CENTRAL RESEARCH LIBRARY

ORNL-5200

Cy 1

# Mechanical Properties Test Data for Structural Materials Quarterly Progress Report for Period Ending July 31, 1976

[redacted]

OAK RIDGE NATIONAL LABORATORY
CENTRAL RESEARCH LIBRARY
DOCUMENT COLLECTION
LIBRARY LOAN COPY
DO NOT TRANSFER TO ANOTHER PERSON
If you wish someone else to see this document, send in name with document and the library will arrange a loan.
UCN-7969
(3 3-67)

OAK RIDGE NATIONAL LABORATORY
OPERATED BY UNION CARBIDE CORPORATION FOR THE ENERGY RESEARCH AND DEVELOPMENT ADMINISTRATION

Printed in the United States of America. Available from
the Energy Research and Development Administration,
Technical Information Center
P.O. Box 62, Oak Ridge, Tennessee 37830
Price: Printed Copy $13.00 ; Microfiche $2.25

This report was prepared as an account of work sponsored by the United States Government. Neither the United States nor the Energy Research and Development Administration/United States Nuclear Regulatory Commission, nor any of their employees, nor any of their contractors, subcontractors, or their employees, makes any warranty, express or implied, or assumes any legal liability or responsibility for the accuracy, completeness or usefulness of any information, apparatus, product or process disclosed, or represents that its use would not infringe privately owned rights.

ORNL-5200
Distribution
Category UC-79b, -h, -k

Contract No. W-7405-eng-26

METALS AND CERAMICS DIVISION

# MECHANICAL PROPERTIES TEST DATA FOR STRUCTURAL MATERIALS QUARTERLY PROGRESS REPORT FOR PERIOD ENDING JULY 31, 1976

Aerojet Nuclear Company

Argonne National Laboratory

Oak Ridge National Laboratory

Naval Research Laboratory

Hanford Engineering Development Laboratory

Westinghouse Advanced Reactors Division

University of Cincinnati

University of California at Los Angeles

General Electric Company

Compiled by M. R. Hill

SEPTEMBER 1976

OAK RIDGE NATIONAL LABORATORY
Oak Ridge, Tennessee 37830
operated by
UNION CARBIDE CORPORATION
for the
ENERGY RESEARCH AND DEVELOPMENT ADMINISTRATION

## FOREWORD

This is the twelfth in a series of progress reports, the purpose of which is to record and distribute quarterly the collected results of all structural materials mechanical properties test programs sponsored by the Reactor Development and Demonstration and the Nuclear Research and Applications Divisions of the Energy Research and Development Administration.

To be useful as resource documents, the reports in this series must be published and distributed in a timely manner to those in the reactor design and materials technology community who have a need of mechanical property test data for nuclear reactor and power plant applications. A test and material index is included to increase the effectiveness of the report.

Reports previously issued in this series are as follows: ORNL-4936, period ending October 31, 1973; ORNL-4948, period ending January 31, 1974; ORNL-4963, period ending April 30, 1974; ORNL-4998, period ending July 31, 1974; ORNL-5103, period ending October 31, 1974; ORNL-5104, period ending January 31, 1975; ORNL-5105, period ending April 30, 1975; ORNL-5106, period ending July 31, 1975; ORNL-5107, period ending October 31, 1975; ORNL-5112, period ending January 31, 1976; and ORNL-5150 for period ending April 30, 1976. The next quarterly report will be for the period ending October 31, 1976, and contributions are due at ORNL by November 15, 1976.

W. R. Martin
Metals and Ceramics Division
Oak Ridge National Laboratory

CONTENTS

SUMMARY . . . . . xi

1. AEROJET NUCLEAR COMPANY . . . . . 1

1.1 INTRODUCTION . . . . . 1

1.2 MECHANICAL PROPERTY PROGRAM OF ALLOY 718 . . . . . 2

1.2.1 Creep-Rupture Tests . . . . . 2

1.2.2 Low Cycle Fatigue Tests . . . . . 2

1.2.3 Creep-Fatigue Interaction Tests . . . . . 2

1.2.4 Mean Stress Effects on Fatigue . . . . . 7

1.2.5 Procurement of Alloy 718 Reference Heat . . . . . 15

1.2.6 Design of Notched Fatigue Specimen . . . . . 18

1.3 REFERENCES . . . . . 20

2. ARGONNE NATIONAL LABORATORY . . . . . 21

2.1 INTRODUCTION . . . . . 21

2.2 FRACTURE AND FATIGUE STUDIES ON STAINLESS STEELS . . . . . 21

2.2.1 Statistical Analysis of Interlaboratory, Heat-to-Heat, and Heat-Treatment Variability of Elevated-Temperature Low-Cycle Fatigue Data on Type 304 Stainless Steel . . . . . 21

2.2.1.1 Interlaboratory Variability . . . . . 23

2.2.1.2 Heat-to-Heat Variability . . . . . 24

2.2.1.3 Heat-Treatment Variability . . . . . 28

2.2.2 A Unified Approach to Creep-Fatigue Damage . . . . 31

2.2.2.1 Basic Equations . . . . . 31

2.2.2.2 Simplifications . . . . . 33

2.2.2.3 Application to Other Materials . . . . . 38

2.2.2.4 Conclusions . . . . . 43

2.2.3 Application of Frequency-Modified Life Approach to the Low-Cycle Fatigue Behavior of Type 304 Stainless Steel . . . . . 43

2.2.3.1 Life-Predictive Parameters . . . . . 44

2.2.3.2 Prediction of Low-Cycle Fatigue Data . . . 47

2.2.3.3 Discussion of Results . . . . . 48

2.2.4 Description of Cyclic Hardening Behavior of Type 304 Stainless Steel . . . . . 60

2.3 REFERENCES . . . . . 72

3. OAK RIDGE NATIONAL LABORATORY . . . . . 75

3.1 INTRODUCTION . . . . . 75

3.2 MECHANICAL PROPERTIES AND BEHAVIOR FOR STRUCTURAL MATERIALS . . . . . 75

3.2.1 Mechanical Property Characterization of Type 304 Stainless Steel Reference Heat . . . . . 75

3.2.1.1 Creep and Rupture Properties of the 51-mm (2-in.) Plate of Reference Heat . . . . . 75

3.2.1.2 Influence of Strain Rate and Test Temperature on Ductility of Type 304 Stainless Steel . . . . . 78

3.2.2 Mechanical Property Characterization of Type 316 Stainless Steel Reference Heat . . . . . 87

3.2.2.1 Tensile Data . . . . . 87

3.2.2.2 Creep Properties . . . . . 88

3.2.3 Heat-to-Heat Variation of Mechanical Properties of Austenitic Stainless Steels of Types 304 and 316 — Time to Rupture and Minimum Creep Rate Modeling for Type 304 Stainless Steel . . . . . 89

3.2.4 Materials Behavior in Support of Development and Evaluation of Failure Criteria for Materials — Development of Creep Equation for Type 304 Stainless Steel . . . . . 109

3.2.4.1 Analysis of Rupture and Minimum Creep Rate Data . . . . . 114

3.2.4.2 Evaluation of Creep Equation Parameters . 117

3.2.4.3 Isochronous Stress-Strain Curves . . . . . 121

3.2.4.4 Variable Load and Relaxation Behavior . . 126

3.2.4.5 Limitations . . . . . 126

3.2.5 Computerized Data Management System . . . . . 129

3.2.6 Elastic Properties of Engineering Construction Materials . . . . . 129

3.2.6.1 Elastic Properties Determined by Dynamic Tests . . . . . 130

3.3 MECHANICAL AND METALLURGICAL BEHAVIOR OF WELDMENTS FOR LMFBR . . . . . 142

3.3.1 Effect of Postweld Heat Treatment and Creep Prestraining on the Creep-Rupture Behavior of Type 308 Stainless Steel Submerged-Arc Welds . . . . . 142

3.3.2 Status of Creep Testing on 16-8-2 Submerged Arc Welds . . . . . 149

3.3.3 Demonstration on Importance of Anisotropy in Welded Pipe Calculations . . . . . 149

3.3.3.1 Description of Finite Element Program . . 149

3.3.3.2 Results . . . . . 153

3.4 MECHANICAL PROPERTIES OF STEAM GENERATOR MATERIALS . . . . 154

3.4.1 Creep and Rupture Behavior of 2 1/4 Cr-1 Mo Steel . 154

3.4.2 Heat-to-Heat Variation of 2 1/4 Cr-1 Mo Steel . . . 168

3.4.2.1 Effect of Heat Treatment on Tensile Properties . . . . . 168

3.4.2.2 Mechanical Properties of a 2 1/4 Cr-1 Mo Steel Forging for LMFBR Tubesheets . . . . 169

3.4.3 Effect of Sodium on the Mechanical Properties of 2 1/4 Cr-1 Mo Steel . . . . . 181

3.4.4 Fatigue Behavior of 2 1/4 Cr-1 Mo Steel . . . . . 185

3.4.4.1 Time-Dependent Fatigue . . . . . 185

3.4.4.2 Creep-Fatigue Data Analysis . . . . . 204

3.4.5 Mechanical Properties Correlations for 2 1/4 Cr-1 Mo Steel — Uniaxial Stress Relaxation of 2 1/4 Cr-1 Mo Steel . . . . . 219

3.4.5.1 Creep Data . . . . . 219

3.4.5.2 Relaxation Data . . . . . 220

3.4.5.3 Analytical Procedure . . . . . 220

3.4.5.4 Results . . . . . 223

3.4.5.4 Limitations . . . . . 223

3.4.6 Mechanical Properties of Transition Weld Joint Materials . . . . . 227

3.4.6.1 Creep Properties . . . . . 227

3.4.6.2 Fatigue Behavior of Transition Joint Materials . . . . . 230

3.5 HIGH-TEMPERATURE DESIGN . . . . . 232

3.5.1 Uniaxial Material Behavior Tests . . . . . 232

3.5.1.1 Exploratory Testing of Type 304 Stainless Steel . . . . . 234

3.5.1.2 Exploratory Testing of Type 316 Stainless Steel . . . . . 241

3.5.1.3 Uniaxial Testing of 2 1/4 Cr-1 Mo Steel . 252

3.5.1.4 Material Testing and Inelastic Analysis in Support of TTTF . . . . . 252

3.5.2 Investigations of Creep Failure Under Uniaxial and Multiaxial Conditions . . . . . 257

3.5.2.1 Uniaxial Tests . . . . . 257

3.5.2.2 Multiaxial Tests . . . . . 257

3.6 MECHANICAL PROPERTIES OF HTGR STEAM GENERATOR AND PRIMARY CIRCUIT MATERIALS . . . . . 265

3.6.1 Tensile Testing . . . . . 265

3.6.2 Environmental Creep Testing . . . . . 265

3.6.3 Fatigue-Life Testing . . . . . 267

3.6.4 Subcritical Crack Growth Studies . . . . . 271

3.7 REFERENCES . . . . . 275

4. NAVAL RESEARCH LABORATORY . . . . . 287

4.1 INTRODUCTION . . . . . 287

4.2 EFFECT OF HOLD TIME ON ELEVATED TEMPERATURE FATIGUE CRACK PROPAGATION IN TYPE 304 STAINLESS STEEL . . . . . 287

4.2.1 Background . . . . . 287

4.2.2 Materials and Test Procedures . . . . . 288

4.2.3 Results and Discussion . . . . . 288

4.3 CREEP-FATIGUE CRACK PROPAGATION IN ALLOY 718 . . . . . 291

4.3.1 Background . . . . . 291

4.3.2 Experimental Procedure . . . . . 292

4.3.3 Results . . . . . 292

4.3.3.1 Crack Growth Rates . . . . . 292

4.4 REFERENCES . . . . . 299

5. HANFORD ENGINEERING DEVELOPMENT LABORATORY . . . . . 303

5.1 INTRODUCTION . . . . . 303

5.2 LMFBR STRUCTURAL MATERIALS . . . . . 303

5.2.1 Creep-Rupture Behavior of Inconel 600 . . . . . 303

5.2.1.1 Objective . . . . . 303

5.2.1.2 Accomplishments and Status . . . . . 303

5.2.1.3 Expected Accomplishments . . . . . 311

5.2.2 Fatigue-Crack Propagation Behavior of Several Pressure Vessel Steels and Weldments . . . . . 314

5.2.2.1 Objective . . . . . 314

5.2.2.2 Accomplishments and Status . . . . . 314

5.2.2.3 Expected Accomplishments . . . . . 327

5.2.3 The Ductile Fracture Toughness Response of Inconel 718 and Inconel X-750 at 75°F and 800°F . . . . . 327

5.2.3.1 Objective . . . . . 327

5.2.3.2 Accomplishments and Status . . . . . 327

5.2.3.3 Expected Accomplishments . . . . . 333

5.3 MATERIALS INFORMATION DOCUMENTATION . . . . . 336

5.3.1 Objective . . . . . 336

5.3.2 Accomplishments and Status . . . . . 336

5.4 REFERENCES . . . . . 336

6. WESTINGHOUSE ADVANCED REACTORS DIVISION . . . . . 339

6.1 INTRODUCTION . . . . . 339

6.2 BASIC SPECIMEN TESTING . . . . . 340

6.2.1 Type 304 Stainless Steel Testing . . . . . 340

6.2.1.1 E2, Tension Plus Bending . . . . . 340

6.2.1.2 BTW-2, Transverse Weld in Type B Model at 19 ksi (131 MPa) and 1100°F (593°C) . . . 347

6.2.1.3 BAW-2 Axial Weld in Type B Model at 22 ksi (151.7 MPa) and 1100°F (593°C) . . . . . 347

6.2.1.4 C-4 B Model Plate with Central Hole at 18 ksi (124.1 MPa) Net Section Stress and 1100°F (593°C) . . . . . 347

6.2.2 Type 316 Stainless Steel Testing . . . . . 347

6.2.2.1 6D2 Notched Bar at 28 ksi (193 MPa) at 1100°F (593°C) . . . . . 347

6.2.2.2 6D3 Notched Bar at 25 ksi (172.4 MPa) at 1100°F (593°C) . . . . . 347

6.3 TUBULAR SPECIMEN TESTING . . . . . 348

6.3.1 Type 304 Stainless Steel Testing . . . . . 348

6.3.2 Type 316 Stainless Steel Testing . . . . . 348

6.4 SODIUM EFFECTS ON MECHANICAL PROPERTIES OF STRUCTURAL MATERIALS . . . . . 351

6.4.1 Type 316 Stainless Steel . . . . . 351

6.2.4 Inconel 718 . . . . . 356

6.5 REFERENCES . . . . . 361

7. UNIVERSITIES . . . . . 363

7.1 UNIVERSITY OF CINCINNATI . . . . . 363

7.1.1 Introduction . . . . . 363

7.1.2 Experimental Program . . . . . 363

7.1.2.1 Creep-Microstructure Evaluation if AISI 330 Stainless Steel . . . . . 364

7.1.2.2 Activation Energy for Creep Calculated from Hot-Hardness Data . . . . . 370

7.1.2.3 Correlation of Hot-Hardness and Hot Tensile Strength of 2 1/4 Cr-1 Mo Steel . . . . . 372

7.1.2.4 Grain Boundary Sliding in AISI 304 Stain-Stainless Steel . . . . . 374

7.1.3 References . . . . . 379

7.2 UNIVERSITY OF CALIFORNIA, LOS ANGELES . . . . . 381

7.2.1 Mechanical Properties Evaluation of Carburized Type 304 SS . . . . . 381

7.2.2 Creep Studies in Stainless Steels . . . . . 386

7.2.2.1 Introduction . . . . . 386

7.2.2.2 Experimental Procedures . . . . . 387

7.2.2.3 Results and Discussion . . . . . 387

7.2.3 Microstructure and High Temperature Deformation of 2 1/4 Cr-1 Mo Steels . . . . . 401

7.2.3.1 Introduction . . . . . 401

7.2.3.2 Experimental . . . . . 401

7.2.3.3 Results and Discussion . . . . . 402

7.2.4 References . . . . . 414

8. GENERAL ELECTRIC COMPANY . . . . . 417

8.1 INTRODUCTION . . . . . 417

8.2 MECHANICAL PROPERTIES OF STAINLESS STEEL IN CARBURIZING SODIUM . . . . . 418

8.2.1 Fatigue Crack Growth Studies . . . . . 418

8.2.2 Creep Investigation . . . . . 422

8.3 DECARBURIZATION KINETICS AND DESIGN METHODS VERIFICATION TESTING . . . . . 446

8.3.1 Background . . . . . 446

8.3.2 Decarburization Studies . . . . . 447

8.3.3 Mechanical Properties of 2 1/4 Cr-1 Mo Steel in Decarburizing Sodium . . . . . 448

8.4 METALLURGICAL CHARACTERIZATION OF VAR AND ESR 2 1/4 Cr-1 Mo Steel . . . . . 459

8.4.1 Summary of Results . . . . . 459

8.5 FRACTURE TOUGHNESS OF LMFBR STEAM GENERATOR MATERIALS . . 488

8.5.1 Background . . . . . 488

8.5.2 Current Progress . . . . . 489

8.6 REFERENCES . . . . . 512

INDEX . . . . . 517

## SUMMARY

### 1. AEROJECT NUCLEAR COMPANY

Mechanical property tests of Alloy 718 given the 1227K (1750°F) solution anneal plus the duplex age are being conducted. Current tests include creep-rupture at 1033K (1400°F), low cycle fatigue at 700K (800°F), creep-fatigue scoping tests at 922K (1200°F), and mean stress effects on fatigue at room temperature.

Product forms of a reference heat of Alloy 718 being procured are described and design parameters of notched fatigue specimens are discussed.

### 2. ARGONNE NATIONAL LABORATORY

A statistical analysis of the influences of the testing laboratory, heat, and pretest heat treatment on the elevated-temperature, low-cycle fatigue life of Type 304 stainless steel is presented. Data representing four test laboratories, eight heats of material, and fifteen pretest heat treatments are considered. No significant variation in life was found for data obtained by three of the laboratories, but cyclic lives from a fourth laboratory displayed lower mean values and a greater variance. No significant variation in life with heat chemistry was observed for zero-hold-time tests. Variations were observed for tension-hold-time data, and these variations could be correlated with previously reported heat-to-heat variations in monotonic creep life. The stress-relieving and the aging heat treatments were found to result in somewhat longer lives than were observed for solution-annealed material, particularly for tests with no hold time.

A damage equation for creep-fatigue interaction is proposed. Instead of separating total plastic strain into time-dependent and time-independent components or using frequency as the controlling parameter, the problem is cast in terms of the total plastic strain and strain rate as the fundamental variables. The damage equation can be integrated to analyze the time to failure for creep and creep-fatigue loading. The method is illustrated for Types 304 and 316 austenitic stainless steel, Incoloy 800, and 2¼ Cr-1 Mo steel at various temperatures. Certain simplifications can be made so that the method is attractive to designers of structures operating at elevated temperatures and loadings which do not necessarily involve a "closed hysteresis loop" type loading.

The application of the frequency-modified life equation to fatigue-life prediction has been critically examined, using the extensive data generated for Type 304 stainless steel at elevated temperature under a variety of cyclic-loading conditions. The accuracy in life prediction is improved when the effect of strain rate on life-predictive parameters is considered. It is shown how the effect of compressive and symmetric

hold time on fatigue life can be taken into account. Finally, a comparison of the creep-fatigue damage using the frequency-modified approach and the recently developed damage-rate approach is made to show the importance of wave-shape effects on low-cycle fatigue life.

A modified version of a Voce-type equation to describe both the initial cyclic-hardening behavior and the attainment of cyclic-saturation state is presented. The application of the proposed equation is demonstrated by considering the cyclic-hardening data generated at ANL for Type 304 stainless steel at 1100°F (593°C).

## 3. OAK RIDGE NATIONAL LABORATORY

Creep and creep rupture testing of type 304 stainless steel reference heat (9T2796) is continuing. The creep curve and microstructural observations are presented for a specimen that ruptured after 30,763 hr.

Three-dimensional plots of total elongation and reduction of area as functions of log strain rate and test temperature have been presented for high-strain-rate tensile, ordinary tensile, and creep data of type 304 stainless steel. An elevated-temperature tensile ductility minimum was confirmed for types 304 and 316 stainless steel. Conditions affecting this minimum have been presented.

Tensile properties of various products of the reference heat (8092297) of type 316 stainless steel are reported. Room-temperature tensile curves (<0.04 strain) were compared with the ORNL tensile model. A table indicates the status of creep tests on 16-mm (5/8-in.) plate of the reference heat of type 316 stainless steel.

Generalized models of time to rupture and minimum creep rate as functions of stress, temperature, and elevated-temperature ultimate tensile strength are described. Several comparisons with the data have been made to show that ultimate tensile strength models can describe the behavior of an individual heat and also the average, maximum, and minimum behavior of several heats of type 304 stainless steel.

The creep strain behavior of type 304 stainless steel was analyzed with an equation giving creep strain as a function of stress, temperature, and elapsed time. The basic strain-time equation form used was the simple rational polynomial. Results obtained include the creep equation itself, plus mathematical models for rupture life and time to tertiary creep. All models include analytical predictions of heat-to-heat variations as reflected by the ultimate tensile strength of a given heat of material.

Development and expansion of a computerized Mechanical Properties Data Storage and Retrieval System (DSRS) are continuing. Capabilities for handling subcritical crack growth data have been added and input has begun. The results from over 8000 tests are now stored in the system.

The dynamic elastic constants ($E$, $G$, and $\nu$) were established for solution-annealed Hastelloy X from room temperature to 1038°C (1900°F). Cubic polynomials are presented for the individual constants, and estimates of the properties at 28°C (50°F) increments are tabulated. The effects of heat-to-heat variations and metal condition (mill annealed vs reannealed) on the dynamic constants of type 304 stainless steel were established. Also the extent of anisotropy of elastic constants in 25-mm (1-in.) plates of reannealed type 304 stainless steel (heat 9T2796) and isothermally annealed 2 1/4 Cr-1 Mo steel (heat 20017) are reported. The heat-to-heat effects and directionality of elastic constants within plates are rationalized.

The creep behavior of a submerged-arc type 308 stainless steel weld in three conditions has been determined at 649°C for rupture times from about 100 to 1000 hr, for both longitudinal and transverse specimen orientations. Weld metal annealed at 982°C (1800°F) for 4 hr has greater ductility than weld metal annealed 4 hr at 607°C (1125°F) or in the as-deposited condition. Prestraining less than 1% in creep for 500 hr at a lower stress severely reduces the ductility of specimens in subsequent testing to failure at a stress producing rupture in about 100 hr. Data from creep testing of a type 16-8-2 stainless steel submerged-arc weld are updated.

Previously obtained anisotropic elastic constants of a type 308 stainless steel electroslag weld have been used in a finite element program to demonstrate the mechanical response of a pipe with a circumferential weld. The limited results show that the anisotropic properties and the orientation of the anisotropy significantly affect the distribution of strain and stress in the vicinity of the weld.

The tertiary creep behavior of annealed 2 1/4 Cr-1 Mo steel was studied at 545, 510, and 566°C (850, 950, and 1050°F). Many of the creep-rupture tests showed nonclassical creep curves with two steady-state stages. Using the values to the end of the second steady-state stage to determine the time to the onset of tertiary creep led to a consistent relationship with the rupture life.

Results are summarized for a report issued on the studies showing the effect of heat treatment on annealed 2 1/4 Cr-1 Mo steel.

We began tensile studies on a 2 1/4 Cr-1 Mo steel tubesheet forging manufactured by current industrial practices. We tested the material as received and laboratory annealed. Tensile tests and metallography on the as-received material indicate nonuniformity in strength and microstructure through the thickness of the forging.

Exposure of 2 1/4 Cr-1 Mo steel to sodium in an LMFBR steam generator can decarburize it and degrade its strength. We have obtained from MSA Corporation some tensile specimens that had been exposed to sodium in a stainless steel retort for 26,500 hr at 566°C (1050°F). This material, along with similar material that had been thermally aged for the same time,

is being creep-rupture tested. This quarter we conducted tensile tests on the sodium-exposed specimens. The results verified the MSA results, which indicate a large drop in tensile properties after decarburization and aging.

Estimated cyclic stress-strain and relaxation behavior for fatigue involving long hold periods at peak strain for 2 1/4 Cr-1 Mo steel have been used to estimate possible damaging effects of creep-fatigue interaction. In addition, the strain range partitioning technique has been used to estimate possible "worst effects" creep-fatigue curves.

Available creep fatigue data for 2 1/4 Cr-1 Mo steel were analyzed by the methods of strain range partitioning and linear summation of damage. Even if modified to reflect the increased damage due to compression rather than tension hold periods, the linear summation approach does not fit the data well. On the other hand, the strain range partitioning approach yields very good results.

From comparisons with limited experimental data for a single heat of isothermally annealed, air-melted plate material of 2 1/4 Cr-1 Mo steel, it appears that isothermal, uniaxial relaxation behavior can be estimated from creep behavior using the hypothesis of strain hardening. Reasonable predictions were obtained by use of strain hardening in conjunction with the creep equation for this material, although this approach tended to overestimate the amount of relaxation at lower temperatures ($\leqslant$ about 538°C) and higher stresses (> yield strength).

Our studies on the mechanical properties of transition joint materials continued. Creep-rupture curves and stress as a function of minimum creep rate curves are presented for tests at 454, 510, and 566°C (850, 950, and 1050°F). Creep-rupture tests were started at 621 and 677°C (1150 and 1250°F).

Continuous cycling and creep-fatigue tests on Inconel 82 weld metal have recently begun. Results of tests employing sound (defect-free) specimens indicated that the continuous cycling fatigue behavior of Inconel 82 at 538°C (1000°F) is similar to that of 2 1/4 Cr-1 Mo steel and type 316 stainless steel at the higher strain ranges (>0.5%); however, the cyclic life for Inconel 82 was superior to that for either of the other two transition weld joint materials at the lower strain ranges (<0.5%). Tests using specimens with flaws showed an 80 to 90% decrease in fatigue life at 538°C (1000°F). Several tests conducted with 0.1-hr strain hold periods each cycle at peak tensile or compressive strain amplitudes indicated an increasing reduction in fatigue life with decreasing strain range.

Results from a metallurgical evaluation of creep-tested specimens of type 304 stainless steel (heat 9T2796) are discussed. Diagrams showing the influence of stress on the kinetics of the $M_{23}C_6$ precipitation are presented. Tensile, strain cycling, creep, and relaxation test results on the reference heat of type 316 stainless steel (heat 8092297) are

described. The creep behavior of materials used to fabricate the third thermal transient test specimen are described. The ability of several creep laws to describe the material response is also discussed.

Results of uniaxial and multiaxial creep tests at Babcock and Wilcox Company on type 304 stainless steel at 593°C (1100°F) are updated. Tests still under way include a uniaxial test at 33,600 hr and multiaxial tests up to 3500 hr.

Data from three creep tests of 2 1/4 Cr-1 Mo steel in simulated HTGR helium are reported. The attack by impurities in helium increased with time of exposure. Data from three creep tests of Hastelloy X (two in helium, one in air) are also presented. In helium the elongation at rupture of Hastelloy X decreased with increasing stress.

The method of strain range partitioning for predicting fatigue-life relations for complex cycles at temperatures within the creep range are discussed. Data from fully reversed strain tests at constant strain rate in which stress hold periods are introduced during the tensile and/or compressive halves of each cycle are presented.

The fatigue crack growth behavior of 2 1/4 Cr-1 Mo steel is discussed. In tests at 593°C in air, the crack growth rate was inversely related to frequency, as expected. The difference in crack growth rate behavior of wedge-opening-load and compact tension specimens has been resolved as a size effect problem. Slightly lower crack growth rates have been found in steam, helium, and vacuum compared with air.

## 4. NAVAL RESEARCH LABORATORY

The influence of thermal aging on fatigue crack propagation behavior during hold time testing was evaluated for solution annealed type 304 stainless steel at 1100°F (593°C). The results show that thermal aging suppressed the increased crack propagation rate in unaged material with increased hold time. Comparison of the data for two heats of Types 304 showed that the inclusion of 1 minute hold times and/or thermal aging prior to testing reduced the effects of composition such that nearly equivalent crack propagation rates were produced in all except the unaged continuous cycle tests.

Crack growth behavior of Alloy 718 under static, cyclic, and combined loads was studied at 538, 649, and 760°C (1000, 1200, and 1400°F). For the combined loads, periods of static load of 0.1, 1, or 10 minutes were imposed at the tensile peak of the cyclic load and these produced an increase in rate of crack growth (da/dN) at 538 and 649°C but not at 760°C. The enhanced crack growth rate is attributed to interaction between creep and fatigue processes. At 760°C, increased plastic flow retards the crack growth process.

## 5. HANFORD ENGINEERING DEVELOPMENT LABORATORY

Creep-rupture properties of unirradiated Inconel 600 were determined over the temperature range from 811 K (1000°F) to 1033 K (1400°F) for rupture times to 3000 hours. Time to rupture, time to onset of tertiary creep, minimum creep rate, and various strain and ductility quantities were described analytically for later comparison with postirradiation test results.

The effect of temperature upon the fatigue-crack propagation behavior of several low-alloy pressure vessel steels and weldments was studied in an air environment over the range 75°-1000°F) 24°-538°C). In general, at a given value of $\Delta K$, fatigue-crack growth rates increased with increasing test temperature. Also, the crack growth behavior of base metal specimens and weldment specimens was similar.

The room temperature and elevated temperature ductile fracture toughness behavior of two nickel-base alloys, Inconel 718 (INEL heat treatment) and Inconel X-750 (double aging heat treatment), have been evaluated by the multi-specimen R-curve technique. $J_{Ic}$ for Inconel 718, 727 in-lb/in$^2$, was found to be superior to that of Inconel-750, 544 in-lb/in$^2$, at room temperature. At 800°F, however, the value of $J_{Ic}$ for Inconel 718 decreased to 555 in-lb/in$^2$, whereas $J_{Ic}$ for Inconel X-750, 563 in-lb/in$^2$, was consistent with that obtained at room temperature.

## 6. WESTINGHOUSE ADVANCED REACTORS DIVISION

Measurements of photographs of Model E2, a Type 304SS plate specimen in bending and tension, indicate that the overall extensometer indicates about 50% higher deflection because of bending of the comparison rods which extend from the gage section to outside the furnace. This necessitated a reanalysis of the test data which resulted in a new graph. Testing of other Type 304SS specimens was continued. Testing of Type 316SS notched bars was initiated.

Creep-rupture tests of Type 316 stainless steel in sodium at 593°C (1100°F) and 275.9 MPa (40.0 ksi) show that the rupture life and ductility are significantly increased by factors of two and three respectively, when the material is sodium pre-exposed at 593°C for 2000 and 5000 hours. The portion of the difference resulting from the sodium pre-exposure and that attributable to time-at-temperature (aging) is not yet known.

Low-cycle fatigue tests of Type 316 stainless steel in sodium at 593°C below a strain range of 1% indicate that the fatigue life is decreased somewhat as a result of sodium pre-exposure at 593°C for 2000 and 5000 hours. At strain ranges of 1% and 2%, essentially the same fatigue life was obtained for the material in the as-received or sodium pre-exposed condition. In addition, the fatigue curve

describing the in-sodium results at 1% and 2% is essentially the same as that reported for tests performed in air (literature data).

Low-cycle fatigue results for Inconel 718 performed in air at 593°C after aging at 538°C for 2000 hours, are the same as those obtained for as-fabricated material, or show a possible increase in fatigue life. The same can be said for tests in sodium at 538°C after sodium pre-exposure at 538°C for 2000 hours. In other words, thermal aging and tested in air or sodium pre-exposure and tested in sodium, for the conditions investigated, does not decrease the fatigue life of Inconel 718 at 538°C.

## 7. UNIVERSITIES

### UNIVERSITY OF CINCINNATI

Creep-rupture tests were performed on AISI 330 stainless steel at 701°C with an applied stress of 20,000, 30,000 35,000, and 40,000 psi, respectively. The minimum creep rate varied from 0.60 to 83.7% hr, and the rupture life ranged from 33.65 to 0.25 hours with the increasing applied stress. A limited amount of TEM observation has been performed on two of the rupture specimens: cells and subgrains were observed in the specimens tested at 40,000 psi and 20,000 psi, respectively.

An experimental plan has been set up to study the substructural developments of AISI 330 SS during creep tests. The creep tests will be interrupted at various levels of creep strain, and the substructures will be examined by TEM. The aim of this experiment is to study the mechanisms of subgrain/cell formation.

Based on the hot-hardness data of AISI 330 SS, the apparent activation energies for indentation hardness and the activation energy for creep were calculated. As with other metals, the apparent activation energy for indentation hardness of this material (7,940 cal/mole) is an order of magnitude lower than the activation energy for creep (93,400 cal/mole).

Hot-hardness tests were performed on four heats of 2 1/4 Cr-1 Mo steel containing various amounts of carbon, and the results were compared with the tensile strength at six temperatures from room temperature to 565°C. The correlation is excellent for the high carbon and the commercial steels and good or fair for the medium and low carbon steels.

A controlled-atmosphere, direct-loading creep testing machine has been constructed for the grain boundary sliding experiments. A preliminary result obtained from AISI 304 stainless steel tested at 750°C with an applied stress of 9,000 psi is in agreement with the data which has been reported in the literature. More detailed experiments are being planned.

UNIVERSITY OF CALIFORNIA, LOS ANGELES

Crack growth rates under sustained load conditions have been evaluated for Type 304 SS at 750°C in both inert and carburizing atmospheres. It was found that both stress intensity factor and net section stress can be employed in correlating the crack growth rates and that carbonization has a significant retarding effect on crack growth.

It is shown that prestraining leads to creep strength improvement of the Type 304 SS only at the low stresses where slow recovery and abundant carbide precipitation are the major factors contributing to creep resistance. The transient creep parameters $\varepsilon_t$ and r in the creep equation

$$\varepsilon = \varepsilon_o + \varepsilon_{st} + \varepsilon_t \ (1 - e^{-rt})$$

and the initial creep rate generally decrease with increasing prestrain.

Characteristics of strain bursts during creep of 2 1/4 Cr-1 Mo steels were evaluated as a function of carbon content and prior heat treatment conditions. Reduction of transient creep strain, steady state creep rate and creep-rupture life were found to correlate with strain bursts.

## 8. GENERAL ELECTRIC COMPANY

Programs designed to study the effects of high temperature sodium environments on the mechanical properties of stainless steels and 2¼Cr-1Mo are continuing. The results of a program evaluating the effect of heat treatment and melting practice on the mechanical behavior of 2¼Cr-1Mo are also reported.

Fatigue crack propagation rates of Type 316 stainless steel are being determined at 510°C (950°F) in air and in carburizing sodium. Preliminary results for annealed base material are reported for both environments. GTA weld specimens are currently being pre-exposed prior to testing. The first series of tests in sodium with hold times are reported.

Fracture toughness properties of 2¼Cr-1Mo steel are being determined through the use of J-Integral test methods. Room temperature test results for base material in several conditions are reported, along with Charpy, drop-weight, and tensile characterizations. The fracture toughness of 2¼Cr-1Mo is considerably above the ASME Code $K_{IR}$ curve at room temperature, but falls below it at higher temperatures. The toughness of 2¼Cr-1Mo SMAW weld metal is similar to that of the base metal; however, the HAZ toughness is much lower.

Characterization of VAR and ESR heats of 2¼Cr-1Mo Steel is continuing. Results of tensile tests, drop-weight tests, Charpy V-notch tests, creep-rupture tests, chemical analyses and microinclusion counts are reported for two additional heats having a variety of heat treatments. Based on the two ESR and three VAR heats characterized to date, the effect of remelting on the tensile and creep properties is small; however, the effect of primary heat treatment and post weld heat treatment is substantial in some cases. Remelting generally improves the fracture toughness properties of this alloy for the heat treatments considered.

The short term creep behavior ($t_r$ < 1000 hrs.) of decarburized 2¼Cr-1Mo in sodium is found to be only slightly dependent on carbon content for the range of bulk carbon 0.03-0.10%. If decarburized below 0.03% the strength decreases rapidly. The carburized case of Type 316SS as determined metallographically is found to be about 2/3 that determined by fracture mode transition studies. Creep of 316SS in carburizing sodium differs from that in air as the carburized case cracks during creep causing a perturbation in the sample geometry. These perturbations have been found not to influence the point of plastic instability under hot tensile conditions.

# 1. AEROJET NUCLEAR COMPANY

D. D. KEISER

## 1.1 INTRODUCTION

Aerojet Nuclear Company is conducting mechanical properties investigations under a program sponsored by ERDA Division of Reactor Development and Demonstration. Program IA-009, Alloy 718 Mechanical Property Program, has as its primary objective the acquisition of the necessary mechanical property data to permit safe, efficient use of this material in LMFBR service. The specific immediate application involves selected structural components of the Clinch River Breeder Reactor Project (CRBRP) where it is necessary to supply design data and to generate design allowables for ASME Code Case approval for high temperature use. Other reactor service applications which require high levels of mechanical properties at temperatures up to 922K (1200$^{o}$F) are also expected to make use of this material.

To provide an adequate data base for the CRBPR additional data has to be generated to complement existing data in the literature. All current tests are being conducted on material given the conventional 1227K (1750$^{o}$F) heat treatment*. The additional data required will include: (1) tensile properties from room temperature to 1033K (1400$^{o}$F), (2) physical properties from room temperature to 977K (1300$^{o}$F) to include density, thermal expansion, heat capacity, and thermal conductivity, (3) creep-rupture properties between 811K (1000$^{o}$F) and 1033K (1400$^{o}$F), (4) low cycle fatigue (to $10^6$ cycles) from room temperature to 977K (1300$^{o}$F), (5) high cycle fatigue (to $10^9$ cycles) from room temperature to 977K (1300$^{o}$F), (6) relaxation properties at 922K (1200$^{o}$F), and (7) long term aging effects from 866K (1100$^{o}$F) to 1033K (1400$^{o}$F) at times up to 30,000 hours.

* Conventional 1227K (1750$^{o}$F) heat treatment: 1227K (1750$^{o}$F) solution anneal 1 h, air cool, duplex age at 991K (1325$^{o}$F) for 8 h, FC to 894K (1150$^{o}$F) and age an additional 8 h.

## 1.2 MECHANICAL PROPERTY PROGRAM OF ALLOY 718

G. E. Korth and G. R. Smolik

### 1.2.1 Creep-Rupture Tests

Test specimens were prepared from 12.7mm (1/2 inch) plate and tested in air at 922K (1200$^{o}$F), 977K (1300$^{o}$F), and 1033K (1400$^{o}$F). These specimens were cut from the plate such that the material was loaded in a direction parallel to the major rolling direction. The test results are tabulated in Table 1.1 and compared in Figure 1.1 with data from Barker, et al[1]. At 1033K (1400$^{o}$F), which is 139K (250$^{o}$F) higher than the lowest aging temperature, the stress-rupture properties are markedly degraded. Stresses as low as 172.4 MPa (25 ksi) yield rupture lives of less than 500 hours.

### 1.2.2 Low Cycle Fatigue Tests

Hourglass test specimens were fabricated from 12.7mm (1/2 inch) plate and tested in strain control at 700K (800$^{o}$F) at a strain rate of $4 \times 10^{-3} s^{-1}$. The tests were conducted in air with a ramp waveform and stress ratio of $A=\infty$. Current test results are listed in Table 1.2 and plotted in Figure 1.2. A few more tests will be conducted to better define the 700K (800$^{o}$F) curve. This curve will then be used as base line data to investigate high cycle ($10^5$ to $10^9$ cycles) behavior, notched behavior and mean stress effects at this same test temperature.

### 1.2.3 Creep-fatigue Interaction Tests

An investigation has been initiated to determine which type of strain controlled loading is the most damaging to Alloy 718. Previous tests[2] conducted on two different heats of Alloy 718 plate material indicated that at 922K (1200$^{o}$F) compression hold times were more detrimental than tensile hold times and the material was quite sensitive to strain effects. This study was undertaken to expand on those results. Tests are being conducted at 922K (1200$^{o}$F) with tensile hold times, compressive hold times, tensile and compressive hold times, and reduced strain rates. In each case, the time to complete one cycle is constant. The strain

Table 1.1 Creep-Rupture Properties of Alloy 718 Plate Material[a]

| Specimen No. | Stress MPa (ksi) | Test Temperature K (F) | Elong in 50.8mm,% | Reduction In Area,% | Min. Creep Rate, $h^{-1}$ | Onset of Tertiary Creep, h | Time to Rupture, h |
|---|---|---|---|---|---|---|---|
| 617-4 | 655 (95.0) | 922 (1200) | 6.7 | 22.8 | $1.4 \times 10^{-4}$ | 205 | 452.9 |
| 617-6 | 381 (55.2) | 977 (1300) | 8.3 | 31.3 | $5.8 \times 10^{-5}$ | 348 | 785.6 |
| 617-1 | 310 (45.0) | 977 (1300) | 12.2 | 34.3 | $1.0 \times 10^{-5}$ | 637 | 1657.4 |
| 617-8 | 414 (59.9) | 1033 (1400) | 12.1 | 34.7 | $2.0 \times 10^{-2}$ | 1.6 | 4.5 |
| 617-7 | 379 (54.9) | 1033 (1400) | 11.5 | 16.7 | $4.0 \times 10^{-3}$ | 5.2 | 18.3 |
| 617-9 | 310 (44.9) | 1033 (1400) | 19.3 | 25.9 | -- | -- | 60.6 |
| 617-10 | 276 (39.8) | 1033 (1400) | 22.6 | 21.8 | $2.2 \times 10^{-4}$ | 26 | 124.8 |
| 617-5 | 207 (29.7) | 1033 (1400) | 24.2 | 38.4 | $1.2 \times 10^{-4}$ | 50 | 276.7 |
| 617-3 | 172 (24.8) | 1033 (1400) | 46.5 | 68.0 | $2.8 \times 10^{-4}$ | 135 | 497.6 |

[a] Heat 2180-4-9478 12.7mm (1/2 inch) thick; heat treatment: 1227K (1750°F) solutional anneal 1 h, AC, age 991K (1325°F) 8 h, FC to 894K (1150°F) and age an additional 8 h.

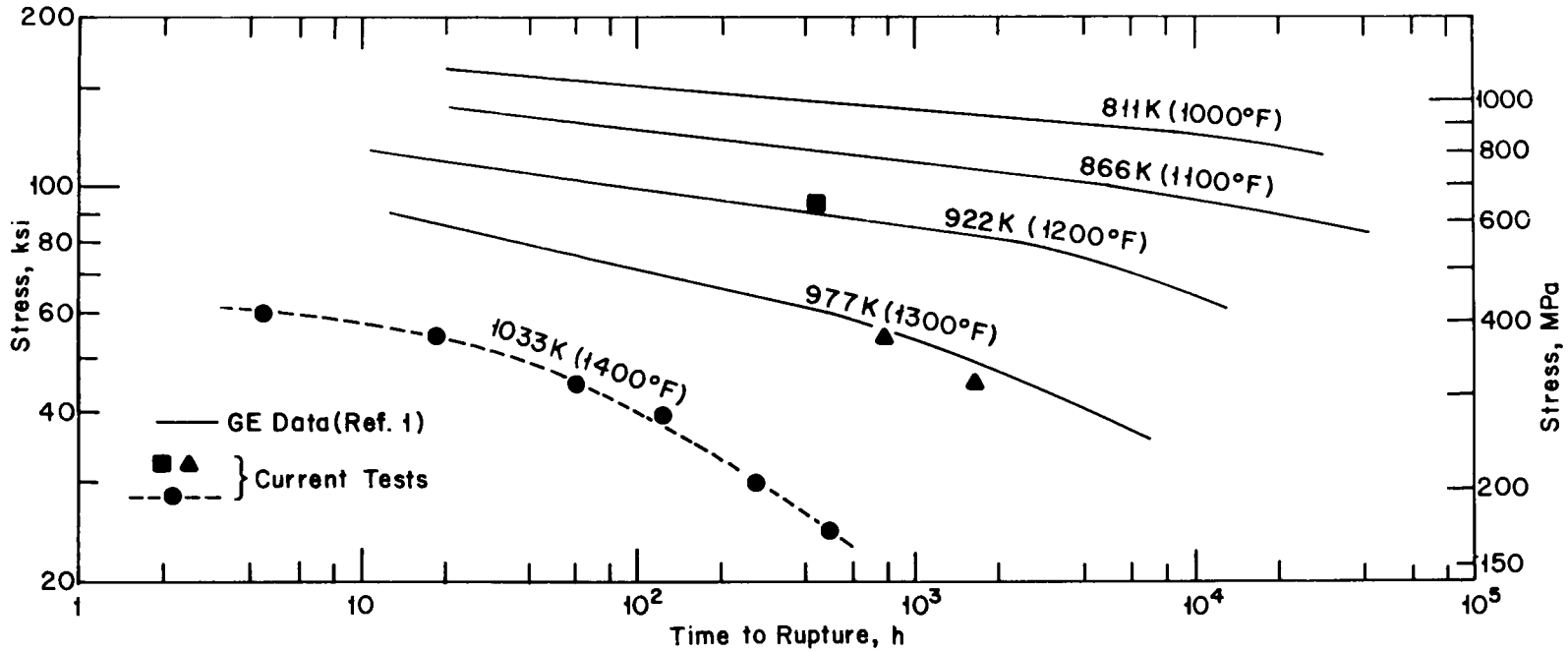


Figure 1.1 Stress-Rupture of Alloy 718 Given the 1227K (1750$^{0}$F) Heat Treatment.

Table 1.2 Strain Fatigue[a] of Alloy 718 Plate[b] Given the 1227K (1750°F) Conventional Heat Treatment

| Specimen Number | $\Delta\varepsilon_t$,% | $\Delta\varepsilon_p$,% | $\Delta\sigma$ @ $N_f/2$ MPa (ksi) | $N_o$ | $N_f$ | Test Temp. K | (F) | Total Test Time Hours |
|---|---|---|---|---|---|---|---|---|
| 614-37 | 4.86 | 3.44 | 2288(331.8) | 172 | 181 | 700 | (800) | 1.13 |
| 614-52 | 4.02 | 2.68 | 2175(315.5) | 307 | 311 | 700 | (800) | 1.56 |
| 614-48 | 3.54 | 2.25 | 2135(309.6) | 385 | 408 | 700 | (800) | 1.93 |
| 614-47 | 3.00 | 1.76 | 2133(309.3) | 467 | 482 | 700 | (800) | 1.96 |
| 614-45 | 2.53 | 1.31 | 2007(291.1) | 755 | 766 | 700 | (800) | 2.59 |
| 614-41 | 2.04 | 0.87 | 1958(289.0) | 1,938 | 2,006 | 700 | (800) | 5.30 |
| 614-36 | 1.97 | 0.84 | 1934(280.6) | 2,200 | 2,252 | 700 | (800) | 5.47 |
| 614-51 | 1.51 | 0.47 | 1868(270.9) | ----- | 4,669 | 700 | (800) | 9.46 |
| 614-34 | 1.26 | 0.22 | 1788(262.8) | 9,095 | 9,433 | 700 | (800) | 16.17 |
| 614-39 | 1.20 | 0.18 | 1812(260.4) | 20,241 | 20,506 | 700 | (800) | 33.06 |
| 614-42 | 1.02 | 0.13 | 1684(244.3) | ----- | 23,259 | 700 | (800) | 31.43 |
| 614-35 | 1.00 | 0.06 | 1655(240.1) | 36,863 | 36,923 | 700 | (800) | 51.76 |
| 614-50 | 0.83 | 0.03 | 1628(236.1) | ----- | 25,606 | 700 | (800) | 28.32 |
| 614-38 | 0.73 | 0.007 | 1204(174.7) | ----- | 1,257,501[c] | 700 | (800) | 1,259.20[c] |

[a] - Fully reversed push-pull tests with a triangle wave form and strain rate of $4 \times 10^{-3}\ s^{-1}$.

[b] - Heat 2180-4-9478, 12.7mm (½ inch) thick.

[c] - Did not fail, test stopped intentionally.

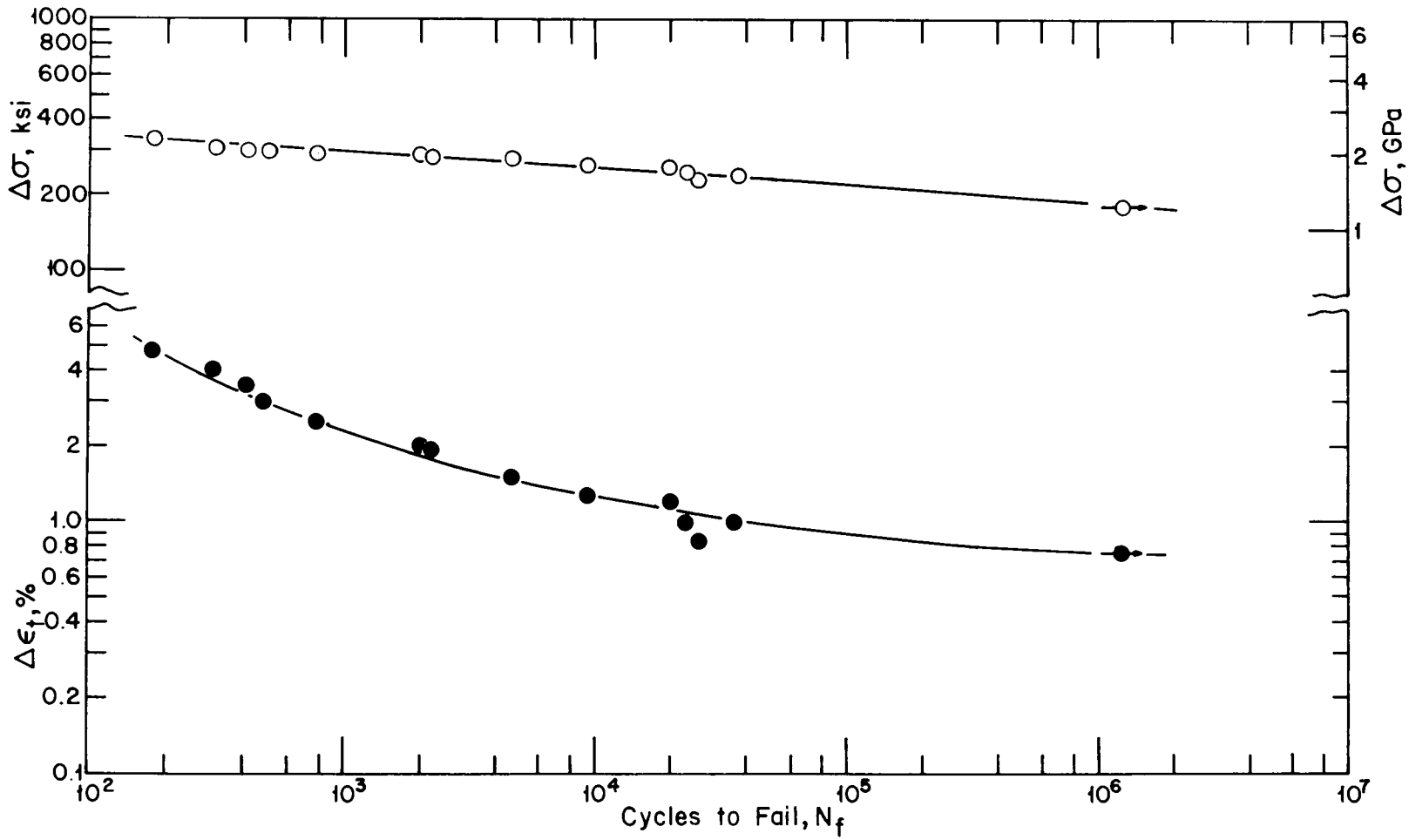


Figure 1.2 Strain Fatigue of Alloy 718 tested at 700K (800°F) at a strain rate of $4 \times 10^{-3} s^{-1}$.

rate between hold periods was $4 \times 10^{-3} s^{-1}$. Tests completed to date include a series at 2% total strain range with a 1.0 hour per cycle, and another series at 1% total strain range with a 0.1 hour per cycle. Results are tabulated in Table 1.3 and compared with a reference test (continuous cycling at a strain rate of $4 \times 10^{-3} s^{-1}$). The tests show that the reduced strain rate is the most damaging except for the combination tension and compression hold time test at 1.0% strain range. The validity of this particular test is somewhat questionable since an identical test, except with twice the time on the hold periods, had a 7% longer cyclic life. Except for the questionable test, the reduction factors compare very well between the 2.0% strain range tests with 1.0 hour per cycle and the 1.0% strain range tests with 0.1 hour per cycle. Further duplicate tests and other strain range-cycle time combinations are currently underway and will prove the validity of the results now available.

### 1.2.4 Mean Stress Effects on Fatigue

The effects of mean stress on the fatigue behavior of Alloy 718 are being investigated. Mean stress can result from any number of sources, including forming operations in fabricating a component, welding stresses, or static preloads due to service conditions. When the loading stresses are totally elastic with a stress ratio A (= stress amplitude/mean stress, $S_a/S_m$) of infinity, ie. $S_m=0$, then the resulting stress-strain is represented by Figure 1.3a. However, when a tensile mean stress is present, then the peak stress shifts upward by an amount equal to the mean stress, $S_m$ (Figure 1.3b). Even though the stress amplitude, $S_a$, remains the same, the cyclic life is shortened due to the increased peak stress. If the temperature is below the creep regime, the mean stress and strain would be expected to remain constant. When service temperatures are high enough for creep to be significant, the mean strain would be expected to increase (ratchet) in a load controlled condition or the stress would relax when the loading is strain controlled. These phenomena have been demonstrated previously.[3] When the cyclic loading is in the inelastic range, the behavior would be expected to be similar to high temperature elastic behavior (ratcheting and relaxation for load and strain controlled

Table 1.3 Creep-Fatigue Interaction Tests at 922K (1200°F)

| Specimen No. | $\Delta\sigma$ at $N_f/2$ MPa (ksi) | Loading Mode[a] | Cycles to Fail, $N_f$ | Cycle Life Reduction Factor |
|---|---|---|---|---|
| | | 2.0% $\Delta\varepsilon_t$ 1.0 hr. Cycle Time | | |
| 614-21 | 1479.6 (214.6) | Reference[b] | 606 | 1.00 |
| 614-31 | 1703.7 (247.1) | 1.0 h T | 290 | 0.48 |
| 614-29 | 1704.4 (247.2) | 1.0 h C | 254 | 0.42 |
| 614-26 | 1586.3 (230.1) | 0.5 h T&C | 268 | 0.44 |
| 614-28 | 1574.1 (228.3) | 1.0 hr/cy, Cont. Cycling[c] | 186 | 0.31 |
| | | 1.0% $\Delta\varepsilon_t$ 0.1 hr. Cycle Time | | |
| 614-32 | 1260.4 (182.8) | Reference[b] | 5822 | 1.00 |
| 614-44 | 1315.5 (190.8) | 0.1 h T | 2833 | 0.49 |
| 614-5 | 1201.1 (174.2) | 0.1 h C | 2520 | 0.43 |
| 614-27 | 1204.5 (174.7) | 0.05 h T&C | 1331 | 0.23 |
| 614-33 | 1283.8 (186.2) | 0.1 hr/cy, Cont. Cycling[c] | 1660 | 0.28 |

[a] - T = tensile hold only, C = compressive hold only, T&C = tensile and compressive hold.

[b] - Reference test, continuous cycling at strain rate of $4 \times 10^{-3} s^{-1}$

[c] - Continuous cycling at slow strain rate such that time to complete a cycle is equal to tests with hold period.

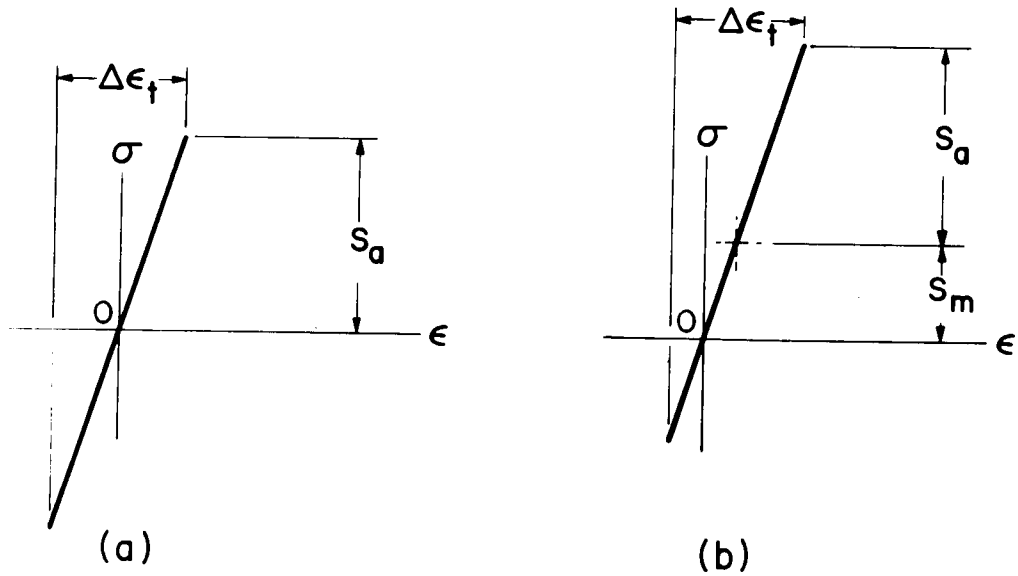


Figure 1.3 Stress-strain representation of fatigue cycling when the stresses are totally elastic without mean stress (a), and with mean stress, $S_m$, (b).

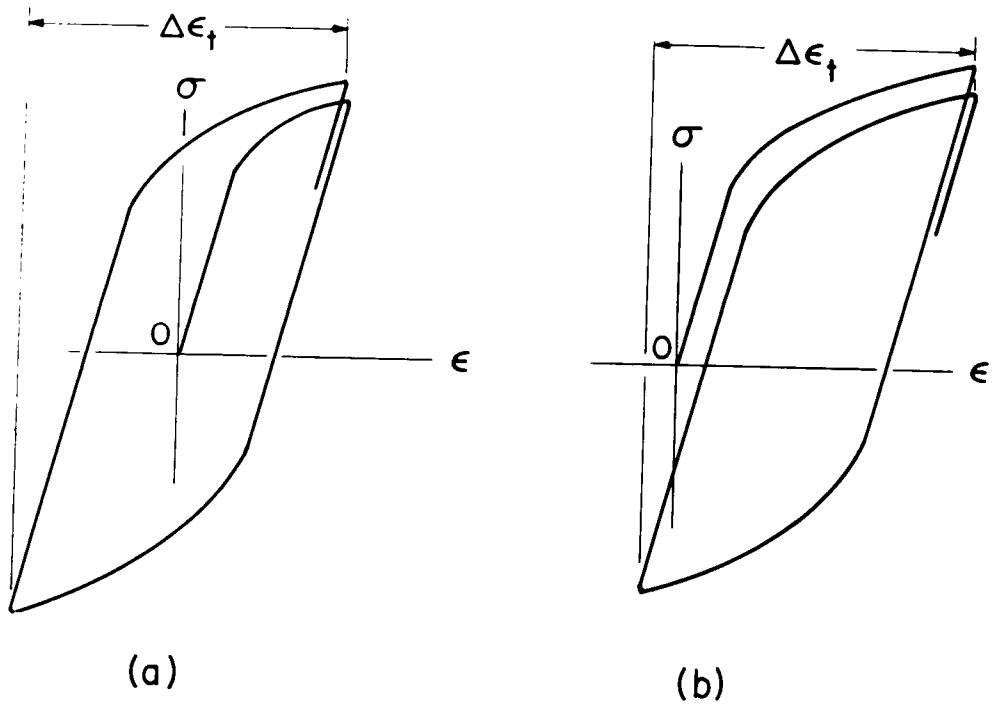


Figure 1.4 Hysteresis loop of strain controlled inelastic fatigue without mean strain (a) and with mean strain (b) with the same strain range, $\Delta\varepsilon_t$.

loadings, respectively). An example of starting strain controlled hysteresis loops is shown in Figure 1.4 for no mean strain (a) and with mean tensile strain (b) when the strain range, $\Delta\varepsilon_t$, is identical. After the first quarter cycle of the mean strain test is completed, the hysteresis loop becomes almost identical to the loop without mean strain, and after a few more cycles, the tensile stress would be expected to relax to a point where the mean strain would no longer be perceptible at all except for the initial offset. The above reasoning is used to justify ignoring mean stress effects in a strain controlled situation when strains are inelastic and accounting for mean stress when the loads are totally elastic. Using this reasoning Langer[4] recommends the Modified Goodman diagram (Figure 1.5) for correcting the stress amplitude to account for mean stress in elastic fatigue cycling where:

$S_e$ = endurance limit
$S_b$ = cyclic yield stress
$S_u$ = ultimate stress
$S_e'$ = adjusted endurance stress

When the mean stress $S_m$, increases such that $S_m + S_e = S_b$, then point C on the diagram is reached and any further increase in $S_m$ will result in yielding and the mean stress will revert back to C which means that a mean stress of C' is the maximum possible. From the geometry of Figure 1.5, the resulting adjustment of the endurance stress becomes:

$$S_e' = S_e \left[\frac{S_u - S_b}{S_u - S_a}\right] \text{ ------- } [1]$$

For a finite number of cycles, $S_e$ becomes stress amplitude, $S_a$, as long as $S_a < S_b$, or,

$$S_a' = S_a \left[\frac{S_u - S_b}{S_u - S_a}\right] \text{ ------- } [2]$$

where $S_a'$ is the stress amplitude corrected for mean stress.

Therefore, according to Langer, the worst case should be when the peak stress ($S_a + S_m$) is just bumping the cyclic yield, $S_b$. Using the Modified Goodman approach and $S_b$ = 1103 MPa (160 ksi), 0.2% yield

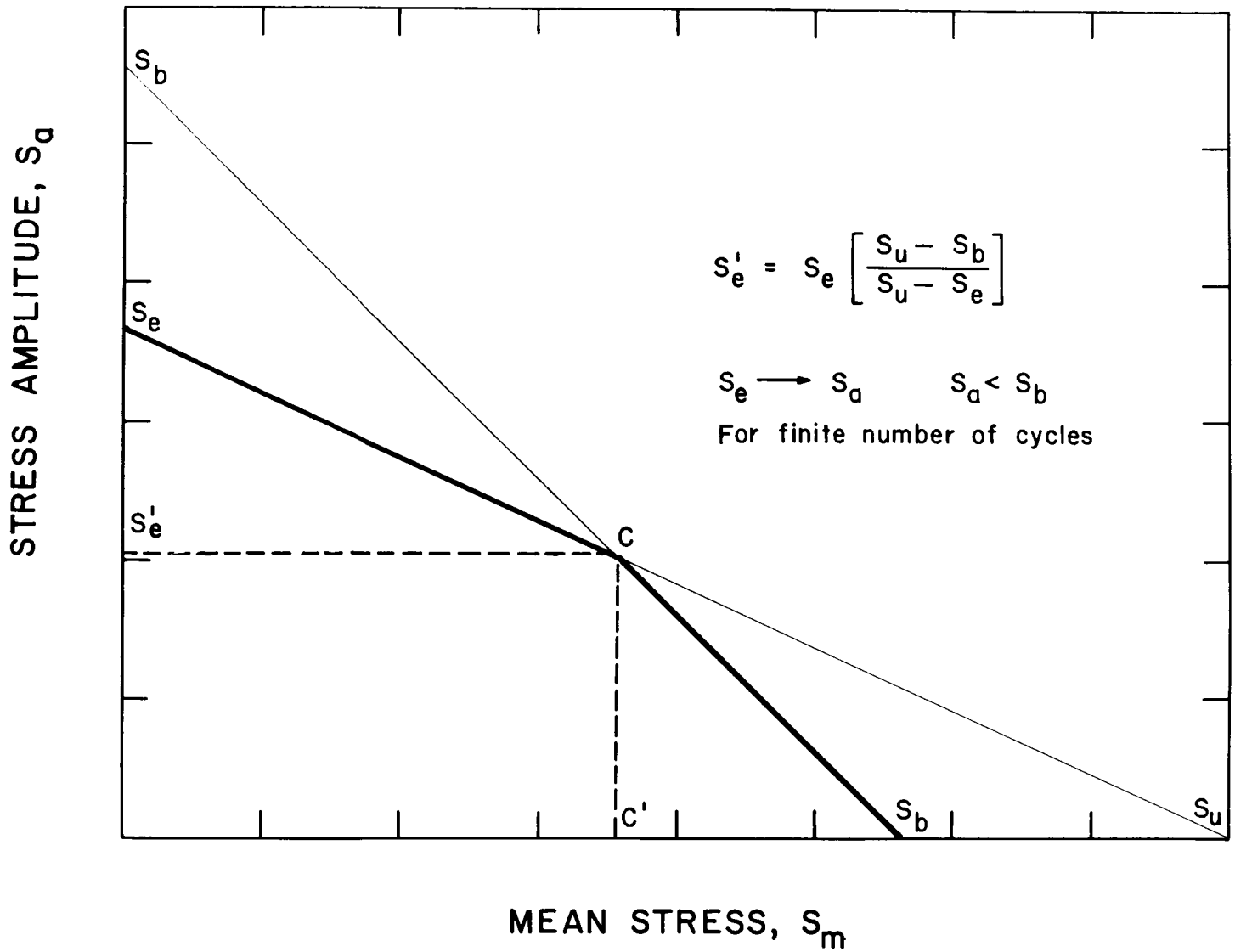


Figure 1.5 Modified Goodman diagram for correcting stress amplitude due to mean stress.

strength, Jaske[5] has shown that with the mean stress correction, Alloy 718 is no better than 304 stainless steel in high cycle fatigue behavior. This observation has a severe impact on Alloy 718 as a candidate material for some critical applications in the CRBRP where resistance to high cycle fatigue is required. Using 0.2% yield strength as $S_b$ is certainly a conservative approach but a much more realistic approach, and not nearly so severe, would be to equate $S_b$ to the proportional limit for the cyclic yield since very little or no cyclic hardening or softening has been observed in Alloy 718 at this laboratory as long as the stresses remain elastic. In an effort to shed some light on the bleak picture of mean stress effects on Alloy 718, a few scoping tests were conducted and compared in a previous report[3] with Jaske's mean curve[5] compiled from a number of tests from a number of sources. This comparison showed the mean stress correction to be too severe. Since then, additional baseline data ($S_m = 0$) has been compiled and generated to compare with the mean stress tests that are more compatible with respect to material heats, specimen geometry, and method of conducting the tests. This data is reported in Table 1.4 and plotted in Figure 1.6 with the stress amplitudes reported as actual test values rather than conversions from strain values, $\varepsilon E$, as Jaske used. The analytical corrections from the Modified Goodman approach are shown for $S_b$ = 965 MPa (140 ksi), the proportional limit, and $S_b$ = 1103 MPa (160 ksi), the 0.2% yield strength. In the $10^5$ cycle region where tests were run with peak stresses ($S_a + S_m$) very nearly equal to the proportional limit, the stress amplitude reduction factor was approximately 0.61 whereas the Modified Goodman diagram indicated the reduction factor to be 0.43 when $S_b$ = 0.2% yield and 0.65 when $S_b$ = the proportional limit, $S_p$. Correlations were fairly close when $S_b$ was chosen as the proportional limit. As the mean stress was reduced such that the peak stress was less than the proportional limit, the mean stress effect was naturally reduced. When $(S_m + S_a)/S_p$ was reduced from 1.00 to 0.88, the $S_a$ reduction factor was increased from 0.61 to 0.68 and to 0.77 when $(S_m + S_a)/S_p$ was 0.84. Figure 1.7 shows the peak stress/proportional limit vs stress amplitude reduction factor relationship.

Table 1.4. Room Temperature Fatigue of Alloy 719 Plate[a]
Showing Mean Stress Effects

| Specimen No.[e] | Stress Amplitude, $S_a$ MPa (ksi) | $N_f$ | Mean Stress, $S_m$ MPa (ksi) | Strain Rate, $\dot{\varepsilon}$, $s^{-1}$ | Stress Ratio, A |
|---|---|---|---|---|---|
| 1-1-3-33 | 1341.7(194.6) | 133 | 0 | $4 \times 10^{-3}$ | ∞ |
| 1-1-3-30 | 1430.0(207.4) | 273 | 0 | $4 \times 10^{-3}$ | ∞ |
| 1-1-4-2 | 1069.4(155.1) | 855 | 0 | $4 \times 10^{-3}$ | ∞ |
| 2-1-3-33 | 1255.9(182.2) | 273 | 0 | $4 \times 10^{-3}$ | ∞ |
| 3-1-2-84 | 1107.3(160.6) | 2,603 | 0 | $4 \times 10^{-3}$ | ∞ |
| 1-1-3-3 | 1102.5(159.9) | 2,277 | 0 | $4 \times 10^{-3}$ | ∞ |
| 1-1-4-18 | 1002.5(145.4) | 4,913 | 0 | $4 \times 10^{-3}$ | ∞ |
| 2-1-3-48 | 994.6(144.2) | 7,197 | 0 | $4 \times 10^{-3}$ | ∞ |
| 1-1-4-3 | 904.6(131.2) | 22,129 | 0 | $4 \times 10^{-3}$ | ∞ |
| 3-1-3-19 | 878.4(127.4) | 13,350 | 0 | $4 \times 10^{-3}$ | ∞ |
| 2-1-3-24 | 933.9(135.4) | 16,652 | 0 | $4 \times 10^{-3}$ | ∞ |
| 2-1-3-43 | 920.1(133.4) | 23,494 | 0 | $4 \times 10^{-3}$ | ∞ |
| 2-1-3-49 | 880.5(127.7) | 33,370 | 0 | $4 \times 10^{-3}$ | ∞ |
| 1-1-4-15 | 747.7(108.4) | 109,972 | 0 | $4 \times 10^{-3}$ | ∞ |
| 3-1-2-81 | 771.9(111.9) | 39,723 | 0 | $4 \times 10^{-3}$ | ∞ |
| 1-4-4-19 | 753.2(109.2) | 99,806 | 0 | $4 \times 10^{-3}$ | ∞ |
| 3-1-3-20 | 742.9(107.8) | 34,472 | 0 | $4 \times 10^{-3}$ | ∞ |
| 2-1-4-17 | 717.0(104.0) | 152,060 | 0 | $4 \times 10^{-3}$[b] | ∞ |
| 1-1-5-16 | 551.6 (80.0) | 6,836,300 | 0 | c | ∞ |
| 2-1-3-10 | 482.6 (70.0) | 118,300 | 386(56.0) | d | 1.25 |
| 2-1-5-20 | 439.2 (63.7) | 119,214 | 519(75.3) | $4 \times 10^{-3}$ | 0.84 |
| 2-1-4-12 | 448.2 (65.0) | 148,620 | 517(75.0) | d | 0.87 |
| 2-1-4-2 | 439.2 (63.7) | 154,839 | 439(63.7) | $9 \times 10^{-3}$ | 1.00 |
| 2-1-3-42 | 448.2 (65.0) | 451,054 | 396(57.5) | $7 \times 10^{-3}$ | 1.13 |
| 2-1-3-3 | 448.2 (65.0) | 3,747,200 | 358(52.0) | d | 1.25 |

[a] - 1227K (1750°F) 1 h, AC, 991K (1325°F) 8 h, FC to 894K (1150°F) age 8 h.

[b] - Switched to load control and 1 Hz at 125,000 cycles.

[c] - Load control with sine wave at 20Hz, did not fail.

[d] - Load control with sine wave at 10Hz.

[e] - Spec. No. 1-x-x-xx = Heat 1 (2180-2-9251)
2-x-x-xx = Heat 2 (2180-2-9247)
3-x-x-xx = Heat 3 (52C9EK)

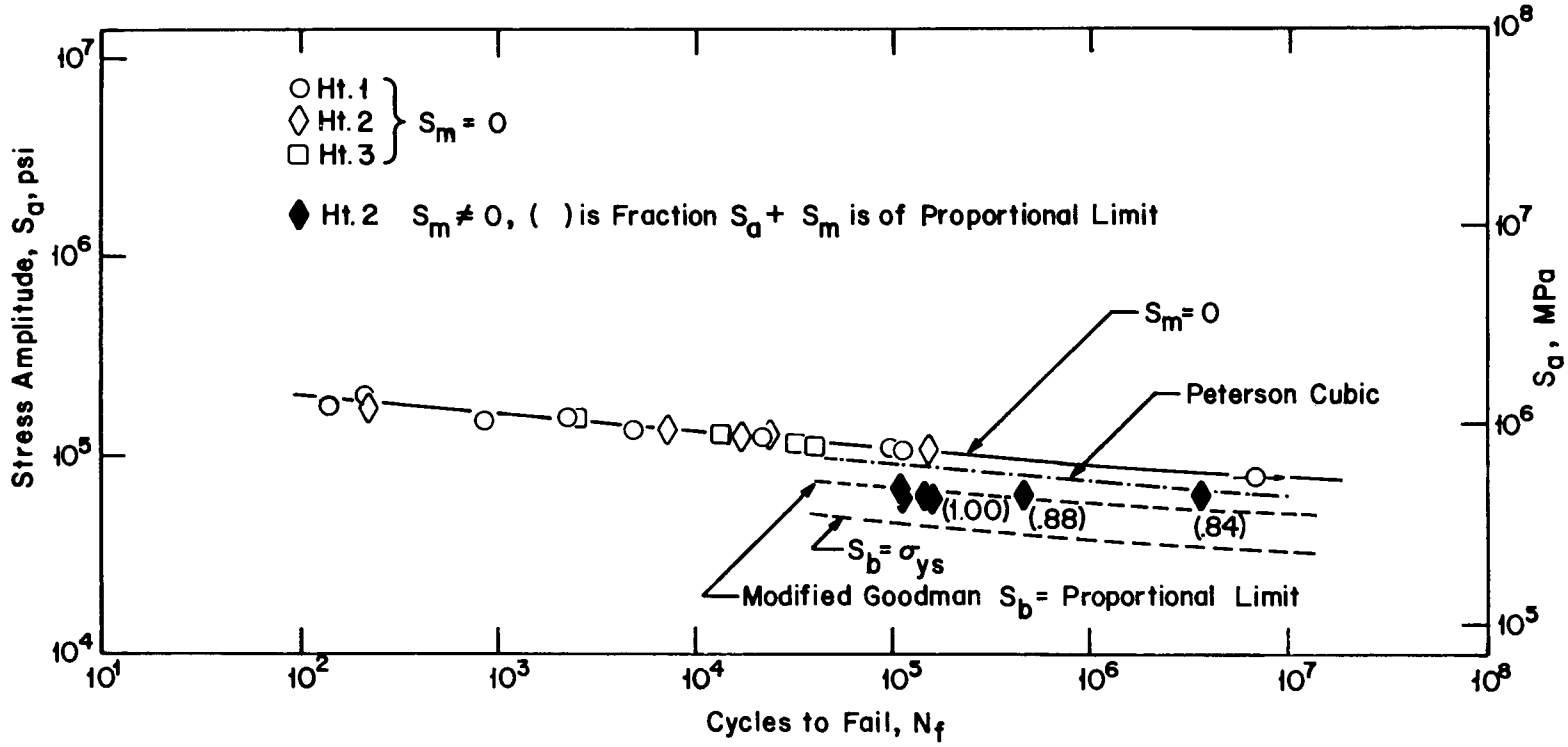


Figure 1.6 Fatigue curve for Alloy 718 at room temperature comparing actual mean stress test data with various analytical methods for determining mean stress effects.

Another model that has been proposed to correct for mean stresses is known as the Peterson cubic equation[6] and is described as:

$$S_a = \frac{7\ S_a'}{8 - \left[1 + \frac{S_m}{S_u}\right]^3} \text{ ----- } [3]$$

where the symbols are the same as identified previously. To put it in the same format as the Modified Goodman correction equation [Eg. 2], it should be written as:

$$S_a' = \frac{S_a \left[8 - \left[1 + \frac{S_m}{S_u}\right]^3\right]}{7} \text{ ------ } [4]$$

If the maximum mean stress is assumed to be equal to the proportional limit, then $S_m + S_a = S_p$ as was reasoned with the Modified Goodman approach, then corrected values, $S_a'$, can be calculated for this maximum $S_m$. When this curve is added to Figure 1.6, it is seen to be non conservative when compared to the test data. With the results obtained to date, it appears that for Alloy 718, the Modified Goodman diagram approach using $S_b$ equal to the proportional limit best represents the data. The Peterson cubic equation appears too nonconservative for Alloy 718, although it has been shown to be successful with AISI 4130 bolting material.[7] Although the correction is not as severe as originally presented, the mean stress effect on fatigue is significant and must be taken into consideration when applying design criteria. On going tests will better define this effect in the future.

### 1.2.5 Procurement of Alloy 718 Reference Heat

Procurement of an Alloy 718 reference heat for research and development programs has been initiated. It is anticipated that various product forms will be fabricated from a master charge of materials melted by vacuum induction melt - electroslag remelt processes. The list of products, which are to total approximately 6700Kg (14800lb) is shown in Table 1.5.

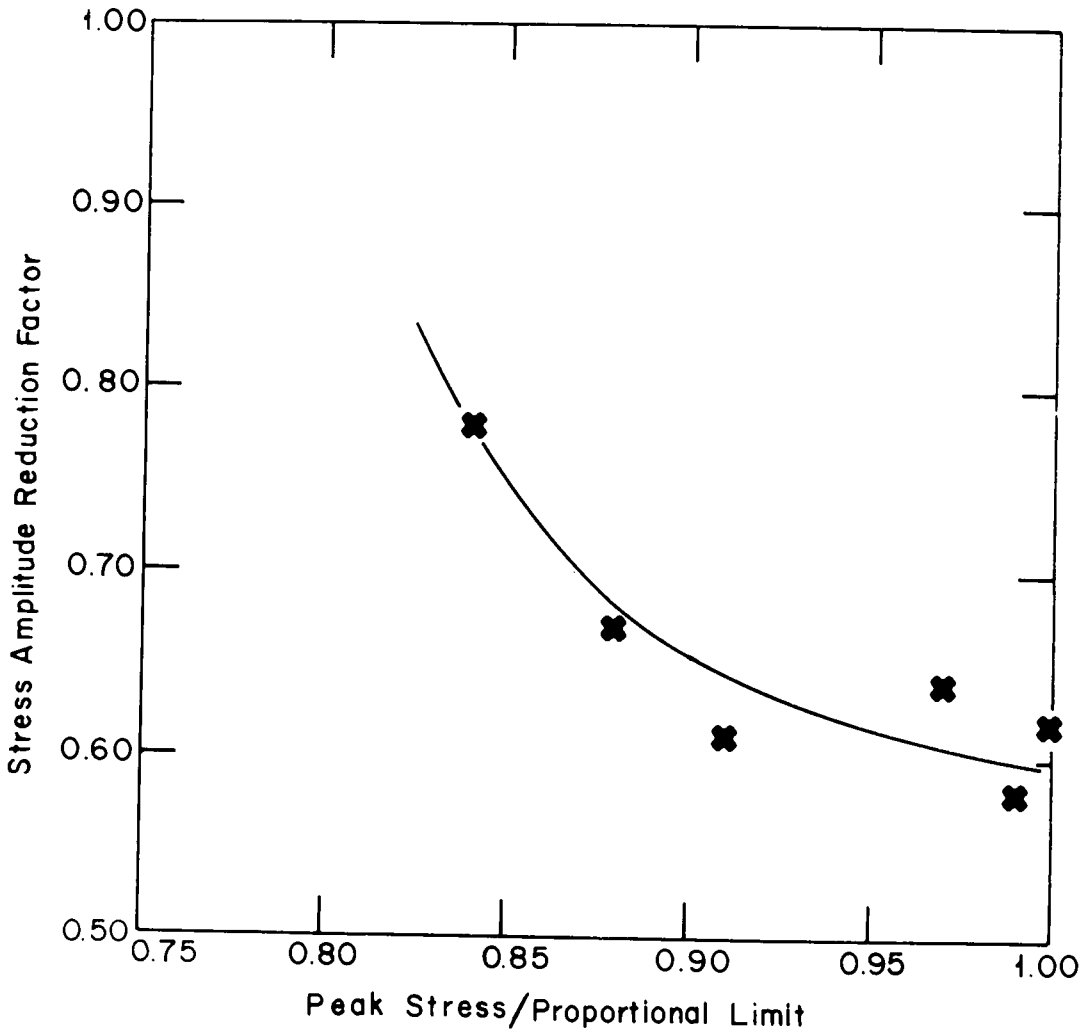


Figure 1.7 Stress amplitude reduction factor for fatigue of Alloy 718 at room temperature versus peak stress $(S_a + S_m)$/proportional limit at varying mean stresses.

Table 1.5 Forms, Sizes, and Quantities of Products from Proposed Alloy 718 Reference Heat

| Product | Description or Size, mm (in.) | Quantity, Kg. (lb.) |
|---|---|---|
| Sheet | 1.57 (0.062) thick | 90 (200) |
| Plate | 12.7 (0.50) thick | 545 (1200) |
| | 19.1 (0.75) thick | 1540 (3400) |
| | 25.4 (1.00) thick | 545 (1200) |
| | 50.8 (2.00) thick | 910 (2000) |
| Bar | 12.7 (0.50) dia. | 135 (300) |
| | 19.1 (0.75) dia. | 225 (500) |
| | 25.4 (1.00) dia. | 225 (500) |
| | 50.8 (2.00) dia. | 225 (500) |
| | 152.4 (6.00) dia. | 275 (600) |
| Forging | Forging Stock | 105 (230) |
| | 3 to 1 upset forgings | 225 (500) |
| | 4 to 1 upset forgings | 120 (265) |
| | 5 to 1 upset forgings | 225 (500) |
| | 203 (8) truncated square forging | 760 (1670) |
| Tubing | 25.4 (1.0) O.D. x 0.34 (.13) wall | 135 (300) |
| | 127(5) O.D. x 9.53 (.38) wall | 320 (700) |
| Weld Wire | 3.18 (.125) dia. x 915 (36) length | 45 (100) |
| | 1.14 (.045) dia. on spools | 45 (100) |

### 1.2.6 Design of Notched Fatigue Specimen

Influences of notch geometry upon high temperature fatigue behavior are to be determined. The necessity for these determinations are implied by the effects of notches upon stress rupture behavior of 304 stainless steel reported by Manjoine[8]. Circumferentially notched specimens having $K_t \simeq 4$ increased rupture life of base and weld metal. Plates having a central hole and $K_t \simeq 2.7$ showed notch softening and reductions in rupture life. Influences of specimen sizes and geometries, stress distribution, elastic stress concentration factors, and plasticity effects upon notched fatigue as reviewed by Frost, et al[9], also illustrate the need for these evaluations.

Tentative plans are to test specimens having notches subjected to high and low constraint. Proposed specimens are illustrated in Fig. 1.8. A circumferential vee-notched specimen, Fig. 1.8(a), exhibiting biaxial stresses at the notch and $K_t = 2.64$ shall be chosen to represent a specimen of high constraint. A plate with a central hole and $K_t = 2.64$, Fig. 1.8(b), shall be tested to establish behavior under conditions of low constraint. Testing such a massive specimen at elevated temperatures and high cycles would be costly. Other specimens, Fig. 18 (c & d), will be tested to determine if results similar to those generated from plate specimens could be obtained. These specimens could then be used as an alternative and allow greater testing flexibility.

The role of stress gradient at a notch is explained by Frost, et al[9]. Grains subjected to lower stresses and located farther from the notch provide support for highly stressed grains near the notch. More support is provided with higher stress gradients and notched fatigue limits are correspondingly improved. Stress gradients at notches were, therefore, used as a basis for selecting specimens of high and low constraint in Fig. 1.8.

Elastic stress concentration factors, $K_t$, shown in Fig. 1.8 are those presented by Peterson[10] and are based upon the net cross-sectional areas at reduced sections. Stress gradients at the notches, S, were determined by the information presented by Seely and Smith.[11] The stress

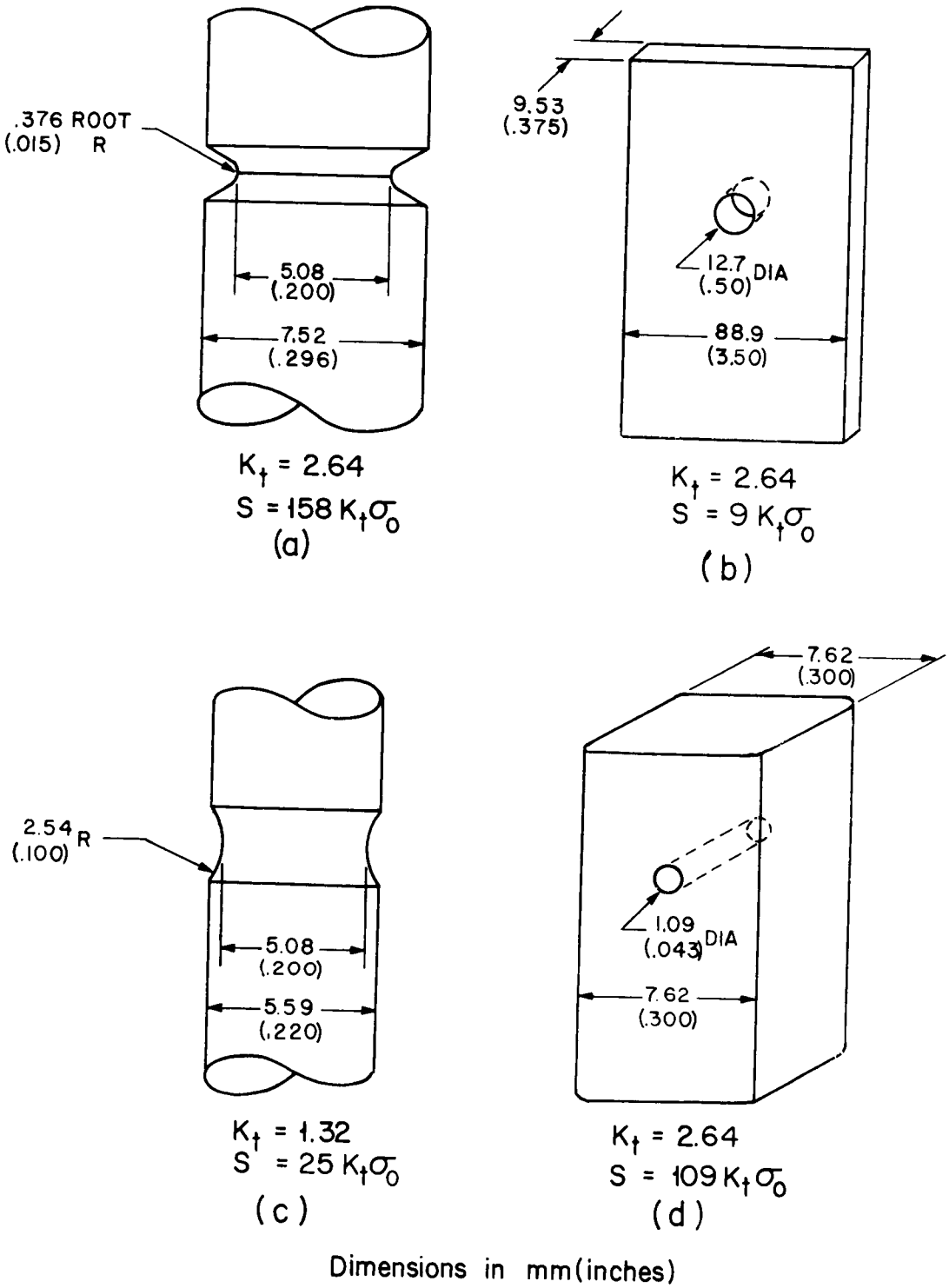


Figure 1.8 Configurations proposed for Reversed Direct Stress Notched Fatigue Tests

gradients have been represented by the general relationship:

$$S = \frac{C}{\rho} K_t \sigma_o$$

where C = constant dependent upon configuration, $\rho$ = radius of notch, and $\sigma_o$ = normal stress based upon the net area at notch.

## 1.3 REFERENCES

1. J. F. Barker, et al, "Long Time Stability of Inconel 718," J. Metals, January 1970, (31-41).

2. D. D. Keiser, et al, "Mechanical Properties Test Data for Structural Materials" for the period ending April 30, 1975, ORNL-4936, (5-9).

3. D. D. Keiser, et al, "National Mechanical Properties Quarterly Progress Report," for period ending January 31, 1976, ORNL-5112, (6,11-14).

4. B. F. Langer, "Design of Pressure Vessels for Low-Cycle Fatigue," J. Basic Engineering, September 1962, (389-402).

5. C. E. Jaske, Battelle Columbus Laboratories, Preliminary draft of "Design Fatigue Curves for Pressure Vessels Alloys," for ASME Fatigue Strength Subgroup Committee work, January 1975.

6. R. E. Peterson, "Brittle Fracture and Fatigue in Machinery," Fatigue and Fracture of Metals, John Wiley & Sons, New York, N.Y. 1952.

7. A. L. Snow & B. F. Langer, "Low Cycle Fatigue of Large-Diameter Bolts," J. Engineering for Industry, February 1967, (53-61).

8. M. J. Manjoine, "Basic Specimen Testing," Mechanical Properties Test Data for Structural Materials Quart, Prog. Rep., Oct. 31, 1975, ORNL-5107, (226-238).

9. N. E. Frost, K. J. Marsh, and L. P. Pook, Metal Fatigue, Oxford University Press (1974), (130-201).

10. R. E. Peterson, Stress Concentration Factors, John Wiley & Sons, Inc. (1974), New York.

11. R. B. Seely and J. O. Smith, Advanced Mechanics of Materials, John Wiley & Sons, Inc. (1955), New York, (514-526).

# 2. ARGONNE NATIONAL LABORATORY

R. W. Weeks

## 2.1 INTRODUCTION

Argonne National Laboratory (ANL) is conducting extensive programs to provide elevated-temperature, low-cycle fatigue data on Types 304 and 316 stainless steel and to study the effects of sodium environment on the elevated-temperature mechanical properties of these materials. Both programs are in support of LMFBR component design. In the present report, additional results of a statistical analysis of available low-cycle fatigue data on Type 304 stainless steel are given, a damage equation for creep fatigue interaction is described, the application of the frequency-modified approach to the low-cycle fatigue behavior of Type 304 stainless steel is discussed, and the results on cyclic-hardening behavior are described.

## 2.2 FRACTURE AND FATIGUE STUDIES ON STAINLESS STEELS -- D. R. Diercks

### 2.2.1 Statistical Analysis of Interlaboratory, Heat-to-heat, and Heat-treatment Variability of Elevated-temperature Low-cycle Fatigue Data on Type 304 Stainless Steel -- D. T. Raske and D. R. Diercks

The results of a regression analysis of the observed fatigue life for the principal test variables of Type 304 stainless steel tested under axial loadings have been reported.[1] In the present report, the results of a statistical analysis of the qualitative variables excluded from that analytical description, or model, will be investigated. These variables include the four laboratories that generated the data, the different heats from which the test specimens were fabricated, and the heat treatments that preceded testing.

The investigation of these variables consisted of a statistical analysis of the residual values of the transformed fatigue lives. The residual is defined as the difference between the observed fatigue life and the fatigue life computed from the analytical model.[1] Residuals offer a convenient means of comparing the fatigue behavior of different samples because deviations from values obtained for all the samples provide a

quantitative measure of performance. The transformation on fatigue life is such that negative residual values are associated with longer lives than predicted by the model.

Sample means and variances constituted the variables studied, using the following assumptions and analyses:

a. Nonrandom samples from the normal population of residuals obtained by the regression analysis ($n = 435$, $\mu = 0$, and $\sigma = 0.01348$)[1] were assumed to be normally distributed with mean $\bar{\chi}$ and variance $s^2$.

b. Heat treatments 5 and 8 as well as 14 and 15 were assumed to be identical (Table 2.1).

Table 2.1. Material Heat Numbers and Heat Treatments Used in Regression Analysis for Type 304 Stainless Steel[1]

A. Material heat numbers

1. 9T2796
2. 55697
3. 346845
4. 346544
5. X22807 (Type 304L Stainless Steel)
6. 600414
7. 8043813
8. 300380

B. Pretest heat treatments

1. Solution annealed
2. Solution annealed and aged 1000 h at 566°C (1050°F)
3. Solution annealed and aged 1000 h at 593°C (1100°F)
4. Solution annealed and aged 1000 h at 650°C (1202°F)
5. Stress relieved 15 min at 760°C (1400°F)
6. Stress relieved and aged 47 h at 566°C (1050°F)
7. Stress relieved and aged 160 h at 650°C (1202°F)
8. Stress relieved 30 min at 760°C (1400°F)
9. Hot rolled
10. As-fabricated or as-welded
11. Aged 3096 h at 410°C (770°F)
12. Aged 8760 h at 400°C (752°F)
13. Aged 8000 h at 593°C (1100°F)
14. Aged 8760 h at 750°C (1382°F)
15. Aged 9240 h at 750°C (1382°F)

c. To compare pairs of samples, the assumption that the mean values of the sample residuals were equal (the null hypothesis $\bar{\chi}_i = \bar{\chi}_j$)

was tested by means of the $t$ test.[2] The $t$-statistic was computed and compared with values from Student's $t$-distribution for $n_i + n_j - 2$ degrees of freedom. The level of significance $\alpha$ of the tests was 5%. Thus, a 5% probability exists that the null hypothesis would be rejected erroneously. All tests were two-sided; therefore, the values from the $t$-distribution were taken at the 0.025 level. This gave a confidence level ($\gamma = 1 - \alpha$) of at least 95% when different sample means were detected. The probability of a Type-II error, i.e., not detecting a difference in the means at $\alpha = 5\%$, was also determined.[3] The probability of this error is strongly dependent on the sample size and is generally not sensitive when small samples ($n \sim 20$) are compared. The sample variances were also compared using the $F$-distribution. When this test indicated that the variances were unequal, an approximate $t$-statistic (recommended for the analysis of fatigue data) was used.[2]

d. When two or more samples were judged equal in mean and variance, they were combined to provide a new, larger sample, which increased the sensitivity of the statistical tests and decreased the Type-II error.

e. To present the results of this analysis in a format that clearly illustrates the basis for the conclusions reached in the text, the samples discussed are plotted as normal probability density functions in terms of their mean $\bar{X}_i$ and standard deviation $s_i$.

2.2.1.1 Interlaboratory Variability

This possible source of variation in results was the first to be investigated because, if present, it would certainly obscure the effects of the other variables. For convenience, the source laboratories were assigned the following numerical designations: 1 - Argonne National Laboratory, 2 - Aerojet Nuclear Company, 3 - General Electric Company-Nuclear Systems Program, and 4 - Battelle-Columbus Laboratories.

Comparisons of the residuals from these four source laboratories were made for specific heats and heat treatments. This was necessary to eliminate any possible effect of these variables on the analysis. The

results are shown in Fig. 2.1 as normal distributions, using the sample mean and variance to determine these curves. The solution-annealed data from laboratory 2 were insufficient to permit a comparison with the other three laboratories (Fig. 2.1a). Therefore, solution-annealed and aged data from laboratory 2 were compared with similar data from laboratory 1 (Fig. 2.1b).

The results of the statistical analysis indicate that data from laboratories 1 and 4 differ in mean and variance at the 5% level of significance. The probability of a Type-II error was 40%. Based on these results, the data from laboratories 1-3 were combined. This new data set was then compared with the data of laboratory 4, with the result that the confidence level for different population means exceeded 90% with a Type-II error probability of ∿60%.

2.2.1.2 Heat-to-heat Variability

Only those heats (1 through 7) from Table 2.1 for which sufficient data existed to provide statistically meaningful results were investigated. The initial comparisons of the residual means and variances by heat were made for data from the same laboratory and with the same heat treatment. The results of these comparisons indicated that the mean values from heats 1 and 3 were significantly different. The next step was to combine the data from laboratories 1-3, as previously discussed. These results revealed that heat 2 also differed from heat 3 and, in addition, heats 1 and 2 differed from heat 7. Finally, the data for heat 2 were increased by combining the data from test specimens that were solution annealed and aged. This consisted of three sets of data from specimens aged for 1000 h, but at temperatures of 566, 593, and 650°C. Statistical comparisons of these data indicated large and significant differences between heats. However, evidence indicated that the cause of these differences might be attributed to the tensile-hold-time data.[4, 5] This was investigated by separating the data into groups consisting of continuous cycling and hold-time waveforms. Because of the many different tensile hold times reported for the data used in this study, no distinction of individual values was attempted. Furthermore, only those data from laboratories 1 and 2 in the solution annealed and aged condition were used.

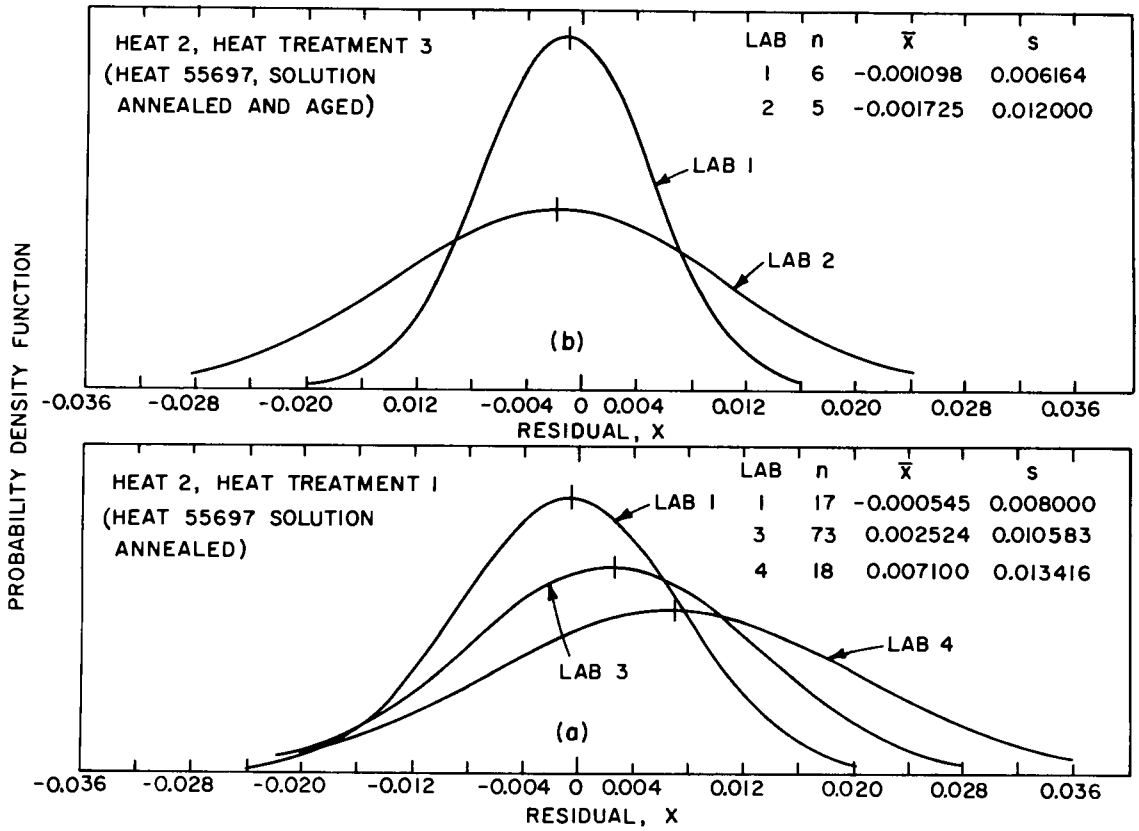


Fig. 2.1. Normal Distribution Probability Density Functions for Residuals from Various Laboratories. Neg. No. MSD-63056.

Five heats (1-3, 6, and 7) provided sufficient data to statistically investigate the variation of the residuals from zero and nonzero-hold-time tests. The results, with the exception of the as-fabricated data from heat 6, are shown in Fig. 2.2. Based on the sample means and variances, these results and the results of uniaxial creep tests[5] indicate the following:

a. Heat 1. The hold-time data have a much lower fatigue life than predicted by the model. In addition, material from this heat also had poor uniaxial creep properties compared with other heats in this study. The continuous cycling and hold-time data differed in the residual mean value at a significance level of 2%, with a Type-II error probability of ∿10%. Therefore, with a confidence level of 98%, it can be concluded that this material will respond differently to zero and nonzero-hold-time tests.

b. Heat 2. This material had fatigue lives slightly higher than predicted by the model for both continuous cycling and hold-time waveforms. It was not possible to distinguish any statistically significant difference in the mean values of samples from this heat subjected to the two waveforms. This means that the difference between the observed and predicted lives is similar for fatigue and creep-fatigue tests.

c. Heat 3. The material from this heat exhibited a considerably different response to the two loading waveforms. Under hold-time waveforms, the observed creep-fatigue lives were much longer than predicted, whereas the continuous cycling lives were similar to those of the other heats investigated in this study. Resistance to uniaxial creep was also reported to be high for this material. The confidence level at which the means differed for these loadings was 99.9% with a Type-II error probability of 1%.

d. Heat 6. Data for this heat were excluded from Fig. 2.2 because the material was tested in the as-fabricated condition and therefore was not directly comparable to the other data. However, the mean values for samples from the two loading waveforms were virtually identical.

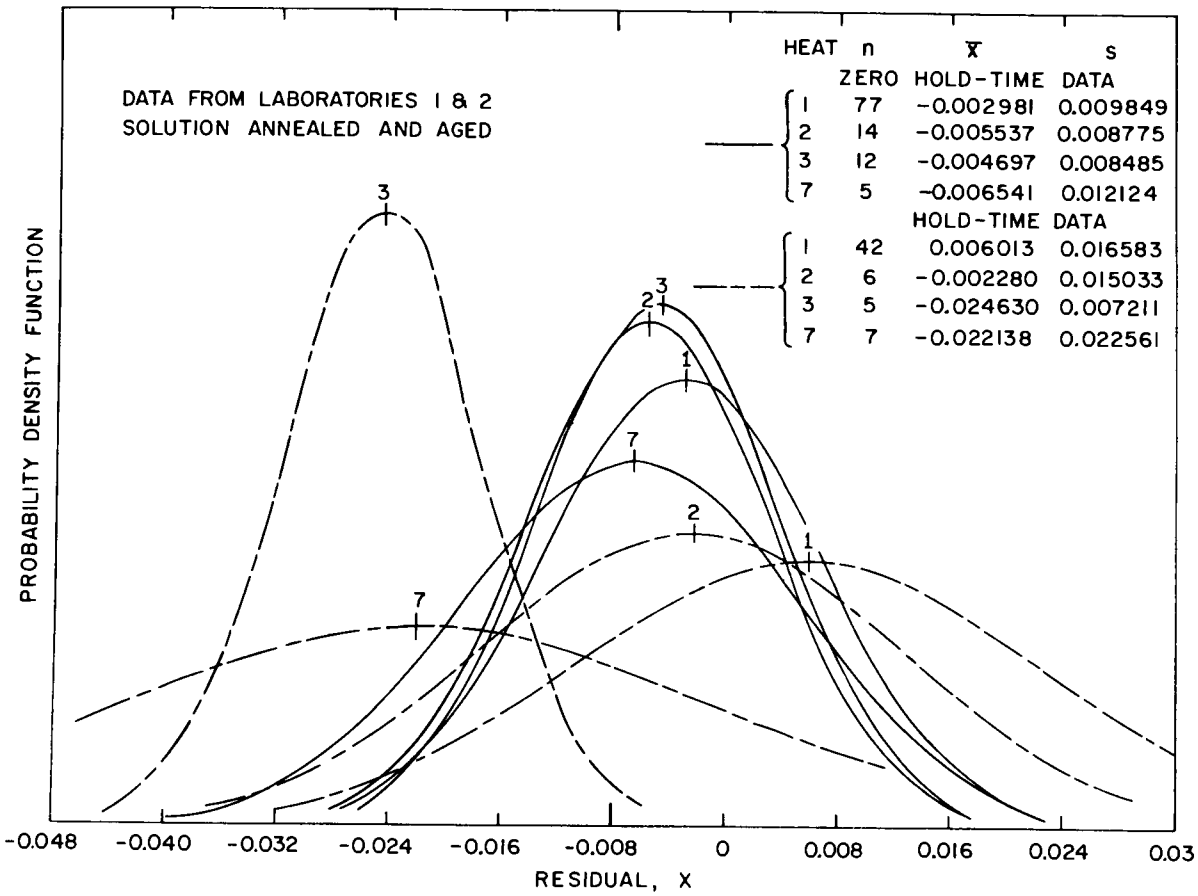


Fig. 2.2. Normal Distribution Probability Density Functions for Zero and Nonzero Tensile Hold-time Data. Neg. No. MSD-63055.

e. Heat 7. This material was similar to heat 3 in that it displayed large differences in response to the different loading waveforms. The hold-time test data had longer fatigue lives than the model predicted, and these results were consistent with the high uniaxial creep resistance observed. The $t$-test did not indicate a statistically significant difference in residual mean values for the samples cycled continuously and with hold times. This was due to the large variance and consequent overlap associated with these data.

The following conclusions regarding heat-to-heat variability are apparent from these results. Waveforms containing tensile hold times produced large variations in fatigue lives with respect to the lives predicted by the model for these heats. These variations were such that those heats with good uniaxial creep resistance also had longer fatigue lives, and those with poor creep resistance were accompanied by shorter fatigue lives than predicted. The confidence levels at which data from the creep-resistant heats (3 and 7) differed from the data for the heats more susceptible to creep damage (1 and 2) exceeded 98%, with Type-II error probabilities averaging 15%. No statistically significant differences were found in the data from heats 1-2, 5, and 7 tested under continuous cycling conditions. In addition, data for three zero-hold-time tests from heat 4 with the same heat treatment had residuals with values within the range of mean values of these heats. Therefore, it is apparent that no significant heat-to-heat variations exist for continuous cycling waveforms, and data from these heats could be considered as identical in subsequent statistical analysis.

2.2.1.3 Heat-treatment Variability

From the results of the previous two sections, continuous cycling data from laboratories 1-3 and heats 1-5 and 7 were combined to investigate the effect of heat treatment on fatigue life. As stated previously, the residual values were grouped with respect to the variable of interest (in this case, heat treatment), and the resultant values were statistically compared. Because of small sample sizes and consequent statistical inaccuracy, a number of heat treatments were not compared. Those samples

that were of sufficient size to be accurately compared are shown as normal probability density functions in Fig. 2.3.

The data from both the stress-relieved and solution-annealed plus aged heat treatments indicated longer mean fatigue lives than predicted by the model. These data had sample means and variances that were nearly identical. For material that was only solution annealed, the mean fatigue life was slightly less than predicted but considerably below the two previous treatments.

The results of the statistical analysis indicate that the solution-annealed sample data differ from the stress-relieved and solution-annealed plus aged data with a confidence level exceeding 98%. The Type-II error probabilities were 35 and 10%, respectively. Consequently, either of these two heat treatments could be expected to result in better fatigue performance than solution annealing alone, under these particular loading and environmental conditions, i.e., continuous cycling in air at a temperature between 430 and 816°C. Earlier work at ANL[6] has shown that specimens stress relieved or solution annealed and aged prior to testing have more carbide precipitation at the grain boundaries and coherent twin boundaries than solution-annealed specimens. Indeed, this work attributed longer fatigue lives to this more advanced carbide precipitation. It was also suggested that, in tests of long duration or higher temperatures, the differences in heat treatment would become obscured due to the precipitation induced by the time at temperature during the test. This hypothesis was statistically tested using tensile hold-time data from heat 1 in the solution-annealed and solution-annealed and aged conditions. No statistically significant difference in the effect of these heat treatments on fatigue life was observed. This is in contrast to the clear and significant difference observed for continuous cycling. Thus the results of the present study support and confirm these conclusions.

Specific conclusions regarding comparisons of the as-fabricated data shown in Fig. 2.3 are uncertain because heat 6 could not be directly compared with the combined heats that constitute the base for the other heat-treatment data. Nevertheless, these data have a mean fatigue life that is considerably below the other heat treatments. In view of the previous heat-treatment effects on fatigue life, this result is not unexpected.

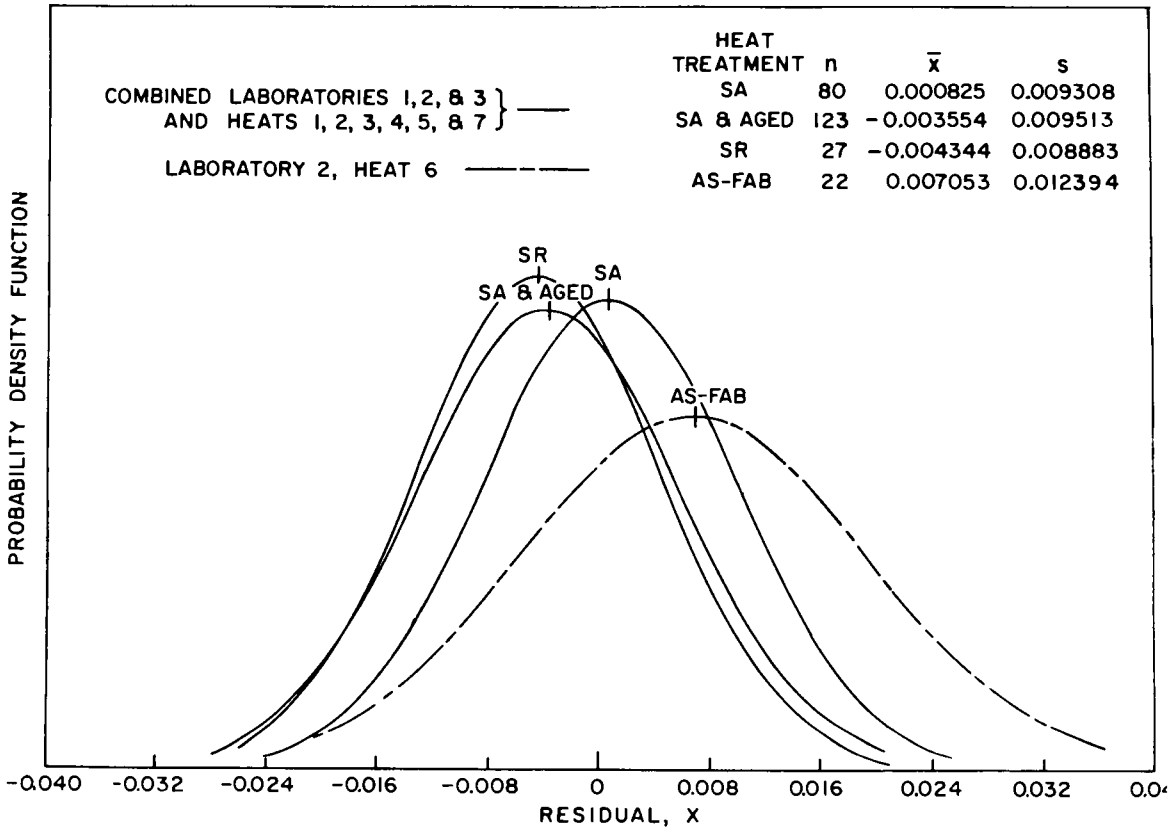


Fig. 2.3. Normal Distribution Probability Density Functions for Continuous-cycling Data with Various Heat Treatments. Neg. No. MSD-63054.

### 2.2.2 A Unified Approach to Creep-fatigue Damage -- S. Majumdar and P. S. Maiya

An incremental damage approach to creep-fatigue interaction has been presented.[1] The method was applied to Type 304 austenitic stainless steel at 593°C (1100°F) for various monotonic and cyclic loading conditions. The present report extends the above approach to analyze creep-fatigue interaction in Types 304 and 316 stainless steel, Incoloy 800, and 2¼ Cr-1 Mo steel at various temperatures. Certain simplifications of the method demonstrated in the present report together with the fact that the strain history for a structural component can often be calculated more reliably than its stress history make this method useful to designers.

#### 2.2.2.1 Basic Equations

It is assumed that the major portion of the life of a low-cycle fatigue specimen is spent in extending preexistent microcracks of length $a_o$ to a final length $a_c$, and the growth of each microcrack is governed by the following equation:

$$\frac{da}{dt} = \begin{cases} aT\ |\varepsilon_p|^m\ |\dot{\varepsilon}_p|^k & \text{(in the presence of tensile stress)} \\ aC\ |\varepsilon_p|^m\ |\dot{\varepsilon}_p|^k & \text{(in the presence of compressive stress),} \end{cases} \quad (1)$$

where T, C, m, and k are material parameters that are functions of temperature, environment, and the metallurgical state of the material. For continuous cycling over a plastic strain range $\Delta\varepsilon_p$ at constant plastic strain rate $\dot{\varepsilon}_p$, Eq. (1) can be integrated to give the cycles to failure[7]

$$N_f = [(m + 1)/4A]\ (\Delta\varepsilon_p/2)^{-(m+1)}\ (\dot{\varepsilon}_p)^{(1-k)}, \quad (2)$$

where

$$A = (T + C)/2\ \ln\ (a_c/a_o). \quad (2a)$$

For tests that involve specimens of identical geometry and microstructure, A can be viewed as a material parameter. Equation (2) is identical to Coffin's frequency-modified equation,[8] provided one replaces the plastic strain rate by the appropriate frequency.

During a monotonic tensile or creep test, a crack-growth law similar to Eq. (1) is assumed, except that the coefficient T is replaced by T'. Integrating the damage equation, one can derive the time to failure as[7]

$$t_f = [(m + 1)\ \ln(a_c/a_o)/T']^{1/(m+1)}\ (\dot{\varepsilon}_p)^{-(m+k)/(m+1)}. \tag{3}$$

For fatigue cycles that include both tensile and compressive hold times, Eq. (1) can be integrated to give the cycles to failure as[7]

$$1/N_f = [4A/(m + 1)]\ (\Delta\varepsilon_p/2)^{(m+1)}(\dot{\varepsilon}_p)^{k-1} + |\varepsilon_{p_{max}}|^m \int_o^{t_H} [2A/(1 + C/T)]\ |\dot{\varepsilon}_p|^k\ dt + |\varepsilon_{p_{min}}|^m \int_o^{t_H} [2A/(1 + T/C)]\ |\dot{\varepsilon}_p|^k\ dt. \tag{4}$$

The first term on the right side of Eq. (4) can be identified as the cyclic damage per cycle, and the second and third terms are the hold-time damages per cycle in tension and compression, respectively. Note that, although the plastic strain is approximately constant during the hold time in a cyclic-relaxation test, the plastic strain rate decreases continuously during the hold-time period, and consequently, the plastic strain-rate term in Eq. (4) cannot be brought outside the integral signs. The plastic strain rate during the hold time at constant total strain is determined by the stress-relaxation rate, i.e.,

$$\dot{\varepsilon}_p = -\frac{\dot{\sigma}}{E}. \tag{5}$$

In the present report, stress relaxation has been assumed to be in the following form:

$$\ln (\sigma_{max}/\sigma) = \frac{B}{1 + p} t^{(1+p)}, \tag{6}$$

where B and p are determined by a least-squares fit of the stress-relaxation data obtained during hold time for each test.

2.2.2.2 Simplifications

The parameters A, k, and m for Type 304 stainless steel at 1100°F (593°C) are shown in Fig. 2.4.[7] These were determined by a least-squares fit of a variety of continuous-cycling fatigue data[9] generated at Argonne National Laboratory (ANL) to Eq. (2). The transitional behavior of the parameters was associated with the transition in the fatigue fracture-surface appearance from a predominantly transgranular to a predominantly intergranular mode. Unfortunately, such elaborate fatigue data at various strain rates are not available for most materials. Thus, to apply this method to analyze creep-fatigue data reported in the literature, certain simplifications are necessary. First, note that the small variation of m from unity in Fig. 2.4 does not influence the damage significantly, and the value of m is consequently set equal to one. Second, the gradual variations of k and A at 1100°F (593°C) in Fig. 2.4 are replaced by step functions, as shown in Fig. 2.5. Figure 2.5 also contains the parameters determined in a similar fashion for Type 304 stainless steel at 1000°F (538°C) and 900°F (482°C). Figure 2.6 shows a plot of the predicted cycles to failure versus the experimentally observed cycles to failure for a representative sample of hold-time fatigue data generated at ANL[9] for Type 304 stainless steel. The predicted values are calculated using Eq. (4) and the values of the parameters from Fig. 2.5. The predicted lives in all cases are within a factor of 1.5 (dotted lines) of the experimentally observed values.

A comparison of the variation of calculated (solid line) and experimentally observed values of time to tensile and creep rupture with plastic strain rate[10-14] for Type 304 stainless steel at 1100°F (593°C),

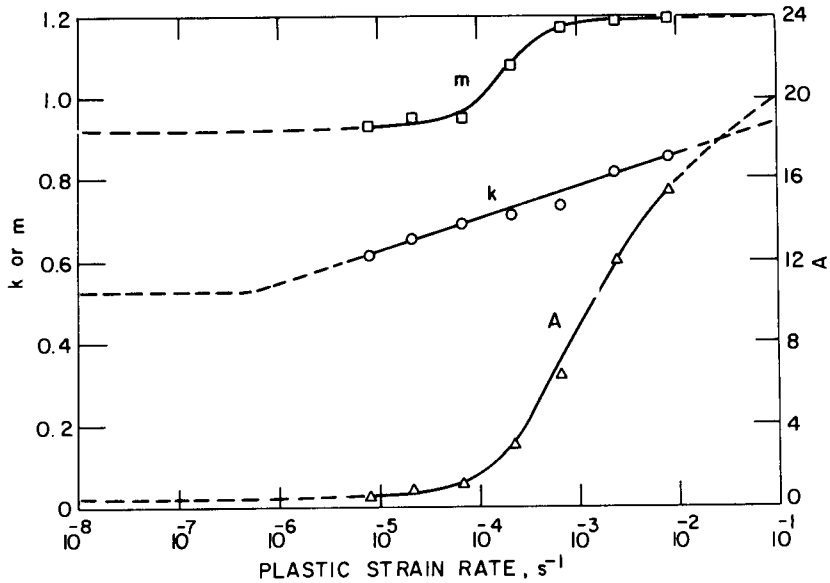


Fig. 2.4. Variation of Material Parameters with Strain Rate for Type 304 Stainless Steel at 1100°F (593°C). Neg. No. MSD-61799.

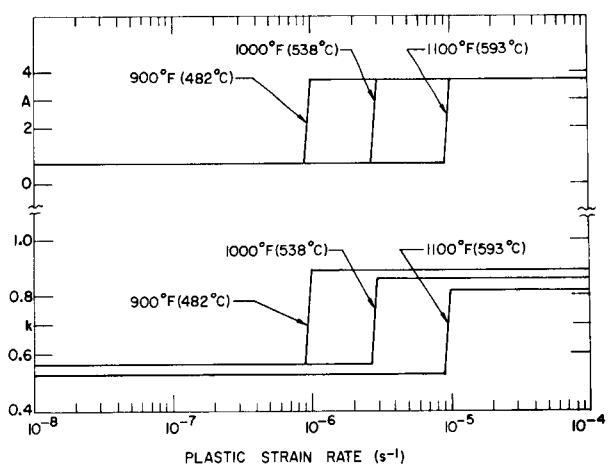


Fig. 2.5. Idealized Variation of Material Parameters with Strain Rate and Temperature for Type 304 Stainless Steel. Neg. No. MSD-62908.

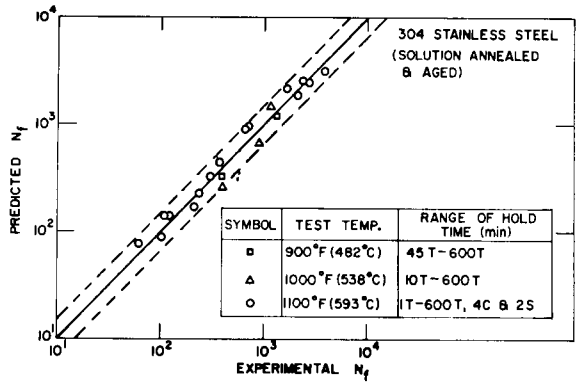


Fig. 2.6. Predicted vs Experimental Hold-time Fatigue Lives for Type 304 Stainless Steel. Neg. No. MSD-62911.

1000°F (538°C), and 900°F (482°C) is shown in Figs. 2.7-2.9. The predicted rupture-time line is calculated using Eq. (3) and the parameters from Fig. 2.5 and is translated along the time axis to match the test data. Since the slope of the time to rupture versus plastic strain rate on a log-log plot is given by the strain-rate exponent in Eq. (3), it is evident that the fatigue parameters k and m are also applicable to monotonic loading cases. In addition, this shows that the lower limit for the value of k can be determined from the slope of the time to creep rupture versus minimum creep rate plot on a log-log basis. This is important because, for most materials, continuous-cycling fatigue data in the low-strain-rate regime ($<10^{-5}s^{-1}$) are not available, whereas extensive creep-rupture data are available at these strain rates.

Furthermore, to determine how sensitive the computed life under creep-fatigue loading is to a change in the parameters A, m, and k due to temperature varation, average values of these parameters were used to compute lives at 1100°F, 1000°F, and 900°F for Type 304 stainless steel, as shown in Fig. 2.10. Note that, although the same values of the parameters are used to calculate lives at these three temperatures, the predicted lives (dotted lines) are within a factor of two of the experimentally observed lives (Fig. 2.6), which is sufficiently accurate for engineering applications.

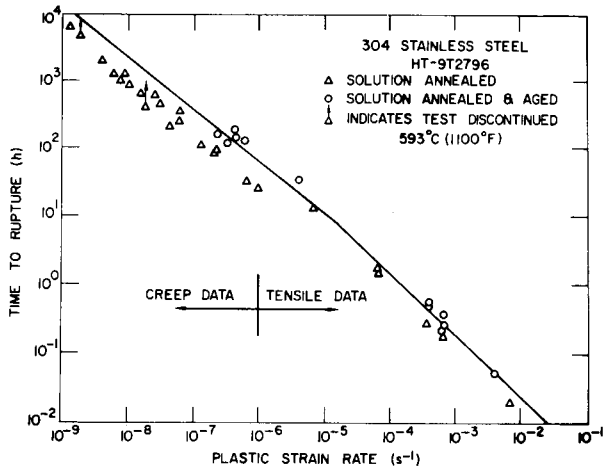


Fig. 2.7. Experimental and Predicted Tensile and Creep-rupture Lives for Type 304 Stainless Steel at 1100°F (593°C). Neg. No. MSD-62905.

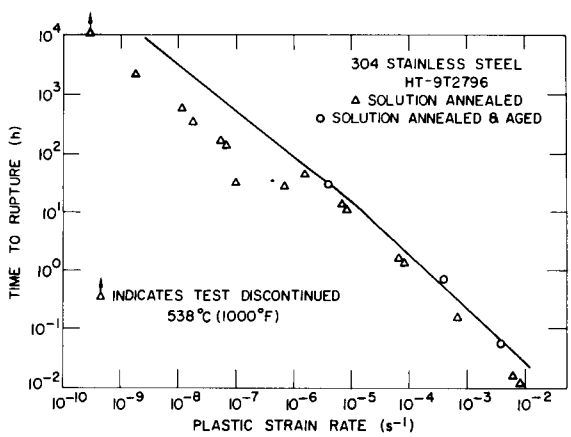


Fig. 2.8. Experimental and Predicted Tensile and Creep-rupture Lives for Type 304 Stainless Steel at 1000°F (538°C). Neg. No. MSD-62914.

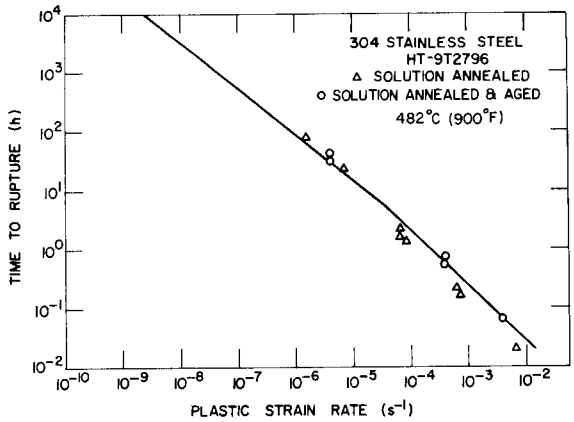


Fig. 2.9. Experimental and Predicted Tensile and Creep-rupture Lives for Type 304 Stainless Steel at 900°F (482°C). Neg. No. MSD-62915.

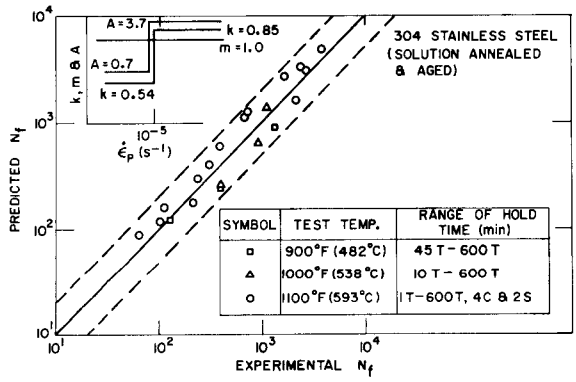


Fig. 2.10. Predicted vs Experimental Hold-time Fatigue Lives for Type 304 Stainless Steel. Neg. No. MSD-62909.

In view of the above observations, the following procedure has been used to determine the parameters A, m, and k for other materials.

a. The upper limit for the values of A, m, and k is determined by a least-squares fit to Eq. (2) of all available continuous-cycling fatigue data at two or more strain rates for different temperatures.

b. The value of m determined in step a is assumed to be constant. The lower limit for the value of k is determined from the slope of time to creep rupture versus minimum creep rate on a log-log plot and Eq. (3).

c. The lower limit for the value of A, together with the T/C ratio, is determined by correlation with a few hold-time fatigue data. In most cases, this value of A coincides with the upper limiting value of A determined in step b. In all cases, the calculated life is found to be relatively insensitive to the T/C ratio.

d. The parameters A, m, and k thus determined are assumed to be independent of temperature.

2.2.2.3 Application to Other Materials

2.2.2.3.1 Incoloy 800 (Solution Annealed). Continuous-cycling fatigue data, used to determine the parameters A, m, and k for Incoloy 800, were obtained from The General Electric Company.[15] Creep-rupture data (Fig. 2.11) used to determine the lower-limit value of k were obtained from Jaske et al.[16] The T/C ratio is found to be equal to four in all cases. Hold-time fatigue data together with the stress relaxation for each test were obtained from Jaske et al.[16] Figure 2.12 shows a comparison between the predicted versus experimentally observed life at 1000°F (538°C), 1200°F (649°C), and 1400°F (760°C). The dashed lines in the figure denote a deviation of a factor of two from the experimentally observed life. It is evident that, for engineering accuracy, the material parameters for Incoloy 800 may be assumed to be independent of temperature in the range from 1000°F (538°C) to 1400°F (760°C).

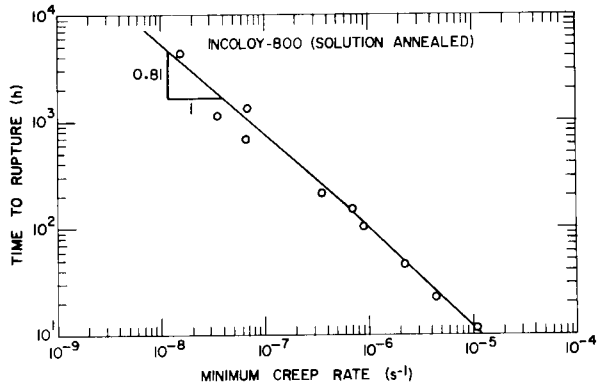


Fig. 2.11. Variation of Time to Creep Rupture with Minimum Creep Rate for Incoloy 800 at 1400°F (760°C). Neg. No. MSD-62916.

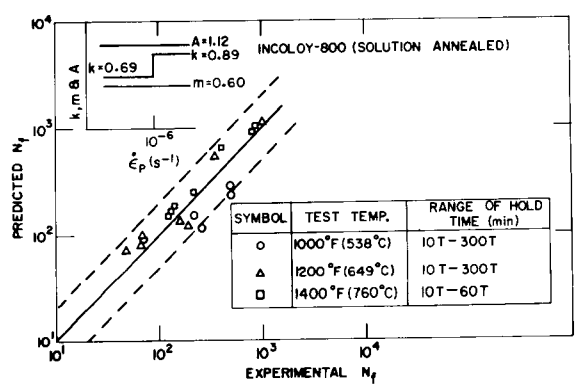


Fig. 2.12. Predicted vs Experimental Hold-time Fatigue Lives for Incoloy 800. Neg. No. MSD-62906.

2.2.2.3.2 2¼ Cr-1 Mo Steel (Isothermally Annealed). Continuous-cycling fatigue data required for determining the parameters A, m, and k for 2¼ Cr-1 Mo steel were obtained from Brinkman et al.[17] Creep-rupture data (Fig. 2.13), used to determine the lower-limit value of k, were obtained from ORNL-5107.[18] The T/C ratio for this material is estimated to be equal to one. However, this ratio is not firmly established because data for sufficiently long compressive hold times are not available. Hold-time fatigue data as well as stress-relaxation behavior for each test were obtained from Ellis et al.[19] and Strizak.[20] Figure 2.14 shows a plot of the predicted versus experimentally observed lives at 900°F (482°C), 1000°F (538°C), and 1100°F (593°C) for a variety of hold-time fatigue tests. The dashed lines in this figure denote a deviation of a factor of two from the experimentally observed life. It is evident that, for engineering accuracy, the parameters for this material may be assumed to be independent of temperature between 900°F (482°C) and 1100°F (593°C).

2.2.2.3.3 Type 316 Stainless Steel (Annealed and Annealed and Aged). Continuous-cycling fatigue data, used to determine the parameters A, m, and k for Type 316 stainless steel, were obtained from Conway et al.[21] and Keller.[22] Unfortunately, creep-rupture data for the same heat of material were not available over a sufficiently wide range of minimum creep rate to reliably determine the slope of the time to rupture versus minimum creep rate curve. Consequently, the lower-limit value of k for material was determined by correlation with some hold-time fatigue data. The value of the T/C ratio of this material is assumed equal to four in all cases. Hold-time fatigue data and stress relaxation for both aged and unaged materials were obtained from Keller.[22] Figures 2.15 and 2.16 show that the predicted life in most cases is within a factor of two (dashed lines) of the experimentally observed life for tests performed at 1050°F (566°C) and 1200°F (649°C). Note that the main effect of aging in this material is to shift the transition in the material parameters from a higher to a lower value of strain rate. This is consistent with the fact that aging causes precipitation of second-phase particles (mainly carbides) at the grain boundaries, and these particles tend to resist grain-boundary

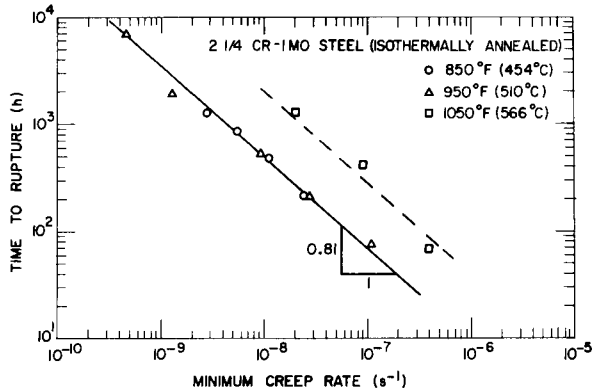


Fig. 13. Variation of Time to Rupture with Minimum Creep Rate for 2¼ Cr-1 Mo Steel. Neg. No. MSD-62913.

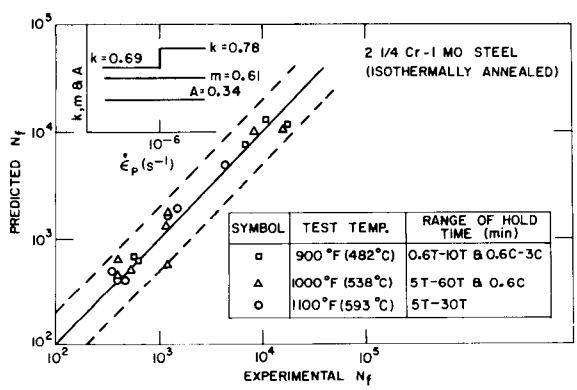


Fig. 2.14. Predicted vs Experimental Hold-time Fatigue Lives for 2¼ Cr-1 Mo Steel. Neg. No. MSD-62907.

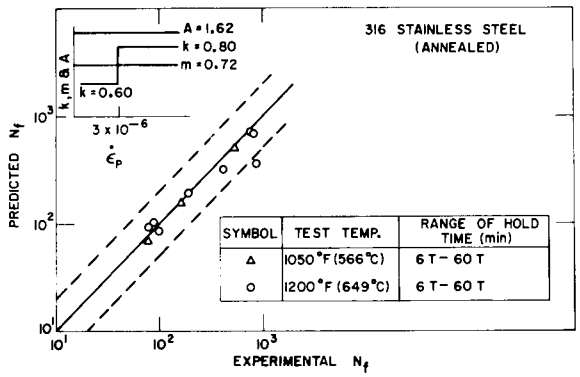


Fig. 2.15. Predicted vs Experimental Hold-time Fatigue Lives for Annealed Type 316 Stainless Steel. Neg. No. MSD-62910.

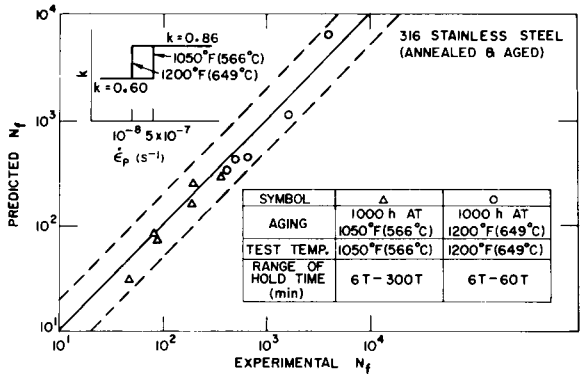


Fig. 2.16. Predicted vs Experimental Hold-time Fatigue Lives for Annealed and Aged Type 316 Stainless Steel. Neg. No. MSD-62912.

sliding. Consequently, the transition from transgranular to intergranular fracture mode occurs at a lower strain rate for a material in the aged condition than for the same material in an initially unaged condition.

2.2.2.4 Conclusions

A damage equation is proposed that takes into account the effect of plastic strain rate under creep and creep-fatigue loadings. The method presents a unified approach to creep and creep-fatigue damage.

Although the various material parameters that appear in the damage equation are, in general, functions of temperature, they may be assumed to be constant over a broad range of temperatures for engineering applications.

The method has been successfully applied to predict failure under a variety of creep-fatigue loadings of Types 304 and 316 austenitic stainless steel, Incoloy 800, and 2¼ Cr-1 Mo steel at various temperatures.

2.2.3 Application of Frequency-modified Life Approach to the Low-cycle Fatigue Behavior of Type 304 Stainless Steel -- P. S. Maiya and S. Majumdar

The application of the frequency-modified life equation (developed by Coffin) has been critically examined using the extensive data available for Type 304 stainless steel. At ANL, a large amount of elevated-temperature, low-cycle fatigue data have been generated for Type 304 stainless steel (Heat No. 9T2796) for various loading conditions. Prior to fatigue testing, the hourglass-shape specimens were solution annealed at 1978°F (1092°C) for 30 min and aged at 1100°F (593°C) for 1000 h. The tests were performed in axial strain control using hydraulically actuated fatigue machines. For the purpose of the present discussion, we will consider only the data at 1100°F (593°C), inasmuch as the data obtained at this temperature are more extensive than those at other temperatures and are thus amenable to a more rigorous testing of the data predictive methods.

To incorporate the time-dependent effects in elevated-temperature, low-cycle fatigue, Coffin[8] has proposed the frequency-modified Coffin-Manson relation given by

$$\left(N_f \nu^{k-1}\right)^{\beta} \quad \Delta\varepsilon_p = C_2$$

or

$$N_f = \left(\frac{C_2}{\Delta\varepsilon_p}\right)^{1/\beta} \nu^{1-k}, \tag{7}$$

where $C_2$ and $\beta$ are constants. The detailed description of Eq. (7) and its application to fatigue-life prediction have been discussed extensively by Coffin in a series of papers.[23-26] Also, a frequency-modified life relationship[26] exists between elastic strain range and fatigue life, which we will not discuss in the present report inasmuch as it is primarily applicable to high-cycle fatigue.

2.2.3.1 Life-predictive Parameters

The constants $C_2$, $\beta$, and k were obtained by a least-squares fit of the continuous-cycling fatigue data to Eq. (7). Only the fatigue data obtained at $\dot{\varepsilon}_t$ from $4 \times 10^{-2}$ to $4 \times 10^{-6}$ $s^{-1}$ and $\Delta\varepsilon_t$ between 0.5 and 2.0% were used. The values for $\Delta\varepsilon_p$ were obtained at half the fatigue life. The regression analysis was performed so that the values of constants were obtained over different frequency ranges. When a geometric mean value was assigned for the frequency range (used in determining the constants), it was found that the predictive parameters vary with frequency in a systematic manner, as shown in Fig. 2.17. All parameters show a gradual transition with frequency. In all cases, it appears that the values vary more slowly with frequency at both the higher and lower end of the frequency spectrum. The transition in the variation of these constants with cyclic frequency coincides approximately with the transition in failure mode from intergranular to transgranular or vice versa. Experimental evidence for this was obtained from an examination of fatigue fracture surfaces and the series of scanning-electron micrographs shown in Fig. 2.18. The transition from transgranular to intergranular failure occurs approximately at frequencies <0.1 cpm, which is consistent with the

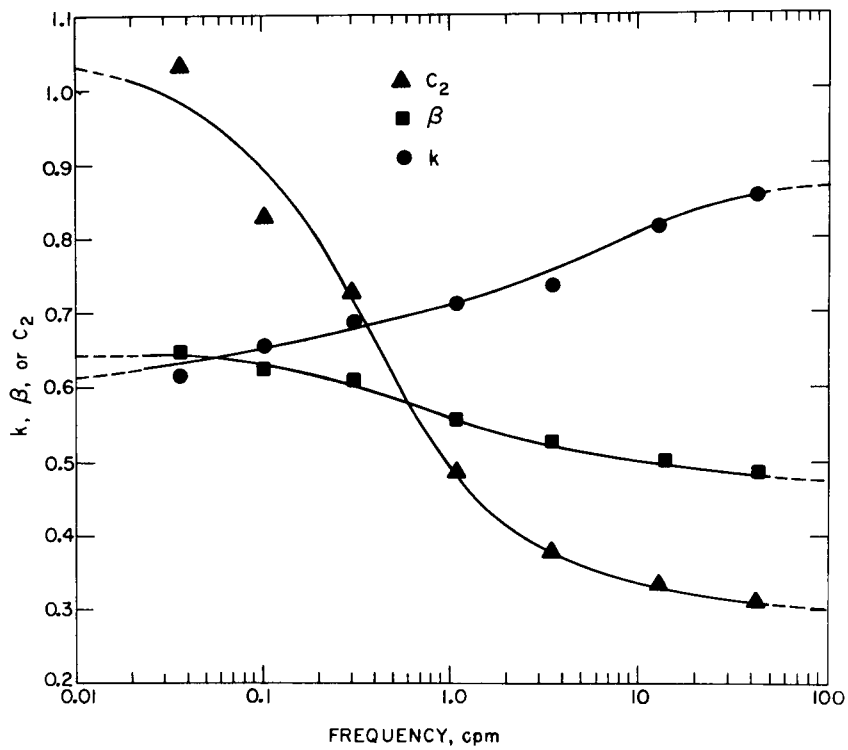


Fig. 2.17. Variation of Life-predictive Parameters with Frequency for Type 304 Stainless Steel at 593°C. Neg. No. MSD-61840.

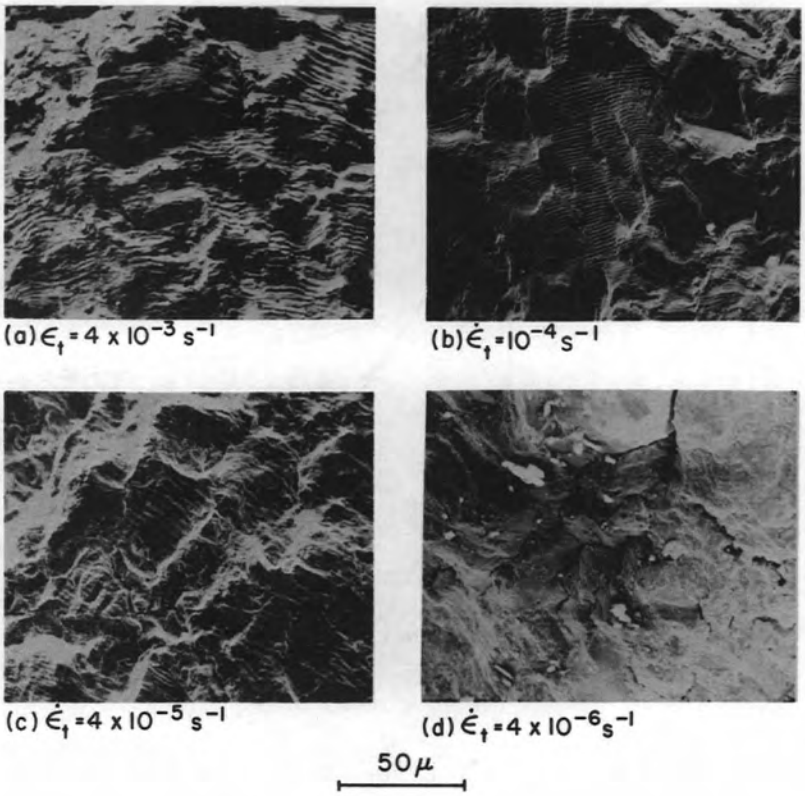


Fig. 2.18. Series of Scanning-electron Micrographs Showing Effect of Strain Rate on Fracture Appearance in Type 304 Stainless Steel. T = 593°C and $\Delta\varepsilon_t$ = 1%. Neg. No. ANL-306-75-230.

transition in the values of the constants observed. Three sets of constants were used in life prediction, and the values are listed in Table 2.2. The constants determined from the data at $\dot{\varepsilon}_t$ between $4 \times 10^{-2}$ and $4 \times 10^{-3}$ $s^{-1}$ will be referred to as transgranular failure mode (TFM) constants and the values obtained at $\dot{\varepsilon}_t$ between $4 \times 10^{-5}$ and $4 \times 10^{-6}$ $s^{-1}$ as intergranular failure mode (IFM) constants. The values of the constants determined over the entire spectrum of $\dot{\varepsilon}_t$ ($4 \times 10^{-2}$ to $4 \times 10^{-6}$ $s^{-1}$) will be identified as mixed failure mode (MFM) constants.

Table 2.2. Fatigue-life Predictive Parameters

| Type of Constants | $C_2$ | $\beta$ | k | A | m |
|---|---|---|---|---|---|
| TFM | 0.303 | 0.475 | 0.866 | 15.42 | 1.2 |
| IFM | 1.03 | 0.641 | 0.614 | 0.45 | 0.93 |
| MFM | 0.39 | 0.535 | 0.74 | 5.62 | 1.13 |

2.2.3.2 Prediction of Low-cycle Fatigue Data

Using the set of parameters listed in Table 2.2 and contained in Eq. (7), the fatigue life was calculated and compared with the experimentally determined fatigue life. The root-mean-square error (RMSE) is used as a measure of predictive capability for the appropriate case. The RMSE is defined as

$$\text{RMSE} = \sqrt{\frac{1}{N} \sum_{i=1}^{N} \left[ \ln N_{f_i} \text{ (calculated)} - N_{f_i} \text{ (experimental)} \right]^2}. \quad (8)$$

In the plots of calculated versus experimental fatigue life discussed in the present report, deviations of a factor of two from the calculated lives are shown by the dashed lines.

We now consider fatigue test results obtained at ANL for Type 304 stainless steel under loading conditions that involve various wave shapes. In one type of test (in addition to cycling at a given strain range with

zero mean strain), a predetermined period of hold time at constant total strain is imposed at both the maximum tensile strain and maximum compressive strain limits. In symmetric hold-time tests, the hold times in tension and compression are equal, and the shape of the strain cycle is trapezoidal. Also, fatigue tests have been run with only tensile hold time imposed in each cycle or compressive hold time. The tensile hold-time tests have been completed with hold times ranging from 1 to 600 min. In the compressive and symmetric hold-time tests, the hold times varied from 1 to 4 min. During the hold time at constant strain, the stress relaxes, which results in additional plastic strain. In a few tests, the tensile stress was held constant during the hold-time period of each cycle, and the specimen was allowed to creep until a predetermined amount of total strain was reached. When Eq. (7) is used for life prediction, the wave-shape effects are generally ignored[26] so that the average frequency $\nu_{av}$ is defined as

$$\nu_{av} = \frac{1}{\tau_{cont} + \tau_{Hold}} \tag{9}$$

where $\tau_{cont}$ is the time spent in continuous cycling, and $\tau_{Hold}$ is the hold-time period. In the cyclic creep tests performed at ANL, the frequency varied from cycle to cycle so that an average time period for each cycle is estimated by dividing the total time to failure by the number of cycles to failure. The frequency-modified life equation together with IFM and MFM constants yield a reasonably good prediction of the hold-time data (generated at ANL, to date, for one heat treatment) within a factor of two (Figs. 2.19 and 2.20). Another point to make is the slightly improved accuracy in life prediction using IFM constants compared with the prediction by means of MFM constants.

### 2.2.3.3 Discussion of Results

The low-cycle fatigue data generated at ANL for Type 304 stainless steel at 1100°F (593°C) for a variety of cyclic-loading conditions can be predicted within a factor better than two from continuous-cycling data using the frequency-modified life equation. However, a trend does exist,

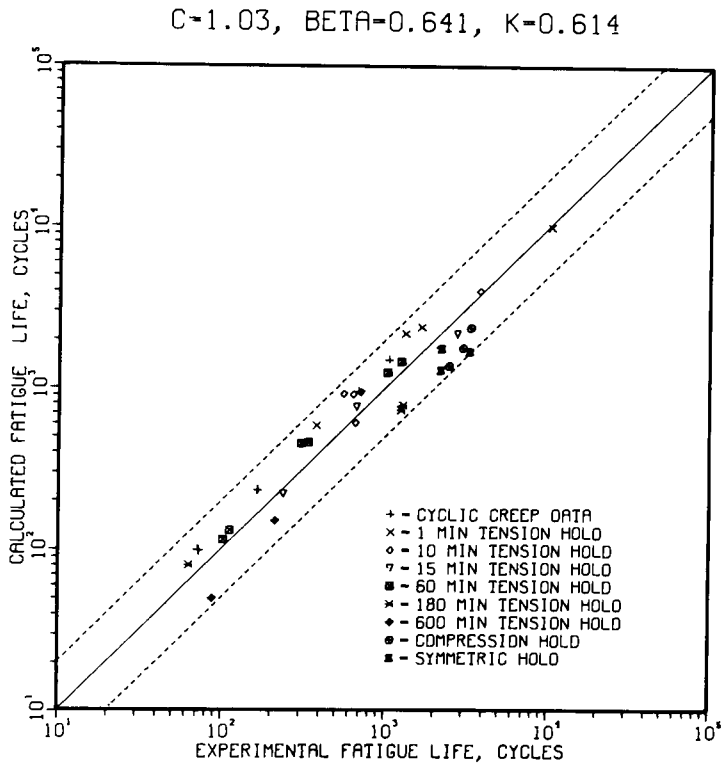


Fig. 2.19. Comparison of Hold-time Fatigue Data with Calculated Life Using IFM Constants. RMSE = 0.36, Type 304 stainless steel, and T = 593°C. Neg. No. MSD-62319.

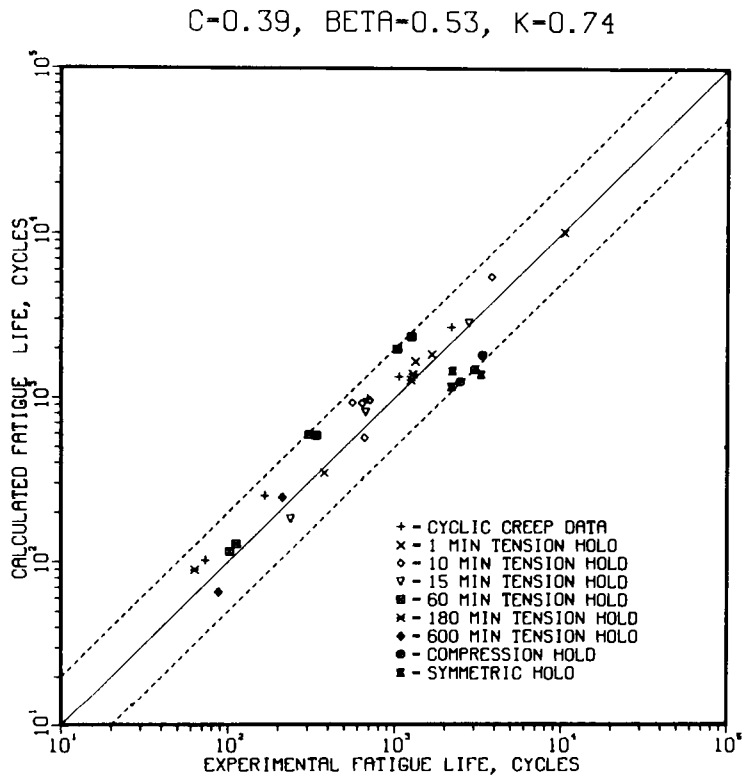


Fig. 2.20. Comparison of Hold-time Fatigue Data with Calculated Life Using MFM Constants. RMSE = 0.41, Type 304 stainless steel, and T = 593°C. Neg. No. MSD-62314.

as has been noted by several other investigators,[9,27,28] that the life prediction is nonconservative for tensile hold-time data and conservative for compressive and symmetric hold-time data. These results can be examined in light of the experimental observation that, for Type 304 stainless steel, the tensile hold-time period produces more damage than compressive or symmetric hold-time periods introduced per cycle. Microstructural evidence is presented by a series of scanning-electron micrographs of fracture surfaces for short hold-time periods involving a few wave shapes (Fig. 2.21). It is clear that a tensile hold time as short as 1 min produces both transgranular and intergranular fracture, whereas symmetric and compressive hold times of the same duration produce transgranular fracture surfaces. These observations are consistent with the work of Cheng and Diercks.[29] Similar results are observed for the 2-min hold-time tests (Fig. 2.21). It should also be mentioned that a compressive hold time as long as 4 min also produces well-defined fatigue striations.[30] Inasmuch as continuous cycling at strain rates $>10^{-4}$ $s^{-1}$ also causes transgranular fracture mode [well-defined fatigue striations visible on the fracture surfaces of specimens (Fig. 2.18)], it should be possible to predict fatigue life (with TFM constants) when compressive and symmetric hold-time periods are imposed. This is demonstrated in Fig. 2.22, and a comparison of Figs. 2.22 and 2.23 shows how the accuracy in life prediction is improved when the variation of predictive parameters with frequency is considered. However, longer compressive and symmetric hold times may be more damaging, resulting in intergranular fracture, and furthermore, the deformation behavior may also be influenced by strain-rate effects. Therefore, additional tests that involve longer compressive and symmetric hold times may impose a limit upon the extent of prediction by means of TFM constants.

From what has been said so far, the low-cycle fatigue data generated with tensile hold times varying from 1 to 600 min, with symmetric and compressive hold times <4 min, and cyclic creep data for Type 304 stainless steel (at 593°C) can be predicted within an accuracy of 30-40% using the Coffin-Manson frequency-modified life equation.

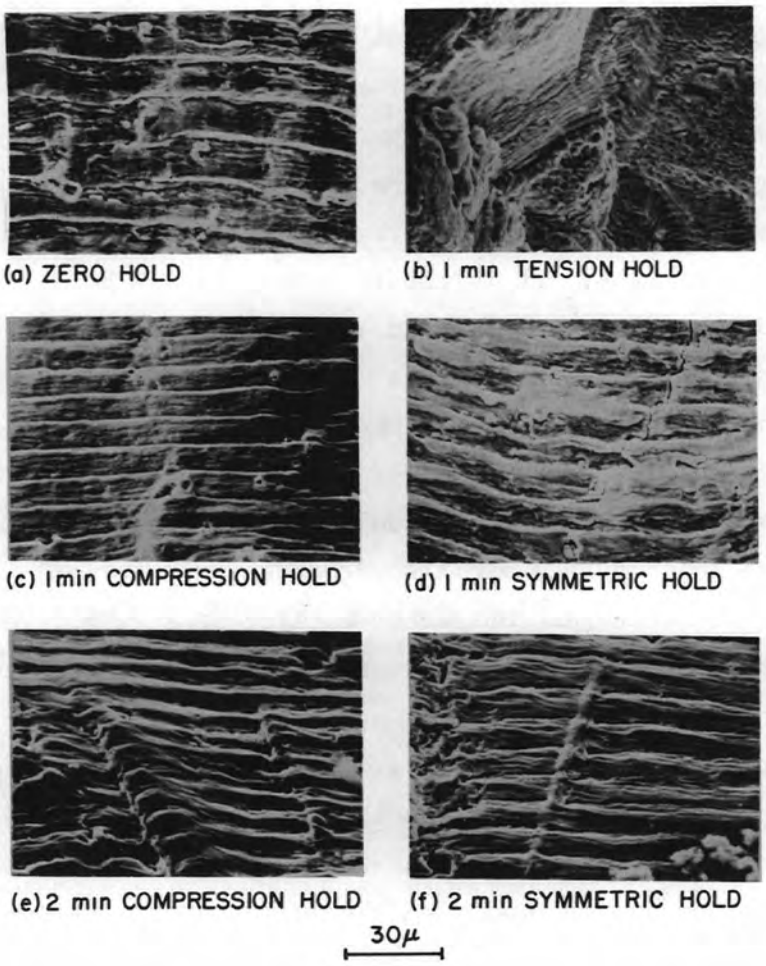


Fig. 2.21. Series of Scanning-electron Micrographs of Fracture Surfaces Showing Effect of Hold Times in Tension and Compression and Hold Times in Both Tension and Compression. Type 304 stainless steel, $\dot{\varepsilon}_t = 4 \times 10^{-3}\ s^{-1}$, $\Delta\varepsilon_t = 1\%$, and T = 593°C. Neg. No. ANL-306-76-116.

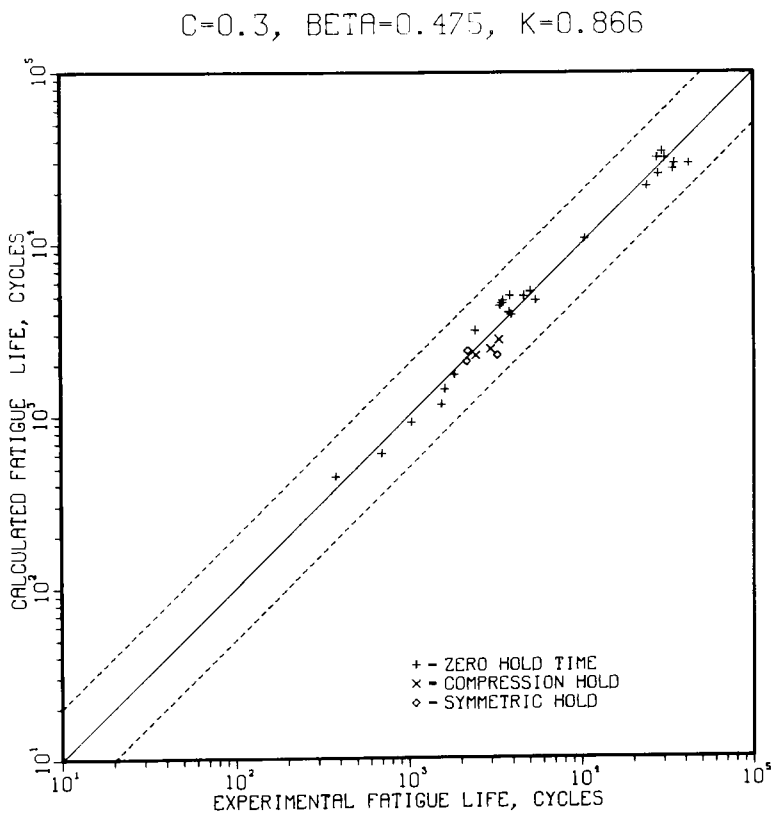


Fig. 2.22. Prediction of Compressive and Symmetric Hold-time Data with TFM Constants. Type 304 stainless steel and T = 593°C. Continuous-cycling data obtained at $\dot{\varepsilon}_t$ between $10^{-2}$ and $10^{-4}$ $s^{-1}$ are included. RMSE = 0.18. Neg. No. MSD-62317.

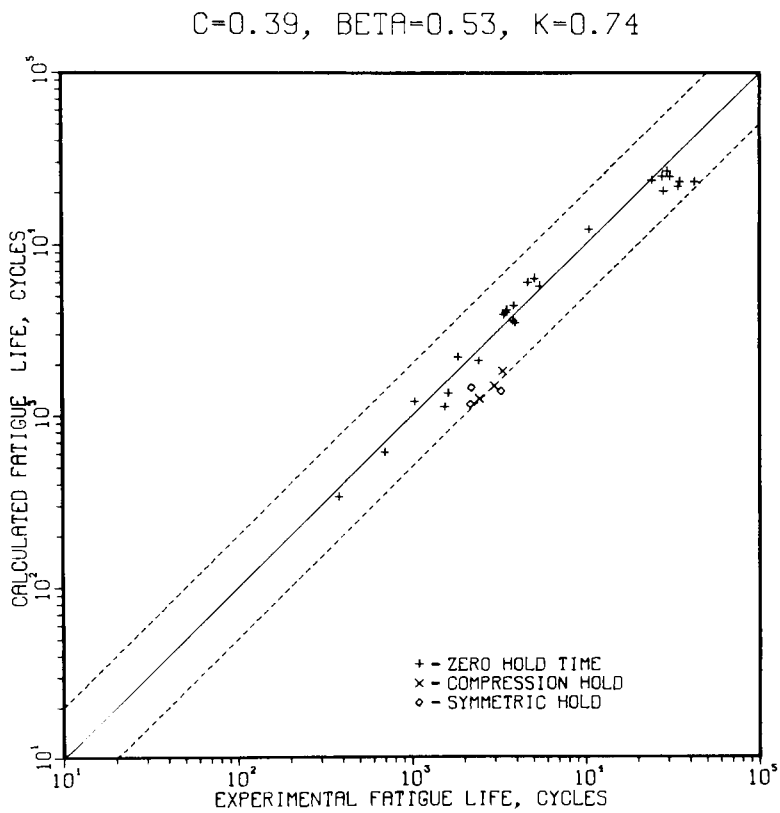


Fig. 2.23. Prediction of Compressive and Symmetric Hold-time Data with MFM Constants. Type 304 stainless steel and T = 593°C. Continuous-cycling data obtained at $\dot{\varepsilon}_t$ between $10^{-2}$ and $10^{-4}$ $s^{-1}$ are included. RMSE = 0.36. Neg. No. MSD-62318.

In earlier reports,[1,7] the damage-rate approach for creep, fatigue, and creep-fatigue interaction was discussed. Basically, the damage-rate approach assumes a failure criterion that involves the growth of an initial microcrack length $a_o$ to a critical crack length $a_c$ and proposes a damage-rate equation in terms of the current crack length a, plastic strain $\varepsilon_p$, and plastic strain rate $\dot{\varepsilon}_p$. The approach is versatile in the sense that the damage accumulation along an arbitrary deformation path can be computed by integrating the damage-rate equation. Because the damage-rate approach has been successfully applied[7] to the same creep-fatigue data as those considered in the present report and also the frequency-modified life equation can be derived from the damage-rate approach, a direct comparison of the life predictions of the two approaches is possible. Integration of the damage-rate equation for continuous cycling over a plastic strain range $\Delta\varepsilon_p$ at a constant plastic strain rate $\dot{\varepsilon}_p$ yields the following relations:[7]

$$N_f = \frac{m+1}{4A} \left(\frac{\Delta\varepsilon_p}{2}\right)^{-(m+1)} (\dot{\varepsilon}_p)^{1-k},$$

where

$$A = \frac{C+T}{2} \Big/ \ln a_c/a_o;$$

or, in terms of frequency $\nu$ (in cpm),

$$N_f = \frac{m+1}{4A} \left(\frac{\Delta\varepsilon_p}{2}\right)^{-(m+k)} (4\nu)^{1-k}. \tag{10}$$

Equation (10) is identical to the frequency-modified life equation, Eq. (9), if

$$\beta = \frac{1}{k+m}$$

and

$$C_2 = \left(\frac{m+1}{A}\right)^{\beta} \frac{2^{(m-k)\beta}}{60^{(1-k)\beta}} . \tag{11}$$

The values of A and m that correspond to $\beta$ and $C_2$ are listed in Table 2.2. Therefore, under continuous cycling, the damage-rate approach yields identical results, provided the same constants are used.

When hold times are imposed in each cycle, the damage-rate equation, upon integration, yields the damage per cycle, as discussed elsewhere.[7]

Let us consider and compare the extent of damage produced during tensile hold time up to 600 min using the two approaches. For this purpose, we include fatigue test results at 593°C for Type 304 stainless steel with the same $\dot{\varepsilon}_t = 4 \times 10^{-3}\ s^{-1}$ and $\Delta\varepsilon_t = 1.0\%$ but with tensile hold times ranging from 1 to 600 min. The damage per cycle in the frequency-modified approach is

$$\frac{1}{N_f} = \frac{4A}{m+1}\left(\frac{\Delta\varepsilon_p}{2}\right)^{m+k}\left(\frac{\tau}{4}\right)^{1-k}, \tag{12}$$

where $\tau$ is the time period per cycle in seconds. Note that in the frequency-modified life equation, no distinction is made between the continuous cycling and the hold-time damages, but a distinction exists in the damage-rate approach. Using the appropriate constants, life with hold time/life without hold time is computed and plotted versus the tensile hold time for the two approaches (Fig. 2.24). The results obtained are in close agreement and imply that, in the frequency-modified approach, wave-shape effects can be ignored for this type of loading considered at least up to tensile hold time <600 min. However, it should be mentioned that the frequency-modified approach continues to predict a decrease in life with longer hold time beyond $t_H = 600$ min, whereas the damage-rate approach predicts a decrease in life as long as $\dot{\varepsilon}_p \neq 0$ and predicts zero damage (saturation) when $\dot{\varepsilon}_p = 0$. The latter situation is of particular interest to designers, but no data exist beyond $t_H = 600$ min to verify whether saturation occurs. For handling the damage during long compressive and/or symmetric hold times, the frequency-modified approach presents problems.

Another situation where wave-shape effects become important involves tests with sawtooth waveforms. Two types of tests of interest are the following: one with slow loading followed by fast unloading (slow-fast)

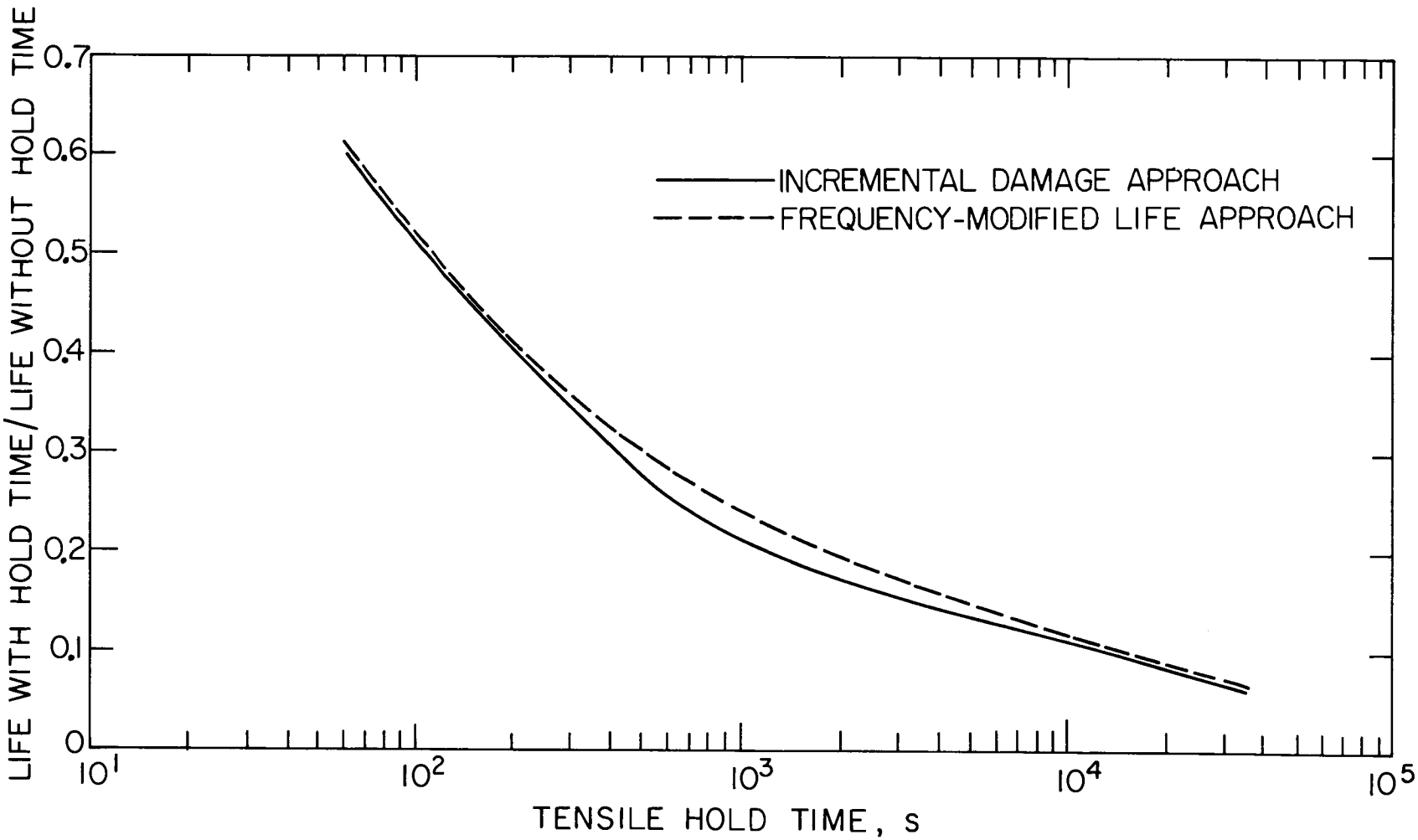


Fig. 2.24. Comparison of Damage That Results from Tensile Hold Time Estimated from Frequency-modified Life and Incremental Damage (or Damage Rate) Approaches. Type 304 Stainless Steel and T = 593°C. Neg. No. ANL-306-76-115.

and the second with fast loading followed by slow unloading (fast-slow). In the frequency-modified approach, the preceding two loading sequences are not distinguished and additional assumptions are necessary to handle the situation. [Recently, the authors have learned that Coffin (private communication) has proposed a frequency-separation technique to handle wave-shape effects.] To examine the damage using the damage-rate approach, we consider two types of tests that involve sawtooth waveforms as shown in Fig. 2.25. From strain-cycling and the corresponding stress-cycling waveforms, shown in Fig. 2.25, it is clear that in a slow-fast test more time is spent when the stress is tensile (also note that a mean compressive stress is present) than when the stress is compressive. Inasmuch as tensile hold time is more damaging than compressive hold time, we conclude that slow-fast cycling is more damaging than fast-slow cycling. To estimate the order of magnitude of life difference involved in sawtooth waveforms, we consider two sets of slow-fast and fast-slow tests, all with $\Delta\varepsilon_p = 0.007$. The strain rates for the first set are $10^{-6}$ $s^{-1}$ ($\dot{\varepsilon}_{p_1}$) and $10^{-4}$ $s^{-1}$ ($\dot{\varepsilon}_{p_2}$), and, for the second set of tests, $\dot{\varepsilon}_{p_1} = 10^{-6}$ $s^{-1}$ and $\dot{\varepsilon}_{p_2} = 10^{-3}$ $s^{-1}$. The damage per cycle in the slow-fast test* is given by

$$\frac{1}{N_f} = \frac{16A}{5(m+1)} (0.0035)^{m+1} \left(\dot{\varepsilon}_{p_1}\right)^{k-1} + \frac{4A}{5(m+1)} (0.0035)^{m+1} \left(\dot{\varepsilon}_{p_2}\right)^{k-1} , \tag{13}$$

and in the fast-slow test

$$\frac{1}{N_f} = \frac{16A}{5(m+1)} (0.0035)^{m+1} \left(\dot{\varepsilon}_{p_2}\right)^{k-1} + \frac{4A}{5(m+1)} (0.0035)^{m+1} \left(\dot{\varepsilon}_{p_1}\right)^{k-1} . \tag{14}$$

*The tensile hold time is assumed to be four times more damaging than compressive hold time to be consistent with our previous work.[7]

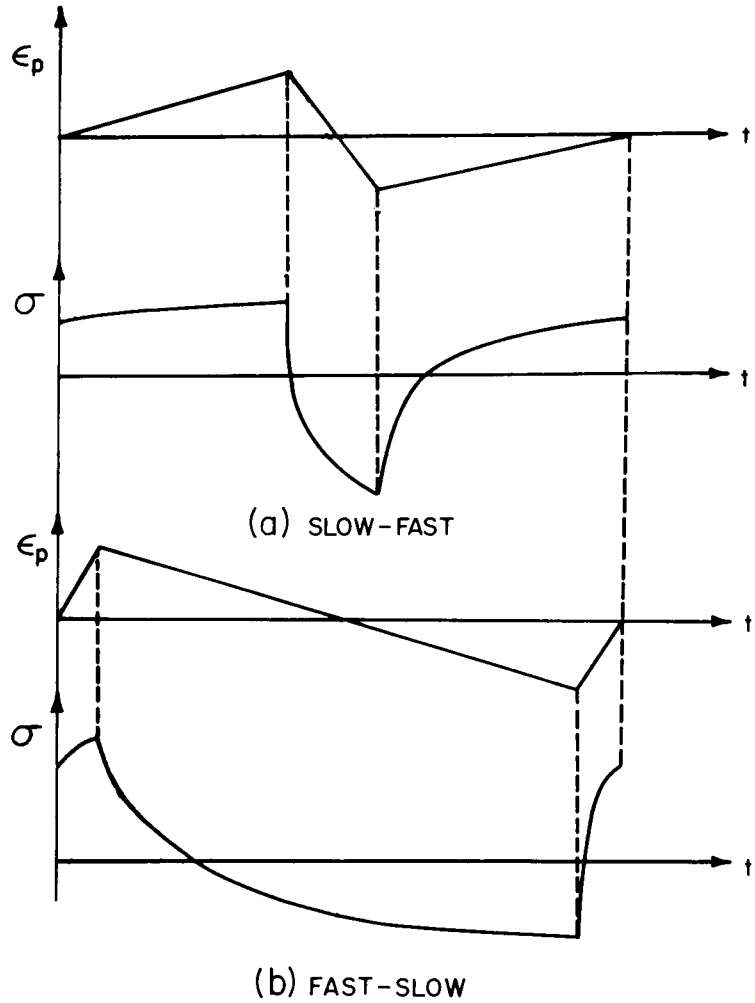


Fig. 2.25. Sawtooth Waveforms. Neg. No. MSD-62311.

Using the appropriate constants (for $\dot{\varepsilon}_p > 10^{-4}\ s^{-1}$, TFM constants are used, and, for $\dot{\varepsilon}_p < 10^{-5}\ s^{-1}$, IFM constants are used) from Table 2.2, the fatigue lives calculated for sawtooth waveform are listed in Table 2.3. The magnitude of the wave-shape effect on fatigue life estimated (slow-fast loading produces three to four times more damage than the fast-slow loading) is consistent with the recent experimental findings of Coffin for Type 304 stainless steel and the A286 alloy.[31]

Table 2.3. Expected Results from Damage-rate Approach for Sawtooth Waveform for Type 304 Stainless Steel, with $\Delta\varepsilon_p = 0.007$ and T = 593°C

| Type of Loading | $\dot{\varepsilon}_{pt}$,[a] $s^{-1}$ | $\dot{\varepsilon}_{pc}$,[a] $s^{-1}$ | $N_f$, cycles |
|---|---|---|---|
| Slow-fast | $10^{-6}$ | $10^{-4}$ | 338 |
| Fast-slow | $10^{-4}$ | $10^{-6}$ | 1032 |
| Slow-fast | $10^{-6}$ | $10^{-3}$ | 378 |
| Fast-slow | $10^{-3}$ | $10^{-6}$ | 1470 |

[a] $\dot{\varepsilon}_{pt}$ and $\dot{\varepsilon}_{pc}$ are the plastic strain rates in tension and compression, respectively.

### 2.2.4 Description of Cyclic Hardening Behavior of Type 304 Stainless Steel -- P. S. Maiya

Type 304 stainless steel in the solution-annealed or solution-annealed and aged conditions cyclically hardens when subjected to cycling at constant strain range. The rate of hardening depends upon the actual strain-range levels, temperature, and other cyclic loading variables of fatigue tests. At total strain ranges between 0.5 and 2.0%, the cyclic-hardening rate decreases with an increase in the number of cycles, and the material typically attains saturation in ∿150-500 cycles. Therefore, a proper description of cyclic-hardening behavior must include both the initial cyclic-hardening stage and the attainment of saturation. Efforts are being made to process the extensive cyclic-hardening data generated at ANL and to describe the cyclic-hardening behavior in a simple manner so that it is easily accessible to designers.

One of the methods[32] of representing the cyclic-hardening behavior at constant strain range is by means of a Voce-type equation

$$\Delta\sigma = (\Delta\sigma_o - \Delta\sigma_\infty) \exp(-KN) + \Delta\sigma_\infty, \tag{15}$$

where $\Delta\sigma$ is the stress range for any cycle N, $\Delta\sigma_o$ and K are constants, and $\Delta\sigma_\infty$ is saturation stress range. As has been recognized earler,[32] Eq. (15) does not describe the cyclic-hardening behavior satisfactorily. In the present report, a modified version of Voce-type equation to describe cyclic-hardening behavior will be discussed. The application of the proposed equation is demonstrated by considering the cyclic-hardening data generated at ANL for Type 304 stainless steel. For simplicity, only results obtained at total strain ranges between 0.5 and 2.0%, a strain rate of $4 \times 10^{-3}$ $s^{-1}$, and a temperature of 1100°F (593°C) are considered.

The cyclic-hardening behavior at constant strain range can be, in general, described by an equation of the following form:

$$\log \frac{\Delta\sigma_\infty - \Delta\sigma}{\Delta\sigma_\infty} = A_o + \sum_{n=1}^{n} A_n N^n , \tag{16}$$

where $\Delta\sigma$ and $\Delta\sigma_\infty$ have the same meaning as in Eq. (15), and $A_o$, $A_1$, $A_2$, and $A_n$ are the coefficients of the polynomial fit. Note that, when n = 1, Eq. (16) simplifies to a form similar to a Voce-type equation.

The cyclic-hardening data obtained for solution-annealed and aged Type 304 stainless steel are fitted to the first, second, and third degree polynomials to determine which gives the best least-squares fit of the data. The polynomials describing the cyclic-hardening data are given as follows:

$$\log \left(\frac{\Delta\sigma_\infty - \Delta\sigma}{\Delta\sigma_\infty}\right) = A_o + A_1 N, \tag{17}$$

$$\log \left(\frac{\Delta\sigma_\infty - \Delta\sigma}{\Delta\sigma_\infty}\right) = A_o + A_1 N + A_2 N^2, \tag{18}$$

and

$$\log\left(\frac{\Delta\sigma_\infty - \Delta\sigma}{\Delta\sigma_\infty}\right) = A_o + A_1N + A_2N^2 + A_3N^3. \tag{19}$$

The coefficients of the polynomial least-squares fit for data obtained at different strain ranges are listed in Table 2.4, and the results are displayed in Figs. 2.26-2.28. The solid curve is calculated from the coefficients listed in Table 2.4, and the experimental points are shown by symbols. It is clear that the best prediction is obtained by fitting the cyclic-hardening data to a third-degree polynomial which predicts both the cyclic-hardening and saturation behavior. The results also reflect that Eq. (15) is not satisfactory and also the higher degree terms $\left(\sum_{n=4}^{n} A_nN^n\right)$ are not required for describing the cyclic-hardening behavior.

It is also shown that the cyclic-hardening data for the solution-annealed Type 304 stainless steel can be represented in a similar manner by Eq. (19) as shown in Fig. 2.29. The coefficients of the polynomial fit for solution-annealed Type 304 stainless steel are listed in Table 2.5.

The above approach for representing cyclic-hardening behavior permits a comparison of hardening behavior of steels with two heat treatments. A comparison is made in Fig. 2.30 in which slight differences in cyclic-hardening behavior are observed (as a result of different initial heat treatments) for Type 304 stainless steel cycled at total strain ranges >0.5%. Using the coefficients of the third-degree polynomial, one can also determine the cyclic-hardening rate $[d(\Delta\sigma)/dN]$ as a function of the number of cycles. A log-log plot of cyclic-hardening rate versus number of cycles for solution-annealed and aged and solution-annealed Type 304 stainless steel is shown in Figs. 2.31 and 2.32, respectively. These figures show that the larger the strain range the higher the cyclic-hardening rate. Furthermore, the rate of hardening decreases more rapidly with the number of cycles (in the first 10 cycles) for larger strain ranges, which is expected.

Table 2.4. Cyclic-hardening Data Fitted to Polynomials for Solution-annealed and Aged Type 304 Stainless Steel at 1100°F (593°C). Strain rate, $4 \times 10^{-3}$ $s^{-1}$.

| Test No. | $\Delta\varepsilon_t$, % | $\Delta\sigma_\infty$, ksi | Coefficients of Polynomial Fit | | |
|---|---|---|---|---|---|
| | | | First Degree | Second Degree | Third Degree |
| 697 | 0.5 | 49.55 | $A_o$ -1.159 | $A_o$ -1.011 | $A_o$ -0.936 |
| | | | $A_1$ -0.0145 | $A_1$ -0.0243 | $A_1$ -0.0343 |
| | | | | $A_2$ $5.256 \times 10^{-5}$ | $A_2$ $2.199 \times 10^{-4}$ |
| | | | | | $A_3$ $-5.98 \times 10^{-7}$ |
| 142 | 0.75 | 61.97 | $A_o$ -0.979 | $A_o$ -0.852 | $A_o$ -0.781 |
| | | | $A_1$ -0.0182 | $A_1$ -0.0265 | $A_1$ -0.0365 |
| | | | | $A_2$ $4.466 \times 10^{-5}$ | $A_2$ $2.12 \times 10^{-4}$ |
| | | | | | $A_3$ $-5.98 \times 10^{-7}$ |
| 464 | 1.02 | 73.65 | $A_o$ -0.885 | $A_o$ -0.738 | $A_o$ -0.61 |
| | | | $A_1$ -0.0384 | $A_1$ -0.0544 | $A_1$ -0.078 |
| | | | | $A_2$ $1.718 \times 10^{-4}$ | $A_2$ $8.324 \times 10^{-4}$ |
| | | | | | $A_3$ $-4.46 \times 10^{-6}$ |
| 149 | 1.52 | 88.45 | $A_o$ -1.032 | $A_o$ -0.559 | $A_o$ -0.389 |
| | | | $A_1$ -0.0344 | $A_1$ -0.0861 | $A_1$ -0.117 |
| | | | | $A_2$ $5.552 \times 10^{-4}$ | $A_2$ $1.427 \times 10^{-3}$ |
| | | | | | $A_3$ $-5.89 \times 10^{-6}$ |
| 132 | 2.02 | 90.95 | $A_o$ -0.78 | $A_o$ -0.447 | $A_o$ -0.261 |
| | | | $A_1$ -0.099 | $A_1$ -0.154 | $A_1$ -0.208 |
| | | | | $A_2$ $1.124 \times 10^{-3}$ | $A_2$ $4.079 \times 10^{-3}$ |
| | | | | | $A_3$ $-3.94 \times 10^{-5}$ |

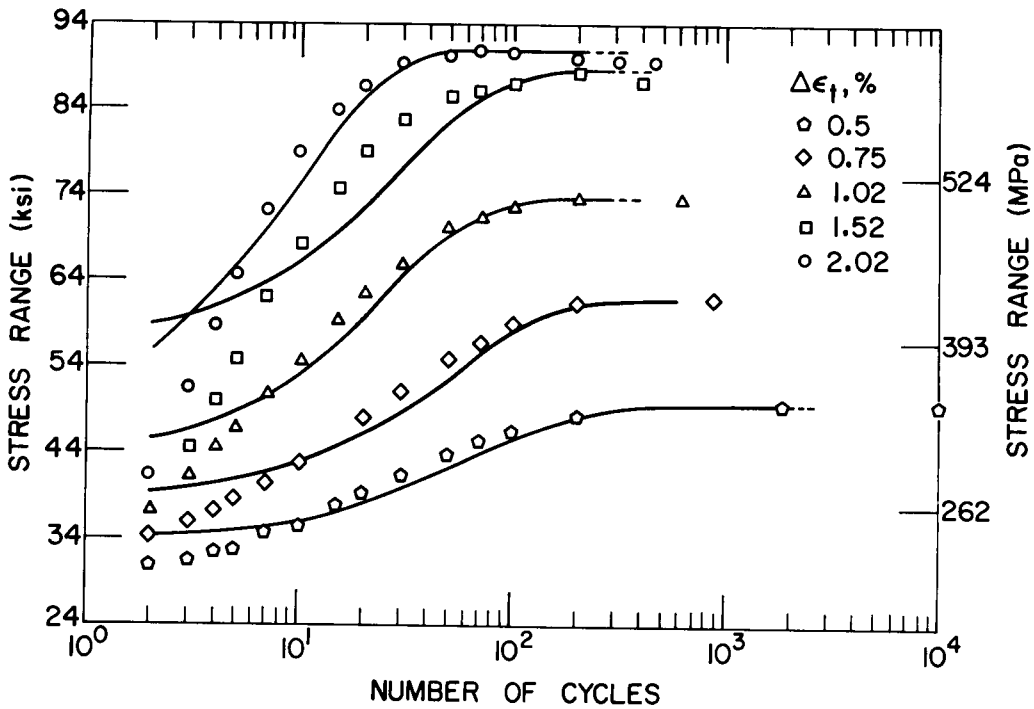


Fig. 2.26. Prediction of Cyclic-hardening Behavior of Solution-annealed and Aged Type 304 Stainless Steel at 1100°F (593°C) and a Strain Rate of 4 x $10^{-3}$ $s^{-1}$ Using First-degree Polynomial. Neg. No. MSD-63089.

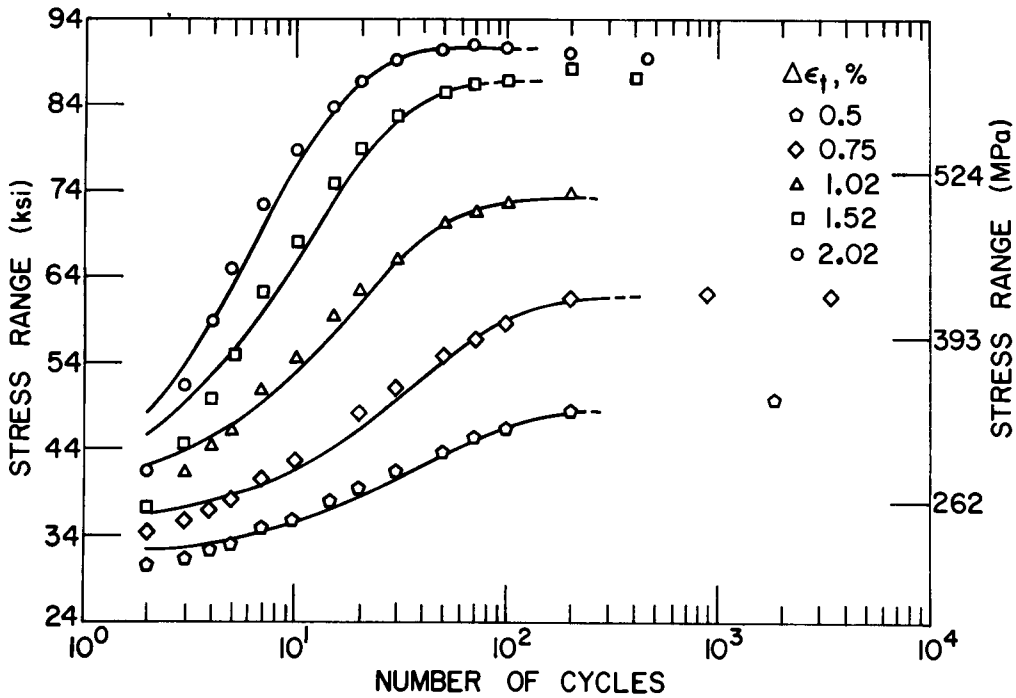


Fig. 2.27. Prediction of Cyclic-hardening Behavior of Solution-annealed and Aged Type 304 Stainless Steel at 1100°F (593°C) and a Strain Rate of 4 x $10^{-3}$ $s^{-1}$ Using Second-degree Polynomial. Neg. No. MSD-63090.

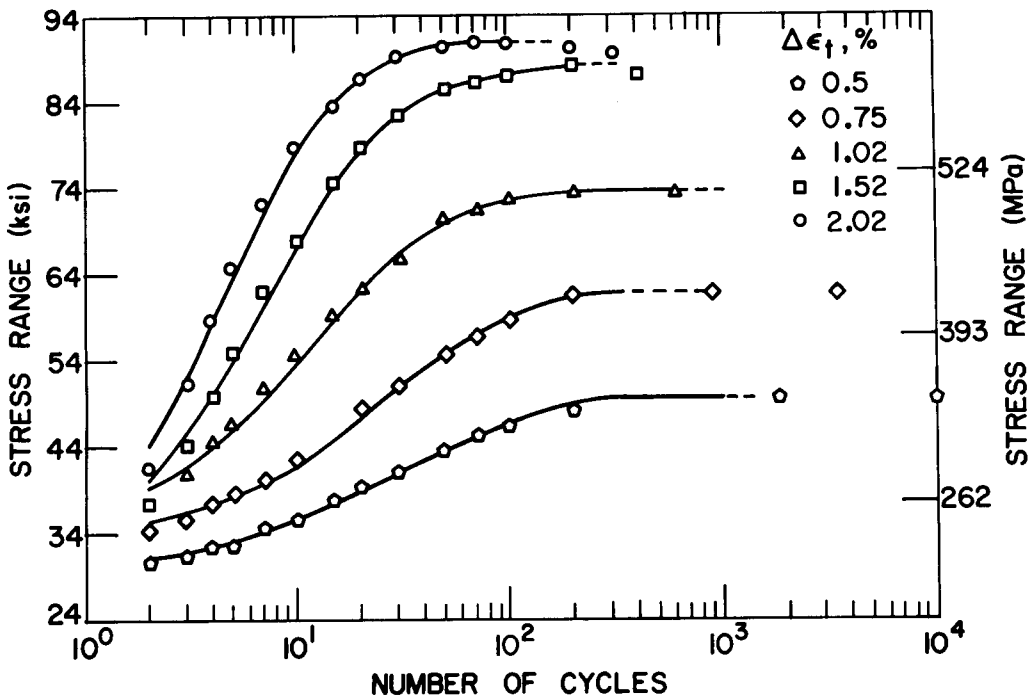


Fig. 2.28. Prediction of Cyclic-hardening Behavior of Solution-annealed and Aged Type 304 Stainless Steel at 1100°F (593°C) and a Strain Rate of 4 x $10^{-3}$ $s^{-1}$ Using Third-degree Polynomial. Neg. No. MSD-63091.

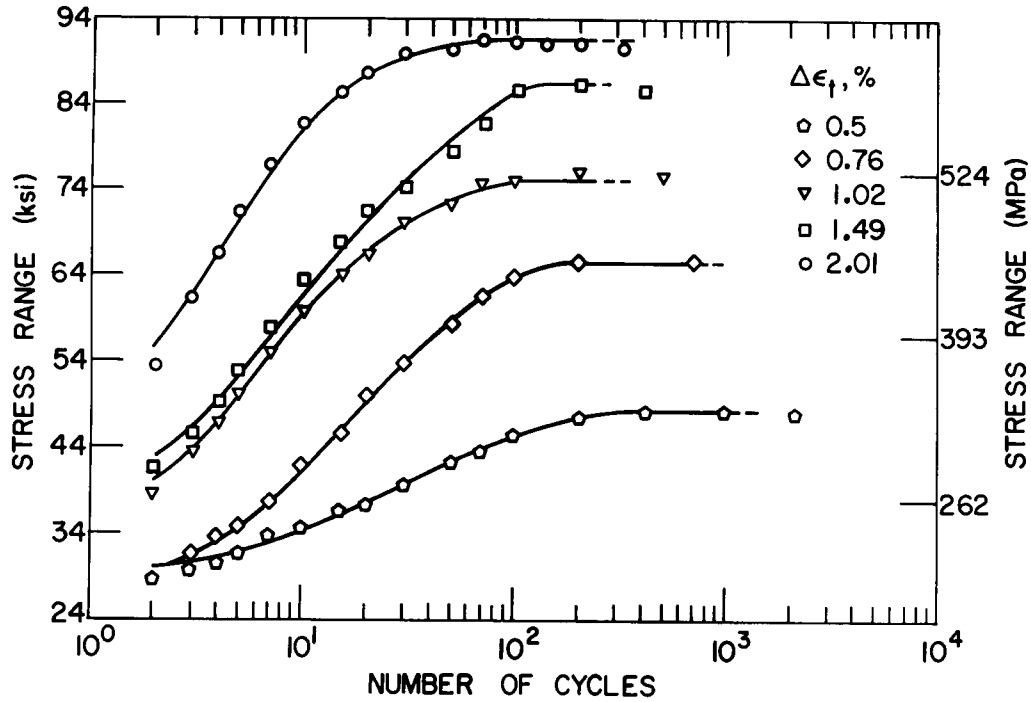


Fig. 2.29. Prediction of Cyclic-hardening Behavior of Solution-annealed Type 304 Stainless Steel at 1100°F (593°C) and a Strain Rate of 4 x $10^{-3}$ $s^{-1}$ Using Third-degree Polynomial. Neg. No. MSD-63088.

Table 2.5. Cyclic-hardening Data Fitted to Third-degree Polynomial for Solution-annealed Type 304 Stainless Steel at 1100°F (593°C). Strain rate, $4 \times 10^{-3}$ $s^{-1}$.

| Test No. | $\Delta\varepsilon_t$, % | $\Delta\sigma_\infty$, ksi | Coefficients of Polynomial Fit |
|---|---|---|---|
| 103 | 0.5 | 48.3 | $A_o$ -0.916 |
| | | | $A_1$ -0.0325 |
| | | | $A_2$ $1.979 \times 10^{-4}$ |
| | | | $A_3$ $-5.554 \times 10^{-7}$ |
| 147 | 0.76 | 65.48 | $A_o$ -0.488 |
| | | | $A_1$ -0.0554 |
| | | | $A_2$ $5.509 \times 10^{-4}$ |
| | | | $A_3$ $-3.253 \times 10^{-6}$ |
| 168 | 1.02 | 74.96 | $A_o$ -0.524 |
| | | | $A_1$ -0.126 |
| | | | $A_2$ $2.32 \times 10^{-3}$ |
| | | | $A_3$ $-1.973 \times 10^{-5}$ |
| 419 | 1.49 | 86.22 | $A_o$ -0.524 |
| | | | $A_1$ -0.0892 |
| | | | $A_2$ $1.688 \times 10^{-3}$ |
| | | | $A_3$ $-1.317 \times 10^{-5}$ |
| 101 | 2.01 | 91.35 | $A_o$ -0.581 |
| | | | $A_1$ -0.192 |
| | | | $A_2$ $3.246 \times 10^{-3}$ |
| | | | $A_3$ $-2.434 \times 10^{-5}$ |

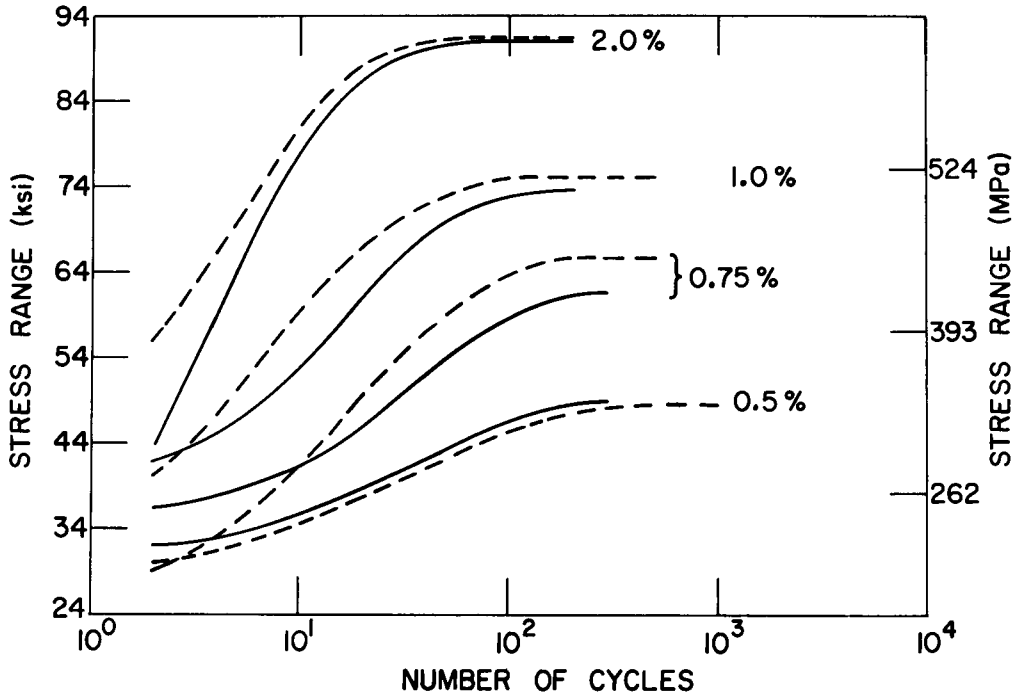


Fig. 2.30. Comparison of Cyclic-hardening Behavior of Type 304 Stainless Steel with Different Initial Heat Treatments. Solid line: solution annealed and aged and dashed line: solution annealed. Neg. No. MSD-63087.

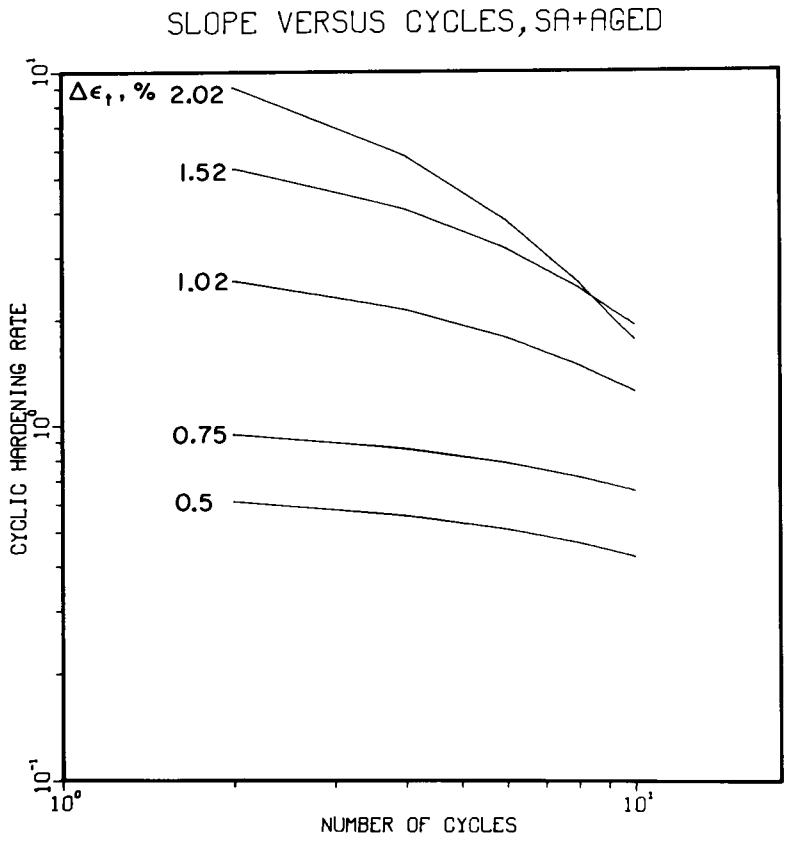


Fig. 2.31. Variation of Cyclic-hardening Rate with Number of Cycles for Solution-annealed and Aged Type 304 Stainless Steel at 1100°F (593°C) and a Strain Rate of 4 x $10^{-3}$ $s^{-1}$. Neg. No. MSD-63085.

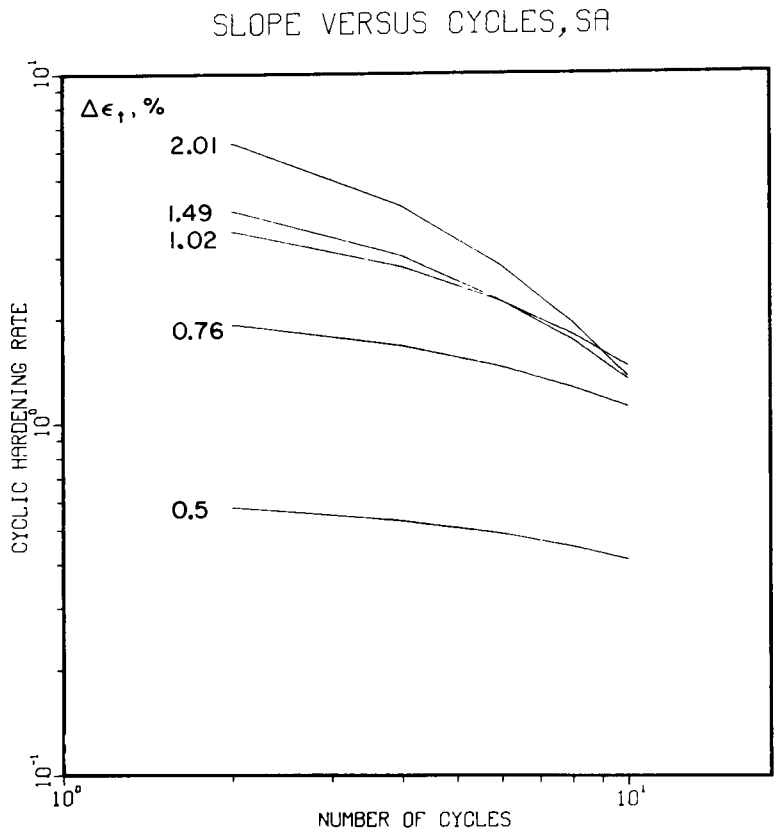


Fig. 2.32. Variation of Cyclic-hardening Rate with Number of Cycles for Solution-annealed Type 304 Stainless Steel at 1100°F (593°C) and a Strain Rate of 4 x $10^{-3}$ $s^{-1}$. Neg. No. MSD-63086.

## 2.3 REFERENCES


1. *Mechanical Properties Test Data for Structural Materials Quarterly Progress Report for Period Ending April 30, 1976*, Oak Ridge National Laboratory, ORNL-5150, pp. 3-40.

2. *A Guide for Fatigue Testing and the Statistical Analysis of Fatigue Data*, ASTM STP 91-A, American Society for Testing and Materials, Philadelphia, 1963.

3. M. G. Natrella, *Experimental Statistics*, National Bureau of Standards Handbook 91, Washington, 1963.

4. C. R. Brinkman and G. E. Korth, "Heat-to-heat Variations in the Fatigue and Creep-fatigue Behavior of AISI Type 304 Stainless Steel at 593°C," *J. Nucl. Mater.* 48: 293-306 (1973); also Aerojet Nuclear Company, ANCR-1097 (May 1973).

5. V. K. Sikka, H. E. McCoy, Jr., M. K. Booker, and C. R. Brinkman, "Heat-to-heat Variation in Creep Properties of Types 304 and 316 Stainless Steels," *J. Pressure Vessel Technol.* 96(J-4): 243-251 (November 1975).

6. C. F. Cheng, C. Y. Cheng, D. R. Diercks, and R. W. Weeks, "Low-Cycle Fatigue Behavior of Types 304 and 316 Stainless Steel at LMFBR Operating Temperature," in *Fatigue at Elevated Temperatures*, ASTM STP 520, American Society for Testing and Materials, 1973, pp. 355-364.

7. S. Majumdar and P. S. Maiya, *A Unified and Mechanistic Approach to Creep-fatigue Damage*, Argonne National Laboratory, ANL-76-58 (1976).

8. L. F. Coffin, "Predictive Parameters and Their Application to High Temperature Low-Cycle Fatigue," *Proc. 2nd Intl. Conf. on Fracture*, Chapman and Hall, London, 1969, p. 643.

9. R. W. Weeks, D. R. Diercks, and C. F. Cheng, *ANL Low-Cycle Fatigue Studies -- Program, Results, and Analysis*, Argonne National Laboratory, ANL-8009 (Nov. 1973).

10. *Mechanical Properties Test Data for Structural Materials Quarterly Progress Report for Period Ending October 31, 1974*, Oak Ridge National Laboratory, ORNL-5103, pp. 109-118.

11. *Mechanical Properties Test Data for Structural Materials Quarterly Progress Report for Period Ending April 30, 1974*, Oak Ridge National Laboratory, ORNL-4963, pp. 61-81.

12. *Mechanical Properties Test Data for Structural Materials Quarterly Progress Report for Period Ending January 31, 1974*, Oak Ridge National Laboratory, ORNL-4948, pp. 177-187.

13. D. R. Diercks and W. F. Burke, "Elevated-Temperature True Stress--True Strain Tensile Behavior of AISI Type 304 Stainless Steel," *Elevated Temperature Properties of Austenitic Stainless Steels*, American Society of Mechanical Engineers, New York, 1974, pp. 19-30.

14. R. W. Swindeman, Oak Ridge National Laboratory, private communication (1975).

15. *Short-Term Tensile and Low Cycle Fatigue Studies of Incoloy 800*, General Electric Company, GEMP-732, Cincinnati, Dec. 1969, pp. 13-16.

16. C. E. Jaske, H. Mindlin, and J. S. Perrin, *Low-Cycle Fatigue and Creep-Fatigue of Incoloy Alloy 800*, Battelle Columbus Laboratories, BMI-1921, Feb. 1972, pp. 20-38.

17. C. R. Brinkman et al., *Interim Report on the Continuous Cycling Elevated-Temperature Fatigue and Subcritical Crack Growth Behavior of 2-1/4 Cr-1 Mo Steel*, Oak Ridge National Laboratory, ORNL-TM-4993, Dec. 1975.

18. *Mechanical Properties Test Data for Structural Materials Quarterly Progress Report for Period Ending October 31, 1975*, Oak Ridge National Laboratory, ORNL-5107, p. 145.

19. J. R. Ellis et al., "Elevated Temperature Fatigue and Creep-Fatigue Properties of Annealed 2-1/4 Cr-1 Mo Steel", *Structural Materials for Services at Elevated Temperatures in Nuclear Power Generation*, American Society of Mechanical Engineers, MPC-1, New York, 1975, pp. 213-246.

20. J. P. Strizak, Oak Ridge National Laboratory, private communication (1976).

21. J. B. Conway, R. H. Stentz, and J. T. Berling, *Fatigue, Tensile, and Relaxation Behavior of Stainless Steels*, TID-26135, U. S. Atomic Energy Commission, 1975, p. 39.

22. D. L. Keller, *Progress on LMFBR Cladding, Structural, and Component Materials Studies During July, 1971 Through June, 1972*, Final Report, BMI-1928, Battelle Columbus Laboratories, July 1972, pp. 16-53.

23. L. F. Coffin, "A Note on Low Cycle Fatigue Laws," *J. Mater.* 6, 388 (1971).

24. L. F. Coffin, "Life Prediction of Metals Subjected to High Temperature, Low Cycle Fatigue," in Proc. of 1971 Kyoto Intl. Conf. of Materials II (1973), p. 234.

25. L. F. Coffin, "Fatigue at High Temperature," in Symp. on *Fatigue at Elevated Temperature*, ASTM STP 520, 5 (1973).

26. L. F. Coffin, *Fatigue at High Temperature,* General Electric Company Technical Information Series, Report No. 72 CRD 135, Class I (April 1972).

27. Masaki Kitagawa and R. W. Weeks, "Analysis of Hold Time Fatigue Test Results of AISI 304 Stainless Steel by Five Existing Methods," in Proc. 1973 Symp. on *Mechanical Behavior of Materials,* Soc. of Matls. Science, Japan, 1974, pp. 233-238.

28. P. S. Maiya and D. R. Diercks, "Analysis of ANL High-temperature Fatigue Data for AISI Type 304 Stainless Steel Using Common Pheonomenological Methods," *Reactor Development Program Progress Report,* Argonne National Laboratory, ANL-RDP-21, October 1973, p. 5.1.

29. C. Y. Cheng and D. R. Diercks, "Effects of Hold Time on Low-Cycle Fatigue Behavior of AISI Type 304 Stainless Steel at 593°C," *Met. Trans.* 4(2), 615-617 (1973).

30. P. S. Maiya, Argonne National Laboratory, unpublished research.

31. L. F. Coffin, General Electric Research and Development Center, private communication (1975).

32. *High-Temperature Structural Design Program Progress Report for Period Ending June 30, 1975,* ORNL-5087, p. 18-25 (March 1976).

# 3. OAK RIDGE NATIONAL LABORATORY

W. R. Martin

## 3.1 INTRODUCTION

The ORNL mechanical properties effort comprises several programs. The program Mechanical Properties and Behavior for Structural Materials deals with materials of general applicability to the LMFBR program. Other programs are concerned with the mechanical properties of weldments in LMFBR components, the specific materials of interest for LMFBR steam generators, collection and correlation of mechanical data needed for design on high-temperature LMFBR systems, and materials for the primary circuit and steam generators of HTGR systems.

## 3.2 MECHANICAL PROPERTIES AND BEHAVIOR FOR STRUCTURAL MATERIALS — C. R. Brinkman

The objective of this program is to collect mechanical property data and material behavior for LMFBR structural and component materials. Included in the scope of this effort are the following: (1) basic tensile, creep, creep-rupture, and relaxation base-line data that are directly applicable to design criteria and methods for types 304 and 316 stainless steel reference heats and cyclic stress-strain tests performed with emphasis on loading and aging history effects, (2) variations in properties for several heats of types 304 and 316 stainless steel determined to allow establishment of minimum and average values of specific properties and the equation parameters required for design purposes. This work will include determination of property variation of samples from different mill products within a given heat of stainless steel.

### 3.2.1 Mechanical Property Characterization of Type 304 Stainless Steel Reference Heat — V. K. Sikka, R. H. Baldwin, and E. B. Patton

#### 3.2.1.1 Creep and Rupture Properties of the 51-mm (2-in.) Plate of Reference Heat

Several creep tests on 51-mm (2-in.) plate of the reference heat of type 304 stainless steel (9T2796) continued. The test times and creep

strains for all tests have been updated and are summarized in Table 3.1. Three creep tests have exceeded 30,000 hr, and two others have exceeded 28,000 hr. All tests are moving smoothly and will be continued during the next quarter.

Table 3.1. Creep Tests on Type 304 Stainless Steel Reference Heat 9T2796 51-mm-Thick (2-in.) Plate[a]

| Test | Temperature | | Stress | | Time in Test | Strain, % | | Ratio of Creep Stress to Yield Stress[b] | Comments[c] |
|---|---|---|---|---|---|---|---|---|---|
| | (°C) | (°F) | (MPa) | (ksi) | (hr) | Loading | Creep | | |
| 11595 | 427 | 800 | 138 | 20.0 | 26,268 | 2.67 | 0.11 | 1.57 | |
| 12368 | 427 | 800 | 124 | 18.0 | 22,940 | 1.91 | 0.02 | 1.42 | |
| 12472 | 427 | 800 | 110 | 16.0 | 22,362 | 1.17 | 0.08 | 1.26 | |
| 12570 | 427 | 800 | 97 | 14.0 | 22,139 | 0.83 | 0.065 | 1.10 | |
| 15319 | 482 | 900 | 207 | 30.0 | 9,553 | 7.86 | 0.27 | 2.54 | |
| 15268 | 482 | 900 | 138 | 20.0 | 10,645 | 3.38 | 0.100 | 1.70 | |
| 11569 | 482 | 900 | 138 | 20.0 | 15,455 | 3.27 | 0.141 | 1.70 | Discontinued |
| 14041 | 482 | 900 | 138 | 20.0 | 12,009 | 3.85 | 0.00338 | 1.70 | Discontinued |
| 12375 | 482 | 900 | 124 | 18.0 | 12,376 | 2.40 | 0.072 | 1.53 | Discontinued |
| 11675 | 482 | 900 | 110 | 16.0 | 2,451 | 1.48 | 0.032 | 1.36 | Discontinued |
| 11693 | 482 | 900 | 97 | 14.0 | 97 | 0.92 | 0.14 | 1.19 | Discontinued |
| 11830 | 482 | 900 | 83 | 12.0 | 83 | 0.35 | 0.04 | 1.02 | Discontinued |
| 13152 | 482 | 900 | 69 | 10.0 | 20,192 | 0.089 | 0.020 | 0.85 | |
| 13020 | 482 | 900 | 69 | 10.0 | 21,002 | 0.085 | 0.05 | 0.85 | |
| 10489 | 538 | 1000 | 138 | 20.0 | 30,763 | 3.80 | 3.16 | 1.80 | Ruptured |
| 12250 | 538 | 1000 | 124 | 18.0 | 23,637 | 2.62 | 0.350 | 1.62 | |
| 11625 | 538 | 1000 | 110 | 16.0 | 19,656 | 1.79 | 0.262 | 1.44 | Discontinued |
| 10491 | 538 | 1000 | 97 | 14.0 | 31,442 | 1.16 | 0.29 | 1.26 | |
| 12444 | 538 | 1000 | 97 | 14.0 | 22,826 | 1.18 | 0.28 | 1.26 | |
| 12445 | 538 | 1000 | 97 | 14.0 | 4,498 | 1.17 | 0.090 | 1.26 | Discontinued |
| 11568 | 538 | 1000 | 83 | 12.0 | 26,400 | 0.53 | 0.140 | 1.08 | |
| 14973 | 538 | 1000 | 83 | 12.0 | 10,000 | 0.723 | 0.0055 | 1.08 | Discontinued |
| 11626 | 538 | 1000 | 69 | 10.0 | 26,067 | 0.071 | 0.123 | 0.90 | |
| 11641 | 538 | 1000 | 55 | 8.0 | 3,170 | 0.040 | 0.027 | 0.72 | Discontinued |
| 10853 | 593 | 1100 | 124 | 18.0 | 4,547 | 2.84 | 5.94 | 1.65 | Ruptured |
| 10852 | 593 | 1100 | 110 | 16.0 | 14,647 | 2.29 | 3.55 | 1.47 | Ruptured |
| 13947 | 593 | 1100 | 110 | 16.0 | 10,000 | 2.13 | 1.54 | 1.47 | Discontinued |
| 10554 | 593 | 1100 | 97 | 14.0 | 8,710 | 1.40 | 0.65 | 1.28 | Discontinued |
| 11596 | 593 | 1100 | 83 | 12.0 | 26,236 | 0.52 | 0.570 | 1.10 | |
| 10490 | 593 | 1100 | 69 | 10.0 | 31,005 | 0.22 | 0.46 | 0.92 | |
| 13710 | 593 | 1100 | 69 | 10.0 | 2,010 | 0.096 | 0.204 | 0.92 | Discontinued |
| 14163 | 593 | 1100 | 69 | 10.0 | 9,980 | 0.228 | 0.230 | 0.92 | Discontinued |
| 11227 | 593 | 1100 | 55 | 8.0 | 6,103 | 0.041 | 0.080 | 0.73 | Discontinued |
| 12459 | 593 | 1100 | 34 | 5.0 | 22,357 | 0.024 | 0.16 | 0.46 | |
| 10855 | 649 | 1200 | 110 | 16.0 | 304 | 2.41 | 12.0 | 1.57 | Ruptured |
| 13764 | 649 | 1200 | 110 | 16.0 | 245 | 2.42 | 14.53 | 1.57 | Ruptured |
| 10854 | 649 | 1200 | 97 | 14.0 | 761 | 1.60 | 13.0 | 1.37 | Ruptured |
| 11563 | 649 | 1200 | 83 | 12.0 | 2,674 | 0.59 | 13.0 | 1.18 | Ruptured |
| 11226 | 649 | 1200 | 69 | 10.0 | 7,278 | 0.18 | 7.0 | 0.98 | Ruptured |
| 10851 | 649 | 1200 | 55 | 8.0 | 20,059 | 0.044 | 5.03 | 0.78 | Ruptured |
| 12255 | 649 | 1200 | 34 | 5.0 | 992 | 0.030 | 0.08 | 0.49 | Discontinued |
| 12443 | 649 | 1200 | 34 | 5.0 | 22,229 | 0.024 | 0.19 | 0.49 | |
| 12460 | 649 | 1200 | 21 | 3.0 | 22,350 | 0.020 | 0.26 | 0.29 | |
| 10856 | 704 | 1300 | 69 | 10.0 | 568 | 0.067 | 15.60 | 0.90 | Ruptured |
| 11562 | 704 | 1300 | 69 | 10.0 | 653 | 0.12 | 22.50 | 0.90 | Ruptured |
| 11222 | 704 | 1300 | 55 | 8.0 | 2,760 | 0.031 | 16.40 | 0.72 | Ruptured |
| 12254 | 704 | 1300 | 34 | 5.0 | 23,550 | 0.030 | 5.12 | 0.45 | |
| 12461 | 704 | 1300 | 21 | 3.0 | 22,467 | 0.018 | 0.37 | 0.27 | |
| 12462 | 704 | 1300 | 14 | 2.0 | 22,061 | 0.010 | 0.250 | 0.18 | |

[a]Annealed 0.5 hr at 1093°C before testing. All tests loaded at a strain rate of 0.004/min.

[b]Yield stresses used in this ratio were 12,700 psi (88 MPa) at 427°C (800°F), 11,800 psi (81 MPa) at 482°C (900°F), 11,100 psi (77 MPa) at 538°C (1000°F), 10,900 psi (75 MPa) at 593°C (1100°F), 10,200 psi (70 MPa) at 649°C (1200°F), 11,000 psi (77 MPa) at 704 °C (1300°F).

[c]Unless otherwise noted, tests in progress.

One test at 538°C (1000°F) and 138 MPa (20 ksi) ruptured recently after 30,763 hr. The creep curve for this test is shown in Fig. 3.1. Included in the figure are the predicted time to rupture ($t_r$), minimum creep rate ($\dot{e}_m$), time to onset of tertiary creep ($t_3$), and creep curve. The predicted values of $t_r$, $\dot{e}_m$, and $t_3$ have been derived from the generalized models of these quantities as functions of stress ($S$), temperature ($t$), and ultimate tensile strength at the creep test temperature ($S_u$). Details of these models are described elsewhere,[1,2] and they are briefly discussed in Sect. 3.2.3. The predicted creep curve was

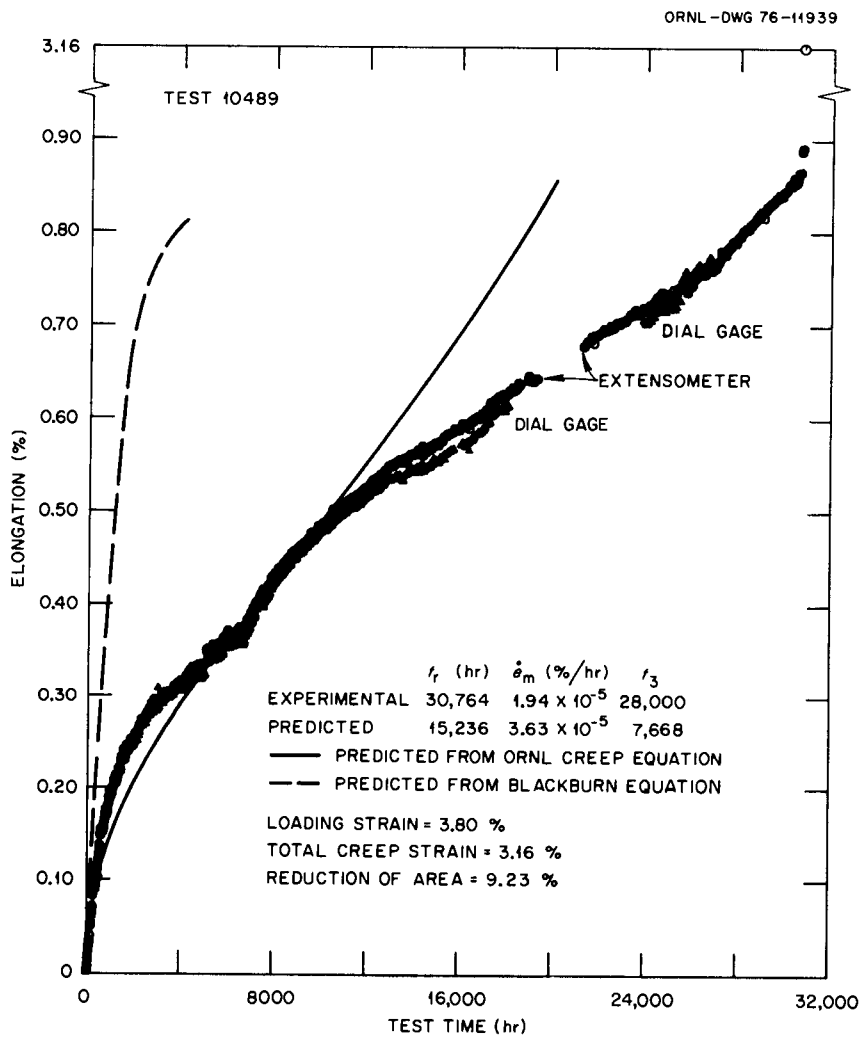


Fig. 3.1. Creep Curve for 51-mm (2-in.) Plate of Reannealed Reference Heat of Type 304 Stainless Steel. Specimen was tested at 538°C (1000°F) and 138 MPa (20 ksi).

derived from the ORNL single rational polynomial creep equation described previously[2] and in Sect. 3.2.4.1. The ORNL creep equation provides for predicting the creep behavior of individual heats by the knowledge of their elevated-temperature $S_u$. The creep curve in Fig. 3.1 was predicted by substituting $S_u$ = 358 MPa (51.9 ksi) in the creep equation.[2] For comparison, we have also included the creep curve predicted from the currently accepted[3] creep equation. This equation does not have any means of predicting the behavior of an individual heat. Several points of interest from Fig. 3.1 are:

1. only 0.8% strain to onset of tertiary creep ($e_3$), indicating thereby a significantly low ductility value at these creep conditions;
2. excellent agreement between the creep curve predicted from the ORNL creep equation and the observed curve;
3. improved predictability of ORNL equation as opposed to most accepted[3] current creep equations;
4. reasonably good agreement between predicted[1,2] and experimental values of $\dot{e}_m$, $t_r$, and $t_3$.

Figure 3.2 shows the ruptured specimen. Intergranular fracture and the absence of any necking are evident. Detailed metallography showing intergranular cracks is presented in Fig. 3.3 and 3.4. The high-magnification micrographs in Fig. 3.4 show the presence of round cavities at the grain boundaries and some indication of grain boundary precipitation. These micrographs showed no indication of intragranular deformation. We believe that round cavities at grain boundaries coalesced to cause intergranular fracture.

### 3.2.1.2 Influence of Strain Rate and Test Temperature on Ductility of Type 304 Stainless Steel — V. K. Sikka, R. W. Swindeman, C. R. Brinkman, and R. L. Stephenson*

Deciding strain limits for elevated-temperature design requires the understanding of the influence of strain rate and temperature, among other variables, on ductility. To obtain an overall picture we have initiated making three-dimensional plots of various ductility indices as functions of strain rate and test temperature. These indices include the following:

---

*Computer Sciences Division.

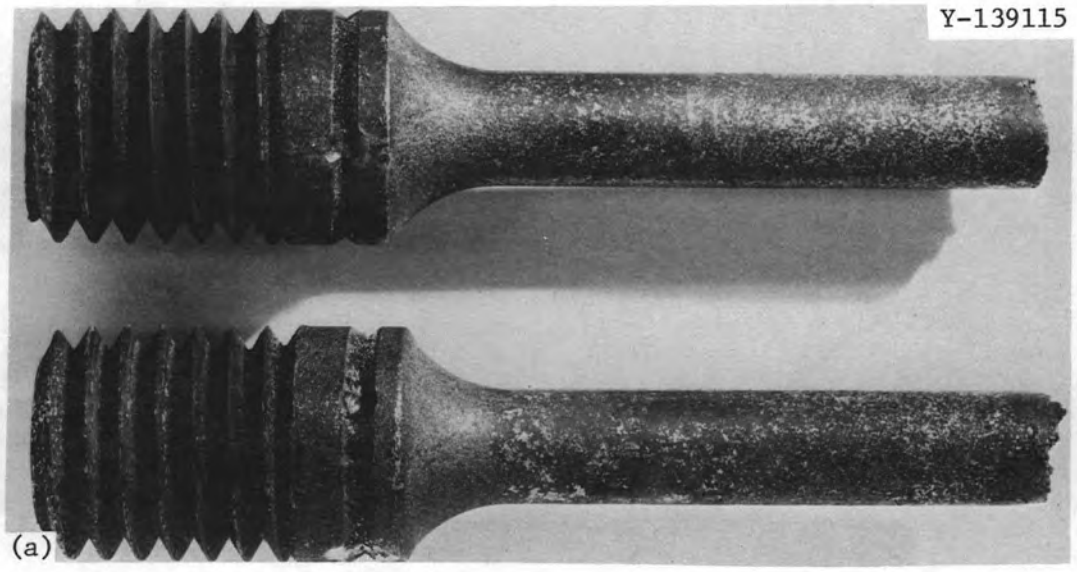


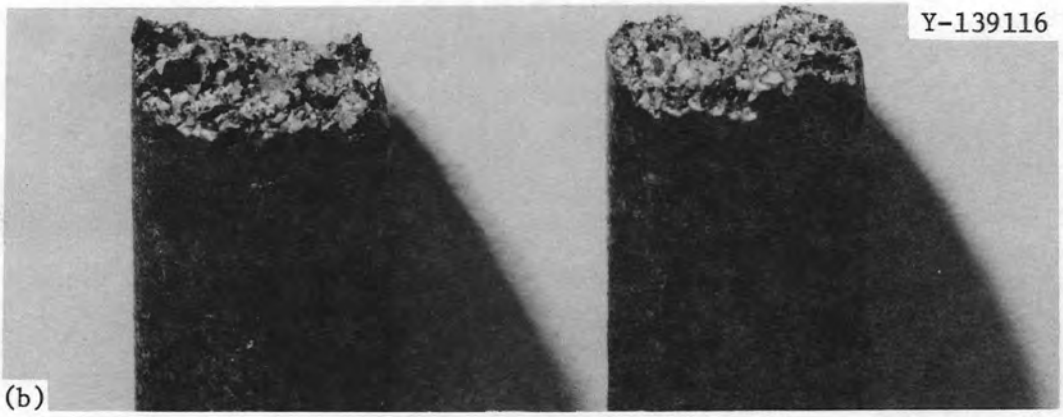


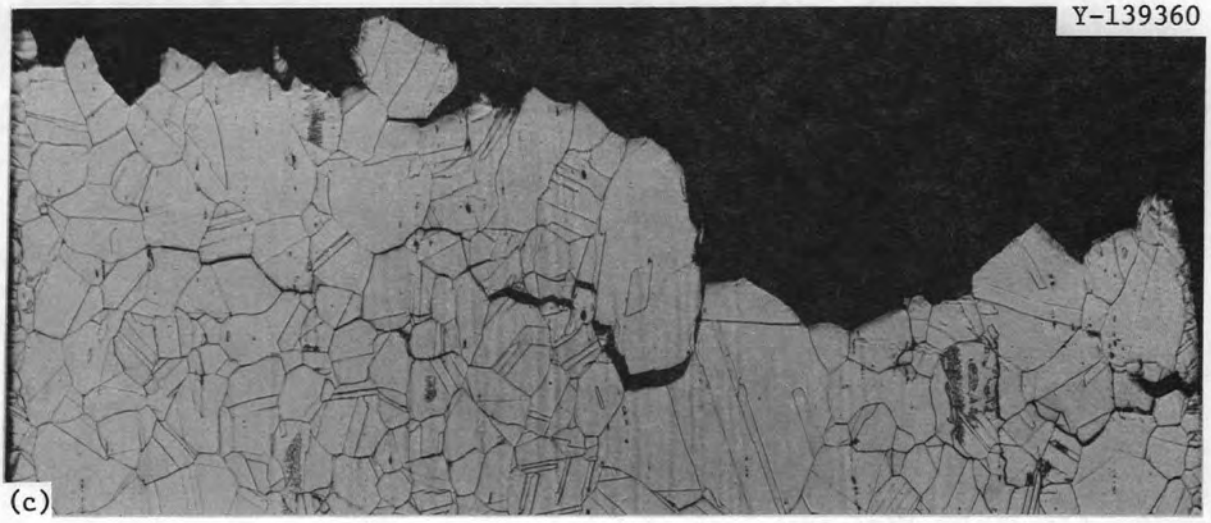


Fig. 3.2. Ruptured Specimen for Test Conditions Described in Fig. 3.1. (a) Side view, 2.3×. (b) Fracture surface, 5.8×. (c) Cross section, 18×, showing intergranular cracks.

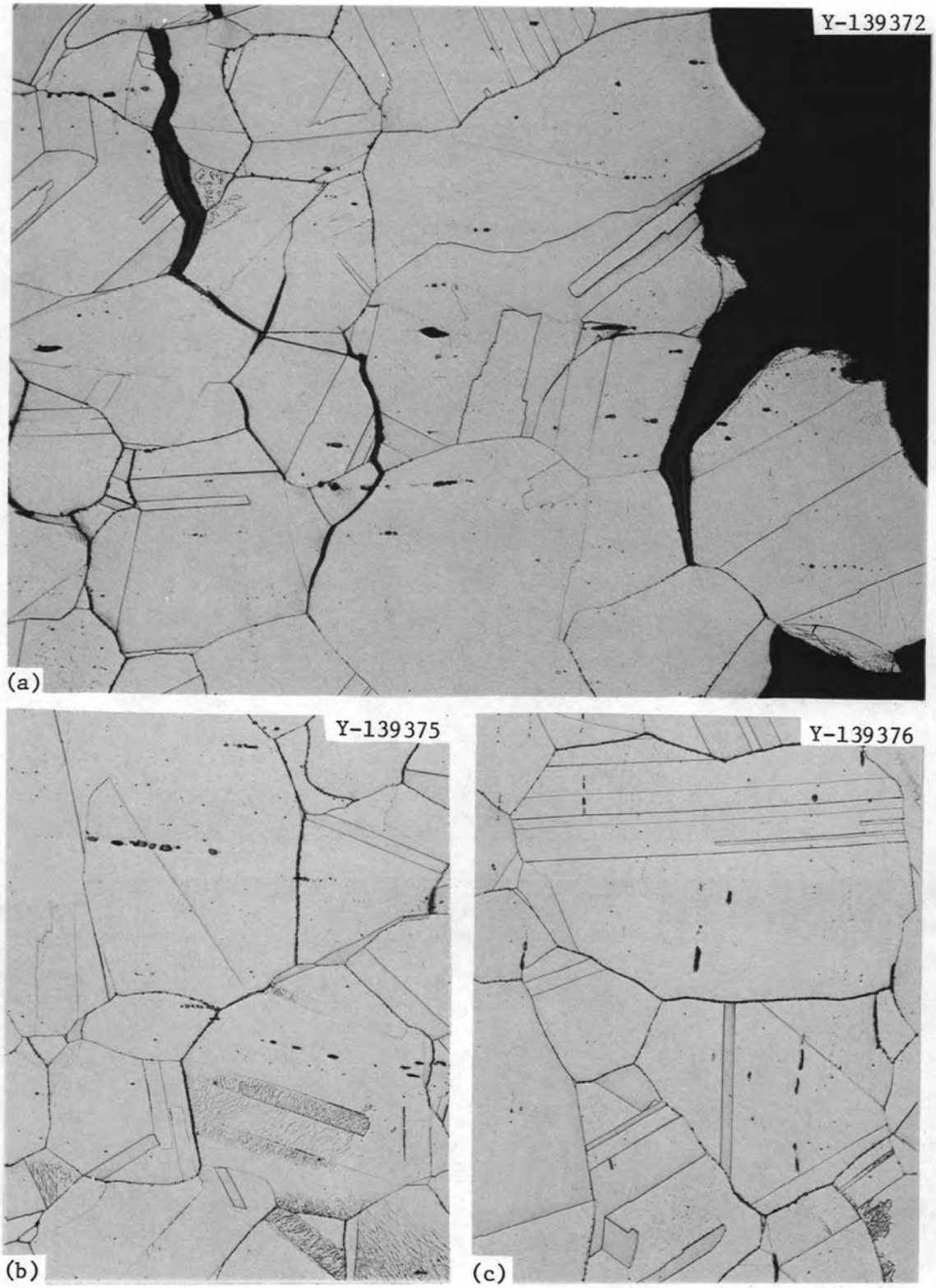


Fig. 3.3. Microstructure of Fractured Creep Specimen. 100×.
(a) Fracture surface. (b) 3 mm (1/8 in.) from fracture surface.
(c) Near end of gage section.

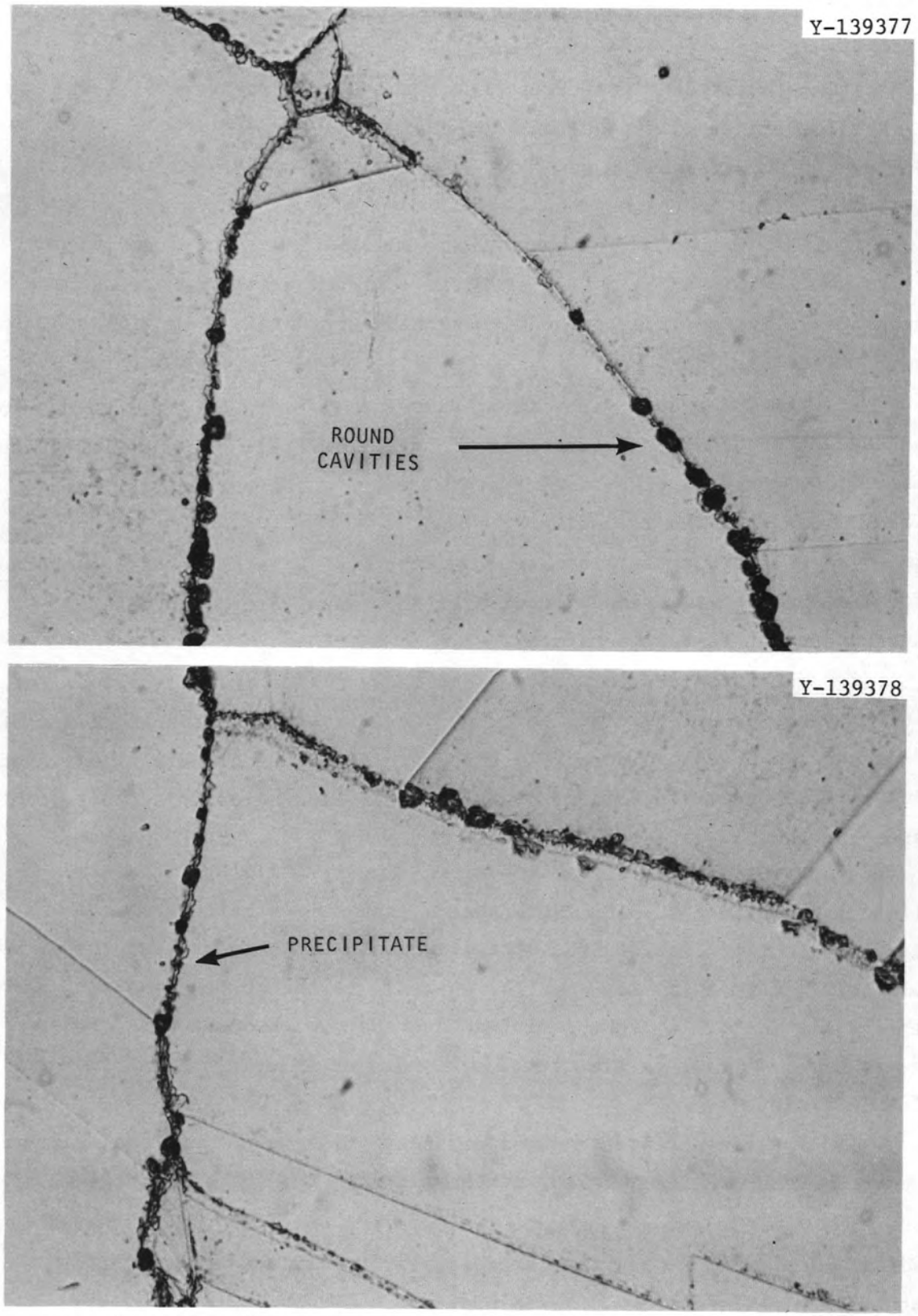


Fig. 3.4. Round Cavities and Precipitates at the Grain Boundaries in the Ruptured Creep Specimen. 100×.

1. uniform elongation for tensile tests and strain to onset of tertiary creep for the creep tests;
2. total elongation — for creep test total elongation refers to the sum of loading strain and elongation during creep;
3. reduction of area.

As a first approximation minimum creep rate is considered as the overall strain rate for creep ductility indices. Data used for these plots are on 25- and 51-mm (1- and 2-in.) plates of the reference heat of type 304 stainless steel. The high-strain-rate data are from Steichen's work[4,5] on heat 55697.

Figures 3.5 and 3.6 show three-dimensional plots of total elongation and reduction of area as functions of log strain rate and test temperature. Each figure shows a high-strain-rate view and a low-strain-rate view. These plots show the following:

1. On the high-strain-rate end (bottom of Figs. 3.5 and 3.6) both total elongation and reduction of area show high values, which are independent of test temperature.

2. The tensile strain rate range shows a loss in ductility in the intermediate temperature region. The ductility loss initiation temperature decreases with decreasing strain rate. This is more clearly illustrated in separate three-dimensional plots of total elongation and reduction of area for tensile data on 25- and 51-mm (1- and 2-in.) plates of the reference heat in Fig. 3.7 and in a two-dimensional plot for 25-mm (1-in.) plate in Fig. 3.8. Note that a change in strain rate from $1 \times 10^{-4}$ to 5/min shifted the ductility loss initiation temperature from 438 to 727°C (0.42 $T_m$ to 0.60 $T_m$), where $T_m$ is the absolute melting point (≈1673 K). Ductility at the minimum decreased with decreasing strain rate, and reduction of area reached a value of 22% at a strain rate of $1 \times 10^{-4}$/min.

3. The creep range shows significantly low values of total elongation and reduction of area. Values of these indices can be seen to reach as low as 10% or below. An example of low creep ductility is presented in Fig. 3.1, and the associated intergranular fracture is illustrated photographically in Figs. 3.2 through 3.4.

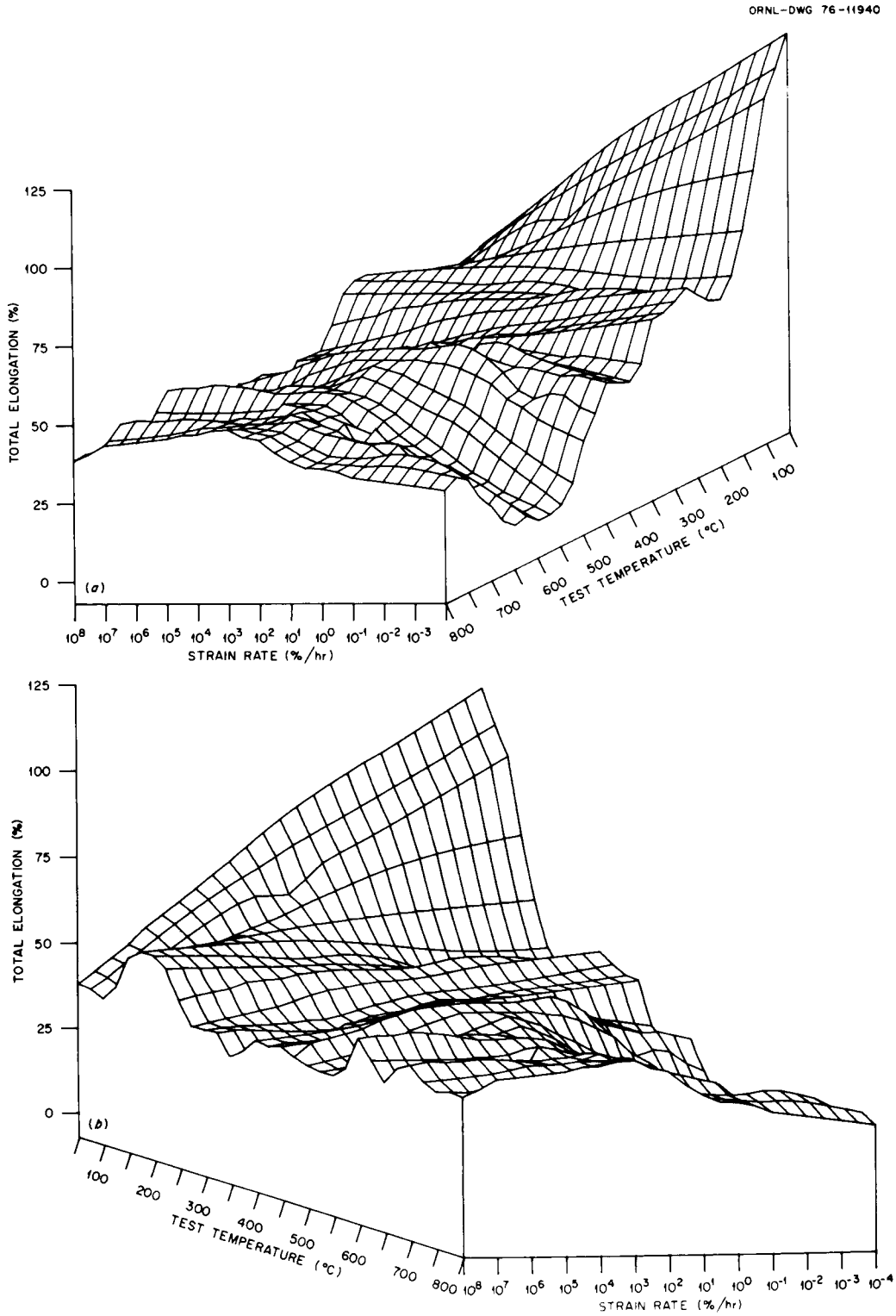


Fig. 3.5. Total Elongation (High Strain Rate, Tensile, and Creep) as a Function of Log Strain Rate and Test Temperature for Heats 55697 and 9T2796 of Type 304 Stainless Steel.

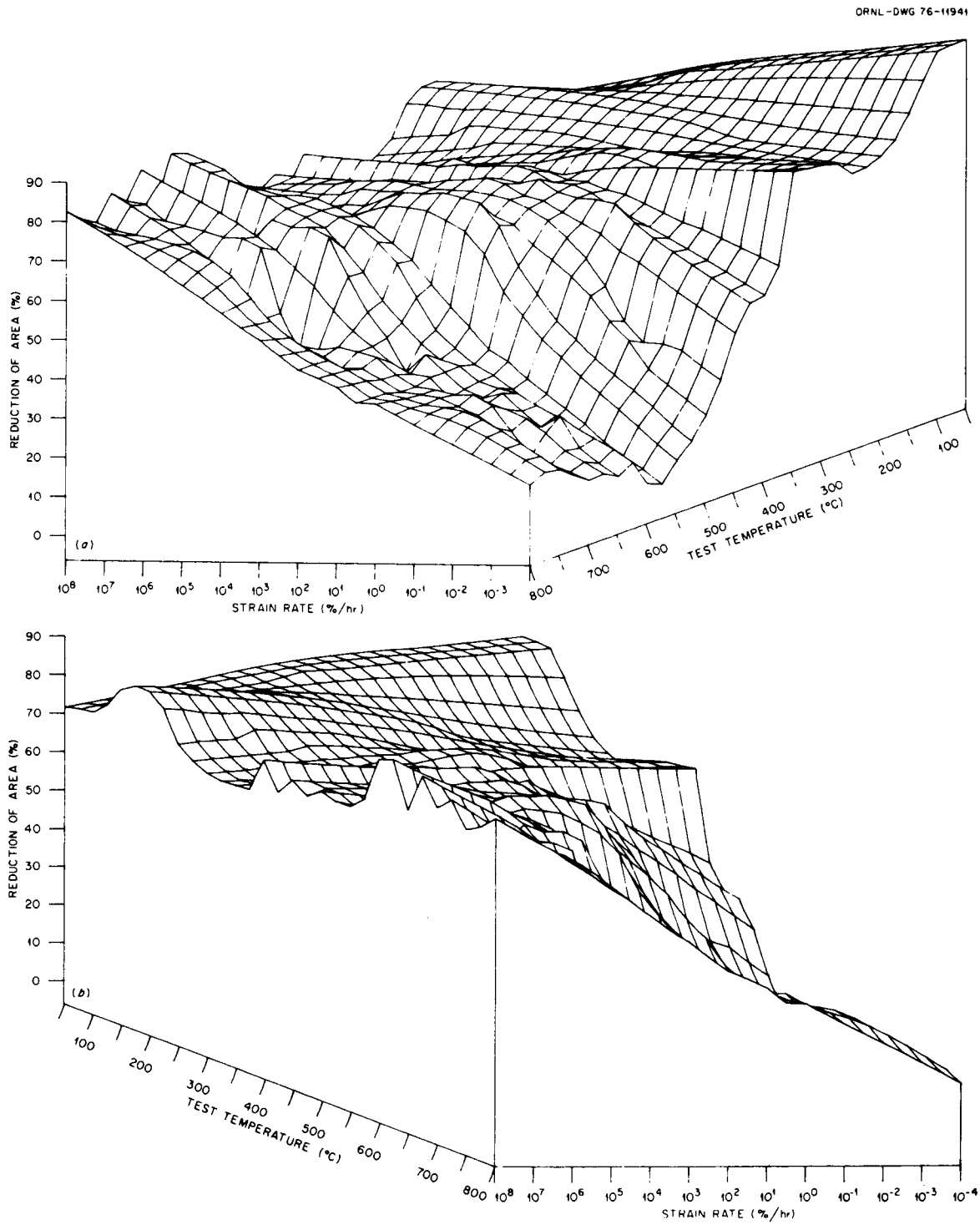


Fig. 3.6. Reduction of Area (High Strain Rate, Tensile, and Creep) as a Function of Log Strain Rate and Test Temperature for Heats 55697 and 9T2796 of Type 304 Stainless Steel.

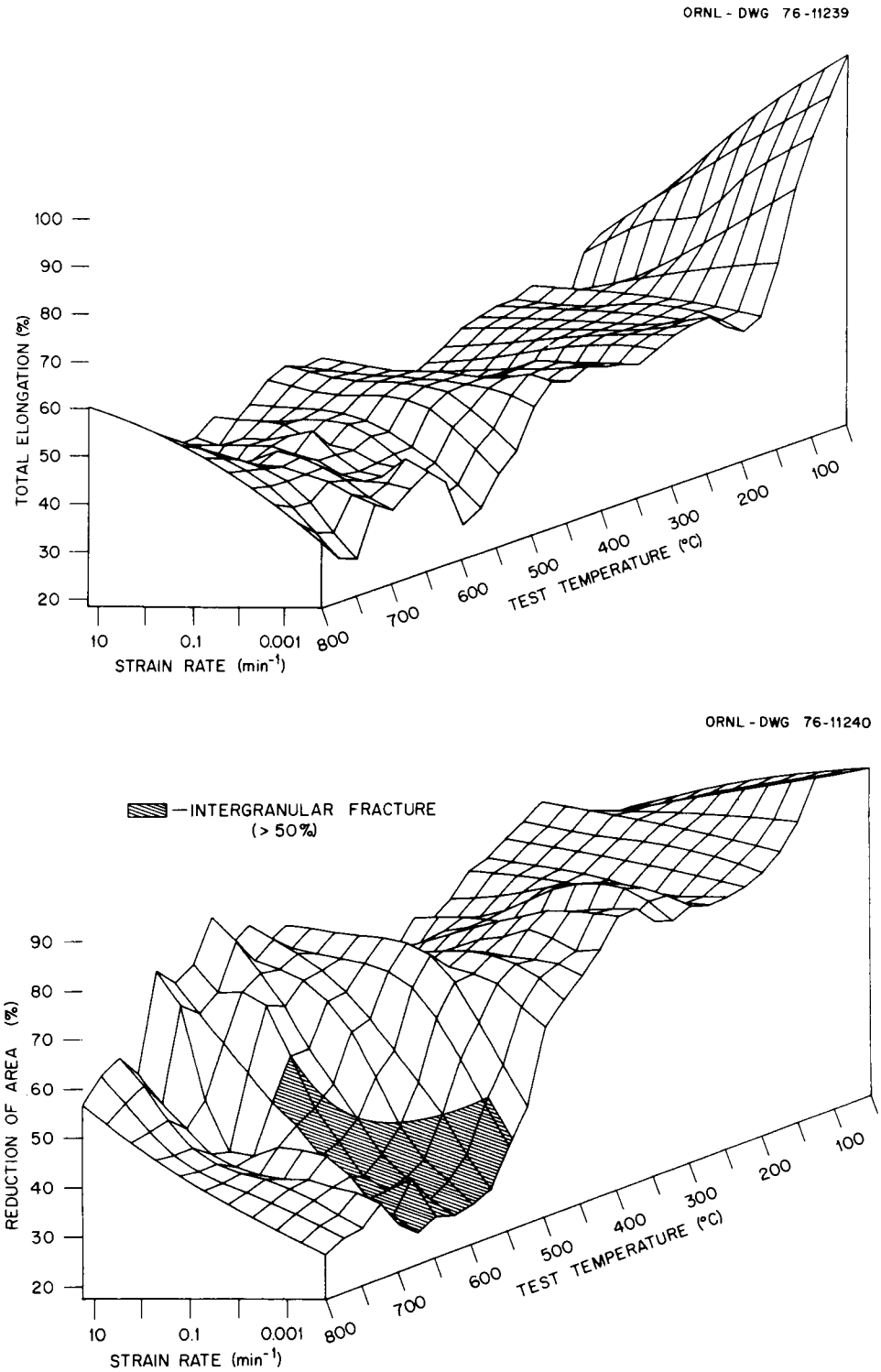


Fig. 3.7. Total Elongation and Reduction of Area as Functions of Log Strain Rate and Test Temperature for 25- and 51-mm (1- and 2-in.) Plates of Type 304 Stainless Steel.

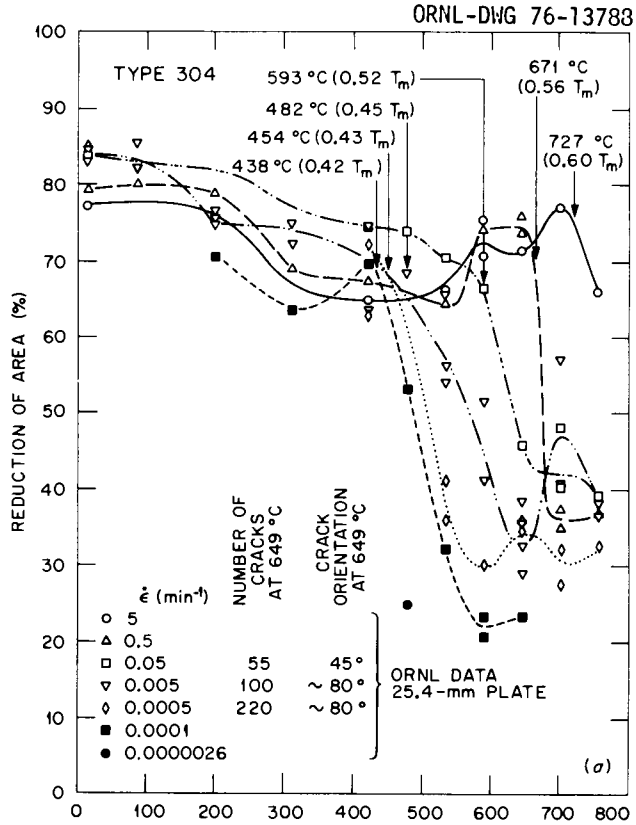


Fig. 3.8. Tensile Reduction of Area as a Function of Test Temperature for 25-mm (1-in.) Plate of the Reference Heat of Type 304.

Work is continuing to get three-dimensional plots of uniform elongation and strain to onset of tertiary creep as functions of strain rate and temperature and also to study the effects on tensile properties of other variables such as:

1. thermal aging,
2. grain size,
3. heat-to-heat variations,
4. cold work, and
5. prior creep deformation.

Similar studies will also be performed on type 316 stainless steel.

### 3.2.2 Mechanical Property Characterization of Type 316 Stainless Steel Reference Heat — V. K. Sikka, R. H. Baldwin, and E. B. Patton

#### 3.2.2.1 Tensile Data

Product form characterization of the reference heat (8092297) of type 316 stainless steel began. Tensile tests have been completed on six different products at room temperature. True stress-strain curves for these tests are shown in Fig. 3.9. The figure indicates that the 0.2% yield strength of various products can vary from 216 to 324 MPa (31.3 to 47.0 ksi). Furthermore, the bar shows higher yield strength than the plate, which is consistent with the previous work[6,7] on type 304 stainless steel. It should be pointed out that all products in the mill-annealed condition showed yield strength values above the ASTM material specifications of 207 MPa (30 ksi) at room temperature.

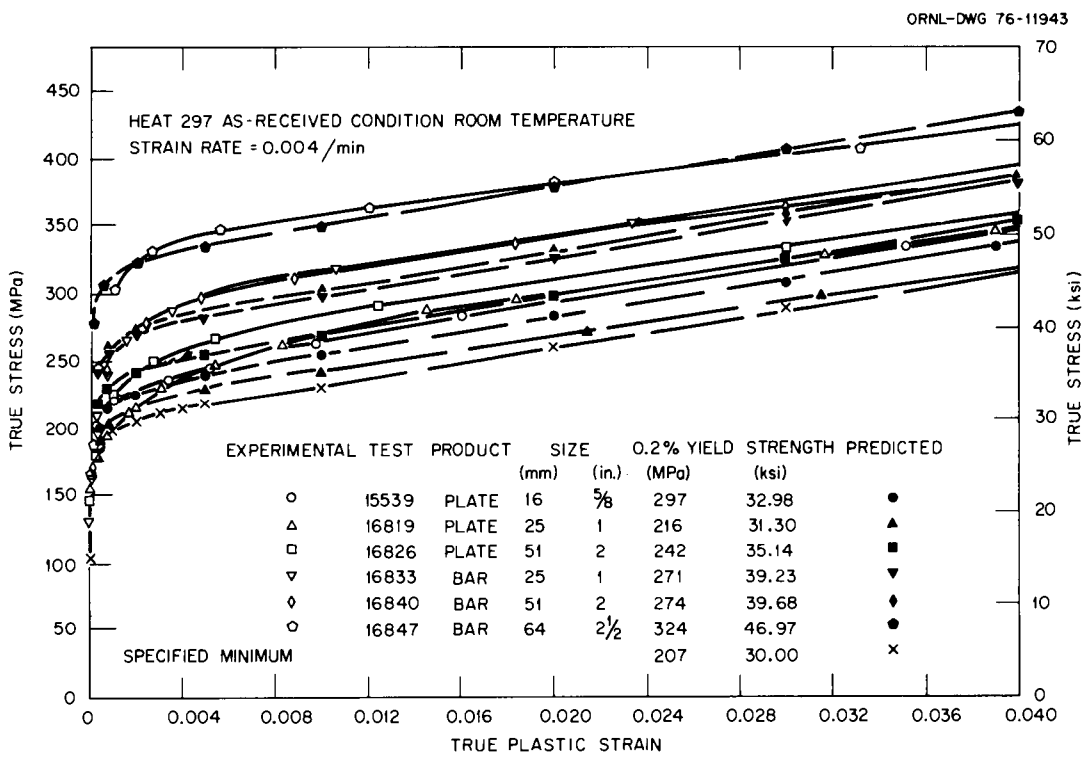


Fig. 3.9. Product Form Variation in the True Stress-Strain Curve of Heat 8092297 of Type 316 Stainless Steel at Room Temperature.

Included in Fig. 3.9 are the true stress-strain plots predicted from ORNL rational polynomial tensile stress-strain equation.[8] Note that predicted values are in excellent agreement with experimental values for six different products. These comparisons provide additional support in that the equation based on a single product form can indeed be extended to several different products.

Tensile testing is continuing on other products.

### 3.2.2.2 Creep Properties

Creep testing of 16-mm (5/8-in.) plate of the reference heat of type 316 stainless steel continued. All creep tests have been updated and are summarized in Table 3.2. The longest test time has exceeded 7000 hr. The table shows that most of the tests are being carried out at stresses and temperatures for which data are limited in the literature.

Table 3.2. Summary of Creep Tests on Type 316 Stainless Steel Reference Heat 8092297 16-mm-Thick (5/8-in.) Plate[a]

| Test | Temperature | | Stress | | Time in Test[b] (hr) | Strain (%) | | Comments |
|---|---|---|---|---|---|---|---|---|
| | (°C) | (°F) | (MPa) | (ksi) | | Loading | Creep | |
| 16019 | 538 | 1000 | 97 | 14 | 5770.9 | 0.071 | 0.080 | |
| 15891 | 538 | 1000 | 110 | 16 | 3000.0 | 0.126 | 0.055 | Discontinued |
| 17119 | 538 | 1000 | 138 | 20 | 929.1 | 0.414 | 0.070 | |
| 15791 | 538 | 1000 | 179 | 26 | 1800.0 | 2.20 | C 275 | Discontinued |
| 17178 | 538 | 1000 | 276 | 40 | .169.8 | 7.41 | 0.360 | |
| 17135 | 538 | 1000 | 276 | 40 | 289.2 | 8.03 | 0.595 | Discontinued |
| 16100 | 565 | 1050 | 69 | 10 | 1626.0 | 0.070 | 0.014 | Discontinued |
| 16357 | 565 | 1050 | 69 | 10 | 3394.4 | 0.059 | 0.060 | |
| 16384 | 565 | 1050 | 172 | 25 | 3060.2 | 2.25 | 0.680 | |
| 16265 | 565 | 1050 | 207 | 30 | 1908.7 | 3.83 | 2.80 | Discontinued |
| 16739 | 565 | 1050 | 207 | 30 | 1763.0 | 3.91 | 1.33 | |
| 16099 | 565 | 1050 | 276 | 40 | 750.3 | 8.63 | 14.0 | Ruptured |
| 15607 | 593[c] | 1100 | 207 | 30 | 831.1 | 3.93 | 34.3 | Ruptured |
| 16279 | 593 | 1100 | 207 | 30 | 3246.0 | 3.91 | 17.8 | Ruptured |
| 16365 | 649 | 1200 | 69 | 10 | 3203.0 | 0.053 | 5.71 | |
| 15842 | 649 | 1200 | 97 | 14 | 7044.7 | 0.139 | 19.0 | |
| 15594 | 649 | 1200 | 124 | 18 | 1983.0 | 0.540 | 16.8 | Discontinued |
| 15538 | 649 | 1200 | 138 | 20 | 1884.2 | 0.790 | 44.4 | Ruptured |
| 15460 | 649 | 1200 | 207 | 30 | 110.2 | 4.27 | 40.2 | Ruptured |
| 15889 | 704 | 1300 | 83 | 12 | 234.0 | 0.0303 | 12.6 | Ruptured |
| 15593 | 760 | 1400 | 97 | 14 | 100.0 | 0.083 | 90.6 | Ruptured |

[a]All tests are being performed for plate in the as-received (mill-annealed) condition.

[b]Unless otherwise noted, tests are in progress.

[c]Shorter rupture time and high creep strain as compared with test 16279 indicate temperature controller malfunctioning.

### 3.2.3 Heat-to-Heat Variations of Mechanical Properties of Austenitic Stainless Steels of Types 304 and 316 — Time to Rupture and Minimum Creep Rate Modeling for Type 304 Stainless Steel — V. K. Sikka

Heat-to-heat variations in rupture life ($t_r$), minimum creep rate ($\dot{e}_m$), and creep curves for 20 heats of type 304 stainless steel are shown in Figs. 3.10 through 3.12. Following are the order of magnitude of variations in these quantities:

$t_r$ — For a given stress and temperature, $t_r$ can vary by factors of 40 to 50. Figure 3.10 shows that the orders of magnitude of variation are approximately the same for all test temperatures.

Creep Curves — Figure 3.12(a) and (b) illustrate the magnitude of variations that can be expected.

In general, large factors of variation in short-term data appear reduced in the long-term data. However, this is probably because so few data are available for such long test times.

Previous reports[9-12] showed the usefulness of elevated-temperature ultimate tensile strengths ($S_u$) in correlating and predicting creep properties. We have now determined generalized models of $t_r$ and $\dot{e}_m$ in terms of stress ($S$), temperature ($T$) and $S_u$. The generalized model development was restricted to ORNL and Blackburn[13] data because these were the only data for which $S_u$ values were known at the creep test temperature and at a single strain rate of $6.67 \times 10^{-4}$/sec. The available $t_r$ and $\dot{e}_m$ data (205 and 226 points) from these two sources were subjected to a systematic analysis involving a generalized set of algebraic models for log $t_r$ and log $\dot{e}_m$ as functions of $S$, $T$, and $S_u$. The final choice of the models was based on

1. least squares fit to the entire set of data,
2. prediction of long-time ($t_r$ > 2000 hr) or low-rate ($\dot{e}_m$ < 0.001 %/hr) data from fits to short-time or high-rate data, and
3. simplicity and physical reasonableness of the models.

The entire modeling procedure is described in detail elsewhere.[2] The final models chosen for type 304 stainless steel were:

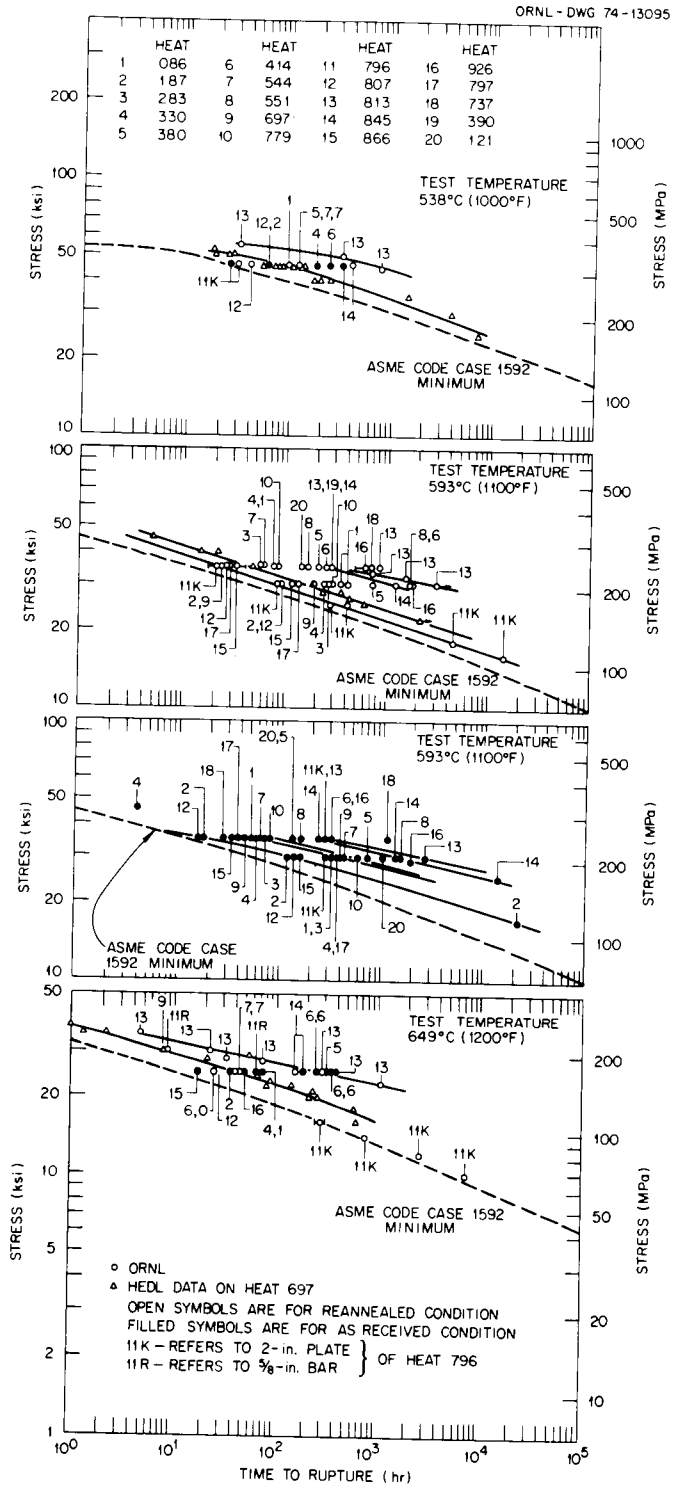


Fig. 3.10. Heat-to-Heat Variations in Stress-Rupture Data at 538, 593, and 649°C (1000, 1100, and 1200°F) for 20 Heats of Type 304 Stainless Steel in Both As-Received and Reannealed Conditions. ASME Code Case 1592 minimum value curves are included for comparison.

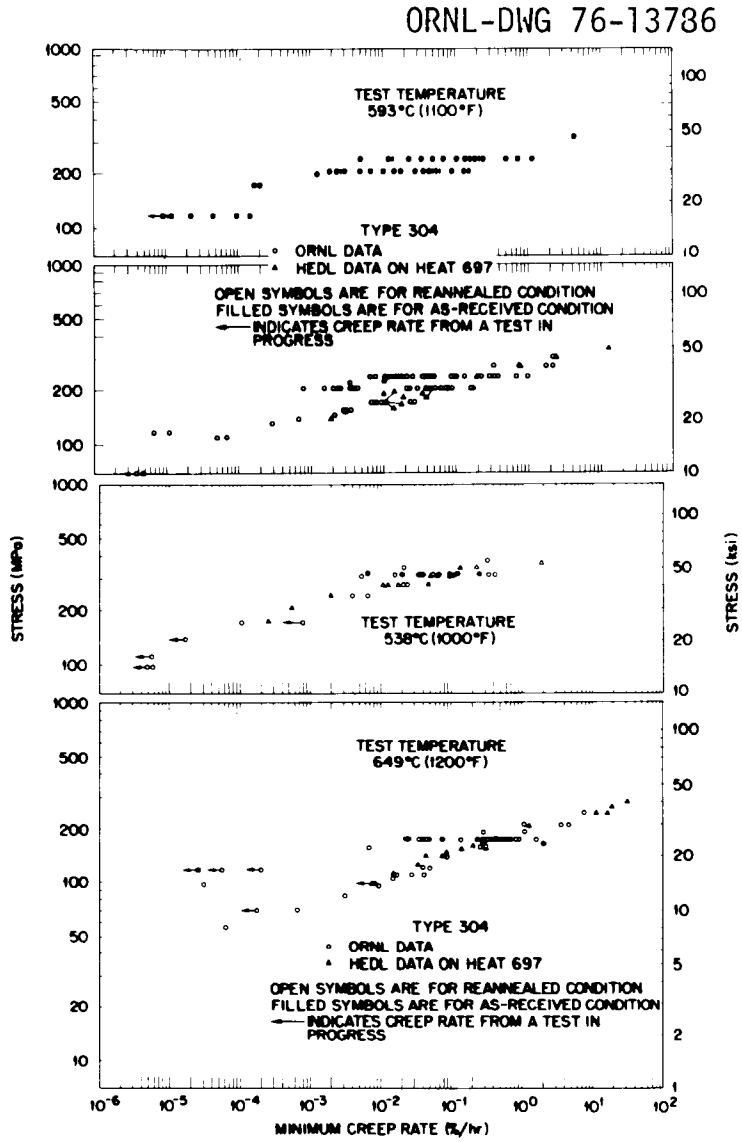


Fig. 3.11. Heat-to-Heat Variations in Minimum Creep Rate Data at 538, 593, and 649°C (1000, 1100, and 1200°F) for 20 Heats of Type 304 Stainless Steel in Both As-Received and Reannealed Conditions.

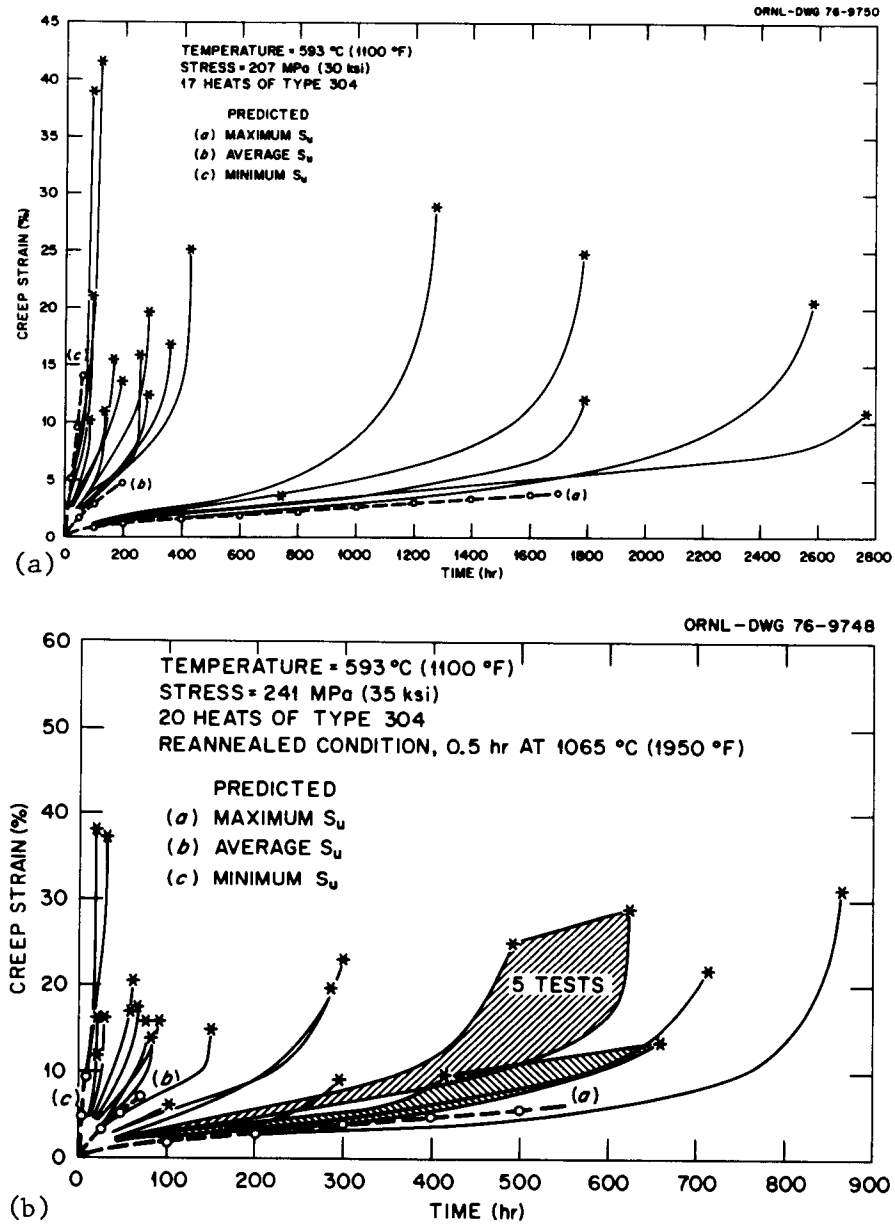


Fig. 3.12. Heat-to-Heat Variations in Creep Curves of Several Reannealed Heats of Type 304 Stainless Steel. (a) Creep tests at 241 MPa (35 ksi) and 593°C (1100°F). (b) Creep tests at 207 MPa (30 ksi) and 593°C (1100°F).

$$\log t_r = 5.716 - 3915 \frac{(\log S)}{T} + 32.60 \frac{S_u}{T} - 0.007303\, S_u \log S \qquad (1)$$

$$\log \dot{e}_m = -2.765 + 3346 \frac{(\log S)}{T} - 51.84 \frac{S_u}{T} + 0.0616\, S_u \log S \qquad (2)$$

for $S$ and $S_u$ in MPa and $T$ in K. Interestingly, Eqs. (1) and (2) are of the same form, both $\log t_r$ and $\log \dot{e}_m$ being linear in $\log S$. The analysis of the same $t_r$ and $\dot{e}_m$ data showed[2] that for models not containing the $S_u$ term, these properties could be represented by:

$$\log t_r = -7.889 - 2.395 \log S - 0.00866\, S + 15324/T \qquad (3)$$

$$\log \dot{e}_m = 15.42 + 3.542 \log S + 0.011199\, S - 23882/T \qquad (4)$$

Figure 3.13 illustrates the plots of predicted versus experimental values of $t_r$ and $\dot{e}_m$ from the models both with and without $S_u$ [Eqs. (1) through (4)]. The improvement in prediction by models with $S_u$ is reflected by the improvement in values of the standard error of estimate (SEE) and the coefficient of determination ($R^2$), Table 3.3. Improvement in predicting $t_r$ and $\dot{e}_m$ of individual heats from Eqs. (1) and (2) is illustrated in Figs. 3.14 through 3.21. These figures indicate that models with $S_u$ predict the experimental data much better than the models without $S_u$. Figures 3.22 through 3.24 compare experimental and predicted values of $t_r$ and $\dot{e}_m$ for a fixed stress and temperature. Again the generalized model, Eqs. (1) and (2), predicts excellently the observed trends.

Equations (1) and (2) can be used to predict the average, minimum, and maximum properties, based on corresponding values of $S_u$. The mean value of $S_u$ as a function of temperature for type 304 stainless steel was predicted from:

$$S_u = 639.2 - 1.813\, T_c + 0.00525\, T_c^{\,2} - 5.068 \times 10^{-6}\, T_c^{\,3} \qquad (5)$$

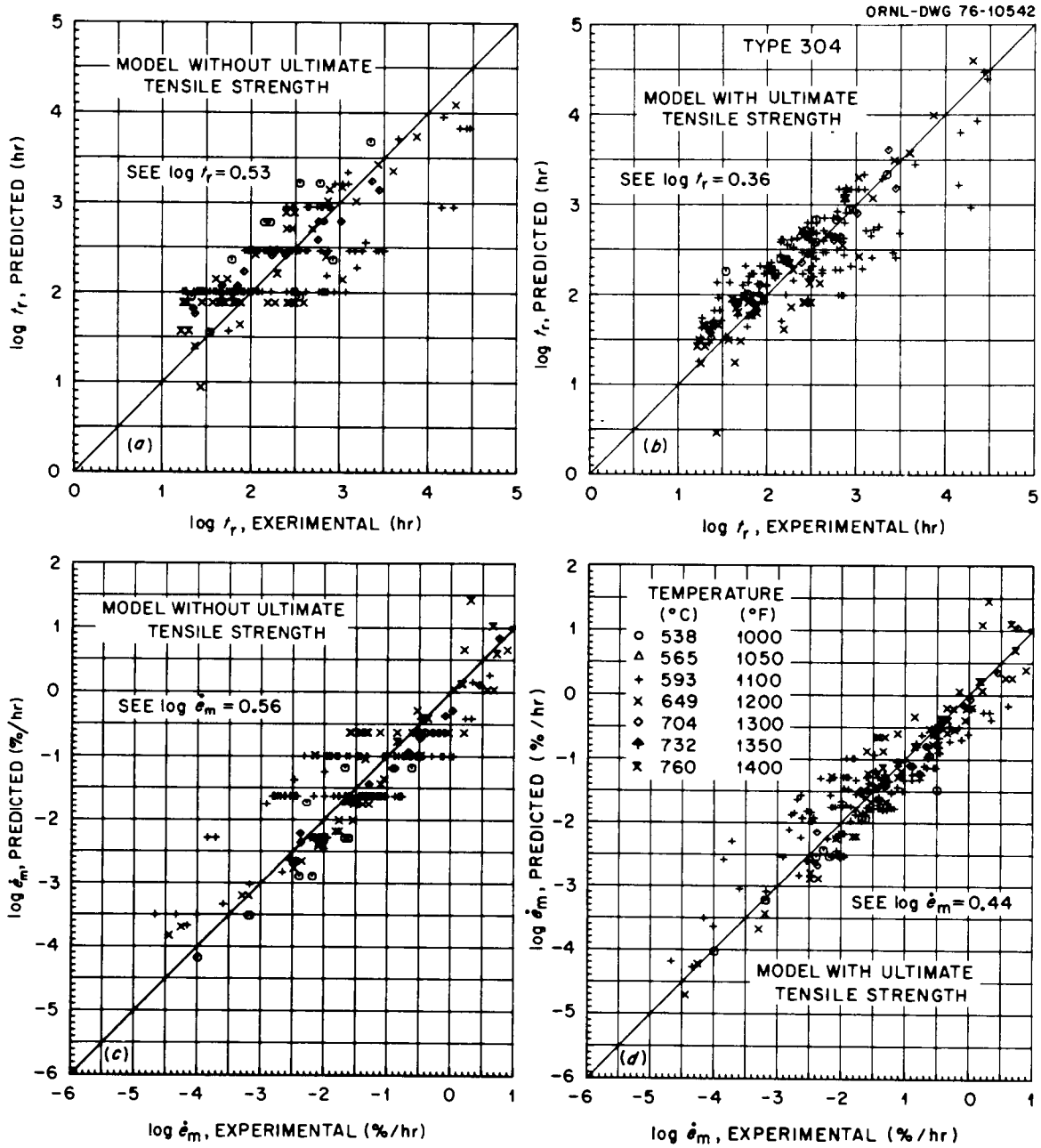


Fig. 3.13. Comparison of Experimental Time to Rupture and Minimum Creep Rate with Predicted Results from Models With and Without Ultimate Tensile Strength for 20 Heats of Type 304 Stainless Steel.

Table 3.3. Summary of the Coefficient of Determination ($R^2$) and Standard Error of Estimate (SEE) for ORNL Data on Type 304 Stainless Steel

| Model | Equation | Data Points | Property | $R^2$ (%) | SEE (log $t_r$) or (log $\dot{e}_m$) |
|---|---|---|---|---|---|
| Without $S_u$ | (3) | 205 | $t_r$ | 56.19 | 0.53 |
| With $S_u$ | (1) | 205 | $t_r$ | 73.37 | 0.36 |
| Without $S_u$ | (4) | 226 | $\dot{e}_m$ | 73.84 | 0.56 |
| With $S_u$ | (2) | 226 | $\dot{e}_m$ | 83.67 | 0.44 |

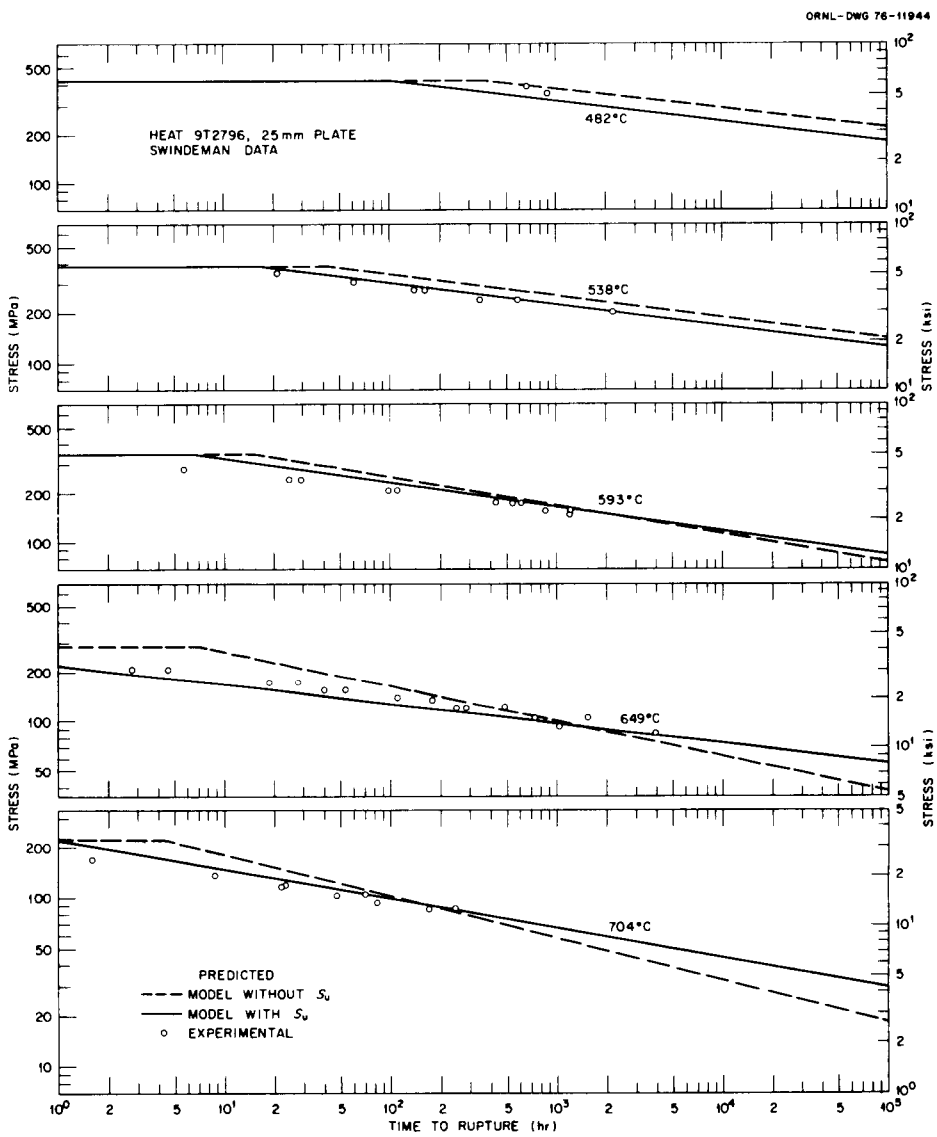


Fig. 3.14. Comparison of Experimental Time to Rupture with Values Computed from Models With and Without Elevated Temperature Ultimate Temperature Strength ($S_u$) for 25-mm (1-in.) Plate of Reannealed Reference Heat of Type 304 Stainless Steel.

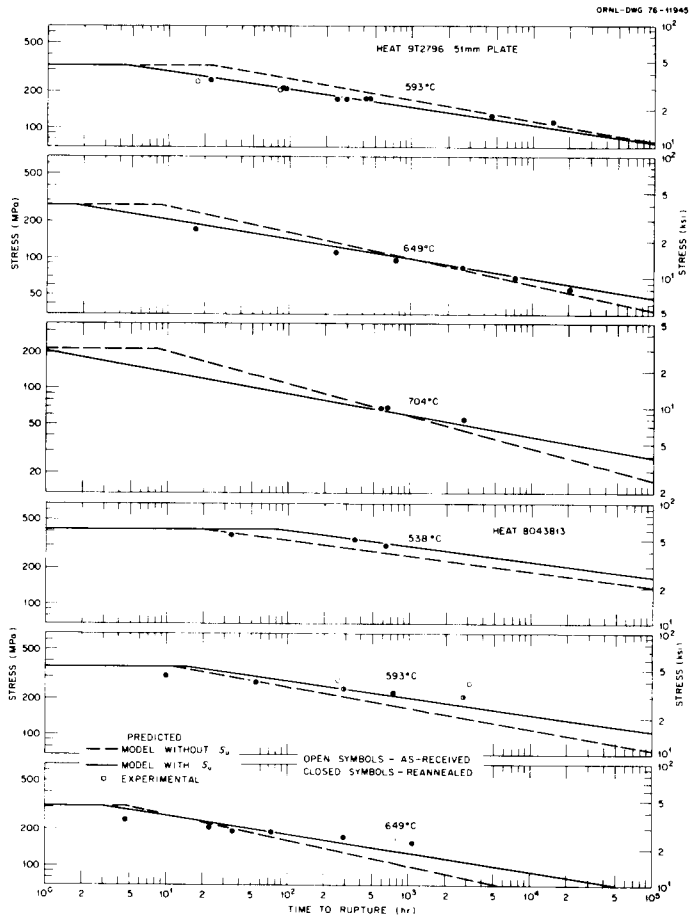


Fig. 3.15. Comparison of Experimental Time to Rupture with Values Computed from Models With and Without Elevated-Temperature Ultimate Tensile Strength ($S_u$) for a Weak (9T2796) and a Strong Heat (8043813).

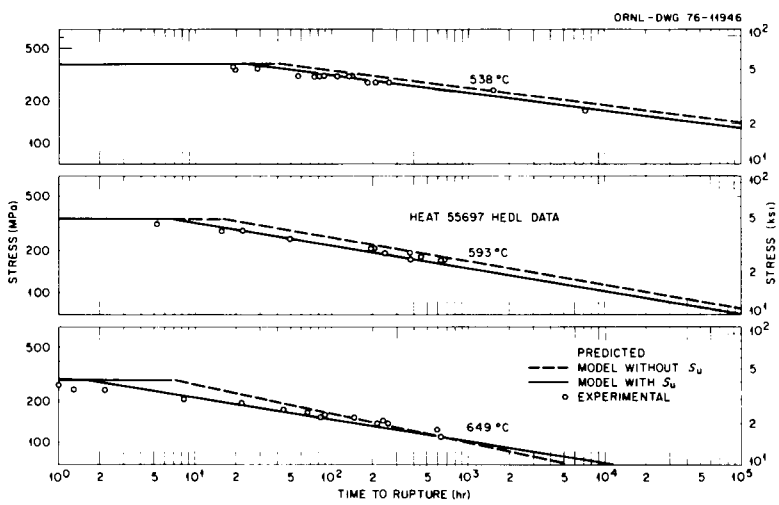


Fig. 3.16. Comparison of Experimental Time to Rupture with Values Computed from Models With and Without Elevated-Temperature Ultimate Tensile Strength ($S_u$) for HEDL Data on Reannealed Heat 55697.

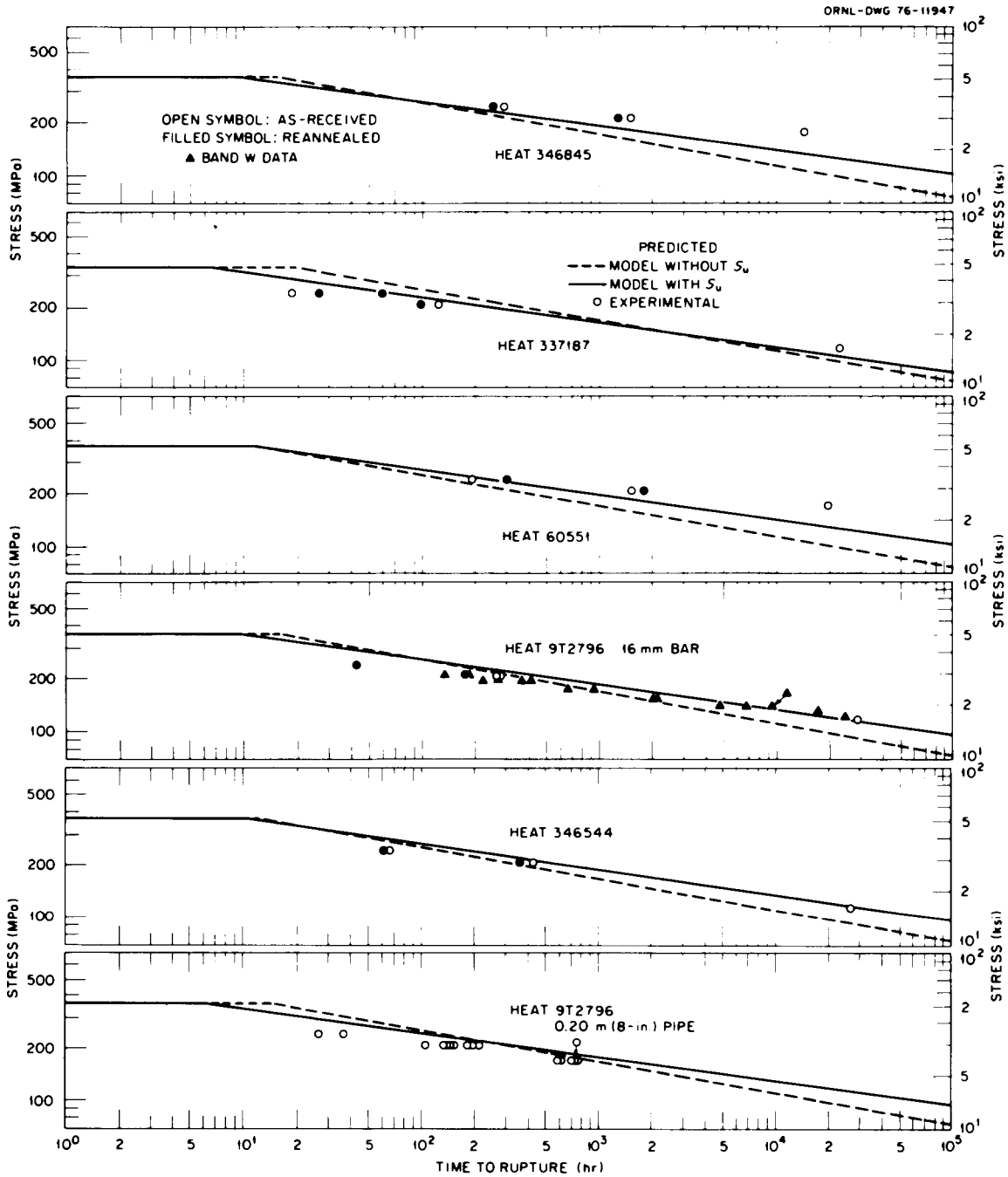


Fig. 3.17. Comparison of Experimental Time to Rupture with Values Computed from Models With and Without Elevated-Temperature Ultimate Tensile Strength ($S_u$) for Several Heats of Type 304 Stainless Steel at 593°C.

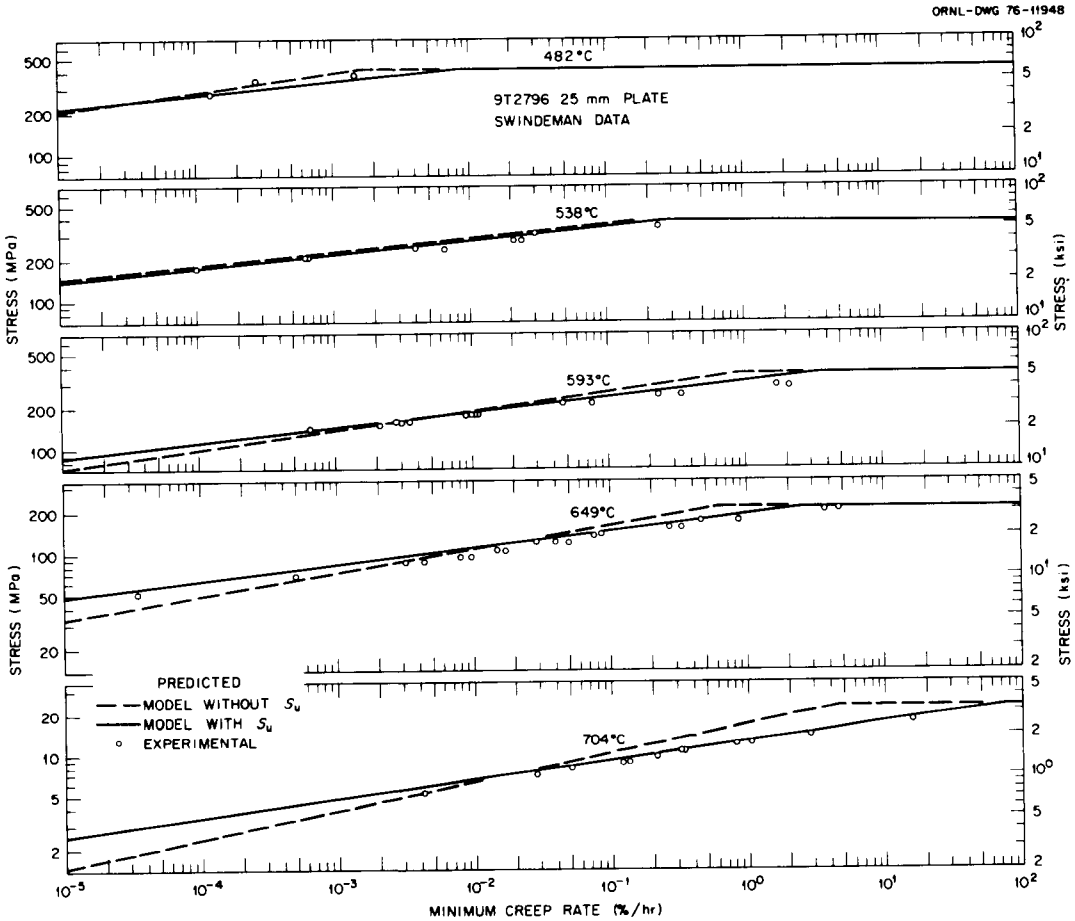


Fig. 3.18. Comparison of Experimental Minimum Creep Rate With Values Computed from Models With and Without Elevated-Temperature Ultimate Tensile Strength ($S_u$) for 25-mm (1-in.) Plate of Reannealed Reference Heat of Type 304 Stainless Steel.

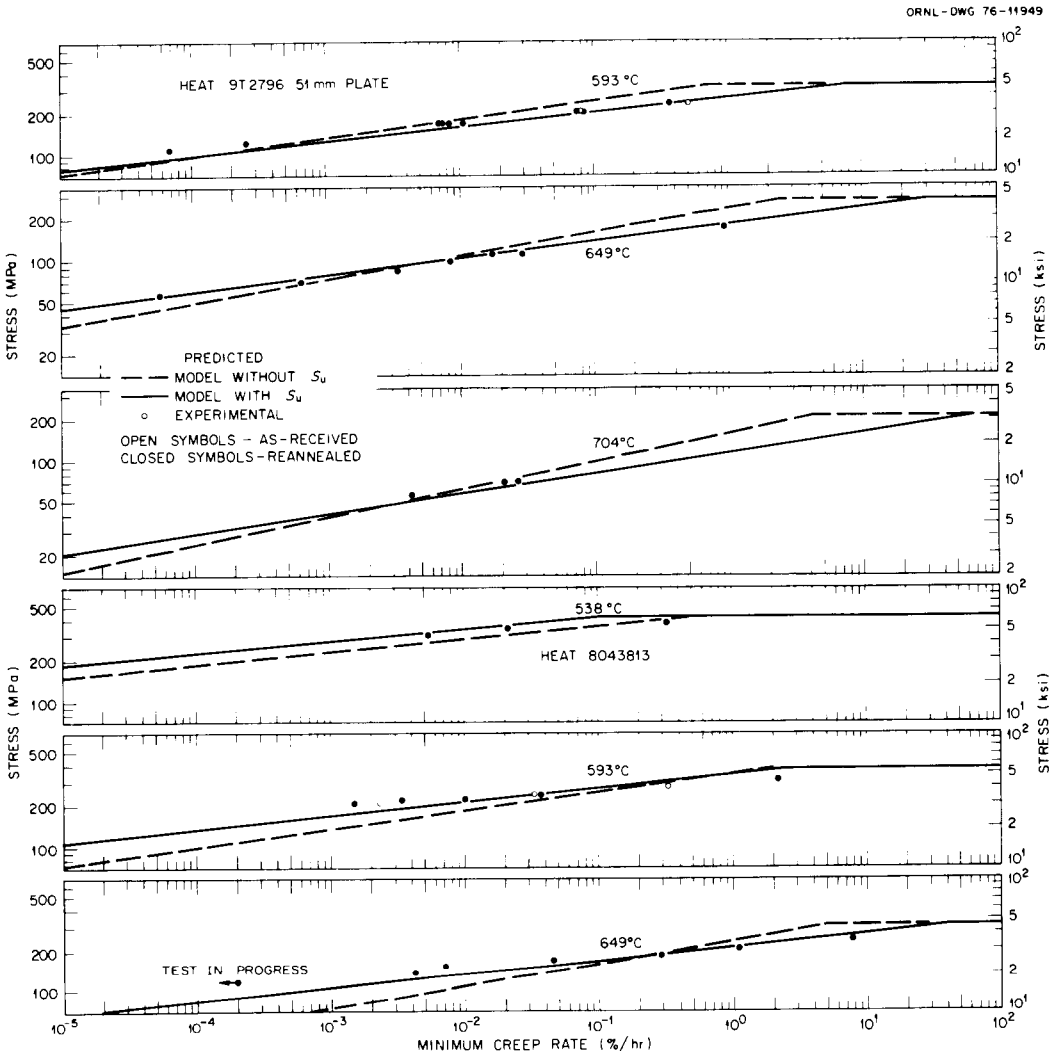


Fig. 3.19. Comparison of Experimental Minimum Creep Rate With Values Computed from Models With and Without Elevated-Temperature Ultimate Tensile Strength ($S_u$) for a Weak (9T2796) and a Strong Heat (8043813).

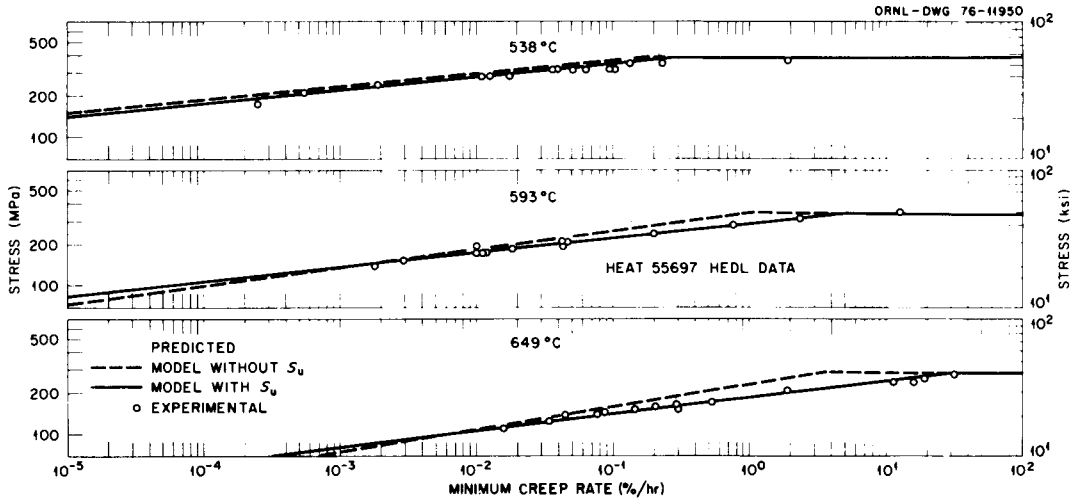


Fig. 3.20. Comparison of Experimental Minimum Creep Rate With Values Computed from Models With and Without Elevated-Temperature Ultimate Tensile Strength ($S_u$) for HEDL Data on Reannealed Heat 55697.

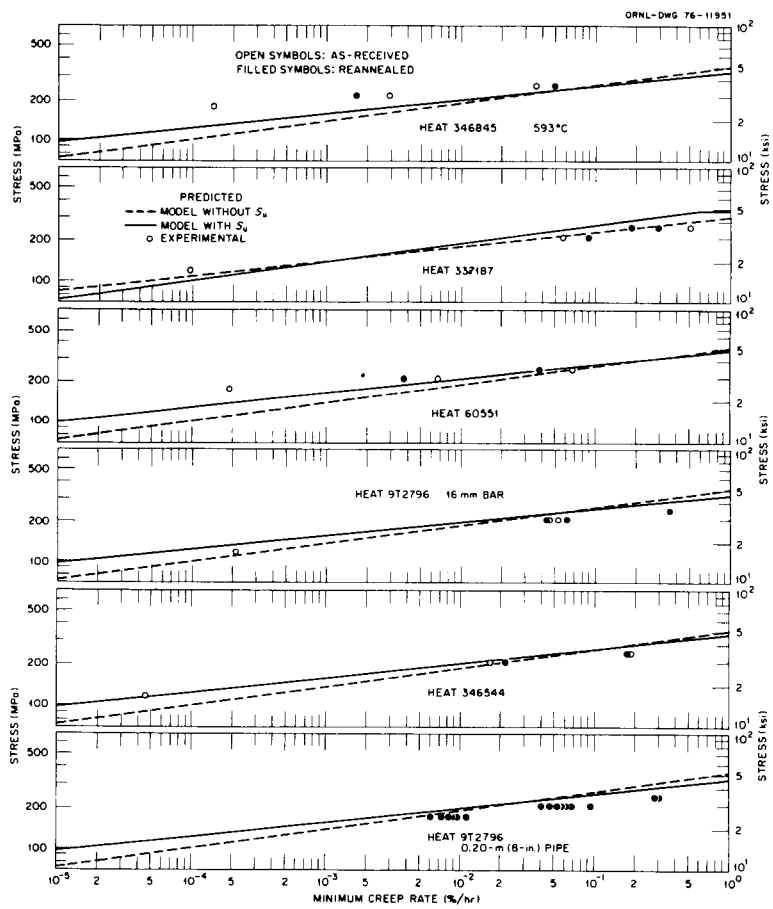


Fig. 3.21. Comparison of Experimental Minimum Creep Rate With Values Computed from Models With and Without Elevated-Temperature Ultimate Tensile Strength ($S_u$) for Several Heats of Type 304 Stainless Steel.

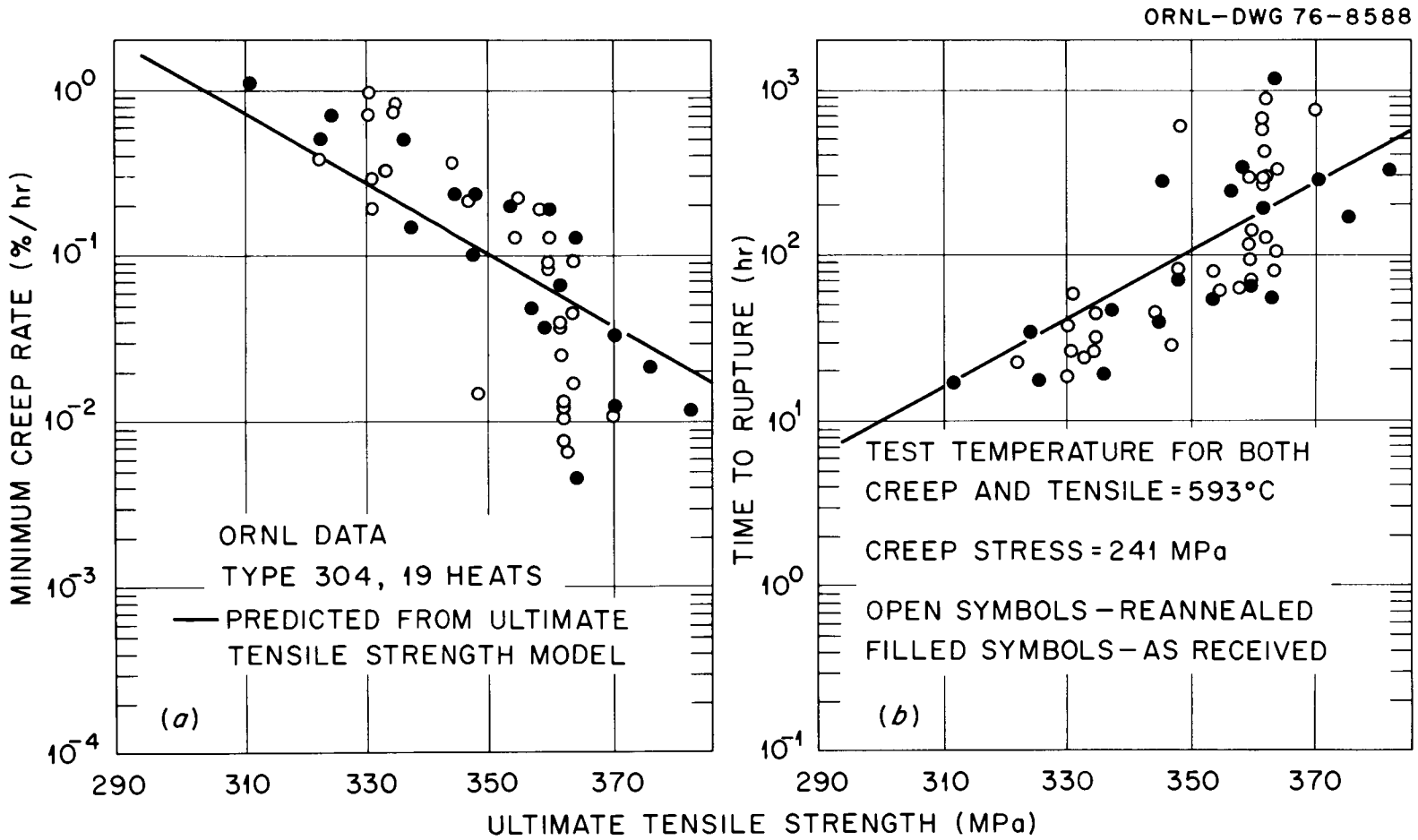


Fig. 3.22. Comparison of Experimental Time to Rupture as a Function of Elevated-Temperature Ultimate Tensile Strength ($S_u$) With Values Predicted from Rupture Model With $S_u$ for Different Heats of Type 304 Stainless. Tests were at 593°C (1100°F) and 241 MPa (35 ksi).

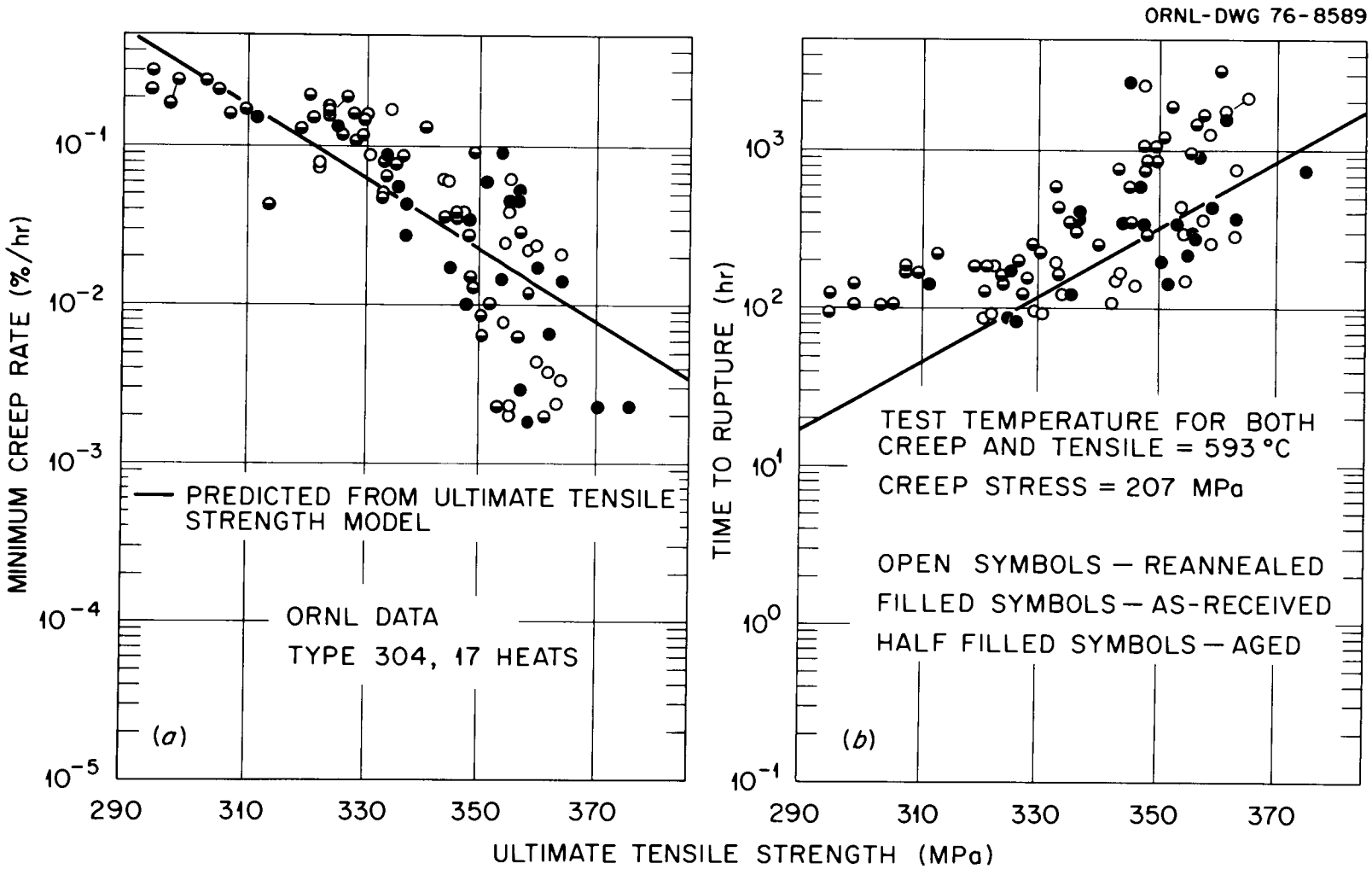


Fig. 3.23. Comparison of Experimental Time to Rupture as a Function of Elevated-Temperature Ultimate Tensile Strength ($S_u$) With Values Predicted from Rupture Model With $S_u$ for Different Heats of Type 304 Stainless. Tests were at 593°C (1100°F) and 207 MPa (30 ksi).

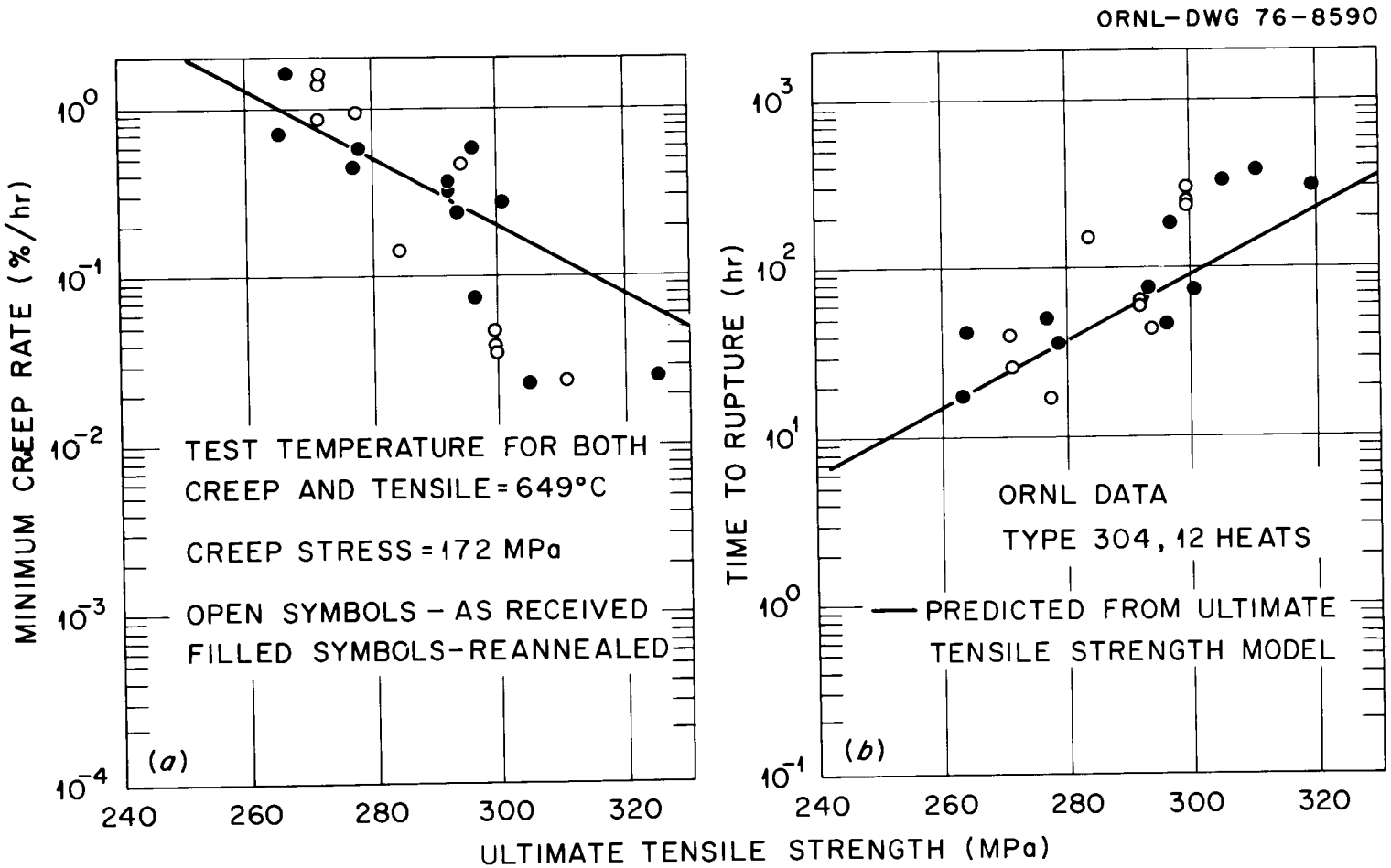


Fig. 3.24. Comparison of Experimental Time to Rupture as a Function of Elevated-Temperature Ultimate Tensile Strength ($S_u$) With Values Predicted from Rupture Model With $S_u$ for Different Heats of Type 304 Stainless. Tests were at 649°C (1200°F) and 172 MPa (25 ksi).

for $S_u$ in MPa and $T_c$ in °C. This equation was taken from a recent report by Sikka et al.[14] and derived from data for reannealed material from the same heats used to develop Eqs. (1) and (2). The standard error of estimate (SEE) for Eq. (5) for 135 data points was 23.4 MPa (3.39 ksi). The maximum and minimum values of $S_u$ were arbitrarily defined as the predicted mean value plus or minus twice the SEE: $S_u \pm 46.8$ MPa ($S_u \pm 6.79$ ksi). Although arbitrary, such a definition of maximum and minimum has been found to give values close to those obtained by central tolerance limits ($P = 0.90$, $\lambda = 0.95$).

Figures 3.25 and 3.26 compare the predicted maximum, average, and minimum values of $t_r$ and $\dot{e}_m$ from Eqs. (1) and (2) and the ORNL experimental data on 20 heats of type 304 stainless steel. The total heat-to-heat variations in $t_r$ and $\dot{e}_m$ are bounded by the predicted maximum and minimum from corresponding values of $S_u$.

Figure 3.27 compares the Japanese (NRIM)[15] heat-to-heat variation data for nine heats of type 304 stainless steel with the predicted maximum-minimum band from Eq. (1). The average and ± 2 SEE values were obtained from Sikka and Booker.[12] These values were obtained at a strain rate of $1.25 \times 10^{-3}$/sec and therefore were corrected to a strain rate of $6.67 \times 10^{-4}$/sec, which was used in the derivation of Eqs. (1) and (2). The strain rate correction was made based on the method discussed by Sikka et al.[14] It can again be noted that the predicted maximum-minimum band encloses the observed variations in the data for test temperatures in the range from 600 to 700°C (1112–1293°F). Thus, we have shown that Eqs. (1) and (2) are not only accurate for ORNL data, but can also be extended to Japanese data.[15]

Booker and Sikka[16] have developed a creep equation that incorporates heat-to-heat variations through elevated-temperature ultimate tensile strength. This model is described in Sect. 3.2.4. The $S_u \pm 46.8$ MPa ($S_u \pm 6.79$ ksi) numbers were inserted into this creep equation to compute average, maximum, and minimum creep curves. The comparison between predicted and experimental curves for short-term tests is illustrated in Fig. 3.12(a) and (b). The comparison for individual heats and long-term creep curves is illustrated in Figs. 3.28 through 3.30.

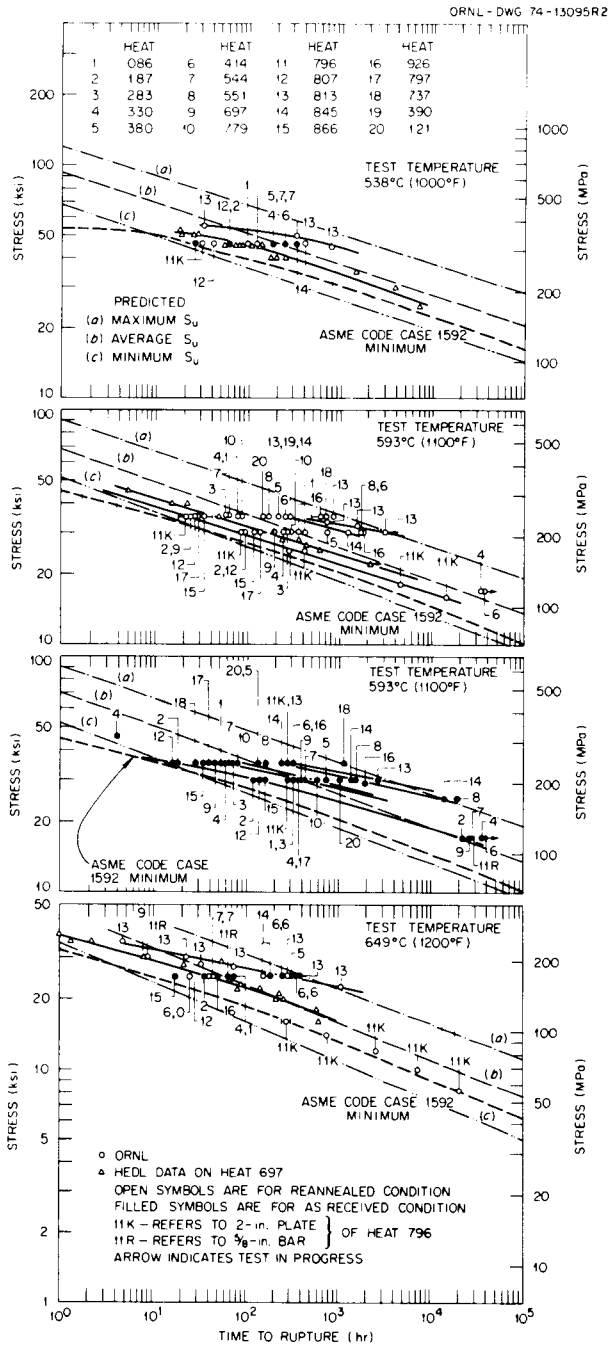


Fig. 3.25. Comparison of Stress-Rupture Data at 538, 593, and 649°C (1000, 1100, and 1200°F) for 20 Heats of Type 304 Stainless Steel in Both As-Received and Reannealed Conditions with ASME Code Case 1592 Minimum and the Predicted Maximum, Average, and Minimum Curves from the Rupture Model with Elevated-Temperature Ultimate Tensile Strength ($S_u$).

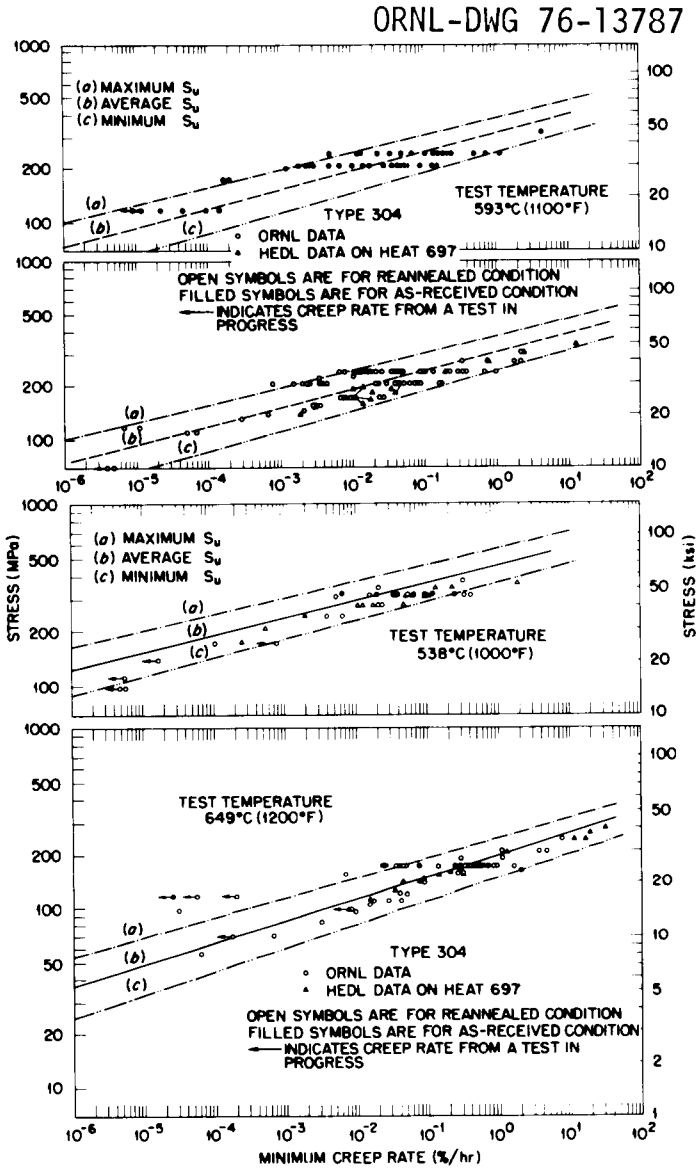


Fig. 3.26. Comparison of Minimum Creep Rate Data at 538, 593, and 649°C (1000, 1100, and 1200°F) for 20 Heats of Type 304 Stainless Steel in Both As-Received and Reannealed Conditions with the Predicted Maximum, Average, and Minimum Curves from Minimum Creep Model with Elevated-Temperature Ultimate Tensile Strength ($S_u$).

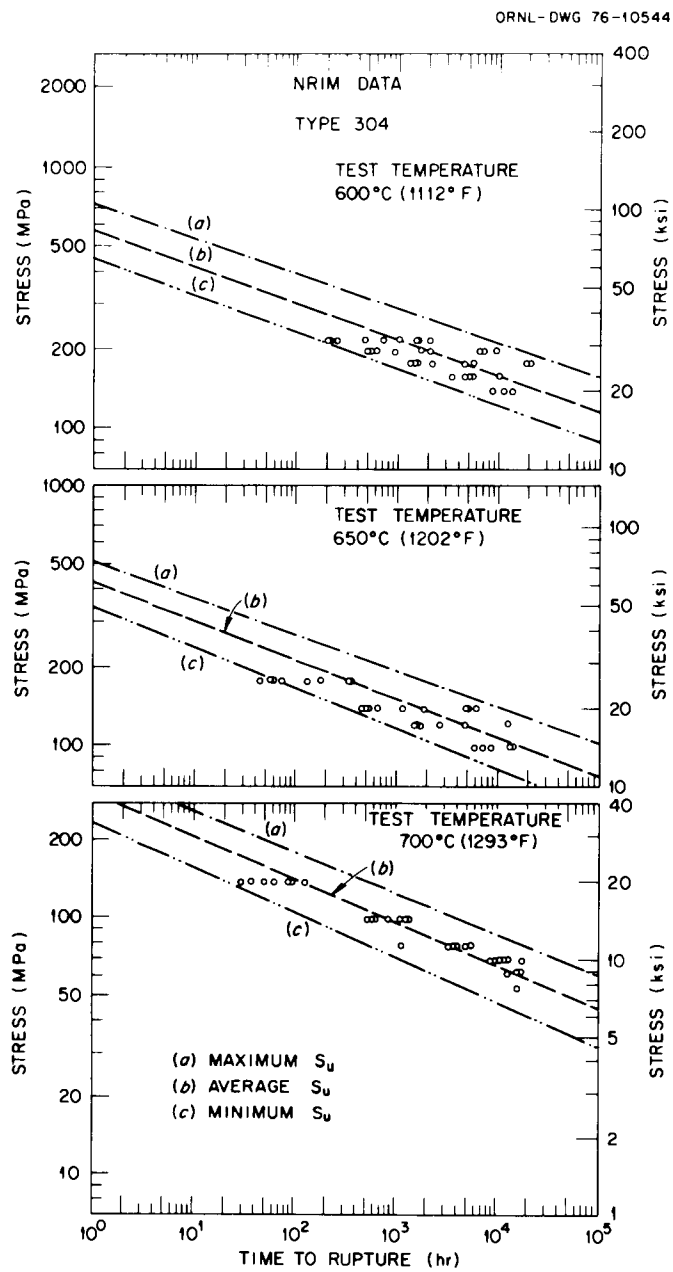


Fig. 3.27. Comparison of NRIM Stress-Rupture Data at 600, 650, and 700°C (1112, 1202, and 1293°F) for 9 Heats of Type 304 Stainless Steel in As-Received Condition with Predicted Maximum, Average, and Minimum Curves from Rupture Model with Elevated-Temperature Ultimate Tensile Strength ($S_u$).

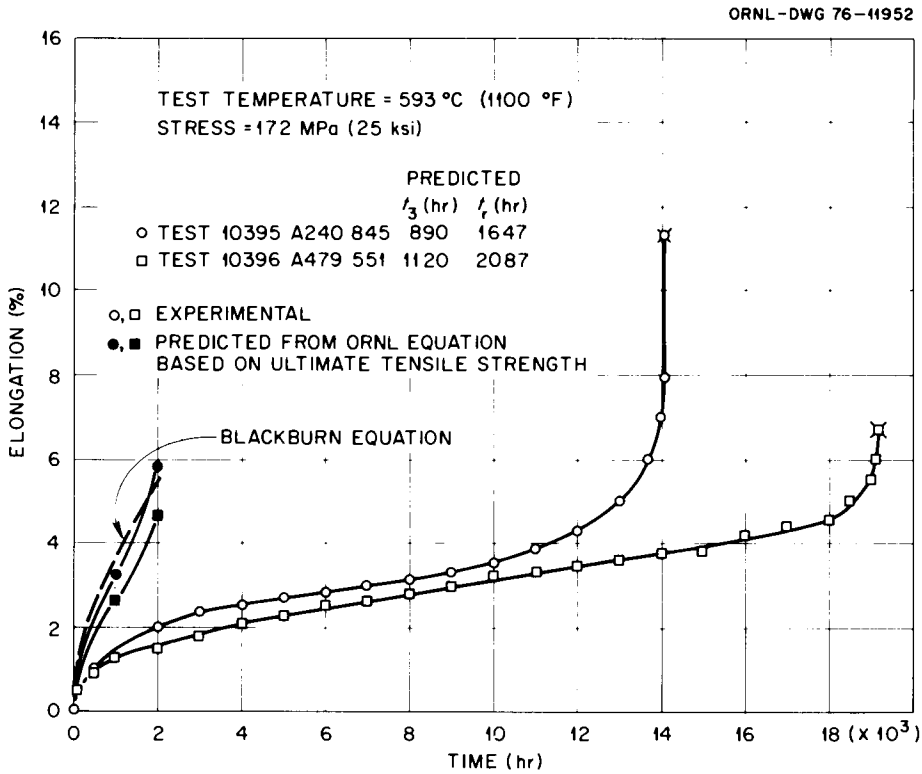


Fig. 3.28. Comparison Between Experimental and Predicted Creep Curves for Two Heats of Type 304 Stainless Steel.

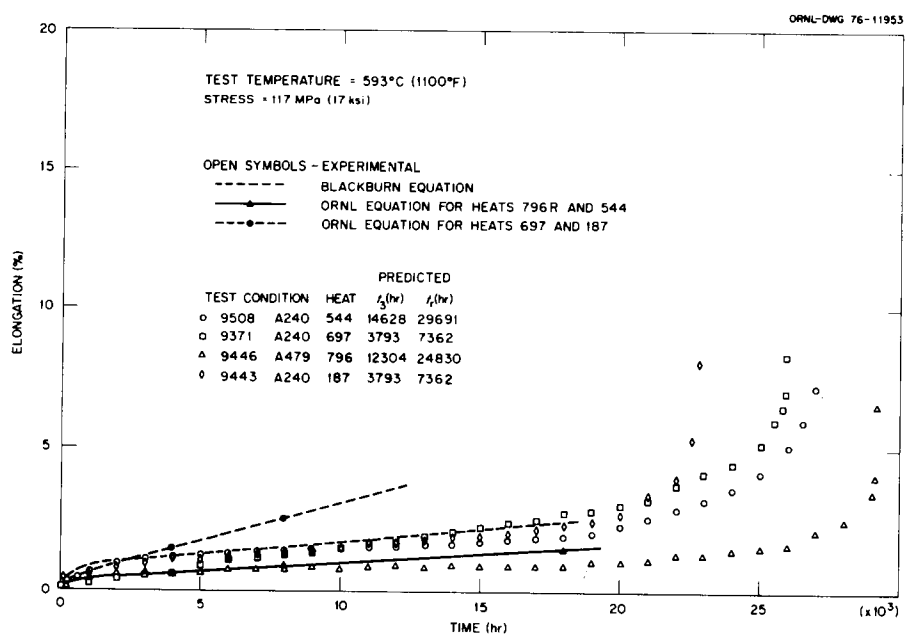


Fig. 3.29. Comparison Between Experimental and Predicted Creep Curves for Four Heats of Type 304 Stainless Steel.

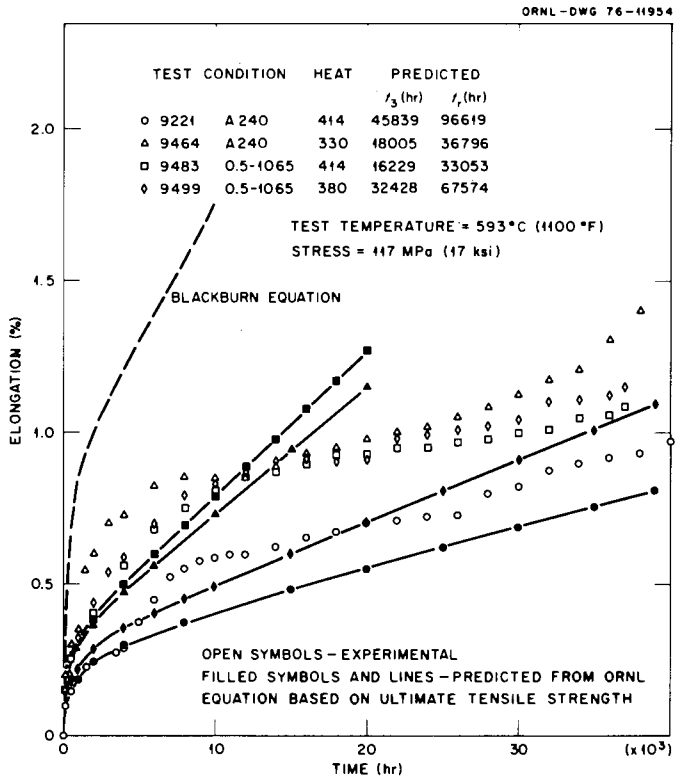


Fig. 3.30. Comparison Between Experimental and Predicted Creep Curves for Three Heats of Type 304 Stainless Steel.

Thus, we have shown that the $t_r$ and $\dot{e}_m$ models and the creep equation containing elevated-temperature ultimate tensile strength describe the behavior of an individual heat and the average, minimum, and maximum behavior of 20 heats of type 304 stainless steel.

### 3.2.4 Materials Behavior in Support of Development and Evaluation of Failure Criteria for Materials — Development of Creep Equation for Type 304 Stainless Steel — M. K. Booker and V. K. Sikka

Progress toward developing an analytical representation of the creep strain-time behavior has been reported previously.[17,18] Final results can be found in ref. 16.

The basic strain-time equation form chosen[17] was the simple rational polynomial equation. The basic properties of that equation are described elsewhere.[19]

As used here, the rational polynomial equation is expressed as:

$$e_c = \frac{Cpt}{1 + pt} + \dot{e}_m t \ , \qquad (1)$$

where $e_c$ = the creep strain,

$t$ = the time,

$\dot{e}_m$ = the minimum creep rate (%/hr), and

$C$ = the limiting value of the transient primary term.

The parameter $p$ is related to the sharpness of the curvature of the primary creep region. From Eq. (1) the instantaneous creep rate $\dot{e}_c$ is given by

$$\dot{e}_c = \frac{Cp}{(1 + pt)^2} + \dot{e}_m \tag{2}$$

and the initial creep rate $\dot{e}_0$ is given by

$$\dot{e}_0 = Cp + \dot{e}_m \ . \tag{3}$$

Figure 3.31 summarizes the properties of the equation.

Next, we evaluated the stress and temperature dependence of the parameters $C$, $p$, and $\dot{e}_m$, using basically the method described last quarter.[18] One of the advantages of the current equation form is that it includes an explicit minimum creep rate term. While analytical fits of Eq. (1) to experimental curves will in general yield slightly different values of $\dot{e}_m$ than graphical measurements, this difference is insignificant in comparison with the overall uncertainty in creep strain-time predictions. Thus, the approach here has been to gather all available minimum creep rate data and to use these data to express $\dot{e}_m$ as a function of stress and temperature.

From Fig. 3.31 it can easily be verified that the value of $C$ (%) is given by:

$$C = e_3 - \dot{e}_m t_3 \ , \tag{4}$$

where $e_3$ and $t_3$ are the strain (%) and time to the onset of tertiary creep (hr), respectively. Methods for the calculation of $e_3$ and $t_3$ have been previously reported.[20,21] Those results, illustrated in Figs. 3.32 and 3.33, found for type 304 stainless steel the relationships

ORNL-DWG 76-3985R

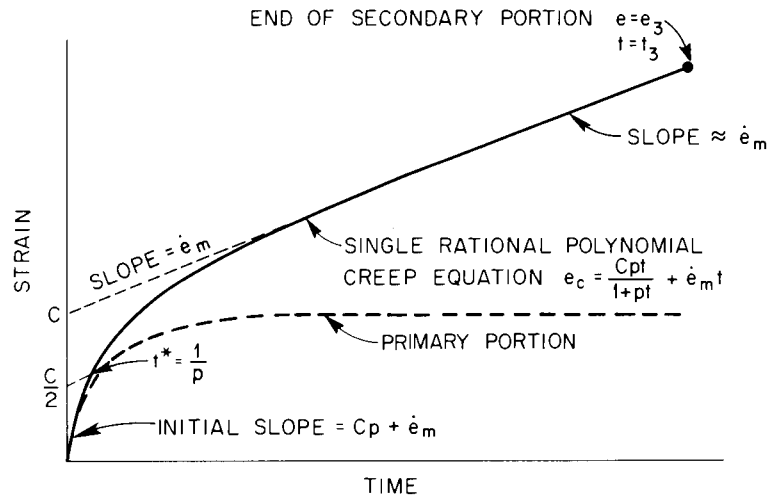


Fig. 3.31. Schematic Illustration of the Properties of the Rational Polynomial Creep Equation.

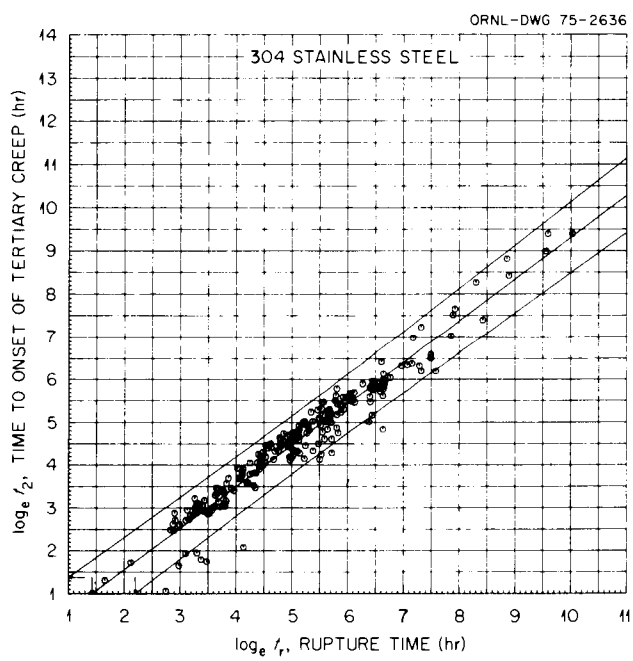


Fig. 3.32. Relationship Between Rupture Life and Time to Tertiary Creep for Type 304 Stainless Steel. The upper and lower lines are central tolerance limits ($P$ = 0.90, $\lambda$ = 0.95). Temperature range 538–649°C.

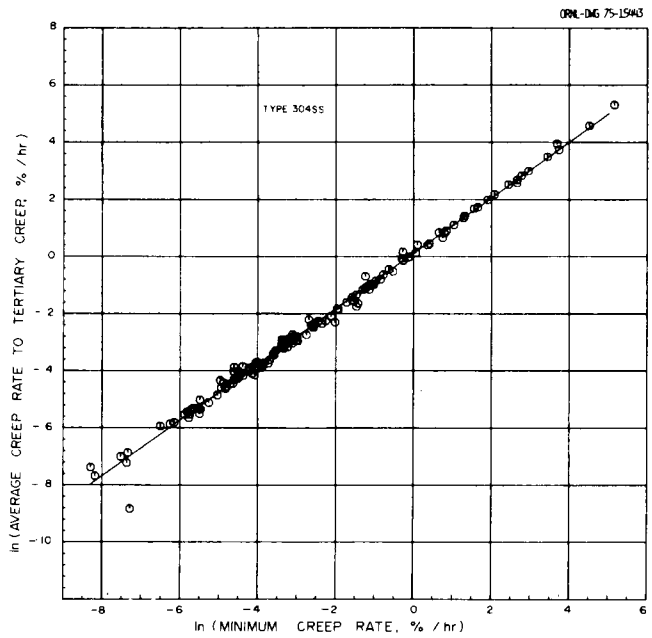


Fig. 3.33. Relationship Between Minimum Creep Rate and Average Creep Rate to Tertiary Creep for Type 304 Stainless Steel. Temperature range 482–816°C.

$$t_3 = 0.685 t_r^{0.968} , \tag{5}$$

and

$$\dot{e}_3 = e_3/t_3 = 1.11 \dot{e}_m^{0.974} , \tag{6}$$

Equations (5) and (6) in turn yield

$$e_3 = \dot{e}_3 t_3 = 0.760 \dot{e}_m^{0.974} t_r^{0.968} . \tag{7}$$

Equations (5) through (7) are independent of heat-to-heat and temperature variations.

After the results of previous investigators,[22,23] we expressed the initial creep rate as a function of the minimum creep rate. Several relationships were examined, the one chosen as optimum being

$$\dot{e}_0 = 3.43 \dot{e}_m^{0.80} , \tag{8}$$

as illustrated in Fig. 3.34. Then, Eq. (3) gives the parameter $p$ ($hr^{-1}$) as

$$p = \frac{(\dot{e}_0 - \dot{e}_m)}{C} \quad . \tag{9}$$

Thus, with the aid of Eqs. (4) through (9) the entire creep equation can be determined from values of only $\dot{e}_m$ and $t_r$.

The creep data used in this analysis were obtained from the experimental program for several heats of material described by Sikka et al,[9] including the data reported by Swindeman.[24,25] Pipe, plate, and bar materials were used, while all material was laboratory reannealed. A full discussion of the data used is given elsewhere.[2]

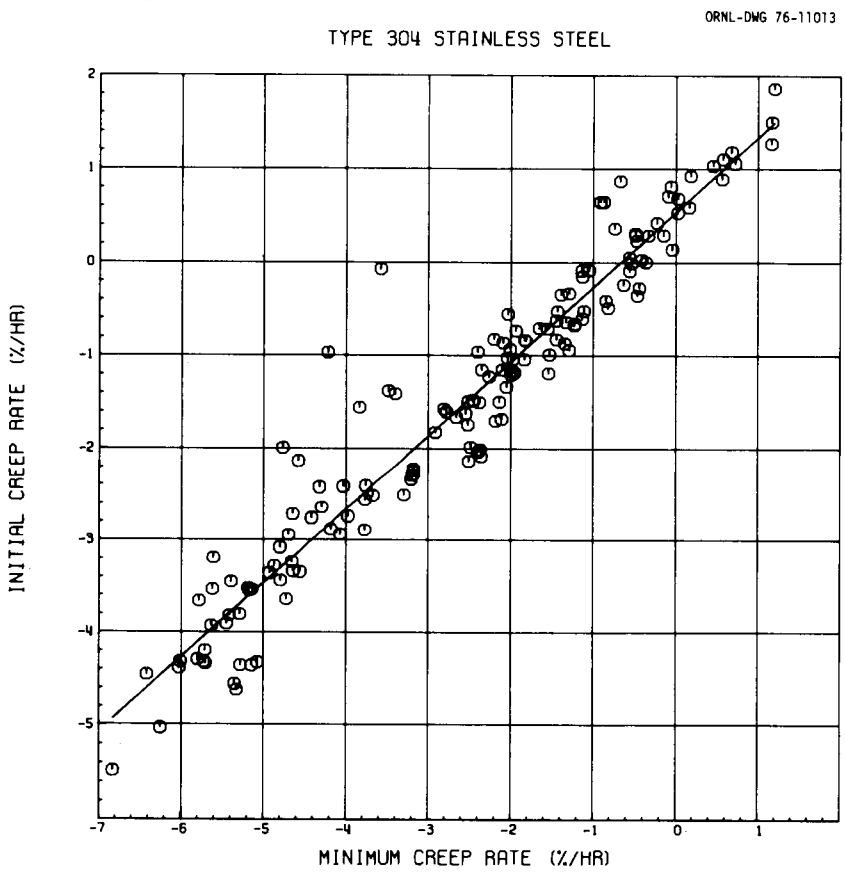


Fig. 3.34. Relationship Between Minimum Creep Rate and Initial Creep Rate for Type 304 Stainless Steel. Temperature range 482–816°C.

3.2.4.1 Analysis of Rupture and Minimum Creep Rate Data

The available rupture data (205 points) and minimum creep rate data (226 points) were subjected to a systematic analysis involving a generalized set of algebraic models for log $\dot{e}_m$ and log $t_r$ as functions of stress $\sigma$, temperature $T$, and ultimate tensile strength $U$. The tensile strengths used were for a given heat at the given temperature, and were included in an attempt to reduce the substantial heat-to-heat variations[9] in properties of this material. We found that ultimate tensile strength is significantly reflected in the creep and rupture strength for this material, consistent with other results.[9,10,26] However, it must be realized that tensile strength is a function of strain rate and testing technique in the temperature range where creep is important.[14] Thus, although a wide range of data is available for this material, for the purposes of the present study only the data described above were used, since a consistent set of tensile data was available for those same heats of material.

The final choices of models were based on

1. least squares fits to the entire set of data,
2. predictions of long-time ($t_r$ > 2000 hr) or low-rate ($\dot{e}_m$ < 0.001%/hr) data from fits to short-time or high-rate data, and
3. simplicity and physical reasonableness of the models.

The entire modeling procedure is described in detail elsewhere.[2] As illustrated in Figs. 3.35 and 3.36, the final models chosen were

$$\log t_r = 5.716 - 3915\ (\log \sigma)/T + 32.60U/T - 0.007303U \log \sigma \qquad (10)$$

and

$$\log \dot{e}_m = -2.765 + 3346\ (\log \sigma)/T - 51.84U/T + 0.0616U \log \sigma \qquad (11)$$

for $\sigma$ and $U$ in MPa and $T$ in K. Interestingly, Eqs. (10) and (11) are of the same form, both being linear in log $\sigma$ and log $t_r$. They may be evaluated for a given heat of material if the ultimate tensile strength

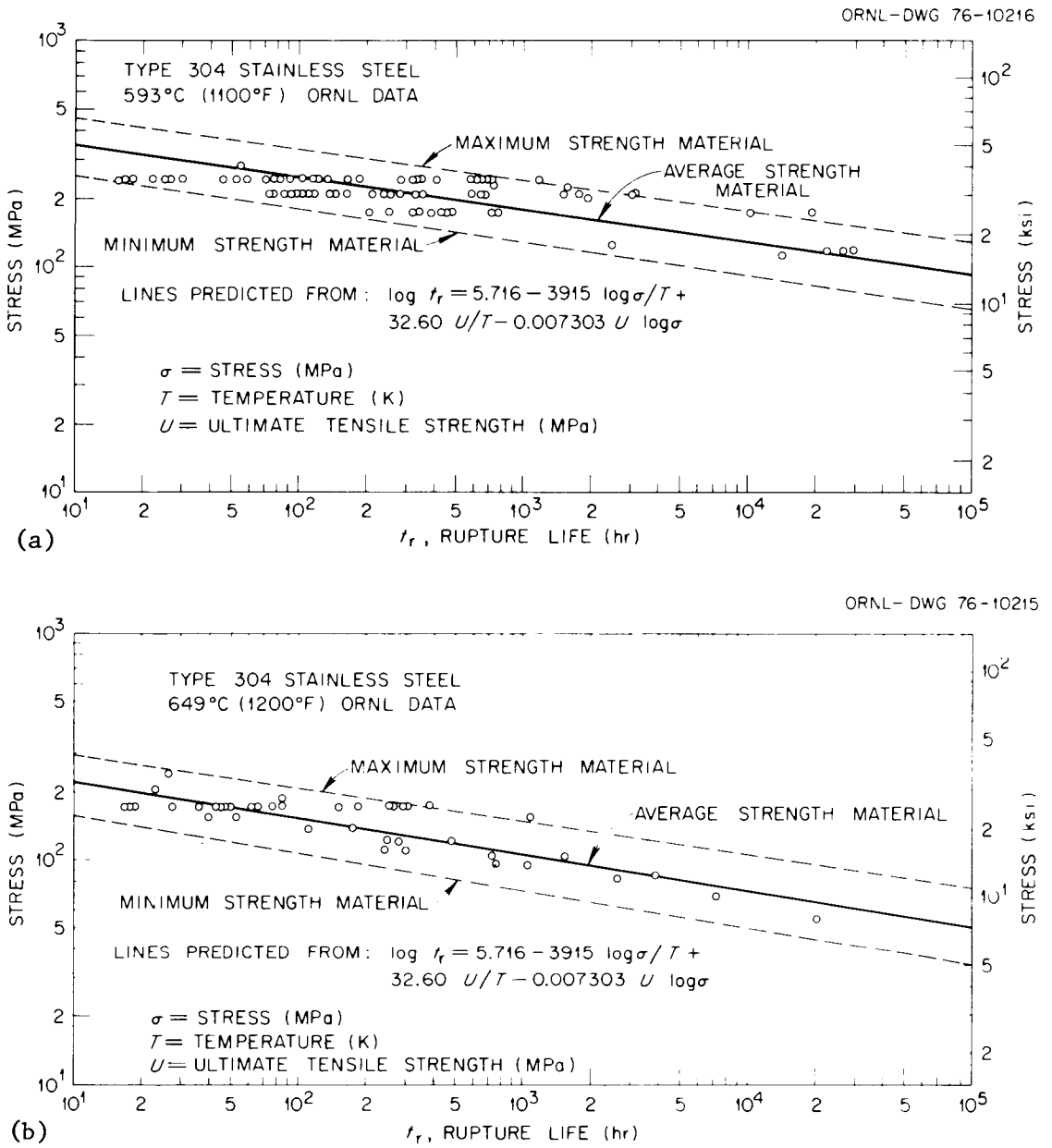


Fig. 3.35. Fits to Experimental Data for Rupture Life of Type 304 Stainless Steel at (a) 593°C (1100°F) and (b) 649°C (1200°F). Lines are predictions from Eq. (10) for average, minimum, and maximum strength material, as reflected by ultimate tensile strength.

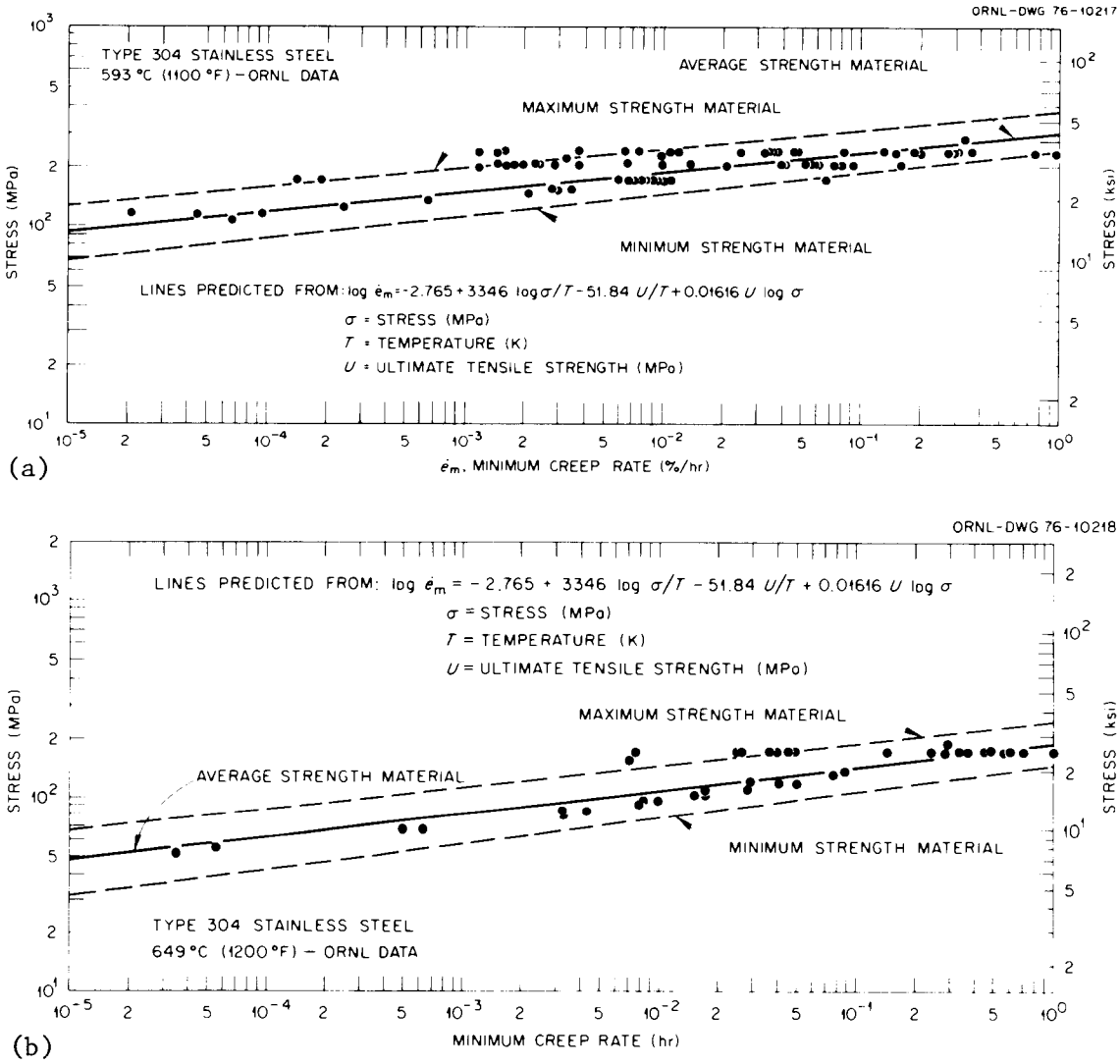


Fig. 3.36. Fits to Experimental Data for Minimum Creep Rate of Type 304 Stainless Steel at (a) 593°C (1100°F) and (b) 649°C (1200°F). Lines are predictions from Eq. (11) for average, minimum, and maximum strength material, as reflected by ultimate tensile strength.

at the temperature desired is known. Mean values of $U$ as a function of temperature used here were predicted from

$$U = 639.2 - 1.813T_c + 0.00525T_c^{\,2} + 5.068 \times 10^{-6}T_c^{\,3} \tag{12}$$

for $U$ in MPa and $T_c$ in °C. This equation, adapted from ref. 14, was derived from data for reannealed material from the same heats used in developing Eqs. (10) and (11). Equations (10) through (12) apply to tensile data measured at a constant strain rate of about $6.7 \times 10^{-4}$/sec. The standard error of estimate of Eq. (12) for 135 data was 23.4 MPa. Maximum and minimum values of $U$ (such as those used in constructing Figs. 3.35 and 3.36) were arbitrarily defined as the predicted mean value plus or minus two standard errors ($U \pm 46.8$ MPa).

3.2.4.2 Evaluation of Creep Equation Parameters

Using the method described above, Eqs. (10) through (12) allow an evaluation of the dependence of the parameters $C$, $p$, and $\dot{e}_m$ upon stress, temperature, and relative strength of a given heat of material (as reflected by the ultimate tensile strength). Figure 3.37 illustrates the predicted behavior of these parameters for the 51-mm-thick plate of heat 9T2796, a relatively weak heat. The predictions used values of ultimate tensile strength for this heat of material from McCoy.[27] The data shown were obtained from fits of Eq. (1) to individual creep curves made by the semigraphical procedure described in ref. 2, after that discussed by Oding.[28] Included in Fig. 3.37(c) are data[24] and predictions for heat 8043813, a relatively strong heat.

Several points are apparent from Fig. 3.37. First, the scatter in the data is large (thus the second objection above to previous evaluation procedures). Second, although the current equations were developed from a large multiheat data base, the predictions still appear to capture the trends in the behavior for a given heat and to reflect to some degree the effect of heat-to-heat variations. It should also be noted that the data shown in Fig. 3.37 are primarily from long-term, low-stress creep tests that had not entered the tertiary creep region. Thus, using the current

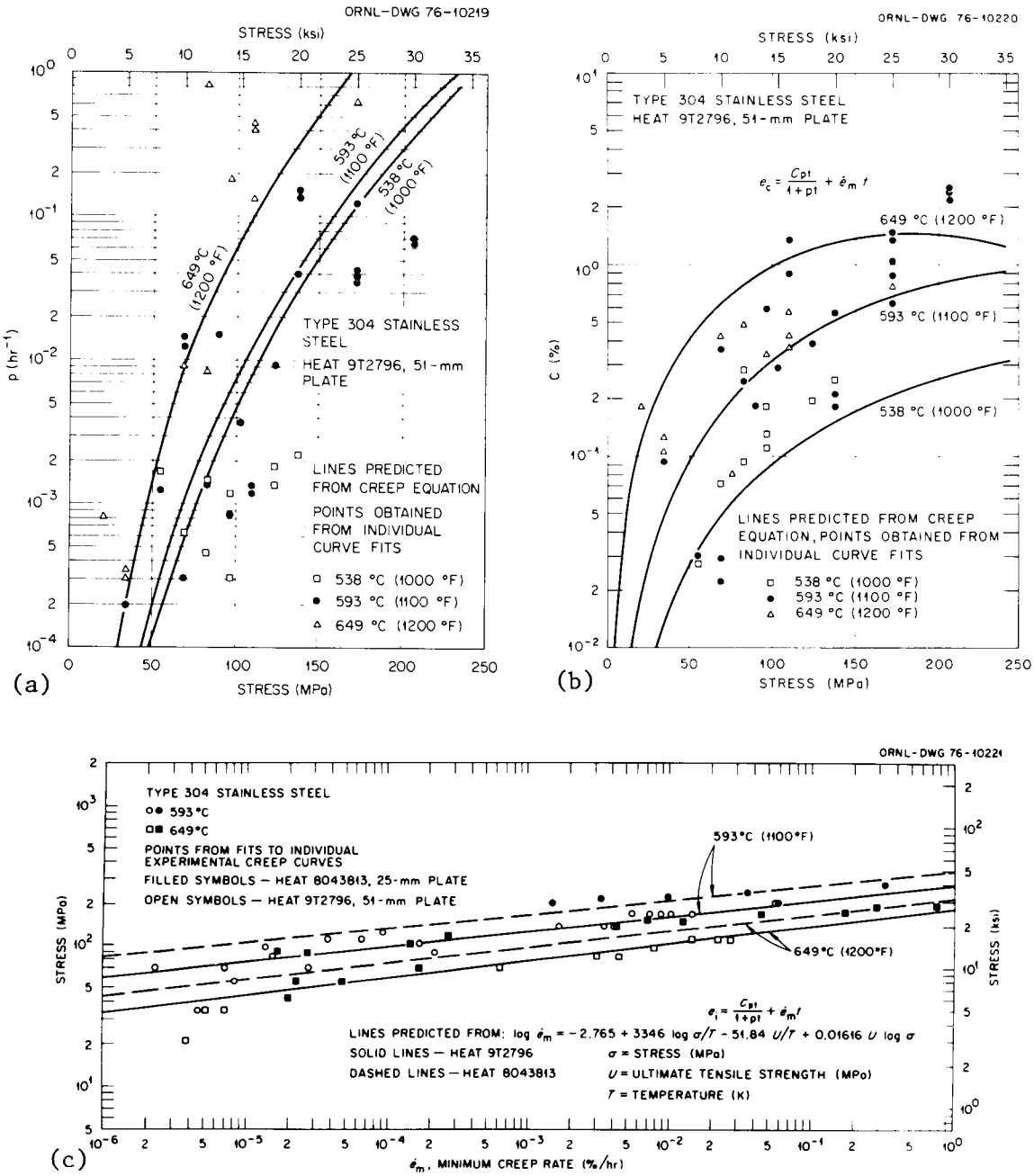


Fig. 3.37. Variation of the Rational Polynomial Creep Equation Parameters with Stress at Three Temperatures for Heat 9T2796, 51-mm Plate of Type 304 Stainless Steel. (a) Experimental data for the parameter $p$, with predictions from the creep equation. (b) Experimental data and predictions for the parameter $C$. (c) Experimental data and predictions for the parameter $\dot{e}_m$. Solid lines predicted for heat 9T2796, a weak heat. Dashed lines predicted for heat 8043813, a strong heat.

method, we did not use the data from most of these tests in determining the various equation constants other than $p$. The comparisons in Fig. 3.37 are therefore primarily extrapolations. Considering this fact, the comparison is quite good. Figure 3.38 illustrates the capability for prediction of heat-to-heat variations in rupture life for these same two heats of material. Clearly, the current models cannot yield precise fits to every individual heat of material. However, Figs. 3.35 and 3.36 show that the current models do provide a good fit to the mass of available data, while Figs. 3.37(c) and 3.38 show that these models somewhat reduce the uncertainty in predictions due to heat-to-heat variations.

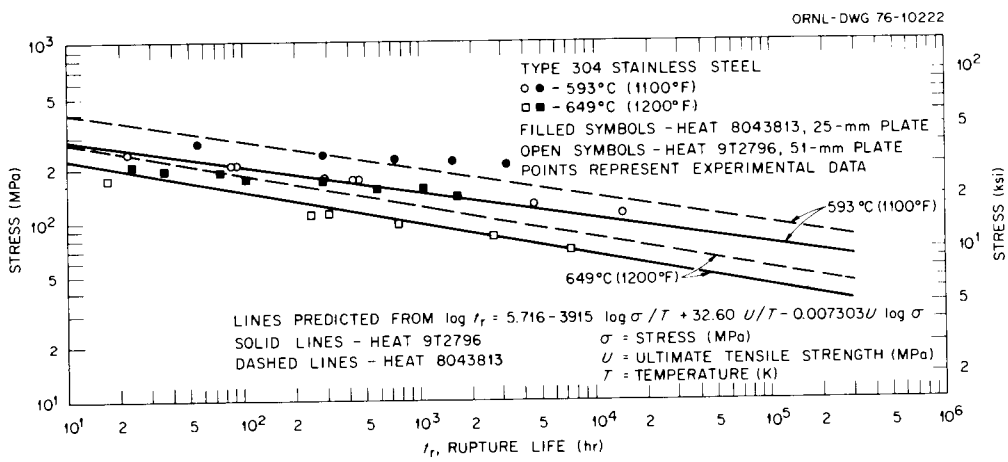


Fig. 3.38. Prediction of Heat-to-Heat Variations in Rupture Life for Two Heats of Type 304 Stainless Steel, Including Experimental Data.

The most meaningful criterion for judging a creep equation is its ability to predict reasonable values for creep strain for a given heat of material under a given loading condition. Figure 3.39 illustrates predictions of individual creep curves for heats 9T2796 and 8043813 from the current equation. Also shown are predictions from Blackburn.[3] Clearly, the current equation more accurately depicts the strain-time behavior of the heats shown, since it does reflect heat-to-heat variation. It should be noted that the data used in establishing the current predictions were almost exclusively from tests conducted at temperatures of 538°C (1000°F) and above. However, creep in this material

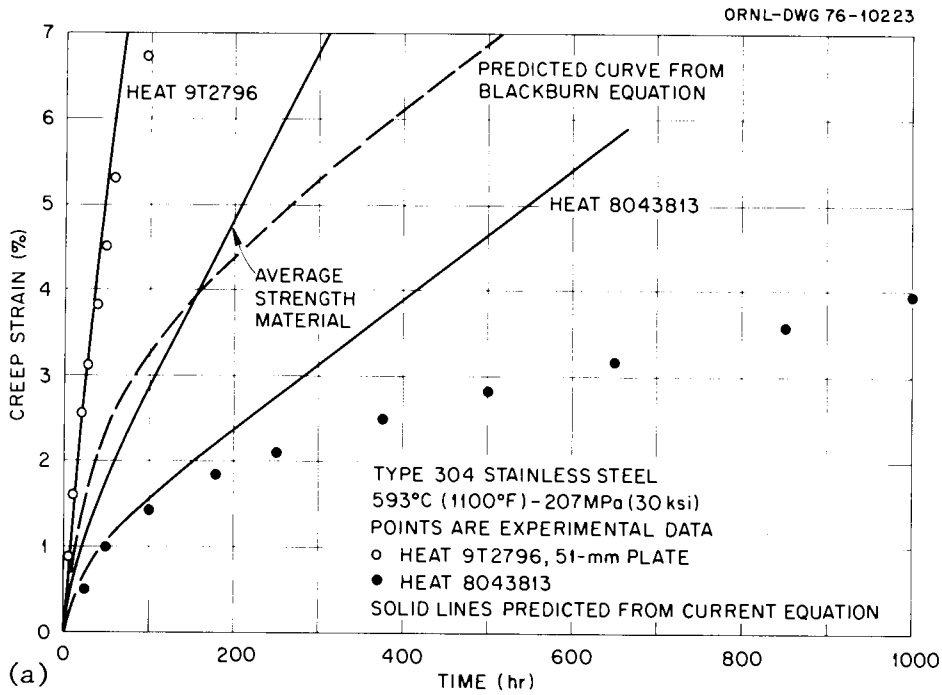


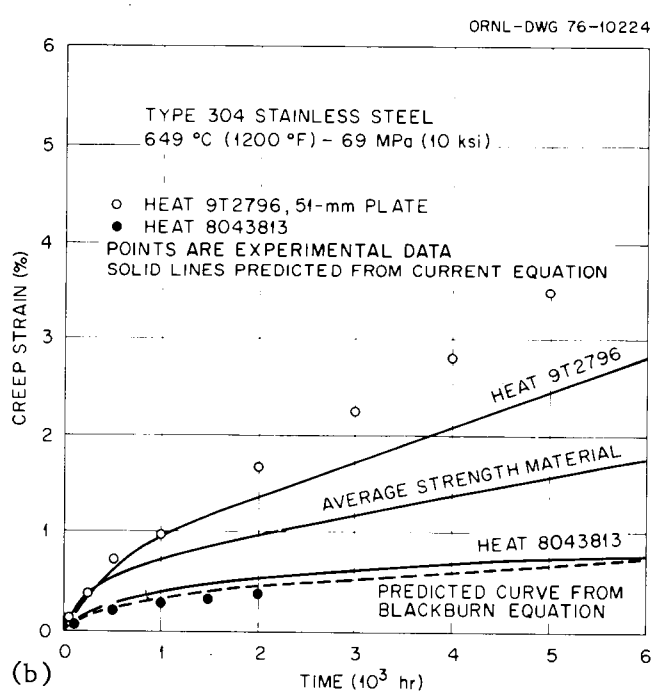


Fig. 3.39. Comparison of Predictions with Experimental Creep Curves for Two Heats of Type 304 Stainless Steel, Including Predictions of Average Behavior from the Current Equation and from the Blackburn Equation. (a) 593°C, 207 MPa; (b) 649°C, 69 MPa.

has been recognized as important at temperatures down to 427°C (800°F), so that the predictions must be extrapolated downward in temperature. Extensive data at such low temperatures are available only for heat 9T2796. Comparisons between the predictions and data at 482°C (900°F) yielded good results. However, limited data indicate the presence of much more creep than predicted at 427°C (800°F). In fact, there is evidence that this material may creep even more at 427°C than at 482°C (see Fig. 3.40). Therefore, we recommend that the predictions at 482°C be used in the range 427 to 482°C, in view of this behavior. (This effect is not yet fully understood, but it may be related to some type of strain aging phenomenon.)

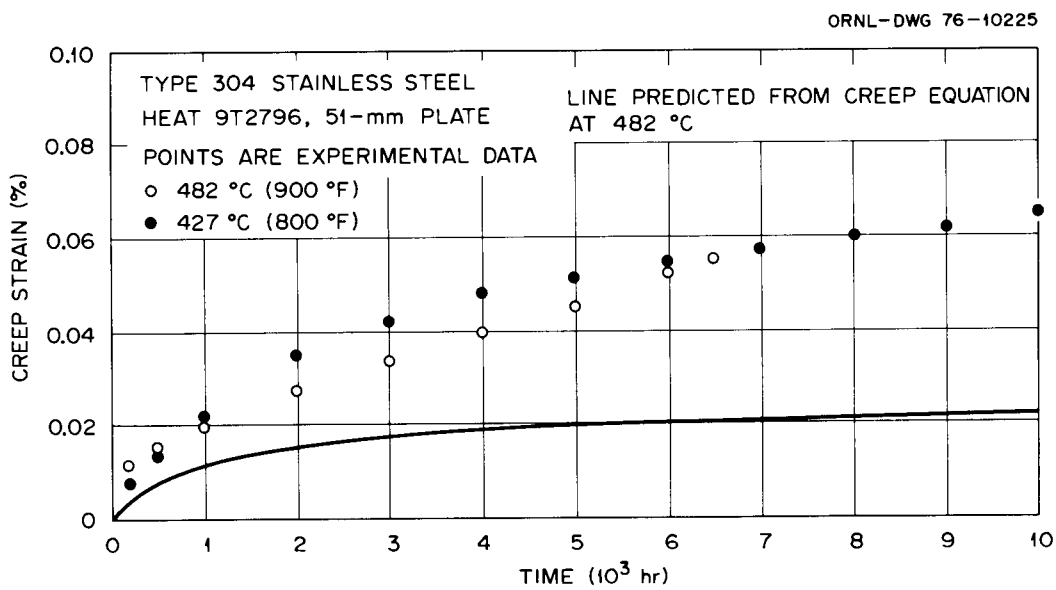


Fig. 3.40. Creep Behavior of Heat 9T2796, 51-mm Plate of Type 304 Stainless Steel at 427 and 482°C. Note the crossover between the curves at 427 and 482°C.

### 3.2.4.3 Isochronous Stress-Strain Curves

One of the most useful forms of displaying creep strain-time behavior is the isochronous stress-strain curve. Various methods exist for the construction of such curves, many of which are summarized in ref. 29.

Equation (1), with the constants $C$, $p$, and $\dot{e}_m$ defined by Eqs. (4), (9), and (11), can easily be used to calculate the creep strain accumulated

in a given time at a given stress and temperature. Thus, given an estimate of the instantaneous strain incurred upon loading, one can develop isochronous stress-strain curves from the equation. This loading strain can be adequately found from monotonic tensile stress-strain curves.

The monotonic tensile stress-strain behavior of this material can be described by:

$$(\sigma - \sigma_0) = \frac{C' p' \varepsilon_p}{1 + p' \varepsilon_p} + \dot{h}_m \varepsilon_p \ , \tag{13}$$

where $\sigma$ is the stress (MPa), $\varepsilon_p$ the plastic strain, and $\sigma_0$ corresponds to the proportional limit. The value of $\sigma_0$ can well be estimated by $0.5\sigma_y$, where $\sigma_y$ is the 0.002-offset yield strength. The constant $\dot{h}_m$ is approximately 2586 MPa, while $p$ is given by $500C$. The value of $C$ is determined by the criterion that $\sigma = \sigma_y$ for $\varepsilon_p = 0.002$. Interestingly, Eq. (13) is of the same form as Eq. (1), reflecting the great flexibility of this equation. Since a knowledge of stress and Young's modulus yields the magnitude of the elastic strain, Eq. (13) can be used to calculate the total strain corresponding to a given stress. A full description of our analysis of stress-strain behavior is given in another report.[30]

Equations (1) and (13) were combined to calculate isochronous stress-strain curves as shown in Fig. 3.41. Average, maximum, and minimum creep strength curves were calculated by using the corresponding values of tensile strength from Eq. (12) as above. For all cases shown in Fig. 3.41, the loading strains were calculated by use of average yield strengths from ref. 14 for as-received material, to allow comparison with the results of ref. 3. Thus, all variations shown are due to the effects of creep strength only.

Figure 3.41 shows considerable differences between the current results and those of ref. 3. Since the current method allows one to calculate a series of isochronous curves for different heats of material, it is generally expected to be more accurate for a given heat of material. At 538°C (1000°F) and below, the results of ref. 3 sometimes fall even below the current minimum predictions. However, on the basis of

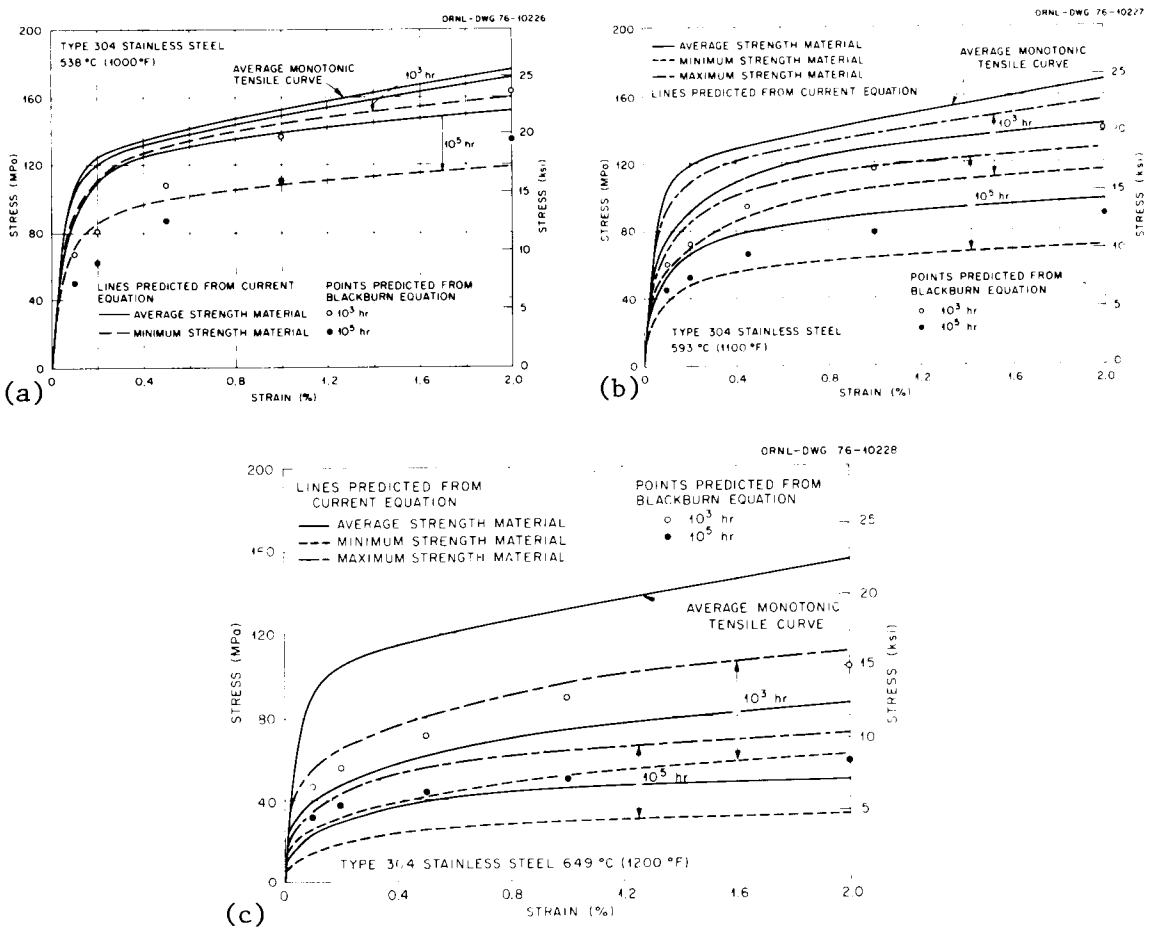


Fig. 3.41. Isochronous Stress-Strain Curves at $10^3$ and $10^5$ hr Predicted from the Creep Equation and the Rational Polynomial Equation for Average Stress-Strain Behavior. Shown are predictions for average, minimum, and maximum creep strength. Also shown are values from curves constructed from the Blackburn equation. (a) 538°C (1000°F), (b) 593°C (1100°F) and, (c) 649°C (1200°F).

available low-temperature data (427–538°C) we feel that our results are the more realistic of the two.

Finally, for comparison, two alternate methods were used to construct isochronous curves for the heat 9T2796 51-mm plate. First, the times to accumulation of given amounts of creep strain $t_x$ were analyzed by parametric techniques similar to those commonly used for rupture data. This method is similar to the one described in ref. 31. No extensive modeling was attempted, although we did fit several standard time-temperature parameters to data for 0.1, 0.25, 0.5, 1, 1.5, and 2% creep strain. The best overall results were obtained by a simple Larson-Miller[32] parameter of the form

$$\log t_x = \alpha_0 + \frac{\alpha_1 \log \sigma}{T} + \frac{\alpha_2}{T} , \tag{14}$$

where $\alpha_0$, $\alpha_1$, and $\alpha_2$ were estimated by least squares methods at each of the above levels of creep strain. Equation (14) allows one to calculate the stress that will cause a given amount of creep strain at a given time and temperature. Using this stress, one can then use Eq. (13) and Young's modulus to calculate isochronous stress-strain curves.

Finally, isochronous curves at 593°C (1100°F) were constructed by use of a form of the Rabotnov[33] parameter. At a given level of strain (loading plus creep), this parameter is given by

$$\phi(\varepsilon) = \sigma(1 + \alpha t^{1/3}) , \tag{15}$$

where $\sigma$ and $t$ are again the stress and time, $\phi$ is the parameter, and $\alpha$ is a constant. We used stress values from the above-mentioned monotonic tensile stress-strain curves for $\phi$ and assumed the time exponent of 1/3. Attempts at determining $\phi$ and the exponent by least squares methods, such as was done by Goldhoff,[34] yielded poor results due to insufficient data. Having thus determined $\phi$ and the time exponent, we obtain the value of $\sigma$ for a given stress by

$$\alpha = \left(\frac{\phi}{\sigma} - 1\right) t^{1/3} . \tag{16}$$

Applying this equation at various points along the experimental creep curves showed that $\alpha$ varied both with stress and strain, rather than being constant. However, we assumed a somewhat average value of $\alpha = 0.01$ for use in further calculations.

Figure 3.42 compares the results obtained by each of these three methods at 593°C (1100°F) for this heat of material. The monotonic tensile curve used to construct the isochronous curves in Fig. 3.42 was based on Eq. (13) using the yield strength for reannealed material from this heat. Reannealing generally lowers the yield strength of type 304 stainless steel by about 35 MPa (5.1 ksi) from that in the as-received condition, although the tensile strength and creep strength are not greatly affected.[14,35] Tensile properties of reannealed material were used in constructing Fig. 3.42 since the Rabotnov parameter always involves total strain, not separate analysis of creep and loading strain. For this reason, the tensile and creep properties should preferably refer to the same material condition. The three methods illustrated in Fig. 3.42 yield similar results, although the creep equation is preferred since it has a wider range of uses than the other methods.

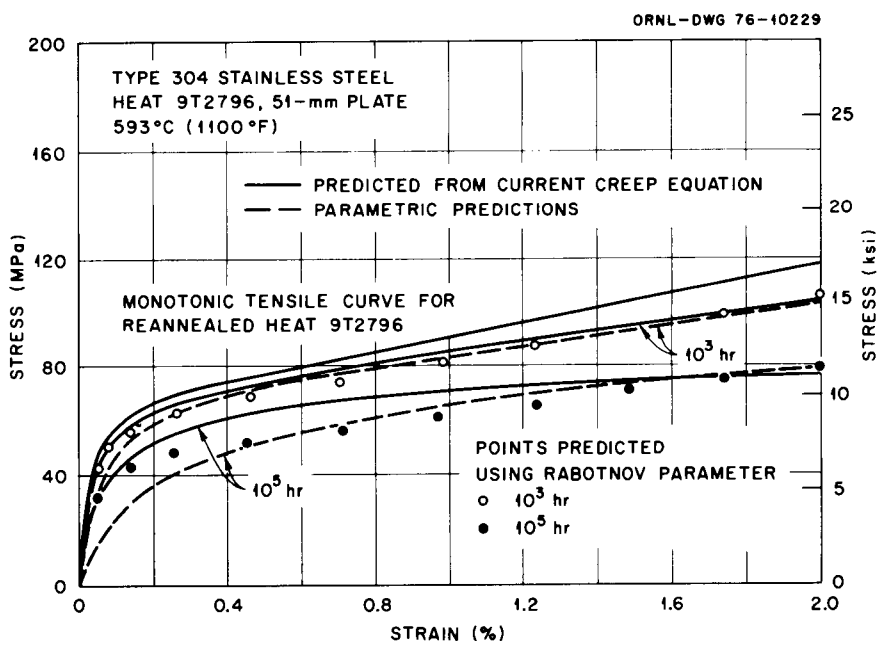


Fig. 3.42. Isochronous Stress-Strain Curves at 593°C for Heat 9T2796, 51-mm Plate Predicted by Various Methods.

3.2.4.4 Variable Load and Relaxation Behavior

Actual design applications will seldom involve simple constant-load situations. Various system transients and other effects will result in repeated changes of stress or temperature or both. Also, many loading situations involve constant-strain stress relaxation rather than constant-load creep straining. To be ot full use, a creep equation must provide some means of accounting for such situations. Little study has been done of variable temperature behavior, but the current equation has been used to predict variable load and relaxation behavior. These predictions have shown good comparison with experimental results.

Currently recommended design rules[36] suggest that the hypothesis of strain hardening be used to evaluate the behavior of type 304 stainless under variable, nonreversed stress conditions (of which relaxation is a special case). Equation (1) can be solved explicitly for time, yielding

$$t = \frac{e_c p - Cp - \dot{e}_m + \sqrt{(Cp + \dot{e}_m - e_c p)^2 + 4e_c p\dot{e}_m}}{2p\dot{e}_m} . \qquad (17)$$

Thus Eqs. (1) and (17) combined provide a simple, convenient method of predicting behavior by the strain hardening approach. Figure 3.43 illustrates a prediction made from the current equation for a variable-load creep test for heat 8043813, while Fig. 3.44 shows results obtained in predicting relaxation behavior for heat 9T2796 (25-mm plate). The predictions show good agreement with experimental data.

3.2.4.5 Limitations

The design lifetimes of operating systems are typically of the order of 30 years, necessitating many design calculations based on extrapolations beyond the time-stress-temperature regime where actual experimental data are available. Such extrapolations must be made with caution, however. Specific limitations on the applicability of the creep equation presented here are as follows:

1. time less than the time to the onset of tertiary creep,
2. temperature in the range 427–704°C (800–1300°F), and

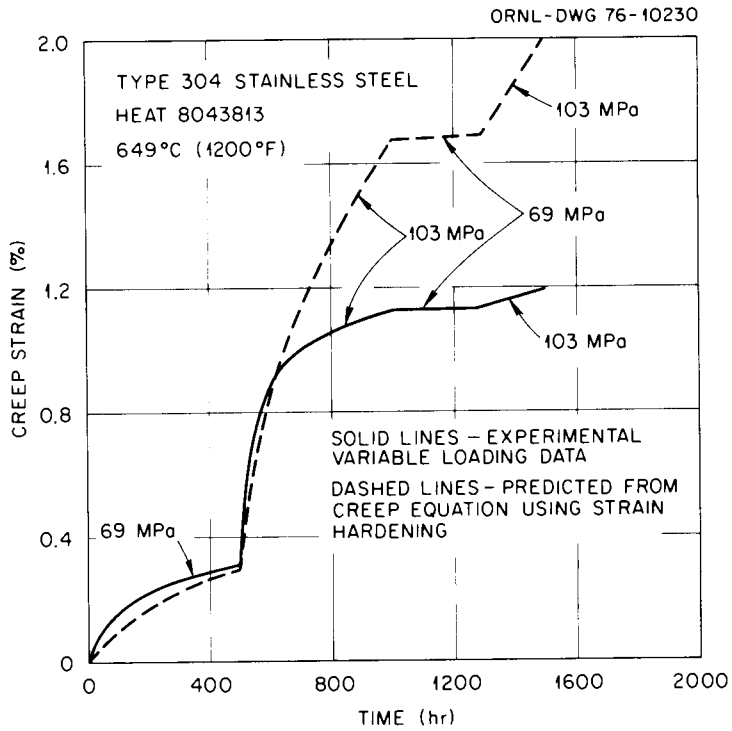


Fig. 3.43. Prediction of Variable Load Creep Behavior at 649°C for Heat 8043813 of Type 304 Stainless Steel Made Using the Creep Equation and Strain Hardening.

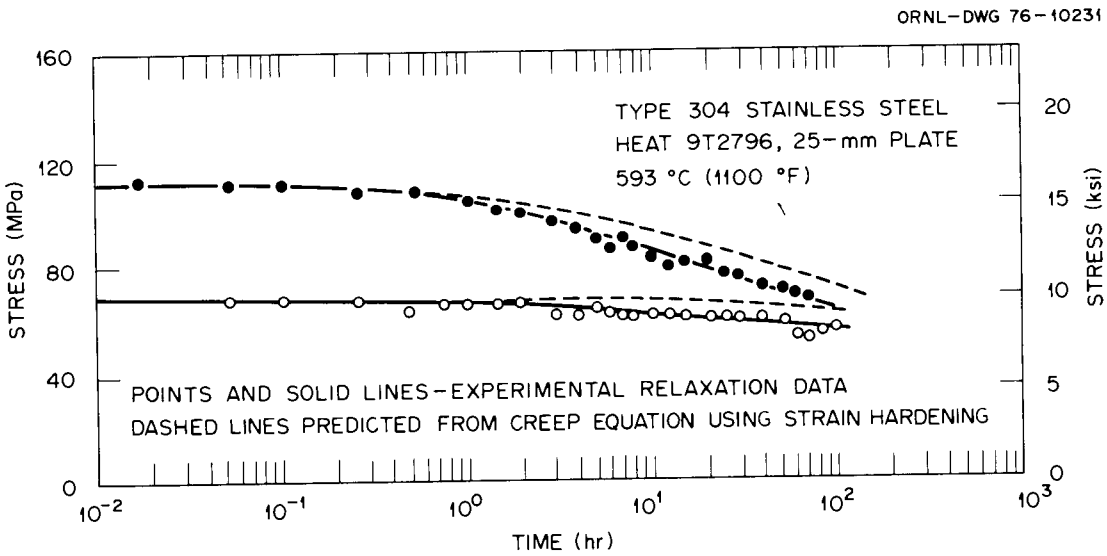


Fig. 3.44. Comparison of Experimental Relaxation Data with Predicted Behavior at 593°C for Heat 9T2796, 25-mm Plate of Type 304 Stainless Steel. Predictions made using the creep equation and strain hardening.

3. ultimate tensile strength within 23.4 MPa of the average strength at temperature as defined by Eq. (12).

In addition, Fig. 3.37(b) shows the parameter $C$ to exhibit a maximum with stress, the stress at the maximum, $\sigma_c$, becoming smaller at higher temperatures. This behavior is consistent with previous results for both types 304 (ref. 24) and 316 (ref. 37) stainless steel. However, to avoid any possible analytical difficulties, the value of $\sigma_c$ can be taken as the maximum applicable stress. Table 3.4 gives the values of $\sigma_c$ at various temperatures. The ranges shown are for minimum (lower values) to maximum strength material. Otherwise, a stress of 414 MPa (the specified minimum room-temperature ultimate tensile strength for this material) is the maximum stress limit. All values of $\sigma_c$ from Table 3.4 are relatively high, well above the range of most design applications. In addition, Eq. (6) predicts $\dot{e}_m > \dot{e}_3$ for values of $\dot{e}_m > 55.36\%/\text{hr}$. However, this anomaly occurs at stresses higher than those cited above and does not affect the stated limits. The equation is analytically valid to zero stress as the lower limit.

Table 3.4. Stress Values Corresponding to Maximum Values of the Parameter $C$

| Temperature | | Stress, for Different Strength Materials | | | |
|---|---|---|---|---|---|
| | | Minimum Strength | | Maximum Strength | |
| (°C) | (°F) | (MPa) | (ksi) | (MPa) | (ksi) |
| 427 | 800 | >414 | >60 | >414 | >60 |
| 482 | 900 | >414 | >60 | >414 | >60 |
| 538 | 1000 | 365 | 53 | >414 | >60 |
| 593 | 1100 | 241 | 35 | 407 | 59 |
| 649 | 1200 | 138 | 20 | 255 | 37 |
| 704 | 1300 | 41 | 6 | 124 | 18 |

### 3.2.5 Computerized Data Management System — M. K. Booker and B.L.P. Booker*

The ORNL Mechanical Properties Data Storage and Retrieval System (DSRS) has been expanded to include capabilities for the storage, retrieval, and analysis of subcritical crack growth data. Initial data input has begun, with the results from 53 tests now stored on line. Over 8000 mechanical properties tests are now stored in the system.

Development of computer programs to increase the power and flexibility of the system is continuing. The initial version of ADOUT, a new generalized data output program, has been implemented. This program allows the user to receive any of the data stored in DSRS, or various transformations of those data, in the form of tabular output or of punched cards.

A report detailing the development of DSRS has been issued.[38] A general description of the various aspects of the system can be found therein.

### 3.2.6 Elastic Properties of Engineering Construction Materials — J. P. Hammond

Precise measurements show that for metals the "elastic" stress-strain relationships are not perfectly linear, even at low stresses and strain levels, and they become progressively more nonlinear as stress increases. Discrepancies thus often occur between elastic constants determined at different strain levels and rates of strain (for example, constants determined by dynamic and static techniques).

The purpose of this program is to correlate the two separate categories of elastic constants (dynamic and static) for reactor materials of interest. Young's modulus, shear modulus, and Poisson's ratio ($E$, $G$, and $\nu$) are being established, with specific attention given to temperature, preference of cystallographic orientation of grains, and other significant test variables. This information is needed to enable more exact and enlightened use of this class of information in engineering design and structural verification work.

---

*Consultant.

### 3.2.6.1 Elastic Properties Determined by Dynamic Tests — J. P. Hammond and M. W. Moyer*

Dynamic (sonic) elastic constants are being established at room temperature on bulk samples by the pulse-echo method (5 MHz) and at elevated temperatures on wires by the remote magnetostrictive technique[39] (0.2 MHz). The modulus data, which consist of sets of 52 or more points from room temperature to 650°C (1200°F) or higher, are fitted with cubic polynomials by regression analysis. The equations are of a form that normalizes the high-resolution but less accurate elevated-temperature data to the accurate (0.1–0.4% standard error) room-temperature values. Results are obtained as computer readout graphs that give best estimates of the elastic property as a function of temperature.

During the last quarter dynamic elastic constants were determined for Hastelloy X (heat 2600-0-2735) from 24 to 1038°C. They were determined on 19-mm-diam (3/4-in.) rod in the solution annealed condition, parallel to the working direction. Also the effects of heat-to-heat variations on the room-temperature dynamic elastic constants of type 304 stainless steel were examined on bulk samples by the pulse-echo method. Finally, the influence of directionality on the room-temperature dynamic elastic constants was determined on reference heats of solution-annealed type 304 stainless steel (heat 9T2796) and isothermally annealed 2 1/4 Cr-1 Mo steel (heat 20017) as 25-mm (1-in.) plate. The elastic constants as a function of temperature of these heats of type 304 stainless steel[40] (24 to 871°C) and 2 1/4 Cr-1 Mo steel[41] (24 to 649°C) were reported earlier. The chemical analyses of the materials reported on here are given in Table 3.5.

3.2.6.1.1 Elastic Constants of Hastelloy X. The polynomials established for $E$, $G$, and $\nu$ of the Hastelloy X alloy are of the usual form:

$$X = X_0[1 + A_x(T - T_0) + B_x(T - T_0)^2 + C_x(T - T_0)^3] ,$$

*Laboratory Development, Oak Ridge Y-12 Plant.

Table 3.5. Chemical Compositions of Alloys in Elastic Constant Studies

| Alloy, Heat | Content, wt % | | | | | | | | | | | | | | |
|---|---|---|---|---|---|---|---|---|---|---|---|---|---|---|---|
| | C | Mn | Si | Cr | Mo | Ni | Nb | V | Ti | Ta | B | O | S | P | N |
| Hastelloy X 2600-0-2735[a] | 0.09 | 0.46 | 0.42 | 21.15 | 9.10 | 48.30 | | 0.07 | <0.01 | | 0.001 | | 0.004 | 0.015 | |
| Type 304 | | | | | | | | | | | | | | | |
| 346845 | 0.057 | 0.92 | 0.53 | 18.4 | 0.10 | 9.28 | 0.010 | 0.050 | 0.008 | <0.0005 | 0.0002 | 0.0092 | 0.006 | 0.023 | 0.024 |
| 346544 | 0.063 | 0.99 | 0.47 | 18.4 | 0.2 | 9.12 | 0.0050 | 0.025 | 0.017 | 0.0006 | 0.0002 | 0.0081 | 0.006 | 0.023 | 0.019 |
| X22807 | 0.029 | 1.26 | 0.50 | 18.8 | 0.20 | 9.67 | 0.0015 | 0.012 | 0.002 | <0.0005 | 0.0005 | 0.010 | 0.023 | 0.024 | 0.021 |
| 9T2796 | 0.047 | 1.22 | 0.47 | 18.5 | 0.10 | 9.58 | 0.008 | 0.037 | 0.008 | <0.0005 | | 0.0110 | 0.012 | 0.029 | 0.031 |
| Type 316 | | | | | | | | | | | | | | | |
| 8092297 | 0.057 | 1.86 | 0.58 | 17.25 | 2.34 | 13.48 | <0.01 | | 0.02 | <0.01 | 0.0005 | | 0.019 | 0.024 | 0.030 |
| 2 1/4 Cr-1 Mo | 0.135 | 0.57 | 0.37 | 2.5 | 0.92 | 0.16 | | | | | | | 0.016 | 0.012 | |

[a]Plus 18.80% Fe and 0.45% W.

where

$X$ = the property ($E$, $G$, or $\nu$),
$X_0$ = same at 24°C (75°F),
$T$ = temperature in °C or °F,
$T_0$ = 24°C (75°F) and
$A_x$, $B_x$, and $C_x$ = constants.

The coefficients for the polynomials and standard deviations of fit of data are given in Table 3.6, while graphical displays of the equations with the data points superimposed are presented in Fig. 3.45. The room-temperature elastic constants of Hastelloy X, to which the elevated-temperature properties were normalized are:

$$E = 202.1 \pm 0.4 \text{ GPa}$$
$$= 29.31 \times 10^6 \pm 0.06 \times 10^6 \text{ psi}$$
$$G = 77.25 \pm 0.15 \text{ GPa}$$
$$= 11.20 \times 10^6 \pm 0.02 \times 10^6 \text{ psi}$$
$$\nu = 0.3081 \pm 0.0006$$

The elastic properties estimated with the polynomials at 24°C (75°F) and at 28°C (50°F) intervals from 38°C (100°F) to 1038°C (1900°F) are given in Table 3.7.

The dynamic Young's and shear moduli of Hastelloy X (Figure 3.45) decrease nearly linearly with temperature, whereas Poison's ratio increases as expected. The slope of the Poison's curve increases at an increasing rate with temperature, tending toward a value of 0.5 at melting.

3.2.6.1.2 Effects of Heat-To-Heat Variations on the Elastic Constants of Type 304 Stainless Steel. To evaluate the effects of heat-to-heat variations on the room-temperature elastic constants of type 304 stainless steel, we selected three heats as plates for examination. To minimize the influence of any preferred crystallographic orientations, plates of comparatively heavy thickness, 51 to 70 mm (2—2.75 in.), were

Table 3.6. Coefficients for Polynomial Fit to Elastic Constants of Hastelloy X[a]

| Constant | Values of Coefficients | | | | |
|---|---|---|---|---|---|
| | $X_0$ | $A_x$, °C$^{-1}$ | $B_x$, °C$^{-2}$ | $C_x$, °C$^{-3}$ | Std Dev of Fit |
| $E$ | 202.1 GPa<br>$29.31 \times 10^6$ psi | $-2.75322 \times 10^{-4}$ | $-5.50494 \times 10^{-8}$ | $-4.74537 \times 10^{-12}$ | 0.559 GPa<br>$8.11 \times 10^4$ psi |
| $G$ | 77.2 GPa<br>$11.20 \times 10^6$ psi | $-2.89929 \times 10^{-4}$ | $-6.43667 \times 10^{-8}$ | $-1.08062 \times 10^{-11}$ | 0.532 GPa<br>$8.35 \times 10^4$ psi |
| $\nu$ | 0.3081 | $7.47238 \times 10^{-5}$ | $-7.43135 \times 10^{-9}$ | $1.32382 \times 10^{-10}$ | $1.7 \times 10^{-4}$ |

[a] $T_0$ = 24°C.

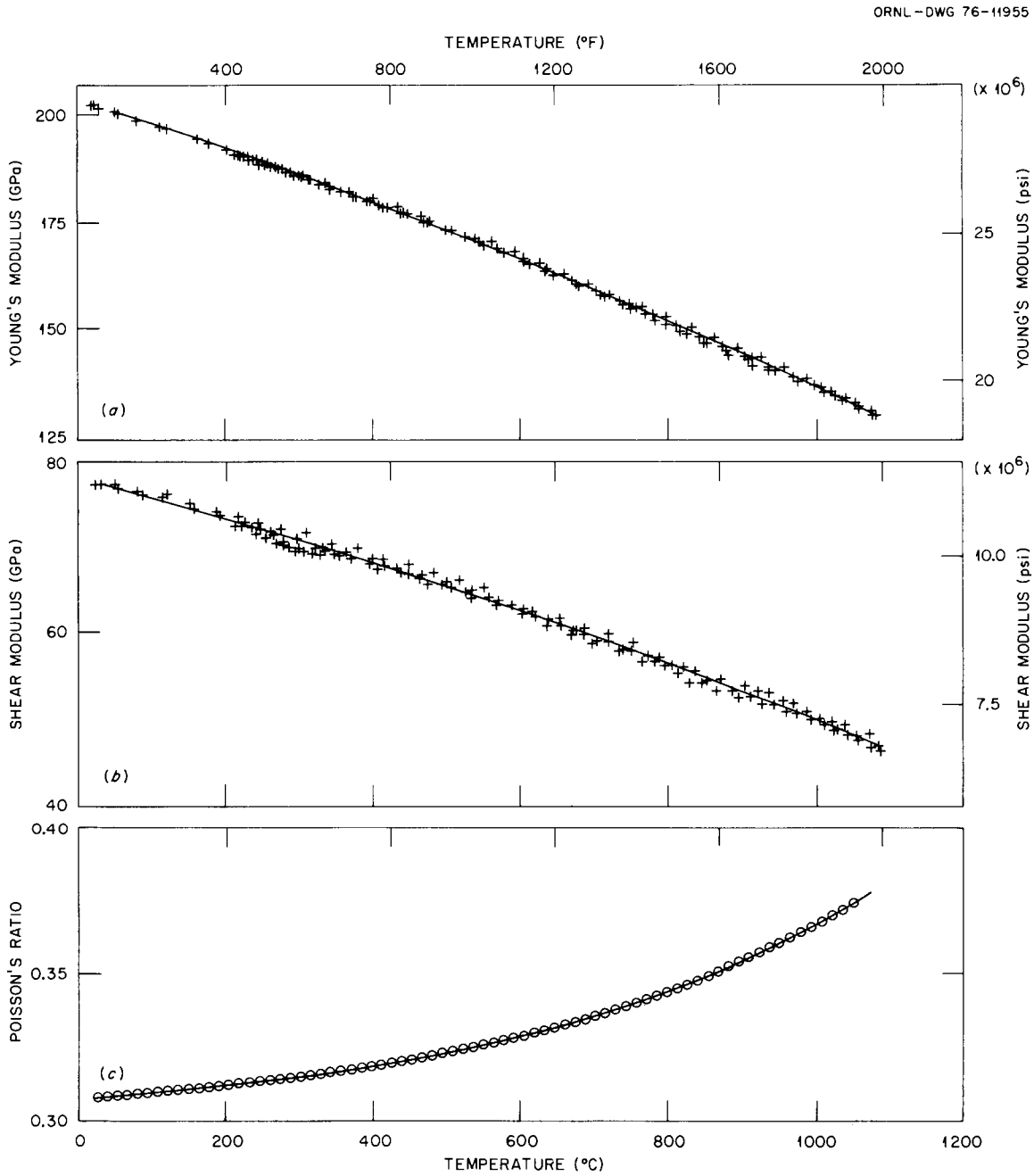


Fig. 3.45. Dynamic Elastic Constants of Hastelloy X, Heat 2600-0-2735.

Table 3.7. Dynamic Elastic Constants of Hastelloy X, Heat 2600-0-2735

| Temperature | | Young's Modulus | | Shear Modulus | | Poisson's Ratio |
|---|---|---|---|---|---|---|
| (°C) | (°F) | (GPa) | (psi) | (GPa) | (psi) | |
| 24 | 75 | 202.2 | $29.32 \times 10^6$ | 77.29 | $11.21 \times 10^6$ | 0.308 |
| 38 | 100 | 201.4 | 29.21 | 76.95 | 11.16 | 0.308 |
| 66 | 150 | 199.8 | 28.98 | 76.32 | 11.07 | 0.309 |
| 93 | 200 | 198.2 | 28.75 | 75.70 | 10.98 | 0.309 |
| 121 | 250 | 196.6 | 28.52 | 75.08 | 10.89 | 0.310 |
| 149 | 300 | 195.1 | 28.29 | 74.39 | 10.79 | 0.311 |
| 177 | 350 | 193.4 | 28.05 | 73.70 | 10.69 | 0.311 |
| 204 | 400 | 191.7 | 27.81 | 73.08 | 10.60 | 0.312 |
| 232 | 450 | 190.1 | 27.57 | 72.39 | 10.50 | 0.313 |
| 260 | 500 | 188.4 | 27.33 | 71.71 | 10.40 | 0.314 |
| 288 | 550 | 186.7 | 27.08 | 71.02 | 10.30 | 0.315 |
| 316 | 600 | 185.0 | 26.83 | 70.33 | 10.20 | 0.316 |
| 343 | 650 | 183.3 | 26.58 | 69.57 | 10.09 | 0.316 |
| 371 | 700 | 181.5 | 26.32 | 68.88 | 9.99 | 0.317 |
| 399 | 750 | 179.7 | 26.06 | 18.12 | 9.88 | 0.319 |
| 427 | 800 | 177.9 | 25.80 | 67.43 | 9.78 | 0.320 |
| 454 | 850 | 176.1 | 25.54 | 66.67 | 9.67 | 0.321 |
| 482 | 900 | 174.2 | 25.27 | 65.91 | 9.56 | 0.322 |
| 510 | 950 | 172.4 | 25.00 | 65.16 | 9.45 | 0.324 |
| 538 | 1000 | 170.5 | 24.73 | 64.33 | 9.33 | 0.325 |
| 566 | 1050 | 168.6 | 24.46 | 63.57 | 9.22 | 0.326 |
| 593 | 1100 | 166.7 | 24.18 | 62.74 | 9.10 | 0.328 |
| 621 | 1150 | 164.8 | 23.90 | 61.98 | 8.99 | 0.330 |
| 649 | 1200 | 162.9 | 23.62 | 61.16 | 8.87 | 0.332 |
| 677 | 1250 | 160.9 | 23.33 | 60.33 | 8.75 | 0.333 |
| 704 | 1300 | 158.9 | 23.04 | 59.50 | 8.63 | 0.335 |
| 732 | 1350 | 156.9 | 22.75 | 58.61 | 8.50 | 0.338 |
| 760 | 1400 | 154.8 | 22.45 | 57.78 | 8.38 | 0.340 |
| 788 | 1450 | 152.8 | 22.16 | 56.88 | 8.25 | 0.342 |
| 816 | 1500 | 150.7 | 21.86 | 56.05 | 8.13 | 0.345 |
| 843 | 1550 | 148.6 | 21.55 | 55.16 | 8.00 | 0.348 |
| 871 | 1600 | 146.4 | 21.24 | 54.26 | 7.87 | 0.350 |
| 899 | 1650 | 144.3 | 20.93 | 53.30 | 7.73 | 0.353 |
| 927 | 1700 | 142.2 | 20.62 | 52.40 | 7.60 | 0.357 |
| 954 | 1750 | 140.0 | 20.31 | 51.43 | 7.46 | 0.360 |
| 982 | 1800 | 137.8 | 19.99 | 50.54 | 7.33 | 0.364 |
| 1010 | 1850 | 135.6 | 19.66 | 49.57 | 7.19 | 0.368 |
| 1038 | 1900 | 133.3 | 19.34 | 48.61 | 7.05 | 0.372 |

employed, and specimens were cut parallel to the metal rolling direction at comparable depths.

Table 3.8 presents the elastic constants ($E$, $G$, and $\nu$) of the heats for the mill annealed and reannealed conditions with average standard errors for their determination and maximum differences in constants between heats, for comparison. The tolerance values given for the individual determinations are standard errors. Heats of high, medium, and low yield strength in the as-received condition were selected to check any correlation of properties with strength, but upon reannealing the order of strength was altered as noted in the table.

Table 3.8. Effects of Heat-to-Heat Variations and Metal Condition on Dynamic Elastic Constants[a] of Type 304 Stainless Steel at Room Temperature

| Heat | Thickness of Plate (mm) | Yield Strength (MPa)[b] | Modulus, GPa[b] | | |
|---|---|---|---|---|---|
| | | | $E$ | $G$ | $\nu$ |
| | | | Mill Annealed | | |
| 845 | 70 | 36.0 | 200.7 ± 0.9 | 77.93 ± 0.22 | 0.2878 ± 0.0012 |
| 544 | 51 | 35.5 | 201.1 ± 0.1 | 78.04 ± 0.07 | 0.2885 ± 0.0003 |
| 807 | 64 | 33.2 | 200.0 ± 0.6 | 77.53 ± 0.09 | 0.2901 ± 0.0008 |
| av std error, three heats | | | 0.26% | 0.15% | 0.26% |
| max difference between heats | | | 0.55% | 0.77% | 0.79% |
| | | | Reannealed | | |
| 845 | 70 | 29.7 | 201.4 ± 0.4 | 78.26 ± 0.12 | 0.2868 ± 0.0006 |
| 544 | 51 | 31.3 | 201.2 ± 0.7 | 78.14 ± 0.07 | 0.2876 ± 0.0008 |
| 807 | 64 | 27.0 | 200.9 ± 0.7 | 78.01 ± 0.14 | 0.2876 ± 0.0009 |
| av std error, three heats | | | 0.28% | 0.14% | 0.27% |
| max difference between heats | | | 0.24% | 0.26% | 0.28% |
| 796[c] | 25 | | 200.1 ± 0.3 | 77.51 ± 0.13 | 0.2905 ± 0.0005 |
| 297[d] | 25 | | 198.0 ± 0.8 | 76.74 ± 0.16 | 0.2901 ± 0.0011 |

[a]Specimen axis aligned parallel to rolling direction.

[b]To convert to psi, multiply GPa values by $1.450 \times 10^5$, MPa by 145.0.

[c]Solution annealed.

[d]Type 316, solution annealed (for comparison).

For comparison, the constants of type 304 (heat 9T2796) and type 316 stainless steel (heat 8092297), both as 25-mm (1-in.) solution annealed plate, are listed at the bottom of Table 3.8. To aid the interpretation of results, the individual values of the constants with magnitude of average standard errors for their determination are shown graphically in Fig. 3.46.

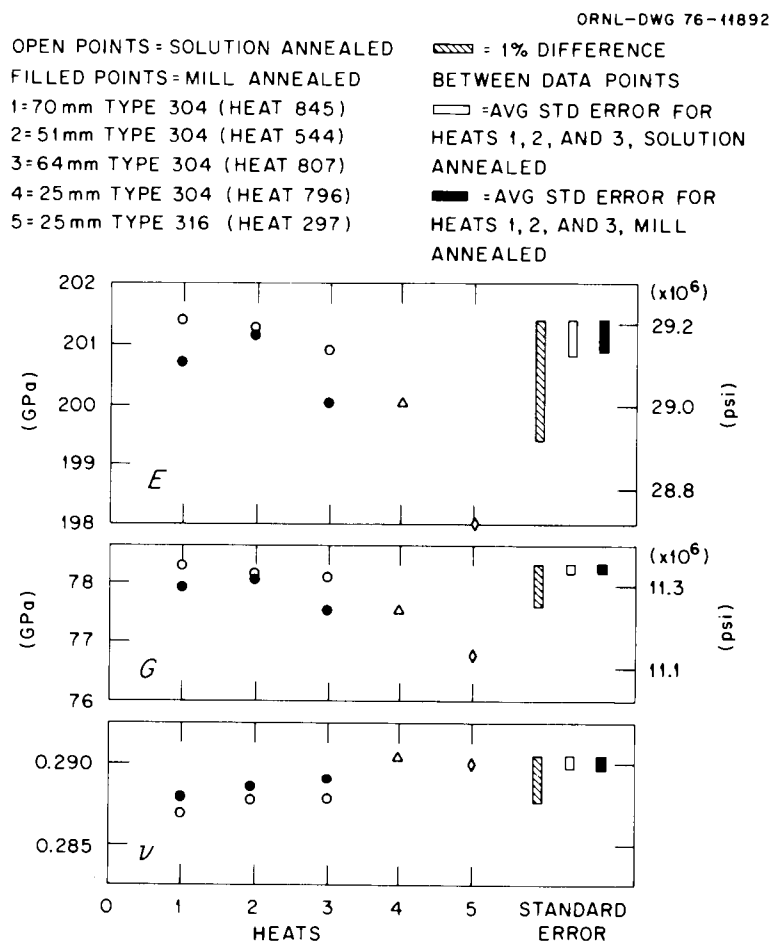


Fig. 3.46. Graphical Comparisons of Elastic Constants of Type 304 Stainless Steels.

Observe that the maximum difference in constants between the three heats of type 304 selected for comparison in each instance was less than 0.8% for the mill annealed condition and less than 0.3% for the reannealed (see Table 3.8). The latter spread was hardly larger than

the standard errors for determining the constants, which ranged in value from only 0.14 to 0.28%. In all instances, the Young's and shear moduli for the reannealed condition exceeded that for the mill annealed, whereas for Poisson's ratio the relationship was reversed (see Fig. 3.46), although in some cases the differences were very small.

The elastic constants of the materials failed to show any correlation with the yield strength data, although this is not surprising in view of the rather shallow spread of elastic constants between heats in relation to magnitude of the standard error for determining them. The Young's and shear moduli for the solution annealed type 304 stainless plate of 25-mm thickness (heat 9T2796) was somewhat lower than those solution annealed plates of heavier thickness, while that for the solution annealed type 316 stainless plate was somewhat lower yet. The Poisson's ratios for the latter materials, on the other hand, ran higher.

As will be shown subsequently, heat 9T2796 displayed significant anisotropy of elastic constants, and it is likely that the lower moduli of the 25-mm plate stem from a small degree of crystallographic preferredness in its grain structure.

The other trends observed in the constant values can be rationalized simply in terms of lattice strain, although several of the differences in values to be noted are not very appreciable. If it is considered that lattice stiffness is greatest when atoms or lattice ions are located at their equilibrium positions — that is, binding forces diminish as atoms are strained out of their energy troughs — then the results are correlatable. Accordingly, the modulus values should be higher for the materials in the reannealed condition than for the mill annealed, where, as a result of final finish rolling or straightening operations, elastic as well as plastic strains are left within the lattice. The lower modulus values for the heats in the mill annealed state as compared with the reannealed then result from atoms being strained out of their equilibrium sites, where binding forces are diminished.

The low values of the moduli for the solution annealed type 316 stainless steel in relation to those for solution annealed type 304 may be attributed to lattice strain introduced in type 316 as a result its

molybdenum solute additive, present at a level of 2.34% (see Table 3.5). Based upon lattice cell size, the atomic diameters of the principal elements of type 304 stainless steel (i.e., Fe, Ni, and Cr) are all within about 1% of one another, whereas the diameter of molydenum is about 10% higher. The atomic diameters of Fe, Ni, Cr, and Mo are 2.48, 2.49, 2.50, and 2.73 Å, respectively. Thus variations of composition within the type 304 stainless steel specification should little influence its elastic constants, whereas introduction of molydenum or variations in the concentration of molydenum in the type 316 stainless steel should significantly affect the constants.

Observe in Table 3.8 that this pattern of behavior is precisely what occurred. For example, heat-to-heat variations for the solution annealed type 304 changed the Young's modulus only 0.24%, whereas introduction of molydenum, as represented by comparing the Young's modulus for the solution annealed type 316 stainless steel, reduced Young's modulus by approximately 1.6%.

3.2.6.1.3 Directionality of Elastic Constants in Plates of Type 304 Stainless Steel and 2 1/4 Cr-1 Mo Steel. The elastic constants established for the principal directions in 25-mm-thick plates of solution annealed type 304 stainless steel and isothermally annealed 2 1/4 Cr-1 Mo steel are presented in Table 3.9. The percent difference in the individual elastic constants with direction in the plate and average standard error values for determining the constants are given at the bottom of the table. Again standard error values for the individual determinations are listed as tolerances.

Observe that whereas the variation in elastic constants with direction in the type 304 stainless steel was substantial (amounting to as much as 5 to over 10 times the average standard errors for their determination), the variation in constants in the 2 1/4 Cr-1 Mo steel was small in comparison. In the instance of the Young's modulus of 2 1/4 Cr-1 Mo steel the difference barely exceeded the average standard error. The substantial variation in elastic constants with direction in the type 304 stainless steel plate was considered to result principally from a condition of preferred crystallographic grain orientation

Table 3.9. Variation of Dynamic Elastic Constants with Direction in 25-mm-Thick Plates of Type 304 Stainless Steel and 2 1/4 Cr-1 Mo Steel

| Orientation of Specimen Axis[a] | Type 304[b] | | | 2 1/4 Cr-1 Mo[c] | | |
|---|---|---|---|---|---|---|
| | $E$ (GPa)[d] | $G$ (GPa)[d] | $\nu$ | $E$ (GPa)[d] | $G$ (GPa)[d] | $\nu$ |
| ∥ to RD | 200.1 ± 0.3 | 77.51 ± 0.13 | 0.2905 ± 0.0005 | 214.5 ± 0.2 | 83.66 ± 0.07 | 0.2819 ± 0.0003 |
| 45° to RD in RP | 197.8 ± 0.9 | 76.15 ± 0.07 | 0.2986 ± 0.0010 | | | |
| 90° to RD in RP | 202.3 ± 0.6 | 78.95 ± 0.2 | 0.2813 ± 0.0010 | 213.8 ± 1.3 | 83.23 ± 0.65 | 0.2842 ± 0.0024 |
| ⊥ to RP | 200.0 ± 1.6 | 77.57 ± 0.8 | 0.2888 ± 0.0031 | 214.4 ± 0.5 | 83.52 ± 0.20 | 0.2837 ± 0.0008 |
| av std error | 0.42% | 0.39% | 0.47% | 0.30% | 0.35% | 0.34% |
| max difference | 2.24% | 3.55% | 5.79% | 0.33% | 0.52% | 0.83% |
| max difference[e] | 1.12% | 1.83% | 3.15% | | | |

[a]∥ = parallel; RD = rolling direction; RP = rolling plane; ⊥ = perpendicular.

[b]Heat 796, solution annealed.

[c]Heat 017, isothermally annealed.

[d]To convert to ksi, multiply by $1.450 \times 10^5$.

[e]With axis 45° to RD excluded.

introduced during its metalworking and annealing operations. Kikuchi[42] has shown that the elastic constants at room temperature can vary by a factor of 3.1 with crystallographic direction in single crystals of type 305 (18 Cr-12 Ni) stainless steel. For example, the $E$ values varied as follows:

$$\langle 111 \rangle,\ 314\ \text{GPa};\ \langle 100 \rangle,\ 101\ \text{GPa};\ \langle 110 \rangle,\ 206\ \text{GPa}.$$

Therefore, to account for the variation of elastic constants with direction, or lack thereof, in our materials, we assess the preferred crystallographic conditions in the respective materials. This was done by x-ray diffraction by establishing the relative intensities of x-ray reflections from the (111), (110), and (100) planes when normal to the specimen axes, for the differently oriented samples. To enable comparisons between samples and plane families, the x-ray reflections were normalized to intensities for random grain orientations established with powder samples of the materials.

This analysis gave equivalent principal plane [(110), (110), and (100)] reflection intensities between sample orientations for the 2 1/4 Cr-1 Mo steel but significantly different intensities in the case of the type 304 stainless steel, indicating an essentially random crystallographic grain orientation in the former material and a moderately preferred one for the latter. The fact that the 2 1/4 Cr-1 Mo steel failed to reveal any appreciable anisotropy of elastic constants with direction in the plate was attributed to the allotropic crystallographic transformation associated with such ferrous alloys. With cycling through the phase transformation range that occurs with the metalworking and heat-treating operations for this material, refinement and crystallographic randomization of grain structure occur.

## 3.3 MECHANICAL AND METALLURGICAL BEHAVIOR OF WELDMENTS FOR LMFBR — P. Patriarca, G. M. Slaughter, W. R. Martin, and C. R. Brinkman

### 3.3.1 Effect of Postweld Heat Treatment and Creep Prestraining on the Creep-Rupture Behavior of Type 308 Stainless Steel Submerged-Arc Welds — E. Bolling and R. T. King

Two related creep experiments at 649°C are being performed on a single type 308 stainless steel weld made by the submerged-arc process in 51-mm-thick (2-in.) type 304 stainless steel plate. First, the creep-rupture properties at 138 and 172 MPa (20 and 25 ksi) of as-deposited longitudinal weld and transverse weldment specimens are being compared with those of longitudinal weld and transverse weldment specimens that have been heat-treated for 4 hr at 607 or 982°C (1125 or 1800°F) in air. The rationale for expecting the latter heat treatment to partially dissolve and agglomerate ferrite, thereby reducing the continuity of sigma phase formed in testing and improving ductility, has been discussed in an earlier report.[43] The materials and testing methods for this experiment were also presented in the earlier report.[43] A second experiment is aimed at examining whether prestraining in creep at 649°C at low stress [110 or 124 MPa (16 or 18 ksi)] for short fractions of the rupture life has a detrimental effect on ductility when the stress is increased (incremented) to cause rupture in a short time at 172 MPa. If sigma phase is formed at low stress, then incrementally stressed specimens should be less ductile than specimens ruptured in short time without prestrain. The testing in the second experiment was performed by methods identical to those used in the first experiment,[43] except that the load was incremented at temperature by supporting the load train, adding weight to the load, and continuously reapplying the load. Thus the high-stress (172 MPa) tests from the first experiment served as no-prestrain controls for the second experiment.

The data from all the tests are combined in Tables 3.10 and 3.11. All terms are as defined previously.[43] The basic creep-rupture data are combined in Figs. 3.47 through 3.50 for specimens from near the surface (L1, T1 types) and at a position intermediate to the surface and root pass regions (L2, T2 types). With the exception of one transverse

Table 3.10. Creep Test Times to Various Events for Type 308 Stainless Steel Submerged-Arc Welds Tested at 649°C (1200°F)

| Specimen Orientation and Level | Stress (MPa) | Stress (ksi) | Approximate Time, hr, to Various Events: End First Stage | End Second Stage | 0.2% Offset Third Stage | Fracture | 0.5% Creep Strain | 1% Creep Strain | 2% Creep Strain | 0.5% Total Strain | 1% Total Strain | 2% Total Strain | $t_{III}/t_r$ |
|---|---|---|---|---|---|---|---|---|---|---|---|---|---|
| | | | | | | As Welded | | | | | | | |
| Longitudinal 1 | 138 | 20 | 43 | 211 | 325 | 530.6 | 16 | 66 | 195 | 0.9 | 31 | 149 | 0.61 |
| | 172 | 25 | 1.0 | 10.2 | 15.0 | 69.1 | 0.8 | 2.8 | 6.8 | 0.08 | 1.2 | 5.2 | 0.22 |
| | 110 | 16 | 82.6 | | | a | 255 | | | 59.8 | | | |
| | 172[b] | 25 | 6.5 | 24.3 | 48 | 95.3 | 8.5 | 20.1 | 55 | 8.5 | 20.1 | 55 | 0.57 |
| | 124 | 18 | | | | a | | | | | | | |
| | 172[b] | 25 | | | | 45.0 | | | | | | | |
| Longitudinal 2 | 138 | 20 | 65.1 | 233.2 | 593.3 | 786.4 | 76.5 | 432.7 | 754.2 | 1.0 | 167.4 | 686.2 | 0.75 |
| | 172 | 25 | 8.0 | 35.0 | 56.0 | 144.9 | 6.1 | 15.6 | 40.0 | 0.1 | 7 | 30.5 | 0.39 |
| Transverse 1 | 138 | 20 | 202.5 | 473.9 | 695 | 757.8 | 92.4 | 372.7 | 740 | 13.7 | 215.5 | 686.8 | 0.92 |
| | 172 | 25 | 2.7 | 30.6 | 42 | 113.2 | 4 | 10 | 23 | 0.8 | 6 | 20 | 0.37 |
| Transverse 2 | 138 | 20 | 74.5 | 444.9 | 620 | 623.9 | 368.2 | 615 | 621 | 57.5 | 602 | 620 | 0.99 |
| | 172 | 25 | 2.0 | 58.2 | 102.7 | 204.5 | 30.5 | 70.9 | 121.6 | 0.05 | 33.2 | 101.1 | 0.50 |
| | | | | | | Annealed 4 hr at 607°C (1125°F), Water Quenched | | | | | | | |
| Longitudinal 1 | 138 | 20 | 73.9 | 370 | 550 | 728.1 | 54 | 241 | 550 | 3.9 | 114 | 473 | 0.75 |
| | 172 | 25 | 1.0 | 17.5 | 22.5 | 71.9 | 1.0 | 3.2 | 7.5 | 0.2 | 1.1 | 5.4 | 0.31 |
| Longitudinal 2 | 138 | 20 | 100 | 650 | 800 | 957.0 | 200 | 622 | 902 | 12 | 344 | 845 | 0.84 |
| | 172 | 25 | 2.4 | 31.6 | 43.5 | 147.9 | 5.2 | 16 | 35 | 0.25 | 6.5 | 29 | 0.29 |
| Transverse 1 | 138 | 20 | 43.2 | 403.6 | 675 | 774.9 | 137 | 386 | 706 | 124 | 370 | 701 | 0.87 |
| | 172 | 25 | 0.8 | 12.5 | 23 | 81.9 | 2.2 | 6.5 | 14 | 0.1 | 2.6 | 11 | 0.18 |
| Transverse 2 | 138 | 20 | 66 | 839 | 1190 | 1190.4 | 791 | 1172 | 1175 | 189 | 1103 | 1173 | 1.00 |
| | 172 | 25 | 7.5 | 66.2 | 120 | 217.1 | 26 | 67 | 123 | 1.3 | 36 | 105 | 0.55 |
| | | | | | | Annealed 2 hr at 982°C (1800°F), Water Quenched | | | | | | | |
| Longitudinal 1 | 138 | 20 | 100 | 498 | 714 | 1346.7 | 9.2 | 73.9 | 401 | 0.2 | 14.6 | 271 | 0.53 |
| | 172 | 25 | 7.1 | 25.0 | 32.5 | 79.2 | 0.2 | 0.7 | 2.2 | ∿0 | 0.01 | 0.7 | 0.41 |
| | 110 | 16 | a | | | | a | | | | | | |
| | 172[b] | 25 | ∿4 | ∿32 | ∿39 | 108.9 | 1.2 | 5 | 14 | 1.2 | 5 | 14 | 0.36 |
| | 124[c] | 18 | | | | a | | | | ∿27 | | | |
| | 172[b] | 25 | | | | 97.8 | 13 | 20 | 22 | 13 | 20 | 22 | ∿0 |
| Longitudinal 2 | 138 | 20 | 46 | 721.5 | 905.7 | 1320.4 | 5.2 | 40 | 386 | 0.3 | 6.5 | 244 | 0.69 |
| | 172 | 25 | 6 | 82.3 | 89.7 | 166.2 | 0.4 | 1.2 | 3.5 | 0 | 0 | 0.1 | 0.54 |
| Transverse 1 | 138 | 20 | 114.6 | 618.5 | 955 | 1278.1 | 5.6 | 193 | 655 | ∿0 | ∿0 | 167 | 0.75 |
| | 172 | 25 | 12 | 54 | 68 | 112.5 | 0.6 | 2.1 | 7.2 | | 0.07 | 2.8 | 0.60 |
| Transverse 2 | 138 | 20 | 187 | 803.9 | 1027 | 1973.1 | 9.7 | 64 | 336 | 0.05 | 10.3 | 181 | 0.52 |
| | 172 | 25 | 27.8 | 107.5 | 131.5 | 211.4 | 0.5 | 2.2 | 6.9 | ∿0 | ∿0 | 0.9 | 0.62 |

[a]Load increased to 172 MPa (25 ksi) after 500 hr.

[b]Same specimen as shown on line above at lower stress. Times are measured from the time the stress was increased.

[c]No sense can be attached to the results because the specimen strained 0.21% on load, jumped from 0.24 to 0.53% strain between 18.4 and 35.5 hr, and then exhibited no significant strain before the load was increased.

Table 3.11. Creep Test Strain Data for Type 308 Stainless Steel Submerged-Arc Welds Tested at 649°C (1200°F)

| Specimen Orientation and Level | Stress (MPa) | Stress (ksi) | Strain, % Loading $\varepsilon_L$ | Strain, % $\varepsilon_I$ Stage I | Strain, % Stage II Real | Strain, % Stage II Offset | Strain, % Rupture $\varepsilon_r$ | Strain Rate, %/hr $\dot{\varepsilon}$ Stage II Real | Strain Rate, %/hr $\dot{\varepsilon}$ Stage II Offset | Strain Rate, %/hr $\varepsilon_r/t_r$ | Reduction of Area (%) | Total Rupture Time, $\varepsilon_r$ (hr) | $\varepsilon_{III}/\varepsilon_r$ |
|---|---|---|---|---|---|---|---|---|---|---|---|---|---|
| | | | | | | As Welded | | | | | | | |
| Longitudinal 1 | 138 | 20 | 0.23 | 0.51 | 0.856 | 1.57 | 7.5 | 0.0051 | 0.0056 | 0.014 | 12.6 | 530.6 | 0.39 |
| | 172 | 25 | 0.26 | 0.35 | 1.44 | 2.4 | 29.0 | 0.160 | 0.17 | 0.34 | 29.1 | 69.1 | 0.13 |
| | 110 | 16 | 0.13 | 0.37 | | | a | 0.00048 | | | | a | |
| | 172[b] | 25 | 0.14 | 0.23 | 0.39 | 0.92 | 8.2 | 0.020 | 0.020 | | | 595.3 | |
| | 124 | 18 | | | | | a | | | | | a | |
| | 172[b] | 25 | | | | | | | | | | 545.0 | |
| Longitudinal 2 | 138 | 20 | 0.25 | 0.31 | 0.128 | 0.52 | 6.3 | 0.00072 | 0.0009 | 0.006 | 6.3 | 786.4 | 0.21 |
| | 172 | 25 | 0.23 | 0.45 | 0.72 | 1.48 | 15.2 | 0.0261 | 0.031 | 0.085 | 26.7 | 144.9 | 0.18 |
| Transverse 1 | 138 | 20 | 0.18 | 0.45 | 0.28 | 0.68 | 5.0 | 0.0010 | 0.0013 | 0.0052 | 3.8 | 757.8 | 0.33 |
| | 172 | 25 | 0.24 | 0.34 | 1.67 | 2.46 | 11.2 | 0.060 | 0.062 | 0.185 | 16.5 | 113.2 | 0.31 |
| Transverse 2 | 138 | 20 | 0.144 | 0.19 | 0.168 | 0.06 | 3.0 | 0.00048 | 0.0073 | 0.0039 | 2.5 | 623.9 | 0.30 |
| | 172 | 25 | 0.29 | 0.10 | 0.41 | 0.896 | 6.7 | 0.0075 | 0.008 | 0.026 | 8.0 | 204.5 | 0.24 |
| | | | | | | Annealed 4 hr at 607°C (1125°F), Water Quenched | | | | | | | |
| Longitudinal 1 | 138 | 20 | 0.20 | 0.36 | 0.49 | 9.2 | 4.7 | 0.0016 | 0.0019 | 0.0054 | 4.8 | 728.1 | 0.40 |
| | 172 | 25 | 0.34 | 0.31 | 2.56 | 3.6 | 24.2 | 0.157 | 0.166 | 0.27 | 33.4 | 71.9 | 0.22 |
| Longitudinal 2 | 138 | 20 | 0.268 | 0.24 | 0.43 | 0.69 | 5.7 | 0.0008 | 0.0009 | 0.0074 | 5.0 | 957.0 | 0.25 |
| | 172 | 25 | 0.28 | 0.21 | 0.912 | 1.46 | 20.4 | 0.031 | 0.035 | 0.68 | 25.7 | 147.9 | 0.11 |
| Transverse 1 | 138 | 20 | 0.024[c] | 0.17 | 0.52 | 1.21 | 5.6 | 0.0013 | 0.0002 | 0.0057 | 8.2 | 774.9 | 0.27 |
| | 172 | 25 | 0.28 | 0.36 | 0.75 | 1.76 | 14.5 | 0.064 | 0.079 | 0.144 | 25.7 | 81.9 | 0.21 |
| Transverse 2 | 138 | 20 | 0.16 | 0.12 | 0.22 | 0.46 | 2.5 | 0.00025 | 0.00040 | 0.0019 | 1.0 | 1190.4 | 0.37 |
| | 172 | 25 | 0.25 | 0.17 | 0.45 | 1.04 | 7.5 | 0.0078 | 0.0093 | 0.026 | 14.0 | 217.1 | 0.24 |
| | | | | | | Annealed 2 hr at 892°C (1800°F), Water Quenched | | | | | | | |
| Longitudinal 1 | 138 | 20 | 0.26 | 0.71 | 0.74 | 1.28 | 9.6 | 0.0018 | 0.0020 | 0.0059 | 7.2 | 1346.7 | 0.29 |
| | 172 | 25 | 0.64 | 2.48 | 3.88 | 5.84 | 33.7 | 0.22 | 0.23 | 0.34 | 36.5 | 79.2 | 0.33 |
| | 110 | 16 | 0.02 | 0.24 | | | a | 0.00023 | | | | a | |
| | 172[b] | 25 | | 0.73 | 2.34 | 3.21 | 25.3 | 0.106 | 0.0942 | 0.18 | 26.3 | 608.9 | 0.2 |
| | 124[d] | 18 | 0.21 | | | | a | | | | | a | |
| | 172[b] | 25 | | | | | 27.3 | | | | 22.3 | 597.8 | |
| Longitudinal 2 | 138 | 20 | 0.24 | 0.66 | 1.22 | 1.73 | 10.1 | 0.0018 | 0.0020 | 0.0060 | 10.9 | 1320.4 | 0.33 |
| | 172 | 25 | 1.2 | 1.75 | 9.92 | 11.04 | 45.6 | 0.130 | 0.132 | 0.23 | 42.4 | 166.2 | 0.36 |
| Transverse 1 | 138 | 20 | 1.00 | 0.60 | 0.73 | 1.36 | 6.9 | 0.0014 | 0.0016 | 0.0043 | 9.5 | 1278.1 | 0.52 |
| | 172 | 25 | 0.53 | 1.72 | 3.2 | 4.53 | 16.5 | 0.076 | 0.180 | 0.12 | 31.4 | 112.5 | 0.52 |
| Transverse 2 | 138 | 20 | 0.304 | 0.99 | 1.11 | 1.65 | 11.3 | 0.0018 | 0.0020 | 0.0045 | 8.5 | 1973.1 | 0.33 |
| | 172 | 25 | 1.2 | 2.96 | 4.8 | 6.4 | 22.4 | 0.060 | 0.062 | 0.085 | 46.0 | 211.4 | 0.59 |

[a]Load increased to 172 MPa (25 ksi) after 500 hr.

[b]Same specimen as shown on line above at lower stress.

[c]Value questionable because of apparent dial gage or specimen bending problem.

[d]No sense can be attached to the results because the specimen strained 0.21% on load, jumped from 0.24 to 0.53% strain between 18.4 and 35.5 hr, and then exhibited no significant strain before the load was increased.

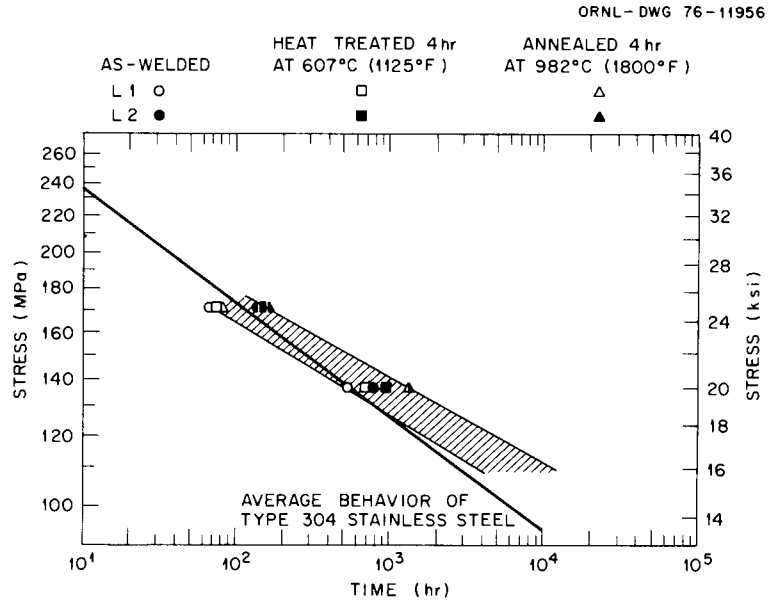


Fig. 3.47. Creep-Rupture Behavior of Longitudinal All-Weld-Metal Specimens of Type 308 Stainless Steel Submerged-Arc Welds at 649°C (1200°F).

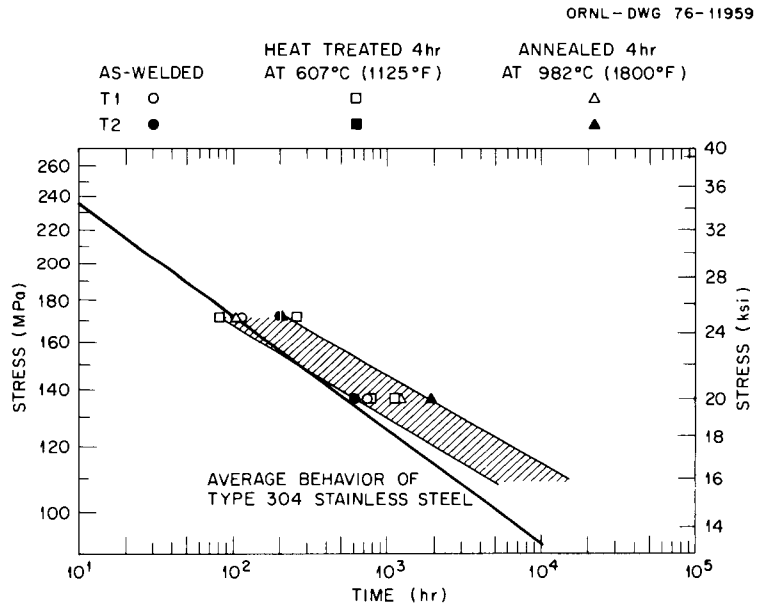


Fig. 3.48. Creep-Rupture Behavior of Transverse Weldment Specimens of Type 308 Submerged-Arc Welds in Type 304 Stainless Steel Base Metal, Tested at 649°C (1200°F).

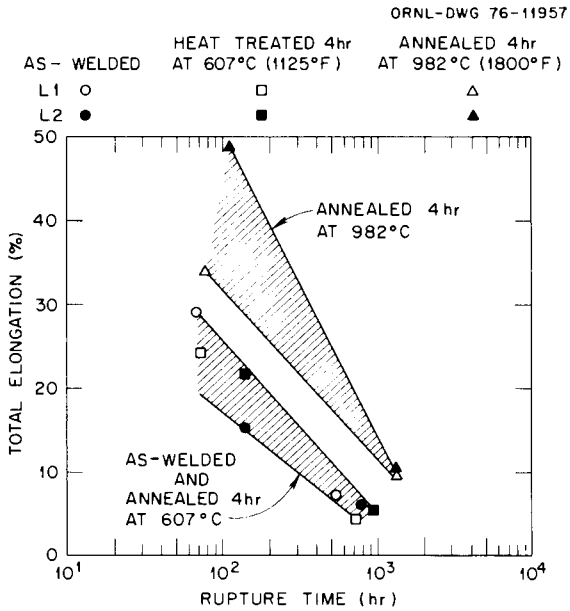


Fig. 3.49. Creep-Rupture Strain Behavior of Longitudinal All-Weld-Metal Specimen of Type 308 Stainless Steel Submerged-Arc Welds at 649°C (1200°F).

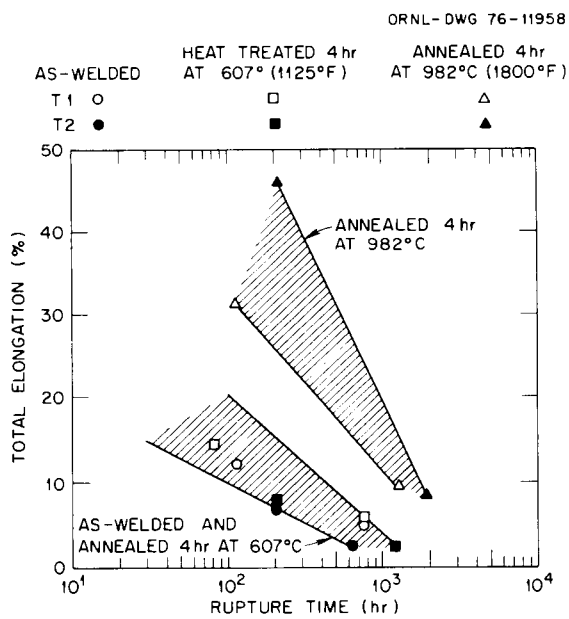


Fig. 3.50. Creep-Rupture Strain Behavior of Transverse Weldment Specimens of Type 308 Submerged-Arc Welds in Type 304 Stainless Steel Base Metal, Tested at 649°C (1200°F).

weldment specimen that apparently failed in the heat-affected zone, all failures were in weld metal and involved substructural separations typical of sigma-phase-affected ruptures.

From the creep-rupture plots (Figs. 3.47 and 3.48), we estimate that prestraining 500 hr at 110 MPa (16 ksi) consumes from 0.01 to 0.02 of the rupture time at that stress, while prestraining 500 hr at 124 MPa (18 ksi) consumes between 0.03 and 0.05 of the rupture time at that stress. The effect of these prestrain treatments is judged by the ratio of total elongation for prestrained specimen to that of a nonprestrained control specimen. These ratios are shown in Fig. 3.51.

The significant results from testing at constant load at 649°C are:

1. Creep-rupture times for this weld metal in all conditions investigated tend to be slightly longer than average rupture times for annealed type 304 stainless steel base metal.

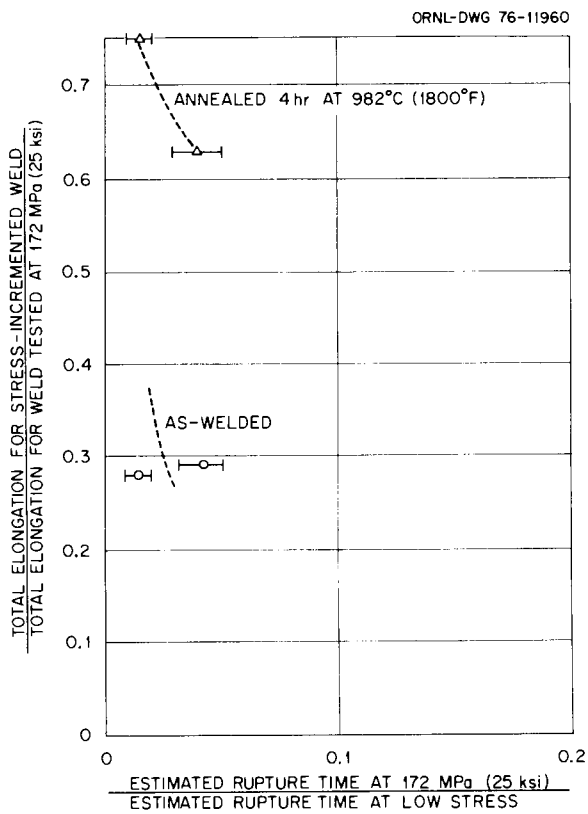


Fig. 3.51. Effect of Prestraining at Low Stress [110 and 124 MPa (16 and 18 ksi)] on Strain for Specimens Incremented to 172 MPa (25 ksi) After 500 hr.

2. At 172 MPa (25 ksi), transverse weldment specimens have longer rupture times than longitudinal all-weld-metal specimens, but at 138 MPa (20 ksi) no distinction can be made.

3. The time to the onset of tertiary creep is between 0.5 and 1.0 times the rupture time at 172 MPa (25 ksi) and between 0.18–0.62 times at 138 MPa (20 ksi).

4. The strain at the onset of tertiary creep is 0.1 to 0.4 of the total fracture strain for as-welded metal and welds heat-treated at 607°C and 0.2 to 0.6 for welds annealed at 982°C.

5. The rupture strains for all the conditions decrease with increasing rupture time from about 100 to about 1000 hr. The lowest rupture strains, in the 2–3% range, occur for transverse as-deposited and 607°C-heat-treated specimens.

6. Weld metal annealed 4 hr at 982°C has greater ductility than as-deposited weld metal or welds heat-treated 4 hr at 607°C.

The significant results from incremented stress tests performed on longitudinal all-weld-metal specimens in the as-deposited condition or after annealing for 4 hr at 982°C are:

1. Prestraining at 110 and 124 MPa (16 and 18 ksi) for times to about 0.01 to 0.05 of the total estimated rupture times at those stresses has no experimentally significant effect on the rupture time when the stress is later raised to 172 MPa (25 ksi).

2. Prestraining as-deposited weld metal reduces the total rupture strains to about one-third the values observed in tests at 172 MPa only.

3. Prestraining weld metal annealed at 982°C reduces the total rupture strains to about 0.7 times the values observed in tests at 172 MPa only.

4. Such testing results in fracture morphologies commonly associated with transformation of ferrite to sigma phase and failures that propagate along sigma phase austenite boundaries. The 500-hr period of prestraining allows the sigma phase to form and causes relatively low-ductility failures when the stress is incremented. Welds annealed at 982°C are suspected of having less continuous ferrite; metallography to demonstrate this point is in progress.

### 3.3.2 Status of Creep Testing on 16-8-2 Submerged Arc Welds — R. T. King, D. P. Edmonds, and E. Bolling

A preliminary report[44] has given details on the materials, experimental and testing methods, and certain characteristics of type 16-8-2 submerged-arc welds made in 25-mm-thick (1-in.) type 316 stainless steel plate. Here we simply update the creep-rupture test data of Table 3.23 of that report and make some corrections. Table 3.12 gives the status of creep-rupture tests together with some of the more important test data that have been obtained.

With two exceptions, all the specimens tested have failed in weld metal. The exceptions are specimens 775-T3 and -T7, both of which were intended to be transverse weld metal specimens. Some base metal was inadvertently included in the gage length, and the fracture surface includes both regions of intergranular separation in the HAZ very near to the fusion line and apparently trans-substructural tearing in the weld metal. Because of possible stress concentration effects near the geometrical discontinuity at the fillet at the end of the gage length and near the metallurgical discontinuity at the fusion line, this failure path does not necessarily imply higher strength for weld metal or HAZ under these test conditions.

We are now preparing impact and aging specimens for characterization. Preliminary results will be reported later.

### 3.3.3 Demonstration on Importance of Anisotropy in Welded Pipe Calculations — B. R. Dewey

Work is continuing in the development of constitutive equations that recognize anisotropy in weld metal. To demonstrate the use of some recently presented data,[45] a finite element program was modified to accept orthotropic elastic constants and has been used to conduct stress analysis in a hypothetical weld joint in a pipe.

#### 3.3.3.1 Description of Finite Element Program

With finite element programs, the user ordinarily inputs the elastic modulus $E$ and Poisson ratio $\nu$ as discrete functions of temperature for each material. Internally, the program takes the values of $E$ and

Table 3.12. Creep-Rupture Test Data for Babcock and Wilcox Type 16-8-2 Stainless Steel Submerged-Arc Welds

| Stress (MPa) | Stress (ksi) | Specimen Type and Number | Test | Rupture Time (hr) | Time to Tertiary Creep: Linearity | Time to Tertiary Creep: 0.2% Offset | Total Strain, %: Onset of Tertiary Creep: Linearity | Total Strain, %: Onset of Tertiary Creep: 0.2% Offset | Total Strain, %: Rupture | Reduction of Area (%) |
|---|---|---|---|---|---|---|---|---|---|---|
| | | | | Tests at 649°C (1200°F) | | | | | | |
| 172 | 25 | L1 776-L35 | FWB-239 | 31.5 | 1.2 | 1.75 | 1.37 | 1.7 | 44.2 | 58.4 |
| 138 | 20 | L1 775-L1 | FWB-249 | 478.5 | 25 | 58 | 1.46 | 3.0 | 42.5 | 54.0 |
| 110 | 16 | L1 775-L6 | FWB-250 | >2485.4 | | | | | >17.9 | |
| 172 | 25 | L2 776-L37 | FWB-237 | 73.9 | ∿4 | ∿5.7 | ∿0.8 | ∿1.1 | 48.5 | 50.1 |
| 138 | 20 | L2 775-L14 | FWB-254 | 609.4 | 34 | 73 | 0.6 | 1.1 | 44.2 | 56.1 |
| 110 | 16 | L2 775-L10 | FWB-257 | >2243.9 | | | | | >12.3 | |
| 172 | 25 | T1 776-T3 | FWB-240 | 121.3 | 6 | 11.5 | ∿0.96 | ∿1.6 | 30.7 | 37.7 |
| 138 | 20 | T1 776-T1 | FWB-252 | 1334.6 | | | | | 30.3 | 32.5 |
| 110 | 16 | T1 775-T5 | FWB-253 | >2363.6 | | | | | >5.96 | |
| 172 | 25 | T2 776-T6 | FWB-246 | 111.8 | 11.4 | 20 | 0.9 | 1.75 | 34.7 | 49.0 |
| 138 | 20 | T2 775-T6 | FWB-256 | 1009.0 | 250 | 300 | 1.1 | 1.39 | 15.7 | 36.9 |
| | | | | Tests at 566°C (1050°F) | | | | | | |
| 310 | 45 | L1 776-L34 | FWB-241 | 45.8 | 29 | 31 | 9.8 | 11.0 | 44.1 | 45.6 |
| 276 | 40 | L1 775-L2 | FWB-255 | 209.3 | 105 | 124 | 7.9 | 9.2 | 23.3 | 29.3 |
| 276 | 40 | L1 775-L3 | FWB-259 | 174.0 | 85 | 95 | 17.0 | 18.4 | 40.3 | 38.0 |
| 310 | 45 | L2 775-L5 | FWB-248 | 78.8 | 27.5 | 29 | 8 | 8.4 | 34.7 | 36.2 |
| 241 | 35 | L2 775-L3 | FWB-259 | 699.8 | 323 | 395 | 4.4 | 5.4 | 26.2 | 62.0 |
| 310 | 45 | T1 776-T1 | FWB-238 | 75.3 | 37.5 | 41.8 | 19.9 | 21.2 | 42.8 | 25.6 |
| 276 | 40 | T1 775-T3 | FWB-263 | 201.5 | 137.5 | 198 | 7.6 | 9.5 | 14.0 | 15.6 |
| 241 | 35 | T1 775-T7 | FWB-260 | 1279.5 | | | | | | |
| 310 | 45 | T2 776-T2 | FWB-245 | 109.6 | 2.8 | 38.4 | 1.6 | 3.0 | 11.5 | 13.9 |
| 310 | 45 | T2 775-T4 | FWB-264 | 142.5 | 38 | 55 | 2.6 | 3.5 | 14.0 | 18.4 |

$\nu$ and forms an elastic stiffness (or compliance) matrix for the material in each element. This computation typically takes the following form, as an example, for the compliance matrix in a three-dimensional solid:

$$[S] = \begin{bmatrix} 1/E & -\nu/E & -\nu/E & 0 & 0 & 0 \\ -\nu/E & 1/E & -\nu/E & 0 & 0 & 0 \\ -\nu/E & -\nu/E & 1/E & 0 & 0 & 0 \\ 0 & 0 & 0 & 2(1+\nu)/E & 0 & 0 \\ 0 & 0 & 0 & 0 & 2(1+\nu)/E & 0 \\ 0 & 0 & 0 & 0 & 0 & 2(1+\nu)/E \end{bmatrix} \quad (1)$$

Hence, a matrix of the form of Eq. (1) can be input directly (instead of just $E$ and $\nu$) in the case of anisotropic material. This has been done using the numerical values for a type 308 stainless steel electroslag weld reported[45] previously.

For the example that follows, axisymmetric welds with two preferential orientations have been compared with one assumed to be isotropic. The mesh shown in Fig. 3.52 was used to model a symmetric pipe segment with a ratio of outside diameter to thickness $d/h$ = 8.0. The $r$ axis represents the center line of a symmetric V-weld with an included angle of 53°. The $Z$ axis represents the center line of the pipe. The mesh in Fig. 3.52 contains 210 elements (linear quadrilaterals and triangles) and 231 nodal points. Loading is by uniform pressure on the inside of the pipe.

Room-temperature elastic properties were used for the base metal and the electroslag weld metal. For the base metal, type 304 stainless steel, $E$ was assumed to be 195 GPa and $\nu$, 0.283. For the weld metal, the properties in Table 3.13 were used, where the subscripts correspond to the unprimed coordinates on the idealized weld shown in Fig. 3.53.

Three different elastic symmetry conditions were used in the finite element demonstrations:

<u>Case 1</u>. Properties of Table 3.13 with the $r$ direction (direction of elongated subgrains) in the weld in the pipe corresponding to the 3-direction in Fig. 3.53, the $z$ direction to the 1-direction, and the $t$ direction (hoop) to the 2-direction.

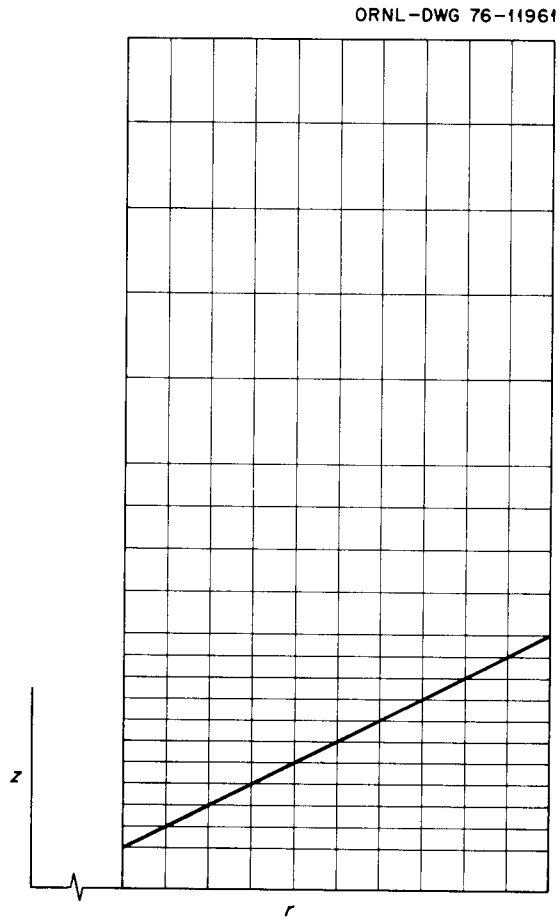


Fig. 3.52. Finite Element Mesh for Idealized Pipe Weld. Weld metal is on lower right.

Table 3.13. Engineering Constants for Specially Orthotropic Model of Electroslag Weld Metal

| Modulus[a] | Value (GPa) | Poisson's Ratio | Value |
|---|---|---|---|
| $E_{11} = E_{22}$ | 142 | $\nu_{12} = \nu_{21}$ | 0.24 |
| $E_{33}$ | 104 | $\nu_{13} = \nu_{23}$ | 0.53 |
| $G_{44} = G_{45}$ | 82 | $\nu_{31} = \nu_{32}$ | 0.39 |
| $G_{66}$ | 57 | | |

[a]$E$ denotes Young's modulus, $G$ shear modulus.

ORNL-DWG 75-13166R

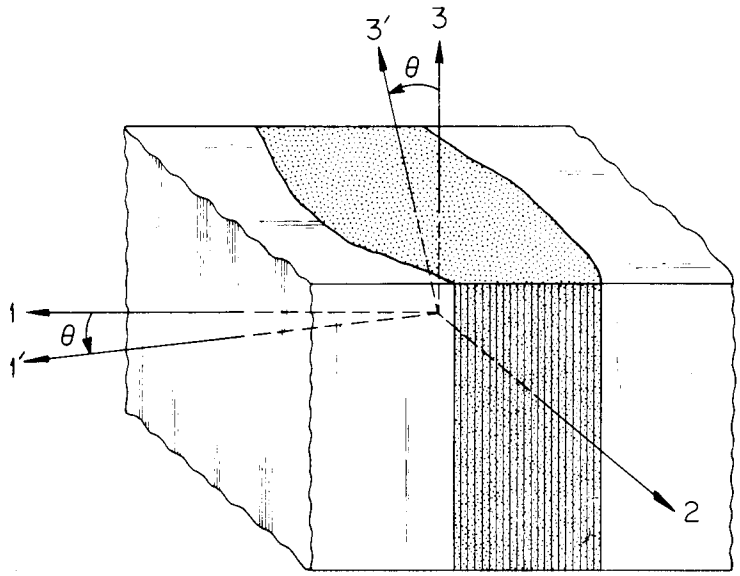


Fig. 3.53. Idealized Electroslag Weld with Coordinate Axes. The elongated subgrains are in the 3-direction. Also shown is a positive rotation around the 2-axis.

Case 2. Same as case 1 except that θ (Fig. 2) equals 126.9°, which places the elongated subgrains perpendicular to the fusion line.

Case 3. Isotropic weld metal with same $E$ and $\nu$ as base metal.

3.3.3.2 Results

Displacements, stresses, and strains are routinely available from the finite element calculations for the three cases. Comparisons among the hoop strain $\varepsilon_\theta$ distributions on the inner and outer surfaces of the pipe are given in Fig. 3.54. Here, we see that the mismatch between weld metal and base metal causes an increase in strain in the vicinity of the weld. Furthermore, the orientation of the weld grains significantly affects the magnitude of the strain increase.

An interesting observation is that the apparent $E$ for weld metal can be much lower than that for base metal. One should note that the transformation equations, when applied to the values given in Table 3.13, give a value of $E$ at $\theta = 45°$ close to the value of $E$ for isotropic material. The directional variation of properties of the weld metal do

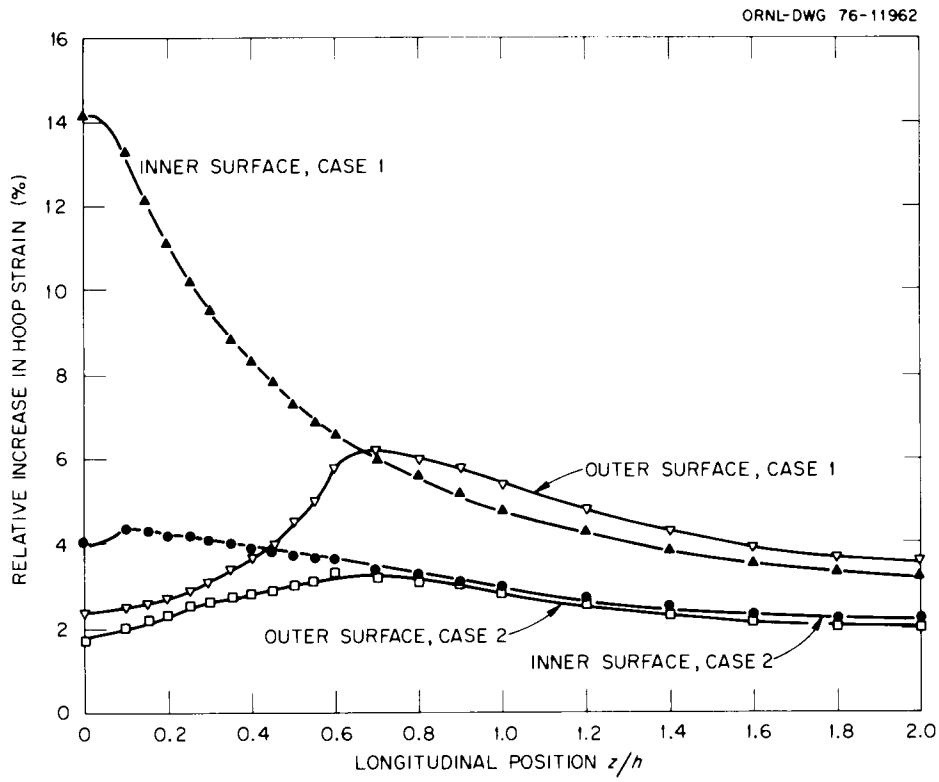


Fig. 3.54. Effect of Orientation of Weld Metal.

significantly affect stress analysis. With such properties routinely incorporated in finite element analysis, improved accuracy and confidence in the design of weld joints will result.

## 3.4 MECHANICAL PROPERTIES OF STEAM GENERATOR MATERIALS — C. R. Brinkman

### 3.4.1 Creep and Rupture Behavior of 2 1/4 Cr-1 Mo Steel — R. L. Klueh

We are studying the effect of heat treatment on the creep and creep-rupture properties of annealed 2 1/4 Cr-1 Mo steel.[46,47] Pieces of a 25-mm-thick (1-in.) plate were given different annealing treatments: two pieces were fully annealed, labeled AN-1 and AN-2 (AN-2 was cooled faster than AN-1), and one piece, labeled IA, was isothermally annealed. The creep-rupture studies were previously reported and discussed.[46,47]

In those studies we noted two types of creep curves: a classical creep curve with single primary (transient), secondary (steady-state), and tertiary stages; nonclassical creep curves were also noted with two

steady-state stages. A schematic diagram of these two types of curves is shown in Fig. 3.55. The transition from the first steady-state stage to the second involved an increasing creep rate, and since, by definition, tertiary creep involves an increasing creep rate, the question arises whether this is tertiary creep or whether the part of the curve after the second steady-state stage, where the creep rate again increases, is tertiary creep. This question will be addressed in this report.

All creep curves were examined for curve shape, and our observations are summarized schematically in Fig. 3.56. At 566°C (1050°F), tests at 103 and 124 MPa (15 and 18 ksi) for both heat treatments AN-1 and IA displayed classical creep curves. At 138 MPa (20 ksi) a nonclassical creep curve was observed. The creep rate for the second steady-state creep stage was quite easily determined for the tests up to and including 172 MPa (25 ksi). At 207 MPa (30 ksi), however, we could only determine one creep rate. Whether this was because a classical strain-time relationship again existed or whether the second steady-state stage was too short to be detected cannot be stated (the question mark after the C in Fig. 3.56 is meant to denote this uncertainty).

When the creep rate for the first steady-state stage for the nonclassical curves at 566°C (1050°F) was plotted against stress, a discontinuity was observed: the two low-stress tests fell on one curve, the rest on a second curve.[46] However, when the creep rate for the second steady-state stage was used for the nonclassical curves, a continuous curve was obtained.[46]

Classical creep curves were observed for all the tests at 454°C (850°C) (Fig. 3.56). At 510°C (950°F), the type of behavior depended on stress and heat treatment. For the AN-2 specimens at 510°C, all the creep curves appeared classical, although there are indications that the curves at 207 MPa (30 ksi) may be nonclassical [the NC(?) region in Fig. 3.56].

For IA at 510°C, only nonclassical curves were observed. All curves for AN-1 were nonclassical below about 241 MPa (35 ksi). Above

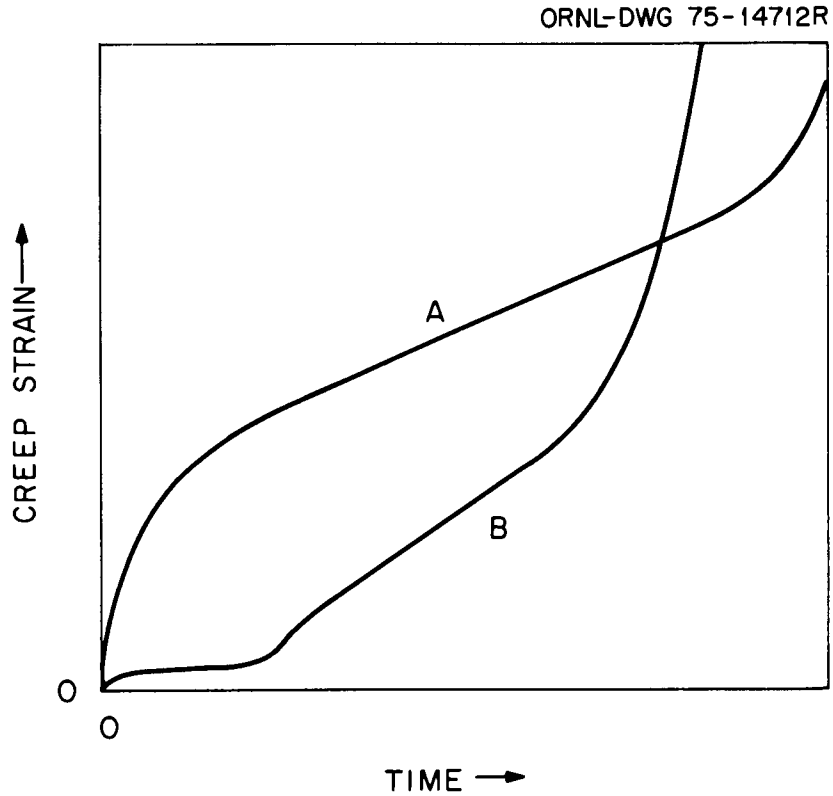


Fig. 3.55. Schematic Diagrams for Classical (A) and Nonclassical (B) Curves of the Type Observed for 2 1/4 Cr-1 Mo Steel.

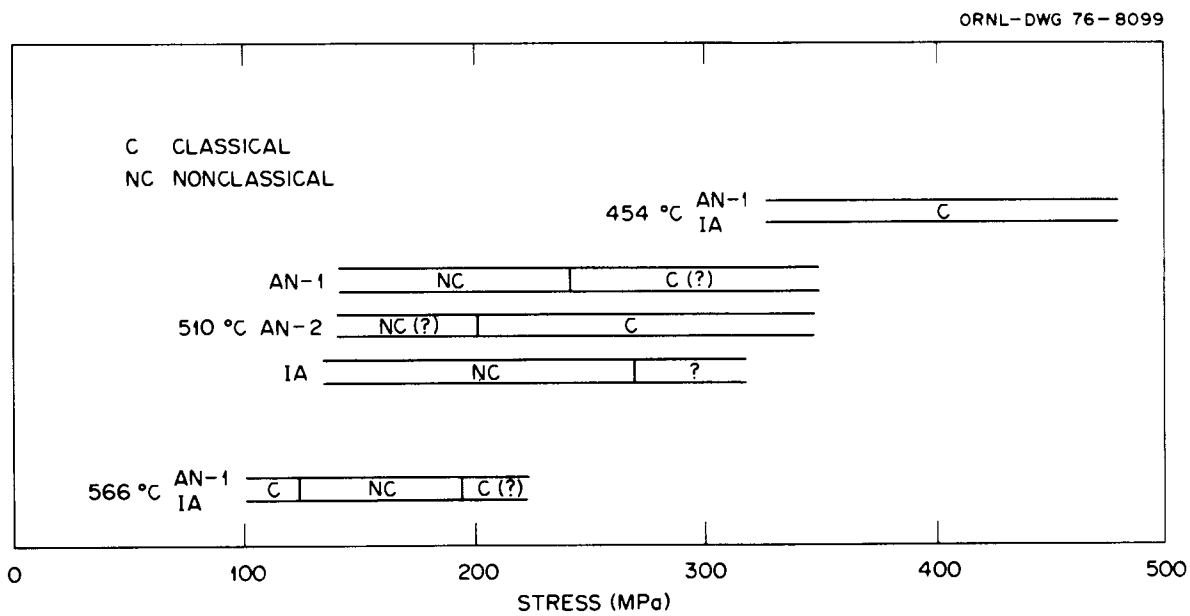


Fig. 3.56. Schematic Representation of Creep Curve Shape as a Function of Stress at 454, 510, and 566°C.

this stress only a single steady state stage could be accurately determinted [again, the reason for this is unknown and shown as C(?) in Fig. 3.56]. When the creep rate for the second steady-state stage was plotted against stress, a continuous curve resulted. This curve fell to the right of the one obtained[46] for the first steady-state stage.

In the present report, the tertiary creep behavior will be examined. Tertiary creep is easily defined for the classical curve (Curve A of Fig. 3.55): it is the point where the creep rate begins to increase after a period of constant creep rate (the minimum creep rate) during the secondary stage (steady-state creep). A 0.2% offset method is generally used to uniformly set the point of departure from steady state. Several investigators[20,48-50] have shown that a relationship exists between the start of tertiary creep and rupture life for various alloys, including 2 1/4 Cr-1 Mo steel. Usually, a relationship of the type

$$t_2 = At_R^{\alpha} \tag{1}$$

is found, where $t_2$ is the time to the start of tertiary creep, $t_R$ is the rupture life, and $A$ and $\alpha$ are constants; $\alpha$ is often found to be unity. According to Eq. (1), a graph of log $t_2$ against log $t_R$ should result in a straight line with a slope of $\alpha$.

We have obtained $t_2$ values from all the creep curves, and in Fig. 3.57 these data are plotted according to Eq. (1). Where nonclassical creep curves were observed, the 0.2% offset from the first steady state stage was used. The data used for Fig. 3.57 are given in Table 3.14.

It is obvious from Fig. 3.57 that the expected straight-line relationship does not apply for all the tests. The data are stratified, and four curves have been drawn. With the exception of the longest test at 454°C, the combined data for AN-1 and IA at 454°C and the AN-2 data at 510°C appear to fall on a straight line (a line with $\alpha = 1$ has been drawn through these data). The other curves in Fig. 3.57 are separate curves for AN-1 and IA at 510 and 566°C. At 510°C, data for IA and AN-1 are roughly parallel. Although the 566°C data parallel the 510°C data for short times, they deviate dramatically for longer rupture times:

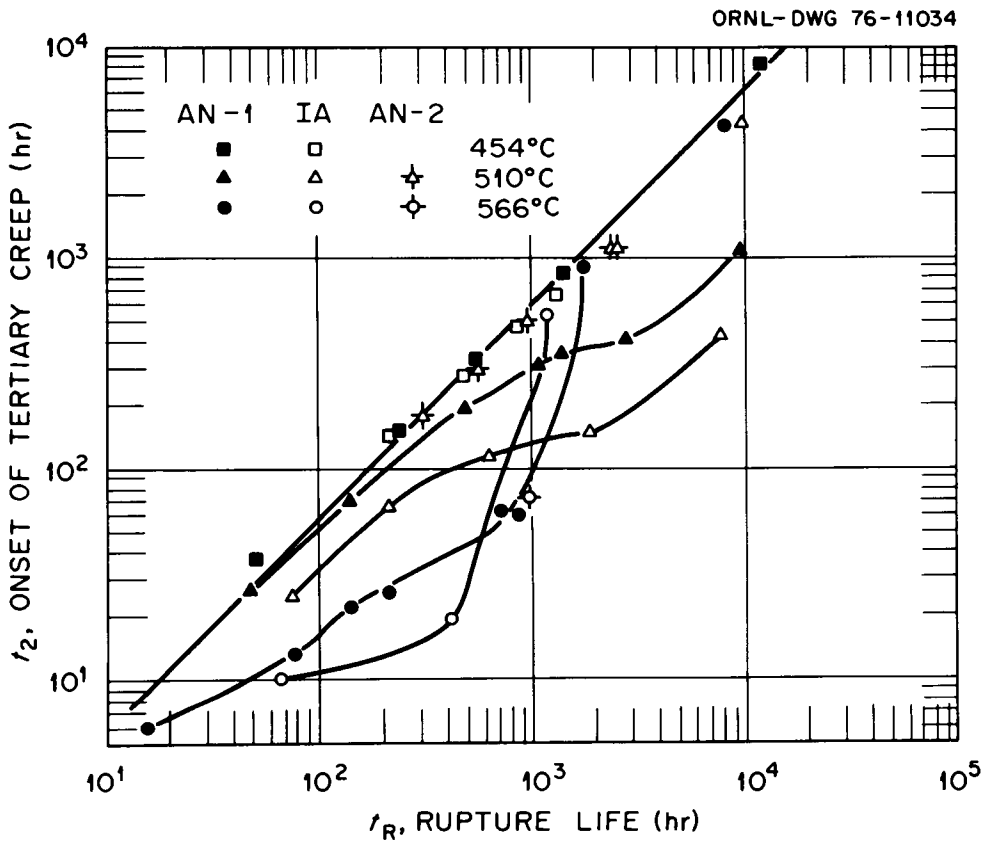


Fig. 3.57. Time to the Onset of Tertiary Creep Plotted Against Rupture Life. For tests where two steady-state stages were observed (i.e., at 510 and 566°C) the time to the end of the first steady-state stage is plotted.

Table 3.14. Time and Strain to Start of Tertiary Creep (0.2% Offset) for 2 1/4 Cr-1 Mo Steel

| Heat Treatment | Temperature (°C) | Temperature (°F) | Stress (MPa) | Stress (ksi) | Rupture Life (hr) | Transition to Tertiary Creep: Time, hr, Stage 1 | Time, hr, Stage 2 | Strain, %, Stage 1 | Strain, %, Stage 2 | $\varepsilon_2/\varepsilon_R$ (%) |
|---|---|---|---|---|---|---|---|---|---|---|
| AN-1 | 454 | 850 | 327 | 47.5 | 12,059.1 | 8,150 | a | 1.48 | a | 9 |
| | | | 358 | 52 | 1,435.3 | 820 | a | 2.28 | a | 13 |
| | | | 379 | 55 | 539.1 | 330 | a | 2.88 | a | 16 |
| | | | 413 | 60 | 233.4 | 150 | a | 2.86 | a | 15 |
| | | | 448 | 65 | 48.9 | 37 | a | 3.13 | a | 18 |
| | 510 | 950 | 152 | 22 | 9,650.3 | 1,100 | 5,300 | 0.38 | 6.63 | 20 |
| | | | 172 | 25 | b | 520 | b | 0.49 | b | |
| | | | 172 | 25 | 2,788.0 | 400 | 1,280 | 0.44 | 4.37 | 12 |
| | | | 189 | 27.5 | 1,396.4 | 350 | 780 | 0.52 | 4.77 | 13 |
| | | | 207 | 30 | 1,089.3 | 300 | 680 | 0.60 | 5.84 | 17 |
| | | | 241 | 35 | 476.0 | 200 | 326 | 1.23 | 4.06 | 15 |
| | | | 276 | 40 | 135.5 | 68 | a | 2.90 | a | 10 |
| | | | 310 | 45 | 47.5 | 26 | a | 2.75 | a | 10 |
| | 566 | 1050 | 103 | 15 | 8,194.8 | 4,200 | a | 3.75 | a | 20 |
| | | | 124 | 18 | 1,804.6 | 900 | a | 5.47 | a | 20 |
| | | | 138 | 20 | 707.3 | 63 | 380 | 0.32 | 5.38 | 17 |
| | | | 138 | 20 | 885.4 | 60 | 440 | 0.41 | 5.16 | 16 |
| | | | 152 | 22 | 222.9 | 26 | 113 | 0.20 | 7.13 | 15 |
| | | | 172 | 25 | 78.2 | 13 | 31 | 1.38 | 3.93 | 11 |
| | | | 182 | 25 | 136.5 | 22 | 78 | 0.85 | 6.75 | 17 |
| | | | 207 | 30 | 16.3 | 6 | | 3.5 | | 9 |
| AN-2 | 510 | 950 | 207 | 30 | 2,372.8 | 1,110 | c | 0.46 | c | 1 |
| | | | 207 | 30 | 2,354.4 | 1,120 | c | 0.46 | c | 2 |
| | | | 276 | 40 | 952.9 | 500 | a | 0.70 | a | 3 |
| | | | 310 | 45 | 563.0 | 300 | a | 1.50 | a | 7 |
| | | | 345 | 50 | 308.4 | 175 | a | 2.41 | a | 12 |
| | 566 | 1050 | 138 | 20 | 982.2 | 83 | 540 | 0.34 | 4.89 | 15 |
| IA | 454 | 850 | 338 | 49 | 1,301.9 | 665 | a | 1.49 | a | 6 |
| | | | 358 | 52 | 854.9 | 475 | a | 2.59 | a | 15 |
| | | | 379 | 55 | 479.1 | 280 | a | 2.33 | a | 10 |
| | | | 413 | 60 | 214.6 | 144 | a | 2.55 | a | 16 |
| | 510 | 950 | 152 | 22 | 6,853.9 | 438 | 4,400 | 0.31 | 7.25 | 22 |
| | | | 172 | 25 | 1,879.5 | 150 | 850 | 0.34 | 3.71 | 9 |
| | | | 207 | 30 | 526.0 | 125 | 270 | 0.65 | 3.53 | 9 |
| | | | 241 | 35 | 204.5 | 69 | 138 | 1.15 | 6.15 | 14 |
| | | | 276 | 40 | 74.2 | 25 | 55 | 1.28 | 5.13 | 23 |
| | 566 | 1050 | 103 | 15 | 9,918.7 | 4,400 | a | 3.30 | a | |
| | | | 124 | 18 | 1,233.1 | 535 | a | 4.86 | a | 16 |
| | | | 138 | 20 | 400.4 | 19 | 175 | 0.48 | 6.15 | 13 |
| | | | 172 | 25 | 68.5 | 10 | 25 | 1.25 | 5.25 | 11 |

[a]Classical creep curve.

[b]Test discontinued after 1321 hr.

[c]There appeared to be a short second steady-state stage, but strains and times could not be accurately determined.

the 566°C curves cross the 510°C curves. It is interesting to observe in Fig. 3.57 that the data at 566°C that led to the deviation from the trends at 510°C (i.e., caused the curves to cross over) are from tests at 103 and 124 MPa (15 and 18 ksi). These were the tests that displayed classical creep curves at 566°C. Note also that at short times all these curves appear to approach the straight line for the 454°C data and the AN-2 data at 510°C. At these high stresses "classical" creep curves were observed (Fig. 3.56).

The above observations clearly indicate that the stratification of data evident from Fig. 3.57 is connected with the different creep curve shapes. To further examine the relationships between creep curve shape and tertiary creep, we determined the creep strain to the start of the two "tertiary creep stages." These values are given in Table 3.14; in Fig. 3.58 the strain values are plotted against stress.

The strain values fall into three distinct categories: (1) For the obviously nonclassical curves at 510 and 566°C (heat treatments AN-1 and IA), the strain to the end of the first steady-state stage is less than 1.5% (most are less than 0.7%); this also applies to the low-stress tests for AN-2 at 510°C, where no second steady-state stage could be clearly deliniated. (2) Strains for AN-1 and IA to the end of the second steady-state stage of the nonclassical curves at 510 and 566°C and the end of the steady-state stage of the classical curves at 103 and 124 MPa (the low-stress tests) at 566°C are from 4 to 7%. (3) The strains for AN-1 and IA at 454°C, for the higher stresses for AN-2 at 510°C, and for the higher stresses for AN-1 at 510 and 566°C — all of which show "classical" curves — are from 1.5 to 2.5%.

Table 3.14 also gives the ratio of $\varepsilon_2/\varepsilon_R$, where $\varepsilon_R$ is the total elongation and $\varepsilon_2$ is the strain to the end of the steady-state stage; for nonclassical curves, it is the end of the second steady-state stage. For AN-1 and IA at 510 and 566°C, values between about 10 and 20% are observed. Similar results (with one exception) are observed at 454°C; the large $\varepsilon_2/\varepsilon_R$ values at 454°C occur, despite the low $\varepsilon_2$ values, because of the lower total elongation. Note also that this ratio is between 10

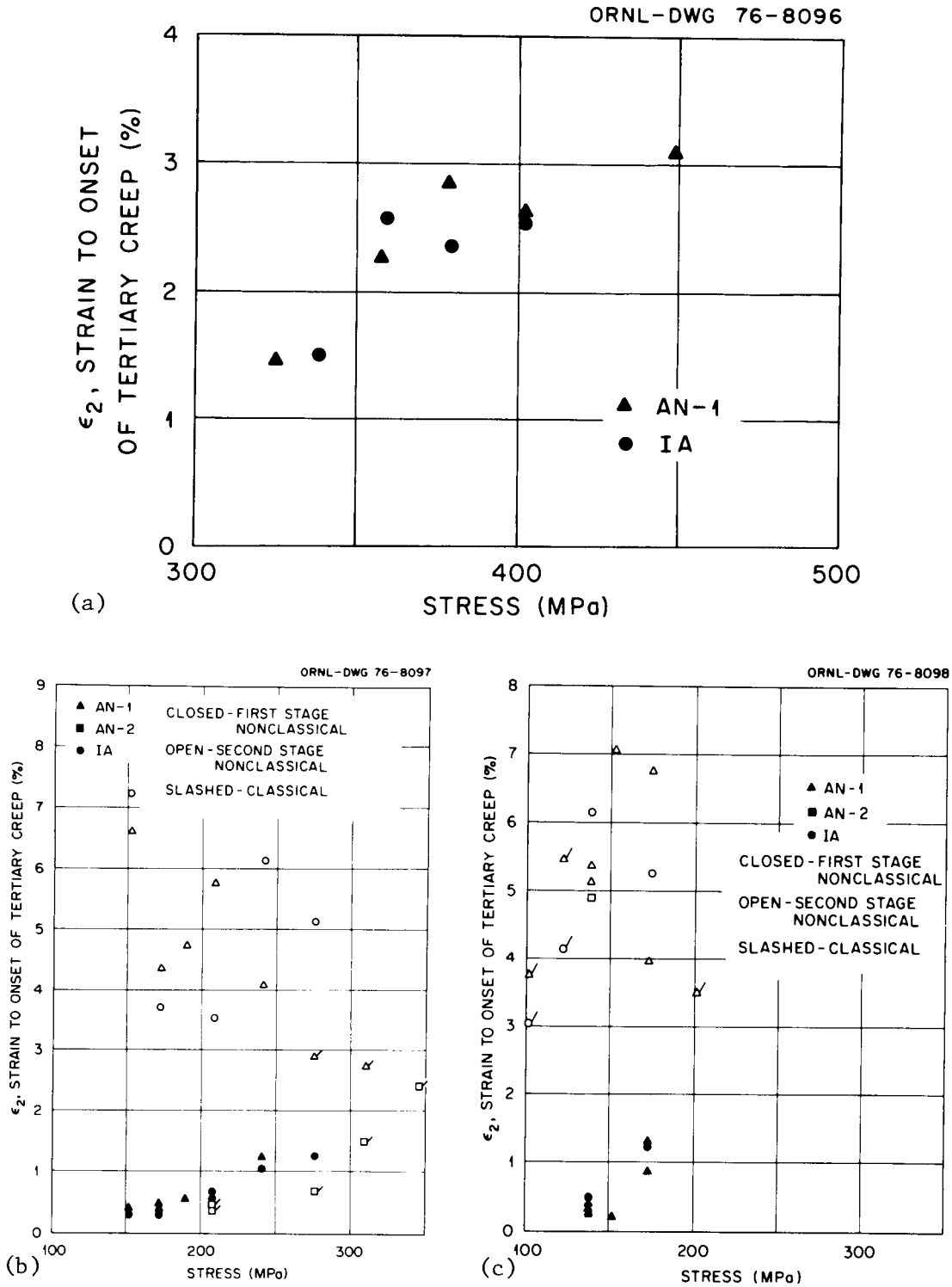


Fig. 3.58. Strain to the Onset of the Two "Tertiary Creep Stages" at (a) 454°C, (b) 510°C, and (c) 566°C.

and 20 for the high-stress tests on AN-1 at 510 and 566°C and the high-stress test on AN-2 at 510°C for a similar reason (i.e., although $\varepsilon_2$ decreases with increasing stress, the total elongation also decreases with increasing stress. Also, note how the $\varepsilon_2/\varepsilon_R$ ratio for the low-stress results for AN-2 at 510°C fall substantially below 10 (a similar low ratio would result if the time to the end of the first steady state stage were used for $\varepsilon_2$).

As a result of these observations on the strains to the onset of tertiary creep and the previous observations[46] when the creep rates were plotted with the creep rate for the second steady state stage used, the data of Table 3.14 were replotted according to Eq. (1). Figure 3.59 shows the data with strains that fall into the second category ($\varepsilon_2 \simeq$ 4–7%), while Fig. 3.60 shows the data for strains that fall into category 3 ($\varepsilon_2 \simeq$ 1.5–3%). For Fig. 3.59, the data for the nonclassical curves at 510 and 566°C are plotted with $t_2$ as the time to the end of the second steady-state stage. The data used in Fig. 3.60 include all the data at 454°C and the high-stress tests for AN-2 at 510°C and AN-1 at 510 and 566°C.

In both cases the data appear to fall on a straight line. The values for $\alpha$ and $A$ for a least squares fit of the data are given in Table 3.15 (in all cases the correlation coefficient $R^2 \approx 0.99$). Since there was little difference in the values of $\alpha$ and $A$ for the curves in Figs. 3.59 and 3.60, the data were combined and are shown in Fig. 3.61. The equation for the combined data is given by

$$t_2 = 0.489\ t_R^{1.016} \ . \tag{2}$$

As seen in Table 3.15, combining the data did not significantly alter the standard error of estimate. Therefore, the combined representation would appear appropriate.

In the above discussion, the four low-stress tests on AN-2 were ignored (these data fall into category 1; they display "classical" curves, with $\varepsilon_2/\varepsilon_R < 10$). It will be pointed out in our next quarterly report that these curves are probably nonclassical, but because of the extended

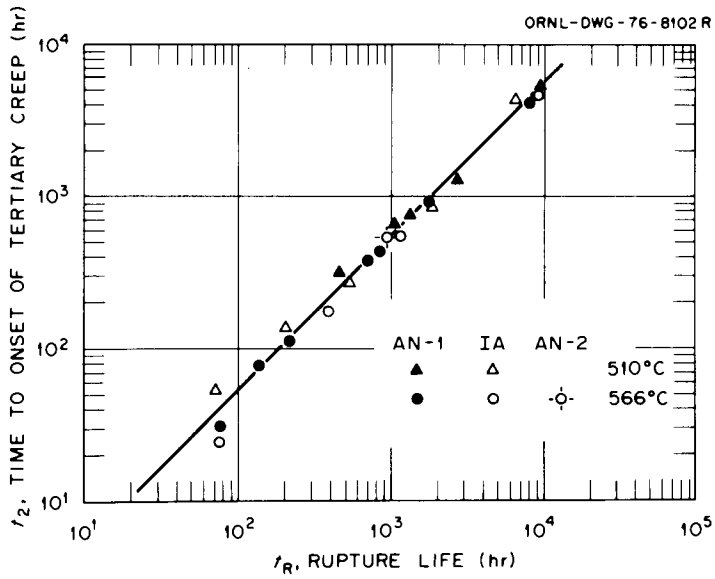


Fig. 3.59. Time to the Onset of Tertiary Creep Plotted Against Rupture Life at 510 and 566°C. For tests that had nonclassical creep curves, the end of the second steady-state stage was used.

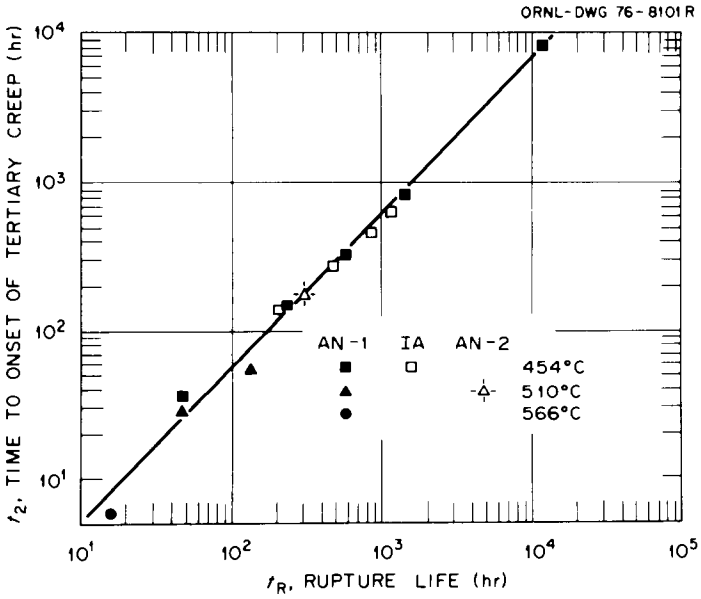


Fig. 3.60. Time to the Onset of Tertiary Creep Plotted Against Rupture Life for the Curves at 454 (AN-1 and IA) and 510°C (AN-2) that Displayed Classical Creep Curves.

Table 3.15. Coefficients for Empirical Relationship Between the Onset of Tertiary Creep and Rupture Life

| Data | log $A$ | $A$ | $\alpha$ | Standard Error of Estimate |
|---|---|---|---|---|
| Category 2[a] | −0.307 ± 0.082 | 0.492 | 1.010 ± 0.028 | 0.0812 |
| Category 3[b] | −0.353 ± 0.088 | 0.444 | 1.044 ± 0.034 | 0.0862 |
| Categories 2 and 3[c] | −0.311 ± 0.059 | 0.489 | 1.016 ± 0.021 | 0.0838 |
| Categories 1, 2, 3[d] | −0.300 ± 0.056 | 0.501 | 1.011 ± 0.020 | 0.0804 |

[a]Category 2: 21 datum points were used. These included: (1) all nonclassical curves at 510 and 566°C, where $t_2$ was taken as the time to the end of the second steady state stage, and (2) the low-stress classical curves at 566°C.

[b]Category 3: 12 datum points were used. These included all points at 454°C and the high-stress classical curves ($\varepsilon_2 \cong 1.5$–3%) at 510 and 566°C for AN-1 and AN-2.

[c]Categories 2 and 3: 33 datum points were used. These included all points used in a and b.

[d]Categories 1, 2, and 3: the 33 datum points used above were combined with the four low-stress tests on AN-2 at 510°C.

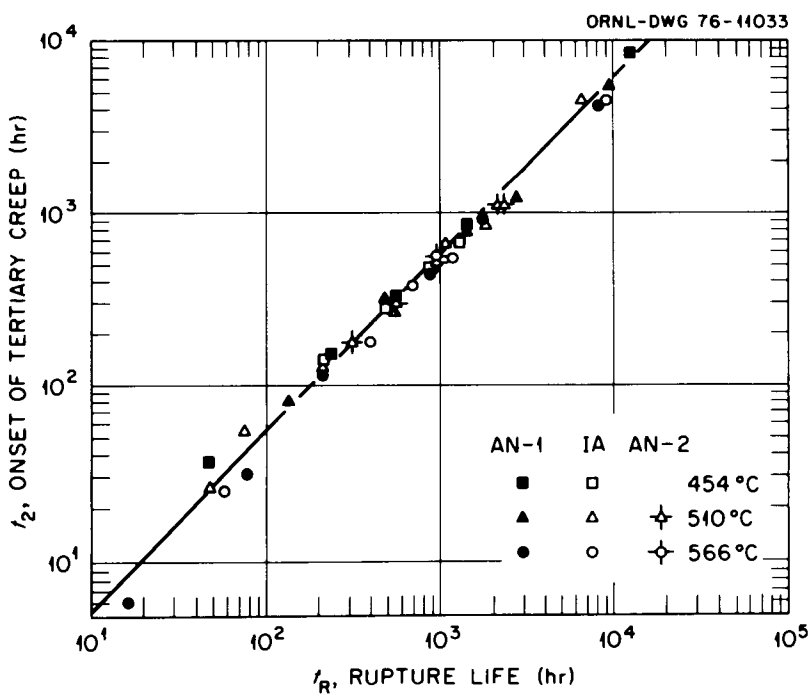


Fig. 3.61. Time to the Onset of Tertiary Creep Plotted Against Rupture Life for All Data. For nonclassical curves, the end of the second steady-state stage was taken as the onset of tertiary creep.

duration of the first steady-state stage, the second steady-state stage cannot be accurately deliniated. Presumably the second steady-state stage is of very short duration. Hence, the time to the end of this stage should not differ substantially from the time to the end of the first steady-state stage for these tests. These four tests are plotted on Fig. 3.61 (they were not used to establish the curve). It is seen that these points fall quite nicely on the curve established for all the data from categories 2 and 3. Finally, when an equation is determined for all the data, including these AN-2 tests, $\alpha$ and $A$ are little changed from Eq. (2) (Table 3.15).

Since tertiary creep is often associated with gross structural instability (i.e., the formation of cracks, voids, or necking, which lower the specimen cross section and thus increase stress), one criterion used in the ASME code case 1592 to set allowable stresses in the creep regime is the time to the onset of tertiary creep. Tertiary creep is generally defined in terms of the classical creep curve as the point on the curve where the creep rate begins to increase (it decreases during the primary stage and is constant in the secondary stage of a classical creep curve). By such a definition, tertiary creep would begin at the end of the first steady-state stage (for nonclassical creep curves). We feel, however, that this is a point of metallurgical instability, not a structural instability (this will be discussed in more detail in the next quarterly report). Hence, for materials that display nonclassical creep curves, the proper start of tertiary creep — the one that precedes fracture and may be associated with structural instability — is that determined after the second steady-state stage is complete. Both the minimum creep rate studies[46] and the tertiary creep correlation in Fig. 3.61 lead to this conclusion.

The present studies have illustrated the difficulty involved in determining tertiary creep when two steady-state stages appear. This is especially true when the test has not gone to rupture. If a creep curve such as that shown in Fig. 3.62(a) is examined, as a first approximation, tertiary creep would be said to begin at about 1000 hr and about 0.07% strain (the 0.2% offset gives values of 0.28% strain and 2100 hr). The creep curve in Fig. 3.62(a) is the first part of a nonclassical curve.

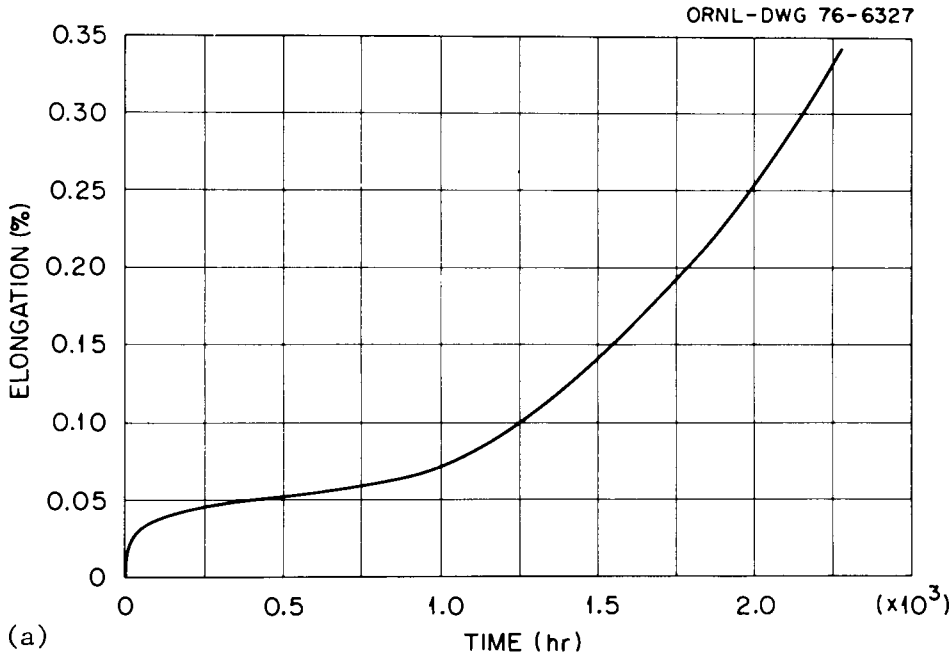


(a)

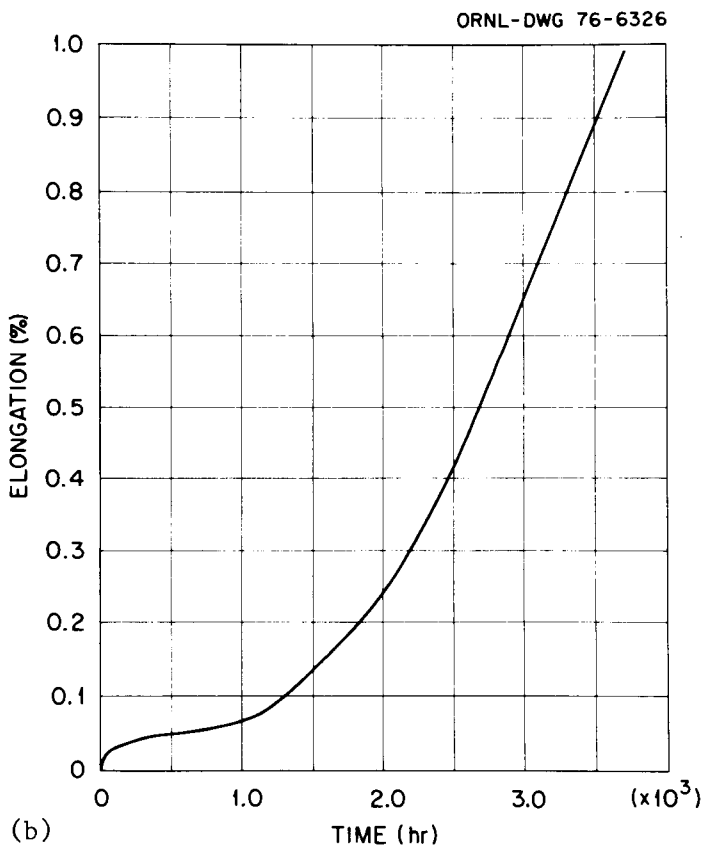


(b)

Fig. 3.62. Creep Curve for AN-2 Specimen Tested at 152 MPa (22 ksi) and 510°C. (a) After 2500 hr. (b) After 3700 hr, showing the second steady-state stage.

Only when the entire creep curve is examined and the second steady-state stage is taken into account can the real start of tertiary creep be determined. Figure 3.62(b) shows the curve after about 3800 hr and the second steady-state stage (the rupture life for this specimen is expected to approach 10,000 hr and tertiary creep has not yet begun). Note also the difference this will make in the determination of the strain to tertiary creep.

We showed that the tertiary creep data could be fit according to Eq. (1), although, interestingly enough, here the strains to the onset of tertiary creep did not seem to affect the fit of the data. For all three strain categories, one curve fit all the data.

Several investigators have found an $\alpha$ of unity[48-50] for a variety of alloys, including 2 1/4 Cr-1 Mo steel.[49,50] Leyda and Rowe[49] fit their data for annealed 2 1/4 Cr-1 Mo steel with

$$t_2 = F_s t_R \ , \tag{3}$$

where $F_s$ is a constant. Their data were taken at 538, 593, and 649°C (1000, 1100, and 1200°F), and they found that $F_s$ decreased slightly with temperature. Since our data showed no obvious stratification with temperature, we did not fit the data according to Eq. (3). Nevertheless, our $\alpha = 1.016$ cannot be assumed to be significantly different from unity, although our $F_s$ is slightly greater than that obtained by Leyda and Rowe, who found an $F_s$ of 0.459 at 538°C. Booker and Sikka,[20] on the other hand, fit tertiary data for 2 1/4 Cr-1 Mo steel from various sources, including some of the data obtained in the present investigation, and found $\alpha = 1.05$. Presently, we have no explanation for this discrepancy.

The results of the observations in this study have certain implications for design. By use of the creep rate for the second steady-state stage to determine the creep strength, the strength is lower, since the creep rate of the second steady-state stage is greater than that of the first. However, the time to the onset of tertiary creep is extended. As we shall show in our discussion next quarter, the first steady-state stage appears to have no relationship to structural instability, which is what the designer is interested in.

### 3.4.2 Heat-to-Heat Variation of 2 1/4 Cr-1 Mo Steel

#### 3.4.2.1 Effect of Heat Treatment on Tensile Properties — R. L. Klueh

We have completed our studies on the effect of heat treatment on the tensile properties of 2 1/4 Cr-1 Mo Steel,[51,52] and a report has been published.[53] The results of these studies are here summarized.

Room-temperature tensile properties were determined on six specimens that had been given different annealing treatments: three were furnace cooled from the austenitizing temperature (described as an anneal or full anneal) at three different controlled cooling rates, and three were isothermally annealed with three different controlled cooling rates from the austenitizing temperature to the isothermal anneal temperature [704°C (1300°F) for this study]. The rate at which the steel was cooled to room temperature during the full anneal had a large effect on both the microstructure and room-temperature tensile properties. With increased cooling rate, progressively more bainite was formed in the microstructure, and the strength increased. For the isothermally annealed steels, the rate at which the steel was cooled to the isothermal anneal temperature had a minor effect (much less than the cooling rate during the full anneal) on the microstructure and room-temperature tensile properties.

In the second part of the study, detailed tensile properties were determined over the temperature range 25 to 593°C (77 to 1065°F) and the strain rate range $2.67 \times 10^{-6}$ to $6.67 \times 10^{-3}$/sec on specimens that had been taken from 25-mm-thick (1-in.) plates (from a single heat of steel) given the following heat treatments: annealed (full anneal), labeled AN-1, which was slow cooled from the austenitizing temperature; annealed, labeled AN-2, which was cooled faster; and isothermally annealed, labeled IA. The following observations and conclusions were made:

1. The microstructure and properties of AN-2 were considerably different than for the other two heat treatments. All three plates were primarily proeutectoid ferrite, but AN-2 contained more bainite, and its strength at all temperatures was significantly greater than that of the other two. The ductility of AN-2 was only slightly less than that of AN-1 and IA.

2. All three heat treatments displayed dynamic strain aging peaks between 200 and 400°C. The peak height for AN-2 was greatest and occurred at a higher temperature than for AN-1 and IA. The peak height for AN-1 was slightly greater than that of IA.

3. The dynamic strain aging was concluded to be the result of interaction solid solution hardening in the proeutectoid ferrite. This phenomenon involves interactions of molybdenum and carbon atoms or atom clusters with dislocations.

4. The larger dynamic strain aging effect in AN-2 was not the result of the greater amounts of bainite in this microstructure. Rather, the faster cooling rate for this plate had not allowed the precipitation of molybdenum and carbon in the proeutectoid ferrite to proceed as far as it had in the more slowly cooled plates. Precipitation removes these species from solid solution, and thus they are no longer available for interaction solid solution hardening.

5. When AN-2 was tempered for 1 hr at 704°C (1300°F), the dynamic strain aging peak was reduced, because tempering removes molybdenum and carbon from solid solution by precipitate formation.

### 3.4.2.2 Mechanical Properties of a 2 1/4 Cr-1 Mo Steel Forging for LMFBR Tubesheets — R. L. Klueh and J. L. Griffith

In an effort to obtain the mechanical properties of typical tubesheet forgings, three 2 1/4 Cr-1 Mo steel tubesheet forgings were purchased from National Forge Company.[54] These were produced from a single 0.69-m-diam (27-in.) big-end-up ingot taken from an electric-furnace air-melted, vacuum-degassed heat. This ingot was upset from a length of 1.9 m (76 in.) to 0.71 m (28 in.), an operation that increased the diameter to 1.1 m (45 in.). The resulting forging was then drawn to a diameter of 0.51 m (20 in.), the top and bottom were cropped, and the remainder was cut into two pieces. One 1.130-m-long (44 1/4-in.) piece was upset forged to 0.840 m diam by 0.483 m thick (33 3/4 × 19 in.). This piece of forging was used in the present study [the remainder was cut to make two 0.46-m-diam by 0.30-m-thick (18- by 12-in.) tubesheets].

The forging was isothermally annealed by holding it at 927°C (1700°F) for 20 hr, then furnace cooling to 732°C (1350°F) at 42°C/hr (75°F/hr);

after holding it for 3 hr at 732°C, it was air cooled. The heat-treated forging was machined to obtain a finished tubesheet 0.69 m diam by 0.30 m thick (27 by 12 in.).

National Forge reported composition, tensile properties, microstructure, and grain size. This information is summarized in Tables 3.16 and 3.17. The microstructure was reported as primarily proeutectoid ferrite with 1—2% pearlite. The ASTM Grain size number was given as 4—6. When the forging was examined ultrasonically with a 3.2-mm-diam (1/8-in.) calibration standard for inspection through the thickness and a 6.4-mm-diam (1/4-in.) calibration standard for inspection radially, no internal defects were detected. Examination of the surface with a magnetic particle technique revealed no surface flaws.

The object of the present study was twofold. First, we were interested in determining the properties of a typical tubesheet forging. Second, data from this product form is of interest for our heat-to-heat variation study, which is considering various product forms. It should be pointed out that the present plans for the CRBRP call for the use of vacuum-arc remelted (VAR) or electroslag-remelted (ESR) material to be used in the tubesheet forgings. Nevertheless, the results from this study should have meaning for forgings manufactured by any technique, since the properties are largely determined by the working procedure and the final heat treatment.

To obtain specimens from the forging, a wedge (pie-shaped cut) was removed from the cylinder. This wedge was sectioned so that specimens could be taken from three different orientations relative to the axis of the forging cylinder. Radial, axial, and tangential specimens were taken. In order that our results from this forging could be compared with other heats being tested in our heat-to-heat variation study, specimen blanks having these three orientations were isothermally annealed in the laboratory: they were heated for 1 hr at 927°C (1700°F), cooled at a rate of 83°C/hr (150°F/hr) to 704°C (1300°F), held at this temperature for 2 hr, then furnace cooled to room temperature. We will refer to the material given this latter heat treatment as laboratory annealed and the other material as as received. Keep in mind, however, that

Table 3.16. Vendor-Supplied Chemical Analyses for 2 1/4 Cr-1 Mo Tubesheet Forging

| Sample | Content, % | | | | | | | | | | | |
|---|---|---|---|---|---|---|---|---|---|---|---|---|
| | C | Mn | P | S | Si | Ni | Cr | Mo | V | Cu | Co | Ti |
| Ladle | 0.10 | 0.36 | 0.007 | 0.009 | 0.35 | 0.30 | 2.40 | 1.03 | | 0.09 | 0.012 | |
| Check 01 | 0.08 | 0.38 | 0.009 | 0.007 | 0.34 | | 2.40 | 1.00 | 0.001 | | | 0.004 |
| Check 02 | 0.09 | 0.39 | 0.009 | 0.009 | 0.35 | | 2.40 | 1.01 | 0.001 | | | 0.004 |

Table 3.17. Vendor-Supplied Tensile Data for 2 1/4 Cr-1 Mo Tubesheet Forging

| Position | Strength, MPa(psi) | | Elongation (%) | Reduction of Area (%) |
|---|---|---|---|---|
| | Ultimate | 0.2% | | |
| 12:00 | 470.5(68,250) | 217(31,500) | 31 | 75.9 |
| 6:00 | 429.2(62,250) | 207(30,000) | 33 | 75.9 |

both have received isothermal anneal heat treatments, although the times and temperatures were somewhat different (the size of the material heat-treated was also quite different).

Tensile tests were made over the range 25 to 566°C (75–1050°F) at nominal strain rates of $2.67 \times 10^{-6}$ and $6.67 \times 10^{-4}$/sec. Specimens having a 6.35-mm-diam by 31.8-mm-long (0.250 × 1.25-in.) reduced section were tested on an Instron testing machine.

Our first tests were run to determine the effect of orientation. Intuitively, one would expect little effect of orientation. The results for tests on the three orientations at 25 and 566°C (77 and 1050°F) are shown in Table 3.18. Specimens from both the as-received and laboratory annealed material were tested.

Table 3.18. Effect of Specimen Orientation (Relative to the Forging Axis) on Tensile Properties[a]

| Orientation | Strength, MPa(ksi) | | Total Elongation (%) | Reduction of Area (%) |
|---|---|---|---|---|
| | Yield | Ultimate | | |
| | As Received — 25°C (77°F) | | | |
| Tangential | 211(30.6) | 475(69.0) | 32.2 | 69.2 |
| Radial | 261(37.9) | 535(77.7) | 24.8 | 57.0 |
| Axial | 254(36.9) | 522(75.7) | 27.8 | 52.7 |
| | Laboratory Anneal — 25°C (77°F) | | | |
| Tangential | 263(38.1) | 506(73.4) | 29.7 | 78.2 |
| Radial | 264(38.3) | 520(75.5) | 28.2 | 77.2 |
| Axial | 262(38.0) | 515(74.7) | 30.1 | 74.9 |
| | As Received — 566°C (1050°F) | | | |
| Tangential | 182(26.4) | 371(53.8) | 29.0 | 71.2 |
| Radial | 219(31.8) | 447(64.9) | 21.1 | 51.6 |
| Axial | 232(33.6) | 478(69.4) | 23.4 | 51.6 |
| | Laboratory Anneal — 566°C (1050°F) | | | |
| Tangential | 196(28.5) | 318(46.1) | 36.6 | 88.2 |
| Radial | 205(29.8) | 327(47.4) | 41.5 | 86.5 |
| Axial | 207(30.1) | 339(49.2) | 33.4 | 82.5 |

[a]All tests at $6.67 \times 10^{-4}$/sec.

The as-received material very definitely shows an orientation effect. At both 25 and 566°C the tangential specimens are weaker than the radial and axial specimens. This shows up both in the 0.2% yield strength and the ultimate tensile strength. There appears to be little difference between the radial and axial specimens. The ductility measurements reflect the strength differences: total elongation and reduction of area for the tangential specimens are larger than those for the other two orientations. Evidently the laboratory anneal has removed the property differences, for after this anneal, the properties for all three orientations appeared to be the same at either temperature.

Figures 3.63 and 3.64 show the microstructure from the unstressed shoulder regions of the room-temperature test specimens of the as-received tangential and axial specimens, respectively. The radial specimen had a microstructure similar to that of the axial specimen. Obviously, there is a significant difference in the microstructures of these materials. The axial (Fig. 3.64) and radial specimens had significantly more bainite present in the microstructure than the tangential specimen did. The tangential specimen, which had the lowest strength, contained small amounts of pearlite (the black regions of Fig. 3.63) and bainite. The axial and radial specimens showed very little pearlite to be present but contained as much as 25% bainite.

Figure 3.65 is a photomicrograph of the unstressed shoulder region for the laboratory-annealed axial specimen tested at 25°C. There was no difference in the microstructure for the different orientations for these specimens. In this case the microstructure was primarily pro-eutectoid ferrite with some pearlite present. Note in Figs. 3.63, 3.64, and 3.65 that the microstructures contain proeutectoid ferrite grains, some of which etch lighter than others. The dark grains at high magnification can be seen to contain a very high density of a fine precipitate, which gives rise to a mottled appearance and causes them to appear darker at low magnification (the ligher grains contain much less precipitate).

We also made tests over the range 25 to 566°C at $2.67 \times 10^{-6}$ and $6.67 \times 10^{-4}$/sec. For the as-received material, the results along

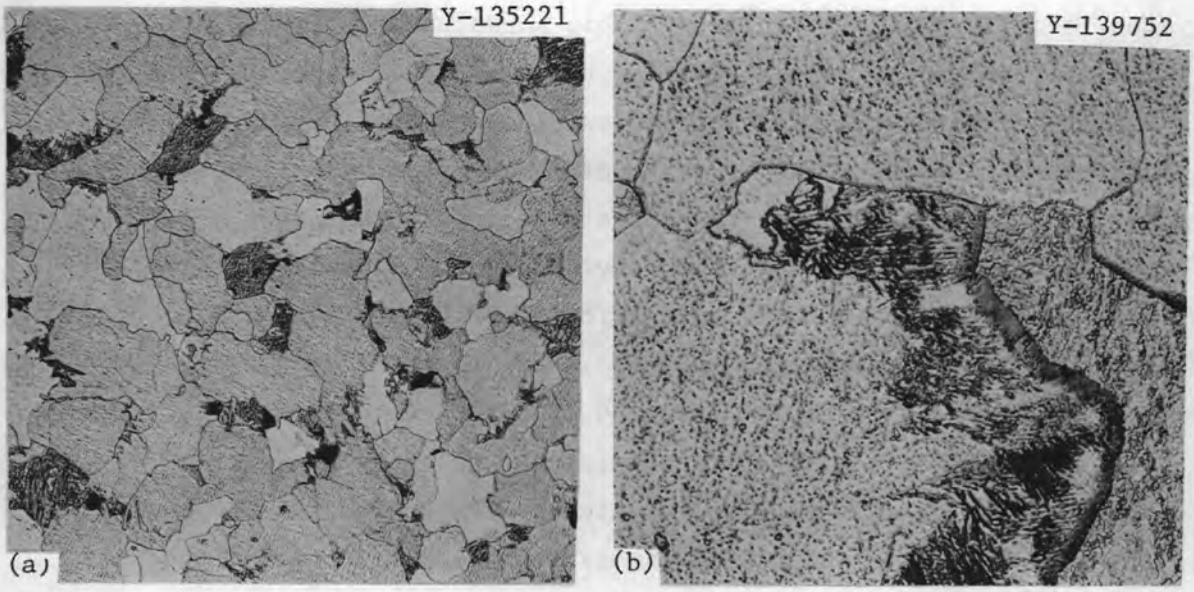


Fig. 3.63. Microstructure of the Unstressed Shoulder Region of the As-Received Tangential Specimens Tested at 25°C. (a) 100×. (b) 500×.

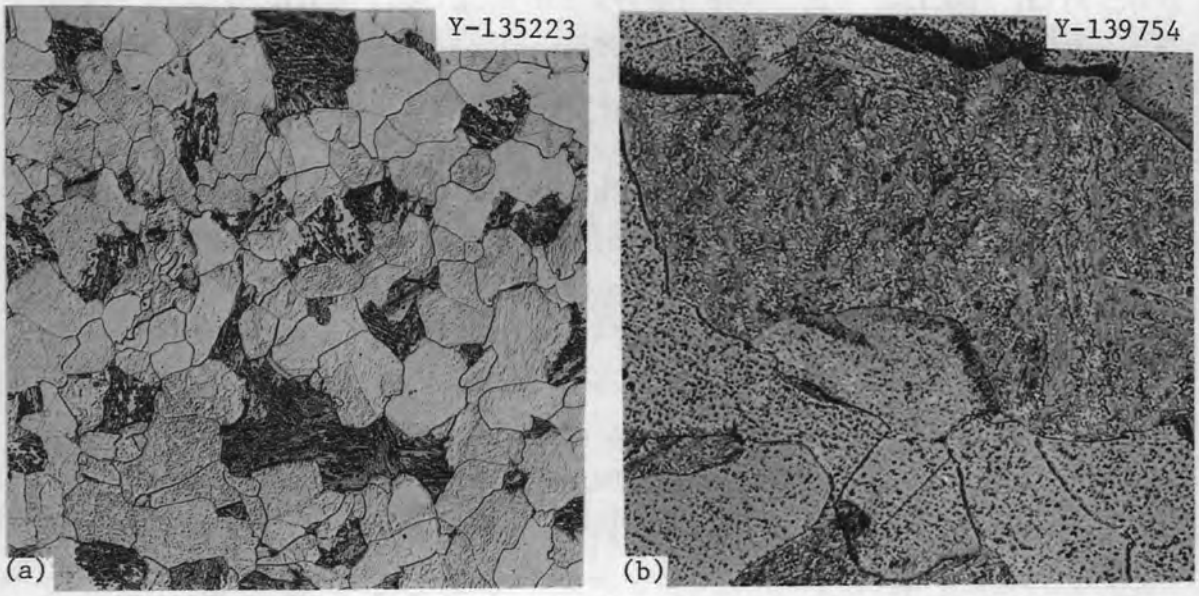


Fig. 3.64. Microstructure of the Unstressed Shoulder Region of the As-Received Axial Specimen Tested at 25°C. (a) 100×. (b) 500×. The radial specimen had a similar microstructure.

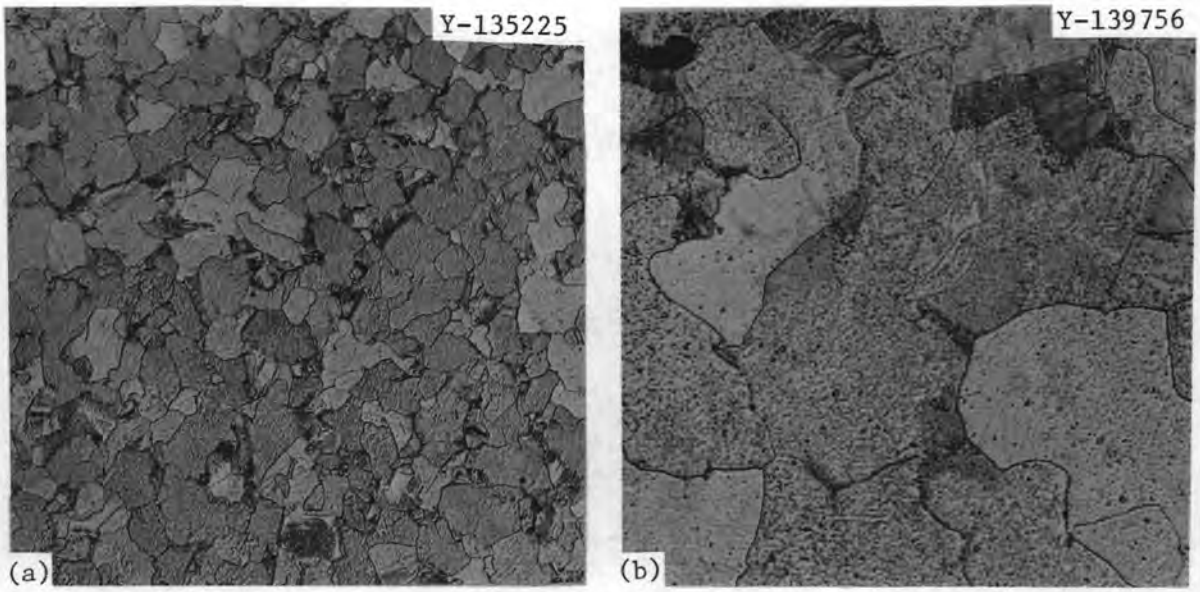


Fig. 3.65. Microstructure of the Unstressed Shoulder Region of the Laboratory-Annealed Axial Specimen Tested at 25°C. (a) 100×; (b) 500×. The radial and tangential specimens had similar microstructures.

with those given previously in Table 3.18 are given in Tables 3.19 and 3.20; Figs. 3.66 and 3.67 show the 0.2% yield strength, the ultimate tensile strength, and the ductility data plotted as functions of temperature for the as-received and laboratory annealed material. The orientation effect for the as-received forging was unexpected; thus not enough axial specimens were available to complete the $2.67 \times 10^{-6}$/sec tests. Only a tangential specimen was tested at 566°C, but it is not plotted because of the lower strength for this orientation.

The most significant effect appears when the ultimate tensile strength data are examined [Fig. 3.66(b)]. Data for the as-received and the laboratory annealed material display dynamic strain aging peaks, but there are quite large differences. The peak height for the as-received forging at both strain rates is considerably greater than that for the laboratory annealed material; the peak for the as-received forging also occurs at a higher temperature. This difference in the temperature of the peaks and the magnitude of the peak heights is similar to the heat treatment effects we noted previously[53] for a single heat of steel given different anneal treatments. In those studies we showed that the temperature of the peak and the height of the peak depended on the anneal treatment.

Table 3.19. Tensile Properties for As-Received 2 1/4 Cr-1 Mo Steel Tubesheet Forging

| Specimen Orientation | Test Temperature (°C) | Test Temperature (°F) | Strength, MPa(ksi) Yield | Strength, MPa(ksi) Ultimate | Strength, MPa(ksi) Fracture | Elongation, % Uniform | Elongation, % Total | Reduction of Area (%) |
|---|---|---|---|---|---|---|---|---|
| | | | Strain Rate $6.67 \times 10^{-4}$/sec | | | | | |
| Tangential | 25 | 77 | 211(30.6) | 475(69.0) | 315(45.7) | 16.2 | 32.2 | 69.2 |
| Radial | 25 | 77 | 261(37.9) | 535(77.7) | 393(57.0) | 12.6 | 24.8 | 57.0 |
| Axial | 25 | 77 | 254(36.9) | 522(75.7) | 393(57.0) | 14.7 | 27.8 | 52.7 |
| Axial | 204 | 400 | 239(34.7) | 473(68.6) | 366(53.1) | 12.2 | 22.3 | 47.5 |
| Axial | 316 | 600 | 246(35.7) | 504(73.1) | 416(60.6) | 10.2 | 17.7 | 43.4 |
| Axial | 371 | 700 | 230(33.4) | 508(73.7) | 422(61.3) | 9.5 | 17.8 | 42.7 |
| Axial | 454 | 850 | 225(32.6) | 521(75.6) | 429(62.2) | 9.9 | 18.2 | 39.7 |
| Axial | 510 | 950 | 231(33.5) | 513(74.4) | 387(56.1) | 10.5 | 19.8 | 42.2 |
| Tangential | 566 | 1050 | 182(26.4) | 371(53.8) | 183(26.6) | 9.9 | 29.0 | 71.2 |
| Radial | 566 | 1050 | 219(31.8) | 447(64.9) | 294(42.7) | 9.8 | 21.1 | 51.6 |
| Axial | 566 | 1050 | 232(33.6) | 478(69.4) | 336(48.8) | 11.9 | 23.4 | 51.6 |
| | | | Strain Rate $2.67 \times 10^{-6}$/sec | | | | | |
| Tangential[a] | 25 | 77 | 198(28.8) | 448(65.0) | 299(43.4) | 15.7 | 29.3 | 64.0 |
| Tangential[a] | 93 | 200 | 178(25.9) | 418(60.6) | 275(39.9) | 13.7 | 27.2 | 68.4 |
| Axial | 204 | 400 | 218(31.7) | 478(69.4) | 392(56.9) | 11.3 | 20.3 | 51.9 |
| Axial | 316 | 600 | 220(32.0) | 552(80.1) | 467(67.8) | 9.8 | 19.4 | 44.6 |
| Axial | 371 | 700 | 225(32.6) | 621(90.2) | 508(73.7) | 13.3 | 21.6 | 40.5 |
| Axial | 454 | 850 | 229(33.3) | 626(90.8) | 499(72.4) | 21.3 | 30.5 | 48.3 |
| Axial | 510 | 950 | 222(32.2) | 558(81.0) | 431(62.5) | 14.7 | 26.8 | 43.1 |
| Tangential[a] | 566 | 1050 | 169(24.6) | 223(32.3) | 138(2.0) | 4.5 | 48.7 | 90.3 |

[a]Since tangential specimens were decidedly weaker, they are not plotted in Figs. 3.66 and 3.67 even though they were the only ones tested at this strain rate and temperature.

Table 3.20. Tensile Properties for Laboratory Annealed 2 1/4 Cr-1 Mo Steel Tubesheet Forging

| Specimen Orientation | Test Temperature (°C) | Test Temperature (°F) | Strength, MPa(ksi) Yield | Strength, MPa(ksi) Ultimate | Strength, MPa(ksi) Fracture | Elongation, % Uniform | Elongation, % Total | Reduction of Area (%) |
|---|---|---|---|---|---|---|---|---|
| | | | Strain Rate $6.67 \times 10^{-4}$/sec | | | | | |
| Tangential | 25 | 77 | 263(38.1) | 506(73.4) | 266(38.6) | 13.9 | 29.7 | 78.2 |
| Radial | 25 | 77 | 264(38.3) | 520(75.5) | 282(41.0) | 12.1 | 28.2 | 77.2 |
| Axial | 25 | 77 | 262(38.0) | 515(74.7) | 289(42.0) | 12.1 | 30.1 | 74.9 |
| Axial | 204 | 400 | 221(32.1) | 446(64.7) | 247(35.9) | 10.5 | 24.2 | 73.1 |
| Axial | 316 | 600 | 240(34.8) | 491(71.3) | 331(48.1) | 8.4 | 20.0 | 68.5 |
| Axial | 371 | 700 | 232(33.7) | 502(72.9) | 336(48.7) | 9.6 | 20.0 | 60.7 |
| Axial | 454 | 850 | 234(34.0) | 466(67.7) | 276(40.1) | 9.1 | 22.8 | 67.9 |
| Axial | 510 | 950 | 231(33.5) | 423(61.4) | 197(28.6) | 7.9 | 24.2 | 72.4 |
| Tangential | 566 | 1050 | 196(28.5) | 318(46.1) | 49(7.1) | 7.4 | 36.6 | 88.2 |
| Radial | 566 | 1050 | 205(29.8) | 327(47.4) | 56(8.1) | 7.1 | 41.5 | 86.5 |
| Axial | 566 | 1050 | 207(30.1) | 339(49.2) | 50(7.2) | 6.4 | 33.4 | 82.5 |
| | | | Strain Rate $2.67 \times 10^{-6}$/sec | | | | | |
| Tangential | 25 | 77 | 243(35.2) | 473(68.7) | 245(35.5) | 12.5 | 29.5 | 77.1 |
| Tangential | 93 | 200 | 227(33.0) | 450(65.3) | 241(35.0) | 11.7 | 26.2 | 79.2 |
| Radial | 204 | 400 | 234(34.0) | 475(68.9) | 303(44.0) | 9.5 | 21.6 | 70.7 |
| Radial | 316 | 600 | 261(37.9) | 555(80.6) | 370(53.7) | 8.6 | 22.1 | 66.6 |
| Radial | 371 | 700 | 238(34.6) | 497(72.2 | 303(44.0) | 9.0 | 22.2 | 66.7 |
| Radial | 454 | 850 | 232(33.7) | 433(62.9) | 140(20.3) | 6.0 | 22.9 | 75.1 |
| Radial | 510 | 950 | 248(36.0) | 349(50.7) | 35.1(5.1) | 3.9 | 31.6 | 88.5 |
| Radial | 566 | 1050 | 183(26.6) | 200(29.0) | 28.2(4.1) | 2.8 | 50.5 | 91.9 |

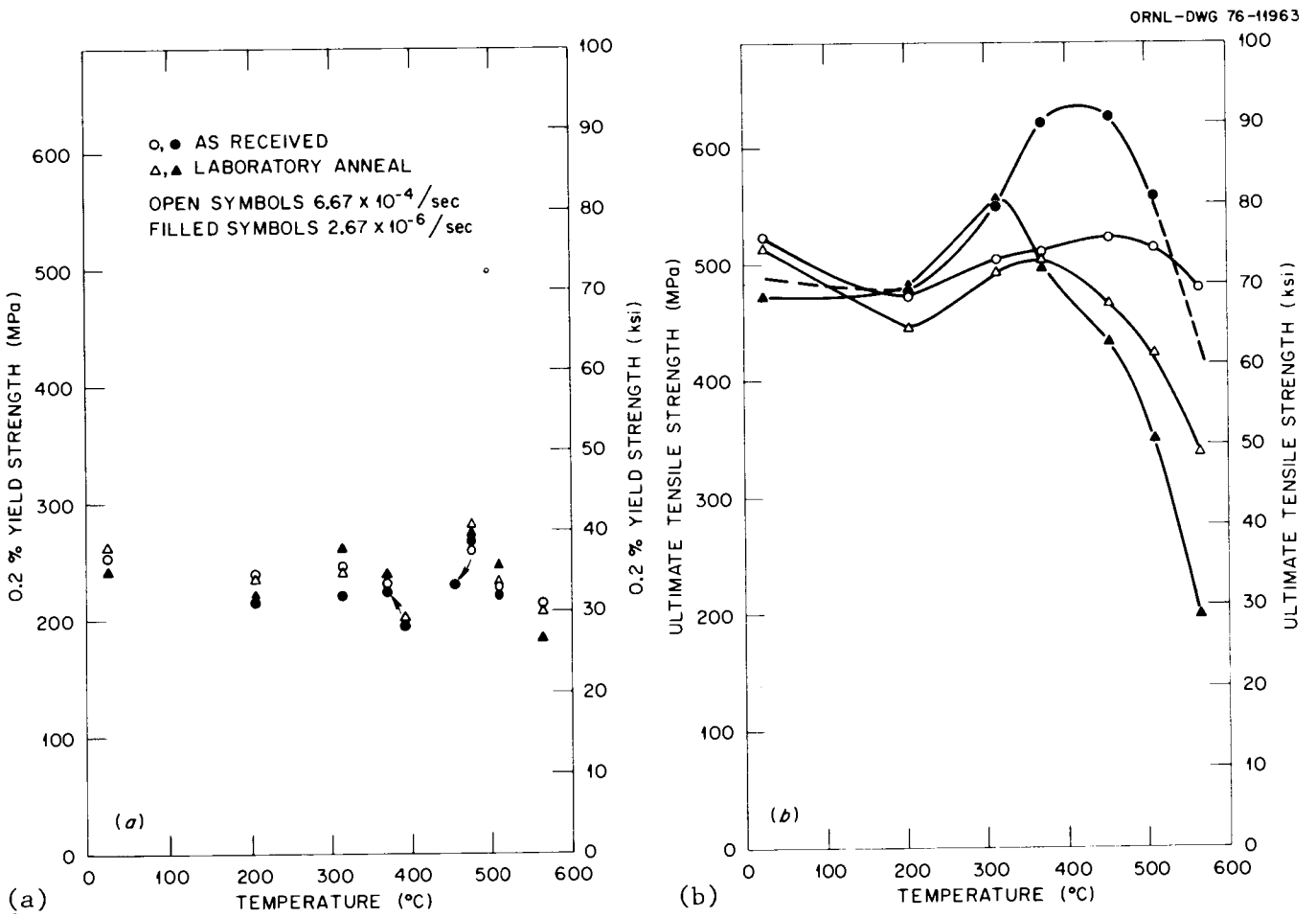


Fig. 3.66. Strength as a Function of Temperature for the As-Received Forging and the Laboratory Annealed Material at two Different Strain Rates. (a) Yield strength. (b) Ultimate tensile strength.

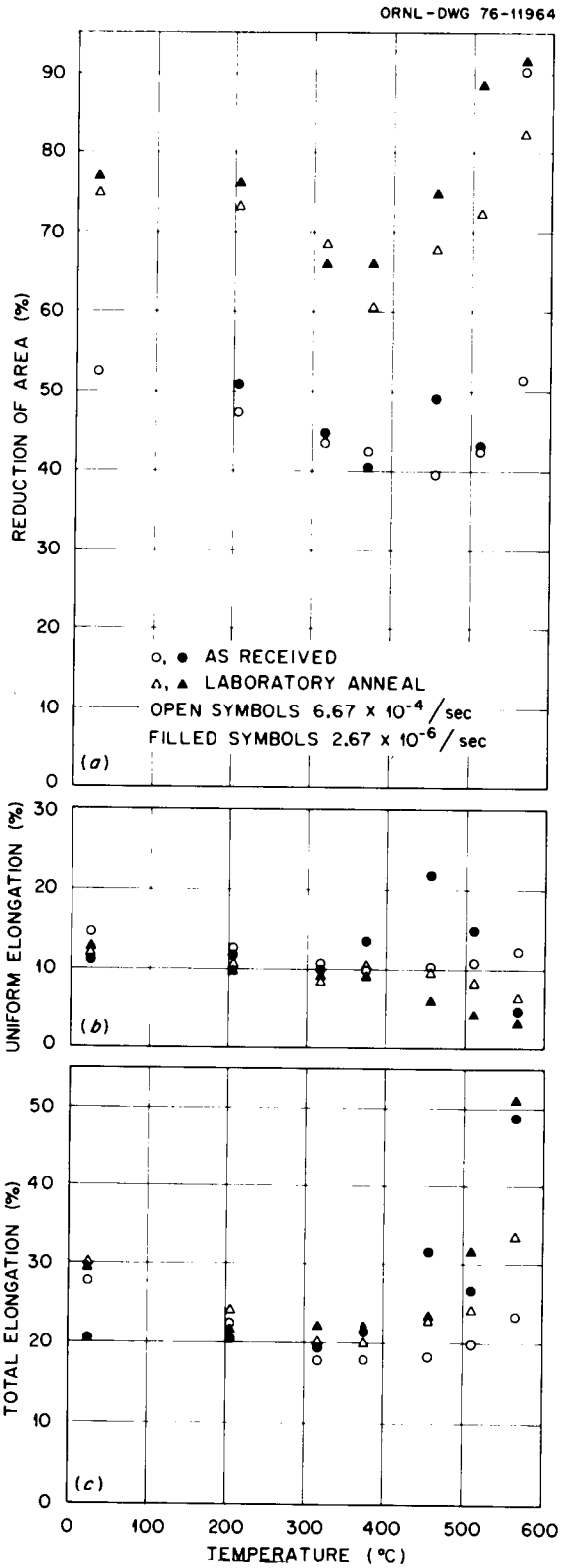


Fig. 3.67. Total and Uniform Elongation and Reduction of Area as a Function of Temperature for the As-Received Forging and the Laboratory Annealed Material at two Different Strain Rates.

The above results lead to some curious, yet interesting and important, results. Consider first the as-received forging. The fact that the microstructure of the tangential specimens was different from the other two orientations indicates that the differences are caused by something other than orientation. We believe this difference is in the position (radial distance from the center of the cylinder) at which the specimens were taken. As stated above, specimens were taken from wedges cut from the cylinder. The tangantial specimens were taken from the wedge edge (i.e., the periphery of the cylinder; 10 to 25 mm (0.5—1 in.) from the edge of the 14-in.-radius cylinder). On the other hand, the radial specimens were taken at approximately 0.25 to 0.28 m (10—11 in.) from the center, while the axial specimens were from less than 0.13 m (5 in.). This would indicate that the strength near the periphery is less than it is at some distance inside the forging as a result of the difference in microstructure. The greater amounts of bainite in the axial and radial specimens would be expected to give a higher strength. It is apparent from these results that the vendor must have taken his tensile and metallography samples (Table 3.17) from the cylinder periphery.

One possible explanation for the difference in microstructure is that the external surface was decarburized during the heat treatment. The lower the carbon content, the less the amount of bainite formed. However, since there is no difference in the microstructure or strength of the laboratory annealed specimens with orientation, this is not too probable. Furthermore, the amount of material machined from the forging after the heat treatment should have included the decarburized material.

The microstructural observations along with the observations on the dynamic strain aging peaks for the as-received material relative to the peaks for the laboratory annealed material [Fig. 3.66(b)] would indicate that although the as-received material was isothermally annealed — held 3 hr at 732°C — it did not transform uniformly. Indeed, if the tranformation was uniform, then the strength of the as-received forging should be less than that of the laboratory annealed material, since the as-received material was transformed at a higher temperature for a longer time.

During the next quarter, we will investigate more closely the variation in microstructure and strength as a function of position in the forging to verify the results reported above. We have also begun creep-rupture tests on these materials, and the preliminary results from those tests will be reported next quarter.

### 3.4.3 Effect of Sodium on the Mechanical Properties of 2 1/4 Cr-1 Mo Steel — R. L. Klueh

In the demonstration liquid-metal fast breeder reactor, the sodium-heated steam generator is to be constructed of 2 1/4 Cr-1 Mo steel. Under the operating conditions of the steam generator, heated sodium flows from the intermediate heat exchanger, which is to be constructed of an austenitic stainless steel, to the ferritic steel steam generator. As a result of the difference in thermodynamic activity of the carbon in the austenitic and ferritic components, decarburization of the 2 1/4 Cr-1 Mo steel and carburization of the stainless steel can result. Such decarburization could significantly alter the properties of the 2 1/4 Cr-1 Mo steel.

Although the starting microstructure for 2 1/4 Cr-1 Mo steel under most typical heat-treated conditions is microstructurally unstable during elevated-temperature exposure,[55–57] little information is available concerning the effect of prolonged exposure (thermal aging) on the mechanical properties. The bulk of the available creep-rupture data is from material in the as-heat-treated condition[58] (i.e., annealed, normalized and tempered, or quenched and tempered). Similarly, little is known about the effect of a carbon loss combined with thermal aging.

In the present study, the creep-rupture properties of 2 1/4 Cr-1 Mo steel exposed to sodium for 26,500 hr at 566°C (1050°F) are being determined. The properties of specimens simultaneously exposed to a helium atmosphere (aged, but not decarburized) are also being determined. Although 566°C is above the peak temperature of the demonstration plant steam generator [520°C (968°F)], these results are nevertheless of interest because this is the longest time and lowest temperature at which commercial 2 1/4 Cr-1 Mo steel has been decarburized by sodium.

The specimens were exposed to sodium in a large type 316 stainless steel retort by Mine Safety Research Corporation (MSA), Evans City, Pennsylvania; the details of that exposure have been published.[59] Because program funding was discontinued, MSA made only a limited study of the effect of sodium and thermal aging on the tensile properties, metallography, and carbon content after 10,000, 20,000, and 26,500 hr.[60—63]

After 10,000, 20,000, and 26,500 hr, Hiltz and co-workers[61,62] found that the carbon content decreased from 0.11 to 0.093, 0.075, and 0.075 wt % C, respectively. By optical microscopy they found that after 10,000 hr, carbide spheroidization of the original pearlite platelets of the annealed steel was well under way in both the aged and decarburized specimens. The particle density of carbides in the decarburized specimen was slightly less than that in the aged specimen, though there was no noticeable difference in density between the edge and center of the decarburized specimen.[60]

We have previously reported[64] in detail on the carbides present in the sodium-decarburized and helium-aged specimens after 26,500 hr (we were only able to obtain 26,500-hr specimens). For a "starting microstructure" to compare with those obtained after decarburization and/or thermal aging, we annealed end pieces from tensile specimens that had been aged in helium and not decarburized.

With optical microscopy, we found that after 26,500 hr, the carbide particle density of the decarburized and aged specimens was considerably less than reported[61] after 10,000 hr, with the density of the thermally aged specimen being considerably greater than that in the decarburized specimen. For the aged specimen, the density decrease was a result of Ostwald ripening, and the total amount of carbide was not noticeably affected. Decarburization, however, resulted in a gradient in carbide density, with the smallest density near the surface.

The proeutectoid ferrite of annealed 2 1/4 Cr-1 Mo steel contains a large number of small particles — mostly $Mo_2C$ — that are replaced during elevated-temperature exposure by $M_{23}C_6$ and η-carbide.[55,56] (Eta-carbide has generally been referred to as $M_6C$; however, it was recently found[65] that in 2 1/4 Cr-1 Mo steel, this is more nearly $M_4C$.) By transmission electron microscopy and electrolytic extraction of

precipitates we found[64] that the precipitates changed from a high density of particles — mostly needles or platelets of $Mo_2C$ — in the annealed steel to a very much smaller density of large globular particles of $M_{23}C_6$ and η-carbide after 26,500 hr.

Tensile specimens were machined from a standard heat of annealed 2 1/4 Cr-1 Mo steel, which was purchased by MSA.[59] According to the vendor's analysis, the steel contained 0.11% C. The specimens, which were aged and decarburized, were in the form of 1.5-mm (0.06-in.) sheet tensile specimens cut from blanks 184-mm-long by 31.8-mm-wide (7 1/4 by 1 1/4 in.) and had a 25.4-mm-long by 12.7-mm-wide (1- × 1/2-in.) gage section. We received from MSA 23 specimens that had been exposed to sodium for 26,500 hr, but only five specimens that had been thermally aged for the same length of time. Unfortunately, none of the starting material was available. Thus, the effect of decarburization and aging will have to be inferred by comparison with literature data.[58]

The tensile properties at 25 and 566°C (75 and 1050°F) were determined by MSA,[62] and after 26,500 hr MSA found that the strength properties of the decarburized and aged specimens had decreased, the greater effect occurring at 566°C (1050°F). At this temperature there was little difference between the specimens decarburized in sodium and those aged in helium. The results are given in Table 3.21.

Because of the large decrease in the strength as a result of decarburization and thermal aging — especially at 566°C — we repeated the tests at 25 and 566°C on decarburized specimens. The results for these tests are also given in Table 3.21. Our results are in good agreement with those obtained by MSA. Because of a lack of specimens, no verification tests were made on helium-exposed specimens. Because of the good agreement on the decarburized specimens, however, no such tests would appear to be necessary.

Creep-rupture tests are now in progress on the decarburized specimens at 510 and 566°C. Selected tests are also being made on the thermally aged specimens at 566°C. Results from these tests will be reported later.

Table 3.21. Changes in Tensile Properties of 2 1/4 Cr-1 Mo Steel After Prolonged Exposure to Helium and Sodium at 566°C (1050°F)[a]

| Exposure Time (hr) | Strength, MPa(ksi) | | Elongation (%) | Reduction of Area (%) |
|---|---|---|---|---|
| | Yield | Ultimate | | |
| | Test Temperature 25°C (75°F) | | | |
| Helium | | | | |
| 0 | 241(35) | 503(73) | 32 | 68 |
| 10,000 | 276(40) | 476(69) | 40 | 68 |
| 26,500 | 234(34) | 455(66) | 36 | 59 |
| Sodium | | | | |
| 0 | 241(35) | 503(73) | 32 | 68 |
| 10,000 | 221(32) | 428(62) | 39 | 68 |
| 20,000 | 234(34) | 434(63) | 37 | 57 |
| 26,500 | 207(30) | 414(60) | 39 | 60 |
| 26,500[b] | 189(27.4) | 411(59.6) | 42 | 51 |
| | Test Temperature 566°C (1050°F) | | | |
| Helium | | | | |
| 0 | 186(27) | 455(66) | 30 | 56 |
| 26,500 | 138(20) | 193(28) | 58 | 72 |
| Sodium | | | | |
| 0 | 186(27) | 455(66) | 30 | 56 |
| 10,000 | 117(17) | 200(29) | 43 | 76 |
| 20,000 | 103(15) | 166(24) | 61 | 71 |
| 26,500 | 131(19) | 200(29) | 50 | 69 |
| 26,500[b] | 112(16.3) | 204(29.6) | 66 | 65 |

[a]Taken from Reference 62; strain rate was not given.

[b]Tested at ORNL; stain rate 0.05/min.

## 3.4.4 Fatigue Behavior of 2 1/4 Cr-1 Mo Steel — C. R. Brinkman

### 3.4.4.1 Time-Dependent Fatigue — Estimates of Worst Effects — M. K. Booker

Last quarter[66] we described our initial attempts to estimate the possible worst effects on fatigue life that can be expected for 2 1/4 Cr-1 Mo steel due to relaxation hold periods at peak strain during strain-controlled cycling. This quarter we will describe additional efforts in that area, including refined calculational procedures and more extensive results.

Actually, this effort consists of two distinct stages: (1) the estimation of fatigue lives with long hold periods (up to 1000 hr); and (2) estimation of shortest fatigue lives that can be expected as a result of hold periods. In Sect. 3.4.4.2 we discuss methods for analyzing the effects of hold periods on fatigue lives in available test data, although practical considerations forced these experimental hold periods to be of relatively short duration. However, those analyses did indicate that the strain range partitioning approach is consistent with the behavior of this material. Therefore, the current projections are based upon that method.

The first step in estimating effects of long hold time is to construct hypothetical hysteresis loops for the tests with long hold periods. The basic method for constructing these loops was discussed last quarter,[66] but it will be briefly described here for completeness. Having chosen a temperature ($T$) and total strain range ($\Delta\varepsilon_t$), one first estimates the corresponding stress range, $\Delta\sigma$. This estimate is based upon plots such as those shown in Fig. 3.68, which gives estimates of the effect of hold periods on the value of $\Delta\sigma$ at 538 and 593°C. The corresponding plot for data at 482°C was shown last quarter.[66]

Next, one must estimate the magnitude of the stress relaxation, $\Delta\sigma_r$, occurring during the hold period (see Fig. 3.69). Available relaxation curves from the experimental creep-fatigue tests indicate that these curves can be well approximated by the Gittus equation,[67]

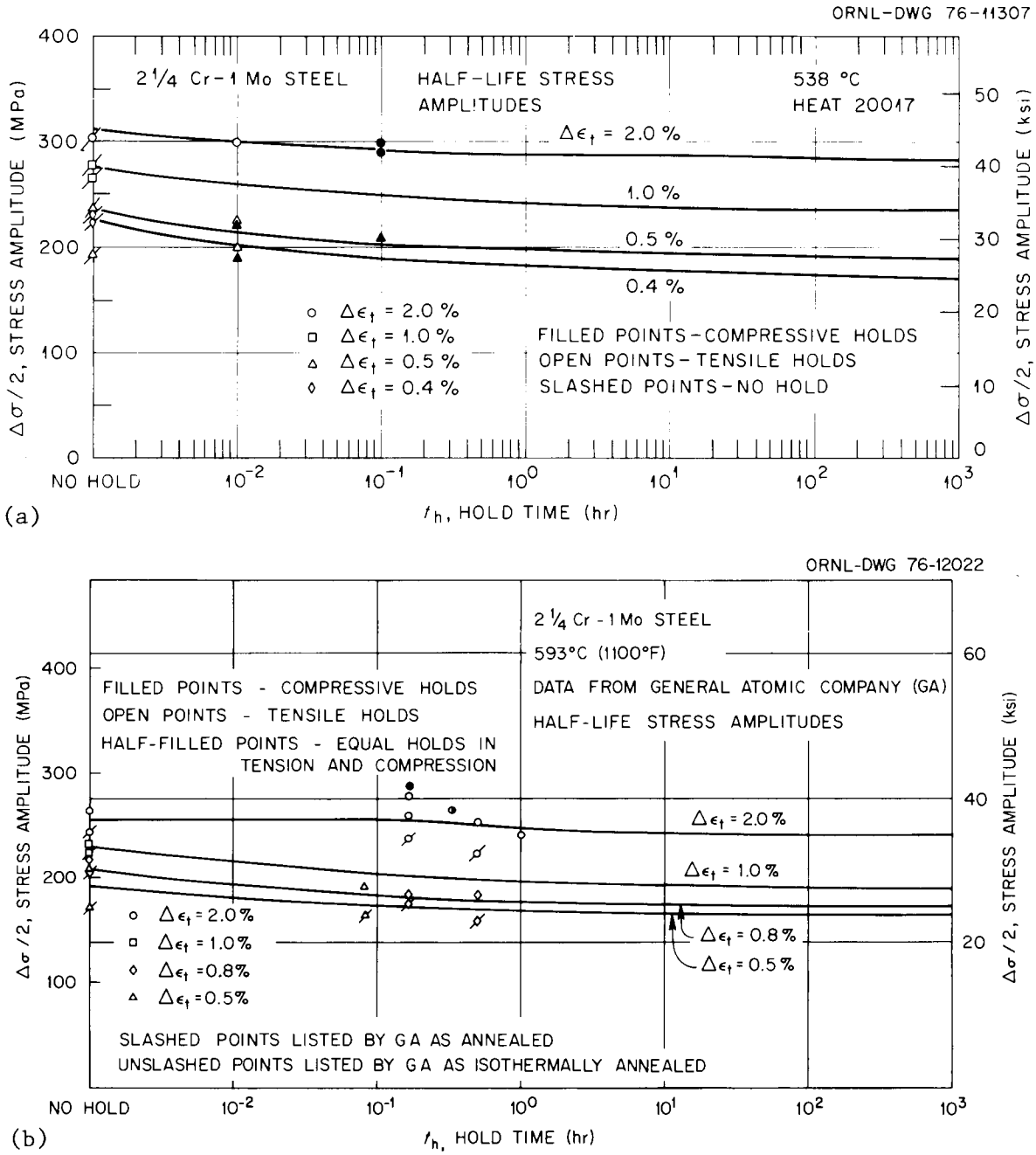


Fig. 3.68. Variation of Half-Life Stress Amplitude with Hold Time for 2 1/4 Cr-1 Mo Steel at (a) 538°C and (b) 593°C.

ORNL-DWG 76-6362

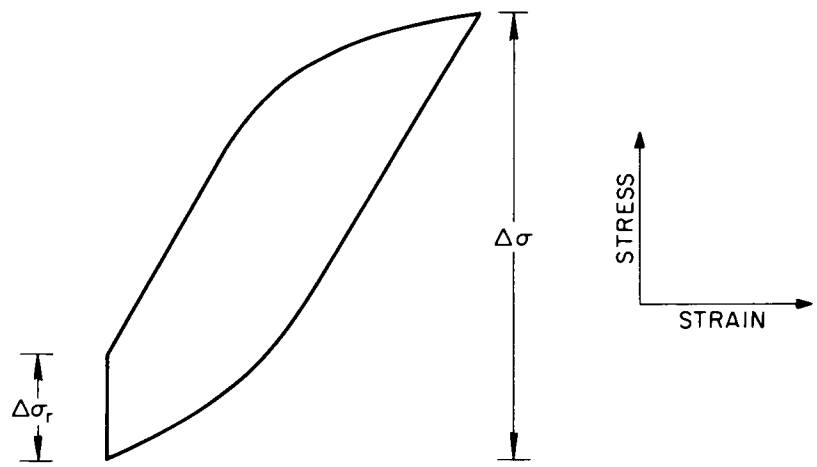


Fig. 3.69. Hysteresis Loop for a Test Involving a Hold Period at Peak Compressive Strain.

which we express as

$$\ln(\sigma_0/\sigma) = Ct^m \ , \tag{1}$$

where $\sigma_0$ is the stress at the beginning of the relaxation ($\sigma_0 = \Delta\sigma/2$), and $\sigma$ and $t$ are the instantaneous stress and time during relaxation. Figures 3.70 and 3.71 illustrate the behavior of the constants $C$ and $m$ from data obtained thus far at 538 and 593°C. (Again, the corresponding plots for 482°C were shown last quarter.) The scatter in the values of $C$ and $m$ is extremely large, although the trends can be estimated as shown in the figures. At each temperature, $m$ appears to be approximately constant. Values of $C$ between strain range levels shown can be estimated by linear interpolation.

Estimates of $\Delta\sigma$, $C$, and $m$ for a given temperature, strain range, and hold period allow construction of an entire hypothetical hysteresis loop. For example, consider a test with a compressive hold period of $t_h$. If $\Delta\sigma_r$ is given by $\sigma_0 - \sigma_f$, Eq. (1) shows that

$$\ln(\sigma_0/\sigma_f) = Ct_h^{\ m} \tag{2}$$

or

$$\sigma_f = \sigma_0 \ \exp\left(-Ct_h^{\ m}\right) \ . \tag{3}$$

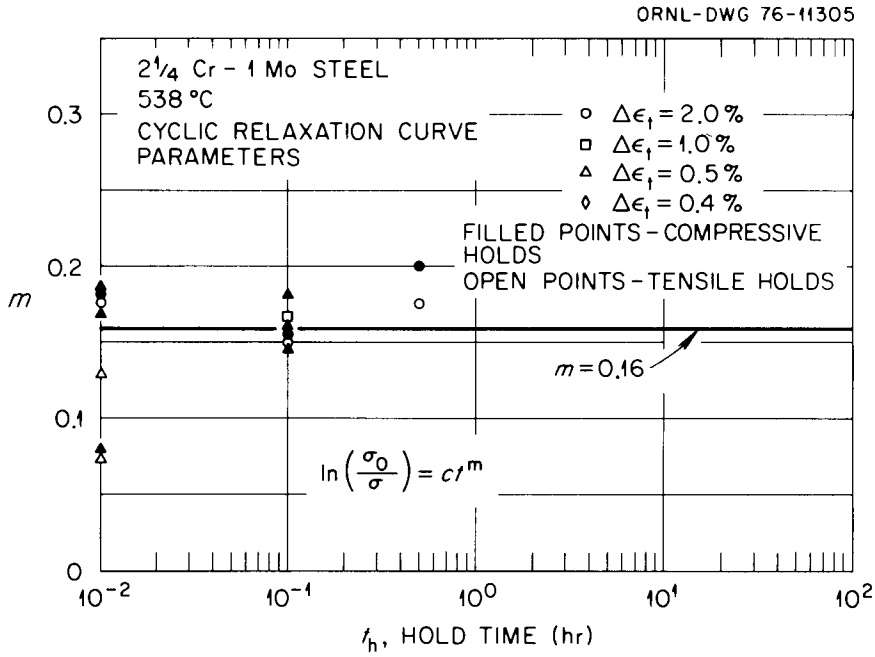


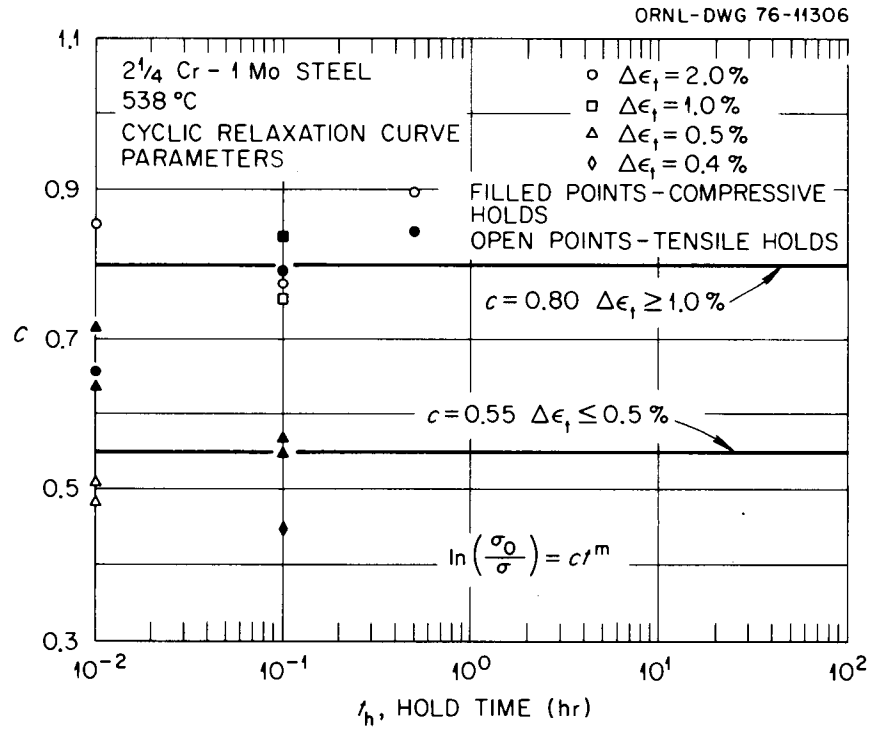


Fig. 3.70. Variation of Gittus Equation Constants with Hold Time at 538°C for 2 1/4 Cr-1 Mo Steel at Various Strain Ranges.

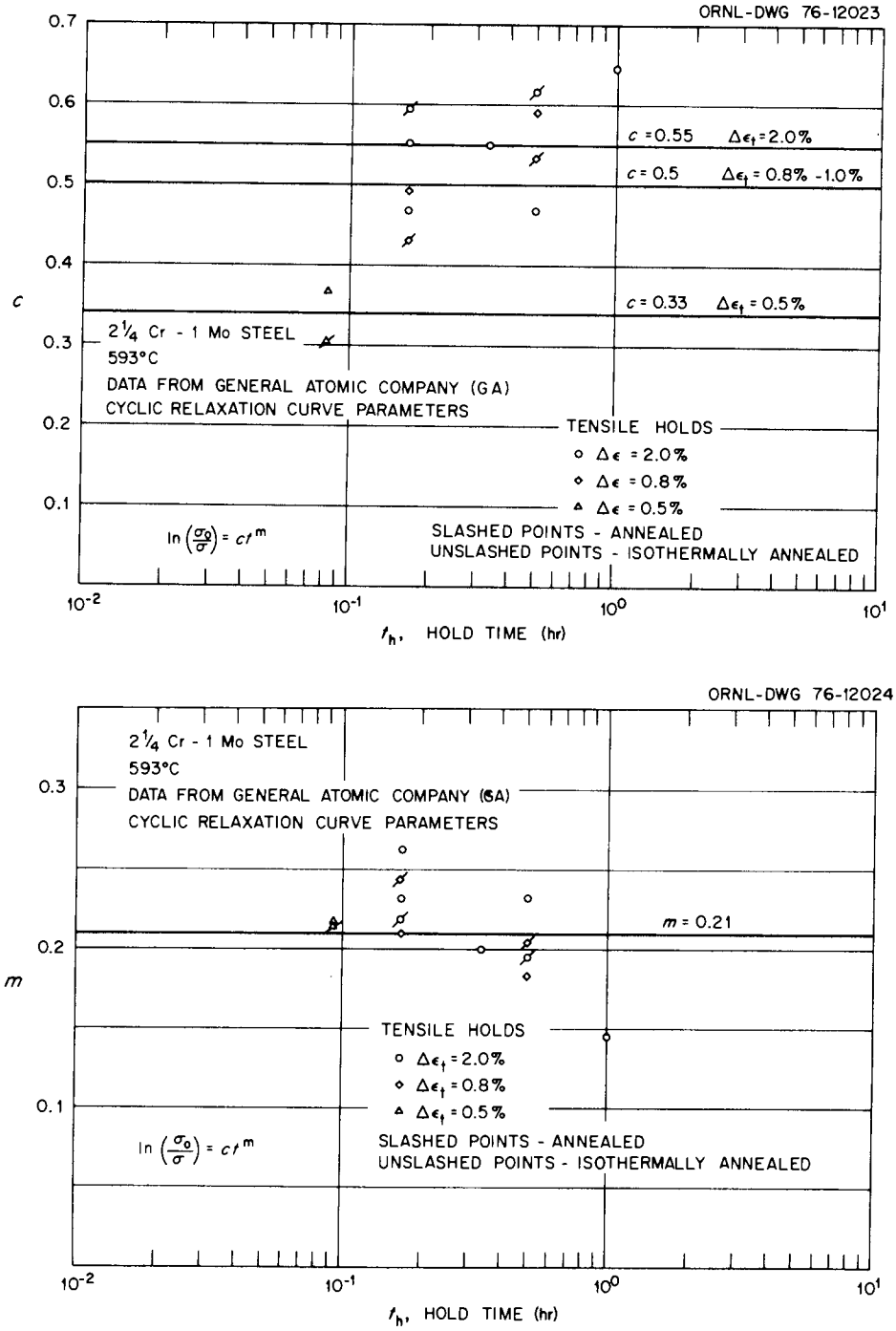


Fig. 3.71. Variation of Gittus Equation Constants with Hold Time at 593°C for 2 1/4 Cr-1 Mo Steel at Various Strain Ranges.

In terms of strain range partitioning,

$$\Delta\varepsilon_{pc} = \Delta\sigma_r/E \ , \tag{4}$$

where $E$ is Young's modulus. The total inelastic strain range is given by

$$\Delta\varepsilon_{\text{inel}} = \Delta\varepsilon_t - (\Delta\sigma - \Delta\sigma_r)/E \tag{5}$$

where $(\Delta\sigma - \Delta\sigma_r)/E$ is merely the total elastic strain range. Finally, one has

$$\Delta\varepsilon_{pp} = \Delta\varepsilon_{\text{inel}} - \Delta\varepsilon_{pc} \ , \tag{6}$$

completing the characterization of the loop.

Tables 3.22 through 3.24 give the hypothetical results constructed by the above method. Several points about these results should be stressed. First, the information at 482°C (Table 3.22) was constructed from data for both heats 20017 and 3P5601 from the ORNL program, although heat 3P5601 generally develops lower values of stress range for a given strain range.[68] At 538°C, the differences between these two heats are even more pronounced, and the $\Delta\sigma$ values (Table 3.23) were estimated from data for heat 20017 only since those were the most numerous at that temperature. All data used at 593°C (Table 3.24) refer to Heat 3 from the program conducted by General Atomic Company.[69] Two heat treatments of this heat were used by Ellis et al.,[69] labelled "annealed" and "isothermally annealed." Their "isothermally annealed" material developed slightly higher stress ranges than their "annealed" material, and the values in Table 3.24 represent estimates of average behavior for this heat of material. Therefore, one must use caution in comparing the values in the tables at different temperatures, since the variations are probably due partially to temperature effects and partially to the fact that the data bases were different at different temperatures.

Table 3.22. Long-Hold-Period Strain Components and Creep Fatigue Lives for 2 1/4 Cr-1 Mo Steel at 482°C (900°F) Calculated from $\ln(\sigma_0/\sigma) = Ct^{0.14}$

| Hold Period (hr) | $\Delta\sigma/2$ (MPa) | Partitioned Strain Components (%) | | Predicted Lives,[b] Cycles | | |
|---|---|---|---|---|---|---|
| | | | | Strain Range Partitioning | | Linear Summation of Damage |
| | | $\Delta\varepsilon_{pp}$ | $\Delta\varepsilon_{pc}$[a] | Tensile Hold | Compressive Hold | |
| | | | Total Strain Range 0.4%, $C = 0.30$ | | | |
| 0 | | | | 93,800 | 93,800 | 93,800 |
| 0.1 | 194 | 0.184 | 0.021 | 18,623 | 12,464 | c |
| 1 | 193 | 0.186 | 0.028 | 15,519 | 10,105 | 30,200 |
| 10 | 193 | 0.186 | 0.036 | 12,937 | 8,228 | 8,210 |
| 100 | 193 | 0.186 | 0.047 | 10,586 | 6,641 | 2,260 |
| 300 | 193 | 0.186 | 0.052 | 9,673 | 6,052 | 1,320 |
| 1,000 | 193 | 0.186 | 0.059 | 8,734 | 5,461 | 792 |
| | | | Total Strain Range 0.5%, $C = 0.30$ | | | |
| 0 | | | | 25,700 | 25,700 | 25,700 |
| 0.1 | 210 | 0.267 | 0.023 | 8,662 | 7,160 | c |
| 1 | 207 | 0.270 | 0.030 | 7,504 | 6,089 | 13,100 |
| 10 | 207 | 0.270 | 0.039 | 6,570 | 5,213 | 4,470 |
| 100 | 207 | 0.270 | 0.050 | 5,649 | 4,406 | 1,320 |
| 300 | 207 | 0.270 | 0.056 | 5,269 | 4,087 | 783 |
| 1,000 | 207 | 0.270 | 0.063 | 4,670 | 3,639 | 472 |
| | | | Total Strain Range 0.75%, $C = 0.385$ | | | |
| 0 | | | | 4,120 | 4,120 | 4,120 |
| 0.1 | 245 | 0.478 | 0.033 | 3,190 | 3,006 | c |
| 1 | 238 | 0.486 | 0.042 | 2,941 | 2,755 | 3,280 |
| 10 | 238 | 0.486 | 0.055 | 2,700 | 2,507 | 2,010 |
| 100 | 238 | 0.486 | 0.069 | 2,479 | 2,288 | 969 |
| 300 | 238 | 0.486 | 0.077 | 2,374 | 2,187 | 684 |
| 1,000 | 238 | 0.486 | 0.085 | 2,267 | 2,085 | 478 |
| | | | Total Strain Range 1.0%, $C = 0.47$ | | | |
| 0 | | | | 2,000 | 2,000 | 2,000 |
| 0.1 | 285 | 0.690 | 0.045 | 1,931 | 1,910 | c |
| 1 | 275 | 0.702 | 0.055 | 1,793 | 1,778 | 1,690 |
| 10 | 270 | 0.702 | 0.072 | 1,650 | 1,640 | 1,230 |
| 100 | 269 | 0.702 | 0.087 | 1,534 | 1,529 | 762 |
| 300 | 269 | 0.702 | 0.097 | 1,463 | 1,462 | 595 |
| 1,000 | 269 | 0.702 | 0.106 | 1,407 | 1,410 | 432 |
| | | | Total Strain Range 2.0%, $C = 0.47$ | | | |
| 0 | | | | 679 | 679 | 679 |
| 1 | 305 | 1.671 | 0.061 | 625 | 665 | 603 |
| 100 | 300 | 1.671 | 0.097 | 563 | 618 | 319 |
| 300 | 298 | 1.671 | 0.105 | 551 | 609 | 257 |
| 1,000 | 296 | 1.671 | 0.117 | 534 | 595 | 192 |

[a]"Creep" component may be $\Delta\varepsilon_{pc}$ or $\Delta\varepsilon_{cp}$.

[b]Values for no hold time calculated from best fits to continuous cycling fatigue data.

[c]Not available.

Table 3.23. Long-Hold-Period Strain Components and Creep Fatigue Lives for 2 1/4 Cr-1 Mo Steel at 538°C (1000°F) Calculated from $\ln(\sigma_0/\sigma) = Ct^{0.16}$

| Hold Period (hr) | $\Delta\sigma/2$ (MPa) | Partitioned Strain Components (%) | | Predicted Lives,[b] Cycles | | |
|---|---|---|---|---|---|---|
| | | | | Strain Range Partitioning | | Linear Summation of Damage |
| | | $\Delta\varepsilon_{pp}$ | $\Delta\varepsilon_{pc}$[a] | Tensile Hold | Compressive Hold | |
| | | | Total Strain Range 0.4%, $C$ = 0.55 | | | |
| 0 | | | | 93,800 | 93,800 | 93,800 |
| 0.1 | 188 | 0.185 | 0.034 | 13,600 | 8,690 | 16,200 |
| 1 | 182 | 0.192 | 0.044 | 10,600 | 6,850 | 5,530 |
| 10 | 178 | 0.196 | 0.056 | 8,530 | 5,510 | 2,170 |
| 100 | 174 | 0.201 | 0.068 | 6,970 | 4,570 | 1,240 |
| 300 | 172 | 0.203 | 0.073 | 6,420 | 4,240 | 969 |
| 1000 | 171 | 0.205 | 0.079 | 5,940 | 3,940 | 652 |
| | | | Total Strain Range 0.5%, $C$ = 0.55 | | | |
| 0 | | | | 25,700 | 25,700 | 25,700 |
| 0.1 | 203 | 0.268 | 0.037 | 6,890 | 5,470 | 8,270 |
| 1 | 198 | 0.274 | 0.048 | 5,710 | 4,500 | 3,030 |
| 10 | 194 | 0.279 | 0.061 | 4,630 | 3,650 | 1,250 |
| 100 | 191 | 0.282 | 0.075 | 4,090 | 3,200 | 668 |
| 300 | 189 | 0.284 | 0.081 | 3,880 | 3,040 | 532 |
| 1000 | 187 | 0.286 | 0.086 | 3,690 | 2,880 | c |
| | | | Total Strain Range 0.75%, $C$ = 0.67 | | | |
| 0 | | | | 4,120 | 4,120 | 4,120 |
| 0.1 | 233 | 0.484 | 0.049 | 2,820 | 2,630 | 2,680 |
| 1 | 226 | 0.492 | 0.063 | 2,540 | 2,360 | 1,610 |
| 10 | 216 | 0.503 | 0.076 | 2,290 | 2,130 | 1,080 |
| 100 | 212 | 0.507 | 0.091 | 2,090 | 1,940 | 700 |
| 300 | 208 | 0.512 | 0.097 | 2,020 | 1,880 | 544 |
| 1000 | 207 | 0.513 | 0.103 | 1,950 | 1,820 | 284 |
| | | | Total Strain Range 1.0%, $C$ = 0.80 | | | |
| 0 | | | | 2,000 | 2,000 | 2,000 |
| 0.1 | 249 | 0.716 | 0.060 | 1,710 | 1,700 | 1,600 |
| 1 | 241 | 0.724 | 0.076 | 1,560 | 1,560 | 1,240 |
| 10 | 238 | 0.728 | 0.093 | 1,430 | 1,440 | 924 |
| 100 | 234 | 0.732 | 0.109 | 1,330 | 1,350 | 612 |
| 300 | 234 | 0.732 | 0.116 | 1,290 | 1,310 | 370 |
| 1000 | 234 | 0.732 | 0.122 | 1,260 | 1,280 | c |
| | | | Total Strain Range 2.0%, $C$ = 0.80 | | | |
| 0 | | | | 679 | 679 | |
| 0.1 | 293 | 1.665 | 0.071 | 609 | 654 | |
| 1 | 289 | 1.670 | 0.091 | 573 | 626 | |
| 10 | 288 | 1.671 | 0.113 | 539 | 600 | |
| 100 | 283 | 1.676 | 0.131 | 511 | 577 | |
| 300 | 283 | 1.677 | 0.139 | 501 | 569 | |
| 1000 | 283 | 1.677 | 0.147 | 491 | 561 | |

[a]"Creep" component may be $\Delta\varepsilon_{pp}$ or $\Delta\varepsilon_{cp}$.

[b]Values for no hold time calculated from best fits to continuous cycling fatigue data.

[c]Not available.

Table 3.24. Long-Hold-Period Strain Components and Creep Fatigue Lives for 2 1/4 Cr-1 Mo Steel at 593°C (1100°F) Calculated from $\ln(\sigma_0/\sigma) = Ct^{0.21}$

| Hold Period (hr) | $\Delta\sigma/2$ (MPa) | Partitioned Strain Components (%) | | Predicted Lives,[b] Cycles | | |
|---|---|---|---|---|---|---|
| | | | | Strain Range Partitioning | | Linear Summation of Damage |
| | | $\Delta\varepsilon_{pp}$ | $\Delta\varepsilon_{pc}$[a] | Tensile Hold | Compressive Hold | |
| | | | Total Strain Range 0.5%, $C$ = 0.33 | | | |
| 0 | | | | 10,830 | 10,830 | 10,830 |
| 0.1 | 172 | 0.296 | 0.019 | 7,313 | 6,428 | 884 |
| 1 | 167 | 0.303 | 0.028 | 5,710 | 4,951 | 197 |
| 10 | 165 | 0.305 | 0.040 | 5,027 | 4,226 | 51 |
| 100 | 164 | 0.306 | 0.056 | 4,374 | 3,582 | 19 |
| 300 | 164 | 0.306 | 0.064 | 4,095 | 3,323 | 14 |
| 1000 | 164 | 0.306 | 0.073 | 3,828 | 3,084 | c |
| | | | Total Strain Range 0.8%, $C$ = 0.50 | | | |
| 0 | | | | 2,270 | 2,270 | 2,270 |
| 0.1 | 183 | 0.584 | 0.029 | 2,594 | 2,525 | 743 |
| 1 | 176 | 0.592 | 0.041 | 2,363 | 2,291 | 272 |
| 10 | 173 | 0.595 | 0.057 | 2,139 | 2,066 | 110 |
| 100 | 172 | 0.596 | 0.075 | 1,938 | 1,870 | 65 |
| 300 | 172 | 0.597 | 0.082 | 1,861 | 1,796 | 56 |
| 1000 | 172 | 0.597 | 0.089 | 1,792 | 1,731 | 43 |
| | | | Total Strain Range 1.0%, $C$ = 0.50 | | | |
| 0 | | | | 1,420 | 1,420 | 1,420 |
| 0.1 | 203 | 0.760 | 0.032 | 1,844 | 1,842 | 427 |
| 1 | 195 | 0.769 | 0.045 | 1,692 | 1,695 | 154 |
| 10 | 192 | 0.773 | 0.063 | 1,543 | 1,553 | 62 |
| 100 | 188 | 0.777 | 0.081 | 1,408 | 1,426 | 40 |
| 300 | 188 | 0.778 | 0.090 | 1,356 | 1,377 | 35 |
| 1000 | 188 | 0.778 | 0.098 | 1,310 | 1,334 | c |
| | | | Total Strain Range 2.0%, $C$ = 0.55 | | | |
| 0 | | | | 556 | 556 | |
| 0.1 | 255 | 1.698 | 0.043 | 647 | 677 | 147 |
| 1 | 248 | 1.707 | 0.062 | 607 | 647 | 52 |
| 10 | 241 | 1.715 | 0.084 | 566 | 616 | 24 |
| 100 | 241 | 1.715 | 0.109 | 529 | 587 | 15 |
| 300 | 241 | 1.715 | 0.120 | 514 | 576 | 12 |
| 1000 | 241 | 1.715 | 0.129 | 502 | 566 | 9 |

[a]"Creep" component may be $\Delta\varepsilon_{pc}$ or $\Delta\varepsilon_{cp}$.

[b]Values for no hold time calculated from best fits to continuous cycling fatigue data.

[c]Not available.

Finally, it must be stressed that the values in Tables 3.22 through 3.24 are merely estimates. The values are consistent with available information for very short hold periods, but extrapolation to extremely long hold periods must be done with caution. For instance, Eq. (1) provides a good description of the experimental relaxation curves, but there is no assurance that it adequately describes long-term behavior. Equation (1) predicts that the stress continues to relax with time toward an asymptotic value of zero. However, the asymptotic value could actually be some finite positive stress, in which case Eq. (1) would probably overpredict the amount of relaxation in long hold periods. Fortunately, from the point of view of strain range partitioning, such an overprediction would simply increase the conservatism of the results.

The softening due to hold periods shown in Fig. 3.68 is consistent with previous estimates[70] of the behavior of this material. However, the actual magnitude of this softening is somewhat uncertain. In terms of strain range partitioning, a decreased $\Delta\sigma$ would increase the total inelastic strain but would decrease the amount of "creep" strain due to relaxation. These opposing effects should decrease the sensitivity of the predictions to variations in $\Delta\sigma$. Therefore, we feel that life predictions from Tables 3.22 through 3.24 can yield useful information, even though those data are somewhat subjective.

Each of the hypothetical tests in the tables was analyzed by strain range partitioning assuming the hold period to be in compression or in tension. Based on available information, the mean stress was considered to be zero, so that the compressive and tensile stress amplitudes were equal. (Again, we recognize that this situation may not be the case for very long hold periods. No available data indicate otherwise, however.) The predicted lives from strain range partitioning using the interaction damage rule are given in Tables 3.22 through 3.24.

The linear summation of damage approach has also been used to estimate the cyclic lives of the hypothetical tests in the tables, although no corrections have been made for the increased damage due to compressive hold periods. (These corrections have been ignored here because the linear summation predictions for long hold times appear overconservative already.) Assuming a damage sum of unity, the predicted life can be obtained from the summation

$$N_h/N_f + N_h D_c(1) = 1 \ , \tag{7}$$

where $N_f$ is the expected continuous cycling life. Equation (7) then yields

$$N_h = [D_c(1) + 1/N_f]^{-1} \ . \tag{8}$$

Finally, the tables also contain estimates of the continuous cycling fatigue life, $N_f$, at each temperature and strain range shown. The values of $N_f$ were calculated from previously reported[71] best-fit fatigue curves. It should be noted that in some cases at high strain ranges (particularly at 593°C) predicted values of $N_h$ by strain range partitioning are greater than the corresponding values of $N_f$. This occurrence is not to be taken as a prediction that the hold period increases the fatigue life. Rather, it is merely a reflection of the uncertainty in predicting fatigue lives. No cyclic life listed in Table 3.22, 3.23, or 3.24 could possibly be considered accurate within less than a factor of 2. Predicted values of the fatigue life reduction factors ($N_f/N_h$) from the tables are shown in Figs. 3.72 through 3.74. (Note that Fig. 3.74 was constructed by using $N_f$ = 1842 at $\Delta\varepsilon_t$ = 1.0% for consistency. Otherwise, the values of $N_f$ in the tables were used.)

The predictions from strain range partitioning seem very reasonable. For instance, at low strain ranges, compressive hold periods are predicted to be more damaging than tensile hold periods. The predicted cyclic lives are generally about the length one would expect from a consideration of the available short-term data. On the other hand, predictions from the linear summation of damage approach appear to be extremely conservative, especially for very long hold times (≥100 hr) and particularly at 593°C. It should be noted that because of differences in data sets, more relaxation is generally predicted at 538°C than at 593°C. The smaller amount of relaxation at 593°C would tend to make linear summation predictions relatively more conservative and strain range partitioning predictions relatively less conservative. This effect can be seen from the values in Tables 3.23 and 3.24.

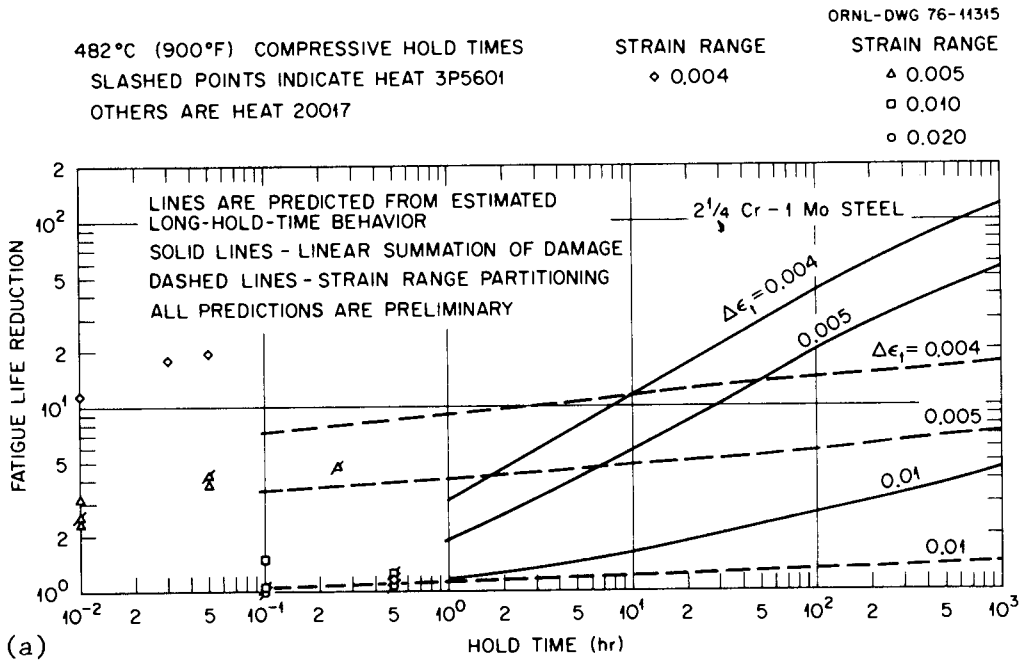


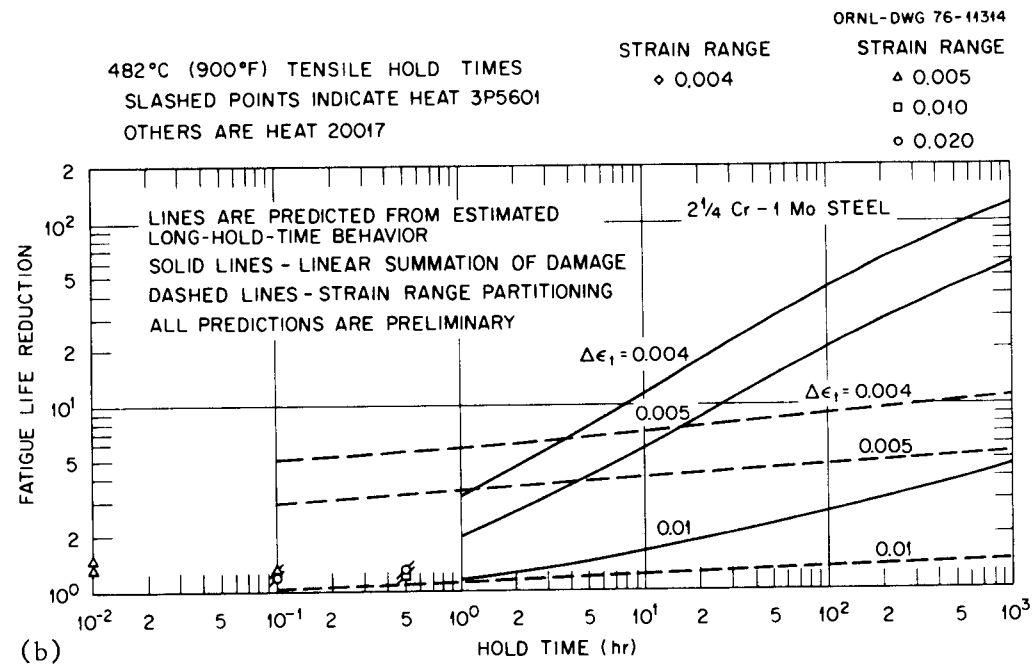


Fig. 3.72. Fatigue Life Reduction Factors, $N_h/N_f$, for 2 1/4 Cr-1 Mo Steel Subjected to (a) Compressive and (b) Tensile Hold Periods at 482°C (900°F).

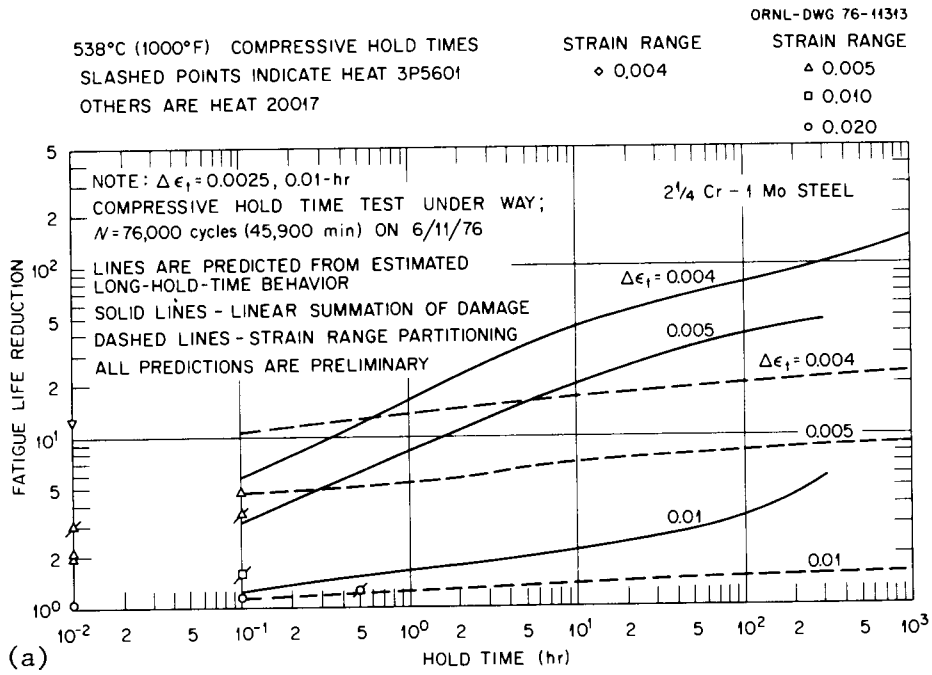


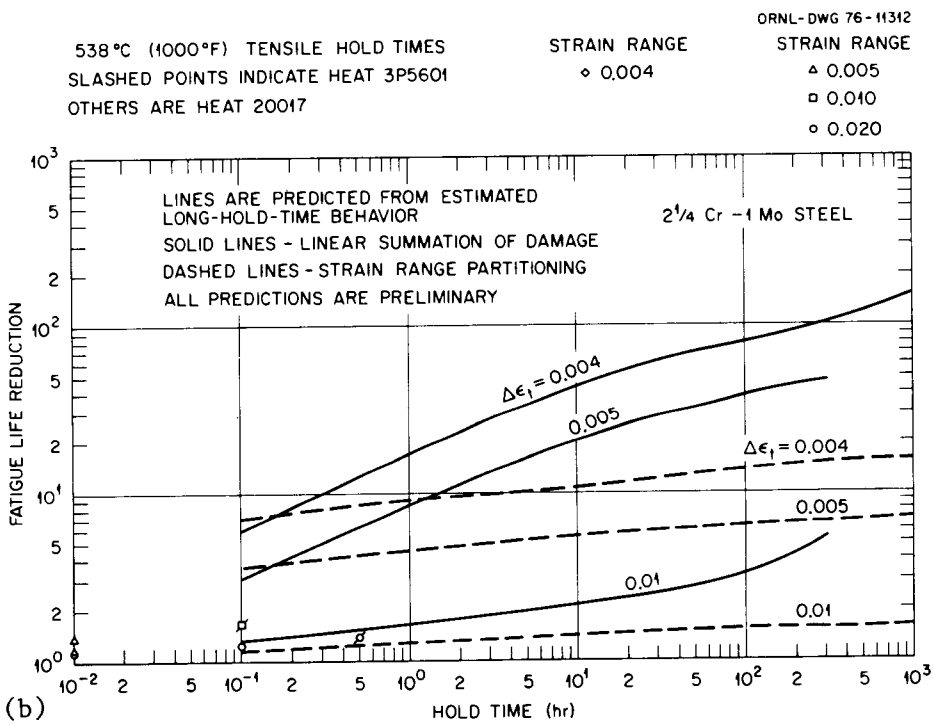


Fig. 3.73. Fatigue Life Reduction Factors, $N_h/N_f$, for 2 1/4 Cr-1 Mo Steel Subjected to (a) Compressive and (b) Tensile Hold Periods at 538°C (1000°F)

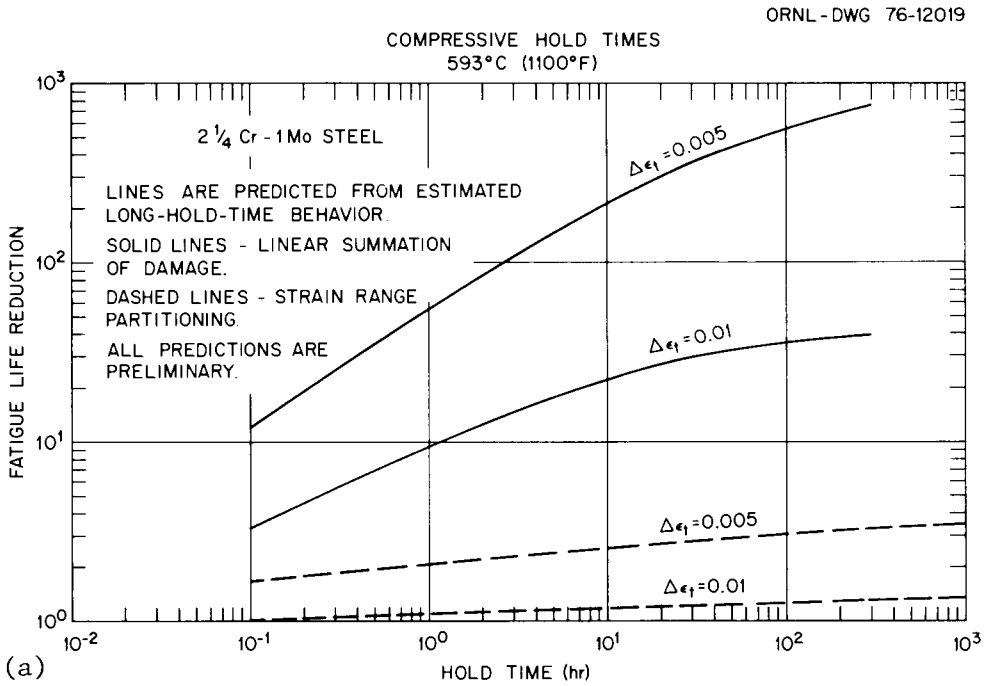


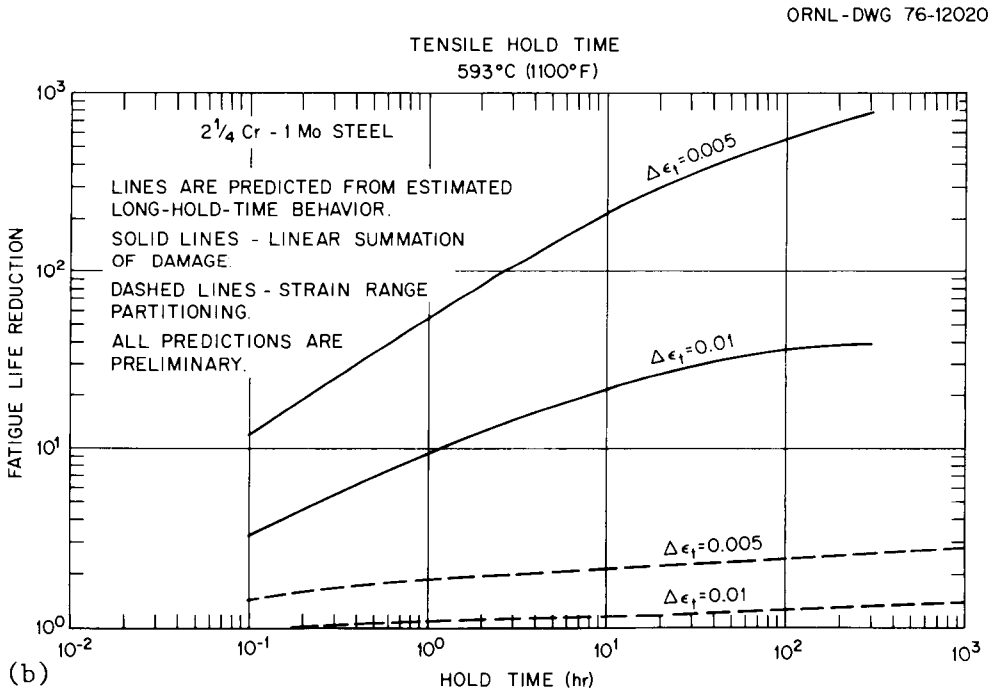


Fig. 3.74. Fatigue Life Reduction Factors, $N_h/N_f$, for 2 1/4 Cr-1 Mo Steel Subjected to (a) Compressive and (b) Tensile Hold Periods at 593°C (1100°F).

Since the above hypothetical predictions cannot be verified by actual experimental data, it is of interest to attempt to predict conservative lower bounds on cyclic life to avoid problems due to possible inaccuracies in the above predictions. One possible way to do this would be to choose a value for $\Delta\sigma$, and then to assume that relaxation proceeds completely to zero stress in compression, yielding the maximum amount of $\Delta\varepsilon_{pc}$ strain ($\Delta\varepsilon_{pc} = \Delta\sigma/2E$). Actually, this approach is equivalent to using Eq. (1) for relaxation, but letting the hold time go to infinity. The choice of $\Delta\sigma$ is still a problem, but we merely chose the value corresponding to $t_h$ = 0.1 hr in Table 3.22, 3.23, or 3.24. This choice was made because (1) that value is known fairly well since actual test data extend that far, and (2) that value is larger than the values for longer hold times and thus yields a greater amount of $\Delta\varepsilon_{pc}$ strain. (Actually predicted lives using $\Delta\sigma$ from $t_h$ = 1000 hr were only a few percent longer than those for $t_h$ = 0.1 hr, so the above choice of $\Delta\sigma$ is not critical.)

Manson[72] has suggested another possible procedure for estimating worst effects due to creep-fatigue interactions. Since $\Delta\varepsilon_{pc}$ is the most damaging of the inelastic strain range components, a lower bound on life could be defined by the predicted life letting all inelastic strain be of $\Delta\varepsilon_{pc}$ type. For a given inelastic strain range, $N_h$ is merely the value of $N_{pc}$ from the strain range partitioning life relationships,[73] here:

$$N_{pc} = (\Delta\varepsilon_{pc}/215)^{-1.10} \tag{9}$$

The remaining problem is to estimate the total amount of inelastic strain corresponding to a given total strain range. We have performed this estimate in two ways.

The more conservative approach is to estimate the amount of inelastic strain, $\Delta\varepsilon_{inel}$, to be expected in an actual test, and then to set $\Delta\varepsilon_{pc}$ equal to this value. In this case it should be noted that

$$\Delta\varepsilon_{pc} = \Delta\varepsilon_{inel} = \Delta\varepsilon_t - (\Delta\sigma' - \Delta\sigma_r')/E \ . \tag{10}$$

Thus, in this case, larger stresses correspond to smaller values of $\Delta\varepsilon_{pc}$, and conservatism requires a small value for $\Delta\sigma' - \Delta\sigma'_r$. We proceeded as follows: first, we choose $\Delta\sigma'$ as the value $(\Delta\sigma - \Delta\sigma_r)$ from a 0.1-hr hold period test. (The subtraction of $\Delta\sigma_r$ was merely an arbitrary safety factor and yields $\Delta\sigma'$ values slightly lower than the $\Delta\sigma$ values from the 1000-hr-hold-time tests. We then assumed the maximum amount of relaxation in a compression hold period (i.e., relaxation to zero). Thus

$$\Delta\sigma'_r = \Delta\sigma'/2$$

and

$$\Delta\varepsilon_{pc} = \Delta\varepsilon_t - \Delta\sigma'/2E \ . \tag{11}$$

Equations (9) and (11) thus allow one to estimate a possible "worst effects" cyclic life for each strain range and temperature. (It should be noted that if the above value of $\Delta\sigma'$ were chosen as $\Delta\sigma$ from the 1000-hr hold tests, estimated worst effects lives became only a few percent longer.)

Since relaxation cannot proceed beyond a zero stress, the maximum possible value for $\Delta\varepsilon_{pc}$ is $\sigma_c/E$, where $\sigma_c$ is the compressive stress amplitude. This maximum value is thus $\Delta\sigma'/2E$ above, for the case of a zero mean stress. The above estimates of $\Delta\varepsilon_{pc}$ are always greater than $\Delta\sigma'/2E$, meaning that they can never occur in a real hysteresis loop unless there is a compressive mean stress. Geometric consideration of a hysteresis with an extended compression hold period indicates that, if anything, a tensile mean stress should develop. Therefore, the above estimates for $\Delta\varepsilon_{pc} = \Delta\varepsilon_{\text{inel}}$ are probably larger than any that might occur in a real situation, which of course means that the above life predictions should be conservative.

Alternatively, we assumed a zero mean stress and set $\Delta\varepsilon_{pc}$ equal to its maximum value of $\Delta\sigma/2E$, so that $\Delta\varepsilon_{pc} = \Delta\varepsilon_{\text{inel}} = \Delta\varepsilon_{\text{el}} = \Delta\varepsilon_t/2$. Such a hysteresis loop is shown in Fig. 3.75.

ORNL-DWG 76-11965

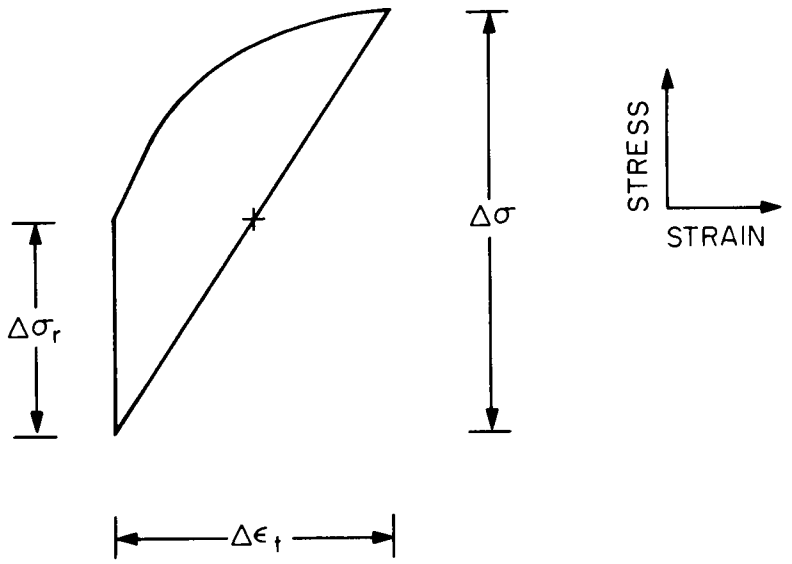


Fig. 3.75. Schematic Hysteresis Loop Illustrating the Basis for Calculation of Worst Effects Curves.

Figure 3.76 compares the two estimates of worst effects curves with the above relaxation to zero stress curves and estimated 1000-hr compression hold period curves with continuous cycling curves at 482, 538, and 593°C. In addition, Fig. 3.77 shows these same predictions for tension hold periods at 538°C. Fig. 3.78 compares the two methods of estimating worst effects curves.

The 1000-hr hold period predictions are quite near the relaxation to zero stress predictions — reflecting the fact that Eq. (1) predicts relaxation to near zero stress in 1000 hr. The two "worst effects" curves are considerably more conservative than the relaxation to zero curves, with those constructed by the first method above appearing overconservative at high strain ranges, since the assumptions upon which they are based are least valid at high strain ranges. It should be noted that the first type of worst effects curves is virtually independent of temperature. The second type is independent of temperature, since the strain range partitioning $\Delta\varepsilon_{pc}$ life relationship is independent of temperature.

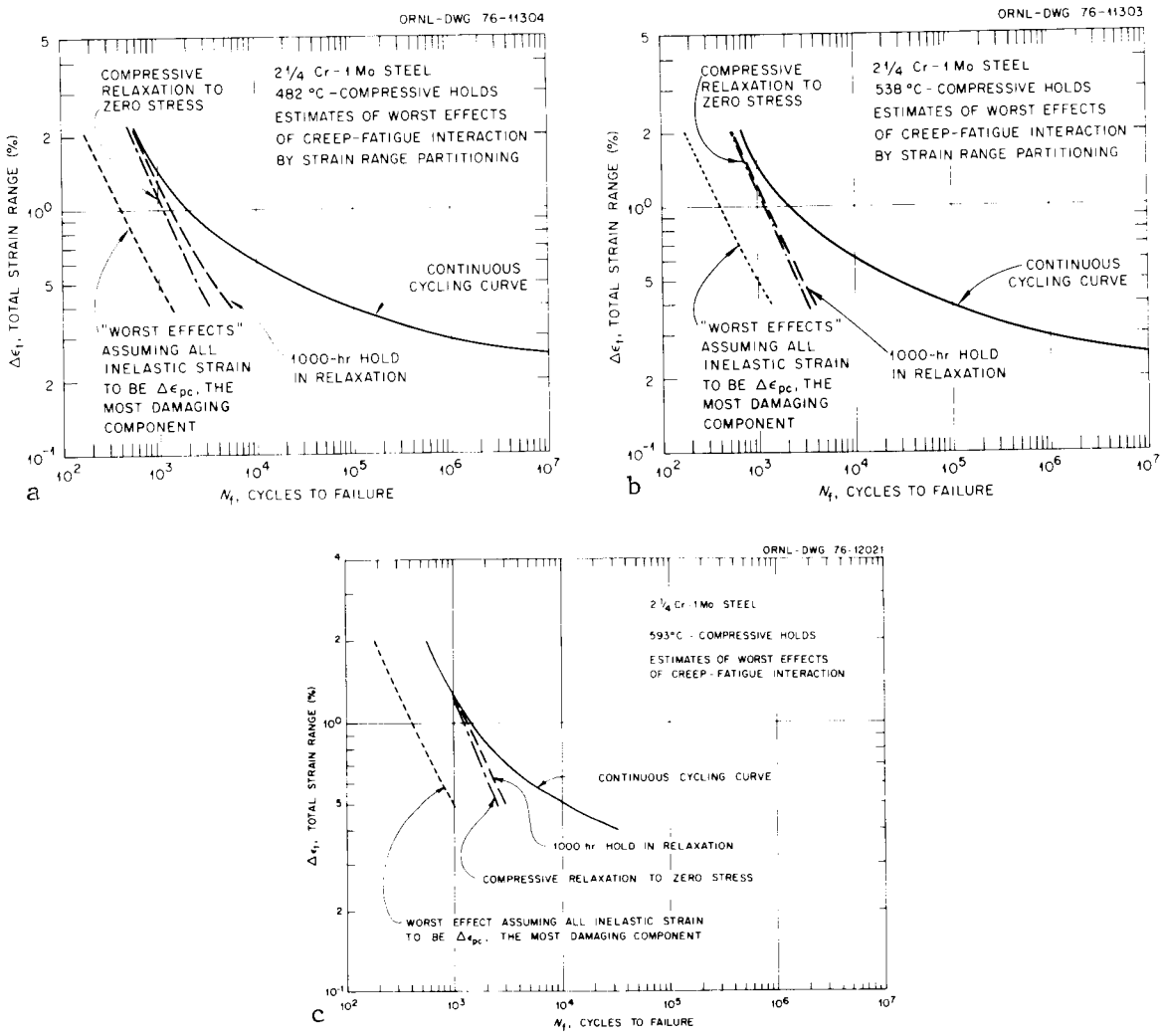


Fig. 3.76. Projected Effects of Long Compression Hold Periods on the Fatigue Life of 2 1/4 Cr-1 Mo Steel at (a) 482°C (900°F), (b) 538°C (1000°F), and (c) 593°C (1100°F).

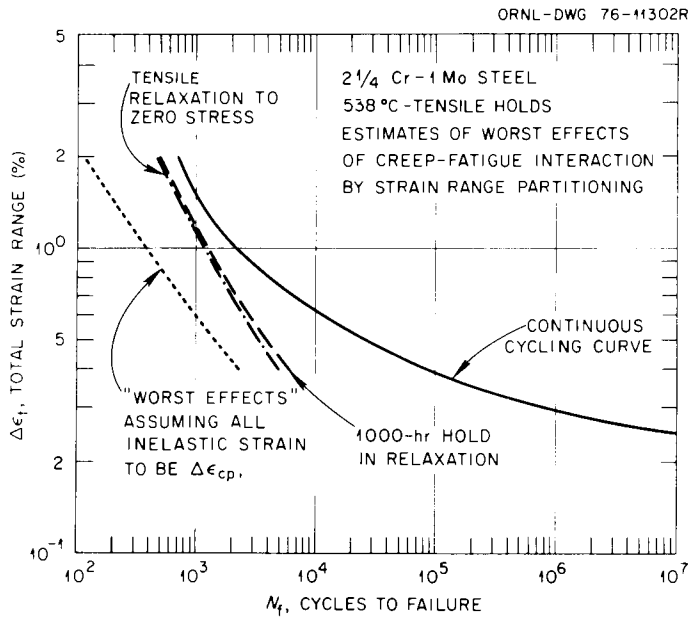


Fig. 3.77. Projected Effects of Long Tension Hold Periods on the Fatigue Life of 2 1/4 Cr-1 Mo Steel at 538°C (1000°F).

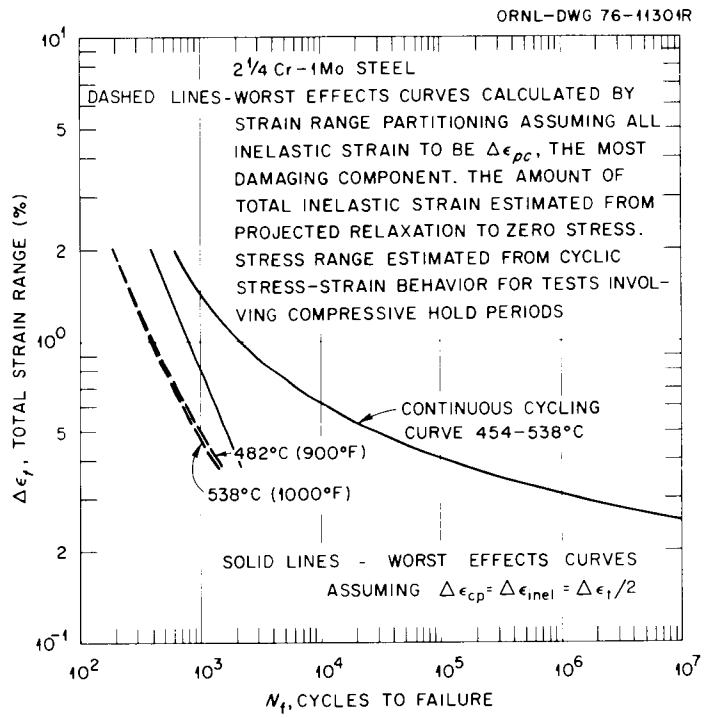


Fig. 3.78. Comparison of Two Methods for Calculating Possible "Worst Effects" Creep-Fatigue Curves for 2 1/4 Cr-1 Mo Steel.

Work is continuing to assess the implications of the above results. The relaxation to zero curves apparently do not represent the worst conceivable situation at low strain ranges. Therefore, the remaining choice is between the two types of worst effects curves. It would appear that the Type II curves are more realistic in terms of actual occurrence. However, scatter and uncertainties in the $\Delta\varepsilon_{pc}$ life relationship mean that the Type II curves may not represent a firm lower bound on life. Still, those curves have several advantages. First, they are independent of temperature, and thus very simple to apply. Second, they merely assume $\Delta\varepsilon_{pc} = \Delta\varepsilon_t/2$ and do not rely on estimates of long-hold-time cyclic stress-strain and relaxation behavior. Work is continuing to assess the possible effects of errors in the estimates of $\Delta\sigma$, $C$, and $m$ on the other predictions. Also, all results will be extended to lower strain ranges when currently planned low-strain cyclic relaxation tests are completed.

3.4.4.2 Creep-Fatigue Data Analysis — M. K. Booker

Interim results of our analyses of creep-fatigue data for 2 1/4 Cr-1 Mo steel have been presented in several previous reports.[74-76] This quarter we present updated results obtained thus far by the methods of strain range partitioning[73] and the linear summation of creep and fatigue damage.[77]

The strain range partitioning approach involves partitioning the plastic strain range traversed by a cycling specimen into four types:

$\Delta\varepsilon_{pp}$ = tensile plastic strain reversed by compressive plastic strain,

$\Delta\varepsilon_{cc}$ = tensile creep strain reversed by compressive creep strain,

$\Delta\varepsilon_{cp}$ = tensile creep strain reversed by compressive plastic strain,

$\Delta\varepsilon_{pc}$ = tensile plastic strain reversed by compressive creep strain.

Here, "plastic" strain is defined as time-dependent inelastic strain, while "creep" strain is defined as time-dependent inelastic strain. Figure 3.79 illustrates the "life relationships" determined for these four types of strain, whereby $\Delta\varepsilon_{pp}$, $\Delta\varepsilon_{cp}$, $\Delta\varepsilon_{pc}$, and $\Delta\varepsilon_{cc}$ are related respectively to $N_{pp}$, $N_{cp}$, $N_{pc}$, and $N_{cc}$, where $N_i$ is the expected cycle life of a specimen cycled in pure $\Delta\varepsilon_i$ strain. Shown in the figure are the lines previously determined by Manson et al.,[73] compared with data from the current ORNL program and from the program at General Atomics Corporation.[69] The scatter in the ORNL and GA data is caused partially by the fact that in all cases the creep strain component ($\Delta\varepsilon_{cp}$, $\Delta\varepsilon_{pc}$, $\Delta\varepsilon_{cc}$) was small in comparison with the total plastic strain range.

It should be noted that both the lines and points in Fig. 3.79 were calculated by the linear damage rule, given by

$$\frac{1}{N_{cp}} + \frac{1}{N_{pc}} + \frac{1}{N_{cc}} + \frac{1}{N_{pp}} = \frac{1}{N} . \tag{1}$$

Ellis et al.[69] report somewhat unsatisfactory results in the analysis of their data using the above rule, being able to predict the cylic life only within a factor of 3. Moreover, their analysis generally overestimated the cyclic lives. Figure 3.80 shows results of analysis of the ORNL data using the life relationships of Fig. 3.79 and the interaction damage rule, given by

$$\frac{F_{cp}}{N_{cp}} + \frac{F_{pc}}{N_{pc}} + \frac{F_{cc}}{N_{cc}} + \frac{F_{pp}}{N_{pp}} = \frac{1}{N} , \tag{2}$$

where, for example, $F_{cp} = \Delta\varepsilon_{cp}/\Delta\varepsilon_{inel}$, $\Delta\varepsilon_{inel}$ being the total inelastic strain range. Results of our analysis of the GA data were reported previously,[68] the margin of error being an acceptable factor of 2 (Fig. 3.81).

The reason for the improvement of our results over those of Ellis et al.[69] can be seen in Fig. 3.82. Comparing Figs. 3.79(d) and 3.82(a), it is clear that the life relationship line used for $\Delta\varepsilon_{cp}$ strain describes the current data significantly better in terms of the interaction

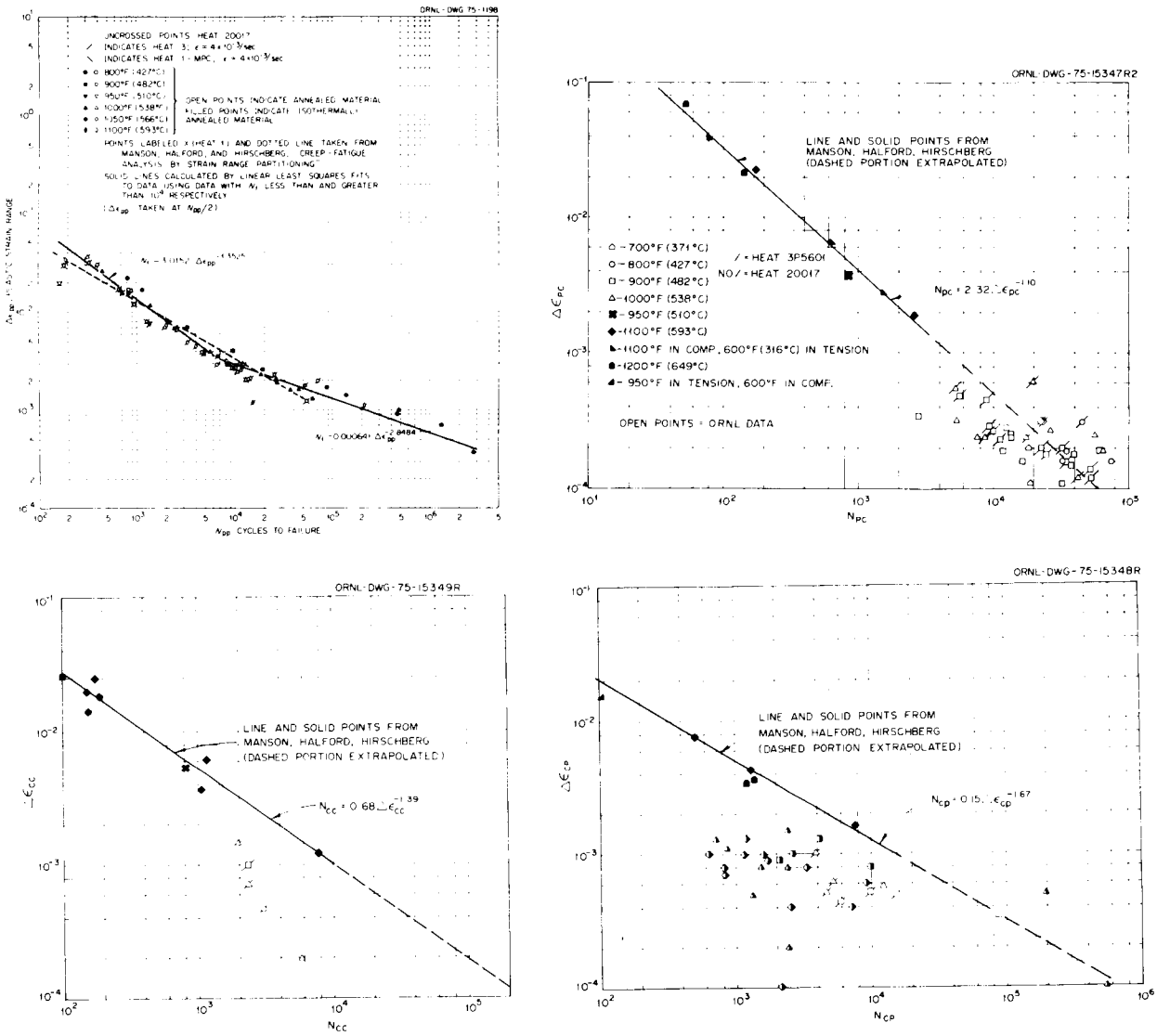


Fig. 3.79. Partitioned Life Relationships for 2 1/4 Cr-1 Mo Steel by the Method of Linear Damage Summation in the Strain Range Partitioning Approach.

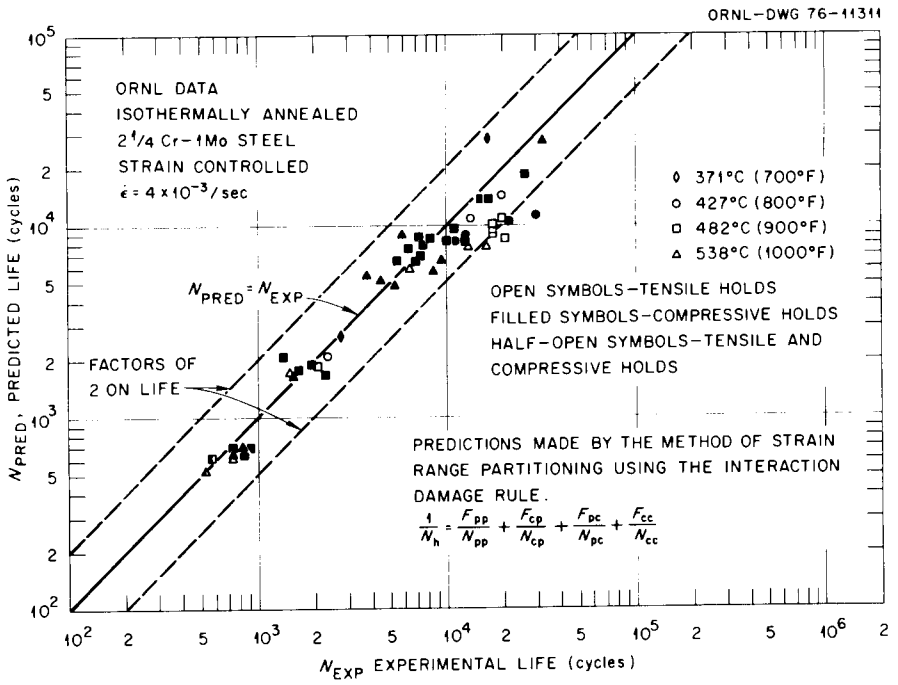


Fig. 3.80. Results of Analysis of ORNL Creep-Fatigue Data for 2 1/4 Cr-1 Mo Steel by the Method of Interaction Damage Summation in the Strain Range Partitioning Approach.

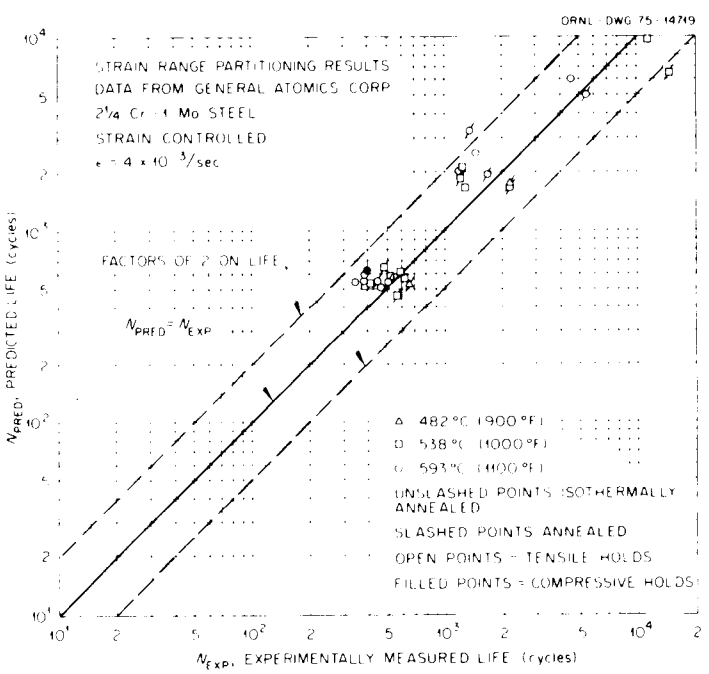


Fig. 3.81. Results of Analysis of GA Creep-Fatigue Data for 2 1/4 Cr-1 Mo Steel by the Method of Interaction Damage Summation in the Strain Range Partitioning Approach.

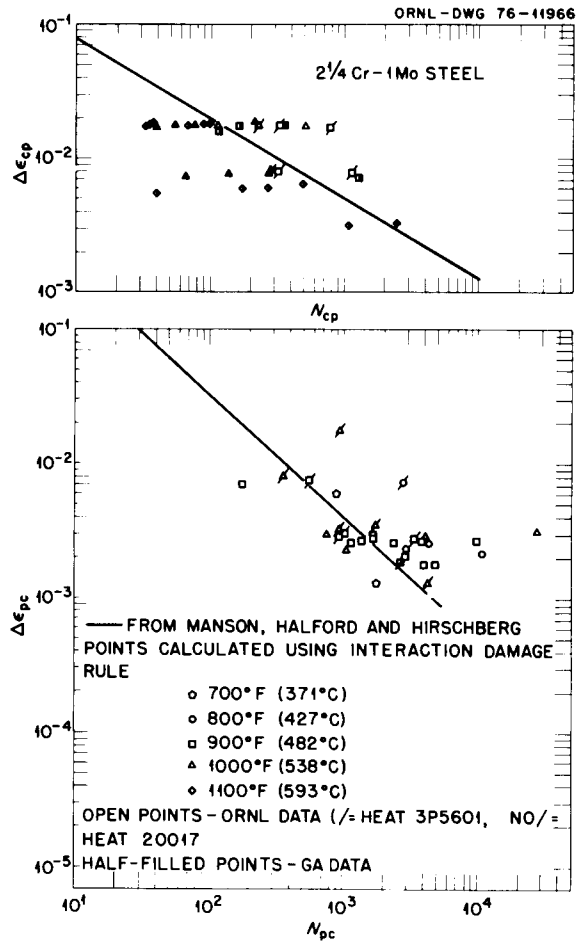


Fig. 3.82. Partitioned *cp* and *pc* Life Relationships for 2 1/4 Cr-1 Mo Steel by the Method of Interaction Damage Summation in the Strain Range Partitioning Approach.

damage rule [Eq. (2)] than in terms of the linear damage rule. On the other hand, data for tests with compressive hold periods seem about equally well-described by either summation procedure. We have used the interaction rule for life predictions in all cases, since most recent results appear to favor that procedure.[78]

A popular method for the analysis of creep-fatigue data in the past has been the method of linear summation of creep and fatigue damage.[77] This method involves numerical integration of a typical relaxation curve during a hold period to calculate the creep damage per cycle as

$$D_c(1) = \int_0^{t_h} dt/t_r \ , \tag{3}$$

where $t_h$ is the total hold time and $t_r$ is the rupture life. The total creep damage is then

$$D_c = N_h D_c(1) \ , \tag{4}$$

where $N_h$ is the total number of cycles to failure in the given hold-time test.

The fatigue damage is given by

$$D_F = N_h/N_f \ , \tag{5}$$

where $N_f$ is the number of cycles to failure that would have been expected with no hold time. Then, the total damage is given by

$$D = D_c + D_F \ . \tag{6}$$

Figures 3.83 through 3.86 show the results of calculations from Eq. (6) for the currently available data. The smaller data points in the figures were calculated by use of expected values of $t_r$ and $N_f$. The larger symbols indicate calculations made by use of lower limit values on $t_r$ and $N_h$ (i.e., $t_m$ and $N_d$). Thus,

$$D_c^{\ d} + D_F^{\ d} = D_d \ , \tag{7}$$

where $D_c^{\ d}$ and $D_F^{\ d}$ are the values of creep and fatigue damage calculated from $t_m$ and $N_d$. In these figures, values of $N_f$ were estimated from continuous cycling data[69,79] for these same heats of material, while $t_r$ at each stress was calculated from a previously published[80] equation for that property.

Values of $N_d$ were obtained from the ORNL fatigue design curves for this material,[79] while calculation of $t_m$ is somewhat more complicated. Current creep fatigue design rules[81] specify that

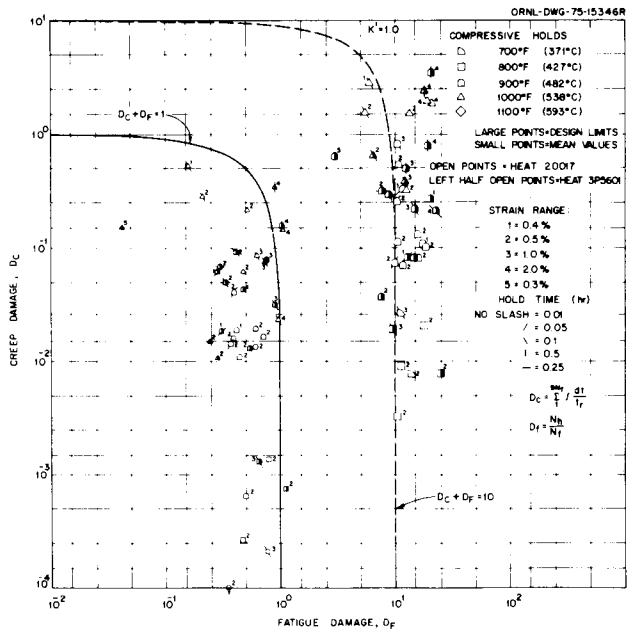


Fig. 3.83. Creep and Fatigue Damage Calculations for 2 1/4 Cr-1 Mo Steel for Use in the Linear Summation of Damage Approach. Data for Tests with Hold Periods at Peak Compressive Strain. $K' = 1.0$.

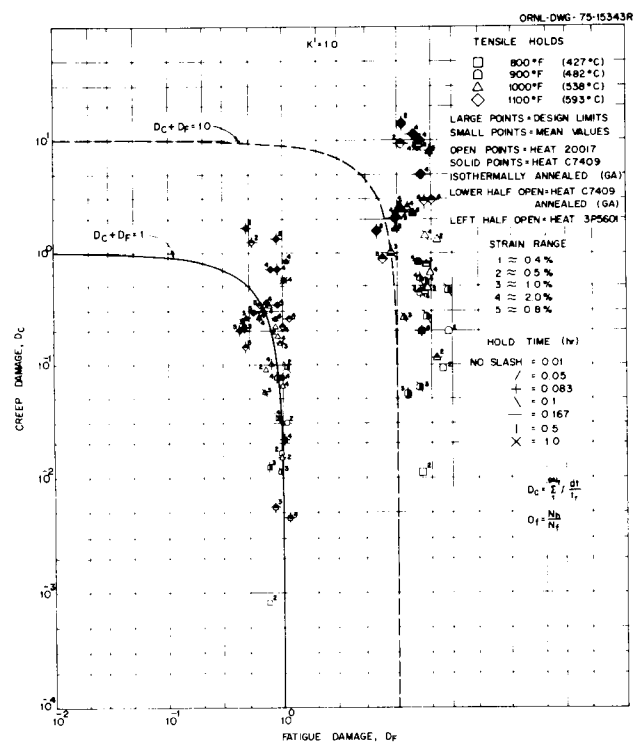


Fig. 3.84. Creep and Fatigue Damage Calculations for 2 1/4 Cr-1 Mo Steel for Use in the Linear Summation of Damage Approach. Data for Tests with Hold Periods at Peak Tensile Strain. $K' = 1.0$.

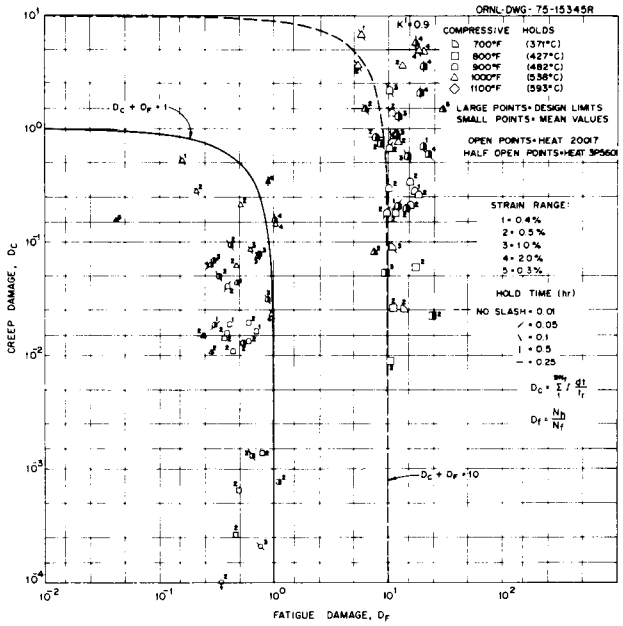


Fig. 3.85. Creep and Fatigue Damage Calculations for 2 1/4 Cr-1 Mo Steel for Use in the Linear Summation of Damage Approach. Data for Tests with Hold Periods at Peak Compressive Strain. $K' = 0.9$.

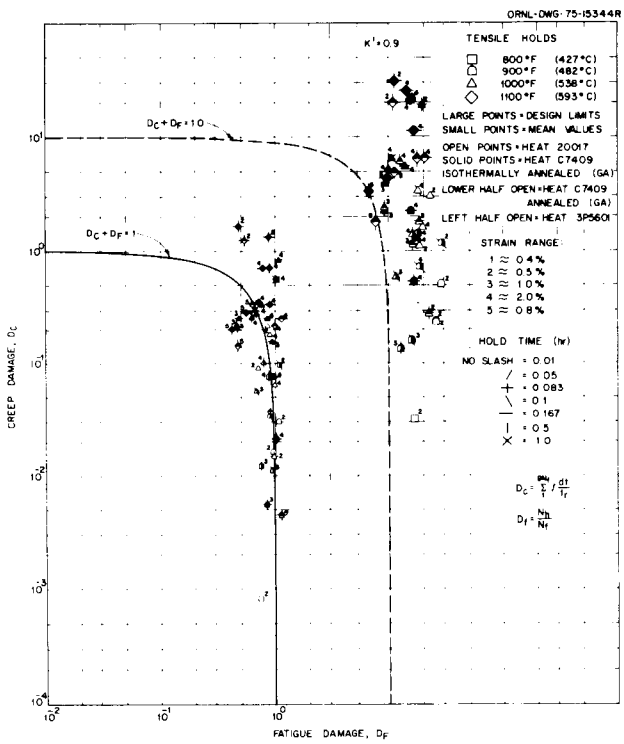


Fig. 3.86. Creep and Fatigue Damage Calculations for 2 1/4 Cr-1 Mo Steel for Use in the Linear Summation of Damage Approach. Data for Tests with Hold Periods at Peak Tensile Strain. $K' = 0.9$.

$$\sum_{j=1}^{P} (n/N_D)_j + \sum_{k=1}^{g} (t/t_m)_k \leq D^* , \tag{8}$$

where

$D^*$ = some specified "damage factor" (currently undefined for 2 1/4 Cr-1 Mo steel),

$n$ = the number of cycles applied under loading condition $j$,

$N_D$ = the number of design allowable cycles under loading condition $j$,

$t$ = time duration of loading condition $k$,

$t_m$ = allowable time under loading condition $k$.

The value of $t_m$ is calculated as the lower limit time to rupture at the temperature of interest under a stress given by the stress from load $k$ divided by factor $K'$, which is defined as 0.9 for austenitic stainless steels and for Incoloy Alloy 800H.

Based on the minimum stress-rupture curves for 2 1/4 Cr-1 Mo steel,[80] the following equation was used for $t_m$:

$$\log t_m = 566 \{46.263 - 0.4194 \ln(\sigma/K') - 0.4589 [\ln(\sigma/K')]^2\}/T - 20 \tag{9}$$

where

$t_m$ = allowable time under loading condition $k$.

$\sigma$ = stress (MPa),

$T$ = temperature (K).

The values shown in Figs. 3.83 and 3.84 were calculated by use of $K' = 1.0$, while the values in Figs. 3.85 and 3.86 were obtained by use of $K' = 0.9$. Figure 3.87 shows the effect of $K'$ on the minimum stress rupture curves, with $K' = 0.9$ yielding values of $t_m$ roughly half those for $K' = 1.0$, thus approximately doubling the value of $D_c^d$ above.

It should be noted that the values in Figs. 3.83 through 3.86 were actually calculated from

$$D_c = 0.9 N_h D_c(1) \tag{10}$$

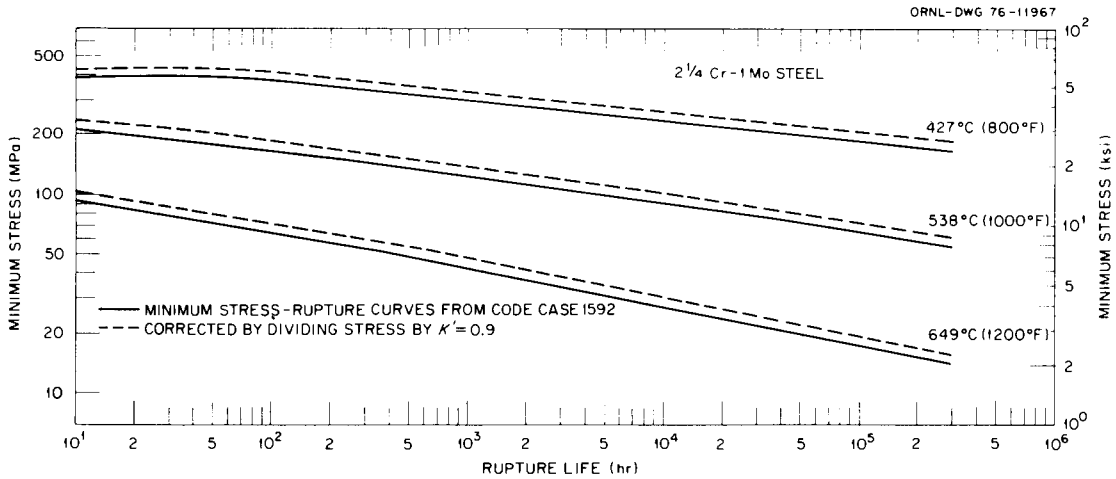


Fig. 3.87. Effect of Using $K' = 0.9$ on Minimum Stress Rupture Curves for 2 1/4 Cr-1 Mo Steel from ASME Code Case 1592.

rather than from Eq. (4). This procedure was based on an estimate that the stress range required to maintain the imposed strain range drops to about 95% of its half-life value at about nine-tenths of the cyclic life. After this point, a sizable crack may exist in the test specimen. However, this correction was found to be a very minor one, and in subsequent life predictions, we used Eq. (4) for simplicity.

Assuming a value of $D = 1$ in Eq. (6), cyclic lives can be predicted by

$$N_h = (1 - D_c)/N_f \ . \tag{11}$$

Figure 3.88 shows the results obtained for the current data by use of this equation. Clearly, the cyclic lives are predicted quite well for the tests involving tension hold periods. However, for this material compressive hold periods are generally more damaging than tension hold periods, especially at low strain ranges. Since the only creep-rupture data available were from tensile creep tests, calculated $t_r$ was in all cases based on these tensile creep-rupture properties. Figure 3.88 shows that the cyclic lives for low-strain-range (long-life) tests involving compression hold periods are generally overestimated at temperatures of 482 to 538°C (900–1000°F).

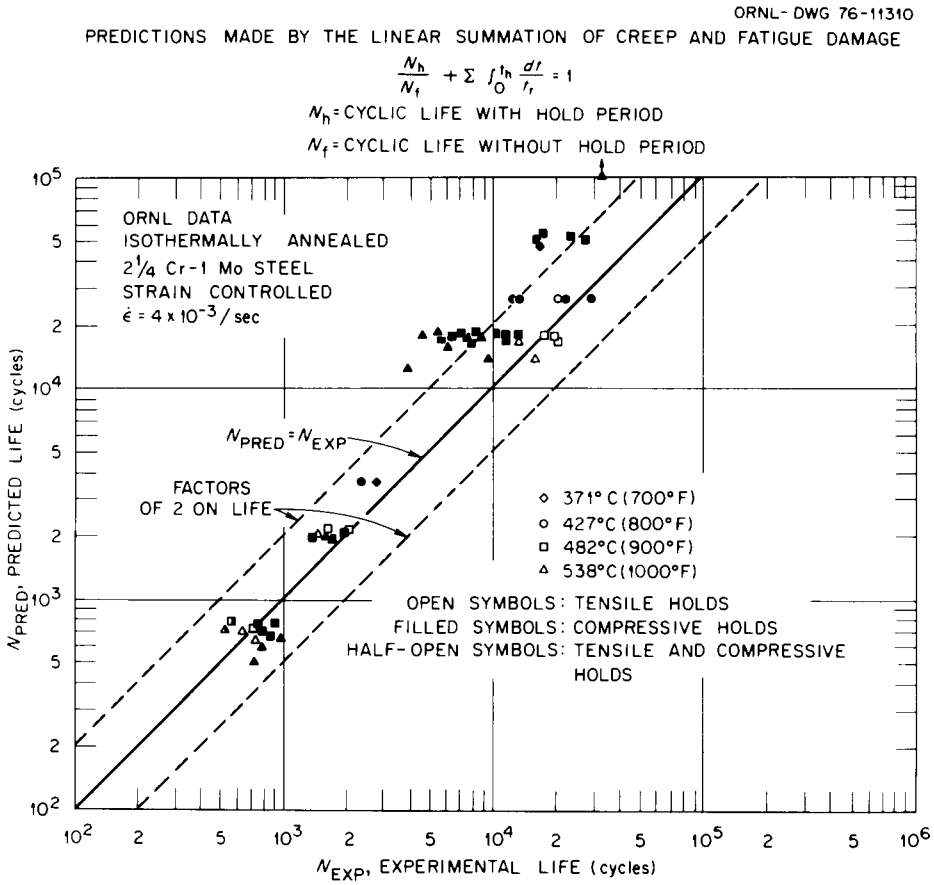


Fig. 3.88. Results of Life Predictions for Creep-Fatigue Tests of 2 1/4 Cr-1 Mo Steel Using the Linear Summation of Damage Approach.

Two possible corrections can be conveniently applied to Eq. (11) to increase the accuracy of the life predictions for compression hold tests. First, the value of the summation of damage can be changed to some number smaller than unity. However, such a correction is probably not warranted. The problem appears to be mainly the inadequacy of predicting compressive creep damage from tensile creep behavior. Thus, a more direct approach would be to attempt to correct $D_c$ to a more realistic value. The simplest way to do this is to correct $D_c$ by some factor β, changing the damage summation equation to

$$D_f + \beta D_c = 1 \ , \tag{12}$$

so that the predicted life is given by

$$N_h = (1 - \beta D_c)/N_f \ . \tag{13}$$

For each of the available compression hold tests in the range 482–538°C from the ORNL program, values of β were calculated from the experimental values of $N_h$ according to

$$\beta = (1 - D_F)/D_c \ . \tag{14}$$

Various relationships were attempted to quantify variations in the values thus obtained for β. The most successful correlation found is illustrated in Fig. 3.89, where β is shown to be approximately given by

$$\beta = 0.22 D_c^{-1.24} \ . \tag{15}$$

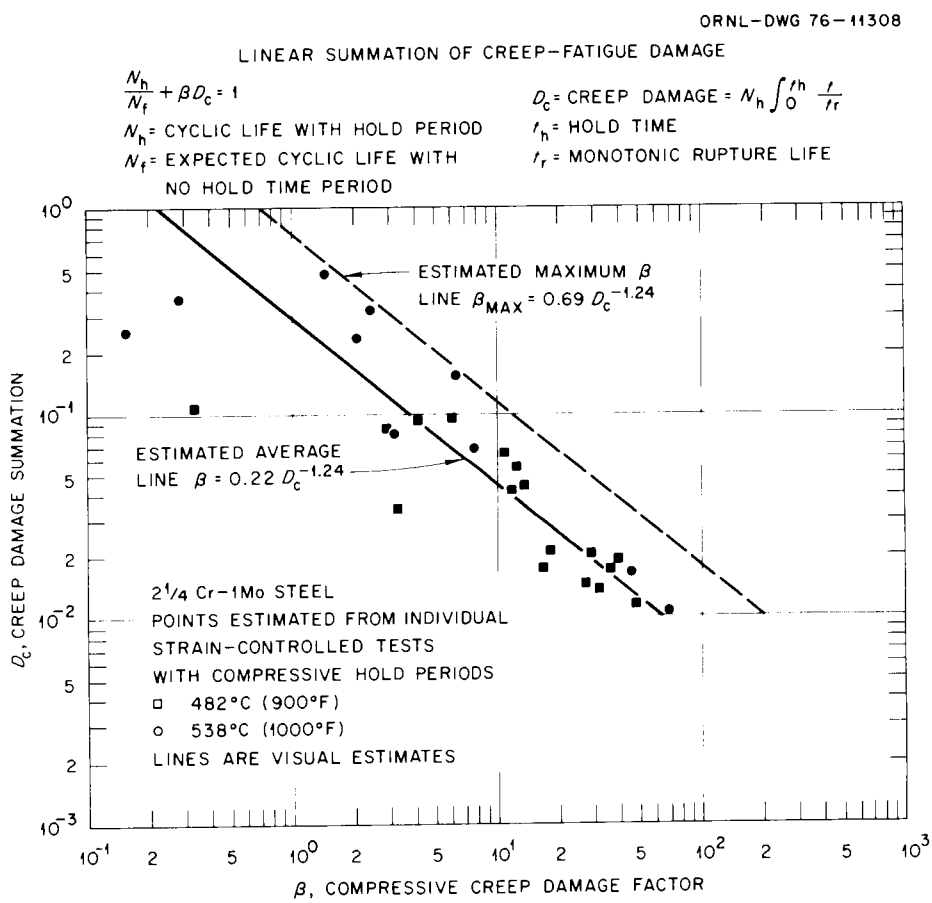


Fig. 3.89. Compressive Creep Correction Factor, β, as a Function of Creep Damage Sum, $D_c$, for Use in the Linear Summation of Damage Approach.

Clearly, the scatter in Fig. 3.89 is large, although a value of $\beta = 0.69D_c^{-1.24}$ could be used as a conservative upper limit for the current data.

Figure 3.90 shows the results of life predictions made using Eq. (13) with β estimated by Eq. (15). For completeness, predictions are shown for all ORNL tests, although only compression tests in the range 482 to 538°C were predicted with the β factor.

In terms of fits to data, the method of strain range partitioning clearly provides the best results of the three methods presented above. The coefficients of determination ($R^2$) given in Table 3.25 show that the β correction significantly improved the fit obtained from the linear summation of damage approach, as is obvious from Figs. 3.88 and 3.90. However, the strain range partitioning predictions are much better still.

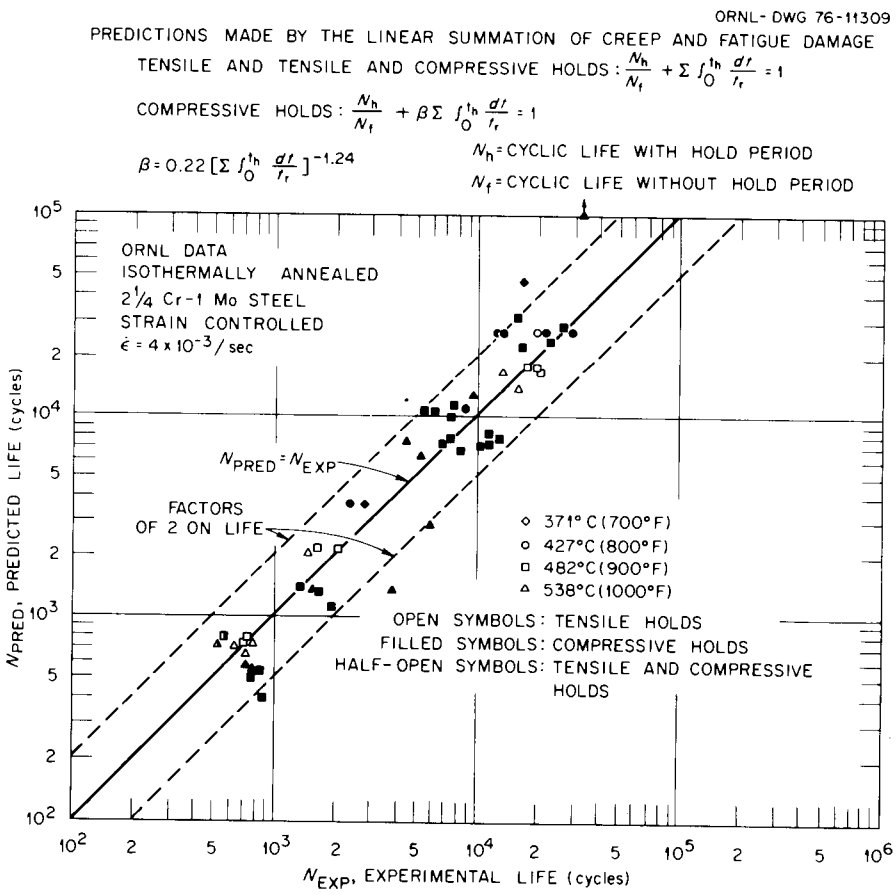


Fig. 3.90. Results of Life Predictions for Creep-Fatigue Tests of 2 1/4 Cr-1 Mo Steel Using the Linear Summation of Damage Approach with Compressive Creep Damage Modified by the β Factor from Fig. 3.89.

Table 3.25. Fits to ORNL Creep-Fatigue Data Using Strain Range Partitioning and Linear Summation of Damage

| Method | $R^2$,[a] Coefficient of Determination, % | |
|---|---|---|
| | Compression Hold Data (39 tests) | All Data (56 tests) |
| Strain Range Partitioning[b] | 92.8% | 91.7% |
| Linear Summation[c] | 41.1% | 67.8% |
| Modified Linear Summation[d] | 63.2% | 79.6% |

[a]The value of $R^2$ represents the percentage of variations in the data that are described by the model.

[b]Using the Interaction Damage Rule.

[c]Using $D_F + D_c = 1$.

[d]Using $D_F + \beta D_c = 1$.

The strain range partitioning technique is thus seen to have several distinct advantages in describing the creep-fatigue behavior of this material. These include: (1) good general fit to the available short-term test data; (2) ability to reflect the larger damage due to compressive vs tensile hold periods at low strain ranges; (3) simplicity in application once the life relationships are determined (at least in uniaxial situations); (4) apparent temperature-independence of life relationships; and (5) ability to construct possible "worst effects" curves, as was discussed in Sect. 3.4.4.1.

However, several uncertainties still remain. For instance, we assumed all inelastic strain during continuous cycling at $4 \times 10^{-3}$/sec to be of the $\Delta\varepsilon_{pp}$ type. Little information is available at higher strain rates, so it is not possible to fully verify that no significant creep component arises during cycling at this strain rate. Also, in a test with a tensile hold period at peak strain, for example, the amount of $\Delta\varepsilon_{cp}$ strain was calculated by $\Delta\varepsilon_{cp} = \Delta\sigma_r/E$, where $E$ is Young's modulus and $\Delta\sigma_r$ is the total change in stress during the hold period.

However, we have seen some evidence that at the beginning of a hold period, the stress undergoes a sudden rapid decrease, followed by a period of more gradual relaxation. Diercks[82] has attributed a similar decrease for type 304 stainless steel to a strain rate effect caused

by a sudden change from the ramp strain rate to the zero strain rate of the hold period, and has thus suggested that the strain corresponding to this initial stress drop be considered plastic rather than creep strain. Interestingly, the fact remains that even with the above simplifications, the method fits our data quite well. The above effects need to be considered, however.

Uncertainties that need to be resolved concerning the strain range partitioning technique in general include the following.

1. The method has no explicit method for dealing with strain rate effects and therefore may not fully account for these effects. Preliminary results from the method recently developed by Majumdar[83] indicate that strain rate plays an extremely important role in determining the damage caused by a given amount of inelastic strain.

2. The method assumes that the damage caused by hold periods is due totally to creep effects, and does not account for environmental effects or for the effects of metallurgical processes such as strain aging. Recent results reported by James[84] show that crack growth studies indicate that the effects of environmental interactions can be a prime cause of damage during hold periods.

3. The life relationships for 2 1/4 Cr-1 Mo steel are yet to be fully verified. Influences due to temperature, heat-to-heat variations, melting practice, etc. need to be determined. In addition, limits of extrapolation of the relationships and their linearity in log-log coordinates need to be verified. Also, the current relations were derived from the linear damage rule, although they seem consistent with our results from the interaction rule over a limited range.

4. Additional long-term complex-wave-form tests are required for full verification.

The relatively poor fits to the data by the linear summation of damage approach raise the question of whether the creep-fatigue rules[81] in current use for austenitic materials are applicable to 2 1/4 Cr-1 Mo steel. Figures 3.83 through 3.86 indicate that the value of $D_d$ from Eq. (7) is well above unity in all cases, typically being 10 or greater. However, for low-strain-range compression hold tests, the factor of

safety can be considerably reduced. The worst situation occurs in the case of specimen MIL-46, which was tested with 0.01-hr hold periods at peak compressive strain at a strain range of 0.3% at 538°C. The predicted damage summation using average properties was only 0.194 for this test. The design value using $K' = 1.0$ was 3.625, and using $K' = 0.9$ was 4.439. If one applies a conservative value of $\beta$ from $\beta = 0.69D_c^{-1.24}$ (where $D_c$ is obtained from average properties) the damage sum becomes 13.32 with $K' = 0.9$ or 7.51 with $K' = 1.0$. Thus, it appears that conservative results can be obtained by using the current procedure with $K' = 0.9$, if $D^*$ from Eq. (8) is unity and if compression hold tests are corrected using $\beta = 0.69D_c^{-1.24}$, where $D_c$ is given from Eq. (4).

### 3.4.5 Mechanical Properties Correlations for 2 1/4 Cr-1 Mo Steel — Uniaxial Stress Relaxation of 2 1/4 Cr-1 Mo Steel — M. K. Booker and R. W. Swindeman

From comparisons with limited experimental data for a single heat of isothermally annealed, air-melted plate of 2 1/4 Cr-1 Mo steel, it appears that isothermal, uniaxial relaxation behavior can be estimated from creep behavior by use of the hypothesis of strain hardening. Resonable productions were obtained using strain hardening in conjunction with the creep equation for this material, described by Booker et al.,[80] although this approach tended to overestimate the amount of relaxation at lower temperatures (≤ about 538°C) and higher stresses (> yield strength).

#### 3.4.5.1 Creep Data

For a discussion of the creep data upon which the creep equation for the material was based, see ref. 80. The data consisted of 37 tests from 5 different heats of material meeting the following restrictions:
room-temperature ultimate tensile strength — 483–517 MPa (70–75 ksi);
room-temperature (0.2% offset) yield strength — ≥207 MPa (30 ksi);
carbon content — 0.07–0.15 wt %;
chromium content — 2.0–2.5 wt %;
molybdenum content — 0.9–1.1 wt %.

Except for the narrower restrictions on tensile strength, these restrictions are given in the *Nuclear Systems Materials Handbook*. The minimum carbon content of 0.07 wt % is in accordance with ASME Sect. III for components in service above 371°C (700°F). The other restrictions are contained in ASME specifications SA-336-F22A and SA-387-22-Cl I. The equation was developed from data for annealed material from tube-pipe, bar, and plate stock. As far as can be determined, all material was air melted.

3.4.5.2 Relaxation Data

Predictions of relaxation behavior were compared with experimental relaxation data for a single heat of annealed air-melted material. This heat was one of the five used in developing the creep equation. The material had the following composition: 0.11% C, 0.55% Mn, 0.29% Si, 2.13% Cr, 0.9% Mo, 0.014% S, and 0.11% P. Bar specimens having a 6-mm-diam by 32-mm-long reduced section were machined from 25-mm-thick plate after annealing at 927°C and furnace cooling. The microstructure consisted of proeutectoid ferrite with about 5% pearlite and 1% bainite. Tests were performed in an electrohydraulic machine, using servocontrol based on the feedback signal from an extensometer attached to the specimen shoulders. Test temperatures included 450, 482, 510, 538, and 566°C (842, 900, 950, 1000, and 1050°F). At each temperature a specimen was tested for approximately 100 hr (run 1), then reloaded to higher strains for subsequent testing (run 2, etc.). In addition, a series of single loading tests extending to 1000 hr at various strain levels at 510°C was available. Most of the data are shown in Sect. 3.4.5.4.

3.4.5.3 Analytical Procedure

Currently recommended interim design rules[70] suggest that relaxation behavior for 2 1/4 Cr-1 Mo steel be estimated from creep behavior in conjunction with the hypothesis of strain hardening. Some results, however, indicate that strain hardening may not be an adequate representation of the variable load behavior of this material.[70,85] For this reason, the strain hardening approach must currently be regarded as interim.

Basically, the strain hardening approach involves the hypothesis that the instantaneous creep rate, $\dot{e}_c$, is uniquely determined by the instantaneous stress, temperature, and accumulated creep strain,

$$\dot{e}_c = \dot{e}_c(\sigma, T, e_c) \ .$$

Booker et al.[80] recommend an equation for creep strain ($e_c$) as a function of time ($t$), stress, and temperature of the form:

$$e_c = \frac{t}{a + bt} + \dot{e}_m t \ , \tag{1}$$

where $a$, $b$, and $\dot{e}_m$ are given by

$$\log a = 12.26 - 3.348 \times 10^{-6} T^2 + 9.353 \times 10^{-4} \sigma^2 - 1.167 \times 10^{-4} T\sigma \ , \tag{2}$$

$$\log b = -52.19 + 0.0868T - 3.368 \times 10^{-5} T^2 - 1.152 \ (\log \sigma)^2 \ , \tag{3}$$

$$\log \dot{e}_m = -30.04 + 0.015167T + 2.001 \times 10^{-3} T(\log \sigma)^2 \ , \tag{4}$$

where

$T$ = temperature, °R;
$0.556T - 273$ = temperature, °C
$\sigma$ = stress, ksi
$6.895\sigma$ = stress, MPa.

Equations (1) through (4) are valid for stresses of from 7 to 448 MPa (1–65 ksi) from 371 to 593°C (760–1100°F), except that below 438°C (820°F), values of $b$ are given by the value at that temperature.

Equation (1) can be solved for time as a function of creep strain to yield

$$t = \frac{be_c - a\dot{e}_m - 1 + \sqrt{(a\dot{e}_m + 1 - be_c)^2 + 4ae_c b\dot{e}_m}}{2b\dot{e}_m} \ . \tag{5}$$

With Eq. (5) one can use Eq. (1) to predict relaxation behavior via the hypothesis of strain hardening.

The exact procedure used to calculate relaxation behavior was as follows:

First, divide the stresses traversed into small intervals (we used 0.5 MPa = 0.072 ksi), then assume that relaxation occurs as a stepwise process through these intervals downward from the initial stress, as shown schematically in Fig. 3.91.

The stress decrease of 0.5 MPa corresponds to a decrease in elastic strain of $100(0.5/E)$, where $E$ is the static Young's modulus (MPa) as given in ASME Code Case 1592 approximately equal to:[86]

$$E = 6895(30.69 - 0.02169T + 7.492 \times 10^{-5}T^2 - 1.170 \times 10^{-7}T^3) \quad (T = {}^\circ\mathrm{C}) \ . \quad (6)$$

Thus, it is assumed that the stress remains at each level for a time period long enough to allow a creep strain of $100(0.5/E)$. If $\Delta\varepsilon$ is the total accumulated creep strain at the beginning of a given stress level, then $\Delta\varepsilon + 100(0.5/E)$ is accumulated creep strain at the end of

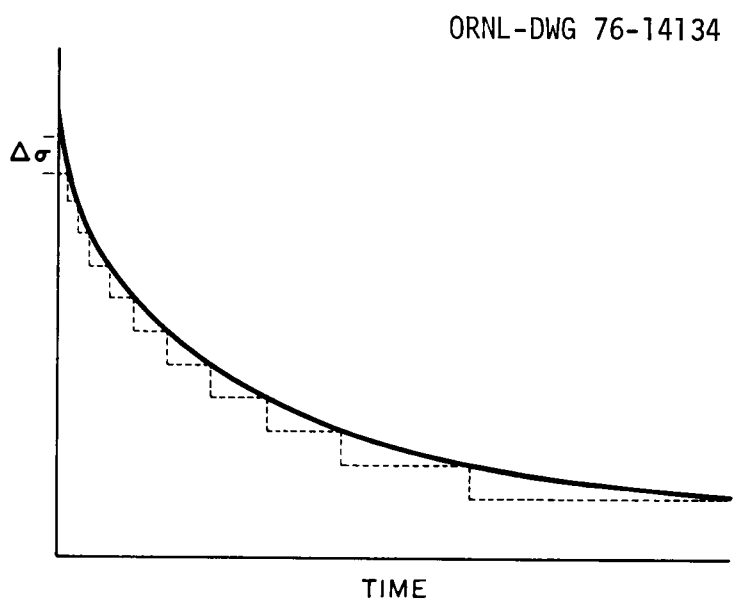


Fig. 3.91. Schematic Illustration of a Relaxation Curve as Approximated in the Numerical Calculation of Relaxation from the Creep Equation Using the Hypothesis of Strain Hardening.

a given stress level. Thus, the time spent at that stress level is $t[\Delta\varepsilon + 100(0.5/E)] - t(\Delta\varepsilon)$, where $t$ is given by Eq. (5) above and where $a$, $b$, and $\dot{e}_m$ are defined at the current stress level. For reloadings, the time is reset to zero at the beginning of subsequent relaxation periods, but the creep strain accumulation continues monotonically.

3.4.5.4 Results

Comparisons between predictions made by the above approach and experimental relaxation data are illustrated in Figs. 3.92 through 3.94 at the various temperatures for which data are available. Clearly, at all the higher stress levels the predictions appear to overestimate the amount of relaxation, at least for the times shown in these figures. This problem worsens at lower temperatures ($\leqslant$538°C), where the relaxation response is consistently overestimated. Figure 3.92 shows that at 450 and 482°C (842 and 900°F) the relaxation curves on subsequent loadings are essentially parallel and the predictions always show more relaxation than do the experimental curves, at least to 100 hr. At 510°C (950°F), the material appears to weaken in terms of resistance to relaxation upon reloading. The predictions (Fig. 3.93) are quite good for initial stresses less than about 170 MPa ($\approx$ 25 ksi), but overpredict relaxation at higher stresses, at least for the single run tests in Fig. 3.93(a). Available tests at 538°C (1000°F) again indicate weakening upon reloading; and the predictions again overestimate relaxation for these high-stress tests [Fig. 3.94(a)]. At 566°C (1050°F), available data [Fig. 3.94(b)] indicate that the predictions agree quite well with curves for reloaded specimens, but overpredict the amount of relaxation upon initial loading, at least at high stresses.

3.4.5.5 Limitations

All limitations and restrictions on the creep equation are inherently a part of this correlation as well. The basic range of applicability of the creep equation is as follows:

1. Stress: 7 MPa < $\sigma$ < 448 MPa (1 ksi < $\sigma$ < 65 ksi). The equation is limited at low stress by the minimum in the $\dot{e}_m$ equation at $\sigma$ = 6.9 MPa (1 ksi).

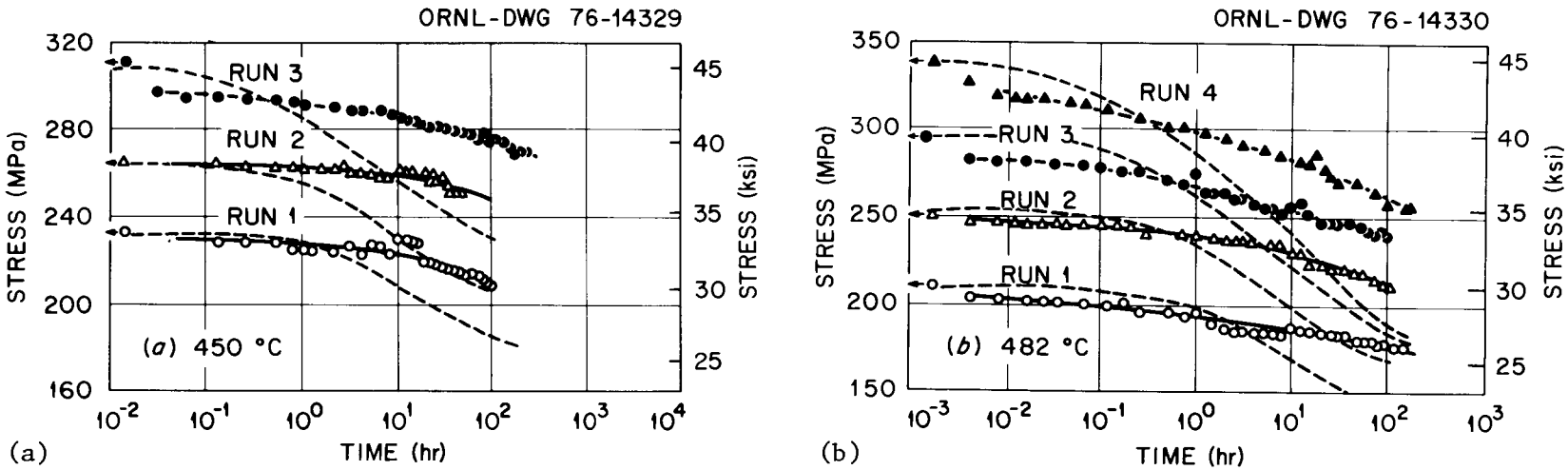


Fig. 3.92. Comparison Between Predicted and Experimental Relaxation Curves in (a) Three Repeated Loadings in a Single Specimen at 450°C and (b) Four Repeated Loading in a Single Specimen at 482°C. Solid lines and points represent experimental data; dashed lines represent predictions.

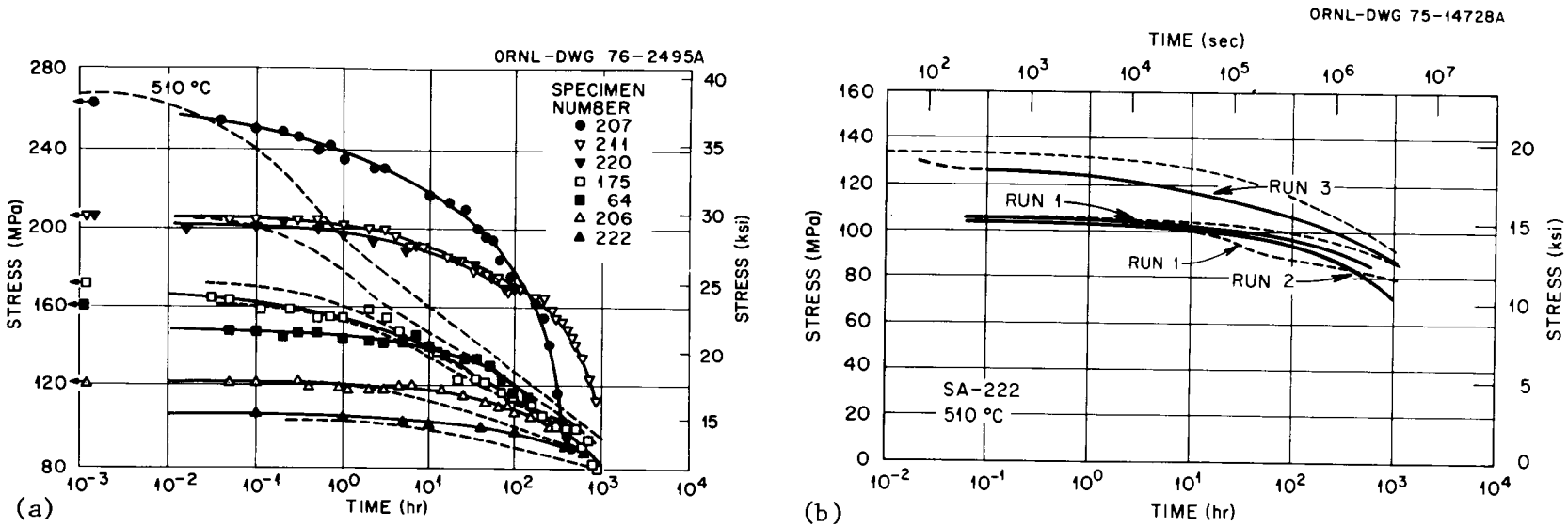


Fig. 3.93. Comparison Between Predicted and Experimental Relaxation Curves at 510°C in (a) Single Loadings of Different Specimens and (b) Three Repeated Loadings of a Single Specimen. Solid lines and points represent experimental data; dashed lines represent predictions.

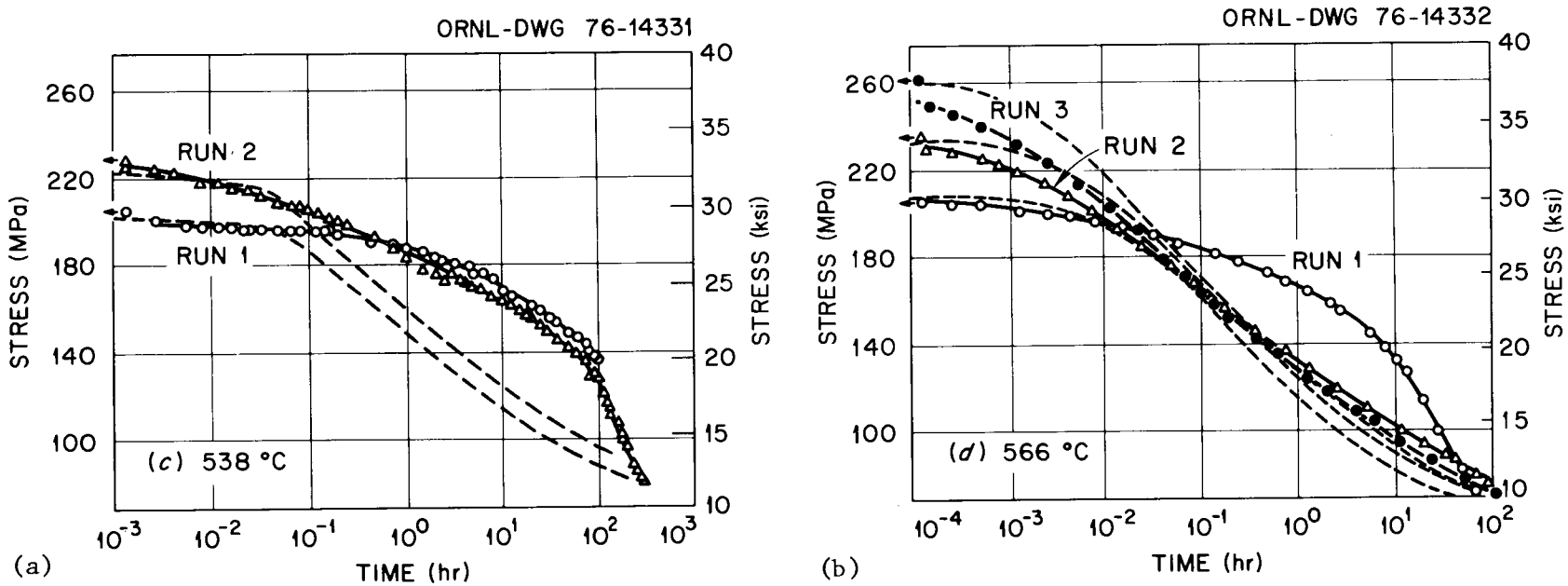


Fig. 3.94. Comparison Between Predicted and Experimental Relaxation Curves in (a) Two Repeated Loadings of a Single Specimen at 538°C and (b) Three Repeated Loadings of a Single Specimen. Solid lines and points represent experimental data; dashed lines represent predictions.

2. Temperature: $371°C \leqslant T \leqslant 593°C$ ($700°F \leqslant T \leqslant 1100°F$)
3. $t_3 = 0.28 t_r^{1.07}$, where $t_r$ = rupture life; $\log t_r = -31.45 + 39{,}320/T - 19.75 \log \sigma + 0.0164T \log \sigma$

   $\sigma$ = stress, MPa,

   $T$ = temperature, K,
4. Calculated strain: $\leqslant$ design criteria strain limits per applicable code or specifications.

Clearly, these restrictions contain some unrealistic regions [e.g., the upper limit of 384 MPa (65 ksi) exceeds the expected ultimate tensile strength]. Also, one must remember the above results, which indicate that the current approach generally overestimates relaxation response at lower temperatures (below about 538°C) and higher initial stresses (> yield strength), although the limited available data do not make it possible to precisely determine the stress-temperature region where problems exist. All results considered, it appears that the current approach will yield reasonably good results for low initial stresses (< yield strength), especially for relaxation after the reloadings. However, the complex nature of this material and the inaccuracies of some predictions indicate a need for further studies of hardening rules.

### 3.4.6 Mechanical Properties of Transition Weld Joint Materials

#### 3.4.6.1 Creep Properties — R. L. Klueh and J. F. King

Last quarter[87] we reported on creep-rupture tests on Inconel 82 weld metal at 454, 510, and 566°C (850, 950, and 1050°F). Several more tests were completed at these temperatures, and the data for all completed tests and those in progress are given in Table 3.26. Examination of the data reveals several premature failures at each temperature. As stated last quarter, the reason for such failures is being investigated.

In Fig. 3.95 the creep-rupture curves are given at 454, 510, and 566°C, while Fig. 3.96 shows the stress as a function of minimum creep rate at these temperatures. For both figures the results from the tests that failed prematurely have not been plotted.

Table 3.26. Creep-Rupture Properties of Inconel 82 Weld Metal

| Stress (MPa) | Stress (ksi) | Rupture Life (hr) | Total Elongation (%) | Reduction of Area (%) | Minimum Creep Rate (%/hr) |
|---|---|---|---|---|---|
| Tests at 454°C (850°F) on Welds in 19-mm (3/4-in.) Plate | | | | | |
| 414 | 60 | a | | | |
| 434 | 63 | a | | | |
| 455 | 66 | b | | | 0.000160 |
| 483 | 70 | c | | | 0.000273 |
| 483 | 70 | 68.1 | 37.0 | 54.2 | 0.00769 |
| 483 | 70 | 75.1 | 33.4 | 50.5 | 0.0187 |
| 496 | 72 | 1012.6 | 36.0 | 38.5 | 0.000769 |
| 510 | 74 | 142.3 | 40.2 | 52.5 | 0.013 |
| 517 | 75 | 3.2 | 33.7 | 53.0 | 0.125 |
| Tests at 510°C (950°F) on Welds in 13-mm (1/2-in.) Plate | | | | | |
| 379 | 55 | a | | | 0.000012 |
| 396 | 57.5 | b | | | 0.0000195 |
| 414 | 60 | 1645.4 | 23.6 | 19.7 | 0.000463 |
| 434 | 63 | 1205.1 | 33.7 | 29.3 | 0.000536 |
| 448 | 65 | 357.1 | 39.1 | 35.9 | 0.00459 |
| 455 | 66 | 4.0 | 40.4 | 39.0 | 0.150 |
| 455 | 66 | 39.4 | 38.7 | 42.9 | 0.138 |
| 465 | 67.5 | 37.1 | 48.4 | 51.8 | 0.209 |
| 483 | 70 | 10.9 | 48.4 | 53.7 | 0.395 |
| Tests at 566°C (1050°F) on Welds in 13-mm (1/2-in.) Plate | | | | | |
| 328 | 47.5 | b | | | 0.0000149 |
| 345 | 50 | 778.8 | 14.5 | 15.6 | 0.000324 |
| 345 | 50 | a | | | 0.000031 |
| 365 | 53 | 1087.5 | 17.2 | 18.2 | 0.000611 |
| 379 | 55 | 841.1 | 18.9 | 18.9 | 0.00105 |
| 396 | 57.5 | 448.2 | 21.4 | 19.6 | 0.00280 |
| 396 | 57.5[d] | 124.6 | 21.9 | | 0.0652 |
| 396 | 57.5[d] | 63.8 | 22.2 | | 0.133 |
| 414 | 60 | 112.8 | 29.7 | 27.4 | 0.0331 |
| 434 | 63 | 29.5 | 37.6 | 36.8 | 0.231 |

[a]Test in progress.

[b]Test discontinued before rupture.

[c]Temperature overshot and test failed after 2430 hr.

[d]Tests made on 19-mm (3/4-in.) plates.

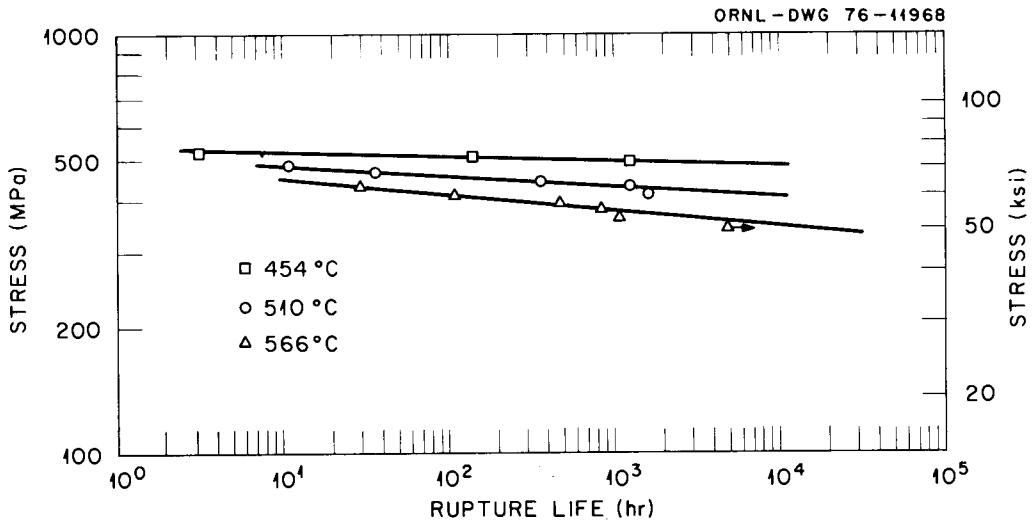


Fig. 3.95. Creep-Rupture Curves for Inconel 82 Weld Metal at 454, 510, and 566°C.

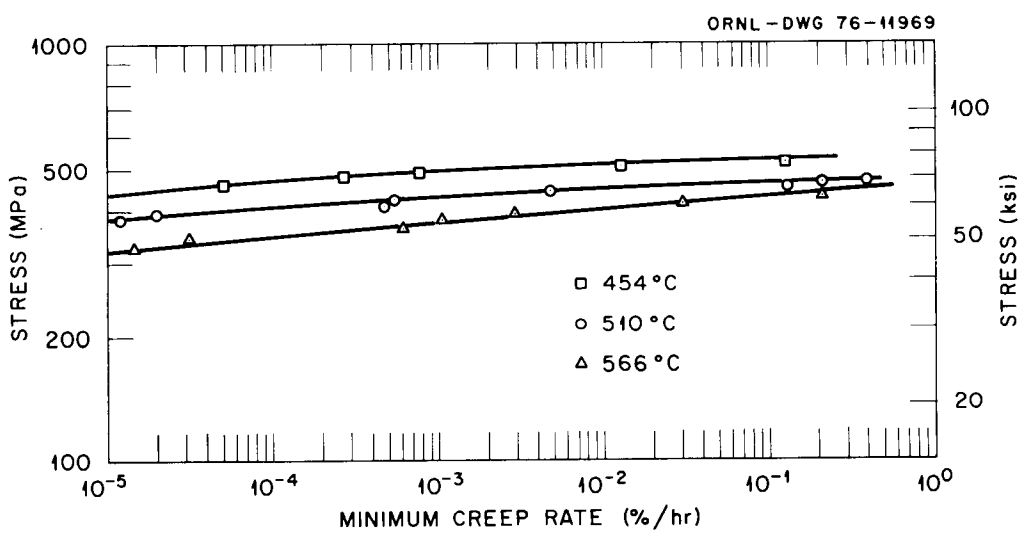


Fig. 3.96. Stress as a Function of Minimum Creep Rate for Inconel 82 Weld Metal at 454, 510, and 566°C.

During this quarter, several tests were started at 621 and 677°C (1150 and 1250°F). The first results from these tests will be reported next quarter. We have also made a weld from which specimens will be obtained to make creep-rupture tests at 732°C (1350°F).

3.4.6.2 Fatigue Behavior of Transition Joint Materials — J. P. Strizak

Collection of fatigue and creep-fatigue data on Inconel 82 filler metal has begun in support of the LMFBR transition joint technology needs and development program. All-weld-metal specimens were made from large deposits of Inconel 82 filler metal with 19-mm-thick (3/4 in.) 2 1/4 Cr-1 Mo steel plates as a base metal. The plates were prepared with a 30°-included-angle V-groove joint geometry with a 32 mm (1 1/4 in.) root opening and a backing strip. Weld deposits were made by the automatic gas tungsten-arc welding process with cold wire filler additions. The welds were stress relieved at 732°C (1350°F) for 1 hr.

Uniform-gage fatigue specimens, 6.35-mm-diam (0.250 in.) by 10.16-mm-long (0.400 in.) gage section, were fabricated with the specimen taken from the center of the weld thickness with its longitudinal axis transverse to the weld direction. The specimens were inspected radiographically, and sound (free from porosity defects) specimens and specimens with defects were identified.

Continuous cycling and creep-fatigue fully reversed strain-controlled tests were conducted on a electrohydraulic closed loop fatigue testing system employing an axial extensometer. Specimens were heated by induction in air. Thermocouples were spot welded to the specimens some distance from the gage area for temperature control and monitoring.

Results of continuous cycling strain-controlled fatigue tests at 538°C (1000°F) are shown in Fig. 3.97. All tests were conducted at a constant strain rate of $4 \times 10^{-3}$/sec with a triangular waveform as shown in Fig. 3.98. Comparison of Inconel 82 weld metal with transition weld joint base materials (type 316 stainless steel and 2 1/4 Cr-1 Mo steel) showed that the fatigue behavior of Inconel 82 weld metal was similar to that of the base metals in the low-cycle region. However, Inconel 82 exhibited superior fatigue resistance in the high-cycle region.

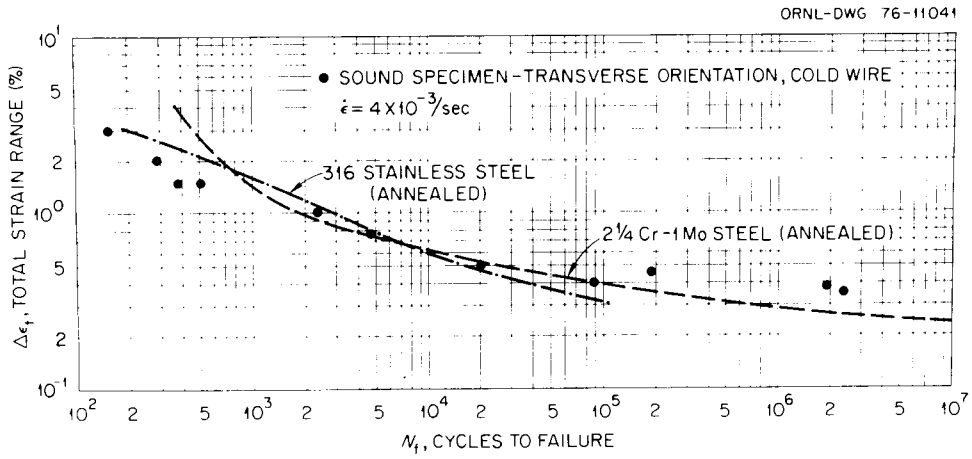


Fig. 3.97. Comparison of the Fatigue Behavior of Inconel 82 Weld Metal with Other Transition Weld Joint Materials at 538°C (1000°F). The type 316 stainless steel curve is for 566°C (1050°F).

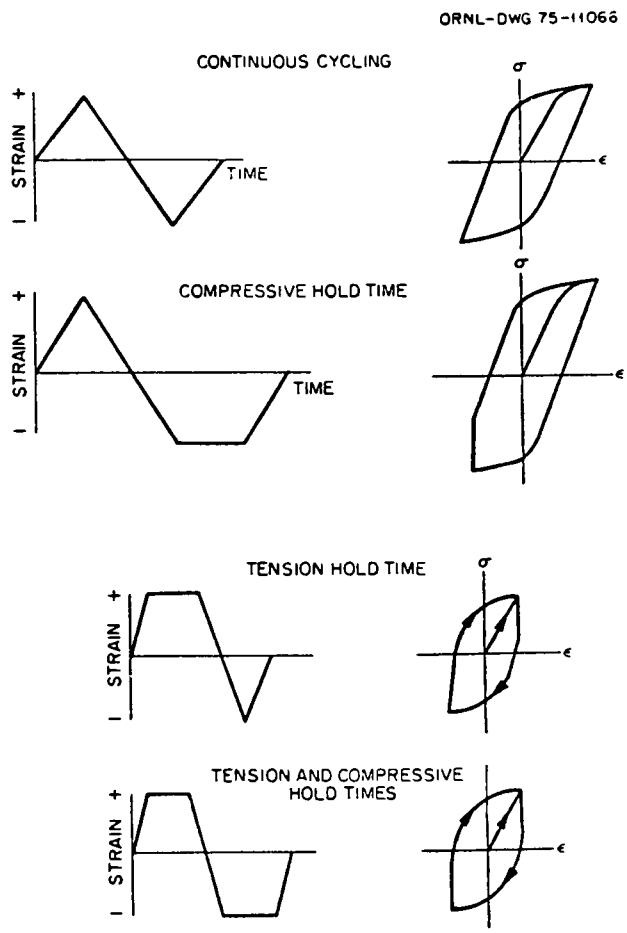


Fig. 3.98. Strain-Time Wave Forms and Associated Stress-Strain Hysteresis Loops for Fatigue and Creep-Fatigue Tests.

In addition to continuous cycling tests, several tests involving hold periods introduced each cycle at peak strain amplitudes (see Fig. 3.98) have been conducted to date to determine the influence of creep-fatigue on the failure behavior of Inconel 82. Results of tests with tensile and compressive strain hold periods of 0.1 hr are shown in Fig. 3.99. Generally, the reduction in fatigue life increased as strain range was decreased. Tests are continuing to determine the most detrimental type of hold period (tensile, compressive, or both) and the influence of increasing hold time on the creep-fatigue behavior of Inconel 82.

Several continuous cycling tests at 538°C (1000°F) were repeated with specimens with defects (porosity). Estimates made from radiographic negatives indicated that the pore sizes in the specimens ranged from 0.3 to 0.7 mm (0.012–0.028 in.) in diameter. As shown in Fig. 3.100 fatigue lives were reduced by 80–90% at the elevated temperature. Ishii[88] has shown that porosity up to 5% had little effect on the room-temperature fatigue behavior of mild steel. However, Buchanan and Young[89] showed that in 2 1/4 Cr-1 Mo steel welds at 649°C (1200°F), 5–8 vol % porosity could reduce fatigue life by 98%.

## 3.5 HIGH-TEMPERATURE DESIGN — J. M. Corum* and C. E. Pugh*

### 3.5.1 Uniaxial Material Behavior Tests — R. W. Swindeman

The objectives of these studies are (1) to perform exploratory uniaxial tests to identify basic inelastic high-temperature material behavior for input into constitutive equation development, (2) to provide characterization data needed as input into inelastic analysis of structural tests, (3) to provide limited data as needed in support of subcontracted activities, (4) to provide limited data in support of failure criteria development, and (5) to identify materials properties data needed for high-temperature design. Studies involve materials of concern for liquid-metal fast breeder reactor (LMFBR) components. The emphasis has been

---

*Reactor Division.

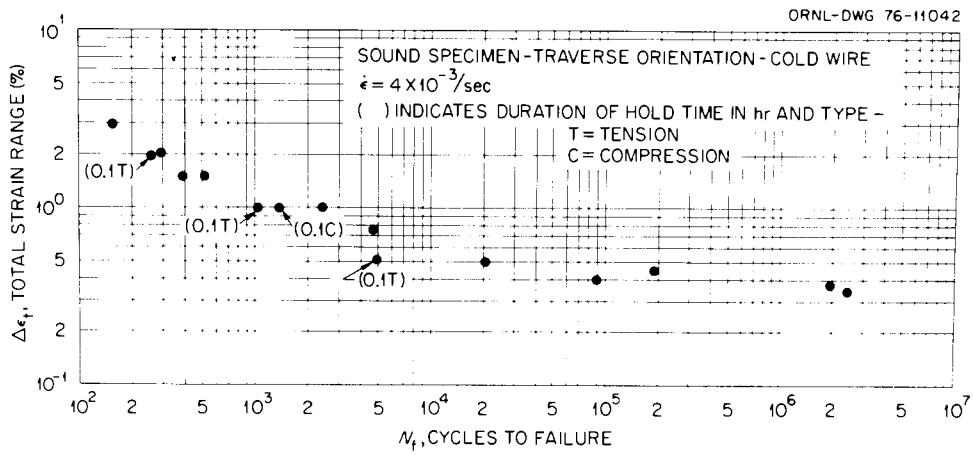


Fig. 3.99. Effect of Hold Periods on the Fatigue Behavior Inconel 82 Weld Metal at 538°C (1000°F).

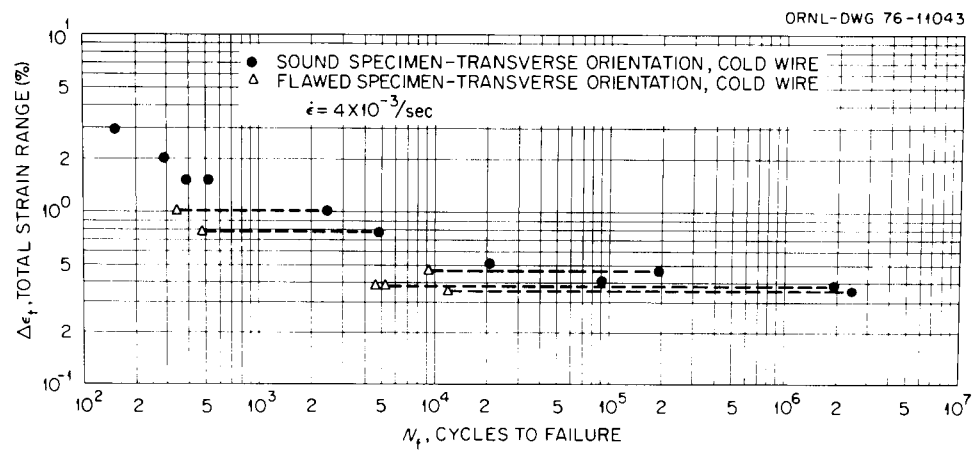


Fig. 3.100. Effect of Material Defects on the Fatigue Behavior of Inconel 82 Weld Metal.

placed on type 304 stainless steel (heat 9T2796), and recently testing of type 316 stainless steel has begun. Studies are separated into three categories — time-independent plasticity (stress-strain behavior), time-dependent creep (creep and relaxation behavior), and creep-plasticity interactions. Monotonic and cyclic tests are involved in each category.

### 3.5.1.1 Exploratory Testing of Type 304 Stainless Steel — R. W. Swindeman, R. K. Bhargava,* J. Moteff,* and V. K. Sikka

The studies on type 304 stainless steel (heat 9T2796) were curtailed during the last reporting period to concentrate manpower and equipment for studies on 2 1/4 Cr-1 Mo steel, materials used for the third Thermal Transient Test, and type 316 stainless steel. It is expected that the effort on type 304 stainless steel will gradually increase over the next two reporting periods.

The low-strain tensile data for the 25-mm (1-in.) plate of the reference heat have been analyzed and a report was issued.[90] A paper that describes the applicability of the model to other product forms of the reference heat has also been written.[7] A somewhat improved model for low-strain tensile flow is currently being developed by Sikka et al.,[30] and this new model could be used to replace the existing representation.

No significant experimental activity involving monotonic or cyclic stress-strain behavior was undertaken in this reporting period.

Creep testing of the reference heat has been limited to a few tests, which involve thermal cycling. The results, in general, reveal that the rate after temperature changes cannot be predicted by the use of a single activation energy term. Data which bear on this are shown in Fig. 3.101, where the creep rate is plotted on a logarithmic scale against creep strain for a test at 121 MPa (17.5 ksi). A temperature change was introduced every week and involved temperatures of 566, 593, and 621°C (1050, 1100, and 1150°F). Examination of the data in Fig. 3.101 reveals that the creep rate at 593°C is less after heating from 566°C than after cooling from 621°C. This phenomenon gives rise to an activation energy that

---

*University of Cincinnati.

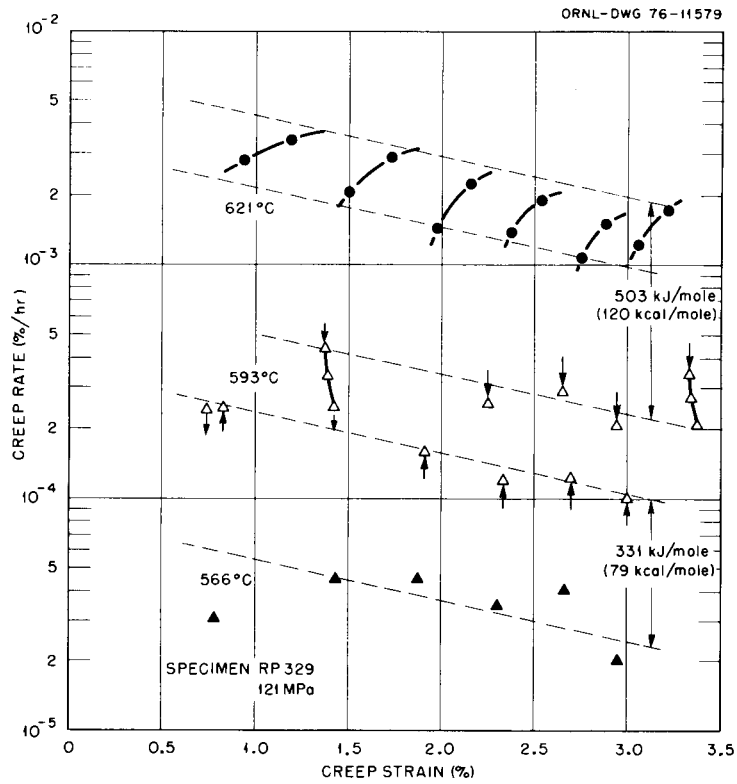


Fig. 3.101. Influence of Thermal Cycling on the Creep Rate of Type 304 Stainless Steel at 121 MPa (17.5 ksi).

depends on the prior history and varies from 331 to 503 kJ/mole (79 to 120 kcal/mole). Another interesting feature of the creep behavior is the acceleration of the creep rate at 621°C after the low-temperature exposure. One interpretation of this behavior is that the internal stress,[91] $\sigma_i$, must be a higher percentage of the applied stress, $\sigma$, at 593°C than at 621°C. If true, the accelerating creep rate period at 621°C could represent the period in which the internal stress is decreasing. This is consistent with observations made in relaxation testing,[92] where the ratio of the internal stress to the flow stress was found to have values near 0.31, 0.39, and 0.50 for temperatures of 760, 704, and 649°C (1400, 1300, and 1200°F), respectively. An extrapolation of this trend leads us to expect a ratio near 0.56 at 566°C and near 0.65 at 593°C for stresses around 121 MPa. Assuming Wilshire and co-workers[93,94] are correct, the creep rate, $\dot{\varepsilon}$, should be related to the effective stress, $(\sigma - \sigma_i)$, according to a power law. Thus:

$$\dot{\varepsilon} \propto (\sigma - \sigma_i)^n \ , \qquad (1)$$

where $n$ is a constant near 4. Just after the temperature change to 621°C, $\dot{\varepsilon}$ might reflect the $\sigma_i/\sigma$ ratio at 593°C (0.65), and gradually this decreases to the ratio for 621°C (0.56). Such a change would result in tripling the creep rate at 621°C, which is not unreasonable. We are now attempting to repeat the test. Further considerations of internal stress concepts are presented later.

No progress was made in this reporting period with respect to creep-plasticity interaction studies for type 304 stainless steel. We expect to resume testing in the next reporting period, however.

Although the constant-load creep and rupture testing of type 304 stainless steel has been completed, the evaluation of the data produced in this test series will continue for some time. Current efforts by Robinson and Clinard[95] to develop deformation models that embody hardening and recovery concepts can be guided, to some extent, by knowledge of the manner in which metallurgical substructure is influenced by thermo-mechanical history. Metallurgical studies currently in progress involve transmission electron microscopy, scanning electron microscopy, and optical microscopy of spcimens tested in tensile, creep, and cyclic modes. This work is intended to supplement research funded under other contracts[96] at the University of Cincinnati. When combined with results obtained by Sikka[97] at ORNL and Etienne, Dortland, and Zeedijk[98] on a similar material, it should provide a very comprehensive picture. This information will serve as a framework on which to evaluate material behavior under variable conditions.

Substructural features that have been examined include the cell and subgrain sizes, subgrain misorientations, dislocation line densities, dislocation-precipitate interactions, precipitate sizes and locations, and microscopic cracking patterns. In a report currently in preparation[99] the kinetics of the precipitation of $M_{23}C_6$ under stress has been studied. Data from this study are plotted in Fig. 3.102, wherein the symbols represent creep-tested specimens that were examined by transmission electron microscopy. Filled symbols indicate the presence and open symbols the

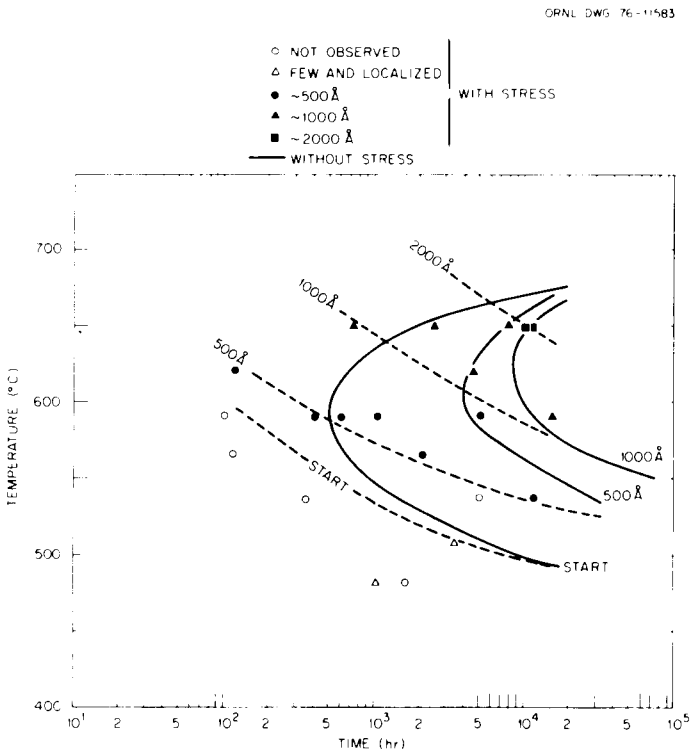


Fig. 3.102. Effect of Stress on the Time-Temperature-Transformation Diagram for Matrix Carbide Precipitation in Type 304 Stainless Steel.

absence of matrix precipitates. Superimposed on these data are solid lines, taken from the work of Etienne, Dortland, and Zeedijk,[98] which represent the time and temperature associated with the development of specific sizes of precipitates in the absence of stress. Finally, dashed lines are shown to represent the development of specific sizes of precipitates in the presence of stress. These lines are based on the University of Cincinnati studies but are consistent with the observations of Etienne, Dortland, and Zeedijk[98] for highly stressed specimens. The data suggest that the size of the precipitate particles is greatly influenced by the stress. For example, at 593°C (1100°F) the time required to develop a precipitate size of 500 Å in the presence of stress is about one-tenth the time for the same size without stress. Above 593°C it appears that the time to initiate the precipitation is also accelerated by the presence of stress.

Grain boundary precipitation kinetics is summarized in Fig. 3.103. Again, the symbols represent specimens examined after creep testing and

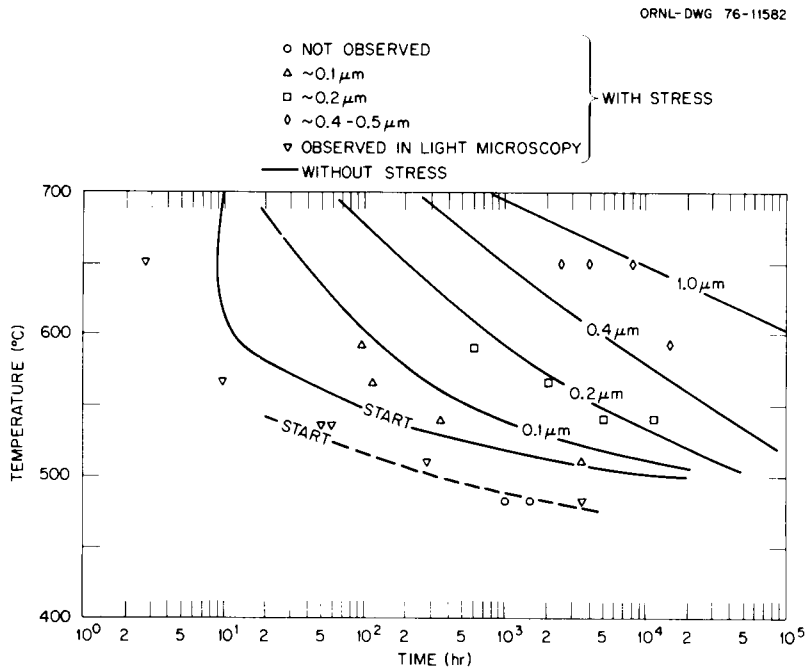


Fig. 3.103. Effect of Stress on the Time-Temperature-Transformation Diagram for Grain Boundary Carbide Precipitation in Type 304 Stainless Steel.

the solid lines represent expected trends, in the absence of stress, as observed by Etienne, Dortland, and Zeedijk.[98] Since all but two of the creep-tested specimens exhibit grain boundary carbides, specimens tested for shorter times were examined by light microscopy to see if grain boundary carbides were present. These specimens also exhibit precipitates in the stressed regions, and the test conditions for these short-time tests are indicated by the inverted triangles. It appears from Fig. 3.103 that the precipitation and early growth of the grain boundary carbides are accelerated by stress. Since $M_{23}C_6$ influences both the strength and the ductility of type 304 stainless steel,[98,100] the data of the type shown in Figs. 3.102 and 3.103 will be of considerable value in the interpretation of mechanical behavior under constant and varying stress-temperature conditions.

Also, the $M_{23}C_6$ precipitate prevents the development of subgrains under some conditions of stress and temperature.[101,102] Further, the fine dispersion of the precipitate tends to stabilize dislocation networks within the grains. A number of investigators, such as Lagneborg,[103]

Davies and Wilshire,[104] and others, believe that the creep response is greatly influenced by the character of the dislocation network. Some investigators invoke the concept of an athermal component of stress or an internal stress, $\sigma_i$, which could be associated with the dislocation structure. Blum et al.,[105] for example, describe the internal stress, $\sigma_i$, by the simple relation:

$$\sigma_i = GMb\alpha\rho^{1/2} ,$$

where $G$ is the shear modulus, $M$ is the Taylor factor, $b$ is the Burgers vector, $\rho$ is the dislocation line density, and $\alpha$ is a constant near 0.25. For type 304 stainless steel we can assume $M$ to be near 3 and $b$ to be $2.54 \times 10^{-10}$ m. Thus, the ratio $\sigma_i/G$ can be estimated from measurements of $\rho$. Data showing the variation of $\rho$ with the ratio $\sigma/G$ at 593 and 649°C are plotted in Fig. 3.104, and from the trend lines it is possible to determine $\rho$ for any value of $\sigma/G$ at either temperature. Using the equation cited by Blum et al.[105] to estimate $\sigma_i/G$ from $\rho$, we can determine the ratio $(\sigma_i/\sigma)$, or $R$, as a function of $(\sigma/G)$. Plots for $R$ vs $(\sigma/G)$ for 593 and 649°C are shown in Fig. 3.105. As may be seen, the ratio increases with decreasing stress and temperature. This seems to be a reasonable trend. The calculated $(\sigma_i/G)$ values can be used to estimate the modulus-compensated effective stress, $\sigma_e/G$, defined by the equation

$$\frac{\sigma_e}{G} = \frac{\sigma - \sigma_i}{G} = \frac{\sigma}{G}(1 - R) .$$

When the effective stress is used instead of the applied stress, we find that the exponent in the power law relating creep rate to stress is significantly reduced, from roughtly 10 to near 7 at 593°C. An exponent of 4, suggested by Wilshire and co-workers,[93,94] is not observed, however, as may be seen in the $\dot{\varepsilon}_s$ vs $(\sigma/G)$ and $(\sigma_e/G)$ curves shown in Fig. 3.106. One possible reason for this is the way in which $\sigma_i$ is determined. Wilshire and co-workers used experimental techniques based on higher resolution strain measurements, which often produce values for $\sigma_i$ that differ from values obtained by conventional techniques.

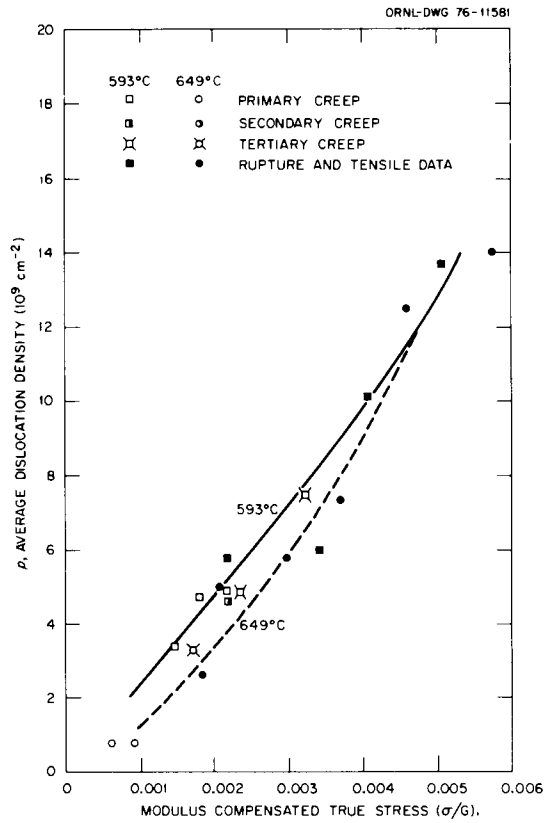


Fig. 3.104. Variation of the Average Dislocation Density with Modulus-Compensated True Stress for Type 304 Stainless Steel at 593 and 649°C (1100 and 1200°F).

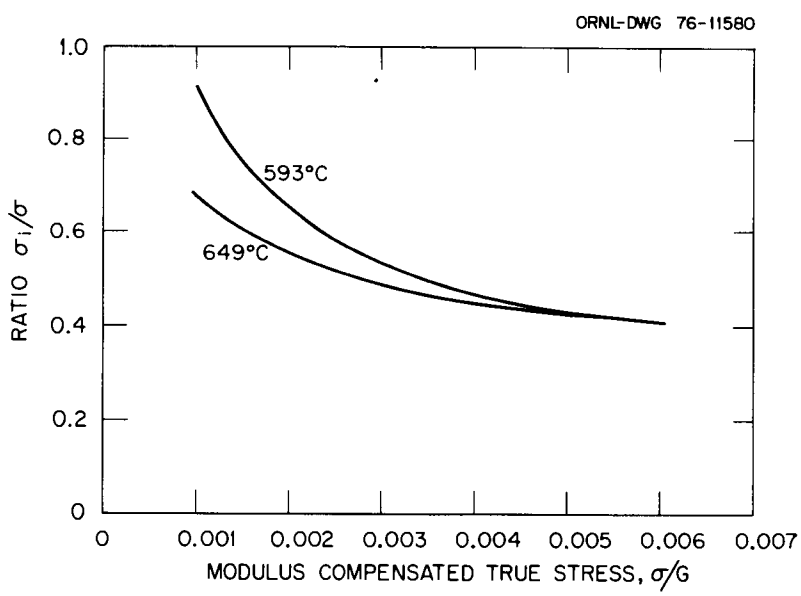


Fig. 3.105. Ratio of the Internal Stress to the Applied Stress for Type 304 Stainless Steel at 593 and 649°C (1100 and 1200°F). The internal stress was calculated from dislocation density data.

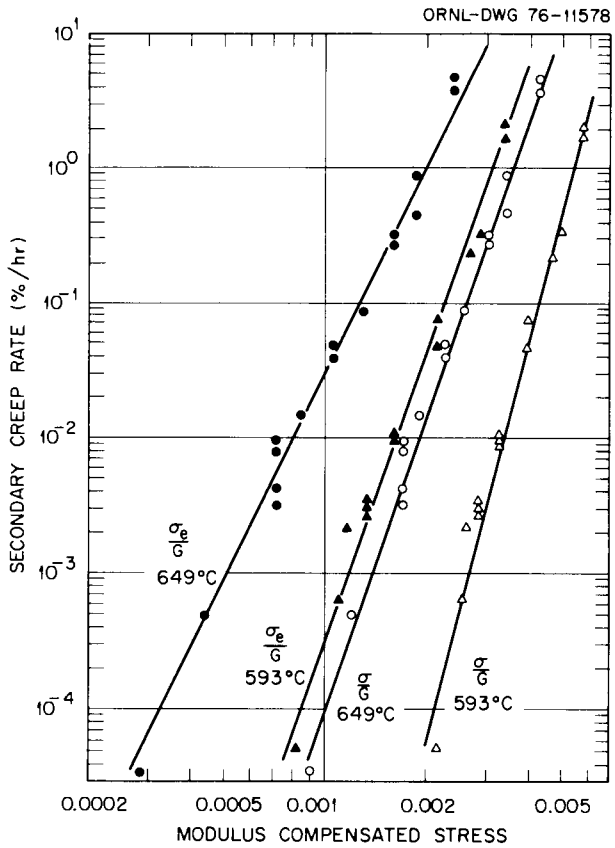


Fig. 3.106. Secondary Creep Rate vs Modulus-Compensated True Stress and Modulus-Compensated Effective Stress for Type 304 Stainless Steel at 593 and 649°C (1100 and 1200°F).

3.5.1.2 Exploratory Testing of Type 316 Stainless Steel — R. W. Swindeman

The exploratory test program on the reference heat of type 316 stainless steel (heat 8092297) concentrates on behavior at 593°C (1100°F), although some short-time studies will be performed at other temperatures. About two-thirds of our testing capability was allocated to testing 25-mm (1-in.) plate material under tensile, strain cycling, creep, and relaxation conditions. In all cases the material was tested in the reannealed condition (0.5 hr at 1065°C). We expect that the effort on type 316 stainless steel will decline during the next reporting period as more testing on type 304 stainless steel and 2 1/4 Cr-1 Mo steel is resumed.

A series of tensile tests was performed over the temperature range 25 to 649°C (77—1200°F) and at a nominal strain rate of 0.004/min. Large-strain tensile curves, obtained from these tests, are plotted in Fig. 3.107. These show that the rate of hardening is relatively

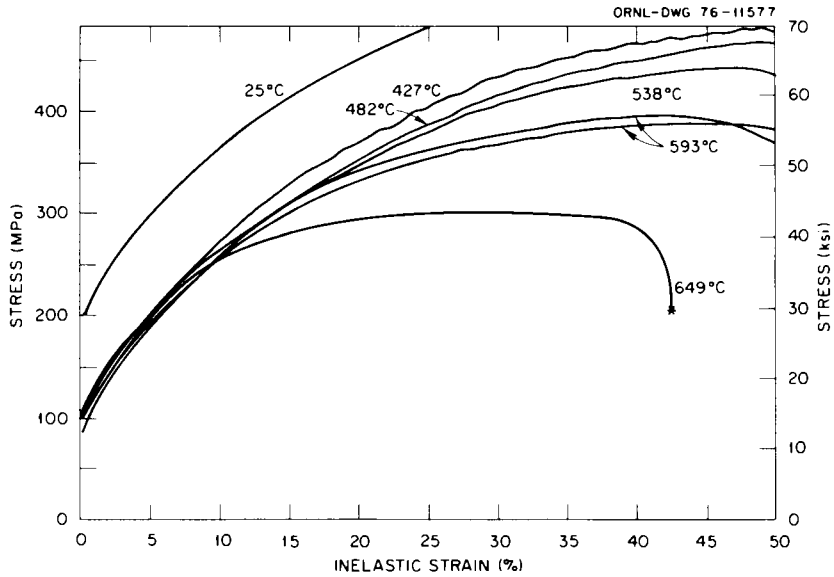


Fig. 3.107. Tensile Curves for Type 316 Stainless Steel (Heat 8092297) at Several Temperatures and 0.004/min Strain Rate.

independent of temperature for strains to at least 5%. Hence, nearly all the temperature dependence could be accommodated by the yield strength term, as was done for type 304 stainless steel.[90] Sufficient data are not available to permit the formulation of an accurate low-strain tensile flow model at this time, however, although either the modified Ludwik[90] or a new model being developed by Sikka et al.[30] could be used to approximate the general shape of the flow curve. One of the difficulties in modeling the flow behavior of the reannealed type 316 stainless steel is the existence of strong strain-aging, which greatly influences the shape of the flow curve.[106] Some idea of the variability in the shape of the flow curves to 0.7% strain can be seen in the extensometer tracings plotted in Fig. 3.108.

Strain cycling tests have been completed for three strain ranges at 593°C (1100°F) — 0.21, 0.42, and 0.59% — and for one strain range — 0.42% — at several other temperatures. The cyclic stress ranges corresponding to the 1st, 10th, 100th, and 1000th cycles are plotted against temperature in Fig. 3.109. The existence of a strong strain-aging phenomenon is apparent in the cyclic data, inasmuch as the strength appears to peak at 538°C (1000°F) and 1000 cycles. Actually, the temperature of the peak will probably shift with strain range and strain rate, but

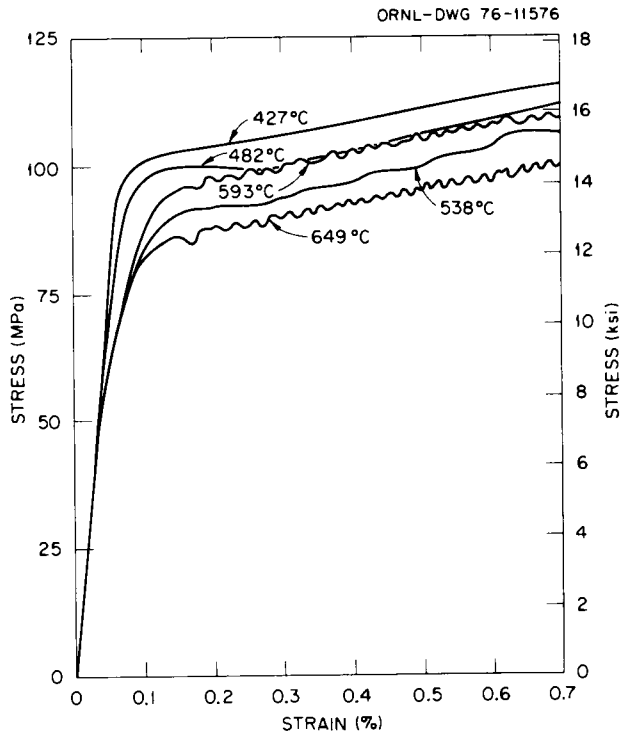


Fig. 3.108. Extensometer Tracing from Tensile Tests on Type 316 Stainless Steel at Several Temperatures and 0.004/min Strain Rate.

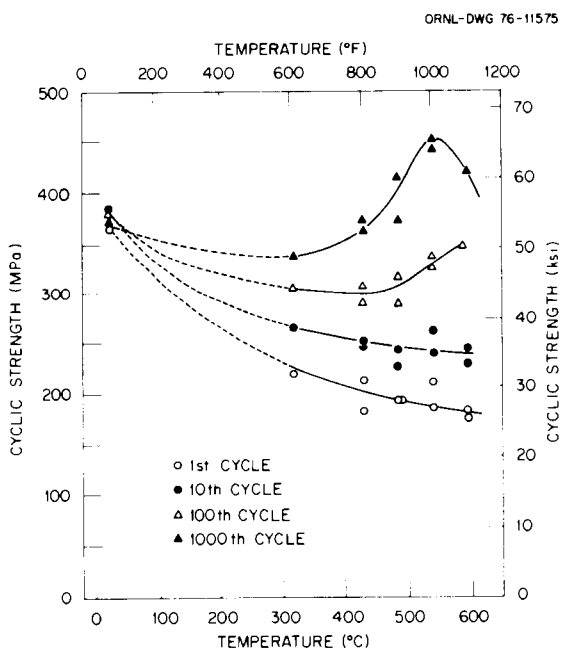


Fig. 3.109. Cyclic Strength vs Temperature for Type 316 Stainless Steel Tested at a Strain Range Near 0.42% and a Strain Rate Near 0.005/min.

insufficient data are available to define this trend. These cyclic hardening data are in qualitative agreement with results obtained at ANL on the 25-mm (1-in.) bar[107] and at Battelle on the 203-mm (8 in.) pipe.[108] All the laboratories observe the peak in strength at 538°C. The 25-mm plate has a much lower cyclic strength in the first cycle than the other products but hardens rapidly to approach the other products by 1000 cycles.

The cyclic hardening behavior can be approximted by a modified Voce[109] equation of the form:

$$\Delta S = (\Delta S_0 - \Delta S_\infty) \exp[-(k\Sigma\Delta e_p)^{1/2}] + \Delta S_\infty ,$$

where

$\Delta S$ = the stress range for any cycle,
$\Delta S_0$ = the initial stress range,
$\Delta S_\infty$ = the saturation stress range,
$\Delta e_p$ = the inelastic strain range,
$k$ = a constant related to the rate of approach to saturation.

The constant $\Delta S_\infty$ is strongly dependent on $\Delta e_p$, while $\Delta S_0$ and $k$ are relatively independent of $\Delta e_p$ for the conditions studied. An example of how the equation fits the hardening curves is shown in Fig. 3.110 for data at 593°C (1100°F). It should be understood, however, that the modified Voce model is not intended to be a very precise representation, but rather a fairly simple empirical approximation. Other models being developed by Eisenberg,[110] Liu,[111] and Jhansale[112] could have better potential for general applicability.

Creep-rupture tests are being performed at 593°C (1100°F) over the stress range 52 to 276 MPa (7.5–40 ksi). Nearly all tests in the constant-load series have been either completed or are in progress. Tests that do not rupture will be terminated by 10,000 hr.

The inelastic strains produced when the creep tests were loaded appear to be related to the applied stress according to a Ludwik-type relation,[90] where the exponent on strain is near 0.75. This behavior

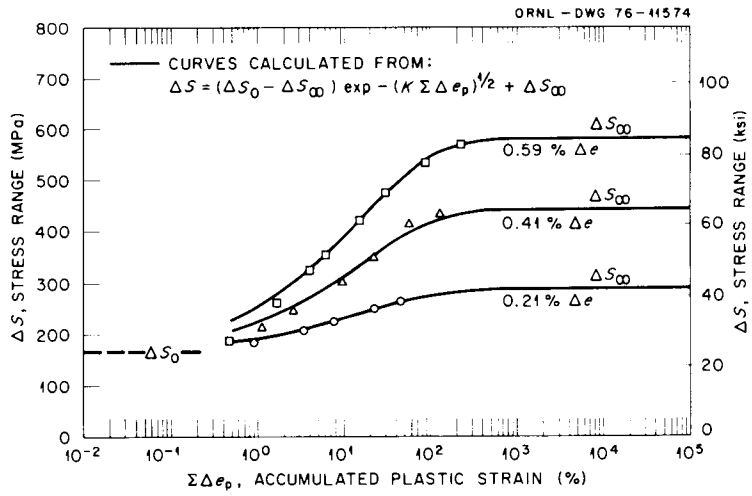


Fig. 3.110. Fit of a Modified Voce Equation to the Cyclic Hardening Behavior for Type 316 Stainless Steel at 593°C (1100°F).

is demonstrated in Fig. 3.111. The trend is similar to that observed[90] for type 304 stainless steel.

The primary creep behavior of the reference heat of type 316 stainless steel appears to be quite complex. The creep curve goes through one or more inflections during the first several hundred hours,

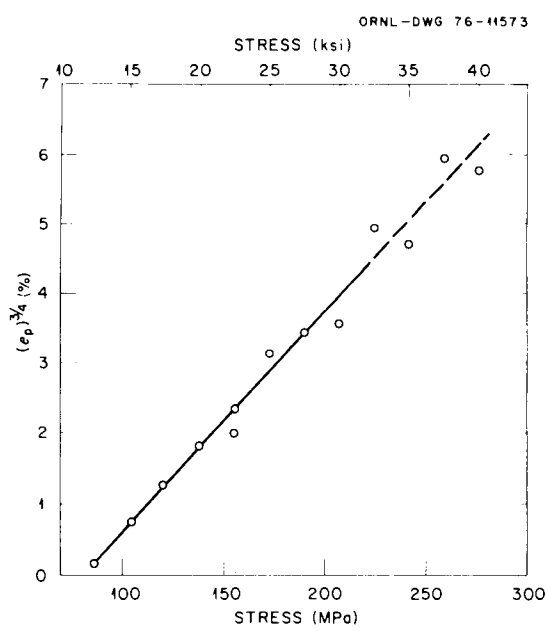


Fig. 3.111. Plastic Strain vs Stress for Type 316 Stainless Steel Obtained from Creep Tests at 593°C (1100°F).

and the transient component, evaluated at stresses above 138 MPa (20 ksi), shows no consistant trend with varying stress. If anything, the transient component, appears to be proportional to the stress. As a first approximation, we can assume a simple exponential creep equation[22] to hold. Then the creep strain is given by:

$$e = e_t[1 - \exp(-rt)] + \dot{e}_s t \ , \tag{2}$$

where

$e$ = the creep strain,
$e_t$ = the transient component,
$r$ = the rate constant evaluated at $rt = 1$,
$t$ = time,
$\dot{e}_s$ = secondary creep rate.

Data for $e_t$, $r$, and $\dot{e}_s$ are plotted against stress in Figs. 3.112, 3.113, and 3.114, respectively. Tensile data are included in Fig. 3.114. An alternative creep equation, based on the single rational polynomial, is being developed by Booker and Sikka,[16] and it appears that this equation could produce a better model than the exponential form. The equation is written:

$$e = \frac{cpt}{1 + pt} + \dot{\varepsilon}_s t \ , \tag{3}$$

where

$c = e_t$,
$p = 1.72r$,
$\dot{\varepsilon}s$ = the same as Eq. (2).

Data are not adequate to determine the constants for either equation for stresses below 138 MPa (20 ksi), however, and to satisfy near-term requirements, a simple power is adequate. A plot of creep data, assuming

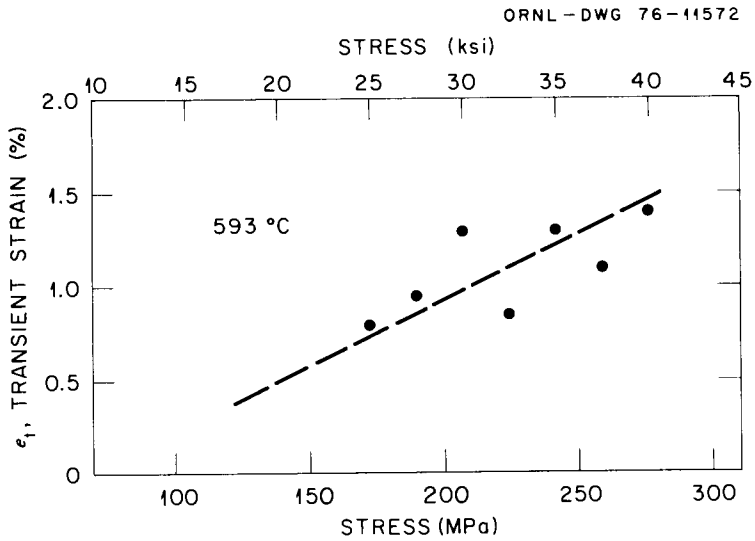


Fig. 3.112. Transient Creep Component vs Stress for Type 316 Stainless Steel at 593°C (1100°F).

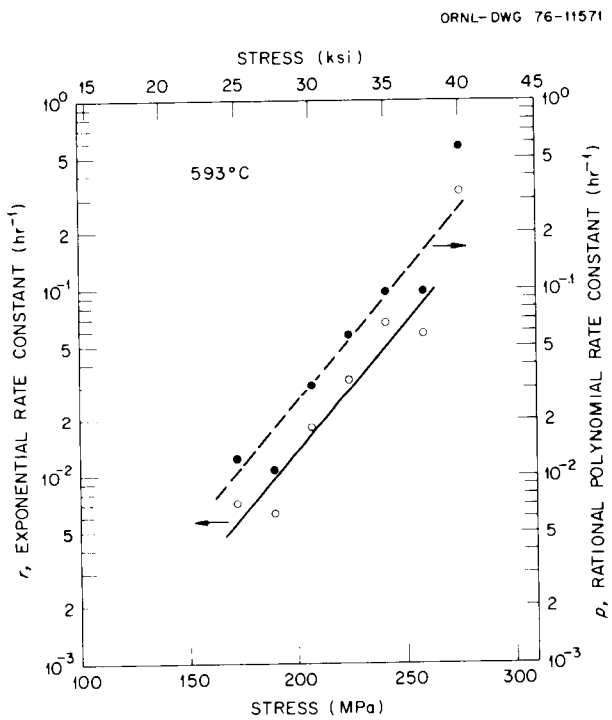


Fig. 3.113. Rate Constants Associated with the Transient Creep Component for Type 316 Stainless Steel at 593°C (1100°F).

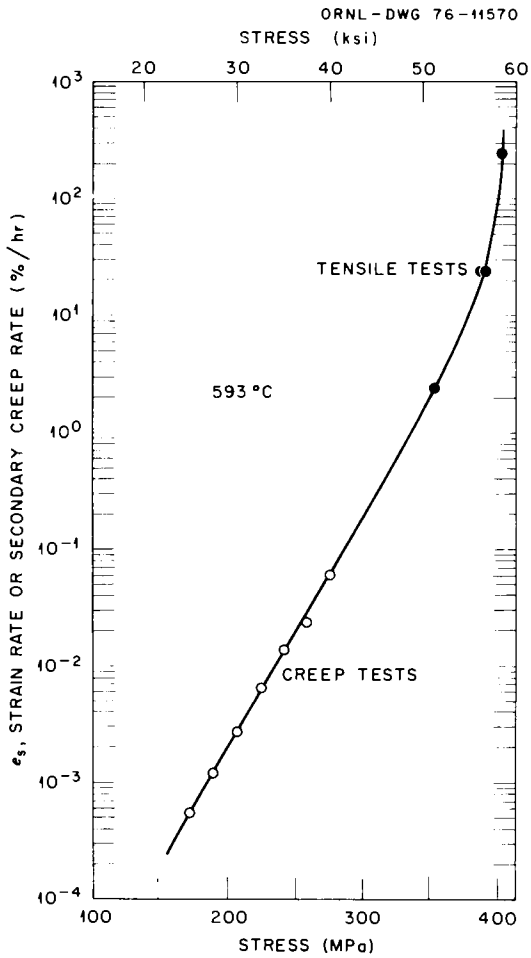


Fig. 3.114. Secondary Creep Rate vs Stress for Type 316 Stainless Steel at 593°C (1100°F).

parabolic behavior, is shown in Fig. 3.115, and such a power law appears to approximate the data trend reasonably for at least 1000 hr.

In the discussion above, three different methods for representing the constant-load creep data were outlined. The real test of any material representation, however, is its usefulness for predicting behavior under varying load or temperature conditions. The relaxation test is one of the most widely used of the variable load test techniques for evaluating creep laws and hardening rules. It provides creep rate data at constant nominal strain. If the creep rate, determined from a relaxation test, is identical to the rate observed in a constant-load creep test at the same stress and temperature, then the structures must be equivalent, at least as far as the mechanical response is concerned.

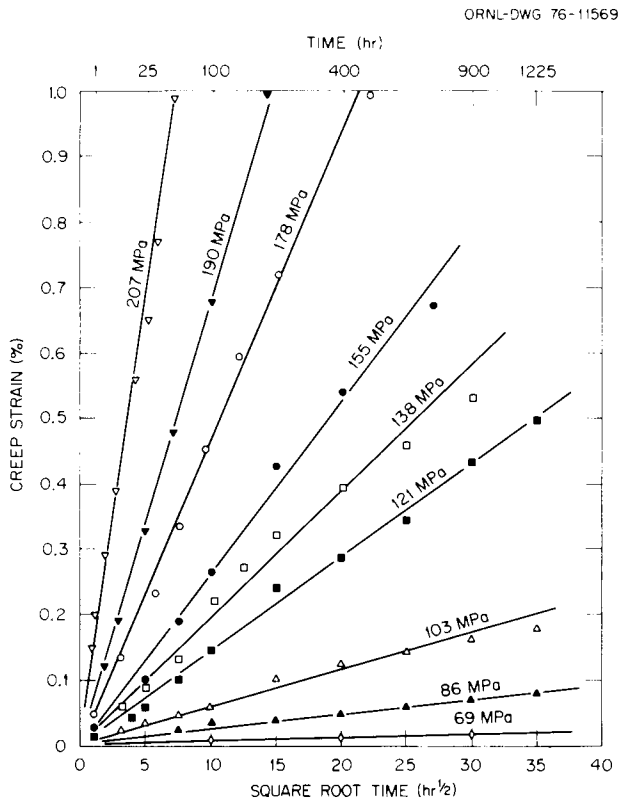


Fig. 3.115. Creep Strain vs Square Root of Time for Tests on Type 316 Stainless Steel at 593°C (1100°F).

The same statement could be made when comparing the results of two relaxation tests, whether they be performed by multiple loadings on the same specimen or single loadings on different specimens with different starting stresses.

We have produced a considerable body of relaxation data on type 316 stainless steel during this reporting period, and some of this information is provided in Fig. 3.116. Each panel corresponds to data on an individual specimen and each run is performed at an increased stress level. In several instances, reloading to the previous stress level was examined, but only one such curve [run 1a in Fig. 3.116(c)] is shown. Some of the relaxation data have already been utilized to demonstrate the applicability of the single rational polynomial creep equation[16,113] to problems of variable stress. Our current effort in the relaxation testing is directed toward collection of data that can be used in the development of rate-type deformation equations,[95,114,115] however. The first thing

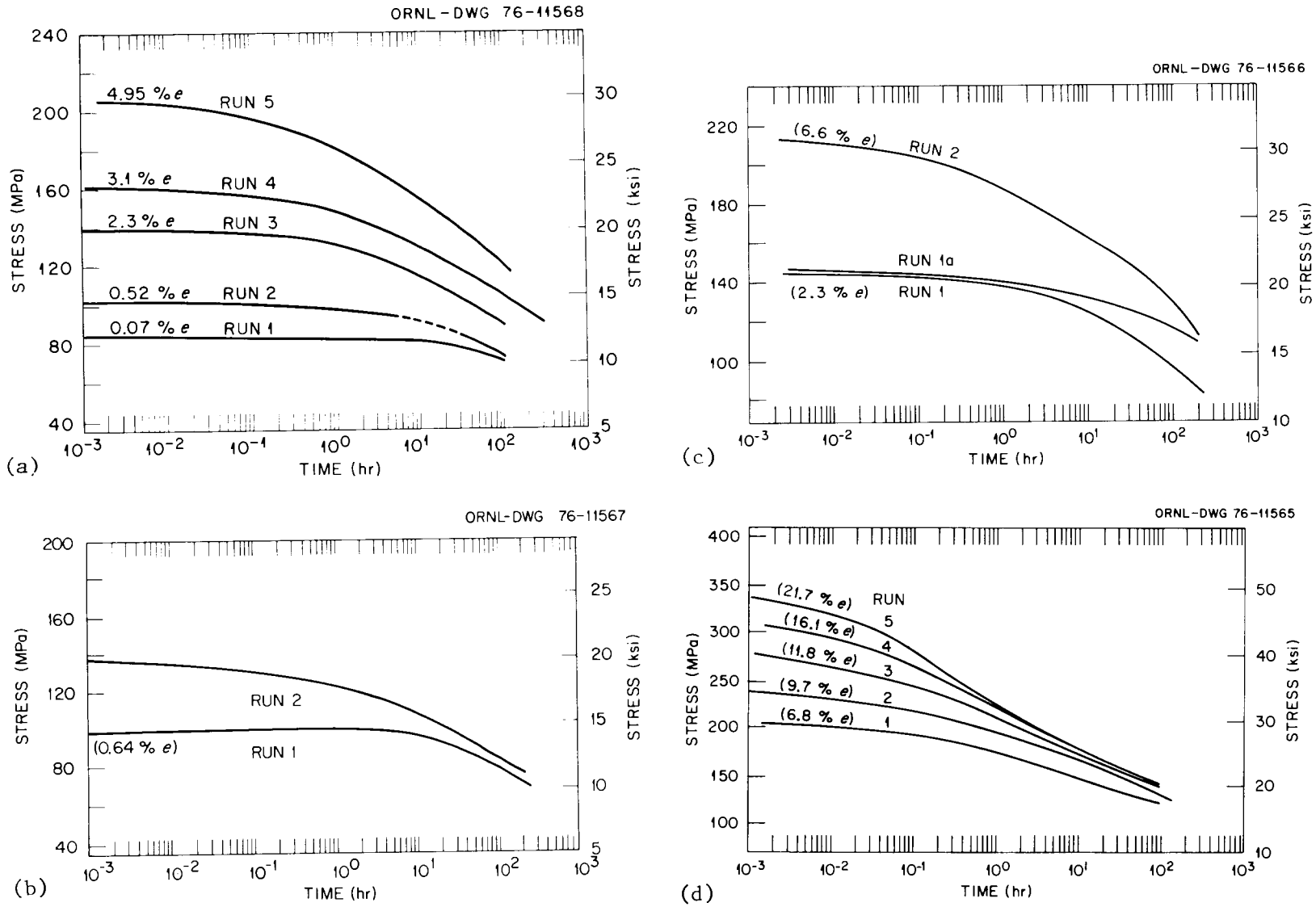


Fig. 3.116. Relaxation Curves for Multiple-Loading Tests on Type 316 Stainless Steel at 593°C (1100°F) and Starting at (a) 86 MPa (12.5 ksi), (b) 100 MPa (14.5 ksi), (c) 148 MPa (21.5 ksi), and (d) 207 MPa (30.0 ksi) (Specimen 22).

that one must recognize in using both creep and relaxation data for the development of rate equations is the fact that true stress, true strain, and true strain rate have greater significance than the corresponding engineering values. Further, the behavioral features, which are very important to constitutive equation development, can differ according to which type of stress-strain response is considered. For example, isochronous relaxation curves constructed from multiple loading data on a single specimen (22) are plotted in Figs. 3.117 and 3.118 for engineering and true values, respectively. Examining Fig. 3.117 one can see that the 100-hr relaxation strength is almost independent of accumulated total or even creep strain. Examining Fig. 3.118, however, one can see that the 100-hr relaxation strength increases significantly (approximately 50%) with accumulated total or creep strain. Admittedly, we have selected a rather extreme case as far as accumulated monotonic strain is concerned but, nevertheless, treatment of behavior on a true-stress true-strain basis is often desirable.

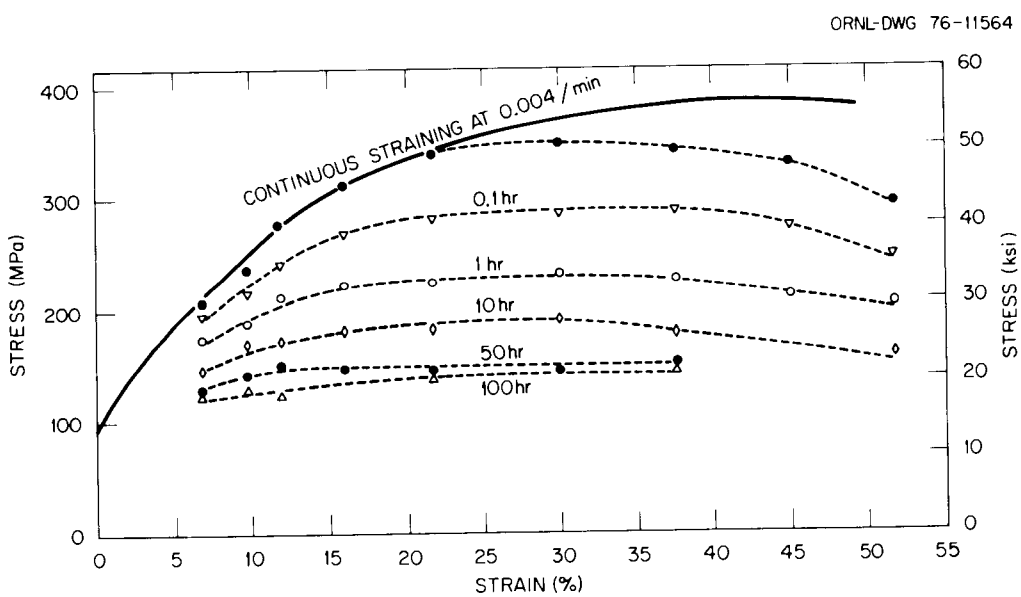


Fig. 3.117. Engineering Stress vs Engineering Strain Isochronous Relaxation Curve for Type 316 Stainless Steel at 593°C (1100°F) Obtained from Multiple Loading Tests (Specimen 22).

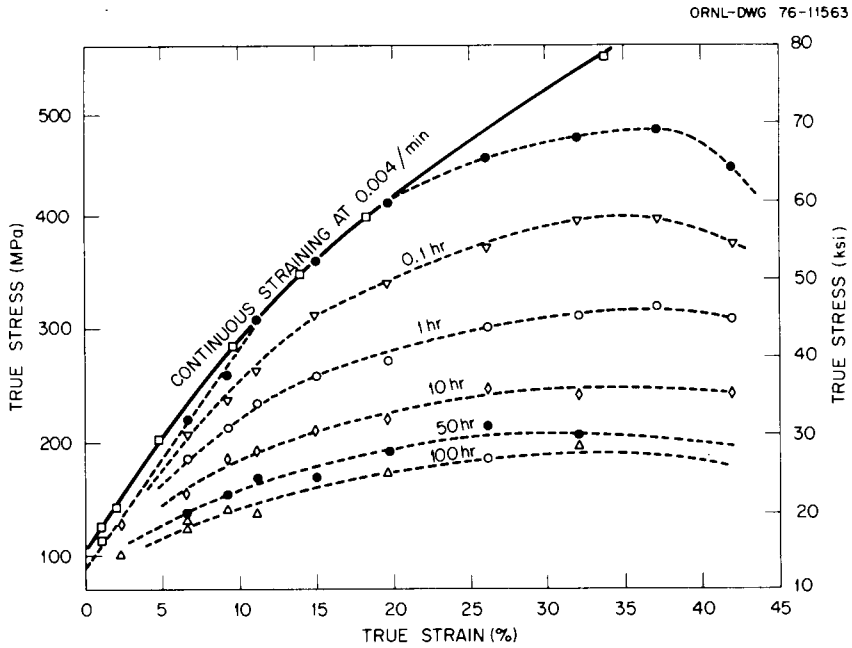


Fig. 3.118. True Stress vs True Strain Isochronous Relaxation Curve for Type 316 Stainless Steel at 593°C (1100°F) Obtained from Multiple Loading Tests (Specimen 22).

### 3.5.1.3 Uniaxial Testing of 2 1/4 Cr-1 Mo Steel — R. W. Swindeman

Creep tests to approximately 2000 hr have been completed at 538°C (1000°F) for heat 3P5601. Strain vs time plots are provided in Fig. 3.119 at several stress levels. Evidence of the "nonclassical" creep behavior, as described by Klueh,[116] exists for stresses in the range 103 to 138 MPa (15–20 ksi). In addition, two compressive creep tests were performed at 103 MPa (15 ksi). The data from the two tests agreed but differed significantly from tensile creep data. The compressive creep curves exhibited lower creep rates.

### 3.5.1.4 Material Testing and Inelastic Analysis in Support of TTTF — R. W. Swindeman

Several tests were performed to provide data for use in the analysis of the third specimen in the Thermal Transient Test Facility (TTTF). Materials of concern were 2 1/4 Cr-1 Mo steel, type 316 stainless steel, and Inconel 82 weld metal. Material was available to fabricate four creep specimens from the 2 1/4 Cr-1 Mo steel pipe. These were tested at stresses and temperatures chosen to supplement the data of Jaske and

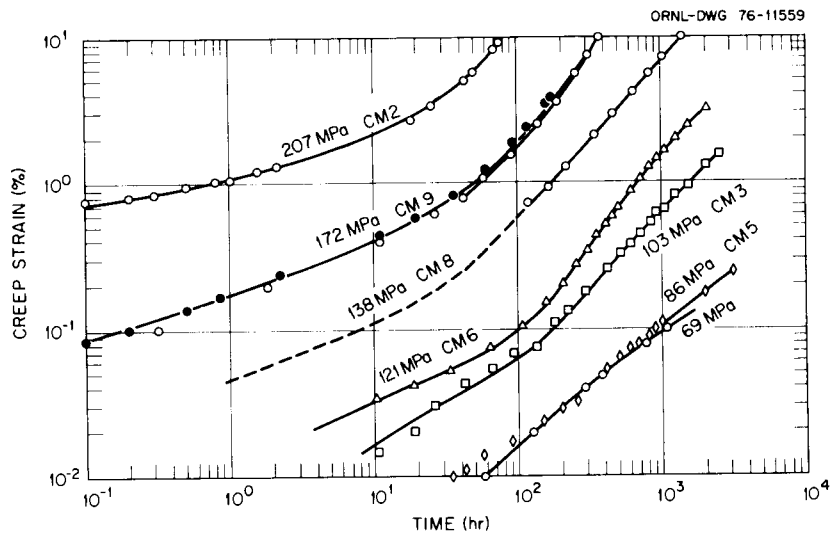


Fig. 3.119. Creep Curves for 2 1/4 Cr-1 Mo Steel (Heat 3P5601) at 538°C (1000°F).

Mindlin[117] and permit the development of an interim creep law for use in the 1D analysis of TTTF. Tests were performed at 51 and 86 MPa (7.5 and 12.5 ksi) at both 538 and 593°C (1000 and 1100°F). The creep curves for the four tests are plotted in Fig. 3.120. These data, as well as data of Jaske and Mindlin, were examined with respect to an interim creep equation and we decided that a simple Norton-Bailey expression combined with an Arrhenius temperature dependency would be adequate for representation of the data over a restricted range of time (1000 hr) and strain (less than 5%). Thus the creep strain $\varepsilon_c$ was represented by:

$$\varepsilon_c = At^m\sigma^n \exp(-Q/RT) \quad , \tag{4}$$

where $A = 4.83 \times 10^{14}$, $m = 0.75$, $n = 8.87$, and $Q = 431.4$ kJ/mole (103.1 kcal/mole), $R = 8.319$ J mole$^{-1}$ K$^{-1}$(1.987 cal mole$^{-1}$ K$^{-1}$), $\varepsilon_c$ is in percent, $\sigma$ is stress in ksi, $t$ is time in hr, and $T$ is temperature in K. The model greatly underestimated the observed creep strains at 51 MPa (7.5 ksi) as shown in Fig. 3.20(c) and (d). This is due, in part, to a significant change in the stress dependency of creep below 86 MPa (12.5 ksi) and 621°C (1150°F), which we chose to ignore. Additional testing is planned to confirm the trend of the data. If verified, then

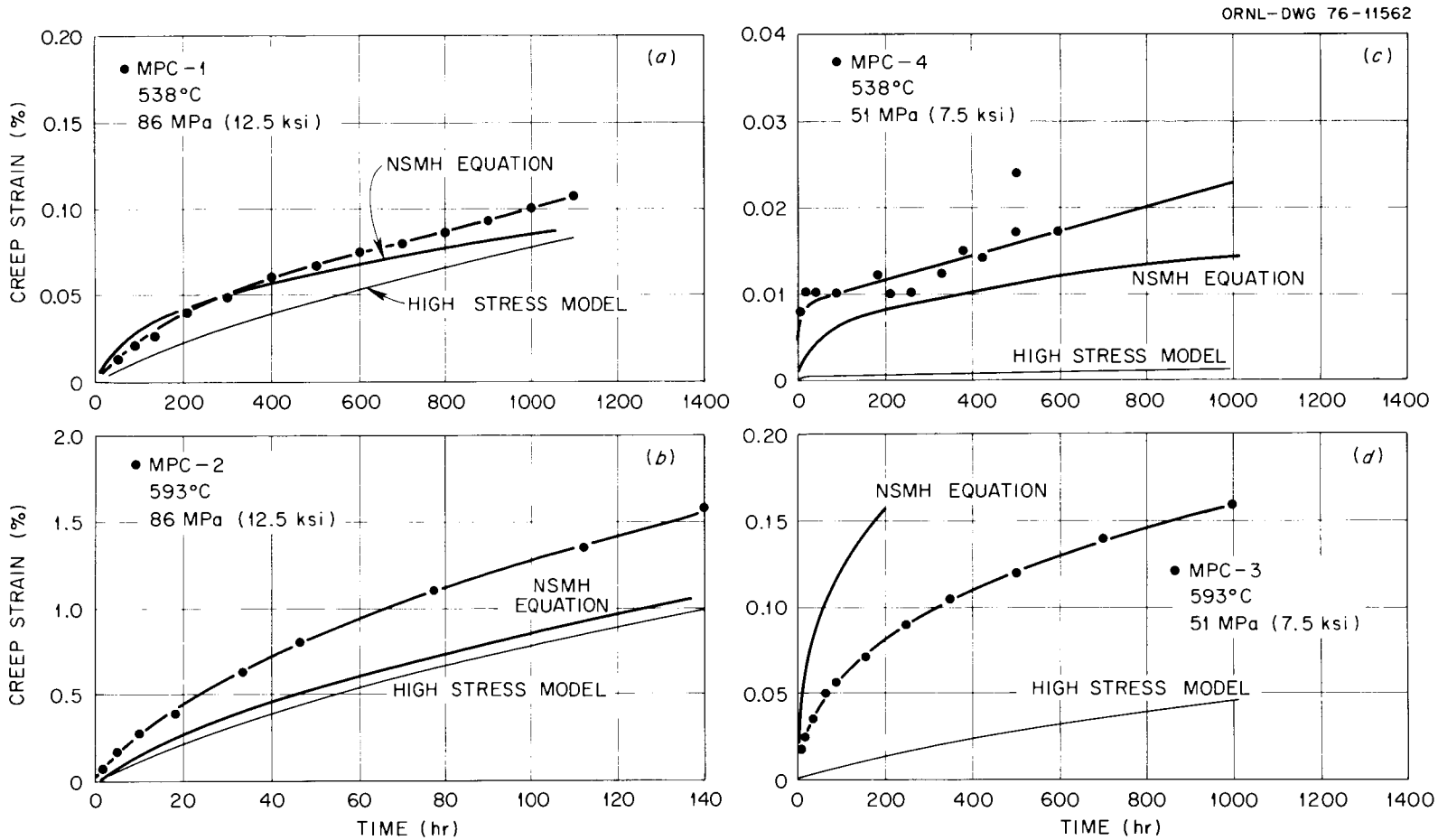


Fig. 3.120. Creep Curves for 2 1/4 Cr-1 Mo Steel (MPC heat) at Two Stresses and Two Temperatures.

the current equation proposed for inclusion in the *Nuclear Systems Materials Handbook* appears to be a better model for the data than the Norton-Bailey equation described above. A possible cause for relatively large creep strains at low stresses could be either eccentric loading of creep specimens or dimensional instability due to metallurgical changes. These factors will be considered in evaluating future test data.

Two specimens fabricated from 203-mm (8-in.) pipe of type 316 stainless steel (heat 8092297) were creep tested at 96.6 MPa (14 ksi) for 1000 hr at 538 and 593°C (1000 and 1100°F). Creep curves are plotted in Fig. 3.121 and compared with data for 16-mm (5/8-in.) and 25-mm (1-in.) plate. Also plotted in Fig. 3.121 are creep curves predicted by the existing *Nuclear Systems Materials Handbook* equation and

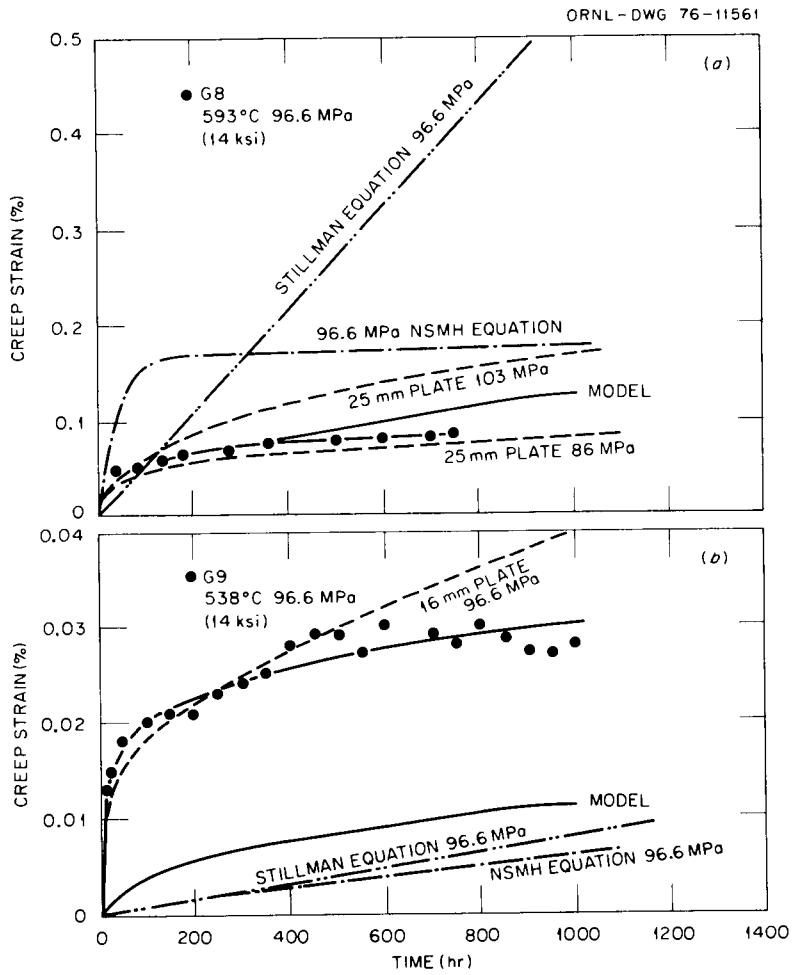


Fig. 3.121. Creep Curves for Type 316 Stainless Steel (Heat 8092297).

a recently developed substitute equation developed by Stillman et al.[113] We did not feel that these equations were a very good representation of the trend and again resorted to a Norton-Bailey model identical to Eq. (4) but having the following values for the constants: $A = 3.23 \times 10^8$; $m = 0.5$; $n = 4$, and $Q = 256.5$ kJ/mole (61.3 kcal/mole), where $\varepsilon_t$ is in percent, $\sigma$ is in ksi, and $T$ is in K. These constants are based on the behavior of 25-mm (1-in.) plate at 593°C (1100°F) and 16-mm (5/8-in.) plate at 538°C (1100°F). Recently, a new model for type 316 stainless steel has been developed by Booker, and it appears to be acceptable for representing this material.

Two creep tests were performed on Inconel 82 weld metal in the transverse orientation. These data, for a stress of 138 MPa (20 ksi), are plotted in Fig. 3.122 for 538 and 593°C (1000 and 1100°F). The data indicate the presence of significant time-dependent strain, and it appears that additional testing will be necessary to define the stress dependence of the creep. We intend to perform tests at 103 and 178 MPa (15 and 25 ksi) at 593°C. In addition to the creep tests, two cyclic tests were performed for comparison with data obtained at Battelle Columbus Laboratory (BCL). We found that our material was about 10% stronger than BCL material. This difference could be associated with either composition or specimen orientation relative to the weld.

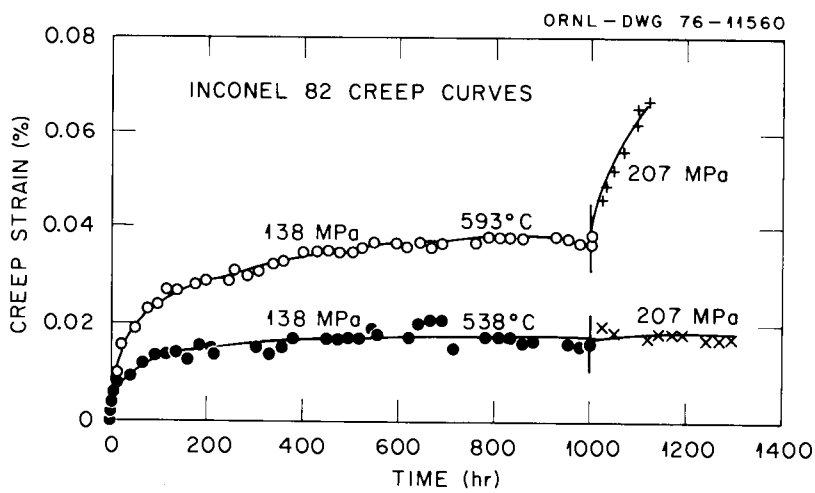


Fig. 3.122. Creep Curves for Inconel 82 Weld Metal at 538 and 593°C.

### 3.5.2 Investigations of Creep Failure Under Uniaxial and Multiaxial Conditions — C. C. Schultz (Babcock and Wilcox)

#### 3.5.2.1 Uniaxial Tests

The only remaining uniaxial test, BWR-7, has been in progress for approximately 33,600 hr at a constant stress of 110 MPa (16 ksi). The creep strain vs time response is shown in Fig. 3.123. Although tertiary creep based on a 0.2% offset from the minimum rate line began at 32,000 hr, rupture is not expected for an additional 5000 to 10,000 hr of testing. The stress vs time-to-rupture data for all constant-load uniaxial tests is shown in Fig. 3.124. Tables 3.26 and 3.27 of ref. 118 summarize the results of these tests.

#### 3.5.2.2 Multiaxial Tests

During this reporting period, tests BWTR-11, -12, and -13 began. The multiaxial tests are listed in Table 3.27, where of the two sets of stresses shown for each test; the first was derived from the mean-diameter formulas, and the second consists of average stresses.*

No tubular specimens ruptured during this reporting period; however, the stress vs time-to-rupture results for the previous multiaxial tests are compared with the uniaxial results in Fig. 3.125 based on the maximum principal stress from the mean-diameter formula.

Test BWTR-7 [equal biaxial tension of 138 MPa (20 ksi)] was completed near the end of the last reporting period, and thus only partial results were reported.[118] Complete creep strain-time results are now available and are shown in Fig. 3.126. The axial creep strain over the center 0.13 m (5 in.) of the 0.20-m (8-in.) test section was obtained by averaging the data from two opposed axial extensometers mounted on opposite sides of the

---

*The average or equilibrium stresses are given by

$$\sigma_r = -p/2 \ , \qquad \sigma_\theta = d_i p/2t \ , \qquad \sigma_z = d_i^2 p/4d_m t + P/\pi d_m t \ ,$$

where $\sigma_r$ = radial stress (sometimes considered negligible), $\sigma_\theta$ = circumferential stress, $\sigma_z$ = axial stress, $p$ = internal pressure, $P$ = superimposed axial load, $t$ = wall thickness, $d_i$ = inside diameter, and $d_m$ = mean diameter. In the corresponding mean-diameter formulas, $\sigma_r$ is usually considered negligible and $d_i$ is replaced by $d_m$.

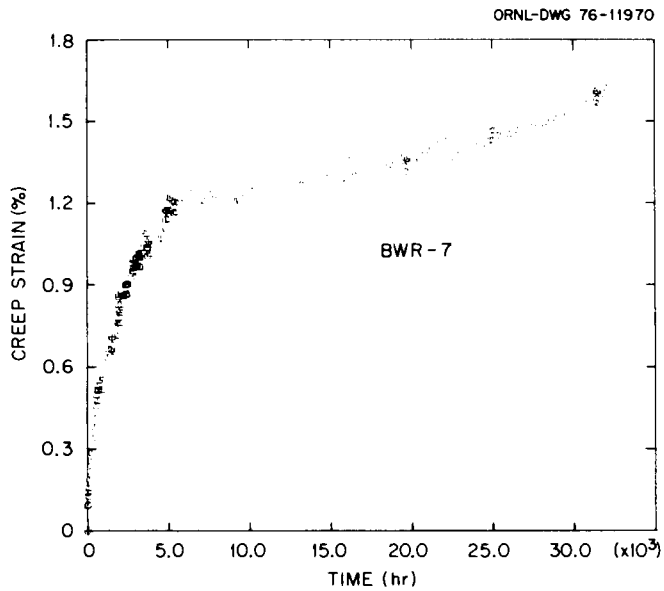


Fig. 3.123. Constant-Load Uniaxial Rupture Test at 110 MPa (16 ksi) and 593°C (1100°F). Type 304 stainless steel, heat 9T2796, 16-mm (5/8-in.) bar, reannealed at 1093°C (2000°F) for 30 min.

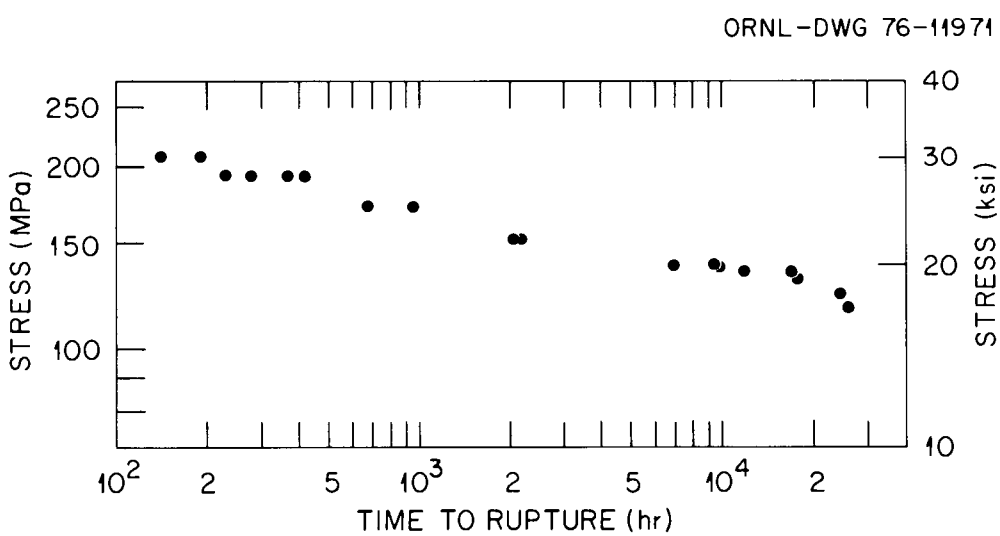


Fig. 3.124. Times to Rupture for Constant-Load Uniaxial Tests at 593°C (1100°F). Type 304 stainless steel, heat 9T2796, 16-mm (5/8-in.) bar, reannealed at 1093°C (2000°F) for 30 min.

Table 3.27. Biaxial Creep-Rupture Tests at 593°C (1100°F) for Type 304 Stainless Steel, Heat 9T2796, 49-mm (1.9-in.) Bar

| Test | Specimen | Internal Pressure | | Additional Axial Load | | Stress,[a] MPa (psi) | | | | | | Estd Rupture Time[b] (hr) | Test Time[c] (hr) |
|---|---|---|---|---|---|---|---|---|---|---|---|---|---|
| | | (MPa) | (psi) | (N) | (lb) | Circumferential | | Axial | | Effective | | | |
| BWTR-1 | 5R-37A | | | 32,637 | 7337 | | | 151 | (21,850) | 151 | (21,850) | 2,000 | 1997 R |
| | | | | | | | | 151 | (21,850) | 151 | (21,850) | | |
| BWTR-2 | 8R- 5A | 15.9 | 2300 | | | 151 | (21,850) | 75 | (10,925) | 130 | (18,920) | 2,000 | 1713 R |
| | | | | | | 143 | (20,700) | 68 | (9,800) | 124 | (17,940) | | |
| BWTR-3 | 7R- 5A | 15.9 | 2300 | 16,316 | 3668 | 151 | (21,850) | 151 | (21,850) | 151 | (21,850) | 2,000 | 584 R |
| | | | | | | 143 | (20,700) | 143 | (20,730) | 143 | (20,710) | | |
| BWTR-4 | 6R-37A | 7.9 | 1150 | 24,465 | 5500 | 75 | (10,925) | 151 | (21,850) | 130 | (18,920) | 2,000 | 3336 R |
| | | | | | | 71 | (10,350) | 147 | (21,280) | 127 | (18,430) | | |
| BWTR-5 | 9R- 3A | 7.3 | 1053 | 22,401 | 5036 | 69 | (10,000) | 138 | (20,000) | 119 | (17,320) | 5,000 | 2800 I |
| | | | | | | 65 | (9,480) | 134 | (19,490) | 116 | (16,880) | | |
| BWTR-6 | 10R- 3A | 14.5 | 2105 | | | 138 | (20,000) | 69 | (10,000) | 119 | (17,320) | 5,000 | 3272 R |
| | | | | | | 131 | (18,950) | 62 | (8,970) | 113 | (16,410) | | |
| BWTR-7 | 8R- 3A | 14.5 | 2105 | 14,937 | 3358 | 138 | (20,000) | 138 | (20,000) | 138 | (20,000) | 5,000 | 1925 R |
| | | | | | | 131 | (18,950) | 131 | (18,980) | 131 | (18,960) | | |
| BWTR-11 | 4X- 3A | 6.5 | 948 | 20,164 | 4533 | 62 | (9,000) | 124 | (18,000) | 107 | (15,590) | 10,000 | 1700 I |
| | | | | | | 59 | (8,530) | 121 | (17,540) | 105 | (15,190) | | |
| BWTR-12 | 3X- 3A | 13.1 | 1895 | | | 124 | (18,000) | 62 | (9,000) | 107 | (15,590) | 10,000 | 3500 I |
| | | | | | | 118 | (17,060) | 56 | (8,080) | 102 | (14,780) | | |
| BWTR-13 | 2X- 3A | 13.1 | 1895 | 13,443 | 3022 | 124 | (18,000) | 124 | (18,000) | 124 | (18,000) | 10,000 | 3200 I |
| | | | | | | 118 | (17,060) | 118 | (17,080) | 118 | (17,070) | | |

[a]The first set of stresses shown is based on the mean-diameter formulas and the second set on average stresses. The radial stress is considered negligible. 38 mm (1.50 in.) outside diameter and 1.9-mm (0.075-in.) wall thickness.

[b]The estimated rupture time is based on the maximum principal stress from the mean-diameter formula.

[c]R indicates rupture; I, in test.

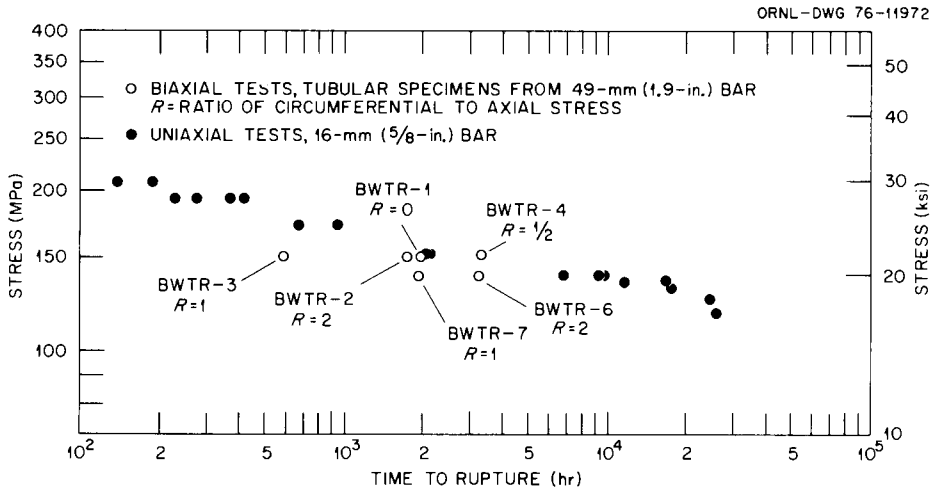


Fig. 3.125. Comparison of Uniaxial and Biaxial Rupture Data at 593°C (1100°F). Type 304 stainless steel, heat 9T2796, 49-mm (1.9-in.) bar, reannealed at 1093°C (2000°F) for 30 min.

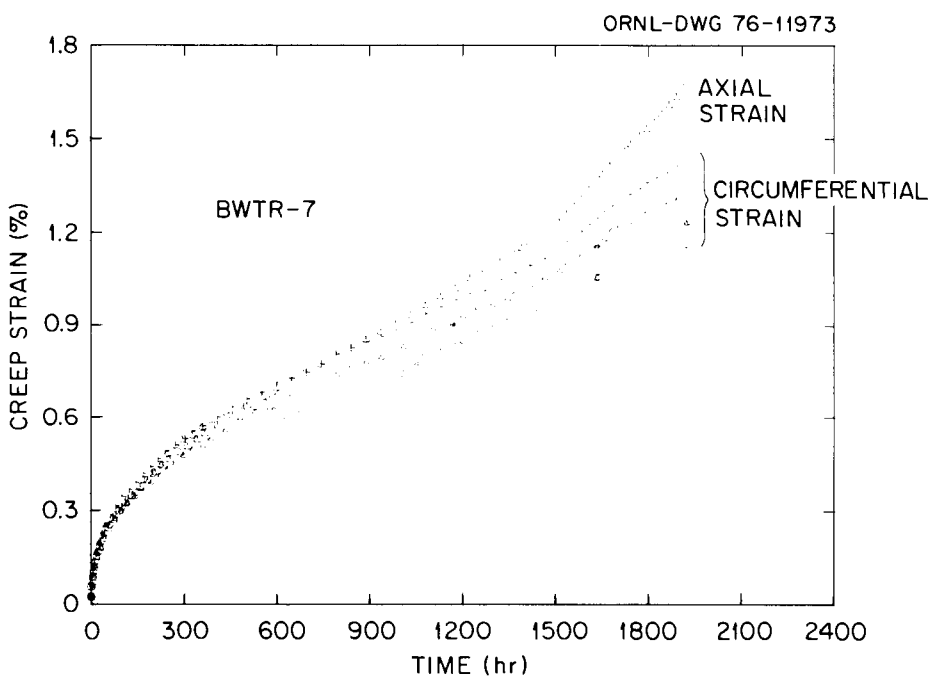


Fig. 3.126. Axial and Circumferential Creep Strains in a Constant-Load Biaxial Rupture Test. Tubular specimen with internal pressure and additional axial load. Equal biaxial tension of 138 MPa (20 ksi) at 593°C (1100°F). Outside diameter of 3.8 mm (1.50 in.) and wall thickness of 1.9 mm (0.075 in.). Type 304 stainless steel, heat 9T2796, 49-mm (1.9-in.) bar.

specimen. Radial displacement at the center of the gage length was monitored by three equally spaced pairs of DCDT probes. The three sets of circumferential strains shown in Fig. 3.126 were obtained by averaging the outputs of both members of each pair of radial probes.

The specimen diameter was measured when the test was interrupted[118] after 1636 hr under load and again upon completion of the test. At the center of the test section the average diametral growth was approximately 1.19 mm (0.047 in.) at failure, which corresponds to 3.1% permanent strain. At this axial location the diameter was constant (with respect to angular location) to within ±0.03 mm (0.001 in.). In-test measurements at this same approximate location indicated an average diametral growth of 1.24 mm (0.049 in.). Near the failure location, post-test measurements indicated an average diametral growth of 1.85 mm (0.073 in.), which corresponds to an average circumferential strain of 4.9%. At this same axial location the diameter was constant to within ±0.08 mm (0.003 in.).

Figure 3.127 shows the axial creep strain for test BWTR-5 at an axial stress of 138 MPa (20 ksi) and a circumferential stress of 69 MPa (10 ksi).

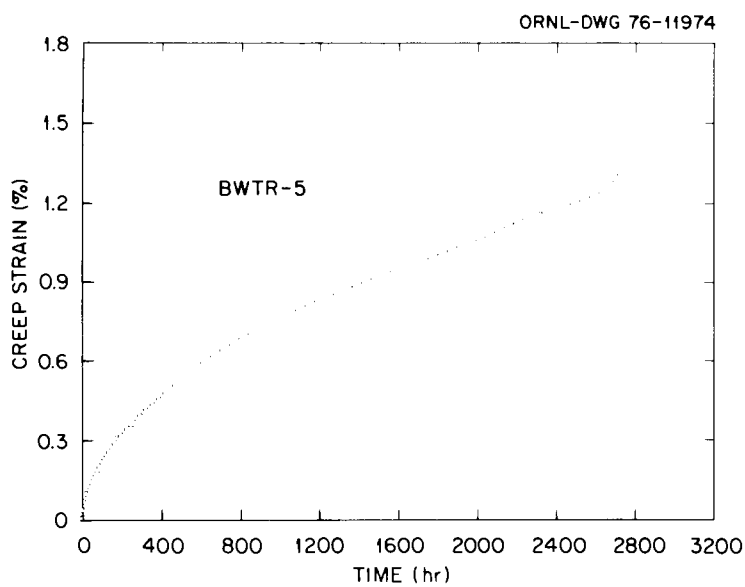


Fig. 3.127. Axial Creep Strain in a Constant-Load Biaxial Rupture Test. Tubular specimen with internal pressure and additional axial load. Axial stress of 138 MPa (20 ksi) and circumferential stress of 69 MPa (10 ksi) at 593°C (1100°F). Outside diameter of 38 mm (1.50 in.) and wall thickness of 1.9 mm (0.075 in.). Type 304 stainless steel, heat 9T2796, 49-mm (1.9-in.) bar.

No in-test measurements of specimen diameter are being made in this test. When the test was interrupted after 2689 hr the diameter had been reduced less than 0.03 mm (0.001 in.).

Figures 3.128 and 3.129 show the axial and circumferential creep strains, respectively, for test BWTR-12. This test, under pure internal pressure, is at a circumferential stress of 124 MPa (18 ksi) and an axial stress of 62 MPa (9 ksi). After approximately 2800 hr, the temperature was intentionally lowered approximately 110°C (200°F) in anticipation of a power outage scheduled for a period when the test would be unattended. When the specimen was returned to the test temperature, the outputs of several of the DCDTs were considerably less than they had been before the power outage. The distinct discontinuities in the data of Figs. 3.128 and 3.129 reflect these changes. The axial strain was expected to be much less than that shown in Fig. 3.128. In the two previous tests with pure internal pressure (BWTR-2 and -6), the measured axial creep strain was about 0.1%.

Figure 3.130 shows the axial and circumferential creep strains for test BWTR-13 at an equal biaxial tension of 124 MPa (18 ksi). The discontinuities in the data at approximately 2000 and 2500 hr were preceeded by temperature drops of 110°C (200°F) and 83°C (150°F) due to temperature controller malfunctions. This unexplained behavior is similar to that during test BWTR-12. This test was interrupted after 3214 hr for diameter measurements, which showed an average increase of approximately 0.91 mm (0.036 in.) at the center of the test section. This corresponds to a permanent circumferential strain of 2.4%. At another axial location, the average diametral growth was 1.32 mm (0.052 in.), or about 3.5% permanent strain.

The axial creep strain vs time results for test BWTR-11 at an axial stress of 124 MPa (18 ksi) and a circumferential stress of 62 MPa (9 ksi), which are shown in Fig. 3.131, are considered unsatisfactory. A DCDT and an extensometer weld failed during this test, and it is too early to tell whether or not repairs have significantly improved the data.

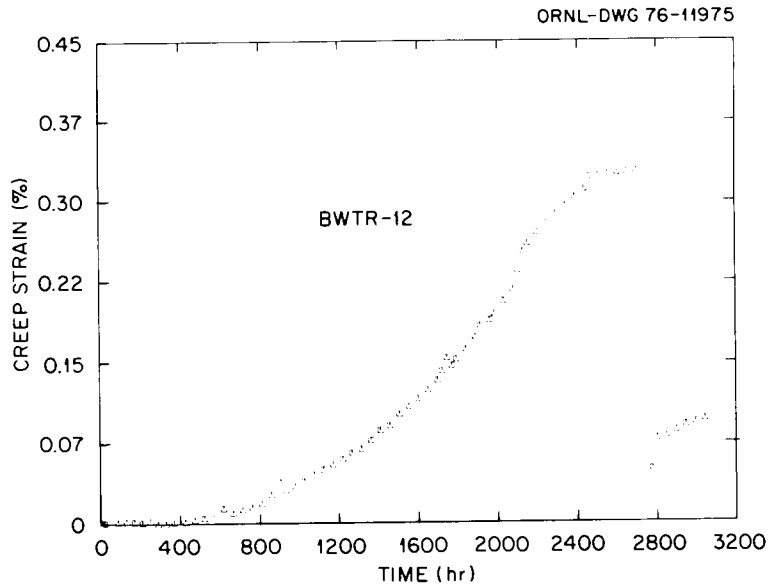


Fig. 3.128. Axial Creep Strain in a Constant-Load Biaxial Rupture Test. Tubular specimen with internal pressure. Circumferential stress of 124 MPa (18 ksi) and axial stress of 62 MPa (9 ksi) at 593°C (1100°F). Outside diameter of 38 mm (1.50 in.) and wall thickness of 1.9 mm (0.075 in.). Type 304 stainless steel, heat 9T2796, 49-mm-diam (1.9-in.) bar.

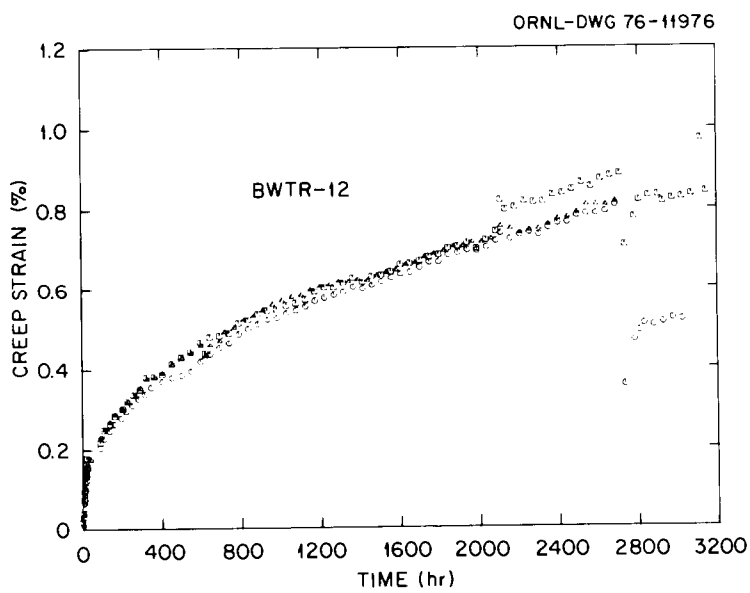


Fig. 3.129. Circumferential Creep Strain in a Constant-Load Biaxial Rupture Test. Tubular specimen with internal pressure. Circumferential stress of 124 MPa (18 ksi) and axial stress of 62 MPa (9 ksi) at 593°C (1100°F). Outside diameter of 38 mm (1.50 in.) and wall thickness of 1.9 mm (0.075 in.). Type 304 stainless steel, heat 9T2796, 49-mm-diam (1.9-in.) bar.

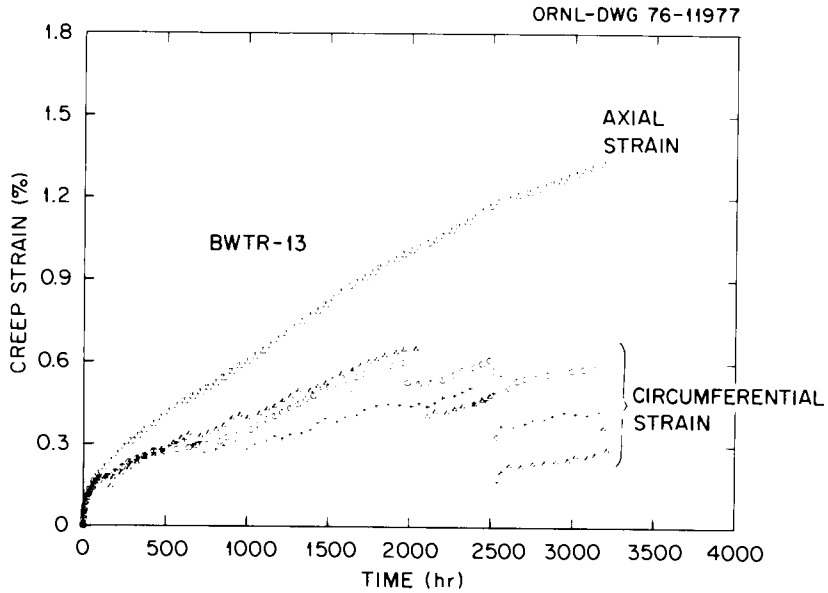


Fig. 3.130. Axial and Circumferential Creep Strains in a Constant-Load Biaxial Rupture Test. Tubular specimen with internal pressure and additional axial load. Equal biaxial tension of 124 MPa (18 ksi) at 593°C (1100°F). Outside diameter of 38 mm (1.50 in.) and wall thickness of 1.9 mm (0.075 in.). Type 304 stainless steel, heat 9T2796, 49-mm-diam (1.9-in.) bar.

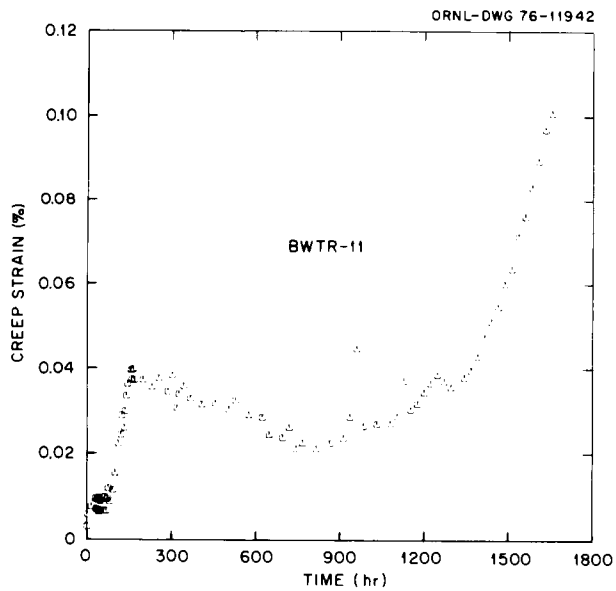


Fig. 3.131. Axial Creep Strain in a Constant-Load Biaxial Rupture Test. Tubular specimen with internal pressure and additional axial load. Axial stress of 124 MPa (18 ksi) and circumferential stress of 62 MPa (9 ksi) at 593°C (1100°F). Outside diameter of 38 mm (1.50 in.) and wall thickness of 1.9 mm (0.075 in.). Type 304 stainless steel, heat 9T2796, 49-mm-diam (1.9-in.) bar.

## 3.6 MECHANICAL PROPERTIES OF HTGR STEAM GENERATOR AND PRIMARY CIRCUIT MATERIALS* — J. R. DiStefano

The major overall objectives of this program are to (1) determine the compatibility of alloys planned for use in the HTGR steam-cycle system with their environment and (2) determine, compile, and analyze materials design data for the commercial HTGR. To achieve these objectives it is necessary to study the mechanical behavior (tensile, creep, low-cycle fatigue, and crack growth) of HTGR alloys at temperatures and in environments (helium and steam) appropriate to their service in the reactor.

### 3.6.1 Tensile Testing — A. Lystrup†

The FY 1976 work plan for tensile tests has been completed.

### 3.6.2 Environmental Creep Testing — A. Lystrup†

Environmental creep tests of HTGR structural alloys in simulated primary coolant helium and comparison tests in air have continued during the quarter. Six tests were completed during this period, and the results are shown in Table 3.28. In the three tests of 2 1/4 Cr-1 Mo steel temperature was constant at 593°C (1100°F), and increasing the stress from 69 MPa (10 ksi) to 103 MPa (15 ksi) lowered the rupture life in helium from 9660 hr (test 15023) to 1337 hr (test 16882) or 436 hr (test 16883). Cross sections of specimens from tests 15023 and 16883 are shown in Figs. 3.132 and 3.133. After 9660 hr exposure to HTGR helium at 593°C (test 15023) 2 1/4 Cr-1 Mo steel showed both intergranular and transgranular attack. Transgranular attack occurred to a depth of 14 to 16 μm in both the gage section and the shoulder section of the sample. In the shoulder section intergranular attack occurred to a depth of 20 μm, but in the gage section (near the fracture) cracks and/or intergranular attack occurred to a depth of almost 40 μm. In test 16883 the increased

---

*This work is supported by the Division of Nuclear Research and Applications.

†On assignment from Risö, Denmark.

Table 3.28. Results of Creep Tests Completed During the Quarter

| Material | Heat | Test | Temperature (°C) | Temperature (°F) | Stress (MPa) | Stress (ksi) | Rupture Life (hr) | Elongation at Rupture (%) |
|---|---|---|---|---|---|---|---|---|
| | | | Tests in Helium | | | | | |
| 2 1/4 Cr-1 Mo | X-6216 | 15023 | 593 | 1100 | 69 | 10 | 9660 | 39 |
| 2 1/4 Cr-1 Mo | 72768 | 16882 | 593 | 1100 | 103 | 15 | 1337 | 51 |
| 2 1/4 Cr-1 Mo | 36202 | 16883 | 593 | 1100 | 103 | 15 | 436 | 47 |
| Hastelloy X | 2600-3-4936 | 15772 | 649 | 1200 | 172 | 25 | 6466 | 35 |
| Hastelloy X | 2600-3-4936 | 16490 | 760 | 1400 | 103 | 15 | 2690 | 19 |
| | | | Test in Air | | | | | |
| Hastelloy X | 2600-3-4936 | 16269 | 816 | 1500 | 69 | 10 | 3453 | 19 |

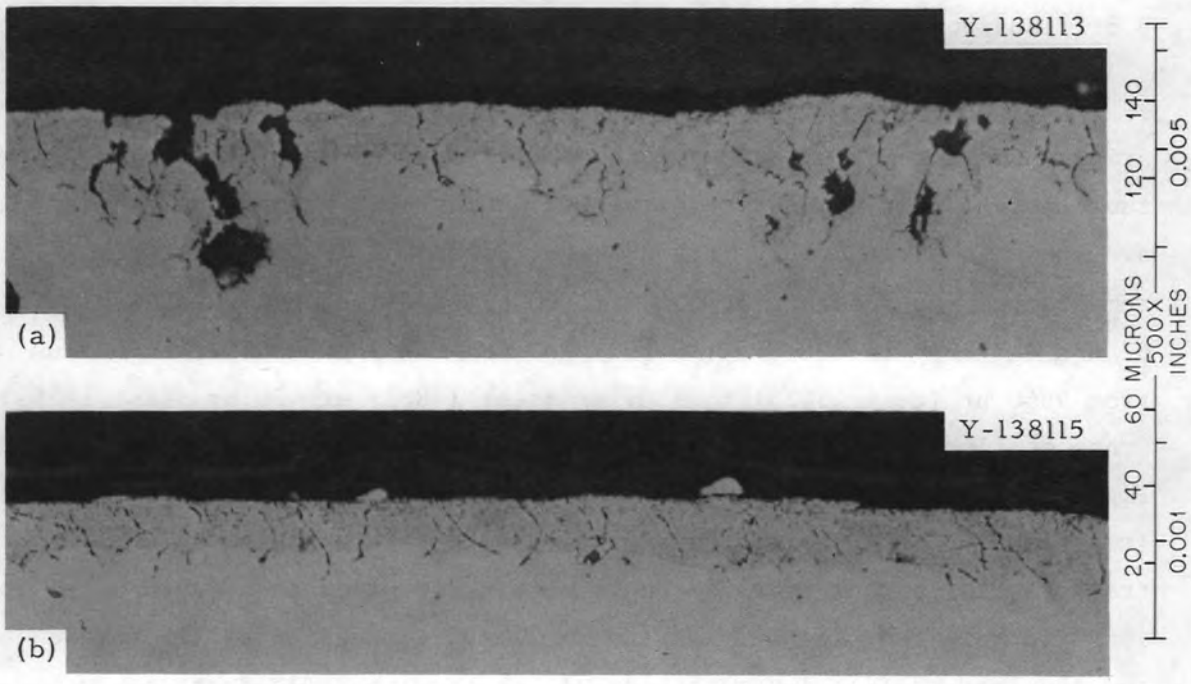


Fig. 3.132. Test 15023: 2 1/4 Cr-1 Mo Steel Exposed in HTGR Helium at 593°C (1100°F) for 9660 hr at 69 MPa (10 ksi). (a) Gage section. (b) Shoulder of the specimen.

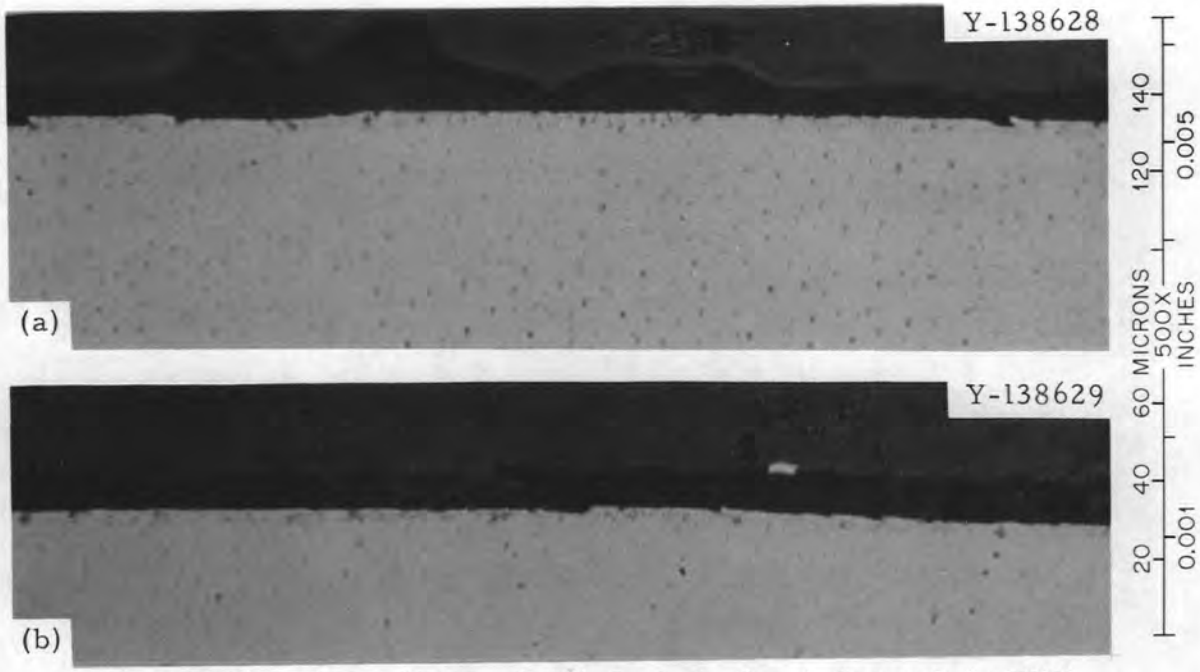


Fig. 3.133. Test 16883: 2 1/4 Cr-1 Mo Steel Exposed in HTGR Helium at 593°C (1100°F) for 436 hr at 103 MPa (15 ksi). (a) Gage Section. (b) Shoulder of the specimen.

stress caused rupture after only 436 hr, and, as indicated by Fig. 3.133, only slight attack of the 2 1/4 Cr-1 Mo steel specimen occurred.

In the three tests of Hastelloy X, temperature, stress, and environment were all varied, so comparisons of the data are not simple. Figure 3.134 shows the Hastelloy X specimen from test 15772. A thin oxide film is visible on the surfaces of both the gage and shoulder sections. In addition the sample from the gage section has some large cracks to a depth of approximately 50 μm.

The matrix of our current creep tests is shown on Table 3.29. Maximum time in test is approaching 11,700 hr on Test 15046.

### 3.6.3. Fatigue-Life Testing — J. P. Strizak

Testing is continuing to characterize the effects of creep-fatigue and environmental interaction on the failure behavior of HTGR materials. Generally, the method of strain range partitioning is being used as a guide in developing data such that the fatigue life of any complex cycle at temperatures within the creep range might be predicted. The method

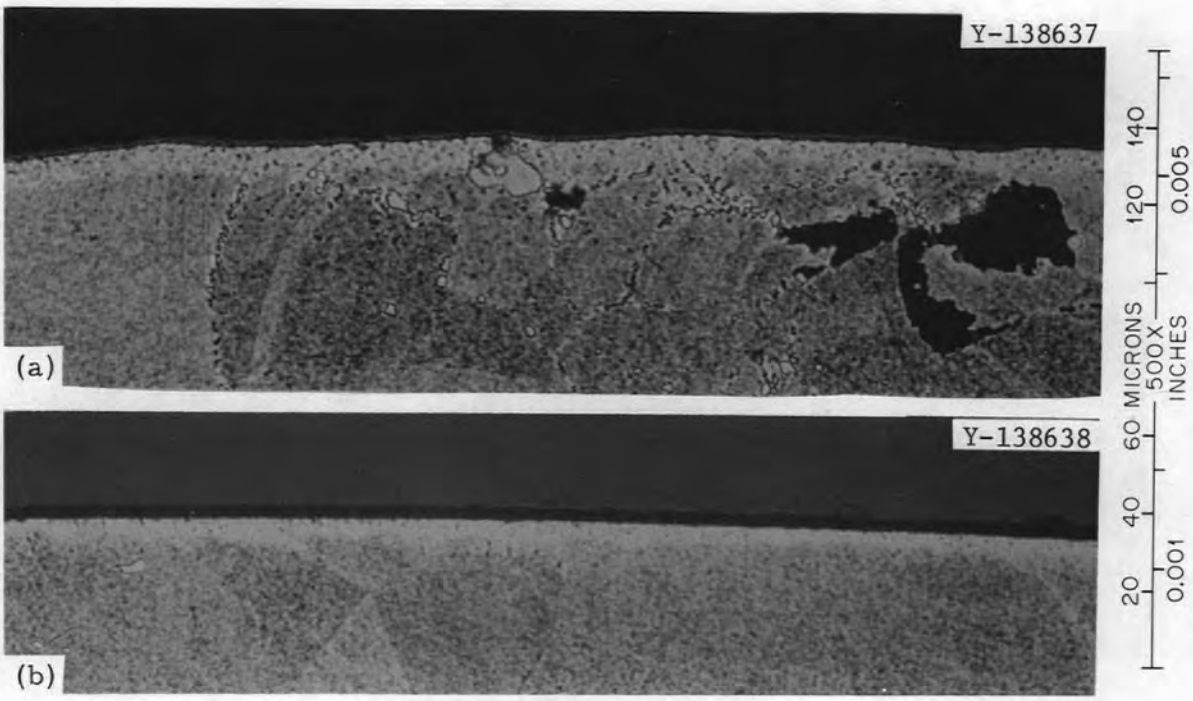


Fig. 3.134. Hastelloy X Exposed in HTGR Helium (Test 15772) at 649°C (1200°F) at 172 MPa (25 ksi) for 6466 hr. (a) Gage section. (b) Shoulder of the specimen.

Table 3.29. Current Creep Tests in Helium and Air

| Test | Test Frame | Material | Heat | Temperature (°C) | Temperature (°F) | Stress (MPa) | Stress (ksi) |
|---|---|---|---|---|---|---|---|
| | | | Helium Tests | | | | |
| 17332 | I-160 | Hastelloy X | 2600-3-4936 | 816 | 1500 | 69 | 10 |
| 15046 | I-161 | 2 1/4 Cr-1 Mo | X-6216 | 538 | 1000 | 103 | 15 |
| 17328 | I-162 | Hastelloy X | 2600-3-4936 | 704 | 1300 | 103 | 15 |
| 15363 | I-163 | 9 Cr-1 Mo | 316381-1A | 538 | 1000 | 103 | 15 |
| 15369 | I-164 | 2 1/4 Cr-1 Mo | 36202 | 538 | 1000 | 103 | 15 |
| 15374 | I-165 | 2 1/4 Cr-1 Mo | 36202 | 482 | 900 | 172 | 25 |
| 16126 | I-166 | Hastelloy X | 2600-3-4936 | 871 | 1600 | 34 | 5 |
| 17329 | I-167 | Hastelloy X | 2600-3-4936 | 649 | 1200 | 138 | 20 |
| 17333 | I-168 | 2 1/4 Cr-1 Mo | X-6216 | 593 | 1100 | 138 | 20 |
| 17334 | I-169 | 2 1/4 Cr-1 Mo | X-6216 | 593 | 1100 | 103 | 15 |
| | | | Air Tests | | | | |
| 16263 | I-170 | 2 1/4 Cr-1 Mo | 36202 | 482 | 900 | 207 | 30 |
| 16264 | I-171 | 2 1/4 Cr-1 Mo | 36202 | 538 | 1000 | 103 | 15 |
| 16360 | I-172 | 2 1/4 Cr-1 Mo | 72768 | 593 | 1100 | 69 | 10 |
| 16267 | I-173 | Hastelloy X | 2600-3-4936 | 649 | 1200 | 172 | 25 |
| 16268 | I-174 | Hastelloy X | 2600-3-4936 | 704 | 1300 | 138 | 20 |
| 17330 | I-175 | Hastelloy X | 2600-3-4936 | 760 | 1400 | 138 | 20 |

involves partitioning the inelastic strain range traversed by a cycling specimen into four types:

$\Delta\varepsilon_{pp}$ = tensile plastic strain reversed by compressive plastic strain,

$\Delta\varepsilon_{pc}$ = tensile plastic strain reversed by compressive creep strain,

$\Delta\varepsilon_{cp}$ = tensile creep strain reversed by compressive plastic strain, and

$\Delta\varepsilon_{cc}$ = tensile creep strain reversed by compressive creep strain.

Here "plastic" strain is defined as time-independent inelastic strain, while "creep" strain is defined as time-dependent inelastic strain. Briefly, the method involves two steps. First, the four types of strain are related, respectively, by "life relationships" to $N_{pp}$, $N_{pc}$, $N_{cp}$, and $N_{cc}$, where $N_i$ is the expected life of a specimen cycled in solely $\Delta\varepsilon_i$ strain. Then for a given complex cycle of known inelastic strain components the predicted cyclic life, $N$, is given by

$$\frac{1}{N} = \frac{F_{pp}}{N_{pp}} + \frac{F_{pc}}{N_{pc}} + \frac{F_{cp}}{N_{cp}} + \frac{F_{cc}}{N_{cc}} \quad ,$$

where, for example, $F_{pp} = \Delta\varepsilon_{pp}/\Delta\varepsilon_{\text{in}}$, $\Delta\varepsilon_{\text{in}}$ being the total inelastic strain range.

Results of analysis of current ORNL data by this technique have been reported previously[76] and are given in Fig. 3.79 (p. 206). Tests were conducted by introducing constant-strain hold periods each cycle at peak tensile and/or compressive amplitudes. If $\Delta\sigma_r$ is the magnitude of the total stress decrease during relaxation, then for a compressive hold test (Fig. 3.69, p. 187), for example, the $\Delta\varepsilon_{pc}$ and $\Delta\varepsilon_{pp}$ strain components are given by

$$\Delta\varepsilon_{pc} = \Delta\sigma_r/E \qquad \text{and} \qquad \Delta\varepsilon_{pp} = \Delta\varepsilon_{\text{in}} - \Delta\varepsilon_{pc} \ .$$

As reported earlier,[66] examination of the relaxation curves obtained for the tests with strain hold periods indicated that the tests could be approximated by a form of the Gittus equation, expressed by

$$\ln\ (\sigma_0/\sigma) = Ct^m\ ,$$

where $\sigma_0$ is the stress at the beginning of relaxation and $\sigma$ and $t$ are instantaneous values of stress amplitude and time during relaxation. The behavior of stress amplitude with increasing hold time is given in Fig. 3.135. Because of the relatively small magnitude of the total stress decrease during relaxation even over long periods of time, the inelastic strain components $\Delta\varepsilon_{pc}$ and $\Delta\varepsilon_{cp}$ are limited to low strain ranges. Further, $\Delta\varepsilon_{pc}$, $\Delta\varepsilon_{cp}$, and $\Delta\varepsilon_{cc}$ account for only 10 to 20% of the total inelastic strain, which might explain the scatter observed in the data plotted in Fig. 3.79. To establish well-defined life relationships $\Delta\varepsilon_{pc}$, $\Delta\varepsilon_{cp}$, and $\Delta\varepsilon_{cc}$ strain components at higher strain values are needed; and, further, these should constitute the major portion (at least 50%) of the total inelastic strain traversed by a specimen for a particular cycle of interest.

Recently, the capability of introducing stress hold periods was developed on an existing ORNL fatigue testing system. Fully reversed

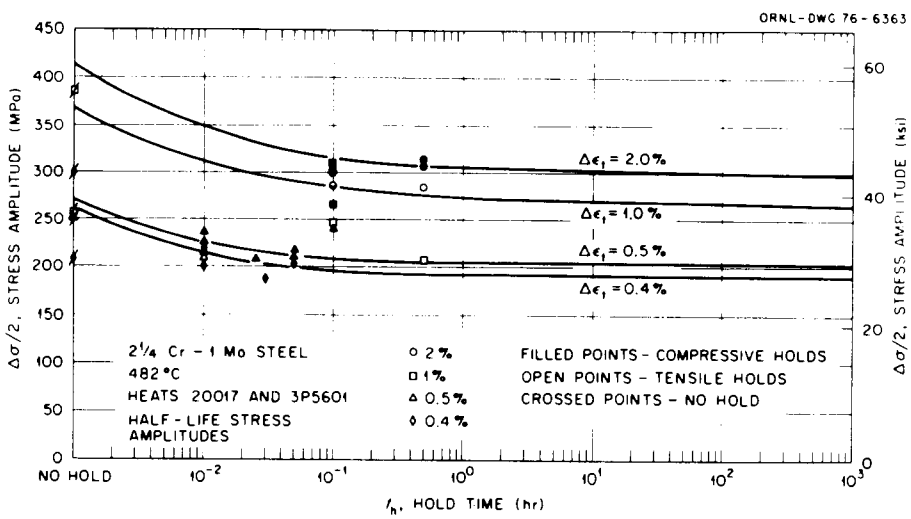


Fig. 3.135. Variation of Half-Life Stress Amplitude with Hold Time for Two Heats of Isothermally Annealed 2 1/4 Cr-1 Mo Steel at 482°C (900°F).

strain tests are conducted at a constant strain rate, and a constant stress hold period is introduced during the tensile and/or compressive halves of each cycle.

A typical hysteresis loop from an actual test is given in Fig. 3.136. The partitioned $\Delta\varepsilon_{pc}$ component for the test accounted for the major portion of the total inelastic strain, $\Delta\varepsilon_{in}$. Data from tests involving stress hold periods conducted to date are given in Fig. 3.137.

Testing will continue in order to develop the life relationships for the four types of inelastic strain ranges. The effects of temperature, heat-to-heat variation, heat treatment, and aging on the creep-fatigue and environmental behavior of HTGR materials will be examined. A second strain controller with a stress hold period capability is presently being fabricated and is intended for installation on the fatigue testing system that will house the environmental chamber for conducting tests in helium and in vacuum. Scheduled delivery of the environmental chamber and strain controller is for mid-August 1976.

### 3.6.4 Subcritical Crack Growth Studies — W. R. Corwin

This study uses isothermally annealed material from two heats of Babcock and Wilcox 2 1/4 Cr-1 Mo ferritic steel, 20017 and 3P5601. Its mechanical properties have been reported in previous quarterlies.

Testing at 593°C (1100°F) in air, steam, simulated HTGR primary coolant helium, and vacuum was emphasized this quarter. Additional data have now been gathered and allow representation of crack growth rate over four decades of testing frequencies at 593°C (1100°F) in air. As shown in Fig. 3.138, the crack growth rate at a given $\Delta K$ level increases with decreasing frequency, as expected. Along with results just obtained at 510°C (950°F) over five decades of frequency, these data form a broad base from which the Fatigue Crack Propagation (FCP) behavior of 2 1/4 Cr-1 Mo steel can be evaluated. Efforts to parametrize all our test results to date are currently under way by use of the general method outlined by Carden[119] or Döner.[120] We expect to complete this task during the next quarter.

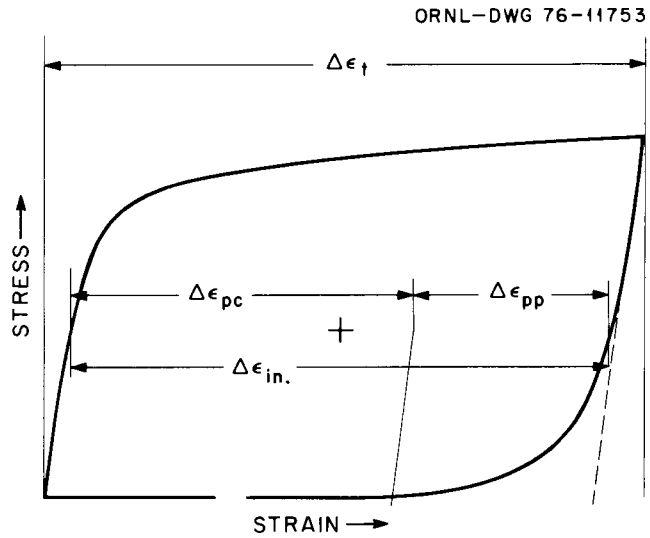


SPECIMEN NO. ITT-11

$\Delta\epsilon_t$ = 2.0%

$\Delta\epsilon_{in.}$ = 1.82%

$\Delta\epsilon_{pp}$ = 0.62%, $F_{pp}$ = 0.34

$\Delta\epsilon_{pp}$ = 1.20%, $F_{pc}$ = 0.66

$\epsilon = 4 \times 10^{-3}$/sec

Fig. 3.136. Partitioned Hysteresis Loop for a Creep-Fatigue Test Involving a Stress Hold Period in Compression at 538°C (1000°F). Material is 2 1/4 Cr-1 Mo steel, heat 3P5601.

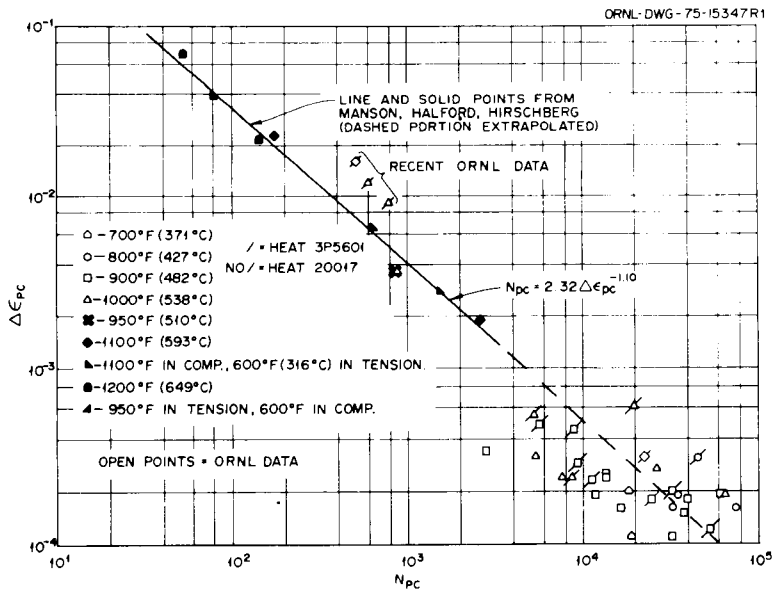


Fig. 3.137. Creep-Fatigue Data for 2 1/4 Cr-1 Mo Steel. Data include $\Delta\varepsilon_{pc}$ components from tests involving stress hold periods.

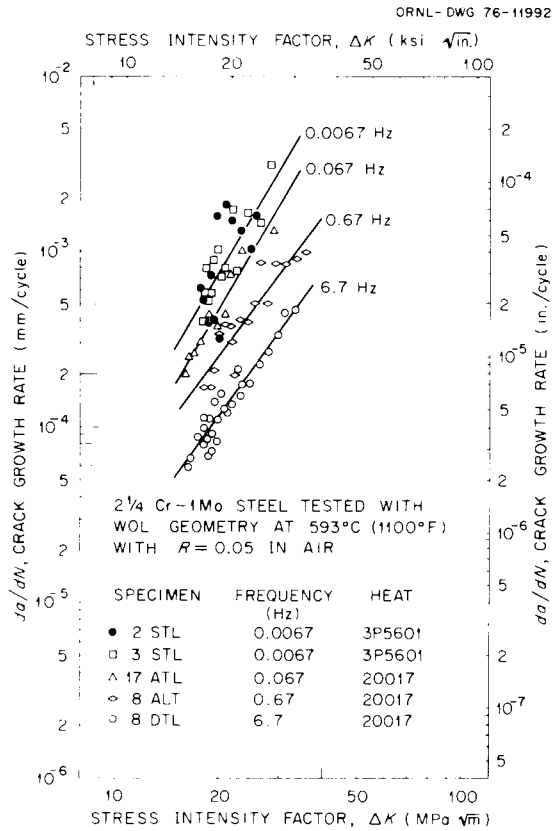


Fig. 3.138. Effect of Test Frequency on Crack Growth Rate.

Last quarter an apparent effect of test specimen geometry [wedge opening load (WOL) vs compact tension (CT)] on crack growth rate was indicated. This has now been tentatively resolved as a size effect. The smaller CT specimen appears to generate an excessively large plastic zone size relative to its planar dimensions, and this does not allow a completely valid calculation of stress intensity. For that reason it will be phased out of our test program. The environmental effects on the crack growth rate observed by use of the CT specimen exclusively are, however, quite real and presumed indicative of fatigue crack propagation completely within the framework of linear elastic fracture mechanics.

Comparative testing in steam at 593°C (1100°F), 0.067 Hz was completed this quarter. The results follow the general trend exhibited in previous tests (i.e. slightly lower crack growth rates compared with identical tests in air), as shown in Fig. 3.139. That the trend line shown for steam (least squares fit) has a smaller slope than the

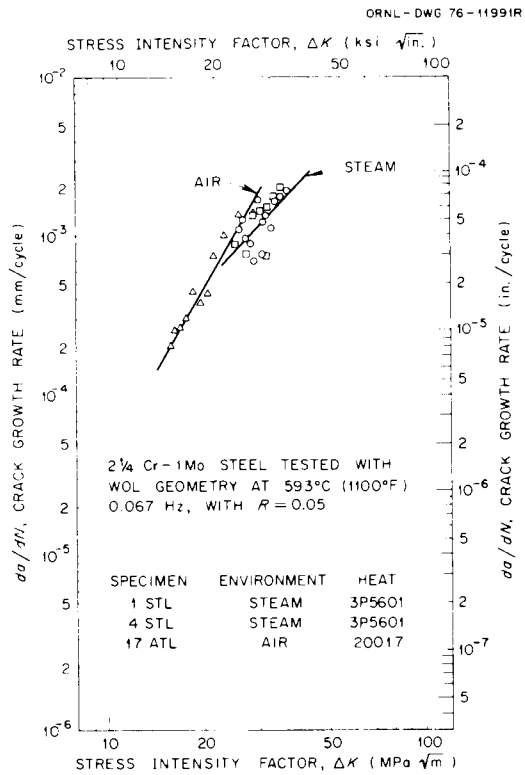


Fig. 3.139. Comparison of Crack Growth Rates in Air and Steam (Supersaturated in Air).

corresponding line for air contradicts our previous data. This appears to be due to the shortness of the data set and the large amount of scatter in it. Difficulties were enountered in obtaining crack growth data under these test conditions at $\Delta K$ values less than 20 to 24 MPa $\sqrt{m}$ (18–22 ksi $\sqrt{in.}$) because of intermittent crack arrest.

Comparison testing to determine the effects of both HTGR helium and vacuum at 593°C (1100°F), 0.67 Hz, were also conducted this quarter. Crack growth rate in the helium environment is less than that observed in air, as shown in Fig. 3.140. This duplicates the behavior seen at 510°C (950°F). That the HTGR helium environment is not completely inert, however, is apparently shown by the further reduction of crack growth rate in a vacuum of approximately $3 \times 10^{-4}$ Pa ($2 \times 10^{-6}$ torr). However, further experimental development of vacuum testing techniques is necessary. In tests discussed above visual crack length measurements necessitated opening the test chamber intermittently, with consequent exposure to the atmosphere and lengthy pump-down times. Work on fracture face marking and potential drop methods to eliminate this problem is under way.

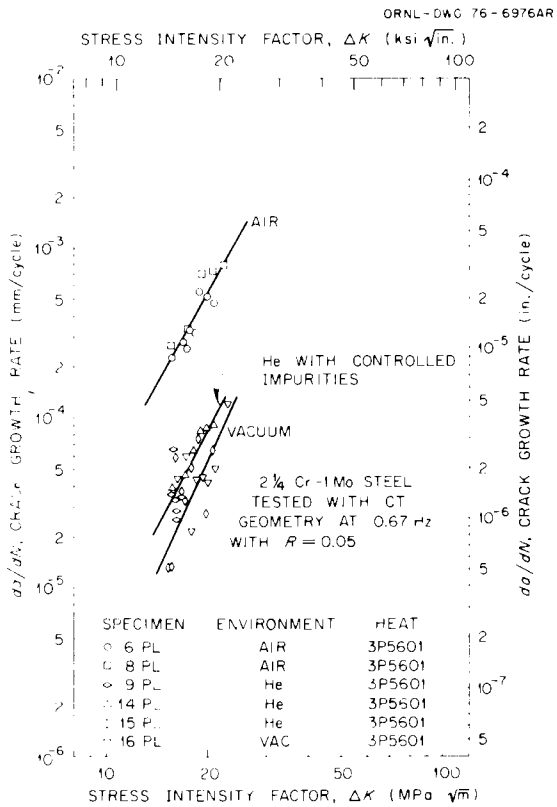


Fig. 3.140. Comparison of Crack Growth Rates in Air, Helium with Controlled Impurity Levels, and Vacuum at 593°C (1100°F).

## 3.7 REFERENCES


1. V. K. Sikka and M. K. Booker, *On the Use of Ultimate Tensile Strength to Correlate and Predict Creep and Creep Behavior of Types 304 and 316 Stainless Steel,* report in preparation.
2. M. K. Booker, *Mathematical Description of the Elevated-Temperature Creep Behavior of Type 304 Austenitic Stainless Steel,* report in preparation.
3. L. D. Blackburn, "Isochronous Stress-Strain Curves for Austenitic Stainless Steels," pp. 15–48 in *The Generation of Isochronous Stress-Strain Curves,* ed. by A. O. Schaefer, American Society of Mechanical Engineers, New York, 1972.
4. J. M. Steichen, *Effect of Thermal Aging on the High Strain Rate Tensile Properties of Type 304 Steel,* HEDL-TME-74-38 (July 1974).
5. J. M. Steichen, Hanford Engineering Development Laboratory, private communication, May 1976.

6. H. E. McCoy, Jr., and R. D. Waddell, Jr., "Mechanical Properties of Several Product Forms of a Single Heat of Type 304 Stainless Steel," *J. Eng. Mater. Technol.* 97: 343–49 (1975).

7. R. W. Swindeman, W. J. McAfee, and V. K. Sikka, "Product Form Variability in the Mechanical Behavior of Type 304 Stainless Steel at Room Temperature and 593°C (1100°F)," paper submitted for publication in the ASTM Symposium on Reproducibility and Accuracy of Mechanical Tests, St. Louis, Missouri, May 1976.

8. V. K. Sikka and M. K. Booker, "Rational Polynomial Tensile Stress-Strain Equation for Low-Strain Behavior of Austenitic Type 316 Stainless Steel," *Mechanical Properties Test Data for Structural Materials Quart. Prog. Rep. April 30, 1976,* ORNL-5150, pp. 55–63.

9. V. K. Sikka, H. E. McCoy, M. K. Booker, and C. R. Brinkman, "Heat-to-Heat Variations in Creep Properties of Types 304 and 316 Stainless Steels," *J. Pressure Vessel Techol.* 97: 243–51 (1975).

10. V. K. Sikka and C. R. Brinkman, "Relation Between Short- and Long-Term Elevated-Temperature Properties of Several Austenitic Stainless Steels," *Scr. Metall.* 10: 25–28 (1976).

11. V. K. Sikka, "Relation Between Tensile and Creep Properties," *Mechanical Properties Test Data for Structural Materials Quart. Prog. Rep. Jan. 31, 1976,* ORNL-5112, pp. 44–56.

12. V. K. Sikka and M. K. Booker, "Assessment of Tensile and Creep Data for Type 304 and 316 Stainless Steels," accepted for publication in *Journal of Pressure Vessel Technology*.

13. L. D. Blackburn, Hanford Engineering Development Laboratory, private communication, November 1973.

14. V. K. Sikka, T. L. Hebble, M. K. Booker, and C. R. Brinkman, *Influence of Laboratory Annealing on Tensile Properties and Time-Independent Design Stress Intensity Limits for Type 304 Stainless Steel,* ORNL-5175 (in preparation).

15. *NRIM Creep Data Sheets: Elevated-Temperature Materials Manufactured in Japan, 1973,* National Research Institute for Metals, Tokyo, 153, Japan.

16. M. K. Booker and V. K. Sikka, "Analysis of the Creep Strain-Time Behavior of Type 304 Stainless Steel," submitted to the Third International Congress on Pressure-Vessel Technology, Tokyo, April 18–22, 1977.

17. M. K. Booker, "Development of Creep Equation for Type 304 Stainless Steel," *Mechanical Properties Test Data for Structural Materials Quart. Prog. Rep. Jan. 31, 1976*, ORNL-5112, pp. 67–74.

18. M. K. Booker, "Development of Creep Equation," *Mechanical Properties Test Data for Structural Materials Quart. Prog. Rep. April 30, 1976*, ORNL-5150, pp. 91–108.

19. D. O. Hobson and M. K. Booker, *Materials Applications and Mathematical Properties of the Rational Polynomial Creep Equation*, report in preparation.

20. M. K. Booker and V. K. Sikka, *Interrelationships Between Creep Life Criteria for Four Nuclear Structural Materials*, ORNL/TM-4997 (August 1975).

21. M. K. Booker and V. K. Sikka, *Predicting the Strain to Tertiary Creep for Elevated-Temperature Structural Materials*, ORNL/TM-5403 (in press).

22. F. Garofalo et al., "Strain-Time, Rate-Stress, and Rate-Temperature Relations During Large Deformations in Creep," pp. 1-31–1-39 in *Joint International Conference on Creep*, The Institute of Mechanical Engineers, London, 1963.

23. D. Sidey and B. Wilshire, "Mechanisms of Creep and Recovery in Nimonic 80A," *Met. Sci. J.* 3: 56–60 (1969).

24. R. W. Swindeman and C. E. Pugh, *Creep Studies on Type 304 Stainless Steel (Heat 8043813) Under Constant and Varying Loads*, ORNL-TM-4427 (June 1974).

25. R. W. Swindeman, "Creep-Rupture Correlations for Type 304 Stainless Steel (Heat 9T2796)," pp. 1–30 in *Structural Materials for Service at Elevated Temperatures in Nuclear Power Generation*, MPC-1, ed. by A. O. Schaefer, American Society of Mechanical Engineers, New York, 1975.

26. V. K. Sikka and M. K. Booker, *Use of Ultimate Tensile Strength in Correlating and Predicting Creep and Creep Rupture Behavior of Types 304 and 316 Stainless Steel,* report in preparation.

27. H. E. McCoy, *Interim Report of Tensile and Creep Data for Type 304 Stainless Steel Plate (Reference Heat 9T2796, 2 in. Thick),* ORNL-TM-4627 (October 1974).

28. I. A. Oding et al., *Creep and Stress Relaxation in Metals,* transl. by E. Bishop, English ed. A. J. Kennedy, Oliver and Boyd, Edinburgh, 1965.

29. A. O. Schaefer, ed., *The Generation of Isochronous-Stress-Strain Curves,* American Society of Mechanical Engineers, New York, 1972.

30. V. K. Sikka, M. K. Booker, and J. P. Hammond, "Rational Polynomial Tensile Stress-Strain Equation for Low Strain Behavior of Types 304 and 316 Austenitic Stainless Steels," submitted for presentation at 1976 ASME Winter Annual Meeting, New York, November 28–December 2, 1976.

31. D. J. Roberts and S. A. Sterling, "A Parametric Method for the Development of Isochronous Stress-Strain Curves," pp. 1–14 in *The Generation of Isochronous-Stress-Strain Curves,* ed. by A. O. Schaefer, American Society of Mechanical Engineers, New York, 1972.

32. F. R. Larson and J. Miller, "Time-Temperature Relationship for Rupture and Creep Stresses," *Trans. ASME* 74: 765–75 (July 1952).

33. Y. N. Rabotnov, "Some Problems on the Theory of Creep," *Vestnik Moskovskovo Universiteta,* No. 10, 1948. Available in English translation as NACA-TM-1353.

34. R. M. Goldhoff, "The Application of Rabotnov's Creep Parameter," *Proc. Am. Soc. Test. Mater.* 61: 908–19 (1961).

35. V. K. Sikka, C. R. Brinkman, R. W. Swindeman, and M. K. Booker, *Residual Cold Work and Its Influence on Tensile and Creep Properties of Types 304 and 316 Stainless Steels,* ORNL/TM-5192 (January 1976).

36. C. E. Pugh et al., *Currently Recommended Constitutive Equations for Inelastic Design Analysis of FFTF Components,* ORNL-TM-3602 (September 1972).

37. W. E. Stillman, M. K. Booker, and V. K. Sikka, "Mathematical Description of the Creep Strain-Time Behavior of Type 316 Stainless Steel," submitted to Second International Conference on Mechanical Behavior of Materials, Boston, August 16–20, 1976.

38. M. K. Booker and B.L.P. Booker, *Development and Implementation of a Mechanical Properties Data Storage and Retrieval System*, ORNL/TM-5330 (June 1976).

39. M. W. Moyer and J. P. Hammond, *Ultrasonic Measurement of Elastic Constants at Temperatures from 24 to 1100°C*, Y-2047 (March 1976).

40. J. P. Hammond, "Elastic Properties of Engineering Construction Materials," *Mechanical Properties Test Data for Structural Materials Quart. Prog. Rep. July 31, 1975*, ORNL-5106, pp. 100–11.

41. J. P. Hammond, "Elastic Properties of Engineering Materials," *Mechanical Properties Test Data for Structural Materials Quart. Prog. Rep. Oct. 31, 1974*, ORNL-5103, pp. 161–67.

42. M. Kikuchi, "Anisotropy and Its Temperature Dependence of Single Crystals and Polycrystal of 18-12 Type Stainless Steel," *Trans. Jap. Inst. Met.* 12: 417–21 (May 1971).

43. E. Bolling and R. T. King, "Preliminary Report on Effect of Postweld Heat Treatment on Type 308 Stainless Steel Submerged-Arc Welds," *LMFBR Materials Development Program Quart. Prog. Rep. Dec. 31, 1975*, ORNL-5131, pp. 175–82.

44. R. T. King and D. P. Edmonds, "Structure and Properties of a 16-8-2 Submerged-Arc Weld," *Mechanical Properties Test Data for Structural Materials Quart. Prog. Rep. April 30, 1976*, ORNL-5150, pp. 135–46.

45. B. R. Dewey, L. Adler, R. T. King, and K. V. Cook, "Measurements of Anisotropic Elastic Constants for Weld Metal," Society for Experimental Stress Analysis Paper WR-11-1975, May 1976.

46. R. L. Klueh, "Creep-Rupture Properties of 2 1/4 Cr-1 Mo Steel," *Mechanical Properties Test Data for Structural Materials Quart. Prog. Rep. Oct. 31, 1975*, ORNL-5107, pp. 141–54.

47. Ibid., *Apr. 30, 1976*, ORNL-5150, pp. 148–51.

48. F. Garofalo et al., "Creep and Creep-Rupture Relationships in an Austenitic Stainless Steel," *Trans. AIME* 221: 310–19 (1961).

49. W. E. Leyda and J. P. Rowe, *A Study of Time for Departure from Secondary Creep for Eighteen Steels*, ASM Technical Report P9-6.1, American Society for Metals, Metals Park, Ohio, 1969.

50. R. L. Klueh, "The Relationship Between Rupture Life and Creep Properties of 2 1/4 Cr-1 Mo Steel," *Nucl. Technol.* 26: 287–96 (1975).

51. R. L. Klueh, "Heat-to-Heat Variation of 2 1/4 Cr-1 Mo Steel," *Mechanical Properties Test Data for Structural Materials Quart. Prog. Rep. July 31, 1975*, ORNL-5106, pp. 131–44.

52. R. L. Klueh, "Heat-to-Heat Variations of 2 1/4 Cr-1 Mo Steel," *Mechanical Properties Test Data for Structural Materials Quart. Prog. Rep. Jan. 31, 1976*, ORNL-5112, pp. 92–101.

53. R. L. Klueh, *Heat Treatment Effects on the Tensile Properties of Annealed 2 1/4 Cr-1 Mo Steel*, ORNL-5144 (May 1976).

54. R. J. Beaver, B. C. Leslie, and G. M. Slaughter, "2 1/4 Cr-1 Mo Steel Tubesheet Forging Development and Characterization," *Fuels and Materials Development Program Quart. Prog. Rep. June 30, 1974*, ORNL-TM-4688, pp. 29–35.

55. R. G. Baker and J. Nutting, "The Tempering of 2 1/4 Cr-1 Mo Steel After Quenching and Normalizing," *J. Iron Steel Inst.* 192: 257–68 (1959).

56. K. F. Hale, "Study of Creep in a Chromium-Molybdenum Steel," *Proc. 4th Intern. Conf. Electron Microscopy*, Vol. 1, 650–58, Springer-Verlag, Berlin, 1960.

57. M. C. Murphy and G. D. Branch, "Metallurgical Changes in 2.25 CrMo Steels During Creep-Rupture Test," *J. Iron Steel Inst.* 209: 546–61 (1971).

58. G. V. Smith, *Supplemental Report on the Elevated-Temperature Properties of Chromium-Molybdenum Steels (An Evaluation of 2 1/4 Cr-1 Mo Steel), ASTM Data Ser. Publ.*, DS 6 S2, American Society for Testing and Materials, Philadelphia, March 1971.

59. E. B. Norris, G. J. Schnabel, and R. D. Wylie, "Properties of Cr-Mo Piping Materials After Service at 1000°F and 1050°F," paper presented at International Conference on Creep and Fatigue in Elevated Temperature Applications, Philadelphia, 1973 and Sheffield, U.K., April 1974.

60. R. H. Hiltz and L. H. Kirschler, *MSAR Evaluation of Candidate Ferritic Alloys for LMFBR Service,* MSAR-69-139, Mine Safety Appliance Research Corp. (July 1969).

61. L. H. Kirschler, R. H. Hiltz, and S. J. Rodgers, *Effect of High Temperature Sodium on the Mechanical Properties of Candidate Alloys for the LMFBR Program,* MSAR-70-76, Mine Safety Appliance Research Corp. (May 1970).

62. R. H. Hiltz, L. H. Kirschler, and R. C. Andrews, *Tensile Strengths of Standard 2 1/4 Cr-1 Mo Steel After 20,000-Hour Exposure in 1050F Sodium,* MSAR-71-78, Mine Safety Appliance Research Corp. (April 1971).

63. R. H. Hiltz, L. H. Kirschler, and R. C. Andrews, *Tensile Strengths of Standard 2 1/4 Cr-1 Mo Steel After 10,000, 20,000, and 26,500 Hour Exposures in 1050F Sodium,* MSAR-72-286, Mine Safety Appliance Research Corp. (December 1972).

64. R. L. Klueh and J. M. Leitnaker, "An Analysis of the Decarburization and Aging Processes in 2 1/4 Cr-1 Mo Steel," *Metall. Trans.* 6A: 2089–93 (1975).

65. J. M. Leitnaker, R. L. Klueh, and W. R. Laing, "The Composition of Eta-Carbide Phase in 2 1/4 Cr-1 Mo Steel," *Metall. Trans.* 6A: 1949–55 (1975).

66. M. K. Booker, "Time-Dependent Fatigue — Estimates of Worst Effects," *Mechanical Properties Test Data for Structural Materials Quart. Prog. Rep. April 30, 1976,* ORNL-5150, pp. 158–64.

67. J. H. Gittus, "Implications of Some Data on Relaxation Creep in Nimonic 80A," *Phil. Mag.* 9: 749 (1964).

68. M. K. Booker, B.L.P. Booker, J. P. Strizak, and C. R. Brinkman, "Cyclic Stress-Strain Behavior of Isothermally Annealed 2 1/4 Cr-1 Mo Steel," to be presented at Second International Conference on Mechanical Behavior of Materials, Boston, Aug. 16–20, 1976.

69. J. R. Ellis et al., "Elevated-Temperature Fatigue and Creep-Fatigue Properties of Annealed 2 1/4 Cr-1 Mo Steel," pp. 213–46 in *Structural Materials for Service at Elevated Temperatures in Nuclear Power Generation,* MPC-1, A. O. Schaefer, ed., American Society of Mechanical Engineers, New York, 1975.

70. C. E. Pugh et al., *Background Information for Interim Methods of Inelastic Analysis for High-Temperature Reactor Components of 2 1/4 Cr-1 Mo Steel,* ORNL/TM-5226 (May 1976).

71. M. K. Booker, "Fatigue Curve Development," *Mechanical Properties Test Data for Structural Materials Quart. Prog. Rep. Jan. 31, 1976,* ORNL-5112, pp. 101–03.

72. S. S. Manson, "The Challenge to Unify Treatment of High Temperature Fatigue — A Partisan Proposal Based on Strain-Range Partitioning," pp. 744–75 in *Fatigue at Elevated Temperatures,* ASTM STP 520, A. E. Carden, A. J. McEvily, and C. H. Wells, eds., American Society for Testing and Materials, Philadelphia, 1972.

73. S. S. Manson, G. R. Halford, and M. H. Hirschberg, *Creep-Fatigue Analysis by Strain-Range Partitioning,* NASA-TM-X-67838 (1971).

74. M. K. Booker, "Creep-Fatigue Data Analysis," *Mechanical Properties Test Data for Structural Materials Quart. Prog. Rep. April 30, 1975,* ORNL-5105, pp. 215–21.

75. Ibid., *July 31, 1975,* ORNL-5106, pp. 144–47.

76. Ibid., *Oct. 31, 1975,* ORNL-5107, pp. 154–58.

77. R. D. Campbell, "Creep Fatigue Interaction Correlation for 304 Stainless Steel Subjected to Strain-Controlled Cycling with Hold Times at Peak Strain," *J. Eng. Ind.* 93: 887–92 (1971).

78. M. H. Hirschberg and G. R. Halford, *Use of Strain-Range Partitioning to Predict High-Temperature Low-Cycle Fatigue Life,* NASA TN D-8072 (January 1976).

79. C. R. Brinkman, M. K. Booker, J. P. Strizak, W. R. Corwin, J. L. Frazier, and J. M. Leitnaker, *Interim Report on the Continuous Cycling Elevated-Temperature Fatigue and Subcritical Crack Growth Behavior of 2 1/4 Cr-1 Mo Steel,* ORNL-TM-4993 (December 1975).

80. M. K. Booker, D. O. Hobson, T. L. Hebble, and C. R. Brinkman, *Mechanical Property Correlations for 2 1/4 Cr-1 Mo Steel in Support of Nuclear Reactor Systems Design,* ORNL/TM-5329 (June 1976). To be published in *International Journal of Pressure Vessels and Piping.*

81. "Case 1592," pp. 327–442 in *1974 Code Cases (ASME Boiler and Pressure Vessel Code),* American Society for Mechanical Engineers, New York, 1974.

82. D. R. Diercks, "The Application of Strain-Range Partitioning to the Prediction of Elevated-Temperature, Low-Cycle Fatigue Life for Type 304 Stainless Steel," pp. 29–38 in *Advances in Design for Elevated Temperature Environment,* S. Y. Zamrik and R. I. Jetter, eds., American Society of Mechanical Engineers, New York, 1975.

83. S. Majumdar and P. S. Maiya, *A Unified and Mechanistic Approach to Creep-Fatigue Damage,* MS-1843 (Rev. 2), Argonne National Laboratory (September 1975).

84. L. A. James, "Some Questions Regarding the Interaction of Creep and Fatigue," ASME Paper 75-WA/Mat-6, to be published in *Journal of Engineering Materials and Technology.*

85. D. N. Robinson, *A Candidate Creep-Recovery Model for 2 1/4 Cr-1 Mo Steel and Its Experimental Implementation,* ORNL-TM-5110 (October 1975).

86. J. P. Hammond, ORNL, private communication, May 1976.

87. R. L. Klueh and J. F. King, "Mechanical Properties of Transition Weld Joint Materials," *Mechanical Properties Test Data for Structural Materials Quart. Prog. Rep. April 30, 1976,* ORNL-5150, pp. 175–86.

88. Y. Ishii and K. Iida, "Low and Intermediate Cycle Fatigue Strength of Butt Welds Containing Defects," *J. Soc. Nondestr. Test. (Japan)* 18(10), (1969); IIW Document XII-560-69.

89. R. A. Buchanan and D. M. Young, "Effect of Porosity on Elevated Temperature Fatigue Properties of 2 1/4 Cr-1 Mo Steel Weldments," *Weld. J. (Miami)* 54(9): 296-s–301-s (September 1975).

90. R. W. Swindeman, *Low-Strain Tensile Behavior of Type 304 Stainless Steel (Heat 9T2796),* ORNL/TM-5245 (February 1976).

91. W. D. Nix and C. R. Barrett, "Interpretation of Steady State Creep in Terms of the Relation Between Dislocation Glide and Recovery," *ASM Trans. Q.* 61: 695–97 (December 1968).

92. R. W. Swindeman, "Exploratory Studies in Support of Structural Design Methods," *Mechanical Properties Test Data for Structural Materials Quart. Prog. Rep. Oct. 31, 1974*, ORNL-5103, pp. 241–60.

93. K. R. Williams and B. Wilshire, "On the Stress- and Temperature-Dependence of Creep of Nimonic 80A," *Met. Sci. J.* 7: 176–79 (1973).

94. P. W. Davies et al., "Stress-Change Experiments During High-Temperature Creep of Copper, Iron, and Zinc," *Met. Sci. J.* 7: 87–92 (1973).

95. D. N. Robinson and J. A. Clinard, "An Alternate Approach to Processing Uniaxial Creep Data for Use in the Currently Recommended Constitutive Equations," *High-Temperature Structural Design Program Prog. Rep. June 30, 1975*, ORNL-5087, pp. 46–50.

96. R. Bhargava, J. Moteff, and R. W. Swindeman, "Correlation of the Microstructure with the Creep and Tensile Properties of AISI 304 Stainless Steel," pp. 31–54 in *Structural Materials for Service at Elevated Temperatures in Nuclear Power Generation*, A. O. Schaefer, ed., MPC-1, American Society of Mechanical Engineers, New York, 1975.

97. V. K. Sikka, "Mechanical Property Characterization of Type 304 Stainless Steel Reference Heat," *Mechanical Properties Test Data for Structural Materials Quart. Prog. Rep. Oct. 31, 1975*, ORNL-5107, pp. 17–34.

98. E. F. Etienne, W. Dortland, and H. B. Zeedijk, "On the Capability of Austenitic Steel to Withstand Cyclic Deformation During Service at Elevated Temperature," paper 225 presented at International Conference on Creep and Fatigue in Elevated Temperature Applications, Philadelphia, September 1973 and Sheffield, UK, April 1974.

99. R. K. Bhargava and J. Moteff, *Metallographic Examination of Type 304 Stainless Steel Specimens Tested in Creep and Fatigue Modes*, report in preparation.

100. R. Tanaka and T. Shinoda, "Carbide Precipitation and High Temperature Strength of 18-8 Stainless Steels," *Zairyo* 21: 198–203 (1972); available in English as ORNL-TR-2686.

101. R. K. Bhargava, J. Moteff, and R. W. Swindeman, "The Dislocation Substructure, Carbides, and the Deformation Mechanism Map for AISI 304 Stainless Steel," *Metall. Trans.* 7A: 879–84 (1976).

102. L.M.T. Hopkin and L. H. Taylor, "Creep Properties of Cr-Ni-Mo Austenitic Steel in Relation to Structure," *J. Iron Steel Inst.* 205: 17–27 (1967).

103. R. Lagneborg, "Dislocation Mechanisms in Creep," *Int. Metall. Rev.* 11: 130–46 (1972).

104. P. W. Davies and B. Wilshire, "On Internal Stress Measurement and the Mechanism of High Temperature Creep," *Scr. Metall.* 5: 475–78 (1971).

105. W. Blum, J. Housselt, and G. König, "Transient Creep and Recovery After Stress Reduction During Steady State Creep of AlZn," *Acta Metall.* 24: 293–97 (1976).

106. D. Fahr, *Analysis of Stress-Strain Behavior of Type 316 Stainless Steel,* ORNL-TM-4292 (November 1973).

107. D. R. Diercks, private communication.

108. R. C. Rice and C. E. Jaske, subcontract progress report to J. M. Corum.

109. E. Voce, "The Relationship Between Stress and Strain for Homogeneous Deformation," *J. Inst. Met.* 74: 537–63 (1946).

110. M. A. Eisenberg, "A Generalization of Plastic Flow Theory with Application to Cyclic Hardening and Softening Phenomena," *ASME Paper* 75-WD/Mat-3.

111. M.C.M. Liu, E. Krempl, and D. C. Nairn, *An Exponential Stress-Strain Law for Cyclic Plasticity,* report in preparation.

112. H. R. Jhansale, "A Friction Stress Method for the Cyclic Inelastic Behavior of Metals," paper presented at the Third International Conference on Structural Mechanics in Reactor Technology, Imperial College, London, Sept. 1–5, 1975.

113. W. E. Stillman, V. K. Sikka, and M. K. Booker, *Creep Evaluation for Type 316 Stainless Steel,* report in preparation.

114. R. Lagneborg, "A Modified Recovery Creep Model and Its Evaluation," *Met. Sci. J.* 6: 127–33 (1972).

115. E. W. Hart, "A Phenomenological Theory for Plastic Deformation of Polycrystalline Metals," *Acta Metall.* 18: 599–610 (1970).

116. R. L. Klueh, *The Creep and Rupture Behavior of Annealed 2 1/4 Cr-1 Mo Steel,* ORNL report in preparation.

117. C. E. Jaske and H. Mindlin, "Elevated-Temperature Low Cycle Fatigue Behavior of 2 1/4 Cr-1 Mo and 1 Cr-1 Mo-1/4 V Steels," pp. 137–210 in *2 1/4 Cr-1 Mo Steel in Pressure Vessel and Piping,* A. O. Schaefer, ed., American Society of Mechanical Engineers, New York, 1971.

118. C. C. Schultz, "Investigations of Creep Failure Under Uniaxial and Multiaxial Conditions," *Mechanical Properties Test Data for Structural Materials Quart. Prog. Rep. Jan. 31, 1976,* ORNL-5112, pp. 151–60.

119. A. E. Carden, "Parametric Analysis of Fatigue Crack Growth," paper C324/73 presented at the International Conference on Creep and Fatigue in Elevated Temperature Applications, Philadelphia, September 1973, and Sheffield, UK, April 1974.

120. M. Döner, "An Analysis of Elevated Temperature Fatigue and Creep Crack Growth," ASME paper 75-WA/GT-16, presented at the ASME Winter Annual Meeting, Houston, Texas, Nov. 30–Dec. 5, 1975.

# 4. NAVAL RESEARCH LABORATORY

L. E. Steele

## 4.1 INTRODUCTION - L. E. Steele

The research program of the NRL Engineering Materials Division, Thermostructural Materials Branch, includes the study of the behavior of structural materials useful in reactor construction. Within the scope of the title above much unirradiated data are developed. This report is developed using such data to support the USERDA and USNRC objective of compiling structural materials properties data for use in national reactor development programs. The NRL program is sponsored by the Office of Naval Research, the U. S. Energy Research and Development Administration, the U. S. Nuclear Regulatory Commission, and the U. S. Army Engineer Power Group. The unirradiated materials properties data contributed here include that developed in the course of research in the areas of high temperature materials, radiation damage, and fracture mechanics.

## 4.2 EFFECT OF HOLD TIME ON ELEVATED TEMPERATURE FATIGUE CRACK PROPAGATION IN TYPE 304 STAINLESS STEEL - H. H. Smith and D. J. Michel

### 4.2.1 Background

The addition of tensile hold periods during cyclic loading has been shown by previous NRL studies (1) to significantly increase fatigue crack propagation rates in austenitic stainless steels. Other NRL studies have shown the influence of prior thermal aging is to reduce the magnitude of the hold time effects in solution annealed and cold worked Type 316 stainless steel (2,3).

During the present reporting period, additional results were obtained for the influence of thermal aging on the crack propagation response of solution annealed Type 304 stainless steel during elevated temperature hold time tests. These results are presented in this report together with a summary of the overall NRL findings of the effects of thermal aging on crack propagation in austenitic stainless steels.

### 4.2.2 Materials and Test Procedures

The chemical composition of the Type 304 stainless steels, the specimen design, and the general test procedure have been previously reported (4,5). Briefly, single-edge-notched cantilever specimens were cycled under zero-to-tension loading to a constant maximum load in air. Specimens utilized for zero hold time tests were loaded in a continuous sawtooth mode. For the hold time tests, tensile loads were imposed on the specimen during each cycle by holding at the maximum load value for 0.1 and 1.0 minutes before returning to zero load. To evaluate the effects of thermal aging, selected specimens were held at 1100°F (593°C) for 5000 hours in air in electric muffle furnaces.

### 4.2.3 Results and Discussion

The experimental data were analyzed to yield crack propagation rate, da/dN, as a function of the stress intensity factor range, $\Delta K$. The effect of thermal aging on crack propagation rates at 1100°F (593°C) for zero and 1 minute tension hold times is presented in Fig. 4.2. Examination of the results in Fig. 4.1 shows that thermal aging slightly reduced the crack propagation rate for zero hold time while producing a significant reduction for the 1 minute hold time tests. A similar effect is seen in Fig. 4.2 for a second heat of 304 stainless steel. It should be noted, however, that the crack propagation rate in the unaged, zero hold time test was approximately a factor of five higher in the Heat B material, Fig. 4.1, than in the Heat A material, Fig. 4.2. Comparison of both figures shows that the inclusion of 1 minute hold times during testing and/or thermal aging prior to testing reduced the effects of material composition variation such that nearly equivalent crack propagation rates were produced.

These results are in agreement with the results of a recent NRL study (5) where Brinell hardness measurements indicated that thermal aging produced a relative strengthening of the annealed Type 304. A similar effect was observed in solution annealed Type 316 stainless steel (5). However, in the cold worked condition, thermal aging produced a bulk softening in both materials. These hardness results are consistent with the overall effect of thermal aging in both steels to

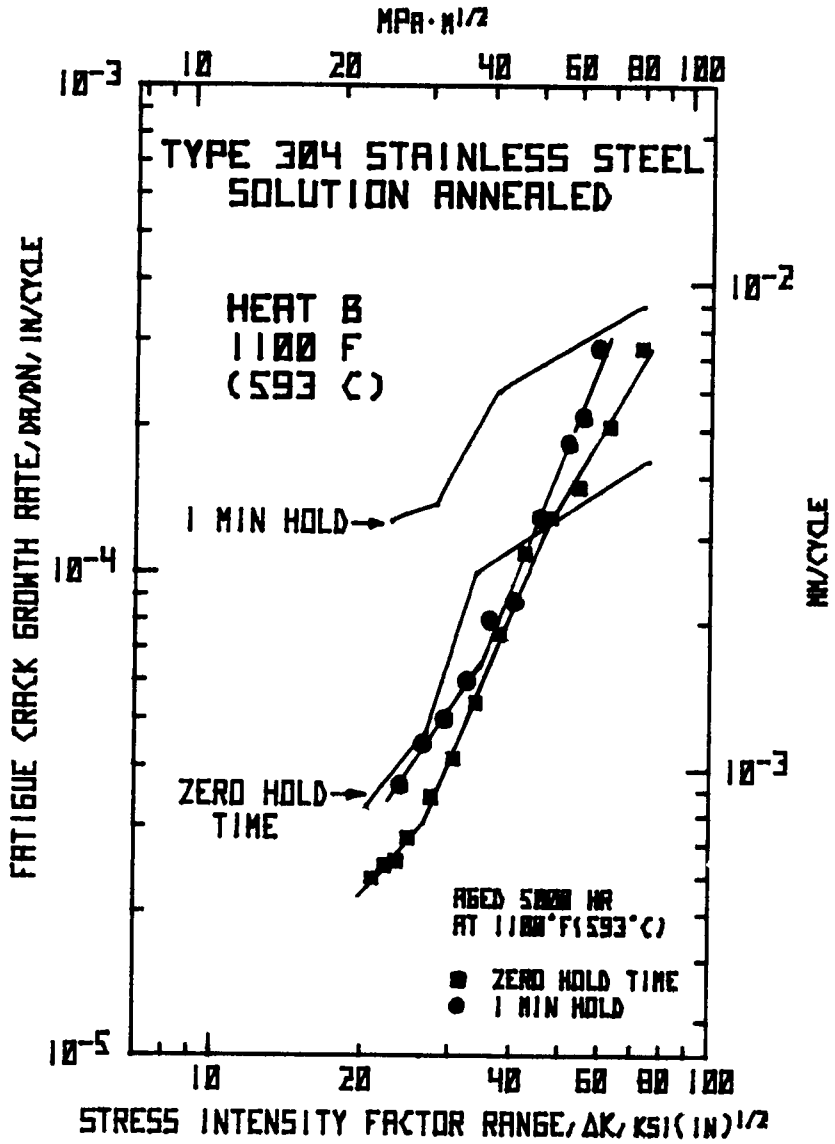


Fig. 4.1 - The effect of hold time on fatigue crack propagation rate, da/dN, in air at 1100°F (593°C) for solution annealed Type 304 stainless steel, Heat B.

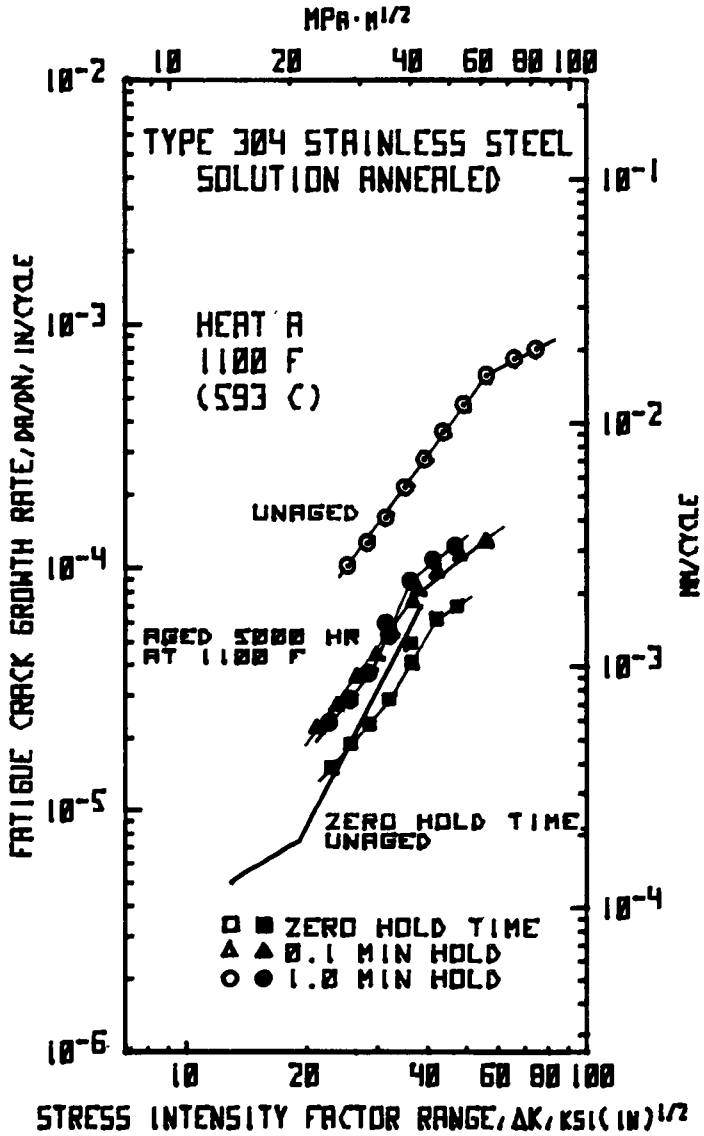


Fig. 4.2 - The effect of hold time on fatigue crack propagation rate, da/dN, in air at 1100°F (593°C) for solution annealed Type 304 stainless steel, Heat A.

reduce crack propagation rate in solution annealed material and increase the rate in cold worked material during continuous cycling tests. With the addition of hold time, the results (5) show that thermal aging reduced the crack propagation rate for both steels in the solution annealed and cold worked conditions.

For the Type 316 stainless steel specimens tested at 1100°F (593°). scanning electron microscopy (SEM) examination of the fracture surfaces (5) showed that only the unaged specimen tested with a 1 minute hold time exhibited a mixed mode (transgranular - intergranular) fracture appearance while unaged, zero hold time and thermally aged, zero and 1 minute hold time specimens showed that crack propagation occurred in a transgranular manner (5). Although comparable results are not yet available for the Type 304 stainless steel specimens, it is expected that the predominate fracture mode will be transgranular. This suggests that the crack propagation response of Type 304 stainless steel is primarily cycle rather than time dependent at 1100°F (593°C) except in the unaged condition at hold times of 1 minute or longer.

## 4.3 CREEP-FATIGUE CRACK PROPAGATION IN ALLOY 718 - P. Shahinian and K. Sadananda*

### 4.3.1 Background

Recognition that many components in high temperature service are subjected to combined cyclic and static loads rather than to either type alone has stimulated investigations of performance under more representative combined loadings. It has become evident that under such conditions material behavior cannot always be predicted simply from pure creep and pure fatigue data, presumably as a consequence of interaction between time-dependent and cyclic-dependent processes.

Studies of creep-fatigue behavior have mainly been directed toward determinations of life under various types of loading and towards development of predictive criteria. Less attention has been given to

---

*On leave from the Department of Mechanical Engineering, University of Maryland, College Park, Maryland.

the detailed aspects of behavior, e.g., crack growth, even though crack growth has been found to be the controlling factor in the life of many cyclically stressed components.

An investigation is being conducted on crack growth behavior in Alloy 718 plate under cyclic and static loads at elevated temperatures over a wide range of conditions. Assessments of creep-fatigue interaction are being made on the basis of crack growth rates, growth characteristics, and failure times.

### 4.3.2 Experimental Procedure

The Alloy 718 used for this study was in the form of a 1-in. thick plate from a vacuum induction melted-electroslag remelted heat having the chemical composition listed in Table 4.1. The standard heat treatment given the alloy is also included. Compact tension (1T) specimens were prepared with a T-L orientation, i.e., crack plane parallel to the rolling direction. To reduce the tendency of the crack front to bow at the start of the test the specimens were fatigue precracked at room temperature.

Continuous cyclic tests using load control were conducted in tension at R = 0.05 (R = max. load/min. load) with a sawtooth pattern at a frequency of 0.17 Hz (10 cpm). For the combined loads, periods of static load (hold time) of 0.1, 1, or 10 minutes were imposed at the tensile peak of the cyclic load. The specimens were heated by induction for the cyclic tests at 538, 649, and 760°C (1000, 1200, and 1400°F) and by a resistance wire-wound furnace for the static load tests. Crack lengths were measured periodically during the tests by means of a traveling microscope. The rates of growth were determined from the slopes of the curves of crack length versus number of cycles, da/dN, or time, da/dt, at suitable intervals.

### 4.3.3 Results

#### 4.3.3.1 Crack Growth Rates

The crack propagation behavior of the alloy and its response to loading mode were significantly different among the three temperatures,

Table 4.1

Chemical Composition and Heat Treatment of Alloy 718

Composition, weight percent

| | | |
|---|---|---|
| 0.04 C | Bal. Fe | 1.00 Ti |
| 0.19 Mn | 51.14 Ni | 0.52 Al |
| 0.05 Si | 17.96 Cr | 0.43 Co |
| 0.005 P | 3.12 Mo | 0.02 Cu |
| 0.005 S | 5.19 Cb and Ta | 0.003 B |

Heat Treatment

Anneal to 955°C for 1 hour - air cool

Age at 720°C for 8 hours, furnace cool at 620°C

Hold at 620°C for total aging time of 18 hours

538, 649, and 760°C (1000, 1200, and 1400°F). The inclusion of a hold period of a 0.1 or 1 minute at the peak of the tensile cycle produced an increase in crack growth rates (da/dN) at 538°C (1000°F), Fig. 4.3. At stress intensity values above about 55 MPa$\sqrt{m}$ (50 ksi$\sqrt{in.}$) the effect becomes quite small. In addition to the deleterious influence of the static load periods, cycling also caused the rate of crack growth for a given $\Delta K$ to increase, as indicated by the growth per unit time (da/dt) data in Fig. 4.4. With increasing hold time, da/dt generally decreased. Or conversely, as the number of cycles per unit time increased, the higher was the da/dt. A static load gave the lowest growth rates, in contrast to the highest rates for the continuous cycling.

At 649°C (1200°F), the increase in da/dN with increasing hold time was substantially greater than at 538°C (1000°F), Fig. 4.5. For example, at 649°C a 10 minute hold period caused the rate to increase by a factor of about 230 over that for continuous cycling. The variation of da/dN with $\Delta K$ shows two stages, a sharp acceleration in rate initially and a stage at higher $\Delta K$ values of less rapid rate increase. The slopes of the second stage curves are generally lower when hold times have been imposed.

While the trend of the hold time effect on growth rate is clear, there was considerable scatter in the data for different test loads or corresponding initial stress intensities. It is not clear whether there was an effect of load on growth rate, however, because of the absence of a systematic change. While the growth rates were the lowest for the highest load, 13.97 kN (3140 lb), at each hold time, they were in reasonable agreement in two cases, zero and 0.1 minute hold, with the rates for the lowest load, 9.34 kN (2100 lb). Thus it does not appear that the dependence of crack growth rate on $\Delta K$ is influenced by load, at least for zero and 0.1 minute hold periods. The results at 649°C show that crack growth is strongly time-dependent.

On a time basis, the crack growth rates for each hold time series at 649°C were grouped within a factor of 7, Fig. 4.6. Within each group, the rates for the continuously cycled and statically loaded specimens were the lowest and those for the 10 minute hold were among

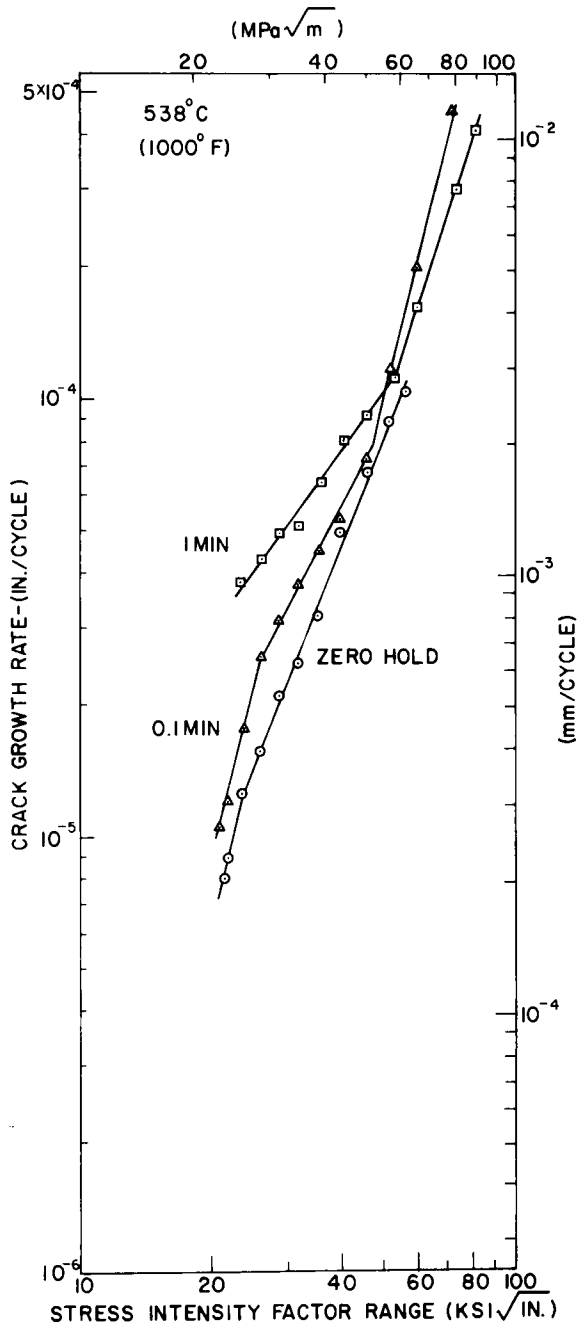


Fig. 4.3 - Effect of hold time on crack growth rate (da/dN) as a function of stress intensity factor ($\Delta K$) at 538°C (1000°F)

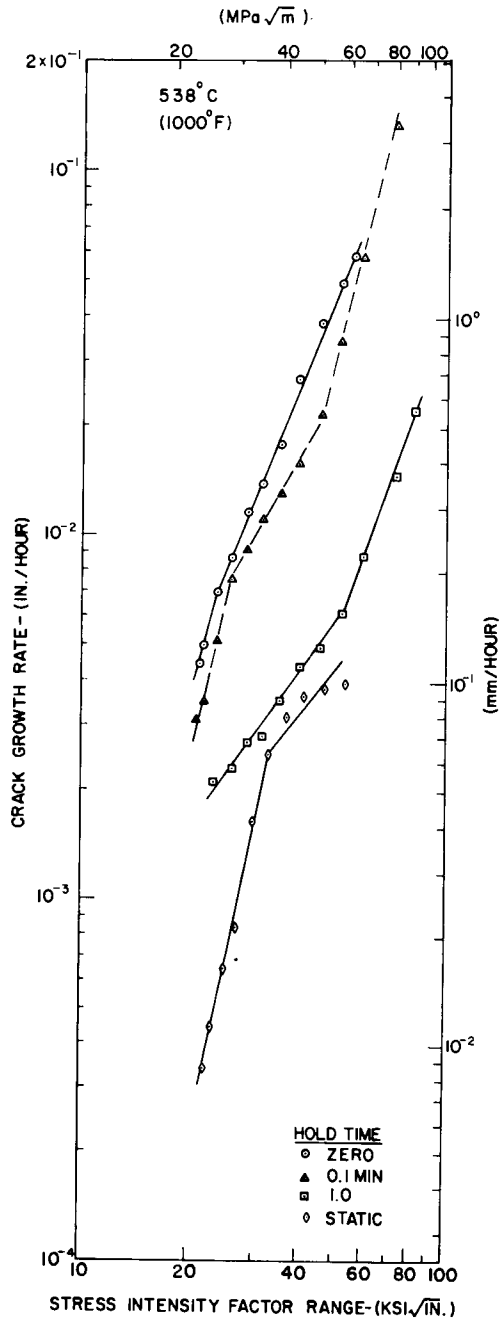


Fig. 4.4 - Crack growth rates (da/dt) for cyclic, static, and combined loadings at 538°C (1000°F).

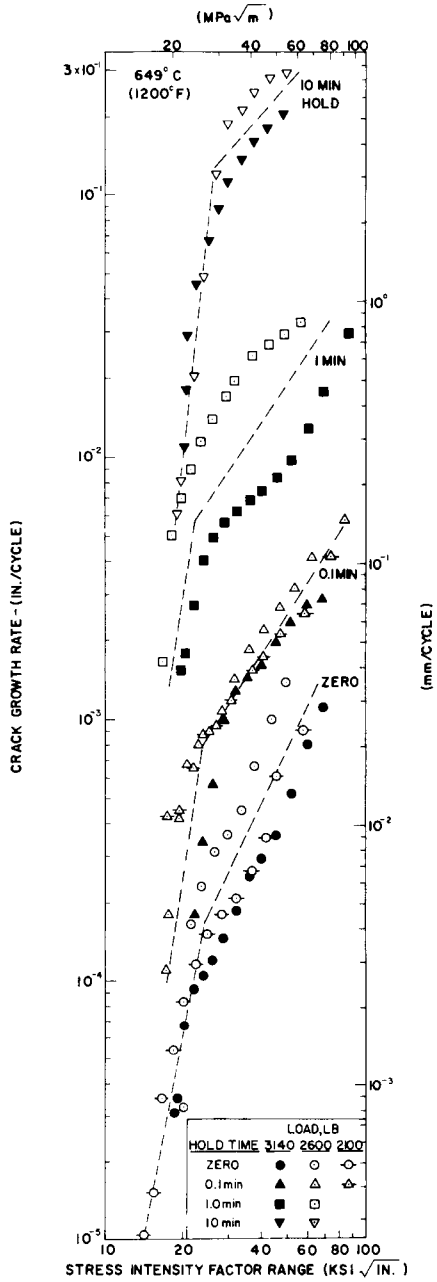


Fig. 4.5 - Effect of hold time on crack growth rates (da/dN) as a function of $\Delta K$ for several loads at 649°C (1200°F).

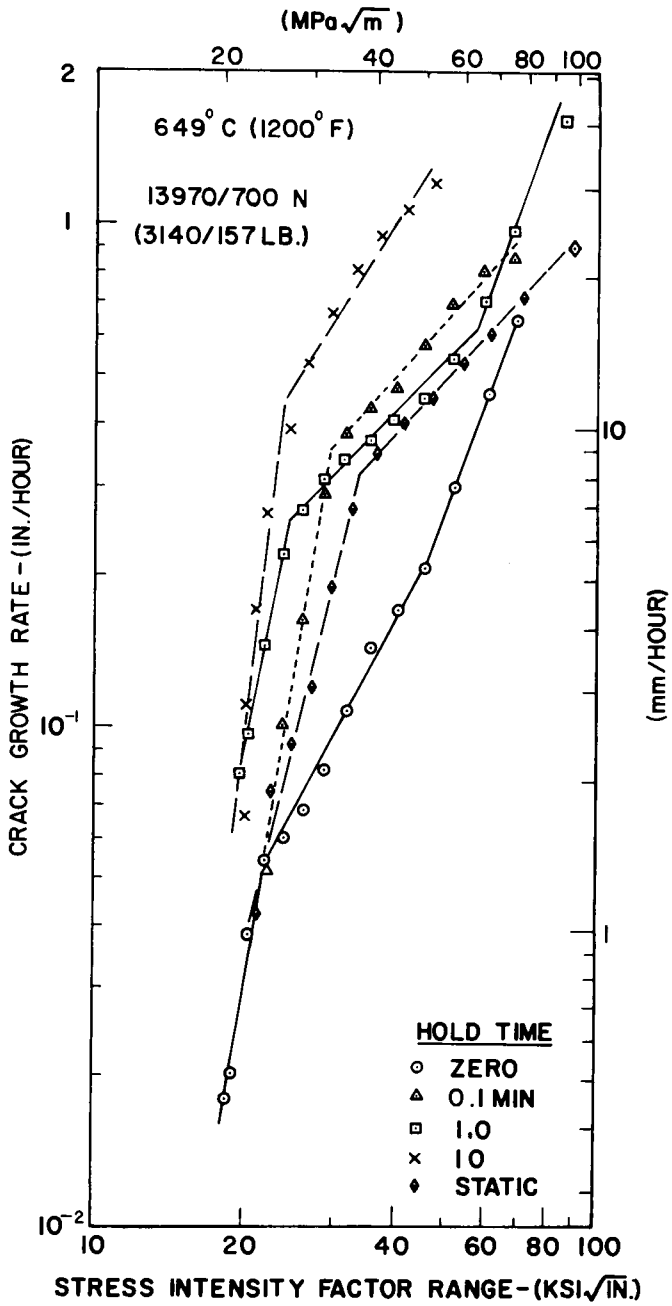


Fig. 4.6 - Crack growth rates (da/dt) for cyclic, static, and combined loadings at a maximum load of 13.97 kN and R = 0.05 at 649°C (1200°F).

the highest. These data suggest a creep-fatigue interaction which enhances crack growth rate.

In contrast to the lower temperature, at 760°C (1400°F) the dependence of da/dN on $\Delta K$ for continuous cycling was significantly affected by load, Fig. 4.7. Lower rates for a given $\Delta K$ were produced by the lower load. Also at this temperature crack growth seemed to be cycle-dependent, judging from the overlap of the zero and 1 minute hold curves. Even with a 10 minute hold, where appreciable crack opening deformation occurred, crack growth appeared to be primarily cycle-dependent. For this specimen the da/dN values were slightly lower than for those for the 1 minute hold time, and the presumed additional creep seemed to have a retardation effect on growth, at least initially. Appreciable crack opening deformation occurred, however, and the validity of the use of the stress intensity parameter for this condition is questionable.

In addition to the correlations of crack growth rate with the stress intensity factor, an attempt was made to correlate the growth rate with the nominal stress at the crack tip for those tests for which the K parameter did not correlate well for different loads, that is at 760°C and long hold times at 649°C. The nominal stress values failed to provide a satisfactory correlation with growth rates at the different loads.

It appears that the stress intensity factor is suitable for correlation of crack growth rates at temperatures where creep is small but not where it becomes appreciable, e.g., 760°C (1400°F) for Alloy 718. Crack growth rates, da/dN, are increased by increases in hold time apparently as the result of a creep-fatigue interaction. This effect was greater at 649°C than at 538°C owing to appreciably more creep. However, at 760°C, retardation of crack growth under static load occurs causing the influence of hold time on growth rate to disappear.

## 4.4 References

1. Michel, D. J., Smith, H. H., and Watson, H. E., "Effect of Hold Time on Elevated Temperature Fatigue Crack Propagation in Fast Neutron Irradiated and Unirradiated Type 316 Stainless Steel," in Structural Materials for Service at Elevated Temperatures

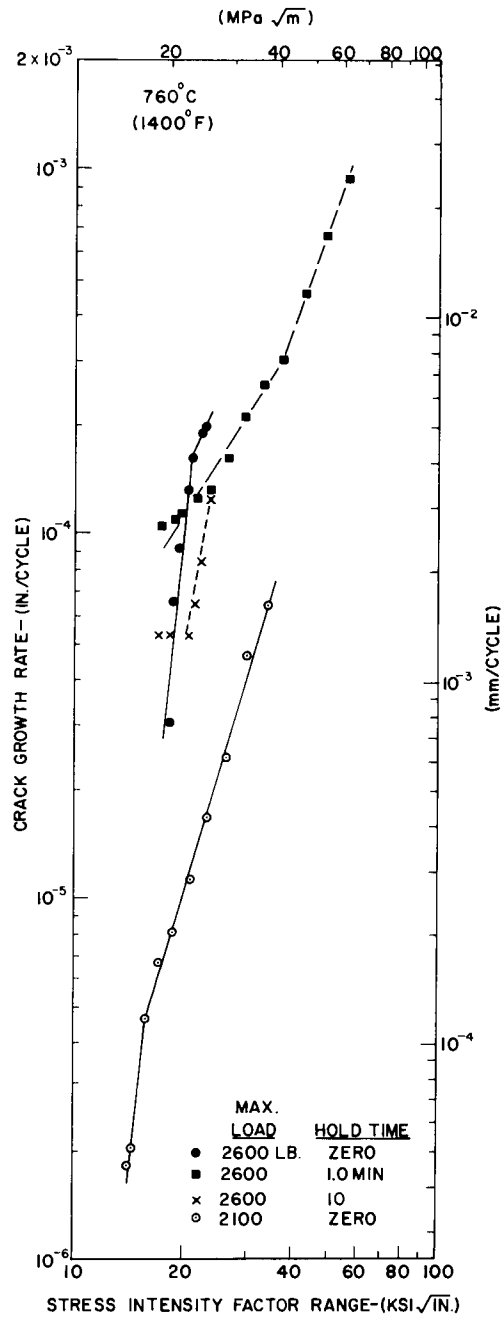


Fig. 4.7 - Effect of hold time and load on crack growth rate (da/dN) as a function of $\Delta K$ at 760°C (1400°F).

in Nuclear Power Generation, American Society of Mechanical Engineers, 1975, pp. 167-190.

2. Michel, D. J., Smith, H. H., and Watson, H. E., "Effect of Hold Time on Fatigue Crack Propagation in Thermally Aged, Solution Annealed and 20% Cold Worked Type 316 Stainless Steel," in Mechanical Properties Test Data for Structural Materials, Quarterly Progress Report, ORNL-5104, Oak Ridge National Laboratory, Oak Ridge, TN, March 1975, pp. 109-113.
3. Smith, H. H., Michel, D. J., and Watson, H. E., "Effect of Aging on Hold Time Effects in Solution Annealed Type 316 Stainless Steel," in Mechanical Properties Test Data for Structural Materials, Quarterly Progress Report ORNL-5106, Oak Ridge National Laboratory, Oak Ridge, TN, September 1975, pp. 216-219.
4. Michel, D. J. and Smith, H. H., "Fatigue Crack Growth in Type 304 Stainless Steel," in Mechanical Properties Test Data for Structural Materials, Quarterly Progress Report, ORNL-4936, Oak Ridge National Laboratory, Oak Ridge, TN, January 1974, pp. 37-45.
5. Michel, D. J. and Smith, H. H., "Effect of Hold Time on Elevated Temperature Fatigue Crack Propagation in Types 304 and 316 Stainless Steel," submitted to ASME, 1976.

# 5. HANFORD ENGINEERING DEVELOPMENT LABORATORY

H. H. Yoshikawa

## 5.1 INTRODUCTION

The objectives of the structural materials investigation conducted at the Hanford Engineering Development Laboratory are mainly to provide control data for in-reactor and postirradiation tests and to provide direct and timely assistance to FFTF and Demonstration plant structural design and analysis programs. The HEDL efforts involve evaluation of mechanical properties in the areas of normal and high strain rate tensile testing, creep testing and analysis, and fatigue crack growth and fracture toughness of such materials as weldments, vessel and piping, core support structures and reflectors as well as duct and cladding. Those test results and analyses appropriate to the "Structural Materials Quarterly Report" will be reported here; however those investigations associated with irradiation effects per se will be reported in HEDL publications.

## 5.2 LMFBR STRUCTURAL MATERIALS - J. J. Holmes and R. L. Knecht

### 5.2.1 Creep-Rupture Behavior of Inconel 600

L. D. Blackburn, J. M. Steichen, R. L. Knecht

#### 5.2.1.1 Objective

The objective of this work is to characterize the creep-rupture behavior of unirradiated Inconel 600 for subsequent comparison with post-irradiation test results.

#### 5.2.1.2 Accomplishments and Status

5.2.1.2.1 Scope. This report presents correlations of creep-rupture properties determined for a single heat of Inconel 600. The test program was conducted to characterize the behavior of unirradiated material for subsequent comparison with test results from irradiated specimens. The material was annealed at 1750°F for 15 minutes and water quenched prior to

testing. Conventional constant-load creep rupture tests were conducted at 811 K (1000°F), 866 K (1100°F), 922 K (1200°F) and 1033 K (1400°F) at stresses which produced rupture in times from 5 to 3000 hours.

5.2.1.2.2 Results Experimental results were described analytically by least squares fitting to equations of the form

$$\log P = A_p + n_p \log \sigma \qquad (1)$$

where P is a particular property, $\sigma$ is the stress, and $A_p$ and $n_p$ are constants. The properties of interest here are time to rupture ($t_r$), time to the onset of tertiary creep ($t_2$), minimum creep rate ($\dot{\varepsilon}_m$), average creep rate to the onset of tertiary creep ($\dot{\varepsilon}_t$), and average creep rate to rupture ($\dot{\varepsilon}_r$). Values of $n_p$ at different temperatures were compared separately for the time and rate quantities using the multiple-comparison approach described by Acton (1), and where differences were not statistically significant, pooled values of $n_p$ were adopted. Temperature dependence of $A_p$ was described for all properties except $t_2$ by an equation of the form

$$A_p = B_o - B_1/T \qquad (2)$$

where T is temperature in degrees kelvin and $B_o$ and $B_1$ are constants.

Experimental $t_r$ results are presented in Figure 5.1. Clearly the analytical description gives an excellent representation of the data. Results for $t_2$ are presented in Figure 5.2. Equation 1 provides a good description of the isothermal stress dependence of $t_2$, but the differences in $n_{t_2}$ are statistically significant, indicating a real temperature dependence. As a result, an analytical representation of $A_{t_2}$ would be more complex than equation 2, so the individual $A_{t_2}$ values are simply retained for present purposes.

Data for $\dot{\varepsilon}_m$ are shown in Figure 5.3, and again the analytical description yields a good representation of the results. In comparing

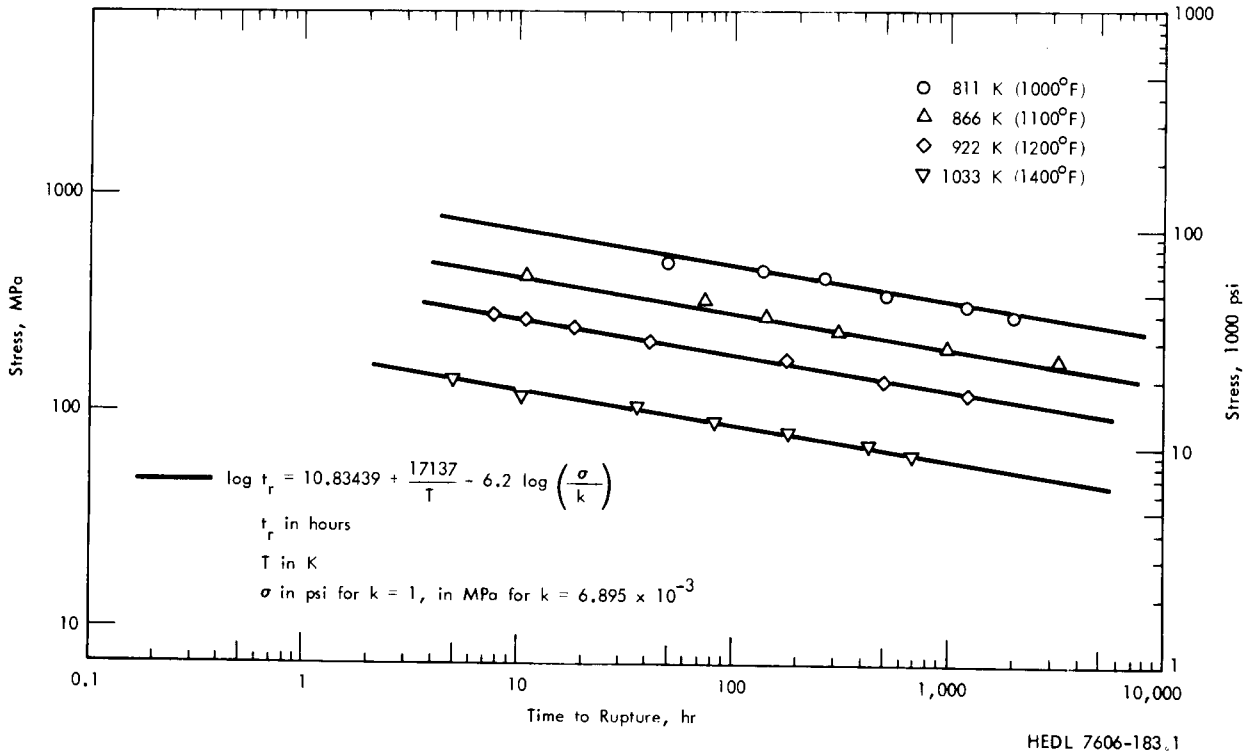


Figure 5.1. Variation of Time to Rupture with Stress for Inconel 600.

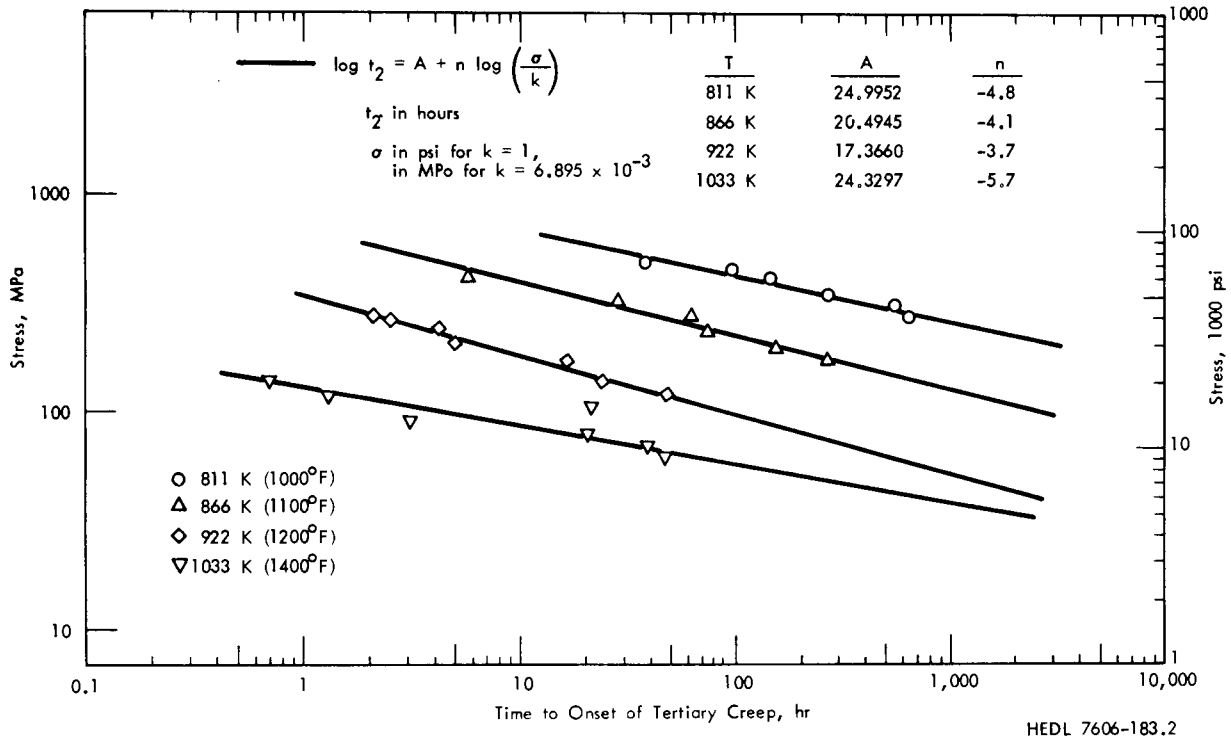


Figure 5.2. Variation of Time to Onset of Tertiary Creep with Stress for Inconel 600.

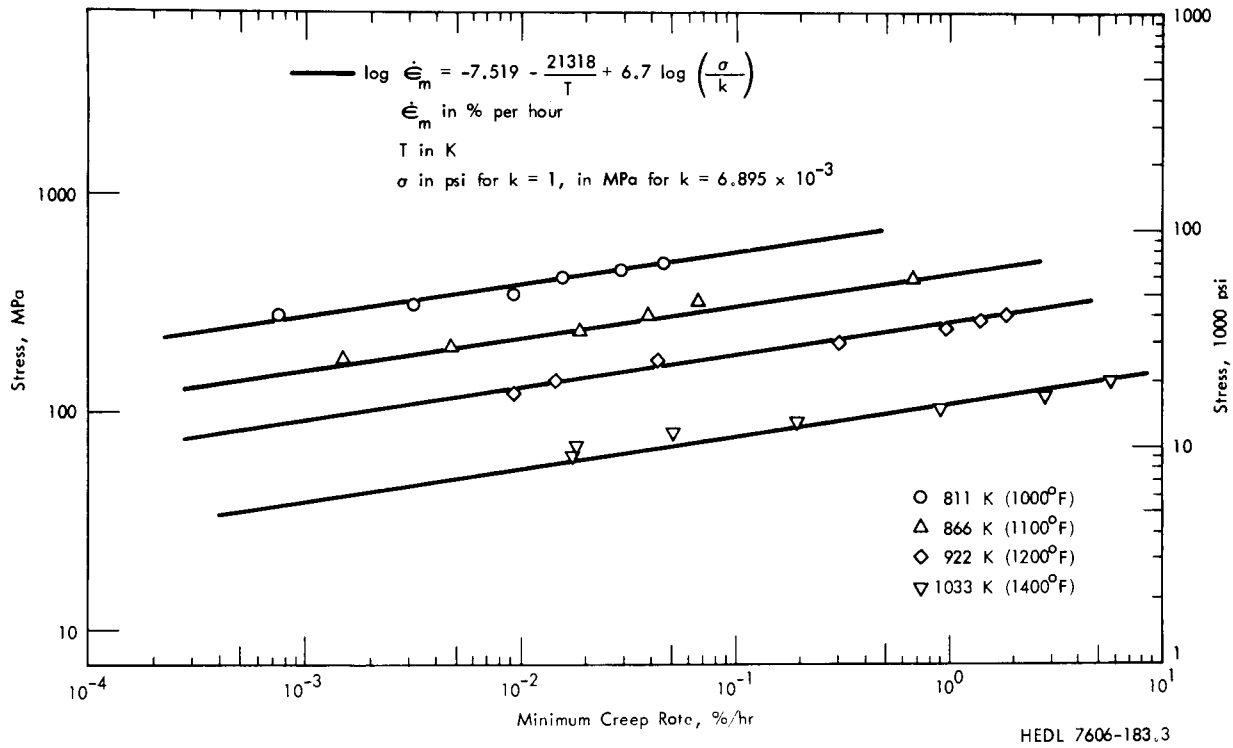


Figure 5.3. Variation of Minimum Creep Rate with Stress for Inconel 600.

the ${}^{n}\dot{\varepsilon}_m$ values, it was found that the value at 1033 K (1400°F) was significantly higher than those at the three lower temperatures. However, only data from the lower temperatures were used in evaluating the analytical description. The resulting fit to the 1033 K (1400°F) data is very acceptable.

Creep ductility or creep strain results are difficult to correlate or extrapolate directly because of inherent scatter in the data. It is possible, however, to estimate the trend behavior for ductility or strain results by making use of average creep rate data, for which the correlation is typically good. The average creep rate quantities $\dot{\varepsilon}_t$ and $\dot{\varepsilon}_r$ are defined by the relations

$$\dot{\varepsilon}_t = \frac{\varepsilon_t^c}{t_2} \qquad \text{and,} \tag{3}$$

$$\dot{\varepsilon}_r = \frac{\varepsilon_r^c}{t_r} \tag{4}$$

where $\varepsilon_t^c$ and $\varepsilon_r^c$ are the creep strain at the onset of tertiary creep and at rupture, respectively. Correlation of the $\dot{\varepsilon}_t$ and $\dot{\varepsilon}_r$ data using equations 1 and 2 is illustrated in Figures 5.4 and 5.5. A correlation of rupture ductility is then obtained by rewriting equation 4 as

$$\log \varepsilon_r^c = \log \dot{\varepsilon}_r + \log t_r \tag{5}$$

and submitting the correlations for $\dot{\varepsilon}_r$ and $t_r$ yields

$$\log \varepsilon_r^c = A_{\dot{\varepsilon}_r} + \frac{6.7}{6.2} A_{t_r} - \left(\frac{6.7}{6.2} - 1\right) \log t_r \tag{6}$$

A similar procedure for equation 4 yields

$$\log \varepsilon_t^c = A_{\dot{\varepsilon}_t} + A_{t_2} + \left(\frac{6.7}{6.2} - \frac{n_{t_2}}{6.2}\right) A_{t_r} - \left(\frac{6.7}{6.2} - \frac{n_t}{6.2}\right) \log t_r \tag{7}$$

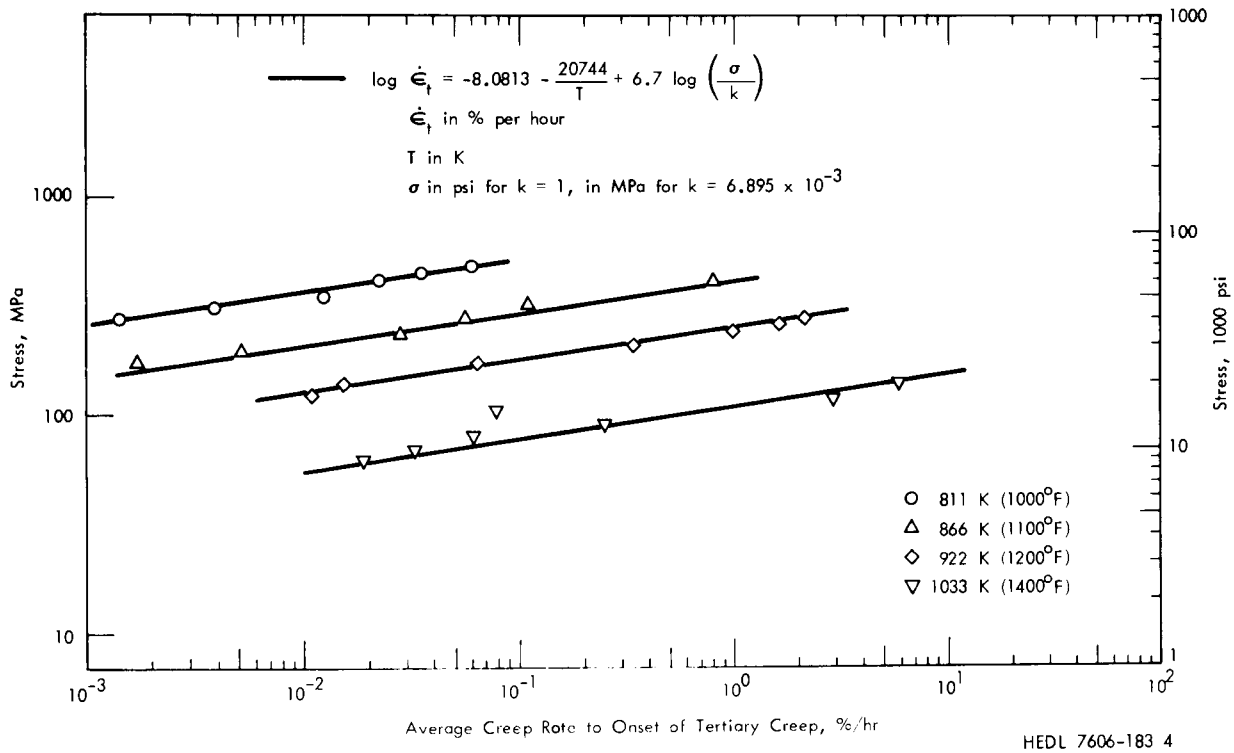


Figure 5.4. Variation of Average Creep Rate to Onset of Tertiary Creep with Stress for Inconel 600.

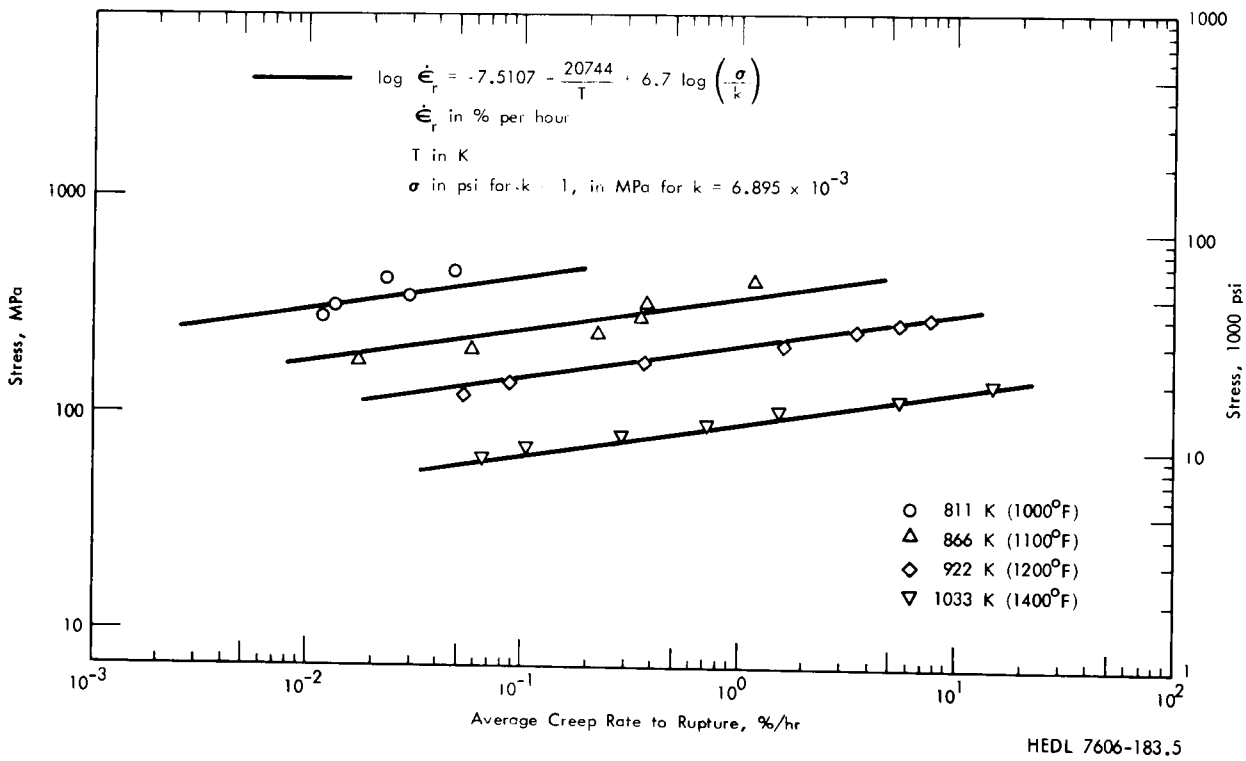


Figure 5.5. Variation of Average Creep Rate to Rupture with Stress for Inconel 600.

Figures 5.6 and 5.7 present the experimental $\varepsilon_r^c$ and $\varepsilon_t^c$ data and illustrate the correlations given by equations 6 and 7. The $A_p$ values obtained from equation 1 with the selected $n_p$ values were used in evaluating equations 6 and 7; this calculation shows better agreement with the data than does an evaluation of $A_p$ from equation 2. The ductility results in Figures 5.6 and 5.7 do exhibit considerable scatter, but the computations appear to give a reasonable estimate of trend behavior.

Estimates of other strain contributions are also possible using the above correlations. For example, the strain at the onset of tertiary creep can be expressed as the sum of a transient creep strain ($\varepsilon_1^c$) and a linear creep strain contribution ($\varepsilon_2^c$)

$$\varepsilon_t^c = \varepsilon_1^c + \varepsilon_2^c \tag{8}$$

and $\varepsilon_2^c$ is given by

$$\varepsilon_2^c = \dot{\varepsilon}_m \, t_2 \tag{9}$$

The correlations can then be used to calculate the ratio $\varepsilon_2^c/\varepsilon_t^c$, obtaining values of 0.363, 0.765, 0.859, and 0.894 at temperatures of 811 K, 866 K, 922 K and 1033 K, respectively. Thus the linear creep strain represents the major contribution to $\varepsilon_t^c$ at high temperatures.

The correlations developed here represent a completely adequate description of the creep-rupture properties of Inconel 600 for subsequent comparison with postirradiation test results.

5.2.1.3 Expected Accomplishments

Correlation of Inconel 600 creep-rupture properties after prior thermal exposures to 10,000 hours will be completed in the next quarter.

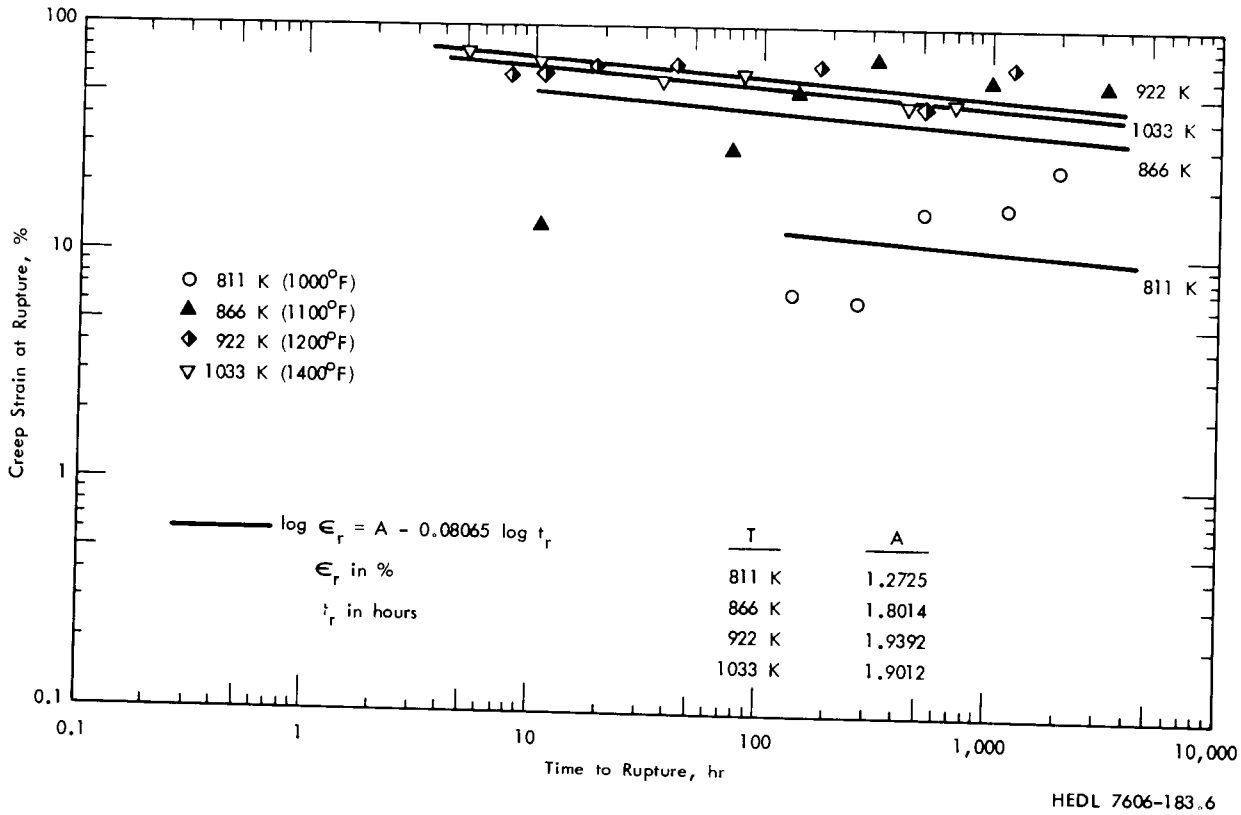


Figure 5.6. Variation of Creep Strain at Rupture with Time to Rupture for Inconel 600.

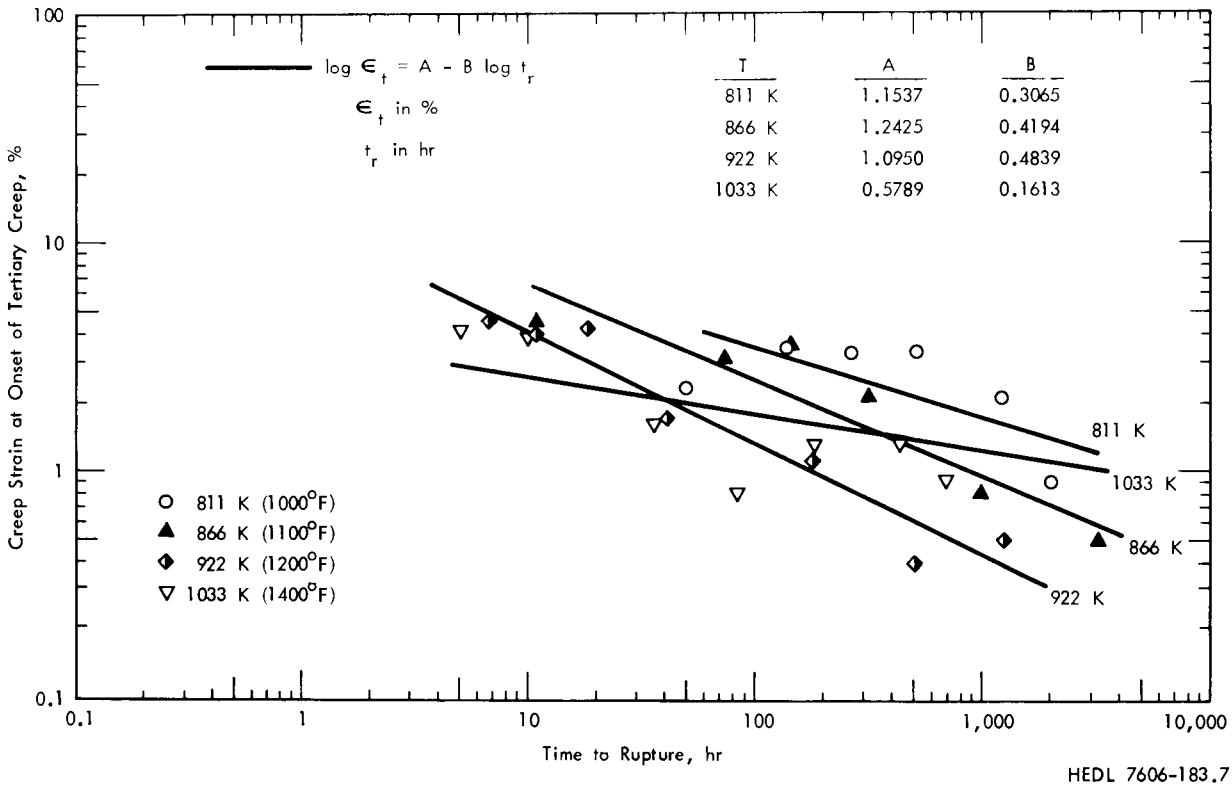


Figure 5.7. Variation of Creep Strain at Onset of Tertiary Creep with Time to Rupture for Inconel 600.

## 5.2.2 FATIGUE-CRACK PROPAGATION BEHAVIOR OF SEVERAL PRESSURE VESSEL STEELS AND WELDMENTS

-L. A. James, R. L. Knecht

### 5.2.2.1 OBJECTIVE

The objective of this report is to characterize the effects of various parameters upon the fatigue-crack propagation behavior of reactor structural materials for use in design, safety analysis and operations support.

### 5.2.2.2 ACCOMPLISHMENTS AND STATUS

The effect of temperature upon the fatigue-crack propagation behavior of several low-alloy pressure vessel steels and weldments was studied in an air environment over the range 75°-1000°F (24°-538°C). The specimens employed were of the ASTM Compact Tension Specimen design (W = 2.00 in., B = 0.40 in.). Four pressure vessel steels (ASME SA-387 grades C and D, SA-516 grade 60, SA-533 grade B class 1) were studied, plus weldments in two of these steels. The identification of these heats is given in Table 5.1, and the chemical analyses and mechanical properties of these heats are detailed in Tables 5.2 and 5.3, respectively. Additional tensile and fracture toughness results on Materials C and D may be found in References 2 and 3, respectively.

The weldment specimens were oriented such that the crack was parallel to the direction of welding, and the crack was placed in the center of the fusion zone. According to the crack orientation system described in Reference 4, these cracks would have a "BA" orientation.

All specimens were tested on a feedback-controlled MTS testing machine using load as the control parameter. A stress ratio ($R = K_{min}/K_{max}$) of 0.05 and sinusoidal waveform were employed for all tests. Tests at elevated temperatures were conducted in an air-circulating furnace at a cyclic frequency of 40 cpm (0.667 Hz).

TABLE 5.1

MATERIAL IDENTIFICATION

| Material | Producer/ Heat No. | Product Form | Material Condition |
|---|---|---|---|
| A | U. S. Steel/ 1P4255 | 3 in. plate SA-387, Gr. C. | Mill annealed. |
| B | Lukens/ B8238 | 3-1/2 in. plate SA-387, Gr. D. | Annealed per Specification RDT M5 -5T. |
| C | Unknown/ 802B06530 | 1 in. plate SA-516, Gr. 60 | Mill annealed. |
| D | Lukens/ A-1195-1* | 12 in. plate SA-533, Gr. B, Cl. 1 | Quenched & tempered. |
| E | RACO/ 2P5022 | Weld filler wire RACO 521S | Auto. Sub. Arc welded. Stress relieved 12 hr @ 1300°F, A.C. |
| F | unknown | Weld filler wire. AWS E8018-C1 | As welded. |

* Heavy Section Steel Technology Program plate No. 02.

TABLE 5.2

CHEMICAL COMPOSITION (percent by weight)

| Material | C | Mn | P | S | Si | Cr | Mo | Ni | Cu | V | Sn | Al | Ti |
|---|---|---|---|---|---|---|---|---|---|---|---|---|---|
| A | 0.15 | 0.56 | 0.016 | 0.013 | 0.91 | 1.35 | 0.52 | 0.06 | 0.05 | 0.006 | 0.009 | 0.020 | 0.01 |
| B | 0.12 | 0.50 | 0.010 | 0.020 | 0.22 | 2.30 | 0.98 | 0.1 | * | * | * | * | * |
| C | 0.15 | 1.20 | 0.005 | 0.025 | 0.23 | 0.005 | 0.01 | 0.008 | 0.020 | * | 0.001 | 0.052 | * |
| D | 0.22 | 1.48 | 0.012 | 0.018 | 0.25 | * | 0.52 | 0.68 | * | * | * | * | * |
| E** | 0.09 | 0.80 | 0.021 | 0.019 | 0.52 | 2.41 | 0.97 | 0.22 | 0.27 | 0.01 | 0.014 | 0.19 | 0.01 |
| F** | 0.08 | 1.12 | 0.017 | 0.021 | 0.45 | 0.02 | 0.01 | 1.50 | 0.02 | 0.012 | 0.001 | 0.003 | * |

* Not determined.

** As-deposited.

TABLE 5.3

MECHANICAL PROPERTIES

| MATERIAL | SPECIMEN N° | TEST TEMP. | 0.2% OFFSET YIELD | ULTIMATE STRENGTH | UNIFORM ELONG. | TOTAL ELONG. | RED. IN AREA | HARDNESS | SITE SEQUENCE N°*** |
|---|---|---|---|---|---|---|---|---|---|
| A | T217 | 75°F | 36,200 psi** | 67,360 psi | 15.59% | 22.55% | 61.16% | $R_B$=77.02 | H03000 |
| A | T218 | 600 | 31,650 | 69,090 | 10.89 | 16.00 | 65.29 | * | H03003 |
| A | T219 | 800 | 29,100 | 59,020 | 9.32 | 18.26 | 68.85 | * | H03004 |
| A | T220 | 1000 | 24,920 | 40,000 | 9.50 | 37.99 | 87.70 | * | H03005 |
| B | T470 | 75 | 35,850 | 71,460 | 13.31 | 20.13 | 59.35 | $R_B$=78.80 | H03001 |
| B | T471 | 600 | 41,220 | 77,400 | 10.33 | 14.35 | 50.41 | * | H03002 |
| B | T472 | 800 | 32,930 | 68,780 | 9.60 | 15.45 | 56.91 | * | H03006 |
| B | T473 | 1000 | 31,220 | 55,120 | 13.14 | 28.33 | 69.92 | * | H03007 |
| C | T475 | 75 | 39,520 | 65,400 | 18.90 | 27.26 | 75.81 | $R_B$=75.47 | H03300 |
| C | T476 | 600 | 33,740 | 69,270 | 16.45 | 28.75 | 76.42 | * | H03301 |
| C | T477 | 800 | 29,670 | 46,910 | 11.27 | 30.33 | 85.37 | * | H03302 |
| C | T478 | 1000 | 19,670 | 24,750 | 7.74 | 65.30 | 88.52 | * | H03303 |
| D | - | 75 | 67,500** | 86,500 | * | 17.50 | * | $R_B$=89.62 | from Ref. 3 |
| D | - | 575 | 55,300 | 80,800 | * | 17.40 | * | * | from Ref. 3 |
| E | T180 | 75 | 65,530** | 82,760 | 10.55 | 18.22 | 65.85 | $R_B$=90.50 | H03200 |
| E | T181 | 600 | 57,850 | 79,830 | 6.96 | 12.63 | 61.98 | * | H03201 |
| E | T182 | 800 | 58,940 | 73,010 | 6.05 | 14.54 | 67.48 | * | H03202 |
| E | T183 | 1000 | 50,490 | 53,410 | 1.20 | 22.20 | 78.86 | * | H03203 |
| F | T485 | 75 | 79,590** | 89,430 | 7.33 | 14.24 | 71.54 | $R_B$=94.10 | H03304 |
| F | T486 | 600 | 73,770 | 99,590 | 11.44 | 17.32 | 60.66 | * | H03305 |
| F | T487 | 800 | 62,950 | 76,070 | 6.00 | 11.99 | 38.52 | * | H03306 |
| F | T488 | 1000 | 40,890 | 41,460 | 0.56 | 28.77 | 86.18 | * | H03307 |

Strain rate = $3 \times 10^{-5}$ $sec^{-1}$ (except for Material D where $6.67 \times 10^{-5} < \dot{\varepsilon} < 1.33 \times 10^{-4}$ $sec^{-1}$).

* Not determined.

** Upper yield strength.

*** HEDL LMFBR Fuel Cladding Information Center.

Crack growth tests were conducted at 75°F (24°F), 600°F (316°C), 800°F (427°C), and 1000°F (538°C), and the results for base metal specimens are shown in Figures 5.8 - 5.11, respectively, and for weldment specimens in Figures 5.12- 5.15 respectively. The results for specimens 317 and 383 (Material D) had been previously reported in References 5 and 6, respectively.

Comparing the crack growth results for the different pressure vessel steels at a given temperature in Figures 5.8 - 5.11, shows that all four steels behave in a similar fashion. This is in agreement with the observations of References 7 and 8 that fatigue-crack growth behavior in the different grades of low-alloy pressure vessel steels does not differ significantly from one alloy to another. Figure 5.8 shows a comparison between the results of the present study, and the equation proposed by Barson[8] for the behavior of ferritic-pearlitic steels at room temperature, and in general the agreement is good. Also, although comparisons are not shown, reasonably good agreement between the present results and those of Brinkman et al[9] for SA-387 grade D, is obtained where test temperatures, stress ratios, and cyclic frequencies are similar.

Comparing the curves for each of the different test temperatures shows that, in general, fatigue-crack growth rates increase with increasing temperature. This is in agreement with similar observations on the effect of temperature upon the crack growth behavior of pressure vessel steels 9-11, as well as observations on other alloys such as austenitic stainless steels (12).

Comparing the results for weldment specimens with those for base metal specimens tested at the same temperatures shows that, in general, the behavior is quite similar. This is in agreement with observations on several studies on pressure vessel steels [13-19], where it was noted that crack growth rates in weldments were generally equivalent to, or lower than, crack growth rates in the base metal tested under similar conditions. Similar observations were also made for weldments in austenitic stainless steels [4, 20, 21].

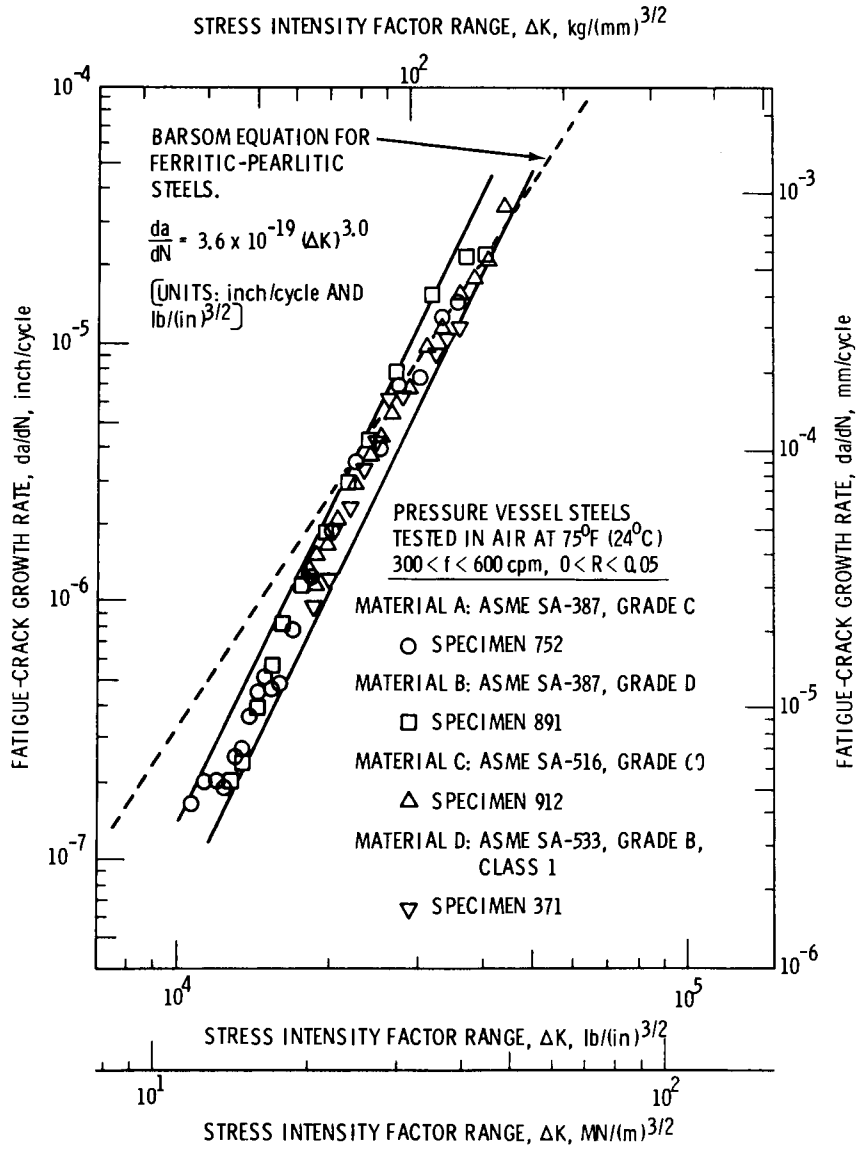


Figure 5.8. Fatigue-crack growth behavior of four ferritic pressure vessel steels tested in an air environment at 75°F (24°C).

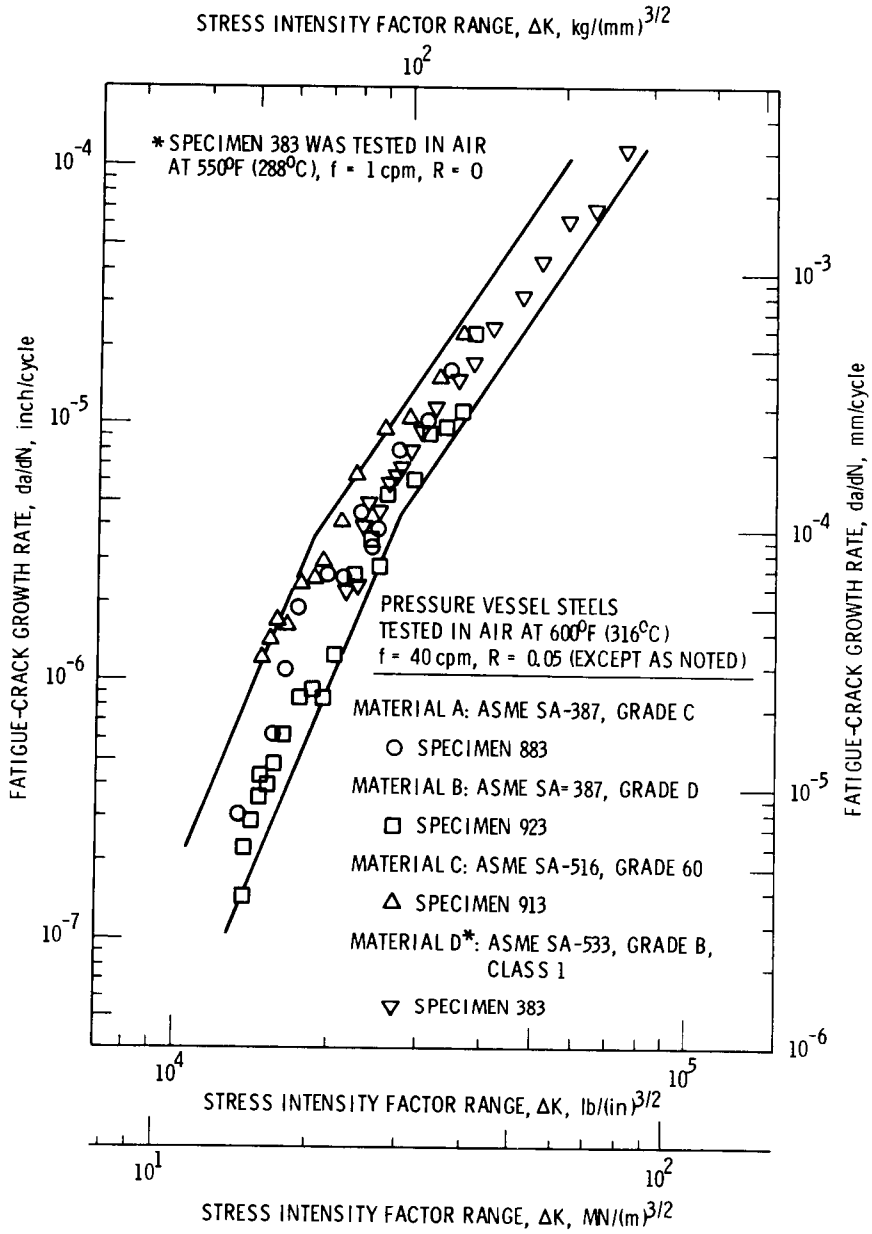


5.9. Fatigue-crack growth behavior of four ferritic pressure vessel steels tested in an air environment at 600°F (316°C).

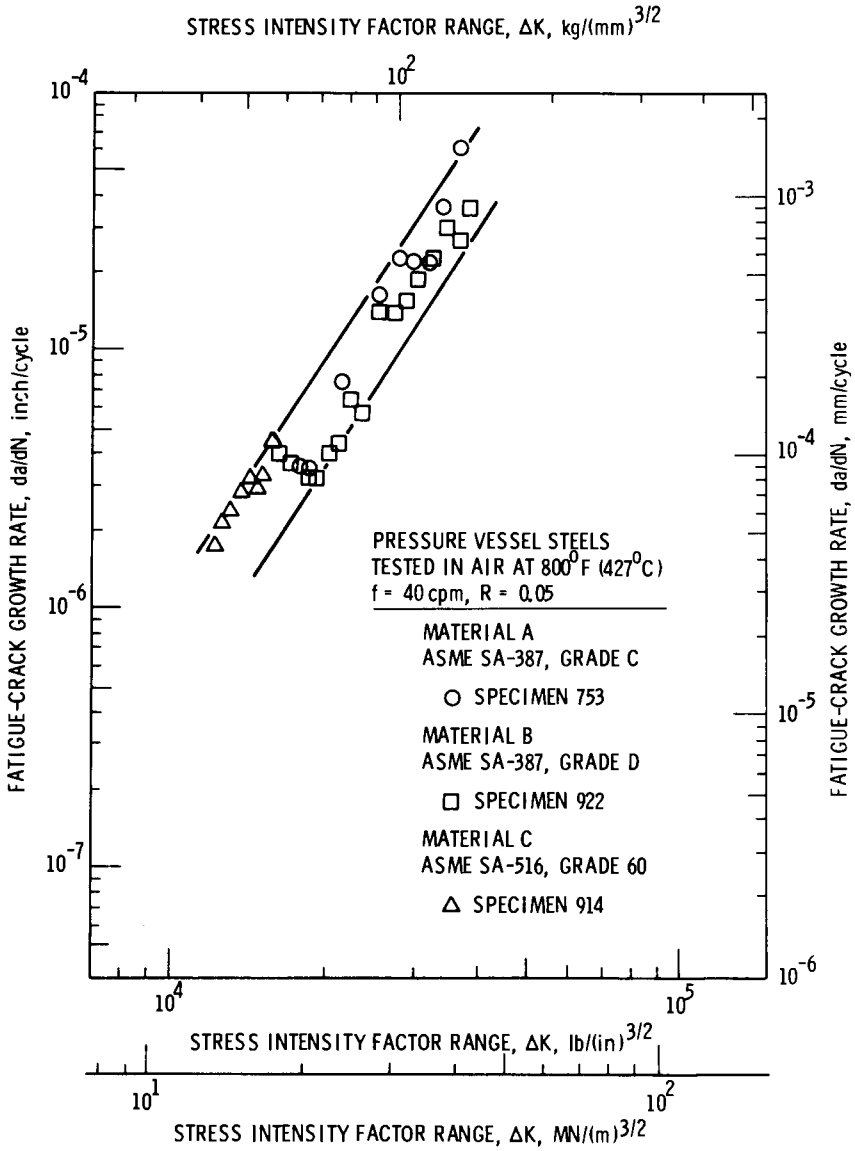


Figure 5.10. Fatigue-crack growth behavior of three ferritic pressure vessel steels tested in an air environment at 800°F (427°C).

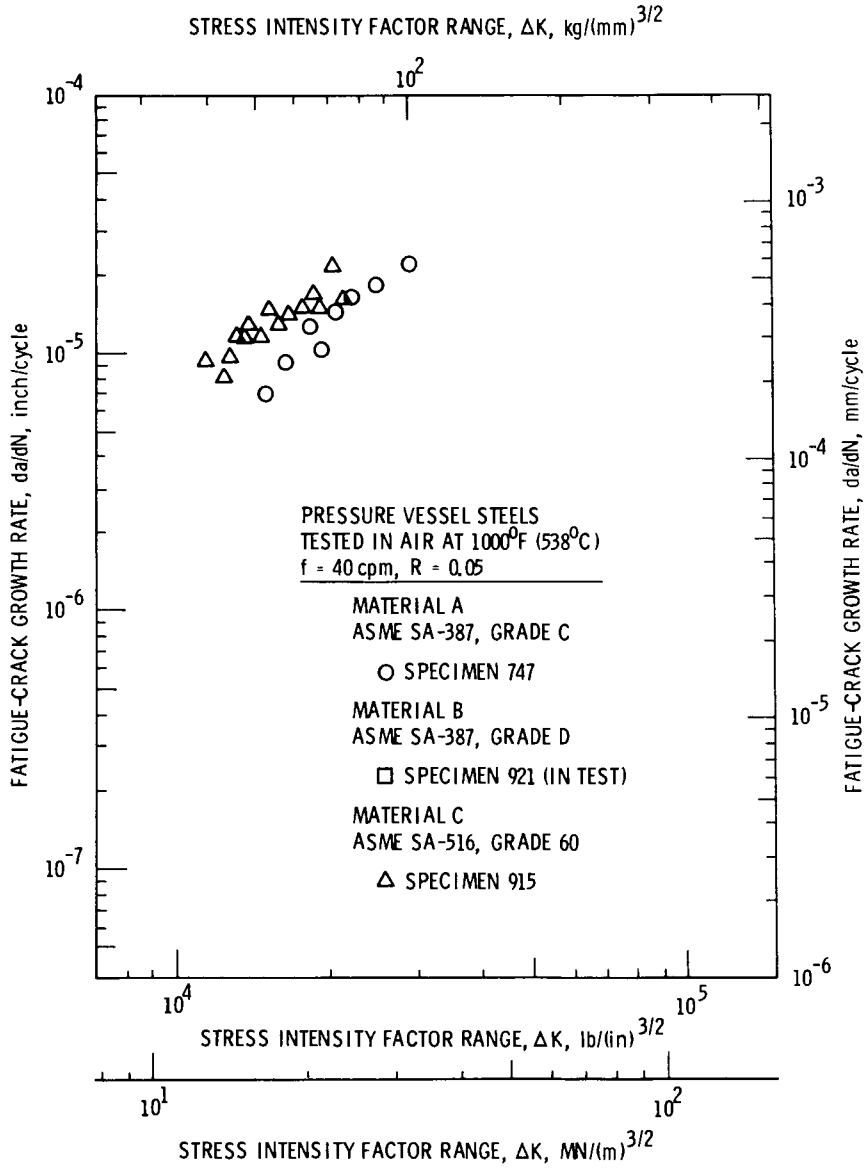


Figure 5.11. Fatigue-crack growth behavior of three ferritic pressure vessel steels tested in an air environment at 1000°F (538°C).

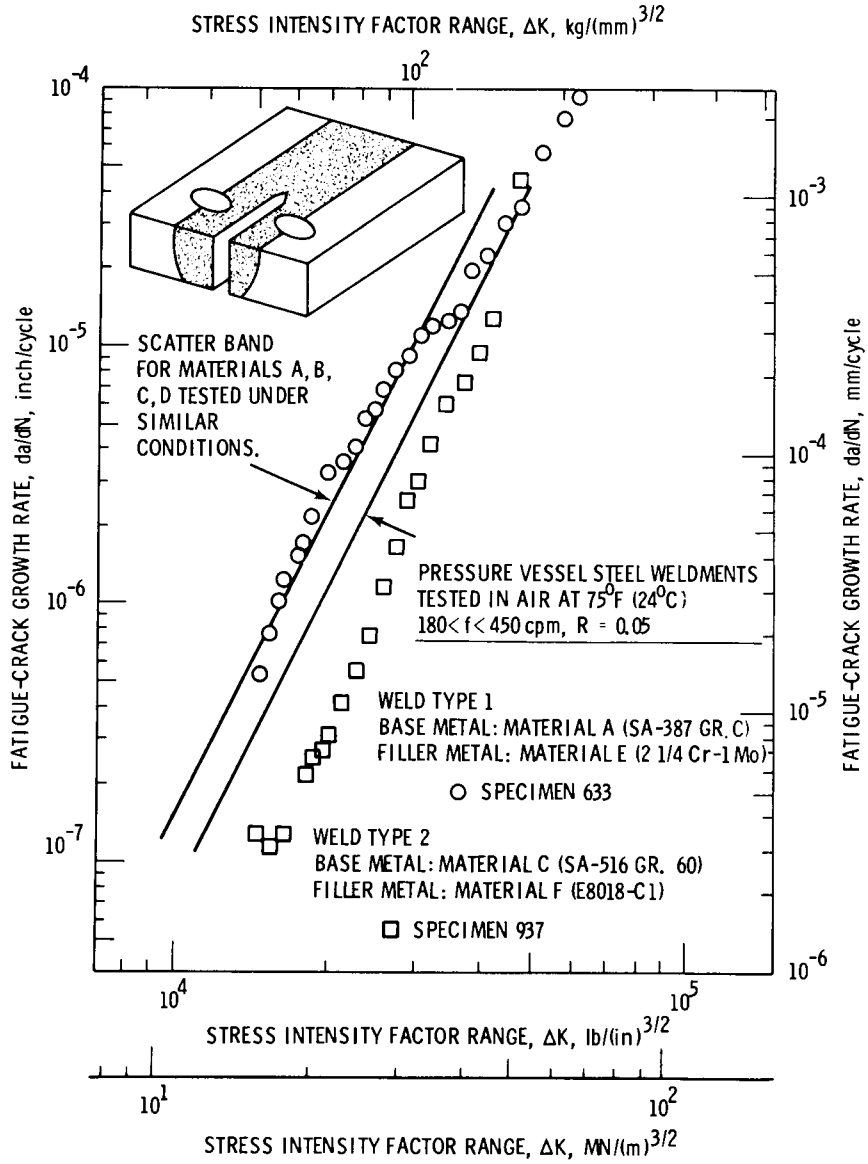


Figure 5.12. Fatigue-crack growth behavior of pressure vessel steel weldments tested in an air environment at 75°F (24°C).

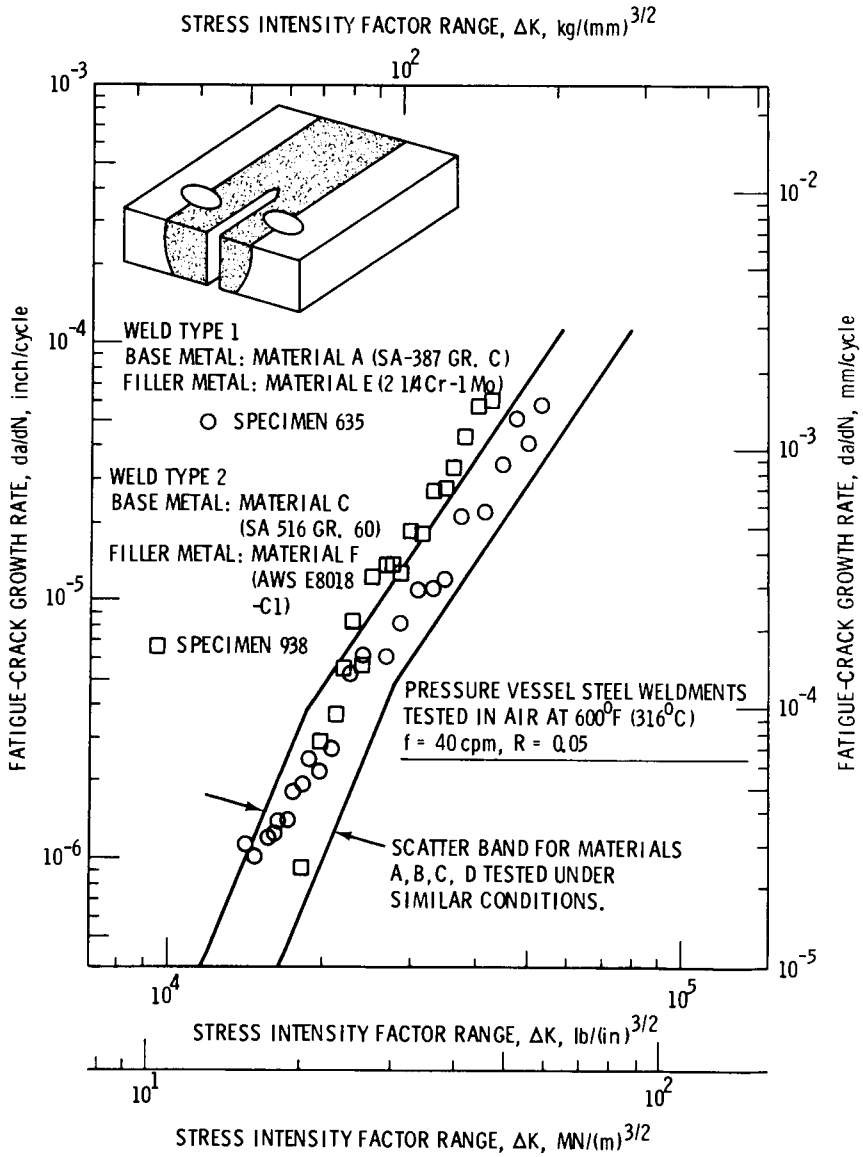


Figure 5.13. Fatigue-crack growth behavior of pressure vessel steel weldments tested in an air environment at 600°F (316°C).

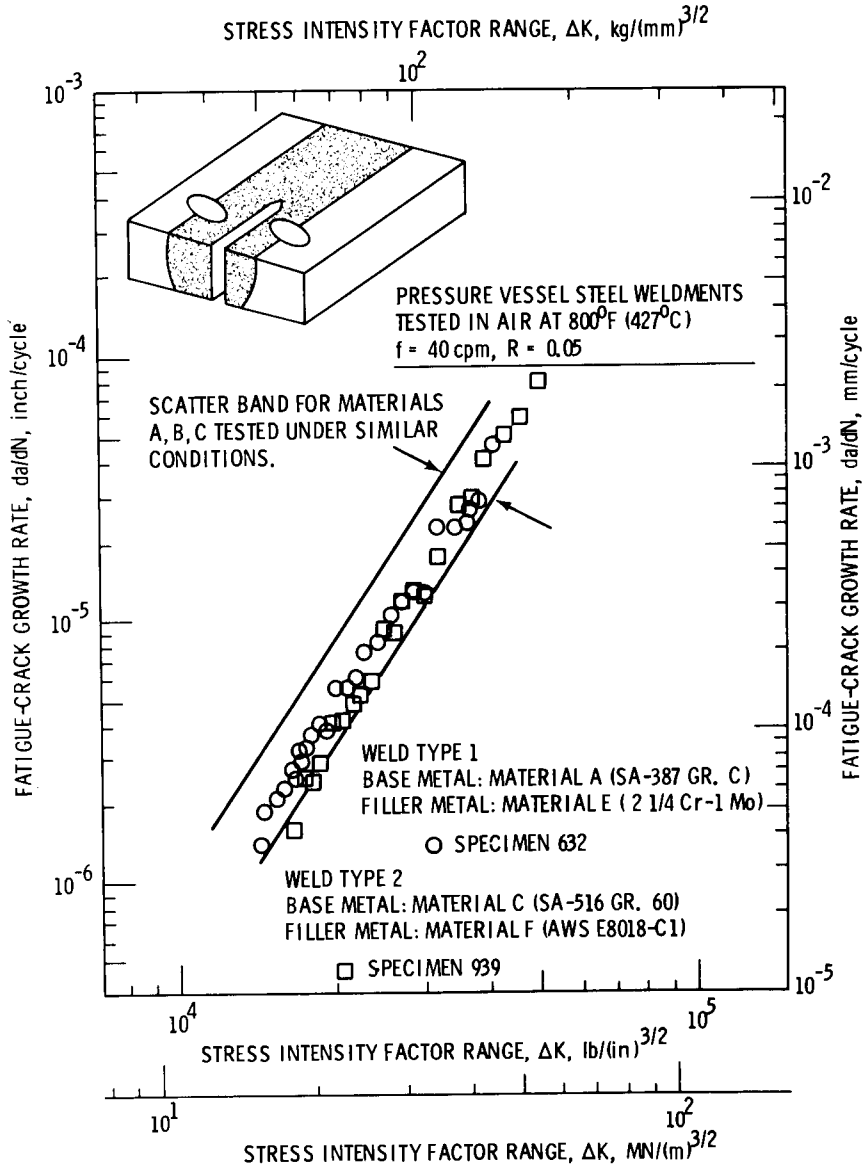


Figure 5.14. Fatigue-crack growth behavior of pressure vessel steel weldments tested in an air environment at 800°F (427°C).

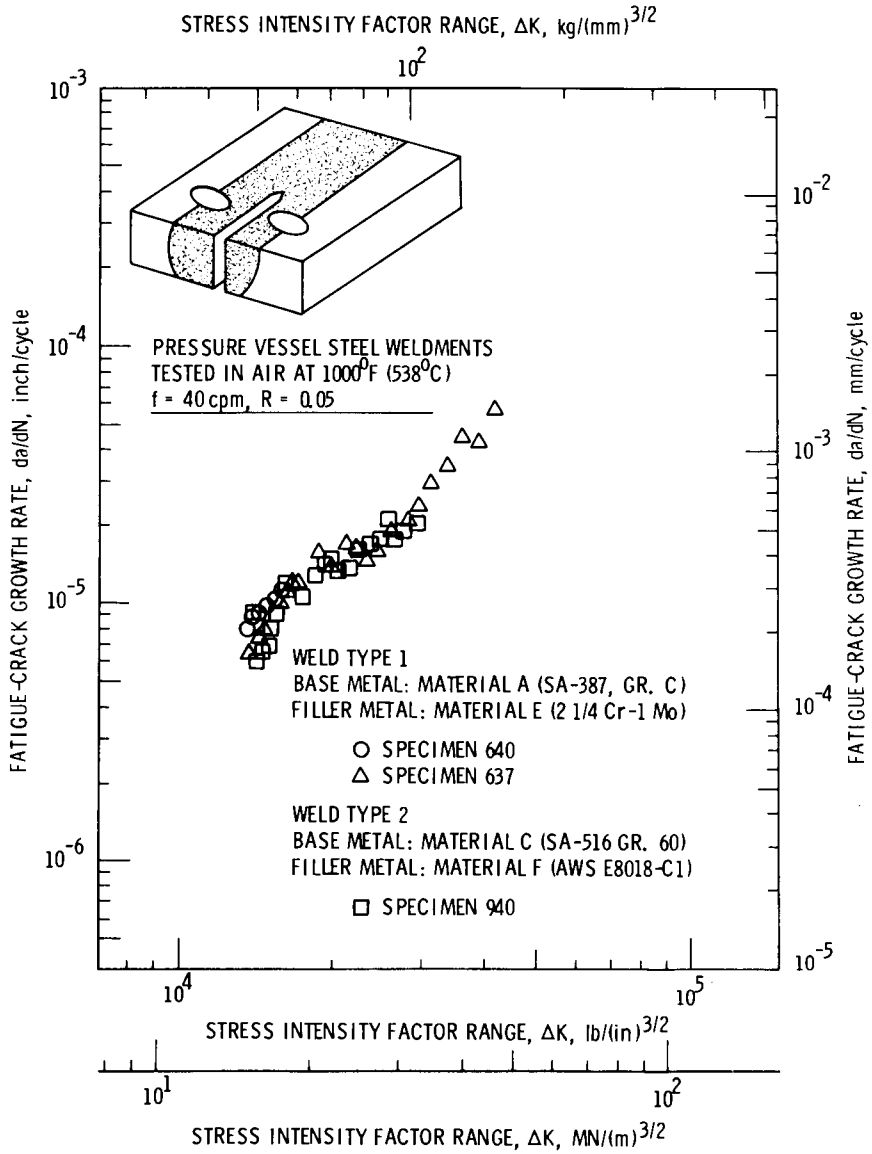


Figure 5.15. Fatigue-crack growth behavior of pressure vessel steel weldments tested in an air environment at 1000°F (538°C).

5.2.2.3 Expected Accomplishments

Testing to characterize the effect of liquid sodium environment upon fatigue-crack growth behavior of austenitic steels, ferritic steels, and nickel-base alloys will continue.

## 5.2.3 THE DUCTILE FRACTURE TOUGHNESS RESPONSE OF INCONEL 718 AND INCONEL X-750 AT 75°F AND 800°F - W. J. Mills, R. L. Knecht

5.2.3.1 Objective

The objective of this work is to characterize the fracture toughness response of LMFBR structural alloys. This information supports the design, operation, and safety analyses of LMFBR structural components.

5.2.3.2 Accomplishments and Status

The elastic-plastic fracture toughness response of Inconel 718 and and Inconel X-750 was determined at 75°F and 800°F. The chemical analysis and mechanical properties of these materials are given in Tables 5.4 and 5.5, respectively. The Inconel 718 INEL heat treatment and the Inconel X-750 double aging heat treatment are reported in Table 5.6.

Fracture tests were performed on deeply cracked (fatigue precracked to a/w > 0.6) .577 T compact tension specimens of Inconel 718 (thickness-0.495 inch) and Inconel X-750 (thickness - 0.577 inch) oriented in the T-L direction (22). The critical value of J associated with crack initiation, $J_{Ic}$, was determined by the R-curve technique outlined in Reference (23).

The R-curves for Inconel 718 reveal that $J_{Ic}$ decreased from 727 in-lb/in$^2$ at 75°F (Figure 5.16) to 555 in-lb/in$^2$ at 800°F (Figure 5.17). The room temperature value of $J_{Ic}$ was considerably higher than that reported by Wells et al. (24), 120 in-lb/in$^2$. This apparent anomaly is believed to be associated with heat treatment and/or melt practice variations. In support of this hypothesis, Logsden (25) has shown that the

TABLE 5.4

CHEMICAL COMPOSITION (percent by weight)

| Material | Producer/Heat No. | C | Mn | Fe | S | Si | Cu | Ni | Cr | Al | Ti | Co | P | Mo | B | Cb & Ta |
|---|---|---|---|---|---|---|---|---|---|---|---|---|---|---|---|---|
| Inconel 718 | Haynes/2180-1-9345 | 0.06 | 0.08 | Bal. | <.005 | 0.07 | 0.04 | 52.88 | 18.06 | 0.51 | 1.11 | 0.22 | <.005 | 2.89 | .004 | 5.04 |
| Inconel X-750 | Huntington/HT6716X | 0.03 | 0.56 | 6.66 | 0.007 | 0.40 | 0.09 | 72.84 | 15.27 | 0.67 | 2.60 | 0.07 | * | * | * | * |

* Not determined.

TABLE 5.5

MECHANICAL PROPERTIES

| Material | Temperature | Specimen No. | 0.2% Yield Strength | Ultimate Strength | Total Elongation | Red. In Area | Site Sequence No. |
|---|---|---|---|---|---|---|---|
| Inconel 718 | 75°F | T41 | 145,350 psi | 190,730 psi | 20.04 % | 33.87 % | H04916 |
| Inconel 718 | 800°F | T40 | 126,830 psi | 168,700 psi | 15.47 % | 28.46 % | H04936 |
| Inconel X-750 | 75°F | T106 | 93,090 psi | 149,190 psi | 14.33 % | 15.45 % | H05986 |
| Inconel X-750 | 800°F | T108 | 82,100 psi | 148,390 psi | 19.62 % | 25.81 % | H05986 |

Strain rate = $1.78 \times 10^{-3}$ $min^{-1}$

TABLE 5.6

HEAT TREATMENTS

INCONEL 718: INEL Heat Treatment

Solution annealed 1 hour at 2000°F
Cooled to 1325°F at 100°F/hour
Aged 4 hours at 1325°F
Cooled to 1150°F at 100°F/hour
Aged 16 hours at 1150°F
Air cooled to room temperature.

INCONEL X-750: Solution Treated and Double Aging Heat Treatment

Solution annealed 2 hours at 2100°F
Air cooled
Aged 24 hours at 1500°F
Air cooled
Aged 20 hours at 1300°F
Air cooled.

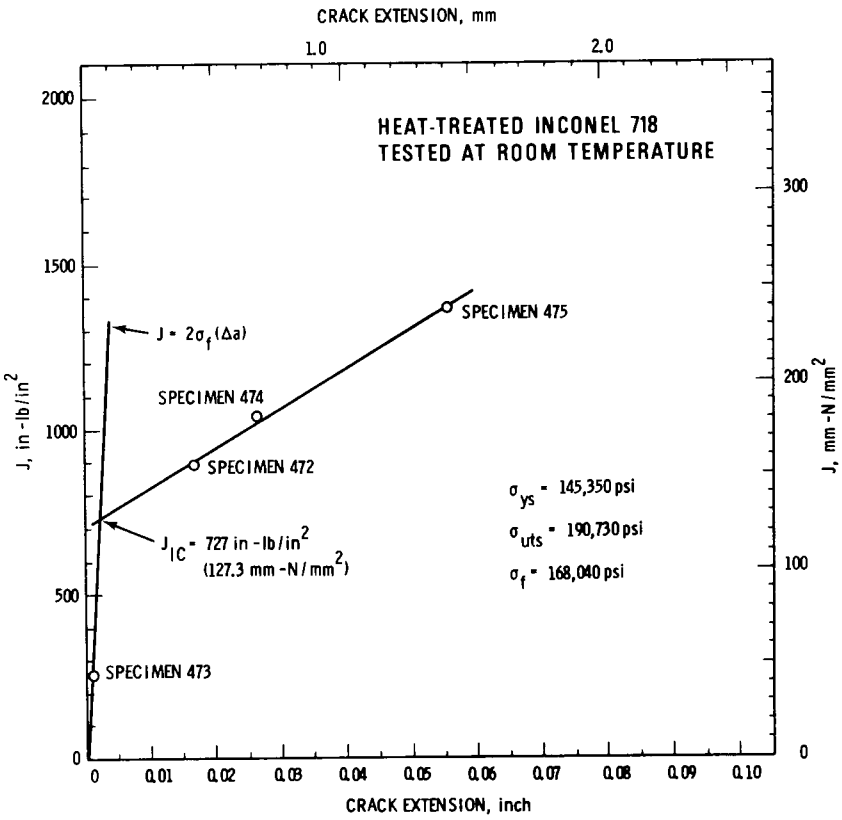


Figure 5.16. R-curve for Inconel 718 (INEL Heat Treatment) tested at room temperature.

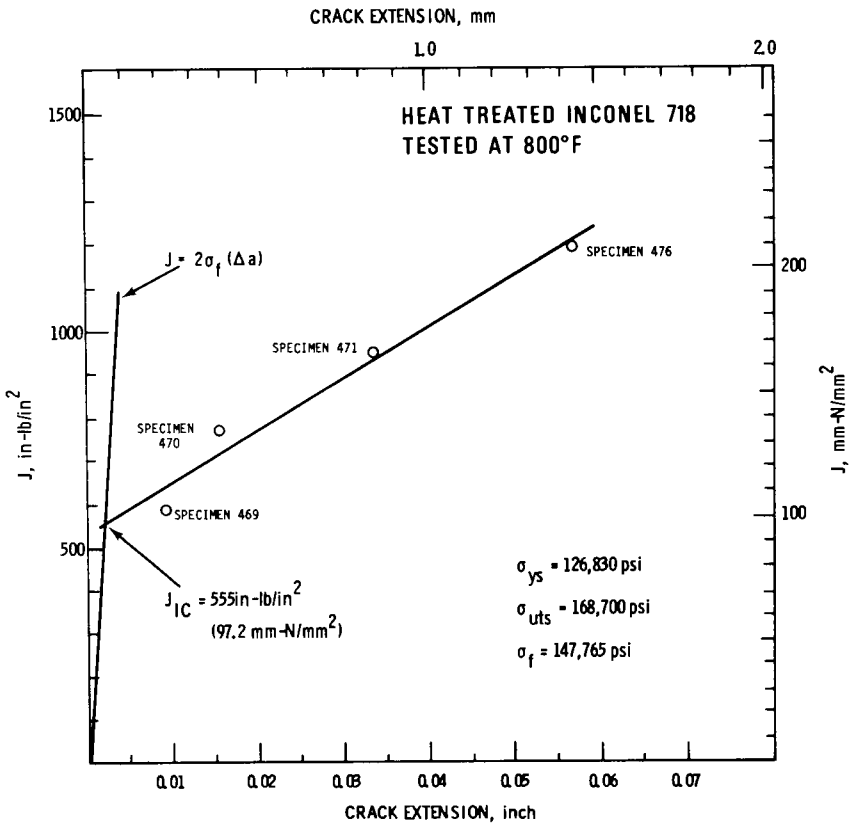


Figure 5.17. R-curve for Inconel 718 (INEL Heat Treatment) tested at 800°F.

fracture toughness of Inconel X-750 (at -452°F) was very dependent on manufacturing process/heat treatment combination. Additional testing is currently underway at HEDL in order to resolve this issue.

The elastic-plastic fracture toughness behavior of Inconel X-750 at 75°F and 800°F is illustrated in Figures 5.18 and 5.19, respectively. The room temperature ductile fracture toughness of Inconel X-750, 544 in-lb/in$^2$, was found to be less than that of Inconel 718. However, contrary to the fracture behavior of Inconel 718, the elevated temperature ductile fracture toughness of Inconel X-750 was essentially the same as the room temperature response. This observation is consistent with Logsdon's findings (24) where $J_{Ic}$ for Inconel X-750 remained essentially constant over a temperature range from 75°F to -452°F.

It is significant to point out that the experimentally determined stretch zone size for both Inconel 718 (Figure 5.16: Specimen 473) and Inconel X-750 (Figures 5.18 and 5.19: Specimens 523* and 955, respectively) were in excellent agreement with the theoretical curve $J = 2\sigma_f (\Delta a)$.

5.2.3.3 Expected Accomplishments

Room temperature and elevated temperature elastic-plastic fracture toughness testing of nickel-base alloys, A-286 stainless steel, and ferritic steels will continue. In addition, fractographic examination of fracture specimens will be performed in order to better characterize the fracture response of these alloys.

* The fracture surface of Specimen 523 exhibited both stretch zone formation and localized crack extension. Therefore, the data point which falls on the line $J = 2\sigma_f (\Delta a)$ represents only those regions exhibiting a stretch zone (approximately 60% of the crack front). The data point which falls on the R-curve is representative of the entire crack front (i.e., a weighted average of stretch zone and crack extension measurements).

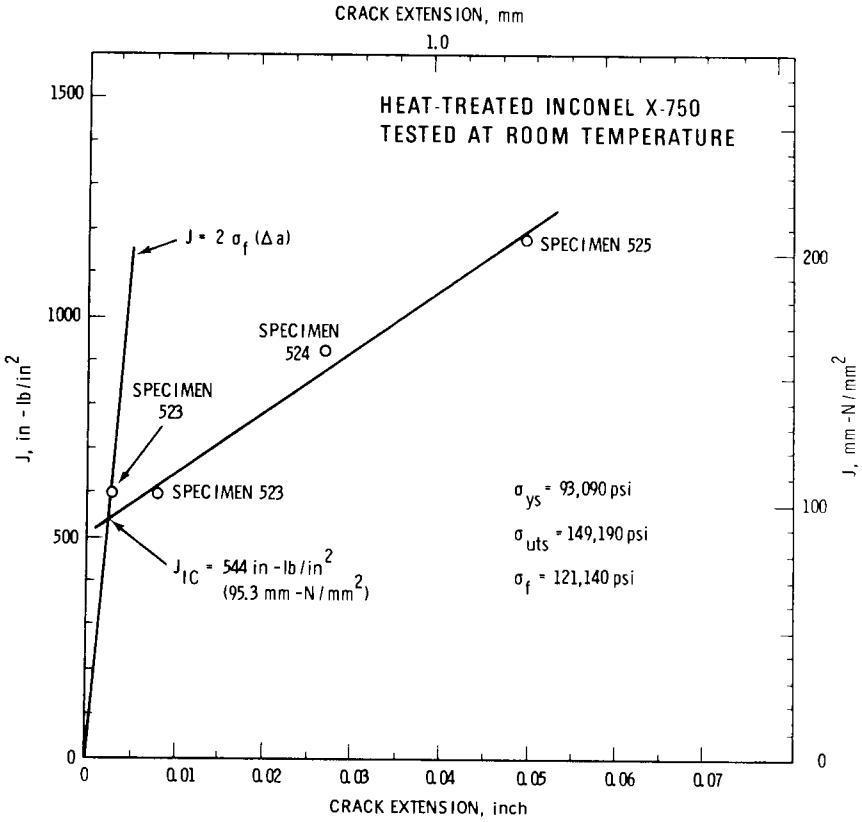


Figure 5.18. R-curve for Inconel X-750 (Solution Treated and Double Aging Heat Treatment) tested at room temperature.

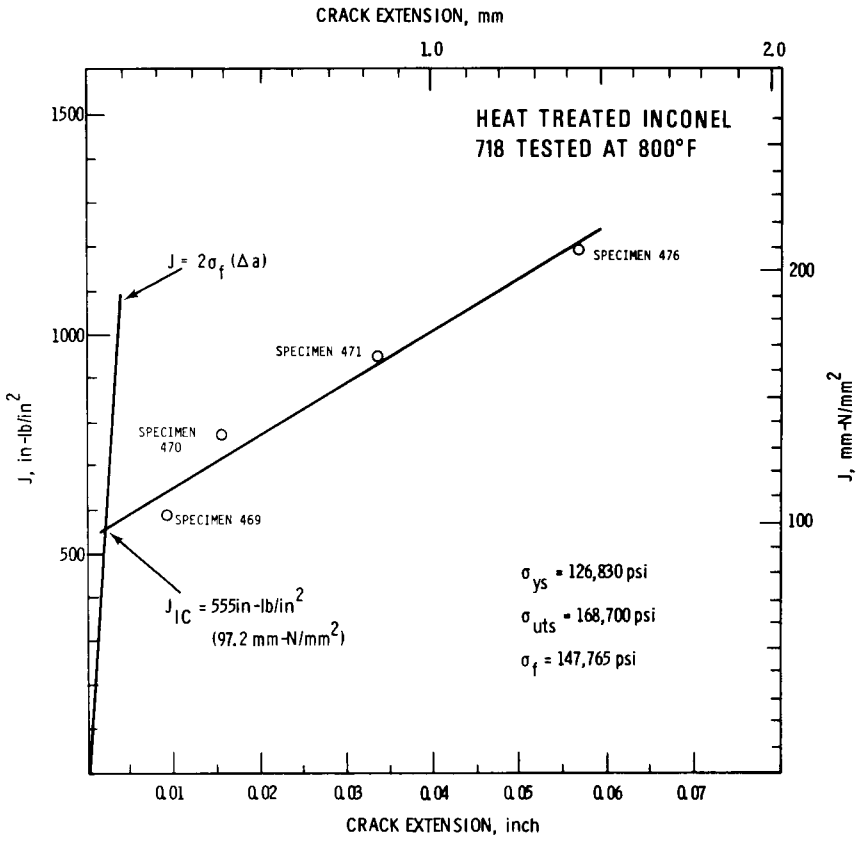


Figure 5.19. R-curve for Inconel X-750 (Solution Treated and Double Aging Heat Treatment) tested at 800°F.

## 5.3 MATERIALS INFORMATION DOCUMENTATION

J. C. Spanner, R. A. Moen, M. F. Marchbanks

### 5.3.1 Objective

The objective of this program is to manage, coordinate and distribute the Nuclear Systems Materials Handbook as a standard materials property reference for the nuclear community.

### 5.3.2 Accomplishments and Status

Nuclear Systems Materials Handbook

Update publication package Number 4 was 95% complete at the end of July and was scheduled for printing early in August, 1976. This package will contain 84 new pages.

## 5.4 REFERENCES


1. F. S. Acton, Analysis of Straight-Line Data, John Wiley & Sons, Inc., New York, 1959, pp. 184-187.
2. L. A. James, "Fracture Toughness of A516 Grade 60 Steel," Welding Journal Research Supplement, Vol. 51, No. 10, pp. 506s-507s, 1972.
3. C. W. Hunter and J. A. Williams, "Fracture and Tensile Behavior of Neutron-Irradiated A533-B Pressure Vessel Steel," Nuclear Engineering and Design, Vol. 17, No. 1, pp. 131-148, 1971.
4. L. A. James, "Crack Propagation Behavior in Type 304 Stainless Steel Weldments at Elevated Temperature," Welding Journal Research Supplement, Vol. 52, No. 4, pp. 173s-179s, 1973.
5. L. A. James and J. A. Williams, "The Effect of Temperature and Neutron Irradiation Upon the Fatigue-Crack Propagation Behavior of ASTM A533-B Steel," Journal of Nuclear Materials, Vol. 47, No. 1, pp. 17-22 1973.
6. L. A. James and J. A. Williams, "Fatigue-Crack Propagation in Unirradiated and Irradiated ASTM A533-B Steel at Low Cyclic Frequency," Journal of Nuclear Materials, Vol. 49, No. 3, pp. 241-243, 1973.
7. J. P. Hickerson, A. W. Pense and R. D. Stout, "The Influence of Notches on the Fatigue Resistance of Pressure Vessel Steels," Welding Journal Research Supplement, Vol. 47, No. 2, pp. 63s-72s, 1968.

8. J. M. Barsom, "Fatigue Behavior of Pressure-Vessel Steels," Bulletin No. 194, Welding Research Council, New York, 1974.

9. C. R. Brinkman, W. R. Corwin, M. K. Brooker, T. L. Hebble, and R. L. Kleuh, "Time Dependent Mechanical Properties of 2-1/4 Cr-1 Mo Steel for Use in Steam Generator Design," Report ORNL-5125, Oak Ridge National Laboratory, 1976.

10. H. I. McHenry and A. W. Pense, "Fatigue Crack Propagation in Steel Alloys at Elevated Temperatures," Fatigue at Elevated Temperatures, ASTM STP-520, pp. 345-354, American Society for Testing and Materials, Philadelphia, 1973.

11. A. W. Pense and R. D. Stout, "Elevated Temperature Fatigue of Pressure Vessel Steels," Welding Journal Research Supplement, Vol. 54, No. 8, pp. 246s-252s, 1975.

12. L. A. James, "Fatigue-Crack Propagation in Austenitic Stainless Steels," Atomic Energy Review, Vol. 14, No. 1, 1976

13. W. G. Clark, Jr., "Fatigue Crack Growth Characteristics of Heavy Section ASTM A533 Grade B, Class 1 Steel Weldments," ASME Paper 70-PVP-24, American Society of Mechanical Engineers, New York, 1970.

14. K. R. Dowse and C. E. Richards, "Fatigue Crack Propagation Through Weld Heat Affected Zones," Metallurgical Transactions, Vol. 2, No. 2, pp. 599-703, 1971.

15. M. Parry, H. Nordberg and R. W. Hertzberg, "Fatigue Crack Propagation in A514 Base Plate and Welded Joints," Welding Journal Research Supplement, Vol. 51, No. 10, pp. 485s-490s, 1972.

16. F. V. Lawrence and W. H. Munse, "Fatigue Crack Propagation in Butt Welds Containing Joint Penetration Defects," Welding Journal Research Supplement, Vol. 52, No. 5, pp. 221s-225s, 232s, 1973.

17. R. J. Bucci, B. N. Greene and P. C. Paris, "Fatigue Crack Propagation and Fracture Toughness of 5Ni and 9Ni Steels at Cryogenic Temperatures," Progress in Flaw Growth and Fracture Toughness Testing, ASTM STP-536, pp. 206-228, American Society for Testing and Materials, Philadelphia, 1973.

18. D. F. Socie and S. D. Antolovich, "Subcritical Crack Growth Characteristics in Welded ASTM A537 Steel," Welding Journal Research Supplement, Vol. 52, No. 5, pp. 221s-225s, 232s, 1973.

19. S. J. Maddox, "Assessing the Significance of Flaws in Welds Subject to Fatigue," Welding Journal Research Supplement, Vol. 53, No. 9, pp. 401s-409s, 1974.

20. P. Shahinian, H. H. Smith and J. R. Hawthorne, "Fatigue Crack Propagation in Stainless Steel Weldments at High Temperature," Welding Journal Research Supplement, Vol. 51, No. 11, pp. 527s-532s, 1972.

21. L. A. James, "Fatigue-Crack Growth in Type 304 Stainless Steel Weldments at Elevated Temperatures," Journal of Testing and Evaluation, Vol. 1, No. 1, pp. 52-57, 1973.

22. R. J. Goode, "Identification of Fracture Plane Orientation," ASTM Mat'ls Res. and Std., Vol. 12, Sept. 1972, p. 31.

23. J. D. Landes and J. A. Begley, "Test Results from J-Integral Studies: An Attempt to Establish a $J_{Ic}$ Testing Procedure," ASTM STP 560, 1974, p. 170.

24. J. M. Wells, W. A. Logdson, R. Kossowsky, and M. R. Daniel, "Structural Materials for Cryogenic Applications," Westinghouse Research Lab., Research Report 75-904-CRYMT-R2, Oct. 10, 1975.

25. W. A. Logsdon, "Cryogenic Fracture Mechanics Properties of Several Manufacturing Process/Heat Treatment Combinations of Inconel X-750," Westinghouse Research Lab., Scientific Paper 75-1E7-CRYMT-P1, May 7, 1975.

# 6.0 WESTINGHOUSE ADVANCED REACTORS DIVISION

E. C. Bishop, W. E. Ray

## 6.1 INTRODUCTION

Two programs are being performed at Westinghouse Advanced Reactors Division (ARD). The first program is "Validation of High Temperature Design Methods and Criteria" (189a CW063). Two of the tasks in this program are "Basic Specimen Testing" and "Tubular Specimen Testing". The specimen material for both tasks was supplied from the ORNL reference heat of Type 304 stainless steel and future tests will include specimens from the reference heat of Type 316 stainless steel. The second program is "Component Materials Compatibility" (189a CW065). One of the tasks in this program is "Mechanical Properties".

The basic specimen tests are performed on plates and bars loaded at 1100°F (593°C). Specimen designs have been selected to provide nonuniform stress distributions (uniaxial, plane stress, and plane strain) and to determine the effects of holes, notches, and welds in various orientations. Uniform and stepped loading is applied at levels sufficient to cause significant creep strain in hundreds of hours and rupture in several thousand hours. Test data are used for: verification of constitutive equations for time-dependent material response, validation of analytical techniques for nonuniform stress states, and investigation of strain limits in base metal, welds, and at geometrical discontinuities.

The tubular specimen tests are being run at 1100°F (593°C) with various combinations of internal pressure and axial load to produce a uniform stress state with a range of biaxiality. Load levels have been selected to determine secondary creep rates in 2000 hours with both steady state and step loading. A limited number of tests will be continued to rupture with geometrical discontinuities. The test data are primarily used for verification of constitutive equations and validation of analytical techniques for shells under multiaxial states of stress.

Westinghouse ARD is performing experiments to identify the effects of a flowing sodium environment on the mechanical properties of LMFBR structural components. The present scope of the program involves three materials: Type 316 Stainless Steel, Type 304 Stainless Steel, and Inconel 718. Work on these materials is in support of the CRBRP upper plenum and hot leg piping components design. Inconel 718 is also being evaluated on a limited basis, relative to the thermal transients to be experienced by the thermal baffles in the upper plenum of the FFTF reactor. More extensive evaluations in the material for the CRBRP will follow. Low-cycle fatigue, creep-fatigue, and creep-rupture experiments are being performed in flowing sodium at elevated temperatures on as-fabricated, aged, and sodium pre-exposed samples in order to identify the environmental effects. In addition, in-air experiments are being performed on the same materials to obtain baseline data.

This report covers the periods: Sections 6.2 and 6.3 - 3/1/76 to 5/31/76 and Section 6.4 - 2/1/76 to 4/30/76.

## 6.2 BASIC SPECIMEN TESTING - M. J. Manjoine (Westinghouse Research Laboratories)

Current basic specimen test data are presented in Table 6.1. Discussions pertaining to specific tests are listed below.

### 6.2.1 Type 304 Stainless Steel Testing

#### 6.2.1.1 E2, Tension Plus Bending

Measurements of photographs of Model E2 indicate that the overall extensometer indicates about 50% higher deflection because of bending of the comparison rods which extends from the gage section to outside the furnace. The specimen geometry is shown in Figure 6.1 with the strain gage location as viewed from the side opposite that for photographic recording. The data from grid measurements and strain gage are plotted in Figure 6.2. The photographs of Model E2 at test termination, Figure 6.3, shows the crack at the upper right hand fillet to be about 12.7 mm long.

Table 6.1 Summary of Creep Data for Type 304SS* and Type 316SS+ at 1100°F (593°C)

| Loading Data | | | Creep Data | | | | | |
|---|---|---|---|---|---|---|---|---|
| | | Plastic | Creep | Increment | | Accumulated | | Permanent |
| Stress (ksi) | Stress (MPa) | Strain (%) | Rate (%/hr) | Strain (%) | Time (hr) | Strain (%) | Time (hr) | Strain (%) |
| C4, 1/3 x 10/3 x 3 in. (8.5 x 85 x 76.2 mm) CENTRAL HOLE, 1/3 in. (8.5 mm) DIA., 304SS | | | | | | | | |
| 18.0[k] | 124.1 | 1.55[n] | $8 \times 10^{-4}$ | 1.26[n] | 1030[a] | 1.26[n] | 1030 | 2.81[n] |
| | | | $4.5 \times 10^{-4}$ | 0.9 | 2013[a] | 2.16[g] | 3043[f] | 3.71 |
| D6-2, NOTCHED BAR, 304SS | | | | | | | | |
| 20.0 | 137.9 | | | 0.94[t] | 4023 | 0.94[t] | 4023[u] | 0.94[t] |
| | | | | | 12869 | 0.12 | 16892[h] | 1.06 |
| E2, TENSION PLUS BENDING (LATERAL STRAIN GAGE DATA), 304SS | | | | | | | | |
| 18.0 | 124.1 | -0.74 | | | | -0.12 | 23[s] | -0.86 |
| ±11.7[w] | ±80.7 | | | | | -0.50 | 1340[a] | -1.24 |
| | | | | | | -0.76 | 3158[a] | -1.40 |
| | | | | | | -0.88 | 4673[s] | -1.62 |
| | | | | | | -0.90 | 5413[s] | -1.64 |
| | | | | | | -0.93 | 6154[s] | -1.67 |
| | | | | | | -0.94 | 6587[a] | -1.68 |
| | | | $4 \times 10^{-5}$ | | | -0.97 | 7424[s] | -1.71 |
| | | | | | | -1.03 | 8216[s] | -1.77 |
| | | | | | | -1.08 | 8500[h] | -1.82 |
| BAW-2, B-TYPE WITH CENTRAL AXIAL WELD, 304SS | | | | | | | | |
| 22.0 | 151.7 | 0.13[n] | $2.4 \times 10^{-3}$ | 5.0[n] | 1509 | 5.0[n] | 1509[a] | 5.1[n] |
| | | | $2 \times 10^{-3}$ | 3.0 | 1077 | 8.0 | 2586[a] | 8.1[g] |
| | | | $2 \times 10^{-3}$ | 2.1 | 954 | 10.1 | 3540[a] | 10.2 |
| | | | $2 \times 10^{-3}$ | 2.1 | 960 | 12.2 | 4500[a] | 12.3[f] |
| CAW-1, C-TYPE WITH CENTRAL AXIAL WELD, 304SS | | | | | | | | |
| 18.0[k] | 124.1 | 0.03[n] | $8 \times 10^{-5}$ | 0.94[n] | 7319[a] | 0.94[n] | 7319[s] | 0.97[n] |
| | | 0.01 | $8.5 \times 10^{-5}$ | 0.25 | 2955[a] | 1.19 | 10274 | 1.23 |
| | | | $7.8 \times 10^{-5}$ | 0.22 | 2829[a] | 1.41 | 13103 | 1.45 |
| | | | $1.6 \times 10^{-4}$ | | | 1.48 | 13500[c] | 1.52 |
| | | | $6 \times 10^{-4}$ | 0.47 | 1468 | 1.88 | 14571[h] | 1.92 |

* HT9T2796, annealed 2000°F (1094°C)
\+ H8092297, annealed 1950°F (1065°C)

Table 6.1 (Continued)

| Loading Data | | | Creep Data | | | | | |
|---|---|---|---|---|---|---|---|---|
| | | Plastic | Creep | Increment | | Accumulated | | Permanent |
| Stress (ksi) | Stress (MPa) | Strain (%) | Rate (%/hr) | Strain (%) | Time (hr) | Strain (%) | Time (hr) | Strain (%) |
| BTW-2, B-TYPE WITH CENTRAL TRANSVERSE WELD, 304SS | | | | | | | | |
| 19.0 | 131 | 0.08 | $1.3 \times 10^{-4}$ | 1.0[n] | 3648[a] | 1.0[n] | 3648 | 1.08[n] |
| | | | | 0.1 | 1410[a] | 1.1 | 5058 | 1.18 |
| | | | $3 \times 10^{-5}$ | 0.04 | 1441 | 1.14 | 6499 | 1.22 |
| | | | $5 \times 10^{-5}$ | 0.08 | 1503 | 1.22 | 8002 | 1.30 |
| | | | $8 \times 10^{-5}$ | 0.08 | 988 | 1.30 | 8990[f] | 1.38 |
| DTW-1, NOTCHED TRANSVERSE WELD, 304SS | | | | | | | | |
| 29.0 | 200 | | | | | | 6020[q] | |
| DTW-2, NOTCHED TRANSVERSE WELD, 304SS | | | | | | | | |
| 25.0 | 172.4 | | | | | 0.003[r] | 5183[e] | 0.16[t] |
| 28.0 | 193 | | | | 5505[m] | | 10688[q] | 0.34[t] |
| DZTW-2, CIRCUMFERENTIAL NOTCH AT HAZ, 304 SS | | | | | | | | |
| 22.0 | 151.7 | | | | | | 903[d] | |
| GTW-1, G-TYPE WITH TRANSVERSE WELD, 304SS | | | | | | | | |
| 25.0 | 172.4 | | | | | | 448[d] | |
| 6D1, NOTCHED BAR, 316SS | | | | | | | | |
| 35.0 | 241.4 | 0.06[r] | | | | 0.01[r] | 335 | |
| 6D2, NOTCHED BAR, 316SS | | | | | | | | |
| 28.0 | 193 | 0.002[r] | | | | 0.013[r] | 1844[f] | |
| 6D3, NOTCHED BAR, 316SS | | | | | | | | |
| 25.0 | 172.4 | | | | | 0.007[r] | 1914 | |

# Footnotes for Table 6.1

[a] Interrupted for photographic measurement

[b] Transition at 0.2% offset

[c] Transition at double minimum rate

[d] Rupture, R

[e] Stress raised (step-loaded test)

[f] Test in progress

[g] Crack initiated

[h] Test terminated, crack tearing

[i] Strain gage average, bending noted

[j] Specimen rotated 180° to investigate bending

[k] Net section stress

[m] Time at final stress

[n] Average overall strain

[p] Test in preparation

[q] Specimen to be sectioned to determine damage.

[r] Deflection of notch, inches (25.4 mm)

[s] Unloaded and reloaded to determine damage

[t] True strain = $l_n$ (Ao/A)

[u] Test interrupted, 1/2 of specimen continued

[v] Peak stress side

[w] Nominal elastic bending stress

NOTE: Previously obtained creep data appeared in earlier issues of "Mechanical Properties Test Data for Structural Materials".

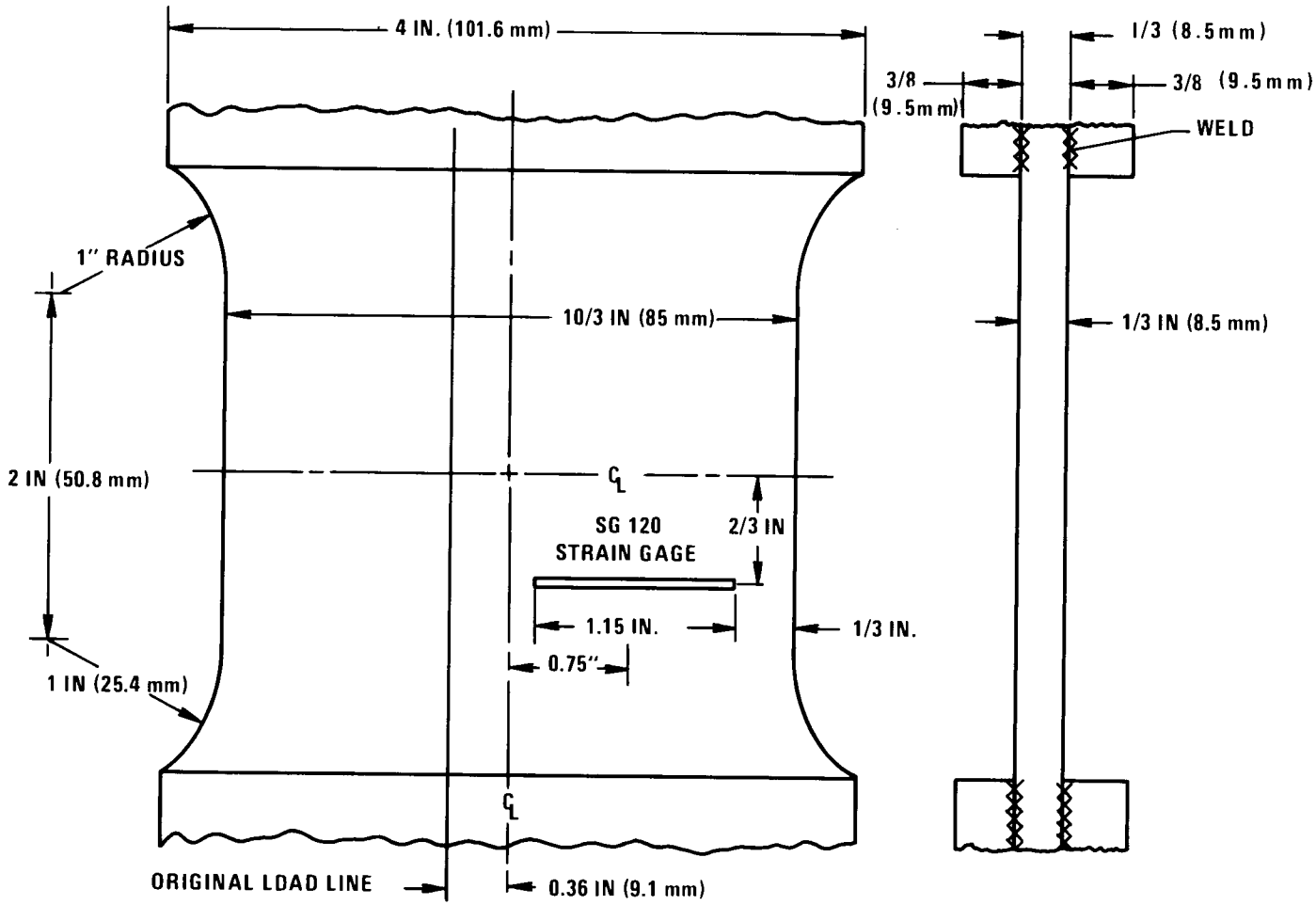


Figure 6.1 Model E2 with Eccentric Load

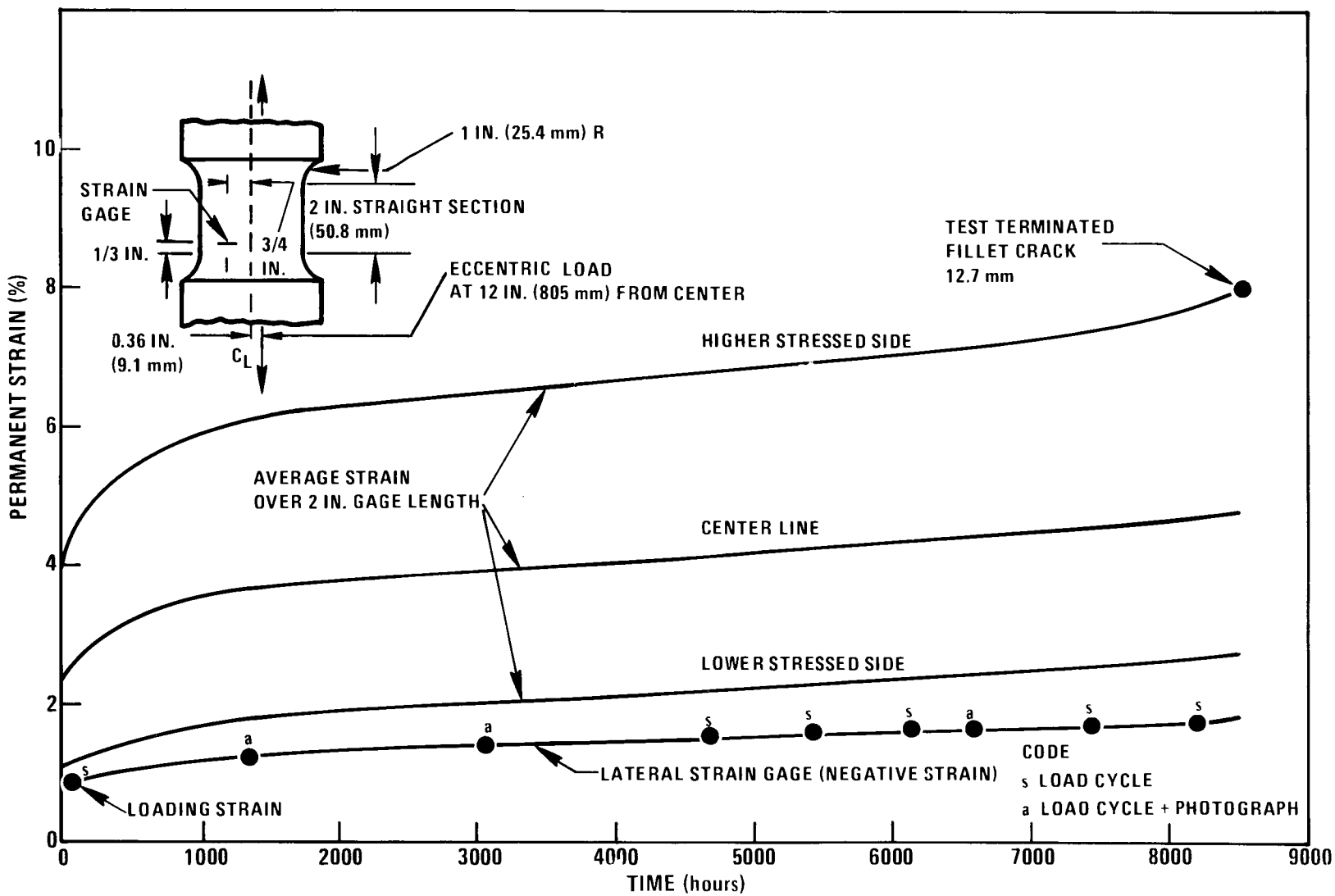


Figure 6.2 Creep of Model E2, 18 ksi Tension Stress plus Bending

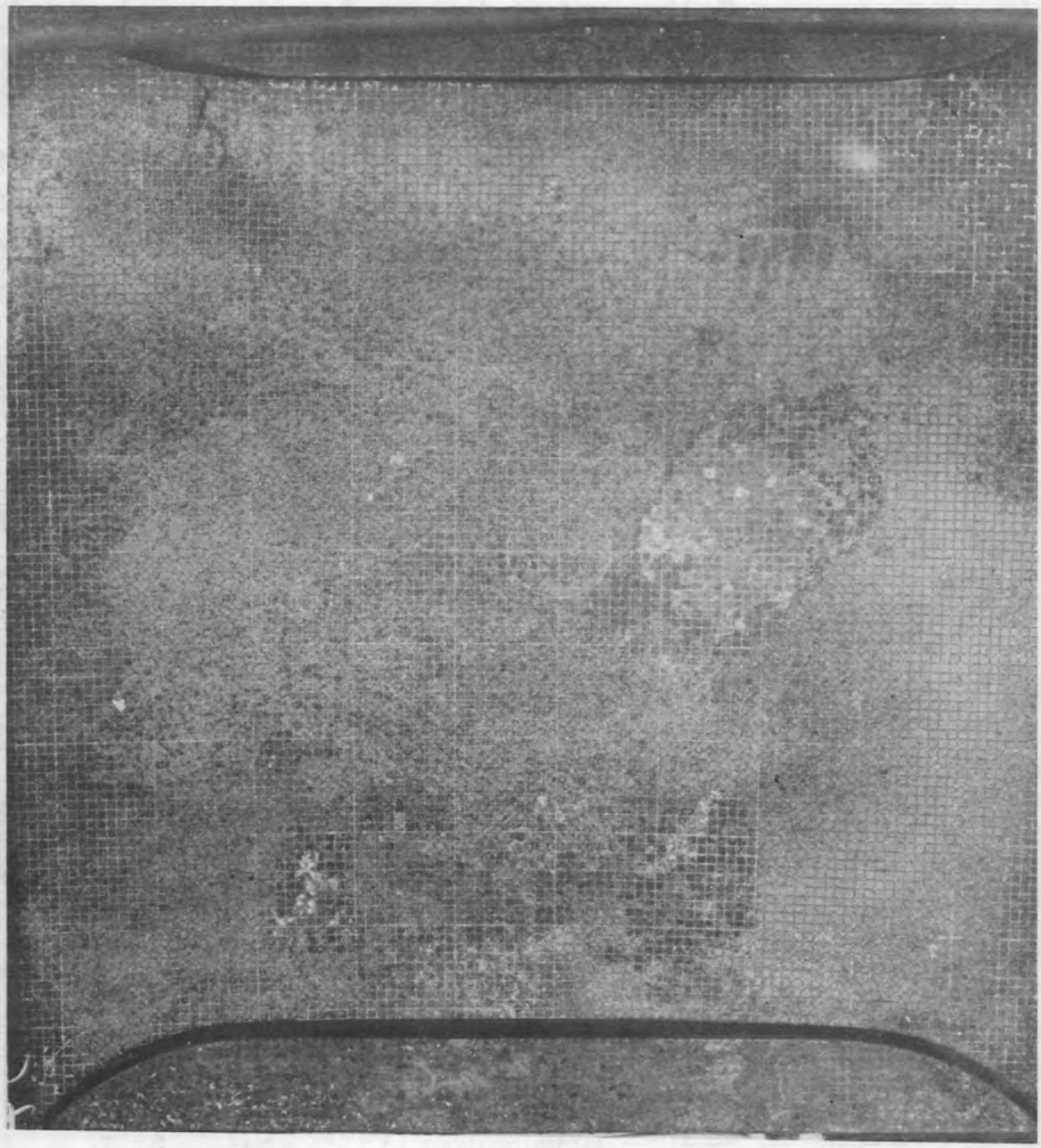

Figure 6.3 Photographs of Model E2 at 8500 Hours (Final)
(Crack at Upper Right Fillet)

6.2.1.2 BTW-2 Transverse Weld in Type B Model at 19 ksi (131 MPa) and 1100°F (593°C)

The creep strain has reached 1.4% after 8990 hours. The creep rate is decreasing slowly and is currently $8 \times 10^{-5}$%/h. Inspection did not reveal any crack initiation. Specimen BTW-1 showed cracks after 2.3% strain.

6.2.1.3 BAW-2 Axial Weld in Type B Model at 22 ksi (151.7 MPa) and 1100°F (593°C)

The cracking at the heat affected zone is shown in Figure 6.4 after 4500 hours. There is little penetration of the cracks into the weld metal but some "forking" can be detected. The initial cracks near mid-length have grown to about 4 mm and additional cracks are initiating as the critical strain spreads along the gage length.

6.2.1.4 C-4 B Model Plate with Central Hole at 18 ksi (124.1 MPa) net section Stress and 1100°F (593°C)

This test was interrupted at 3043 hours for photographic inspection. As shown in Figure 6.5 cracking has initiated at each side of the central hole and the cracks have started to fork. Testing will be continued to investigate the crack propagation.

6.2.2 Type 316 Stainless Steel Testing

6.2.2.1 6D2 Notched Bar at 28 ksi (193 MPa) at 1100°F (593°C)

This test is in progress at 1844 hours.

6.2.2.2 6D3 Notched Bar at 25 ksi (172.4 MPa) at 1100°F (593°C)

This test is in progress at 1914 hours.

## 6.3 TUBULAR SPECIMEN TESTING - C. Daniels, K. C. Thomas, P. C. S. Wu

### 6.3.1 Type 304 Stainless Steel Testing

Two topical reports were issued on the 304 SS tubular specimen program: WARD-HT-3045-13, Design and Analysis of Multiaxial Cylindrical Creep Test Specimens, by R. H. Mallett, A. K. Dhalla and J. T. Yocolano, and, WARD-HT-3045-14, Data Package for Type 304 Stainless Steel Tubular Specimen Creep Test Program, by P. C. S. Wu. These two reports present a detailed record of how the tubular specimen tests were performed and how the data were processed to provide a comprehensive set of 304 SS creep measurements from this program.

Analysis of the 304 SS data was continued with six inelastic analyses on the .05 inch thick specimens. The results can be summarized as follows:

1) The effective gage length varies with the thickness of the tube
2) The effective gage length varies with the stress ratio and not the stress level. However, this variation is highly non-linear for the 0.05 inch thick tube as compared with a nearly linear distribution obtained for the 0.1 inch thick tube. Therefore, discrete values of the effective gage length for various stress ratios will be used in creep data reduction of tubular specimens.

### 6.3.2 Type 316 Stainless Steel Testing

The annealing procedure for the 316 SS was modified to eliminate the soak time at the annealing temperature. Specimens were allowed to reach the annealing temperature and were then immediately air-cooled. Subsequent tensile testing at a strain rate of $4 \times 10^{-3}$/sec. produced a .2% offset yield stress of 29.2 Ksi, which is within the reported ORNL range of 28-32 Ksi.

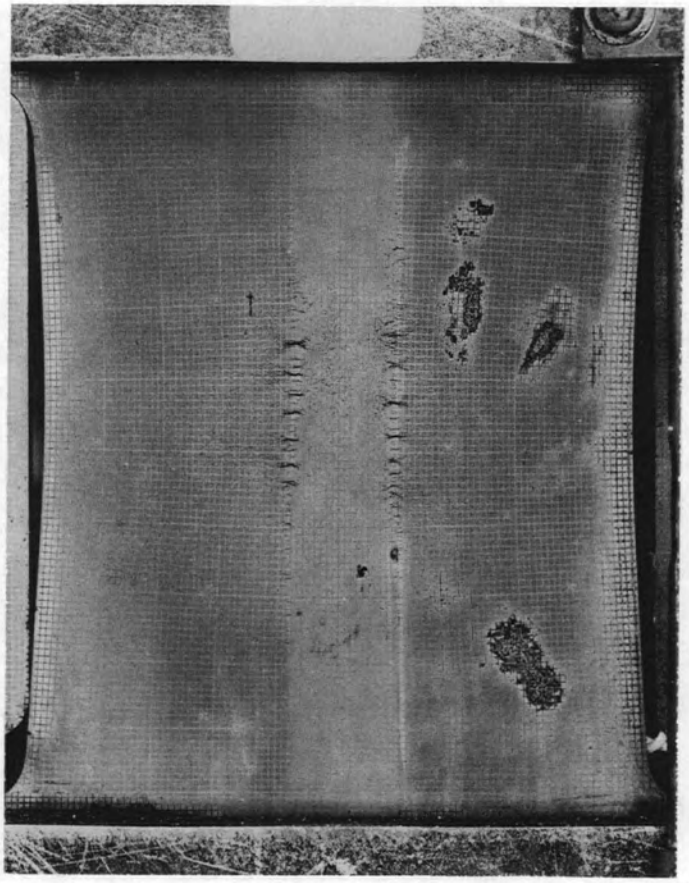

Figure 6.4 Photograph of Model BAW-2, Axial Weld at 22 Ksi and 1100°F, after 4500 Hours

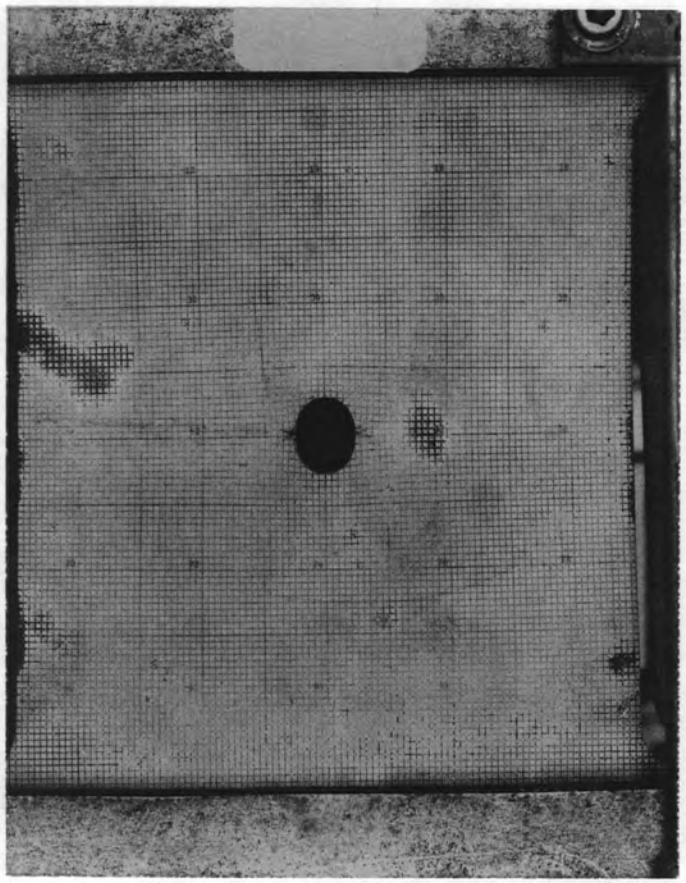

Figure 6.5 Photograph of Model C4 at 3043 Hours

## 6.4 SODIUM EFFECTS ON MECHANICAL PROPERTIES OF STRUCTURAL MATERIALS

P. N. Flagella, J. Kahrs, J. Denne, P. Wu, S. L. Schrock

### 6.4.1 Type 316 Stainless Steel

During this reporting period, creep rupture and low cycle fatigue tests in sodium on the HEDL heat of 2.5 cm (1 inch) plate material (65805) were initiated. Creep rupture results for tests performed at 593°C (1100°F) and 275.8 and 240.1 MPa (40.0 and 32.5 ksi) are given in Table 6.2. Figure 6.6 presents the strain-time creep curves for the tests performed at 275.8 MPa (40.0 ksi). These curves show that the rupture life and ductility are significantly increased as a result of the sodium pre-exposure. The minimum creep rate is lowest for the as-fabricated sample. Somewhat surprising is the decreased loading strain for the pre-exposed samples, which also have the higher minimum creep rates. This is consistent with the tests of Type 316 stainless steel in sodium at 593°C (1100°F) from the W heat of material, reported previously[1]. The differences in creep-rupture properties for sodium pre-exposed samples when compared to the as-fabricated sample are apparently due to changes in the material's microstructure resulting from time-at-temperature during the pre-exposure. The effect of the sodium environment on the creep-rupture properties is not clear at this time, and will require additional data for evaluation. In addition, tests in sodium at lower stress levels are in progress to determine if the differences in creep rupture properties will persist for longer test times.

Low-cycle strain-controlled fatigue tests in flowing sodium for the HEDL heat of solution annealed Type 316 stainless steel plate material were also initiated during this reporting period. Test results obtained to date at 593°C (1100°F) are given in Table 6.3. Figure 6.7 presents both the total and plastic strain range values as a function of cycles-to-failure. Also included in the figure are the data for two tests of the W-ARD heat of material, previously reported. With the exception of the one test of as-fabricated material at a $\Delta\varepsilon_t$ = 0.33%, the indication is that the fatigue life for the sodium pre-exposed

Table 6.2 Creep-Rupture Results for S.A. Type 316 SS[a] Tested in Flowing Sodium at 593°C (1100°F)

| Sample Number | Na Pre-Exposure Hours at 593°C | Stress MPa | Stress ksi | Loading Strain % | Minimum Creep Rate %/hour | Rupture Time hour | Total Elongation[b] % |
|---|---|---|---|---|---|---|---|
| A017 | 5,000 | 275.8 | 40 | 6.7 | $2.5 \times 10^{-1}$ | 110 | 68 |
| A084 | 2,000 | 275.8 | 40 | 8.6 | $1.8 \times 10^{-1}$ | 129 | 68 |
| A149 | 0 | 275.8 | 40 | 10.7 | $8.0 \times 10^{-2}$ | 75.2 | 18.5 |
| A146 | 0 | 240.1 | 32.5 | 4.6 | $8.5 \times 10^{-3}$ | 640 | 21 |

(a) HEDL Heat 65805 (2.5 cm thick plate).

(b) Gage section 0.64 cm diameter x 2.54 cm lg.

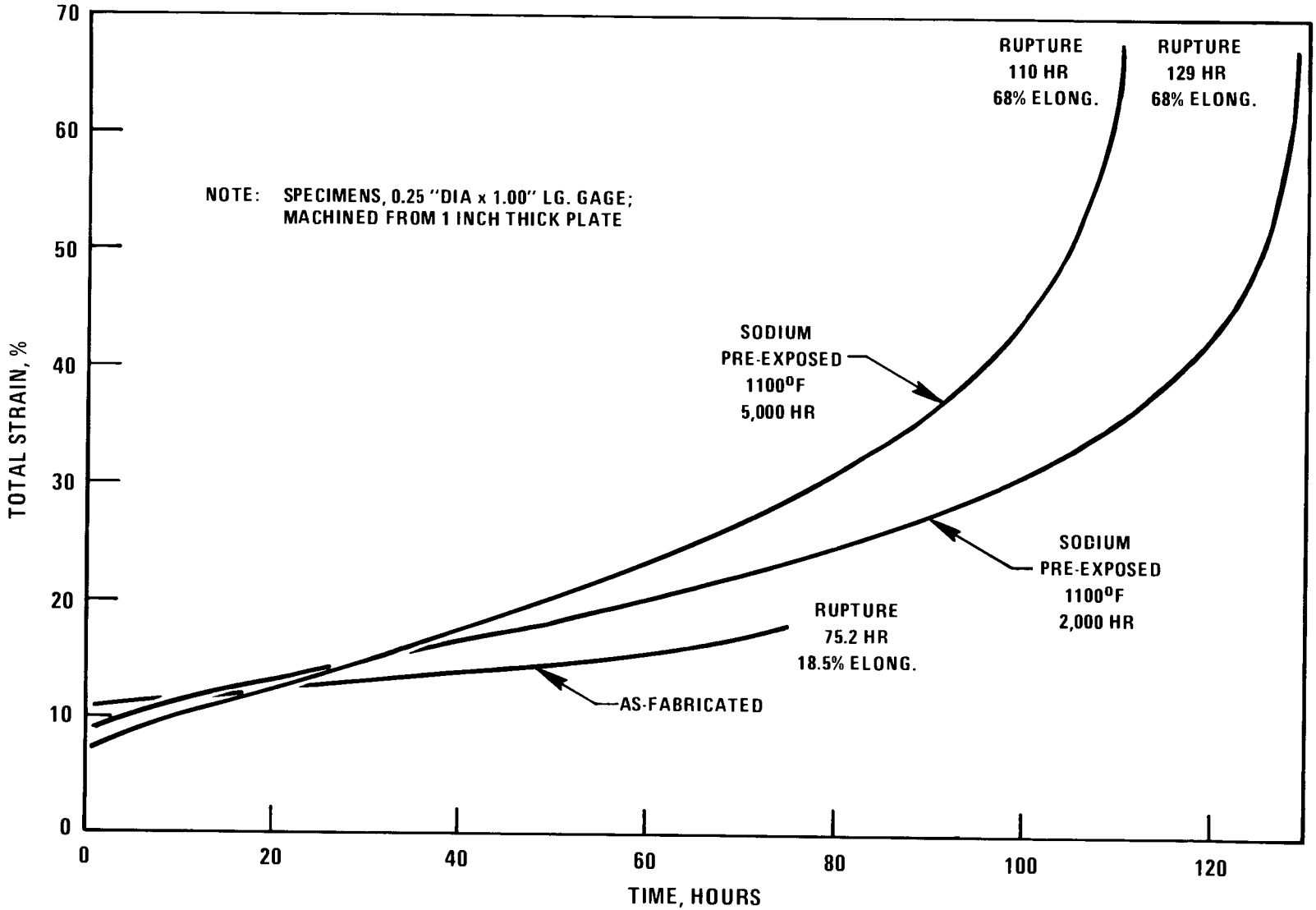


Figure 6.6 Creep Rupture Curves for Solution Annealed Type 316 Stainless Steel Plate Tested at 1100°F and 40.0 ksi in Flowing Sodium

Table 6.3 Low Cycle Fatigue Results[a] for S.A. Type 316 SS[b] Tested in Flowing Sodium at 593°C (1100°F)

| Sample Number | Na Pre-Exposure Hours at 593°C | Strain Range | | Stress Range[c] | | $N_f$ |
|---|---|---|---|---|---|---|
| | | $\Delta\varepsilon_t$ | $\Delta\varepsilon_p$ | MPa | ksi | |
| A144 | 0 | 2.14 | 1.53 | 837.0 | 121.4 | 394 |
| A050 | 2,000 | 2.16 | 1.63 | 780.5 | 113.2 | 332 |
| A141 | 0 | 1.06 | 0.68 | 670.2 | 97.2 | 2,265 |
| A045 | 2,000 | 1.10 | 0.69 | 593.0 | 86.0 | 1,927 |
| A032 | 5,000 | 1.13 | 0.69 | 586.8 | 85.1 | 2,355 |
| A140 | 0 | 0.66 | 0.27 | 581.2 | 84.3 | 18,245 |
| A047 | 2,000 | 0.70 | 0.36 | 514.4 | 74.6 | 7,864 |
| A160 | 0 | 0.33 | 0.04 | 508.8 | 73.8 | 124,900 |
| A105 | 2,000 | 0.34 | 0.06 | 401.3 | 58.2 | 382,119 |
| A033 | 5,000 | 0.34 | 0.12 | 386.1 | 56.0 | 59,592 |

(a) Control Mode: Axial strain
Wave Form: Triangular, zero mean strain
Strain Rate: $4 \times 10^{-3}$ sec.$^{-1}$

(b) HEDL Heat 65805 (2.5 cm thick plate)

(c) At $N_f/2$

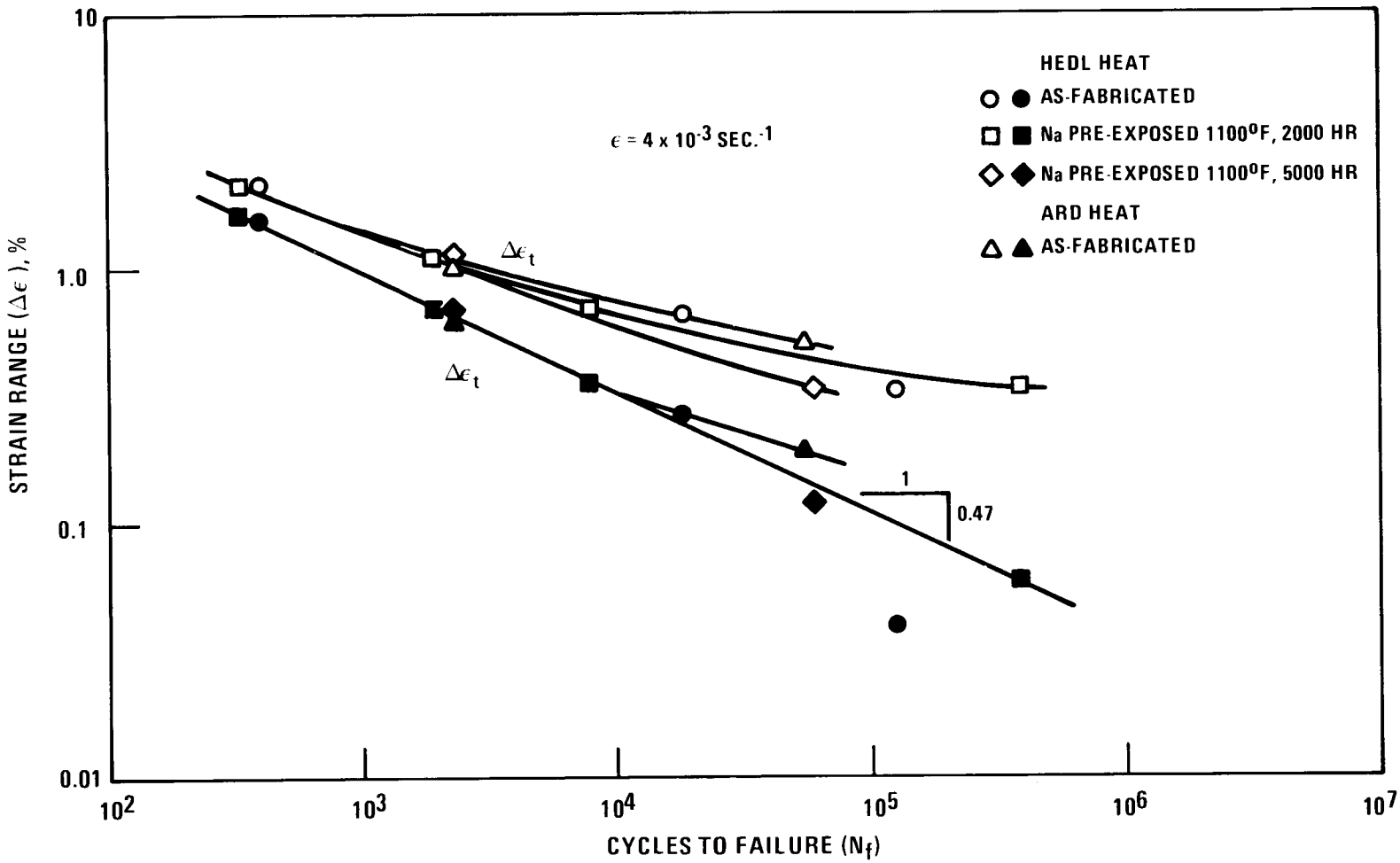


Figure 6.7 Fatigue Results for Solution Annealed Type 316 Stainless Steel Tested at 1100°F in Flowing Sodium

material below $\Delta\varepsilon_t$ = 1% is lower than the as-fabricated material. In addition, the fatigue life, at the same total strain range, appears to decrease as the sodium pre-exposure time at 593°C increases. This is apparently related, at least in part, to the microstructural changes in the material as a result of the temperature and time during the sodium pre-exposure. Effects of corrosion and interstitial transfer which result from the sodium exposure are probably additional factors influencing the results. Metallurgical evaluations are planned for the next reporting period.

The total strain range curve for the as-fabricated material at 1% and above is in good agreement with reported date[2] obtained in air. The two tests below 1% (0.66 and 0.50%) performed in sodium, indicate an increasing fatigue life when compared to the in-air data. This may be due to the longer time of testing and the increasing influence of the environments.

### 6.4.2 Inconel 718

Low-cycle strain-controlled fatigue tests on Inconel 718 are being performed in-air and in-sodium to evaluate the effect of the environment on the fatigue life. Using the same heat of material, grain size effects on the fatigue life are being determined by subjecting the material to two different heat treatments. In addition to testing the material in the as-heat treated condition (as-fabricated), tests are also performed after vacuum aging and sodium exposure of samples at 538°C for 2,000 hours. Table 6.4 presents results obtained to date for samples pre-exposed and tested in sodium at 538°C. Table 6.5 presents results obtained for in-air tests of as-fabricated samples and samples vacuum aged at 538°C for 2,000 hours. The data are presented in terms of strain range versus fatigue life in Figures 6.8 and 6.9. Also included in each figure are the data reported by the Aerojet Nuclear Corporation[3], using the same heat of material. All test results for the material solution annealed at 1040°C (1900°F) and double aged per AMS-5597A are presented in Figure 6.8 (grain size ∿ASTM 4). Good agreement is shown between the two data sources for the material tested in air in

Table 6.4 Low Cycle Fatigue Results[d] for Inconel 718[e] Tested in Flowing Sodium at 538°C after Sodium Exposure at 538°C for 2,000 Hours

| Sample Number | Strain Range, % | | Stress Range[b] | | $N_f$ |
|---|---|---|---|---|---|
| | $\Delta\varepsilon_t$ | $\Delta\varepsilon_p$ | MPa | ksi | |
| 21[a] | 1.59 | 0.54 | 1803.7 | 261.6 | 1,614 |
| 13[a] | 1.09 | 0.14 | 1621.0 | 235.1 | 27,200 |
| 5[a] | 0.82 | 0.01 | 1382.4 | 200.5 | 200,000[g] |
| 6[b] | 1.50 | 0.53 | 1656.2 | 240.2 | 3,363 |
| 34[c] | 1.39 | 0.37 | 1745.8 | 253.2 | 3,518 |

(a) S. A. 940°C + D. A. (AMS-5596C)

(b) S. A. 1040°C + D. A. (AMS-5597A)

(c) S. A. 1065°C + D. A. (AMS-5597A)

(d) Control Mode: Axial strain
Wave Form: Triangular, zero mean strain
Strain Rate: $4 \times 10^{-3}$ sec.$^{-1}$

(e) ANC Heat #2 (2.5 cm thick plate)

(f) At $N_f/2$

(g) Tested in load control at 23.5 cpm

Table 6.5 Low Cycle Fatigue Results[a] for Inconel 718[b]
Tested at 538°C in Air

| Sample Number | Strain Range, % | | Stress Range[c] | | Comp. Hold, Hour | $N_f$ | Notes |
|---|---|---|---|---|---|---|---|
| | $\Delta\varepsilon_t$ | $\Delta\varepsilon_p$ | MPa | ksi | | | |
| | 940°C S. A. + D. A. (AMS-5596C) | | | | | | |
| 9 | 0.95 | 0.22 | 1610.7 | 233.6 | 0 | 2,050 | |
| 17 | 0.97 | 0.15 | 1592.7 | 231.0 | 0 | 3,340 | |
| 25 | 1.96 | 0.96 | 1972.0 | 286.0 | 0 | 377 | |
| 1 | 2.04 | 1.09 | 1434.2 | 308.0 | 0 | 400 | |
| 31 | 2.01 | 0.98 | 1778.9 | 258.0 | 0.5 | 357 | |
| 55 | 2.00 | 0.90 | 1834.1 | 266.0 | 1.0 | 333 | |
| | 940°C S. A. + D. A. (AMS-5596C); Vacuum Aged, 1,000°F, 2,000 Hours | | | | | | |
| 11 | 0.87 | 0.03 | 1406.6 | 204.0 | 0 | >45,556 | |
| 27 | 1.02 | 0.06 | 1627.2 | 236.0 | 0 | 3,725 | compressed to 2% on 2nd cycle |
| 7 | 1.26 | 0.18 | 1820.3 | 264.0 | 0 | 2,286 | |
| 19 | 1.45 | 0.42 | 1820.3 | 264.0 | 0 | 1,482 | |
| 3 | 1.90 | 0.71 | 1903.0 | 276.0 | 0 | 627 | overheated to 1300°F for ∿ 1/2 hour during heat-up |
| 15 | 1.90 | 0.94 | 1875.4 | 272.0 | 0 | 457 | |
| 29 | 2.01 | 0.78 | 1847.9 | 268.0 | 0.5 | 419 | |
| 45 | 1.27 | 0.17 | 1999.6 | 290.0 | See Note | 2,590 | 1.0 hour comp. hold during 1st 290 cycles |
| | 1065°C S. A. + D. A. (AMS-5597A) | | | | | | |
| 48 | 0.96 | 0.045 | 1452.8 | 210.7 | 0 | 12,454 | tested at $\Delta\varepsilon_t$ = 0.76% for 10,545 cycles first |
| 40 | 0.97 | 0.045 | 1434.2 | 208.0 | 0 | 8,137 | |
| 2 | 2.00 | 0.60 | 1889.2 | 274.0 | 0 | 760 | |
| 18 | 2.00 | 1.05 | 1875.4 | 272.0 | 0 | 457 | |
| 56 | 2.00 | 0.66 | 1889.2 | 274.0 | 1.0 | 639 | |
| | 1065°C S. A. + D. A. (AMS-5597A); Vacuum Aged, 1,000°F, 2,000 Hours | | | | | | |
| 38 | 2.10 | 0.75 | 1918.9 | 278.3 | 0 | 605 | |
| 42 | 2.00 | 0.74 | 1892.0 | 274.4 | 0 | 610 | |

(a) Control Mode: Axial strain
Wave Form: Triangular, zero mean strain
Strain Rate: $4 \times 10^{-3}$ sec.$^{-1}$

(b) ANC Heat #2 (2.5 cm thick plate)

(c) At $N_f/2$

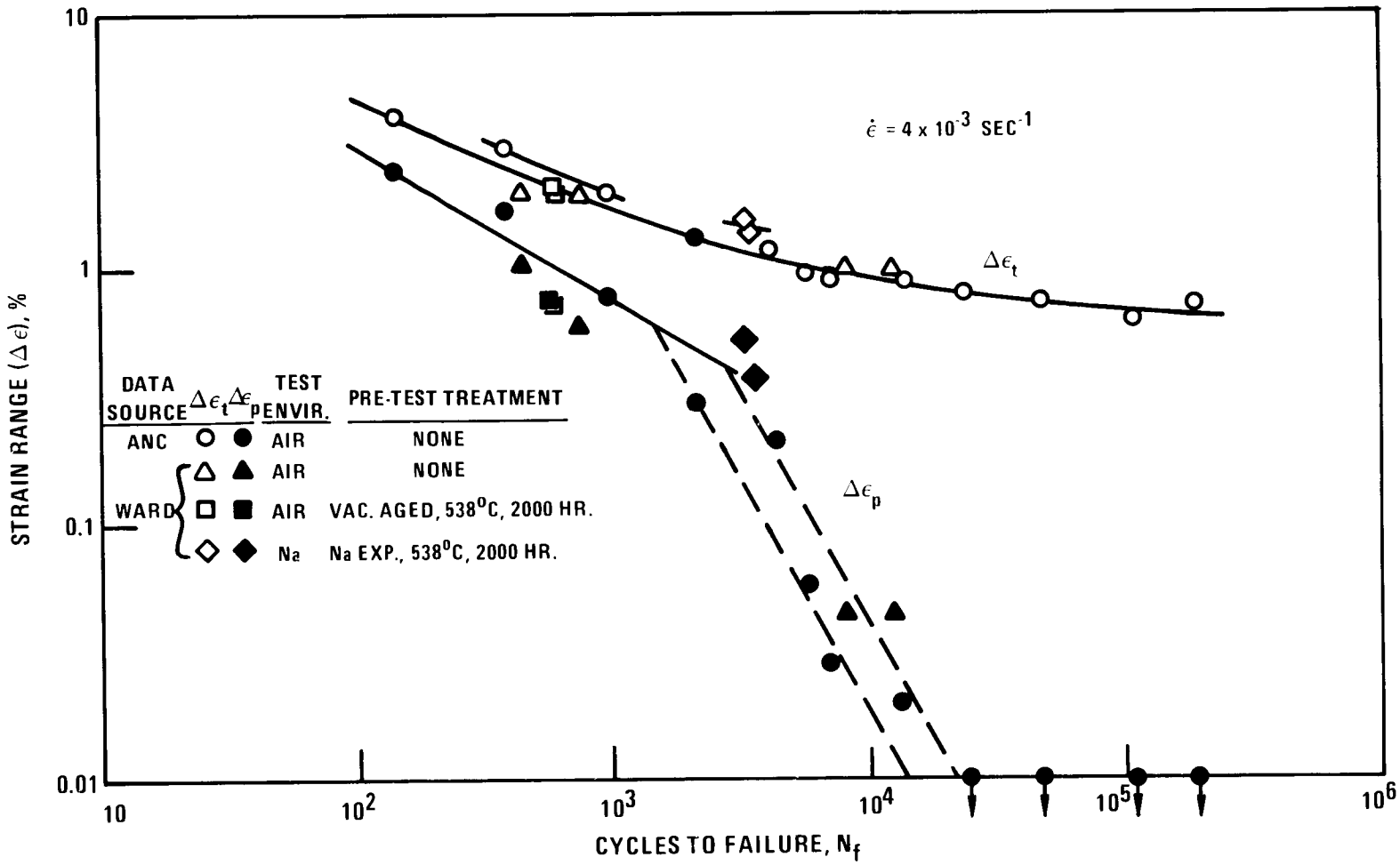


Figure 6.8 Comparison of Low Cycle Fatigue Results for Inconel 718 Tested at 538°C. All Material Solution Annealed at 1040°C + Double Aged.

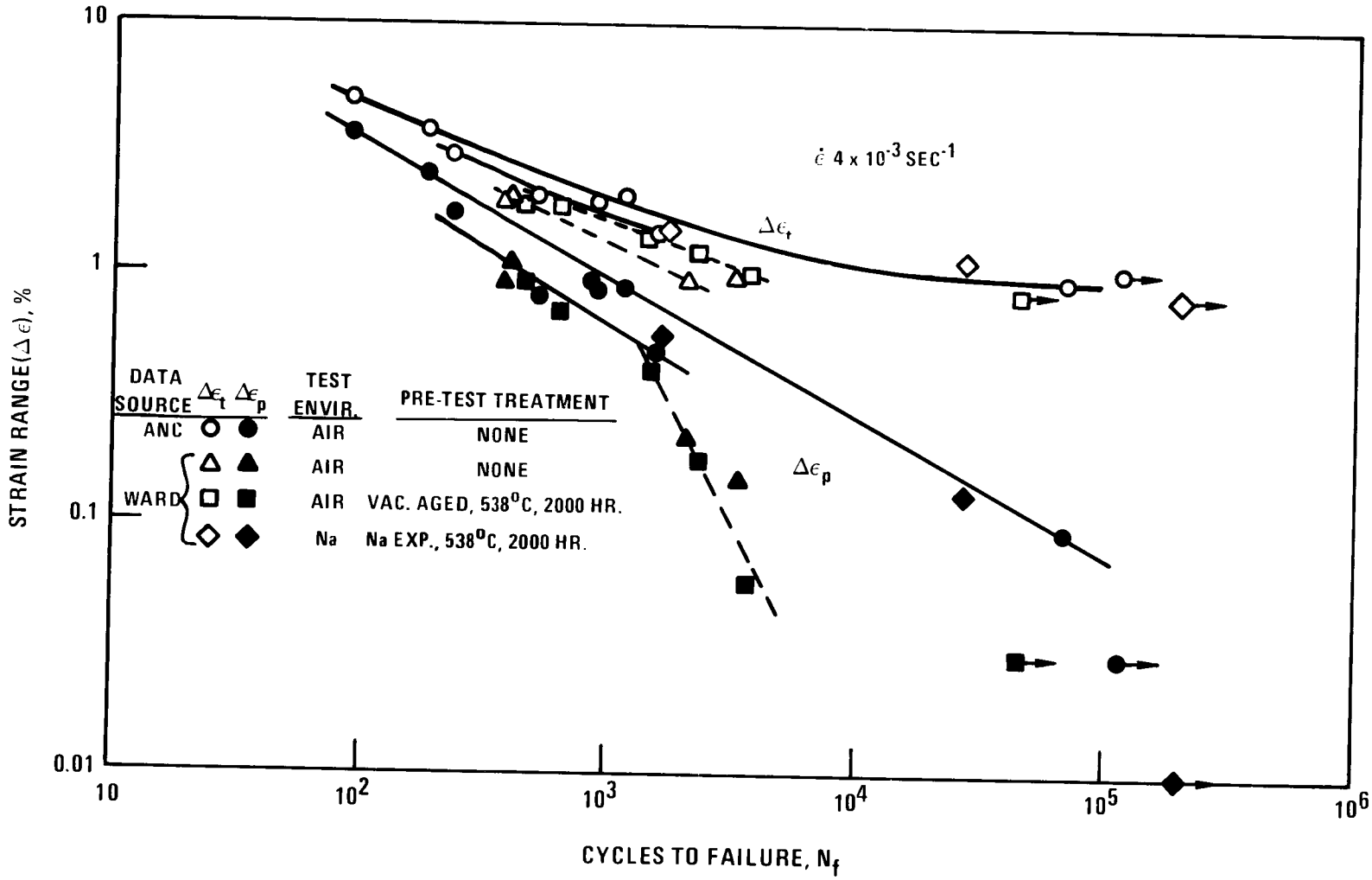


Figure 6.9 Comparison of Low Cycle Fatigue Results for Inconel 718 Tested at 538°C. All Material Solution Annealed at 940°C + Double Aged.

the as-fabricated condition. No effect of vacuum aging the material at 538°C for 2,000 hours is indicated, based on the two tests performed at a total strain range of 2%. The two samples sodium pre-exposed at 538°C for 2,000 hours and tested in sodium at a total strain range of approximately 1.5% imply an increase in fatigue life over the results obtained in air for as-fabricated material. Since no effect was indicated for the aged material, the increase in fatigue life is apparently an environmental effect. Additional tests will be required before this can be substantiated. The data trend for the plastic strain range values strongly suggest two linear regions, one below about 2,000 and another above 2,000 cycles to failure. The actual slopes are not clear because of the large data scatter, but the curve representing the ANC data below 2,000 is shown at a slope of -0.59, and the curves representing the ANC data above 2,000 are shown at a slope of -1.8.

All test results given in Figure 6.9 are for the same heat of material; solution annealed at 940°C (1725°F) and double aged per AMS-5596C (grain size $\sim$ ASTM 10). Two populations of data are indicated for both the ANC and W-ARD total strain range results obtained in air, with the W-ARD data displaced to somewhat lower fatigue lives. The reason for this is not known, but planned metallurgical studies may offer an explanation. No effect of vacuum aging the material at 538°C for 2,000 hours is apparent if in fact there are two populations of data. If not, a significant increase in fatigue life is indicated, 50% at $\Delta\varepsilon_t$ = 2% and 100% at $\Delta\varepsilon_t$ = 1%. The effect of the sodium environment on the fatigue life is also unclear based on the three tests performed, but no deleterious effects are indicated. It appears likely that the fatigue life is increased for $\Delta\varepsilon_t \cong 1\%$.

## 6.5 REFERENCES

(1) ORNL-5112, Mechanical Properties Test Data for Structural Materials Quarterly Progress Report for Period Ending January 31, 1976, page 209.

(2) C. R. Brinkman and G. E. Korth, "Low Cycle Fatigue and Hold-time Comparisons of Irradiated and Unirradiated Type 316 Stainless Steel,"

Met. Trans. 5, pp. 792-794 (1974).

(3) C. R. Brinkman and G. E. Korth, Strain Fatigue and Tensile Behavior of Inconel 718 from room temperature to 650°C, ANCR-1125, August 1973.

# 7. UNIVERSITIES

## 7.1. UNIVERSITY OF CINCINNATI

J. Moteff and H. I. Jang

### 7.1.1. INTRODUCTION

The objective of this program is to (a) evaluate the time, temperature, and stress-dependent mechanical properties of reactor structural materials, (b) determine the relationship of these properties to the microstructure, (c) show the contribution of the microstructure to the internal stress fields and the subsequent influence on microcracking and the grain boundary sliding behavior during the normal plastic deformation at elevated temperatures, and (d) demonstrate the relationship of the hot micro-hardness properties with the hot-tensile properties of a class of commercial and advanced alloys presently under investigation at other laboratories. Special consideration is being given to operating conditions typical of nuclear reactor applications, including the knowledge that radiation environment can influence the substructure of these metals, a circumstance which can lead to significant changes in the conventional mechanical property behavior.

### 7.1.2. EXPERIMENTAL PROGRAM

Transmission electron microscopy has been used as the primary tool to study the deformation substructure of reactor structural materials resulting from creep, fatigue, and tensile testing at elevated temperatures. Complementary work

using optical microscopy, scanning electron microscopy, and hot-hardness testing has been performed to characterize the deformation and failure behavior. New work is underway to perform similar studies on the Commercial, the Developmental, and the Fundamental alloys being evaluated in the National Alloy Developmental Program with particular attention on the application of hot-hardness measurement as a strength microprobe.

7.1.2.1. Creep-Microstructure Evaluation of AISI 330 Stainless Steel

7.1.2.1. (A) Stress-Temperature Effects on Substructures (B. Billings)

Table I shows the results of the creep-rupture testing completed to date. All testing was performed at 701°C with the exception of one sample which has been discussed elsewhere[1]. The specimen geometry, type of creep testing machine, and testing methods pertinent to this work have been reported before[1]. Figure 1 shows the creep curves obtained through this testing. It can be observed qualitatively that AISI 330 demonstrates the stress dependence of the overall creep rate as documented in the literature[2]. However, as the present time period is being utilized mainly for raw data collection, a detailed interpretation of the experimental results will be withheld pending further data accumulation.

A limited amount of TEM observation has been performed on two (2) of the ruptured specimens: AN330-CB01 and AN330-

TABLE 7.I

AISI 330 RAW CREEP-RUPTURE TEST DATA,
TEST TEMPERATURE 701°C (1294°F)

| Sample Number | Applied Stress, ksi | $e_p$ % | $e_t$ % | $\dot{e}_s$ %/hr | $t_2$ hr | $t_R$ hr | $e_R$ % | RA % |
|---|---|---|---|---|---|---|---|---|
| AN330-CB01 | 40 | 5.0 | 12.0 | 83.7 | 0.15 | 0.25 | 60.0 | 44.1 |
| -CB03 | 35 | 2.7 | 6.0 | 33.3 | 0.17 | 0.68 | 65.0 | 54.1 |
| -CB02 | 30 | 1.5 | 2.7 | 8.82 | 0.85 | 2.90 | 64.0 | 56.4 |
| -CB04 | 20 | 0.19 | 0.95 | 0.60 | 5.0 | 33.65 | 62.3 | 58.5 |

$e_p$ = plastic loading strain
$e_t$ = transient creep strain
$\dot{e}_s$ = minimum secondary creep rate
$t_2$ = time to reach end of secondary creep (0.2% offset)
$t_R$ = time to rupture
$e_R$ = rupture strain
% RA = % reduction in cross sectional area
NOTE: Values obtained through graphical methods

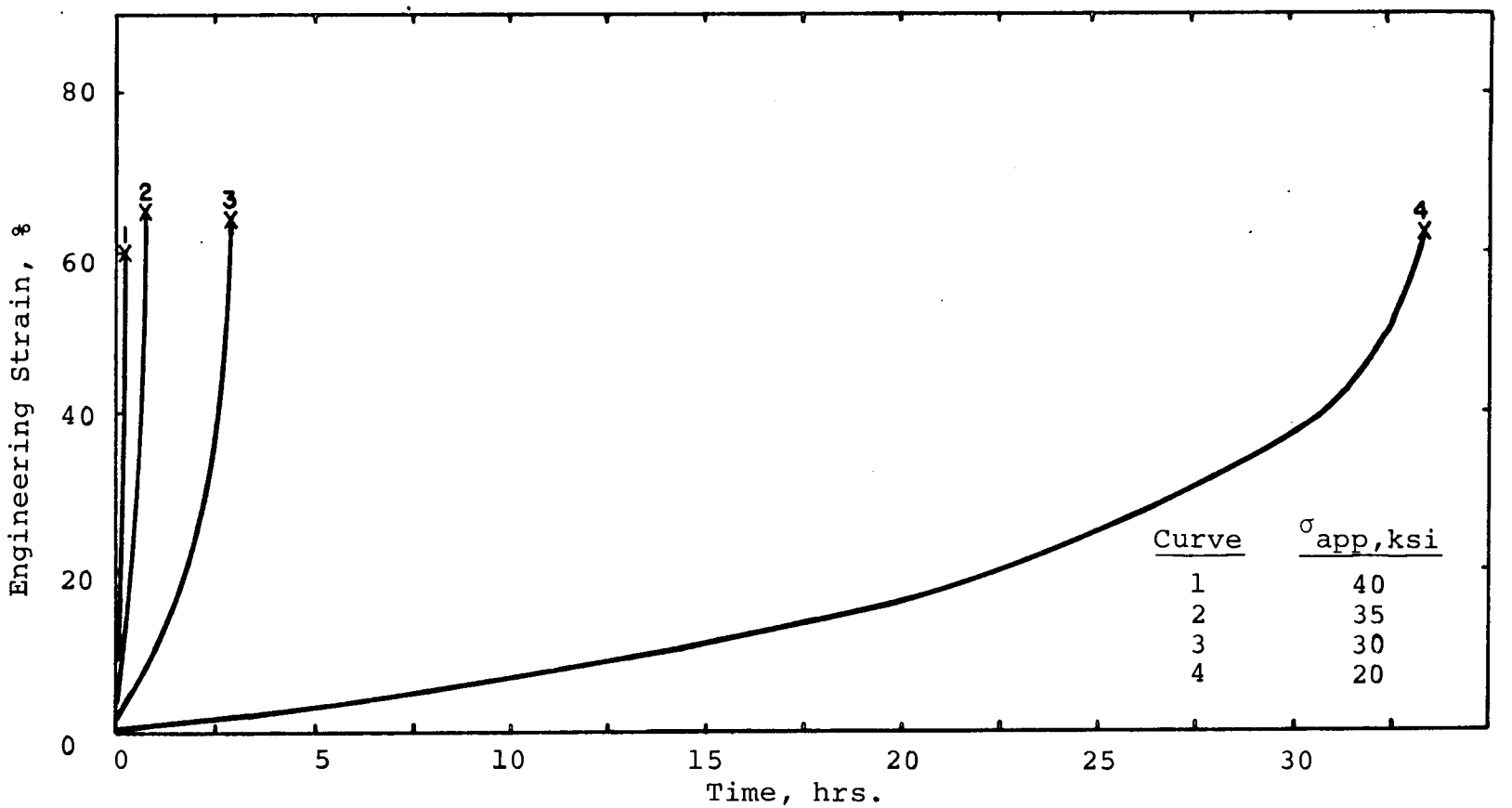


Fig. 7.1. Constant Load Creep-Rupture Curves for AISI 330 Stainless Steel Tested at Various Applied Stresses ($\sigma_{app}$) at 701°C.

CB04. These samples were tested at 40 ksi (275.8 MPa) and 20 ksi (137.9 MPa), respectively. The microstructure of the former was cellular in nature, while that of the latter was subgranular, as was expected. At the present time, however, no quantitative microscopy work will be discussed.

7.1.2.1. (B) A Study on Subgrain/Cell Development During Creep Deformation (J. Foulds)

The specimens for creep testing were machined from 1/4 in. dia. bar stock obtained from the Hanford Engineering Development Laboratory (reference heat = BB8951) and annealed at 1100°C $\pm$ 10°C and less than $1 \times 10^{-6}$ torr in two batches of twelve specimens each.

Microstructural features will be observed and the grain size determined. Creep testing and TEM work will be carried out according to the plan described below.

The strain behavior of the material will be studied at a fixed temperature above 0.5 Tm and at two stress levels. The temperature and stress levels will be selected such that subgrains are obtained at one stress level and cells at the other, and such that the strain rates involved are not too high or too low to result in very short-term or long-term tests. For this, a few preliminary tests will be run using as a first approximation an Ashby deformation map for 304 SS and operating at temperatures and stress levels in the region of separation between dislocation glide and climb. Constant load creep tests will be run using an Arcweld model C creep-

rupture tester, the electric furnace being of the zone controllable type and capable of a constant temperature zone of maximum variation ± 1°C over a length twice the specimen gage length.

The dislocation substructures will be studied at various points in the deformation process using a different specimen each time and stopping the test at the desired level of completion. The cross-marked points in Fig. 2 indicate the points at which substructure studies will be made,which with increasing strain,represent:

(i) Before test (annealed).

(ii) At start of primary creep stage.

(iii) At approximately 50% primary creep strain.

(iv) At completion of primary creep stage.

(v) At 50% secondary creep strain.

(vi) At completion of secondary creep.

(vii) At approximately 50% of tertiary creep strain.

(viii) At rupture.

At these strains the substructure will be evaluated with regard to

(i) Dislocation density.

(ii) Cell or subgrain size.

(iii) Misorientation between cells or subgrains.

(iv) The identification of any second phase formed and its effect on strain behavior.

These will enable a quantitative correlation between the

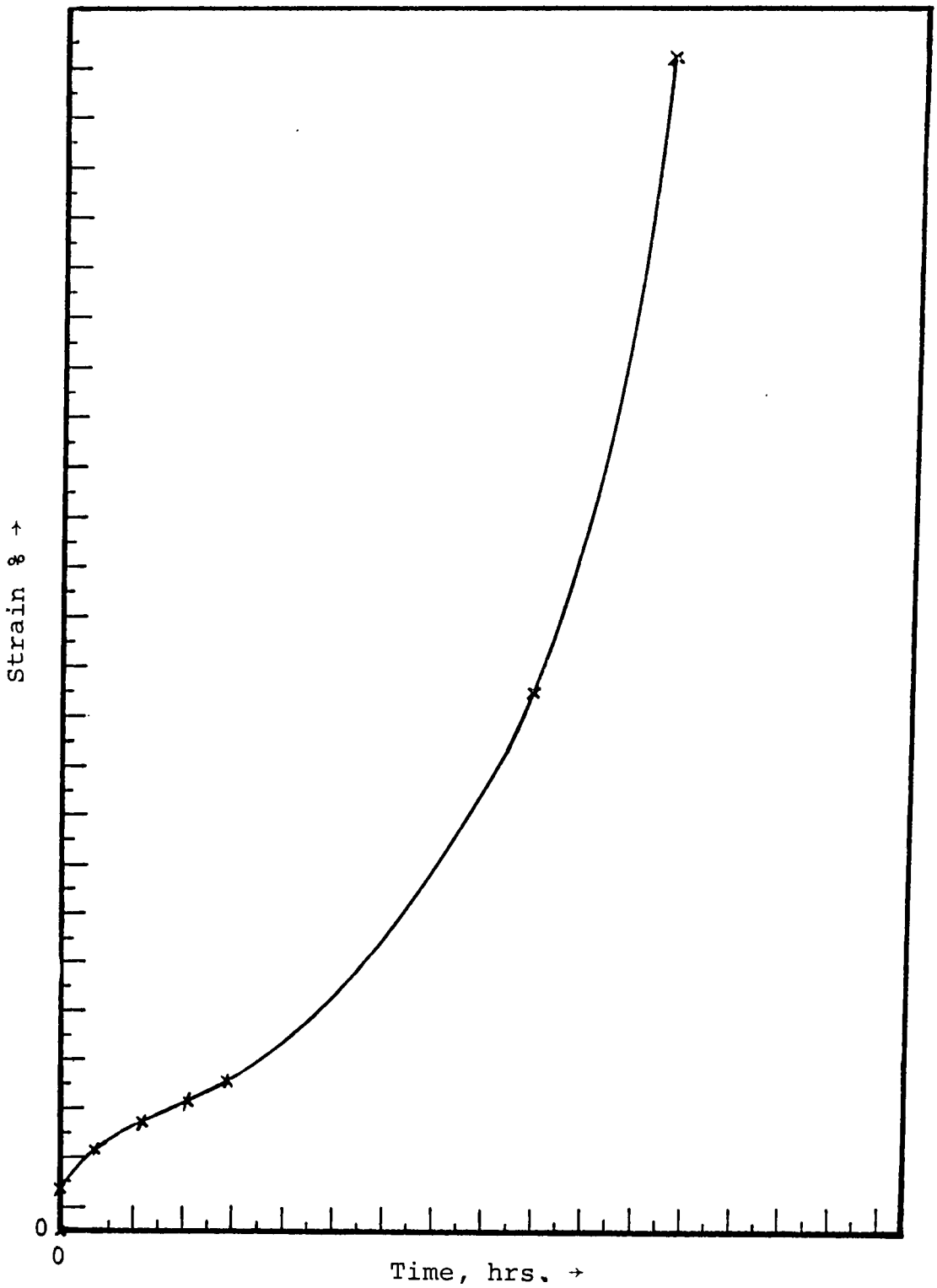


Fig. 7.2. Typical Creep Curve for AISI 330 Stainless Steel. X Denotes Strain Levels at Which Substructure Studies will be made.

various facets of substructure development and the observed strain behavior in the creep mode.

7.1.2.2. Activation Energy for Creep Calculated from Hot-Hardness Data (H. I. Jang)

Most of the empirical equations relating hardness with temperature are of the form:

$$H = Ae^{-BT} \qquad [7.1]$$

$$H = Ae^{B/T} \qquad [7.2]$$

$$H = A + B/T \qquad [7.3]$$

Although it is considered[3] that the Ito-Shishokin relationship (Equation 7.1) is the most satisfactory expression to fit the experimental data, it is difficult to interpret in terms of other metal characteristics[4]. For a large number of metals, in fact, the data fit all three expressions quite well, and Equation 7.2 is suggestive of thermally activated deformation processes[4].

The influence of temperature on the hardness of AISI 330 SS is shown in Fig. 3. The logarithmic scale of hardness vs. 1/T is used in accordance with Equation 7.2. The shape of the hardness/temperature curve can be described as two straight lines intersecting at about 0.55 Tm. The inflection of the curve at around 0.5 Tm has been observed in many other metals, and it has been attributed to a change in the deformation mechanism from normal slip processes below the inflection to diffusion-controlled processes above the inflection. From

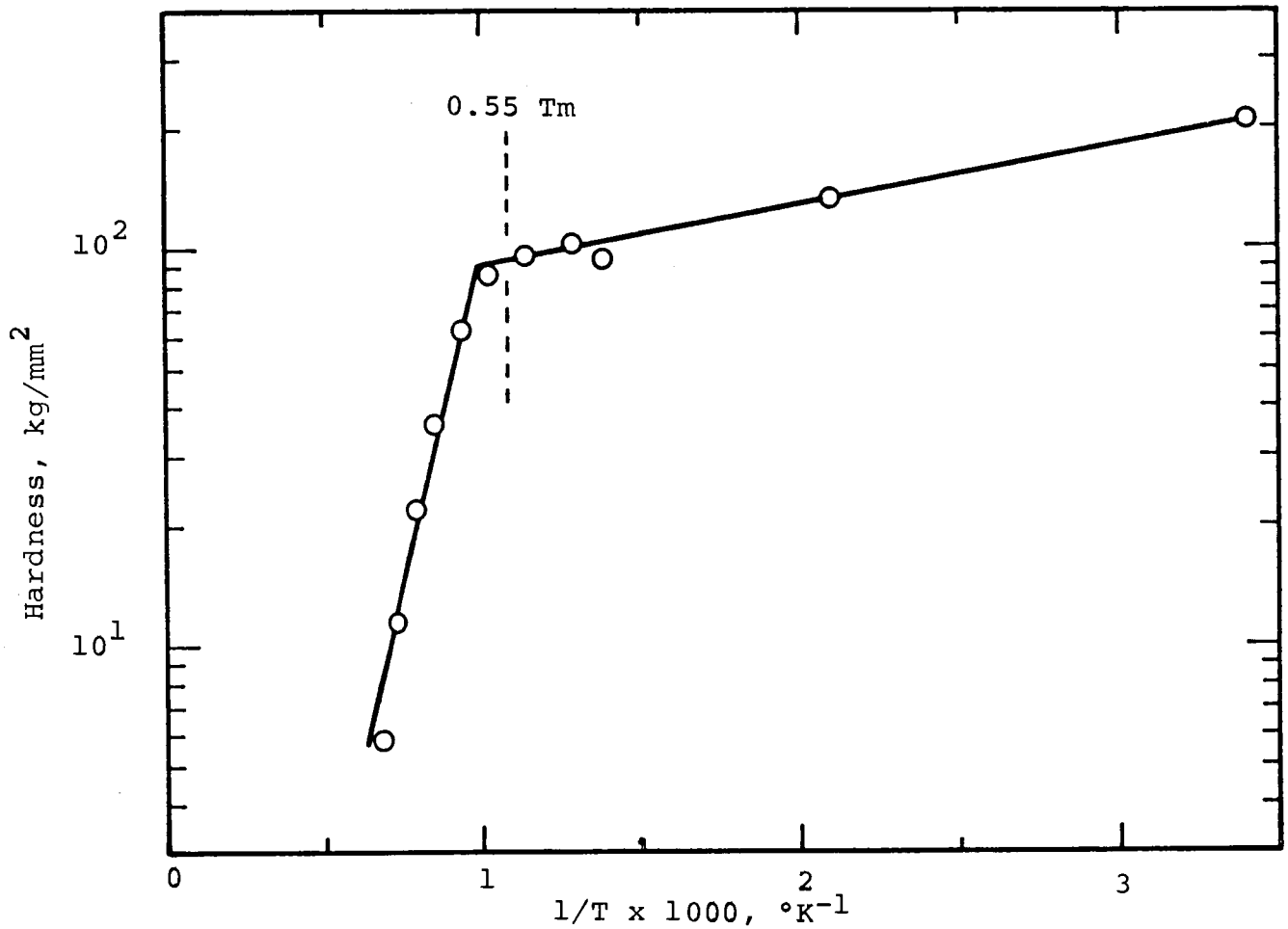


Fig. 7.3. Log Hardness of AISI 330 Stainless Steel Plotted Against 1/T.

the slope of the curve in Fig. 3, the "apparent activation energies for indentation hardness" were determined by using the Larsen-Badse relation[4]:

$$H = Ae^{2Q'/RT} \qquad [7.4]$$

The results are:

$$Q' = 7.940 \text{ cal/mole for } T > 0.55 \text{ Tm}$$

$$Q' = 340 \text{ cal/mole for } T < 0.55 \text{ Tm.}$$

The apparent activation energy for indentation hardness is low, and this has been explained by Sherby and Armstrong[5]. They have shown that the activation energy for creep can be determined from hot-hardness data above 0.75 Tm by using the expression

$$H/E = G \exp \frac{L}{nRT} \qquad [7.5]$$

The hot-hardness data of AISI 330 stainless steel above 0.5 Tm plotted as logarithm H/E vs. 1/T is shown in Fig. 4. As can be seen two straight lines can be drawn with a break occurring at about 0.75 Tm. In this plot the Young's modulus of AISI 304 SS[6] was used with an extrapolation to 1200°C. Utilizing Equation 7.5 with n = 5, the activation energy for creep of 93,400 cal/mole was obtained for T > 0.75 Tm.

7.1.2.3. Correlation of Hot-Hardness and Hot Tensile Strength of 2 1/4 Cr - 1 Mo Steel (R. Dorning)

Hot-hardness tests were performed in a high purity argon (99.999%) atmosphere on 2 1/4 Cr - 1 Mo steel at four different carbon levels between 0.009% and 0.135% by weight. The

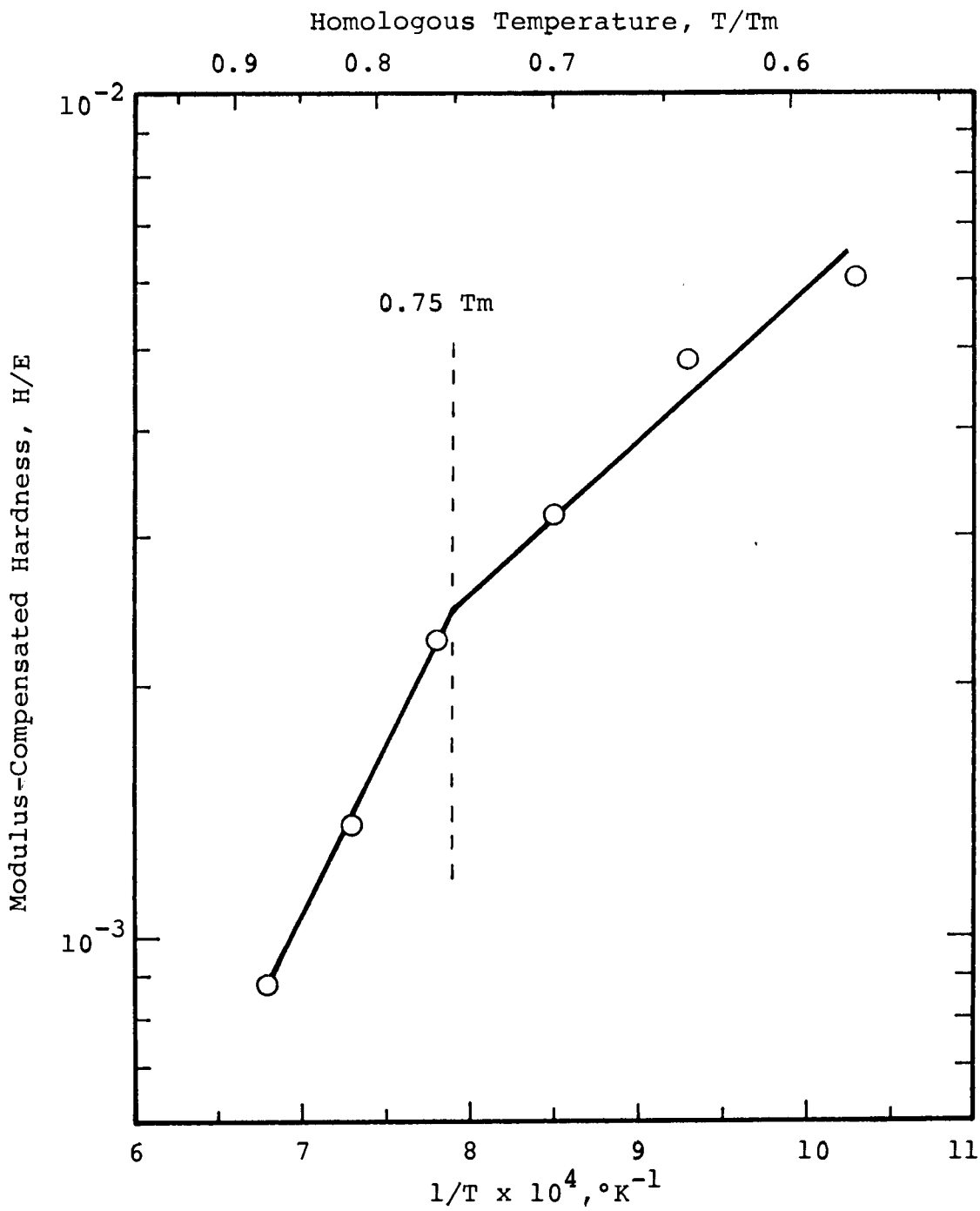


Fig. 7.4. Modulus-Compensated Hardness vs. 1/T of AISI 330 Stainless Steel.

hardness results are related to the tensile strength at six temperatures ranging from room temperature to 565°C by the relationship[7]

$$\sigma = \frac{H}{3}\left(\frac{n}{0.217}\right)^{n} \qquad [7.6]$$

As can be seen in Fig. 5, the correlation between UTS and hot-hardness is excellent for the high carbon (0.120% C) and the commercial (0.135% C) steels for all the temperatures tested. The medium (0.030% C) and low (0.009% C) carbon steels show good correlation at test temperatures above ∿ 350°C and fair correlation at the lower temperatures. Figure 6 shows the comparison between the UTS obtained from the tensile data and that calculated from the hot-hardness data for all four different carbon-level steels. A straight line is drawn with a 45° angle through the data points, and it can be seen that there is an excellent correlation between the experimental and the calculated tensile strength.

7.1.2.4. Grain Boundary Sliding in AISI 304 Stainless Steel (J. Costa)

Preliminary grain boundary sliding (GBS) data has resulted from the testing of a direct-loading, ultra-pure argon atmosphere creep furnace. Creep specimens 2.5 x 0.5 x 25 mm long were machined from a 304 SS sheet. The sheet product form, after undergoing a series of cold rolling and annealing treatments, resulted in an average grain size of 93 microns. Specimens were mechanically polished, etched lightly, and a rectangular grid pattern was scribed by hand

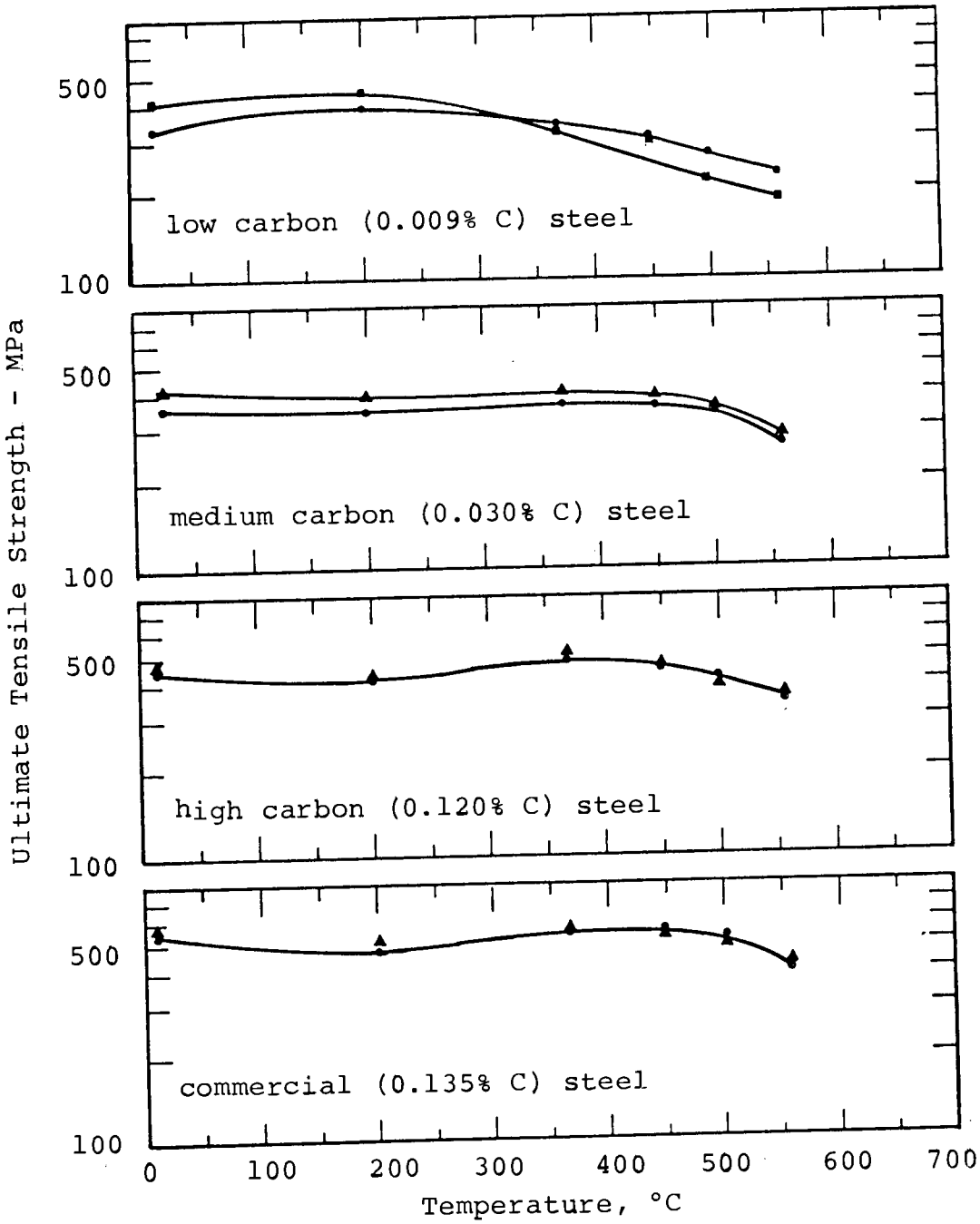


Fig. 7.5. Ultimate Tensile Strength of 2 1/4 Cr - 1 Mo Steels with Varying Carbon Contents Plotted Against Temperature. (● - Experimental Data From R. L. Klueh; ▲,■ - Calculated Values Based on Hot-Hardness Data)

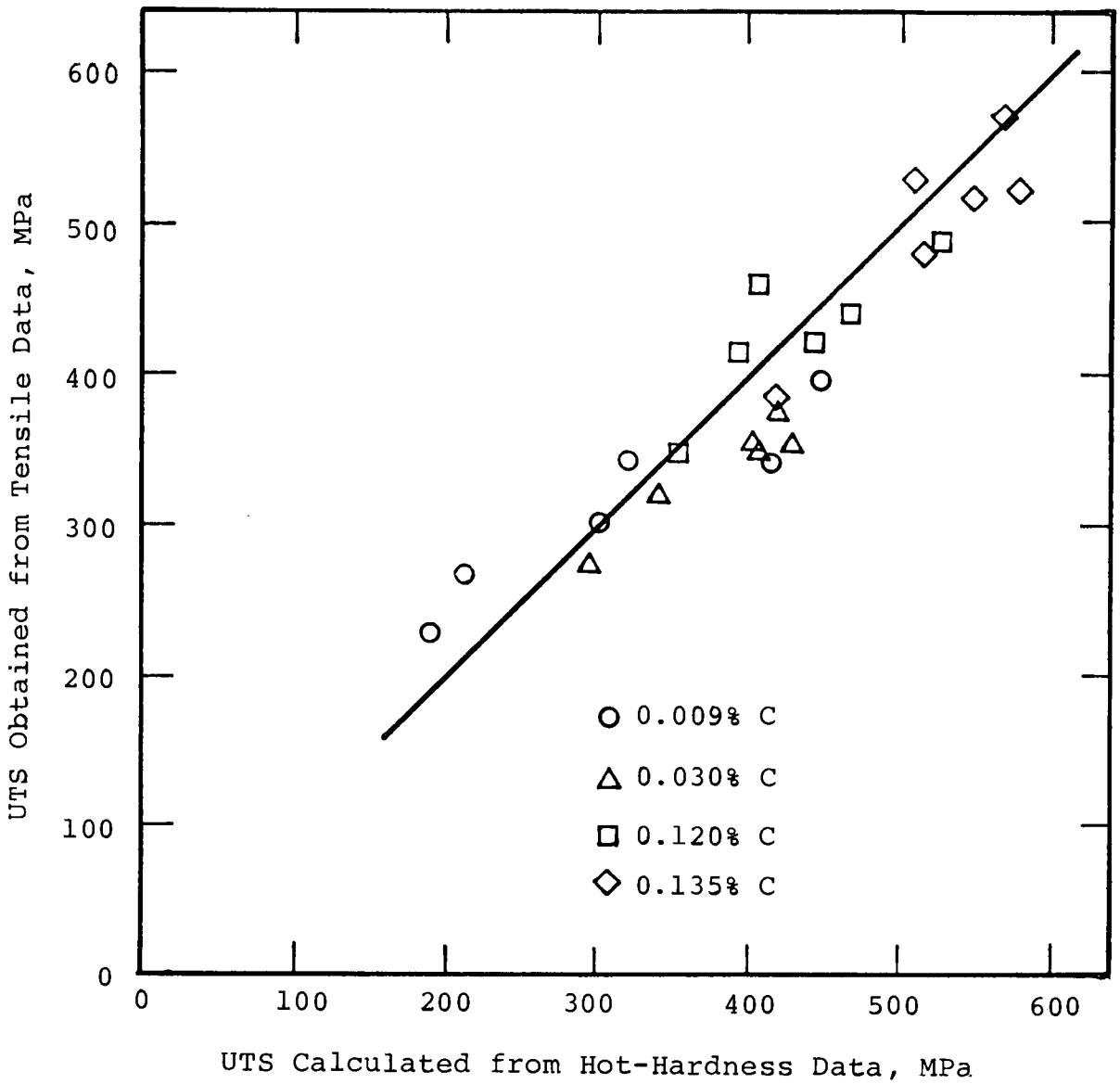


Fig. 7.6. Comparison of the Calculated and Experimental Tensile Strength of 2 1/4 Cr - 1 Mo Steels with Varying Carbon Contents in the Temperature Range of RT ∿ 565°C.

over the midsection using a SiC scriber.

The specimen was then heated to 750°C in an argon atmosphere and a 9,000 psi stress applied. At random intervals the testing was interrupted and the specimen removed. Using the traveling and optical microscopes, strain and grain boundary sliding parameters were measured. The offsets of both the transverse and longitudinal marker lines were measured and applied in Equation 7.7, previously used by Rachinger[8] and, in Equation 7.8, a simplified version from Stevens[9].

$$\varepsilon_{gb} = N_L \bar{l}_T \qquad [7.7]$$

$$\varepsilon_{gb} = 2\ N_L \bar{d}_L \qquad [7.8]$$

where $N_L$ is the number of boundaries per unit length in the longitudinal direction, $\bar{l}_T$ is a mean value of the longitudinal component of displacement of a transverse line, $\bar{d}_L$ is a mean value of the transverse component of displacement of the longitudinal marker line.

It should be noted that these equations are applicable under specific assumptions. Present investigations are verifying the validity of these simplifying assumptions.

At least 400 total measurements were taken at the intersections of the grain boundary and the longitudinal and transverse marker lines to compute values for $\varepsilon_{gb}$. The single plot of $\bar{\varepsilon}_{gb}$ in Fig. 7 was the computed mean value of the results as obtained from Equations 7.7 and 7.8. Photomicrographs of the more distinguishable sliding grains were

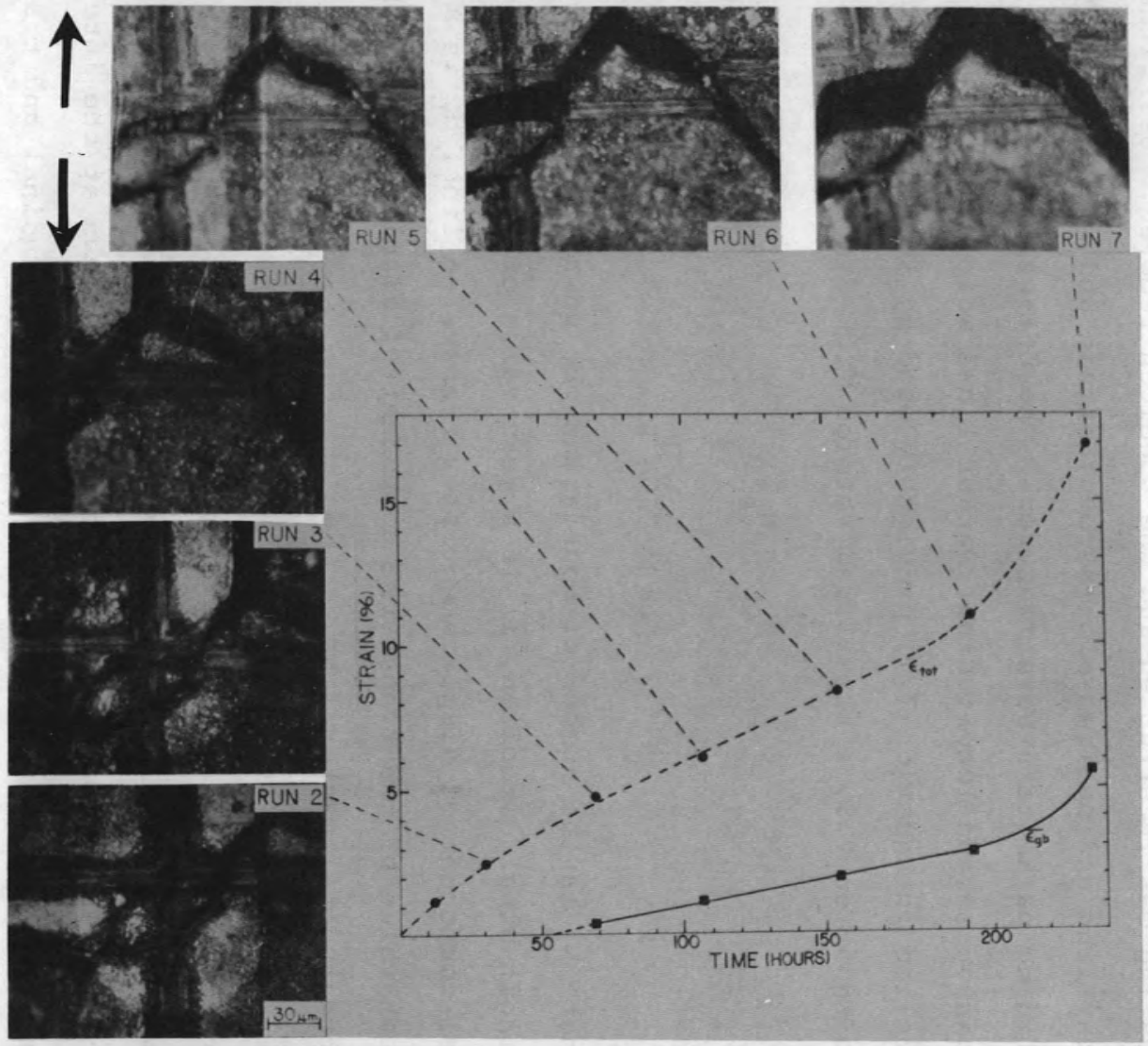


Fig. 7.7. Total Strain and Grain Boundary Sliding Behavior in AISI Stainless Steel Creep Tested at 9 ksi and 750°C.

included in Fig. 7.

Another fact to be emphasized is that only one specimen was employed in this test of interrupted runs which could appreciably affect the rupture life and total strain to rupture.

### 7.1.3. REFERENCES


1. Oak Ridge National Laboratory, Mechanical Properties Test Data for Structural Materials Quarterly Progress Report for Period Ending April 30, 1976, ORNL-5150, pp. 375-379.

2. F. Garofalo, Fundamentals of Creep and Creep-Rupture in Metals, The Macmillan Co., NY, 1965, pp. 46-66

3. J. H. Westbrook, Trans. Amer. Soc. Metals, 45 (1953) 221.

4. J. Larsen-Badse, Trans. JIM, 9 (1968) 312.

5. O. D. Sherby and P. E. Armstrong, Met. Trans., 2 (1971) 3479.

6. F. Garofalo, P. R. Malenock, and G. V. Smith, ASTM STP No. 129 (1952) 10.

7. J. R. Cahoon, Met. Trans., 3 (1972) 3040.

8. W. A. Rachinger, J. Inst. Metals, 81 (1952-53) 33.

9. R. N. Stevens, Met. Rev., II (1966) 133-136.

## 7.2 UNIVERSITY OF CALIFORNIA, LOS ANGELES - K. Ono, A.J. Ardell and A.S. Tetelman

### 7.2.1 Mechanical Properties Evaluation of Carburized Type 304SS (P.L. Jones and A.S. Tetelman)

This research program is designed to provide a basic understanding of the effects of surface carburization on the elevated temperature mechanical behavior of Type 304SS. The basic research has been dividied into two parts: 1) evaluation of short-term mechanical and fracture behavior; and 2) characterization of the time-dependent mechanical behavior and corresponding changes in microstructure, crack growth rate and fracture behavior. Since our last report, work has continued on the second portion of the research program.

A constant load creep frame with a 9.5:1 lever ratio is being used to study the elevated temperature through-the-thickness crack growth characteristics of surface flawed Type 304SS sheet specimens. The present report describes the baseline data obtained at 750°C.

Constant load creep rupture tests were interrupted periodically and the crack depth determined by a clip gauge displacement technique. Material characterization, specimen configuration

and the clip gauge displacement technique have been discussed in a previous report.[1] Crack growth experiments were performed in both helium and in two gas mixtures of hydrogen and methane. The calculated equilibrium surface carbon concentration was taken as a direct measure of the carburizing potential.[2] To insure a significant amount of carburization in the specimens exposed to the hydrogen-methane gas mixture, the tests were conducted at 750°C. total exposure time varied from 12.5 to 23.6 hours.

Crack growth rates were analyzed as a function of both the stress intensity factor, K, and the net section stress, $\sigma_{NET}$. K was calculated from the Paris and Sih[3] equation for a semi-elliptical surface crack in tension. This relation can be expressed as:

$$K_I = \left[1 + 0.12\ (1 - a/c)\right] \frac{\sigma\sqrt{\pi a}}{\Phi} \left(\frac{2t}{\pi a} \tan \frac{\pi a}{2t}\right)$$

for $a/t < 0.75$ and $a/c \leq 1$

where $a$ = flaw depth

$2c$ = flaw length

$\sigma$ = far field stress

$t$ = specimen thickness

and $\Phi$ = elliptical integral of the second kind, given by

$$\Phi = \int_0^{\pi/2} \left[1 - \left(\frac{c^2 - a^2}{c^2}\right) \sin^2\theta\right]^{1/2} d\theta .$$

The crack growth rate was determined graphically by plotting crack depth as a function of time. The corresponding stress intensity

factor and net section stress was calculated from the average crack depth and length over the time interval used to determined the crack growth rate.

Figures 1 and 2 are log plots of the crack growth rate, da/dt, as a function of the stress intensity factor and the net-section stress, respectively. It appears that the constant load crack growth behavior at 750°C in both inert and carburizing atmospheres can be correlated with either K or $\sigma_{NET}$ using equations of the form

$$\frac{da}{dt} = CK^n \quad \text{or} \quad \frac{da}{dt} = D\sigma_{NET}{}^m,$$

where n and m are 3.4 and 7.0, respectively. However, the physical significance, if any, of either correlation remains to be shown.

Comparing the crack growth behavior in an inert vs. carburizing environment discloses that the growth rate is strongly affected by the carburizing potential, taken as the theoretical equilibrium surface carbon concentration, $C_s$, which can be calculated from the hydrogen to methane ratio and thermodynamic considerations. Increasing $C_s$ from 0 to 0.29 wt.% C had no significant effect on the flaw growth characteristics. However, at equivalent values of K and $\sigma_{NET}$ the crack growth rate was reduced by a factor of approximately 0.5 in the test conducted with $C_s$ = 0.88 wt.% C. Thus, under static load conditions at 750°C exposure of Type 304SS to a carburizing atmosphere has a beneficial effect (if any) on crack growth.

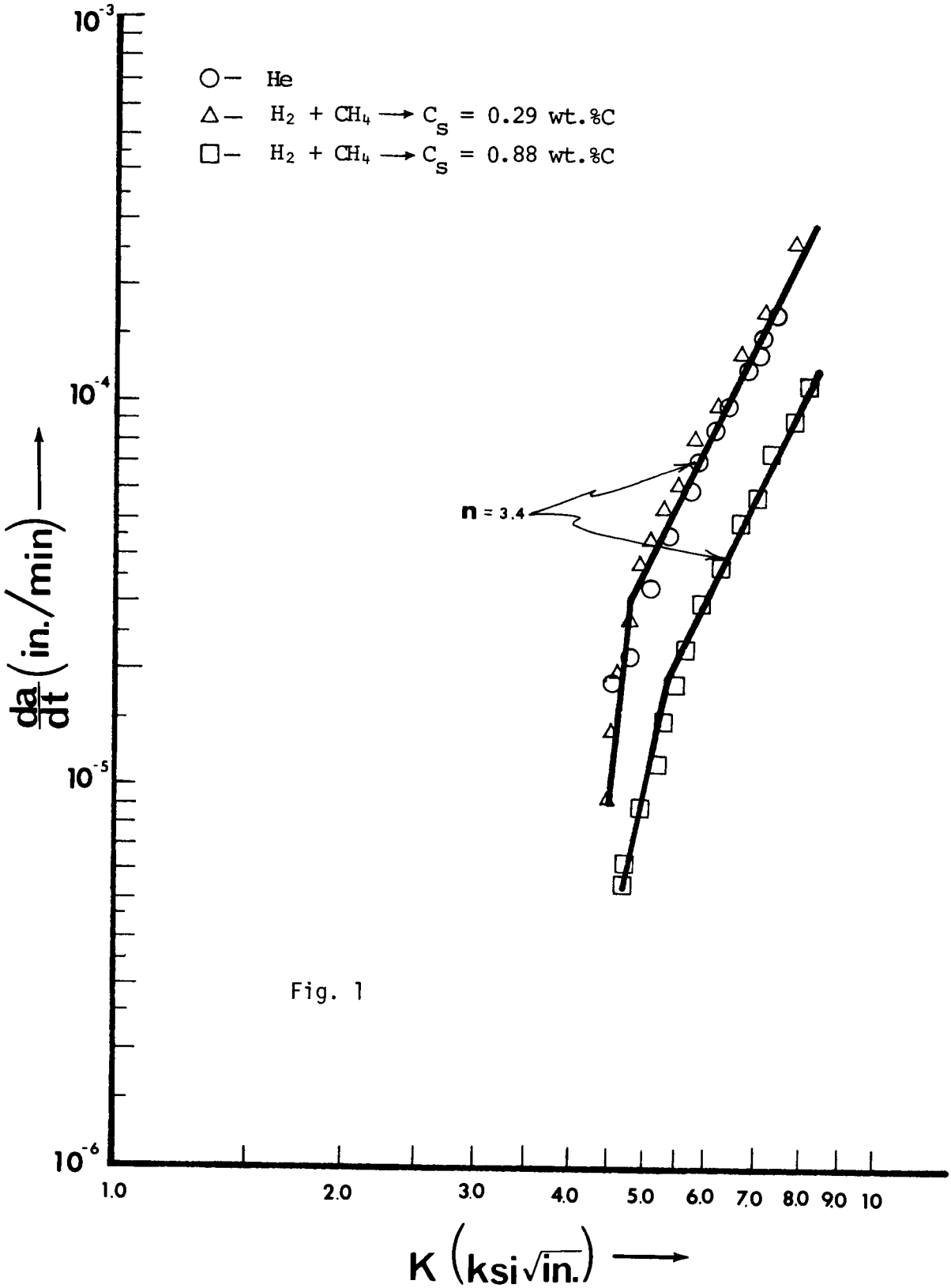


Fig. 1

Crack growth rate as a function of stress intensity factor at 750°C.

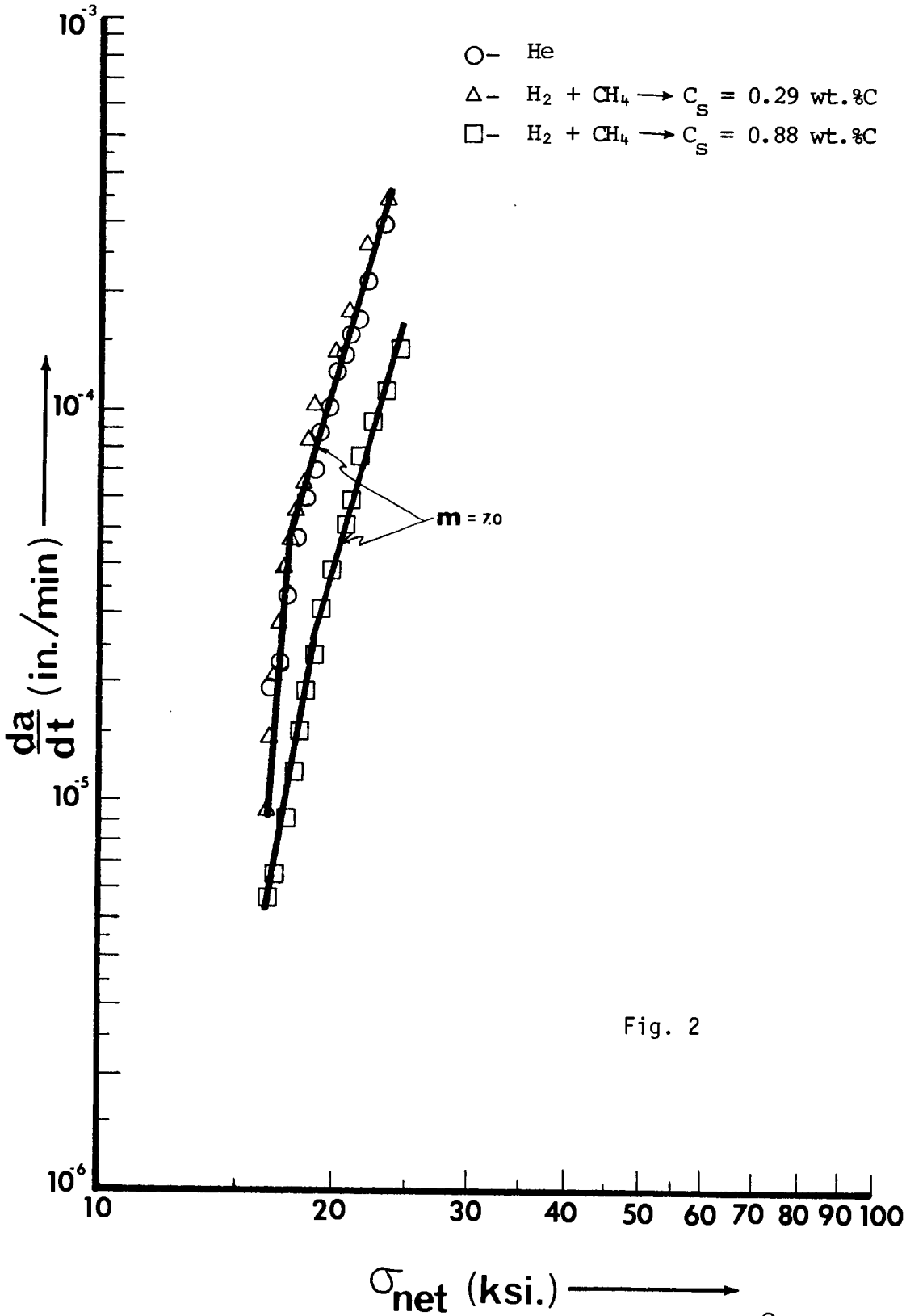


Fig. 2

Crack growth rate as a function of net section stress at 750°C.

## 7.2.2 CREEP STUDIES IN STAINLESS STEELS

(O. Ajaja and A. J. Ardell)

### 7.2.2.1 INTRODUCTION

The effect of prior cold work (0-10%) on the creep behavior of Type 304SS is under investigation. Our efforts have been particularly concentrated on the primary and secondary creep characteristics. As we pointed out in a previous progress report,[4] the strain-time relationship that has provided the best fit to our data is of the form:

$$\varepsilon = \varepsilon_o + \dot{\varepsilon}_s t + \varepsilon_t(1 - e^{-rt}) \qquad (3)$$

where $\varepsilon$ is the creep strain at time t, $\varepsilon_o$ and $\varepsilon_t$ are the loading strain and the limiting transient creep strain, respectively, $\dot{\varepsilon}_s$ is the secondary creep rate and r is the transient creep rate parameter. The creep strength improvement resulting from prestrain was shown to be greatly limited by the creep stress and temperature, and we suggested that while prestraining resulted in a decrease of creep rate at low stresses, rapid recovery at high stresses and/or temperatures contributed to a partial or total loss of creep resistance. In this report, we present and analyze more creep data obtained from creep testing done at three different temperatures: 677, 704 and 760°C. The sensitivity of the stress dependence of creep rate to prestrain is examined. The influence of prestrain on the transient creep parameters is being delineated. By investigating how each parameter responds to prestrain and the corresponding microstructural changes involved, we hope to gain a better understanding of the mechanism of transient creep in particular,

and of the overall creep behavior of the material.

### 7.2.2.2 EXPERIMENTAL PROCEDURES

The techniques of prestraining and creep testing have been reported earlier.[4] Cylindrical tensile specimens of Type 304SS are solution-treated at 1040°C for 1 hr., prestrained in tension at room temperature using an Instron machine, and subsequently creep tested under conditions of constant (true) stress in the temperature range 677-760°C. Thin foils for TEM are spark machined from crept specimens and jet electropolished using an electrolyte made up of 40 parts acetic acid, 30 parts phosphoric acid, 40 parts nitric acid and 90 parts distilled water. Final electro-thinning is done with a solution containing 940 mℓ ethanol, 6 mℓ distilled water and 54 mℓ perchloric acid (70%) at 0°C.

### 7.2.2.3 RESULTS AND DISCUSSION

#### A. Secondary Creep

The secondary creep rate, $\dot{\varepsilon}_s$, decreases with increasing cold work (CW) level at low test stresses (Fig. 3). This enchancement of creep strength by prestrain becomes less apparent as the stress increases, and at the highest stresses, CW has no significant effect. It is obvious from Fig. 3b that CW levels up to about 6% have little effect on the creep strength at T = 704°C and $\sigma$ = 172.4 MN/m$^2$. This trend is frequently observed at the intermediate stresses, suggesting that higher prestrain levels are necessary in order to improve the creep resistance.

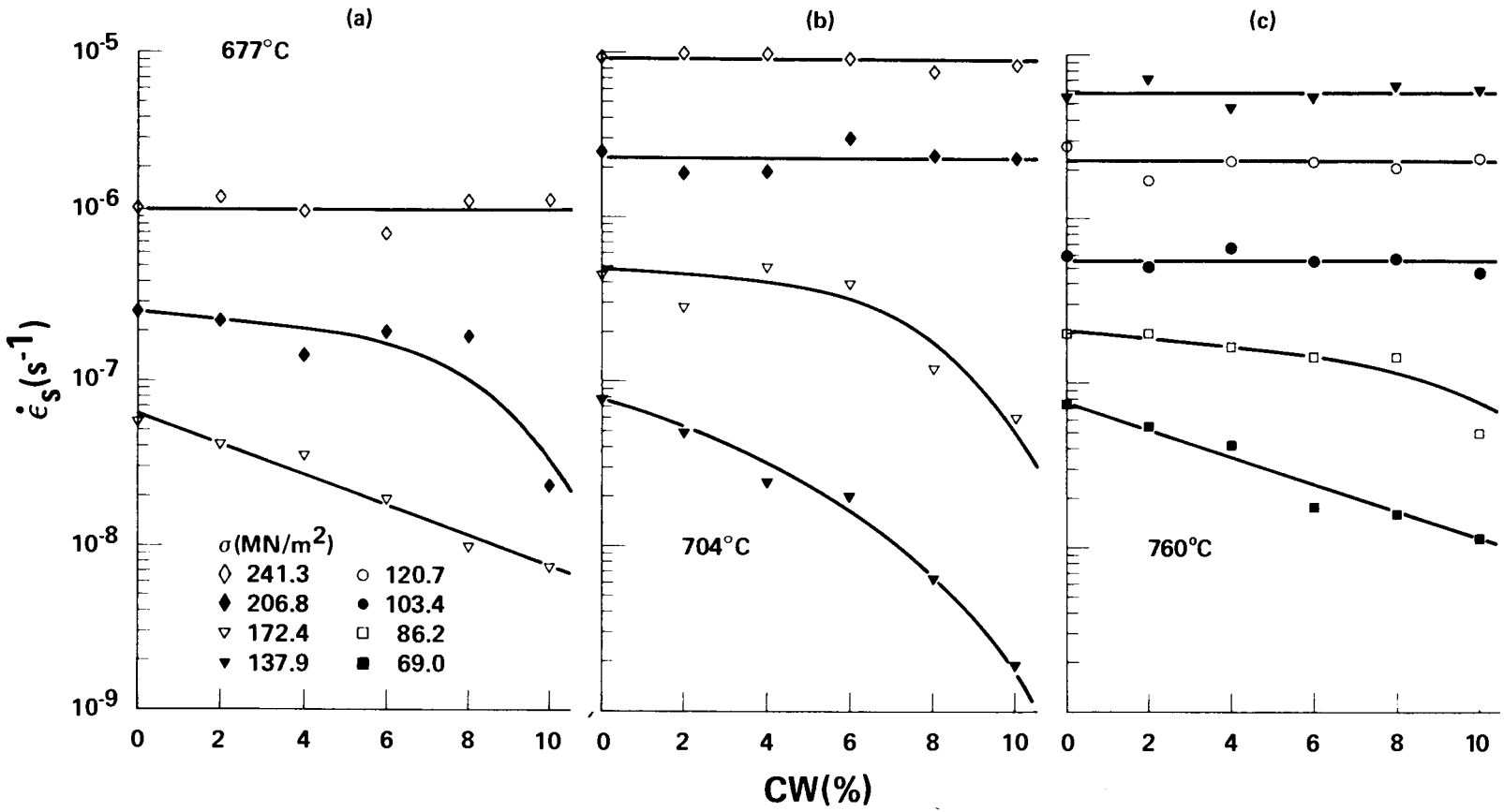


Fig. 3. Illustrating the Dependence of the Steady State Creep Rate, $\dot{\varepsilon}_s$ on Prior Cold Work.

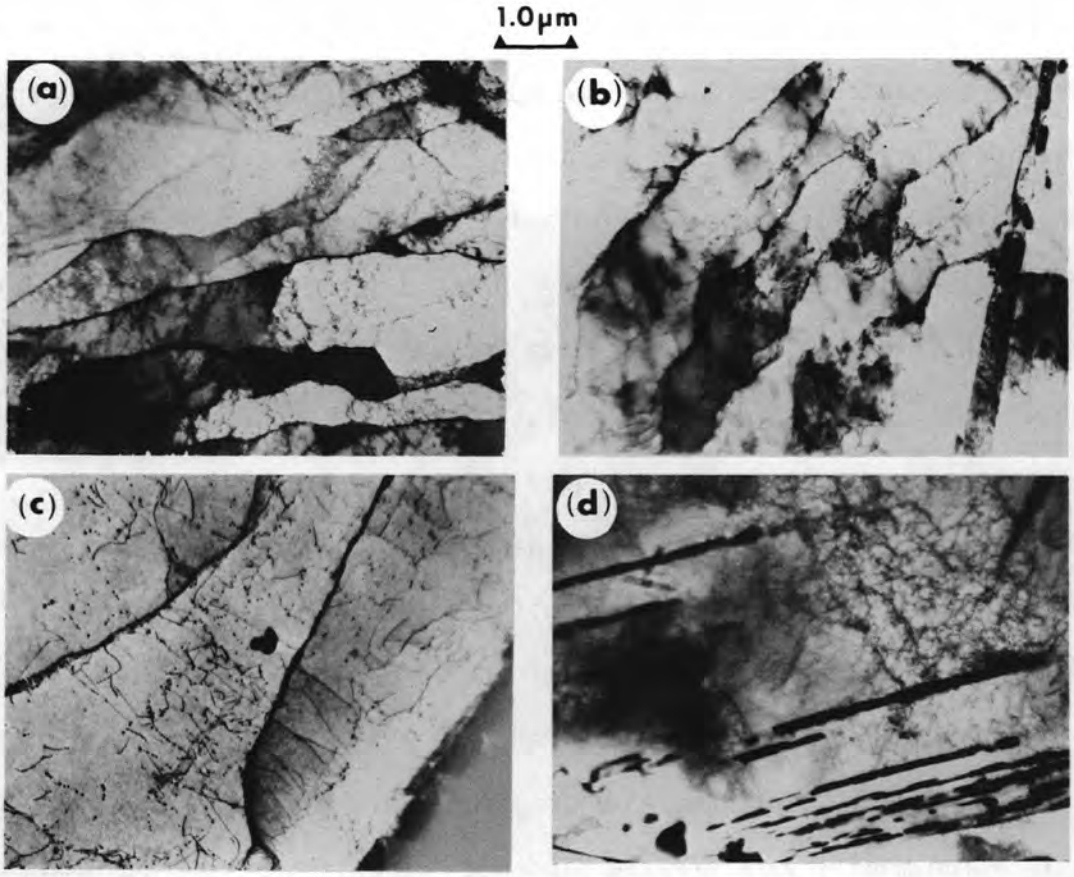


Fig. 4: Transmission electron micrographs of specimens creep-tested at 760°C (a) CW = 0%, $\sigma$ = 137.9MN/m$^2$, $\dot{\varepsilon}_s$ = 5.44x10$^{-6}$s$^{-1}$ (b) CW = 10%, $\sigma$ = 137.9MN/m$^2$, $\dot{\varepsilon}_s$ = 6.17x10$^{-6}$s$^{-1}$, (c) CW = 0%, $\sigma$ = 69.0 MN/m$^2$ $\dot{\varepsilon}_s$ = 7.47x10$^{-8}$s$^{-1}$; (d) CW = 10%, $\sigma$ = 69.0 MN/m$^2$, $\dot{\varepsilon}_s$ = 1.16x10$^{-8}$s$^{-1}$.

Thin foil electron microscopy performed on the crept specimens shows that the steady state creep substructures developed at the high stresses are characterized by extensive subgrain formation. Figures 4a and b show the substructures developed by the annealed and (10%) pre-strained specimens tested at 760°C and 137.9 MN/m$^2$ - the highest stress used at that temperature. The creep rates are almost identical, so also are the microstructures; the only visible difference being the presence of an extensive array of deformation bands in the CW specimen. Tests carried out at 760°C and 69.0 MN/m$^2$ showed the prestrained specimen to be

about an order of magnitude stronger than the annealed specimen (Fig. 3c). The microstructure of the annealed specimen was characterized by extensive grain boundary precipitation and a limited subgrain formation, while the prestrained specimen revealed, in addition, an array of banded carbide platelets nucleated intragranularly on the deformation bands generated during CW (Figs. 4c and d). We have not yet identified the nature of these bands, although previous investigators have characterized them as clusters of stacking faults produced by slip on closely spaced slip planes[5] or microtwins.[6] These bands have been known to provide ready nucleation sites for carbide precipitates in aged stainless steels.[5-7] If the banded carbide platelets nucleate very early in the creep process, which they probably do, the mean free path of the dislocations is reduced and the propensity for subgrain formation, which depends very strongly on dislocation mobility is greatly hindered. The lack of intragranular precipitation at the high stress (partly due to the short test duration), combined with faster recovery are clearly some of the factors responsible for the lack of creep strength enhancement. The transient creep substructures for the preannealed and prestrained specimens are currently under study. The processes of precipitation and subgrain formation as functions of creep testing time will be investigated.

The stress dependence of $\dot{\varepsilon}_s$ is strongly influenced by all the parameters $\sigma$, T and CW. For all the temperatures investigated and for specimens prestrained less than 4%, the creep rate follows a stress dependence of the type

$$\dot{\varepsilon}_s = A \exp(\beta_s \sigma) \tag{4}$$

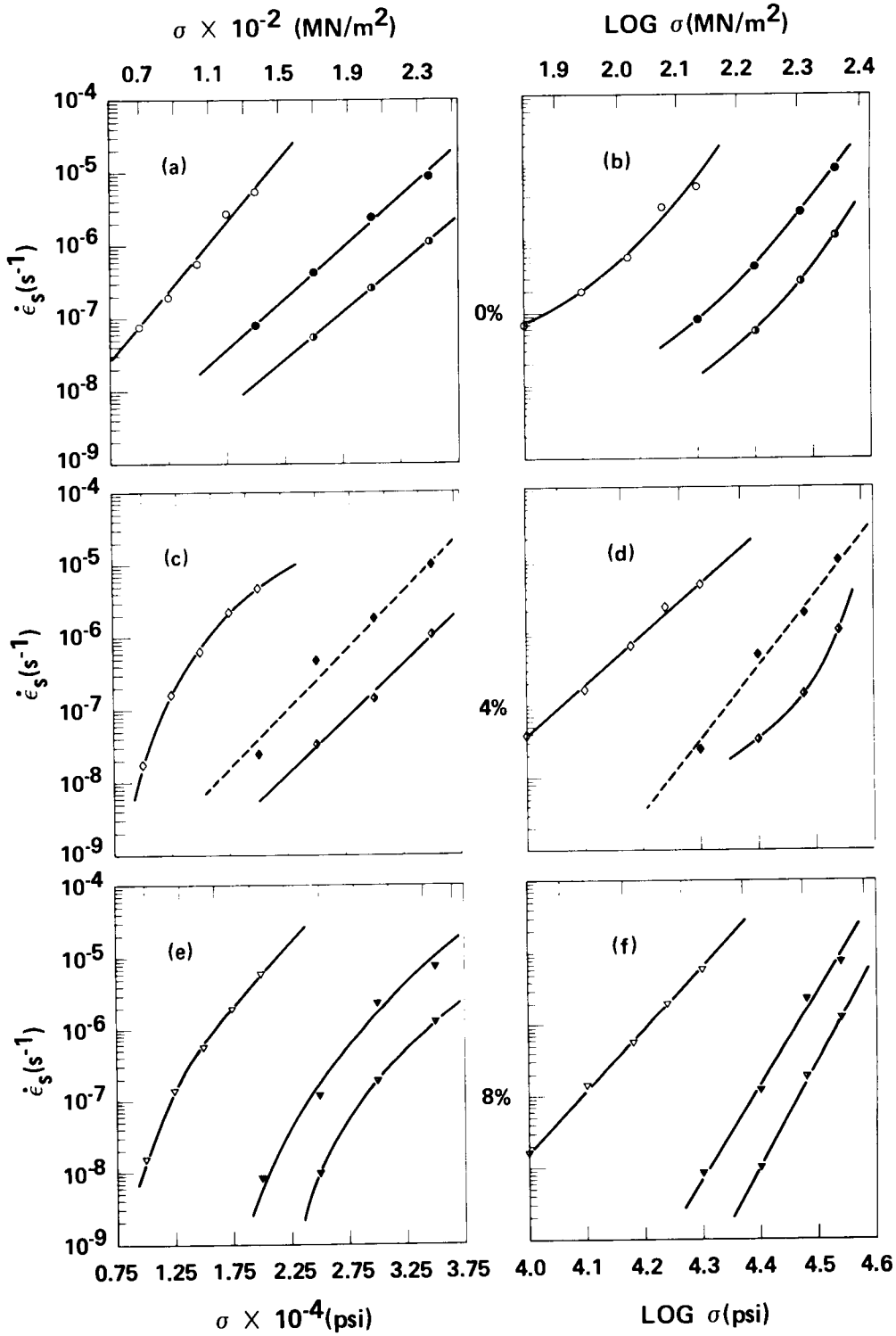


Fig. 5. The Relationship Between $\varepsilon_s$ and the Applied Stress, σ. a, c and e: Log $\dot{\varepsilon}_s$ vs. σ; b, d and f: Log $\dot{\varepsilon}_s$ vs. Log σ. Open Symbols Represent Tests at 760°C, Filled Symbols: 704°C, Half Filled Symbols: 677°C.

where A and $\beta_s$ are constants. For CW levels greater than 4%, a better fit is obtained with the polynomial stress function

$$\varepsilon_s = A'\sigma^n \tag{5}$$

where A' and n are constants. The plots presented in Fig. 5 indicate that the creep rate for the annealed specimen follows the $\exp(\beta_s\sigma)$ - type while the specimen prestrained 8% follows the $\sigma^n$ - type dependence. A prestrain level of 4% represents the transition from the exponential to the polynomial stress dependence at 704°C (Fig. 5c and d). This transition lies between 2 and 4% CW at 760°C and between 4 and 6% at 677°C, suggesting that the transition CW level decreases with increasing temperature. The values of $\beta_s$ (for 0 to 4% CW) and n (4 to 10% CW) are listed in Table I. Evidently, $\beta_s$ increases with temperature and CW; the value of n, however, increases with increasing CW, but with decreasing temperature.

It has been shown[8,9] that Eqs. (4) and (5) are both limiting cases of a more general relation of the type:

$$\dot{\varepsilon}_s = A'' \sinh^n(\alpha\sigma) \tag{6}$$

where A", $\alpha$ and n are all constants. Equation (6) reduces to (4) at high stresses ($\alpha\sigma > 1.2$) and to (5) at low stresses ($\alpha\sigma < 0.8$) with $\beta_s \equiv n\alpha$, $A \equiv A''/2^n$ and $A' \equiv A''\alpha^n$. It is clear from Table I that although $\beta_s$ increases with prestrain, n increases much more rapidly. Since $\alpha = \beta_s/n$, the net effect is to decrease $\alpha$ as the CW level increases. The fact that the transition from the $\sigma^n$ - type to the $\exp(\beta_s\sigma)$ - type dependence for a given specimen occurs at $\alpha\sigma \simeq 1$ implies that a decrease in the value of $\alpha$ would result in an increase in the value of the transition stress. It is

TABLE I

| Cold Work (%) | $\beta_s \times 10^2 (m^2/MN)$ | | | n | | |
|---|---|---|---|---|---|---|
| | 677°C | 704°C | 760°C | 677°C | 704°C | 760°C |
| 0 | 4.34 | 4.77 | 6.43 | -- | -- | -- |
| 2 | 4.77 | 5.13 | 7.11 | -- | -- | -- |
| 4 | 4.99 | 5.57 | --- | --- | 10.87 | 7.09 |
| 6 | -- | -- | --- | 12.17 | 11.29 | 8.33 |
| 8 | -- | -- | --- | 15.00 | 13.33 | 8.75 |
| 10 | -- | -- | --- | 15.63 | 15.15 | 9.09 |

obvious, then, that for prestrain levels > 6% the transition stress was raised above the stress range investigated, hence the $\sigma^n$ - type dependence. We hope to perform more tests in order to evaluate $\alpha$ and the transition stress for all CW levels.

B. Transient Creep

As previously reported[4], prior CW significantly influences the transient creep kinetics in the Type 304SS under investigation. The limiting transient creep strain, $\varepsilon_t$, decreases fairly rapidly with increasing prestrain at stresses $\leq$ 206.8 MN/m$^2$ (Fig. 6). At 704°C and $\sigma \geq$ 206.8 MN/m$^2$, $\varepsilon_t$ is not significantly affected by prestrain levels less than some critical value (about 6% for $\sigma$ = 206.8 MN/m$^2$ and > 10% for $\sigma$=241.3 MN/m$^2$) beyond which a further increase in prestrain results in a rapid decrease in the value of the transient creep strain. Note

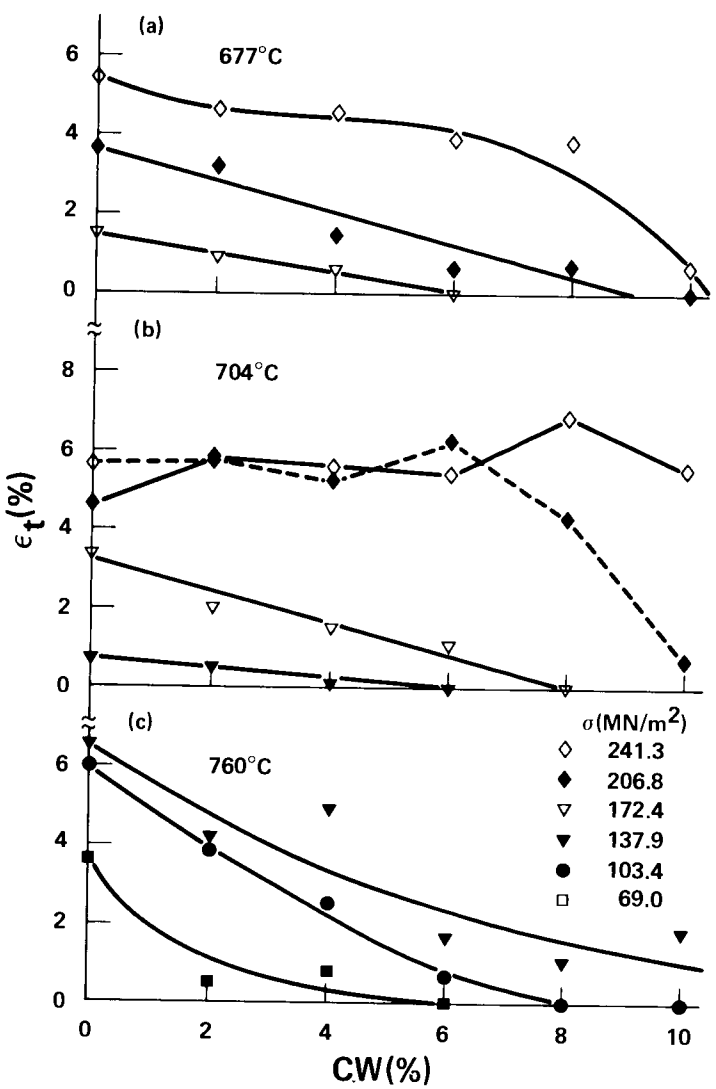


Fig. 6. Illustrating the Dependence of the Transient Creep Strain, $\varepsilon_t$ on Pre-strain.

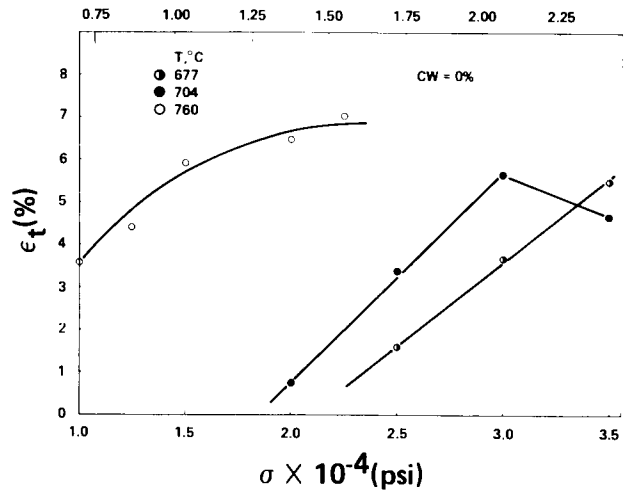


Fig. 7. The Relationship between $\varepsilon_t$ and $\sigma$ for the Annealed Material.

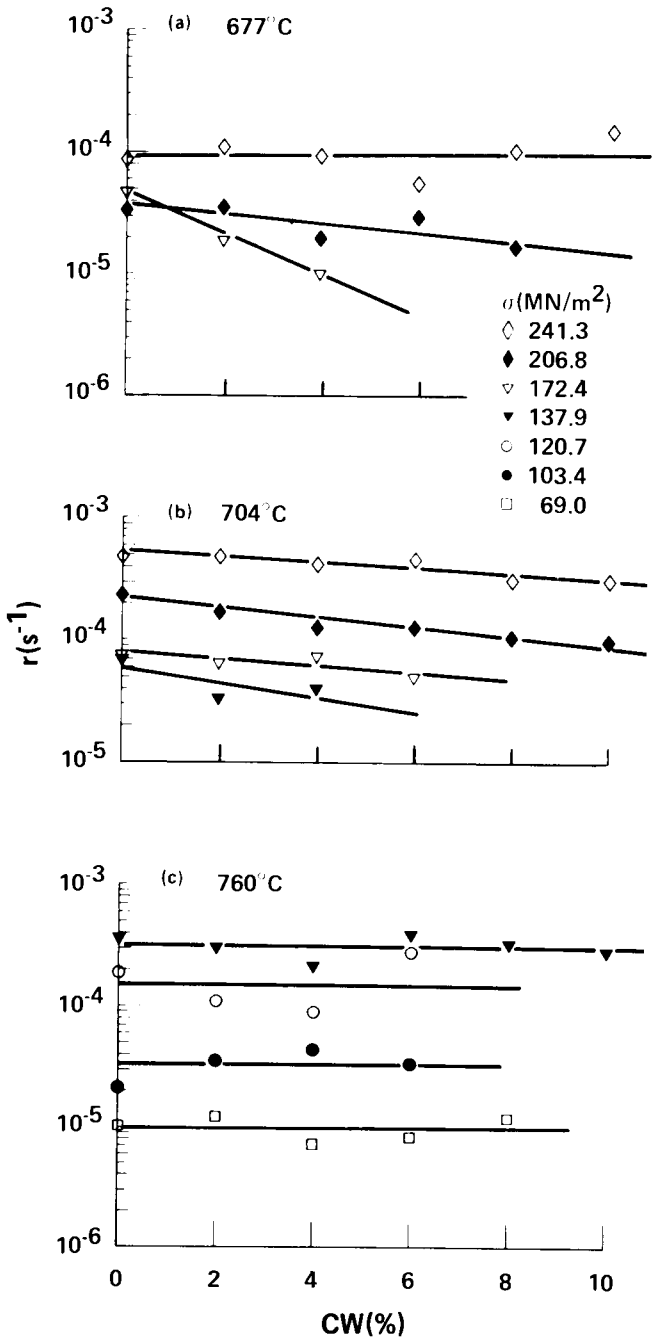


Fig. 8. The dependence of the transient creep parameter, r on prior cold work.

that at the lowest stress investigated at each temperature, transient creep was completely eliminated ($\varepsilon_t$ = 0) by a prestrain of 6% or more. Figure 7 illustrates the variation of $\varepsilon_t$ with $\sigma$ for the annealed specimen. It is noted that $\varepsilon_t$ increases initially with increasing stress and then reaches some saturation value beyond which a further stress increase results in no appreciable change (T = 760°C) or a slight decrease (T = 704°C) in the value of $\varepsilon_t$. This is true for all CW levels investigated. The saturation value of $\varepsilon_t$ thus observed has been approximately 6 to 7%, also independent of CW level. It is clear from Fig. 7 that $\varepsilon_t$ also increases with increasing

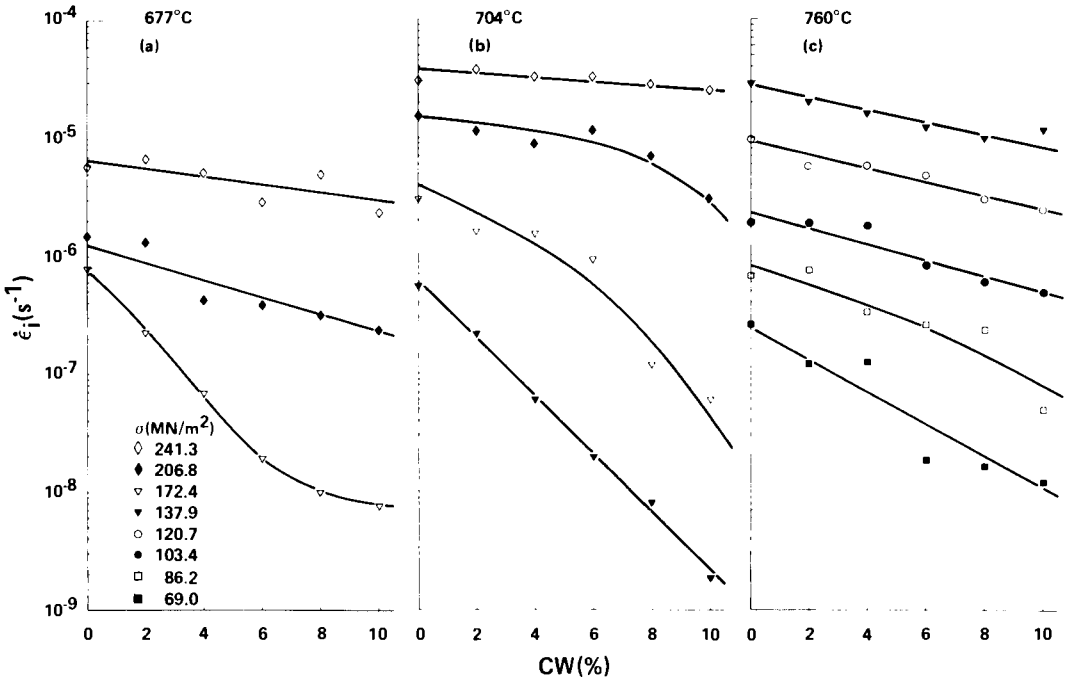


Fig. 9. The relationship between the initial creep rate, $\dot{\varepsilon}_i$ and prior cold work.

temperature for any given stress level. The maximum value of $\varepsilon_t$, however, is again limited to the saturation value mentioned above.

The creep parameter r characterizes the rate at which transient creep is exhausted, or the rate of approach to steady state. The results presented in Fig. 8 indicate that r decreases rather mildly with increasing prestrain at 677°C and 704°C, this effect becoming more pronounced at the lowest stresses. The plots for 760°C do not show a significant variation of r with CW at any stress level investigated. However, its value is very sensitive to stress and temperature changes, which is not unexpected since r is directly related $\dot{\varepsilon}_s$, as is demonstrated below.

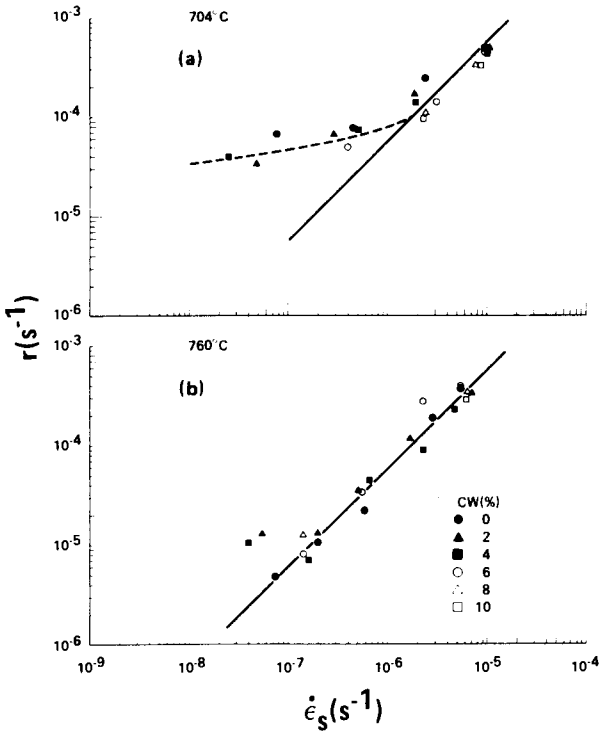


Fig. 10. Log-Log plot of r vs. $\dot{\varepsilon}_s$

All values of the initial creep rate, $\varepsilon_i$, reported in this paper are obtained by differentiating Eq. (3) w.r.t. time and setting t = 0, giving:

$$\dot{\varepsilon}_i = \dot{\varepsilon}_s + r\,\varepsilon_t \tag{7}$$

This is necessary because of the difficulty involved in making accurate measurements of the strain rate immediately after loading. The values of $\dot{\varepsilon}_i$ thus obtained are displayed as a function of prestrain in Fig. 9. The mode of variation of $\dot{\varepsilon}_i$ with CW is very similar to that observed for $\dot{\varepsilon}_s$ and r. Prestraining results in a reduced initial creep rate, this effect becoming more drastic as the test stress decreases. For example, at 704°C and 241.3 MN/m$^2$, $\dot{\varepsilon}_i$ is reduced by < 50% by a 10% prestrain, whereas the same prestrain level at the same test temperature and $\sigma$ = 137.9 MN/m$^2$

leads to a reduction of the initial creep rate by more than two orders of magnitude (Fig. 9).

The strain-time relation [Eq. (3)] has been theoretically derived using different approaches based on dislocation kinetics,[10-12] and unimolecular reaction kinetics.[13-15] It has also been shown to provide a good fit for creep data obtained for stainless steels.[4,9] Based on the assumption that the same creep mechanism is rate controlling for both transient and secondary creep, both r and $\dot{\varepsilon}_s$ are supposed to have the same stress and temperature dependence.[10-14] Hence

$$r = B\,\dot{\varepsilon}_s \tag{8}$$

where B is a constant, independent of $\sigma$ and T. A log-log plot of r vs. $\dot{\varepsilon}_s$ shown in Fig. 10 appears to be in good agreement with Eq. (5) at the higher stress levels. At the lowest stresses, especially at 704°C (Fig. 10a) the values of r are clearly higher than predicted by Eq. (8). Webster, et al.[13] made a similar observation in the course of their analysis of Garofalo's creep data on Type 316SS. They attributed the deviation at low stresses to the increased contribution of grain boundary sliding to the measured creep strain. It is noted in Fig. 10, however, that the applicability of Eq. (8) at the high stresses, as well as the low -stress deviation, is true for all CW levels. The value of B obtained in this investigation is 55.6 and it remains unaltered by prestrain. (Webster's analysis of Garofalo's data for 316SS yielded B = 38.)

The initial creep rate, $\dot{\varepsilon}_i$, has been shown to be directly proportional to the steady state creep rate for annealed materials.[9,13-14]

Hence

$$\dot{\varepsilon}_i = K\dot{\varepsilon}_s \tag{9}$$

where K is a constant. From Eq. (7),

$$\varepsilon_t = (\dot{\varepsilon}_i - \dot{\varepsilon}_s)/r,$$

and, combining this with (8) and (9) yields:

$$\varepsilon_t = (K - 1)/B \tag{10}$$

This led Webster et al.,[12] and Ahmadieh and Mukherjee[14,15] to conclude that $\varepsilon_t$ is a material constant, independent of stress and temperature. The results of Garofalo et al.[9] and Threadgill et al.,[16] however, showed that $\varepsilon_t$ is dependent on both $\sigma$ and T, in contradiction to Eq. (10). Both found that $\varepsilon_t$ showed an initial increase with increasing $\sigma$ and T, and later reached a limiting value beyond which it remained constant[16] or even decreased[9] with a further increase of $\sigma$ or T. Their observations are entirely consistent with our present results. Threadgill et al. associated the stress dependence with the breakdown of Eq. (8) at low stresses, making Eq. (10) inapplicable. The same reason may account for the rather strong temperature dependence of $\varepsilon_t$. Further research is clearly necessary, particularly on the transient creep microstructure, in order to fully appreciate the significance of the parameters r and $\varepsilon_t$ and gain a better understanding of the effect of creep stress and temperature on them.

Referring to Fig. 10b, it is noted that although at the higher stresses, where $r \propto \dot{\varepsilon}_s$, the validity of Eq. (6) is not altered by pre-strain, but $\varepsilon_t$ nevertheless decreases as the CW level increases. Equation (7) can be rewritten as

$$\dot{\varepsilon}_i = \dot{\varepsilon}_s(1 + B\varepsilon_t)$$

upon substitution of Eq. (6). This clearly suggests that Eq. (9) would hold true only when both B and $\varepsilon_t$ remain constant. Since $\varepsilon_t$ changes with prestrain, it follows that Eq. (9) would have to be modified for prestrained specimens. This is consistent with our earlier observation[4] that in the stress range investigated

$$\dot{\varepsilon}_i = k\,\dot{\varepsilon}_s^{\,m}\,, \tag{11}$$

where both k and m are prestrain dependent. As reported for the annealed 304SS, $m \simeq 1$ and $k \simeq 5.4$ for tests performed at 704°C. Two special cases of Eq. (11) are worth noting. First, at very high stresses when the effect of prestrain is quickly eliminated by rapid recovery, all prestrained specimens show basically the same creep characteristics as the annealed specimen. Eq. (11) then reduces to Eq. (9) with $m = 1$ and $k \equiv k$. Also, at creep stresses low enough to render $\varepsilon_t = 0$ (complete elimination of transient creep), $\dot{\varepsilon}_i$ and $\dot{\varepsilon}_s$ are clearly the same, hence Eq. (11) relaces to $\dot{\varepsilon}_i = \dot{\varepsilon}_s$ with both k and m equal to unity. The stress range over which Eq. (11) is applicable, therefore, represents a transition stage from the "No Transient Creep" condition (CW effect maximum) to the "Full Transient Creep" condition (CW effect virtually nonexistent). More creep data are being generated at two other temperatures in order to investigate the effect of temperature, if any, on k and m.

## 7.2.3 MICROSTRUCTURE AND HIGH TEMPERATURE DEFORMATION OF 2-1/4 CR - 1 MO STEELS

(S. Y. Hsu and K. Ono)

### 7.2.3.1 INTRODUCTION

We have reported previously large instantaneous loading strain or strain burst, due to a stress increment during high temperature creep tests of 2-1/2 Cr-1Mo steels.[17,18] It is believed to be one of the mechanical instability phenomena during plastic deformation, but its relation to microstructures and test conditions is not understood. The objective of this study was to systematically evaluate the variables which are responsible for the strain burst phenomenon.

### 7.2.3.2 EXPERIMENTAL

Flat tensile specimens having four different carbon contents and various heat treatment conditions were used in creep tests. Materials and experimental details were identical to those reported previously. Each specimen was tested at several stress levels corresponding to minimum creep rates in the range of $10^{-6}$ to $10^{-3}$ per hour. For strain burst experiments, a steady state creep condition was first established, after which additional load of 10 lb or 20 lb was carefully added. This was equivalent to an increase in the applied stress level of 2 to 2.5 ksi for 10 lb weight (4 to 5 ksi for 20 lb weight), depending on the original cross sectional area and prior deformation of the specimen.

### 7.2.3.3 RESULTS AND DISCUSSION

#### A. Strain Burst Observations

Table II summarizes the results of a series of tests performed using the 10 lb load increment. As reported previously, four alloys are referred to as Alloy H, I, M and L, according to the carbon contents, which are 0.12%, 0.03%, 0.021% and 0.009%, respectively. Observed strain burst behaviors can be classified into three types. Type 1 exhibited no strain burst phenomenon throughout the entire stress range and the sum of instantaneous loading strain ($\Sigma\varepsilon_i$) was less than 0.5%. Type 2 behavior indicated occasional strain bursts, usually at relatively high stress levels. $\Sigma\varepsilon_i$ reached 2 to 3%. The value of $\Sigma\varepsilon_i$ was over 5% in Type 3, and large strain bursts were consistently observed upon a load increment during the test. The following observations are pertinent:

(i) In the normalized and tempered (N&T) condition, Alloy H showed no strain burst (Type 1) at either 850 or 1050°F. Alloys I, M and L also showed no strain burst in the N&T condition, when test temperatures was 1050°F.

(ii) When test temperature was 850°F, the N&T materials of Alloy I and L showed Type 3 behavior and that of Alloy M Type 2 behavior. Alloy I and L showed much strain burst, the values of $\Sigma\varepsilon_i$ exceeding 5%. Instantaneous loading strains larger than 0.5% were consistently observed throughout the high stress range.

(iii) In Alloys I and L, the propensity for strain bursts diminished after long time tempering at elevated temperatures. Tests # 5 ~

TABLE II. Strain Bursts in 2-1/4Cr-1Mo Steels

| Test Number | Alloy | Heat Treatment After N & T | Test Temp (°F) | Applied Stress (ksi) | $\Sigma \varepsilon_i$ (%) | Type |
|---|---|---|---|---|---|---|
| 1 | H | | 850 | 47~70.2 | 0.4 | 1 |
| 2 | H | | 1050 | 8.8~30.3 | 0.13 | 1 |
| 3 | I | | 850 | 29.5~54.1 | 5.5 | 3 |
| 4 | I | | 1050 | 9.57~21.2 | 0.3 | 1 |
| 5 | I | 4 Mo at 850°F | 850 | 26.1~51.8 | 4.56 | 2 |
| 6 | I | 8 Mo at 950°F | 850 | 26.4~43.8 | 2.93 | 2 |
| 7 | I | 4 Mo at 950°F | 850 | 23.7~41.6 | 2.25 | 2 |
| 8 | I | 1 Mo at 1050°F | 850 | 21.8~41.3 | 2.05 | 2 |
| 9 | I | 12 Mo at 1050°F | 850 | 22.3~36.4 | 0.5 | 1 |
| 10 | M | | 850 | 29.5~57.5 | 1.4 | 2 |
| 11 | M | | 1050 | 6.8~18.4 | 0.12 | 1 |
| 12 | L | | 850 | 36.5~49.6 | 5.2 | 3 |
| 13 | L | | 1050 | 6.8~22.9 | 0.2 | 1 |
| 14 | L | 8 Mo at 950°F | 850 | 26.2~41.1 | 1.01 | 2 |
| 15 | L | 12 Mo at 1050°F | 850 | 10.4~29.8 | 0.88 | 2 |

# 9 reveal this trend for Alloy I. Tempering temperatures seem to have more effect than tempering time. Tempering for one month at 1050° (#8) reduced $\Sigma\varepsilon_i$ value to 2.05%, whereas tempering for four months at 850° (#5) produced a minor reduction to 4.56%. Strain bursts were greatly diminished when a specimen was tempered for 12 months at 1050°F (#9). Similar trends were found in the tests of Alloy L. It should be noted here that $\Sigma\varepsilon_i$ of 0.88% was observed in a sample tempered for 12 months at 1050°F. However, a single strain burst at the highest stress level (29.9 ksi) accounted for much of the total (i.e., 0.74%). Thus, this sample could well be categorized as Type 1 in concert with the results of Alloy I tests.

(iv) Under conditions where no strain burst occurred by using 10 lb load increment, 20 lb increment usually triggered a much larger instantaneous strain. However, the general trend of strian burst appears to be identical. This stress dependence will be shown later together with stress dependence of creep rate.

B. Effects of Strain Burst on Creep Properties

The transient creep stage was reduced when a large instantaneous strain was produced upon a load increment. Figure 11 shows three typical creep curves from three successive stress levels performed on a single specimen. Note that the true strain coordinates have the same scales with shifted origins and the time scale begins at the load increment. A large strain burst (1.15%) was observed at the beginning of the test at 41 ksi. As Fig. 11 clearly shows, the transient strain was smaller than those from higher and lower stress curves and the steady state condition was achieved at a shorter time.

Figure 11 illustrates another interesting observation related to strain burst. The steady state creep rate was smaller in a test with a large strain burst than that of a test without. Apparently, hardening attributable to strain burst increased the creep resistance. The effect was widely observed especially between tests with different stress increments. The variations of minimum creep rate with applied stress of Alloy I samples tested at 850°F are presented in log-log plots of Figs. 12 to 16. For each tempering condition, effects of load increments were evaluated using 10 and 20 lbs increments. The filled data point indicates that preceeding instantaneous strain was larger than 0.2%.

The N&T specimens (Fig.12) showed unusual discontinuities in the $\sigma$ - $\dot{\varepsilon}$ curves, as first observed by Chalco et al.[17,18] These discontinuties were also observed in specimens tempered at 850°F for 4 months and for 12 months (see Figs. 13 and 14). When strain bursts were small under the condition of 10 lbs load increment, the $\sigma$ - $\dot{\varepsilon}$ curves were normal; that is, the stress exponent is high at high stresses and is 4 to 6 at lower stresses. With the occurances of strain bursts, the strain rate was reduced at a given stress level. These results indicate that the unusual discontinuities in the $\sigma$ - $\dot{\varepsilon}$ curves are closely related to strain bursts.

When tempering temperature was increased to 950°F and 1050°F, the magnitude of strain burst was reduced with 10 lb load increments, but was nearly unchanged with 20 lb load increments. In both cases, however, no unusual discontinuity in the $\sigma$ - $\dot{\varepsilon}$ curves was observed as shown in Fig. 15 and 16. This discrepancy, possibly of microstructural origin, cannot be understood presently.

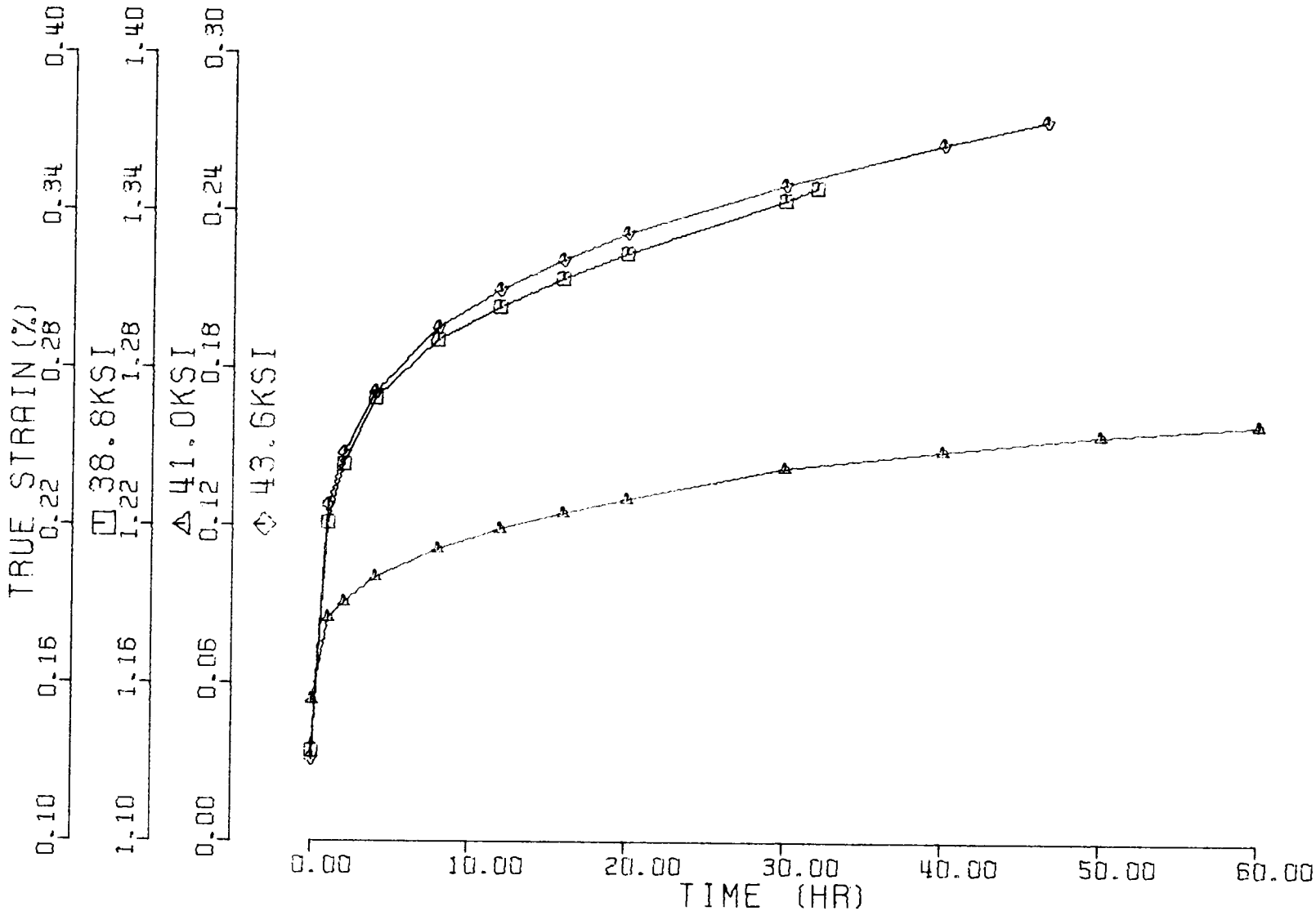


Fig. 11. Typical Creep Curves of Alloy I (4 months tempering at 850°F, tested at 850°F) With (41.0 ksi) and Without (38.8 ksi, 43.6 ksi) strain burst.

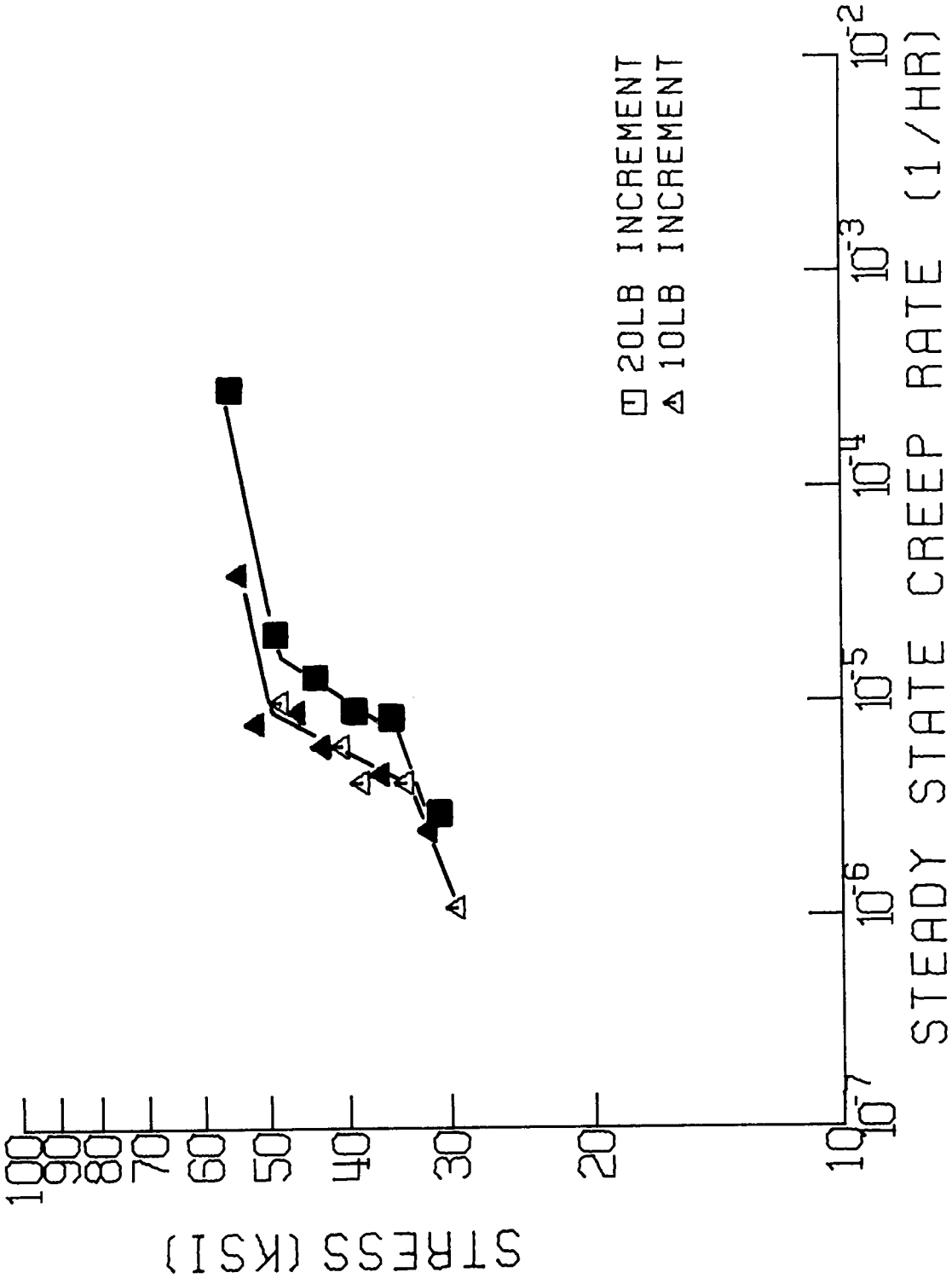


Fig. 12. Creep Stress vs. Steady State Creep Rate of Normalized and Tempered Alloy I. Test Temperature: 850°F.

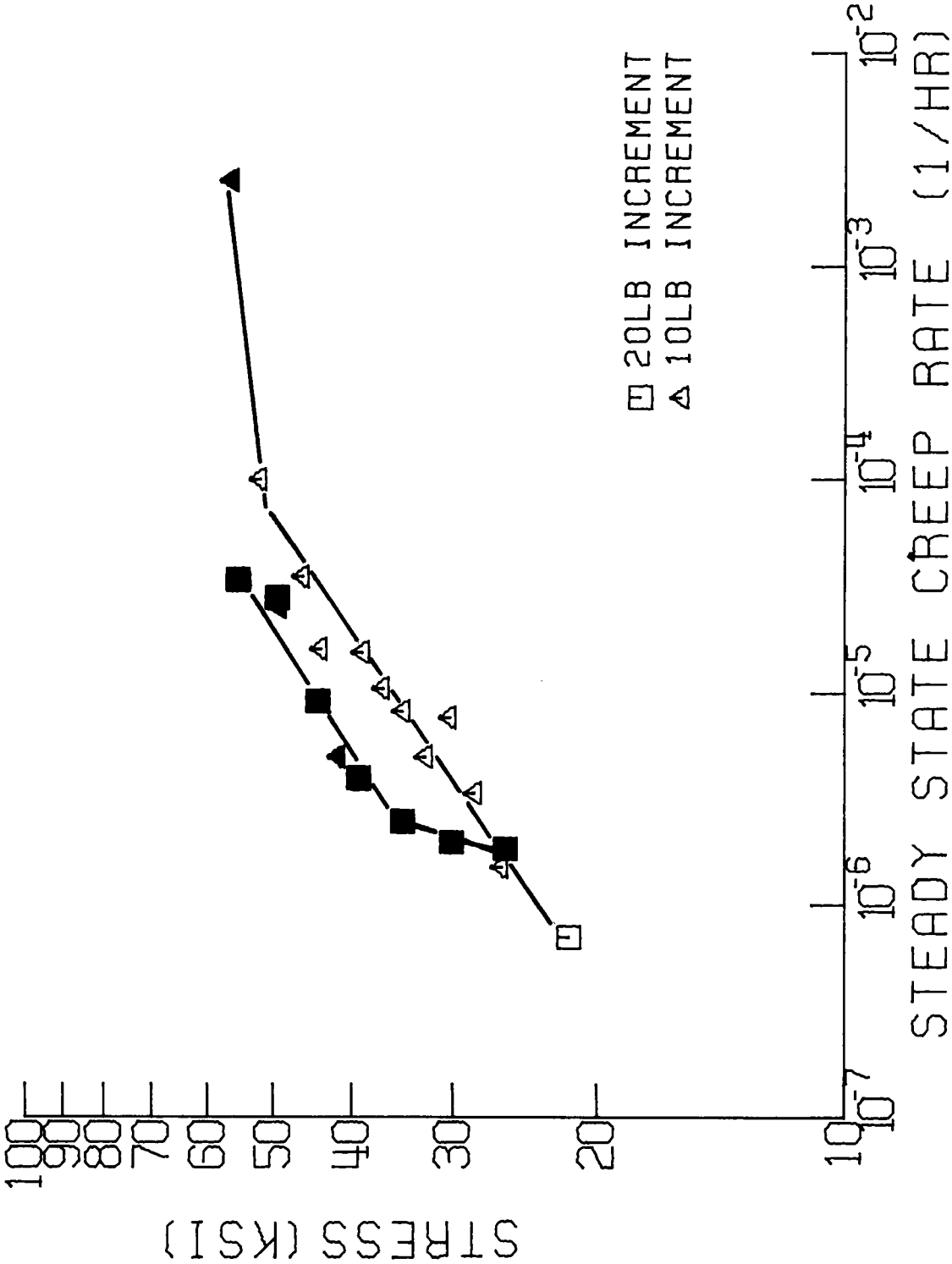


Fig. 13. Creep Stress vs. Steady State Creep Rate of Normalized and Tempered Alloy I, Tempered at 850°F for Four Months. Test Temperature: 850°F.

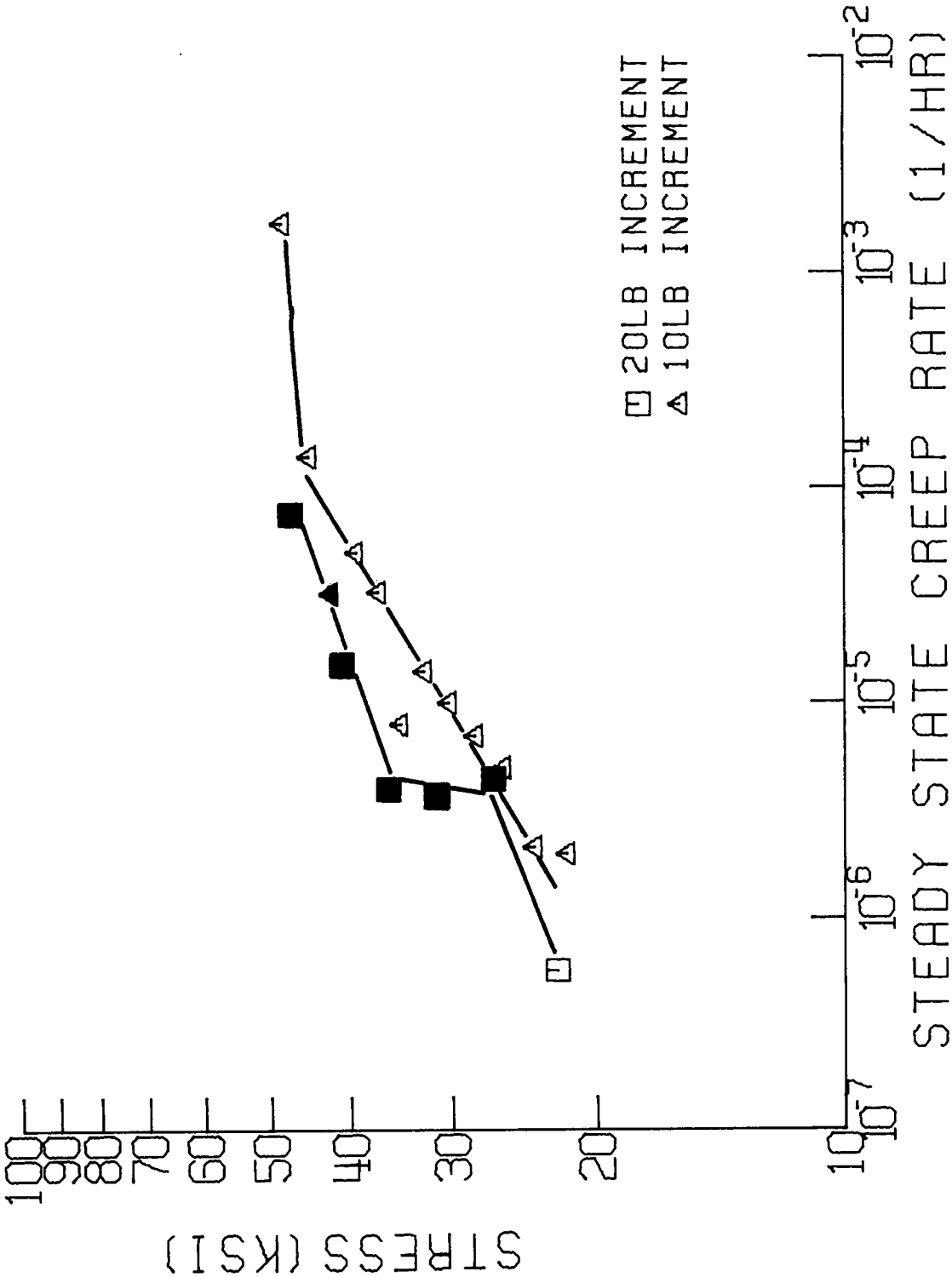


Fig. 14. Creep Stress vs. Steady State Creep Rate of Normalized and Tempered Alloy I, Tempered at 850°F for 12 Months. Test Temperature: 850°F.

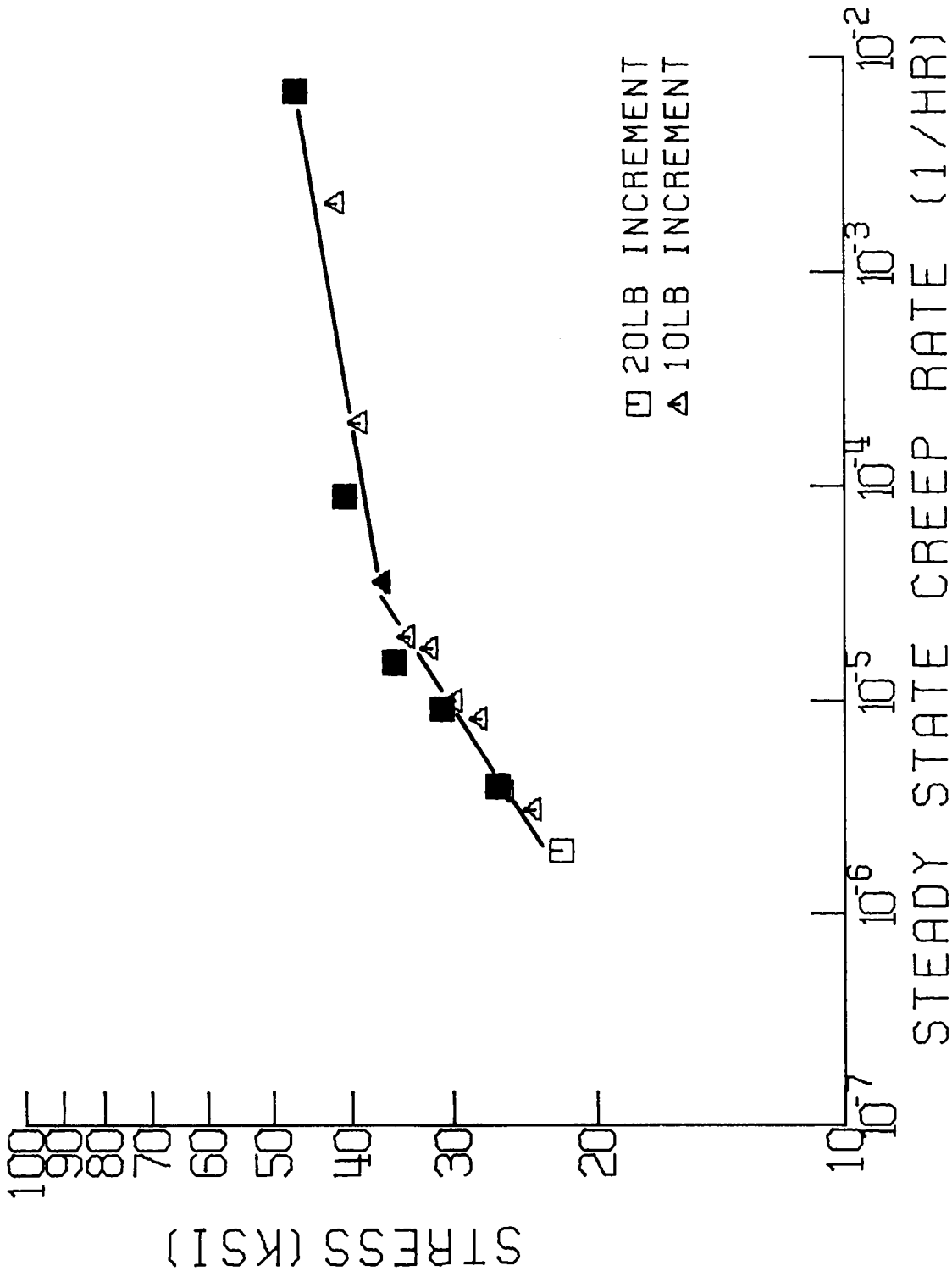


Fig. 15. Creep Stress vs. Steady State Creep Rate of Normalized and Tempered Alloy I, Tempered at 850°F for 4 Months. Test Temperature: 850°F.

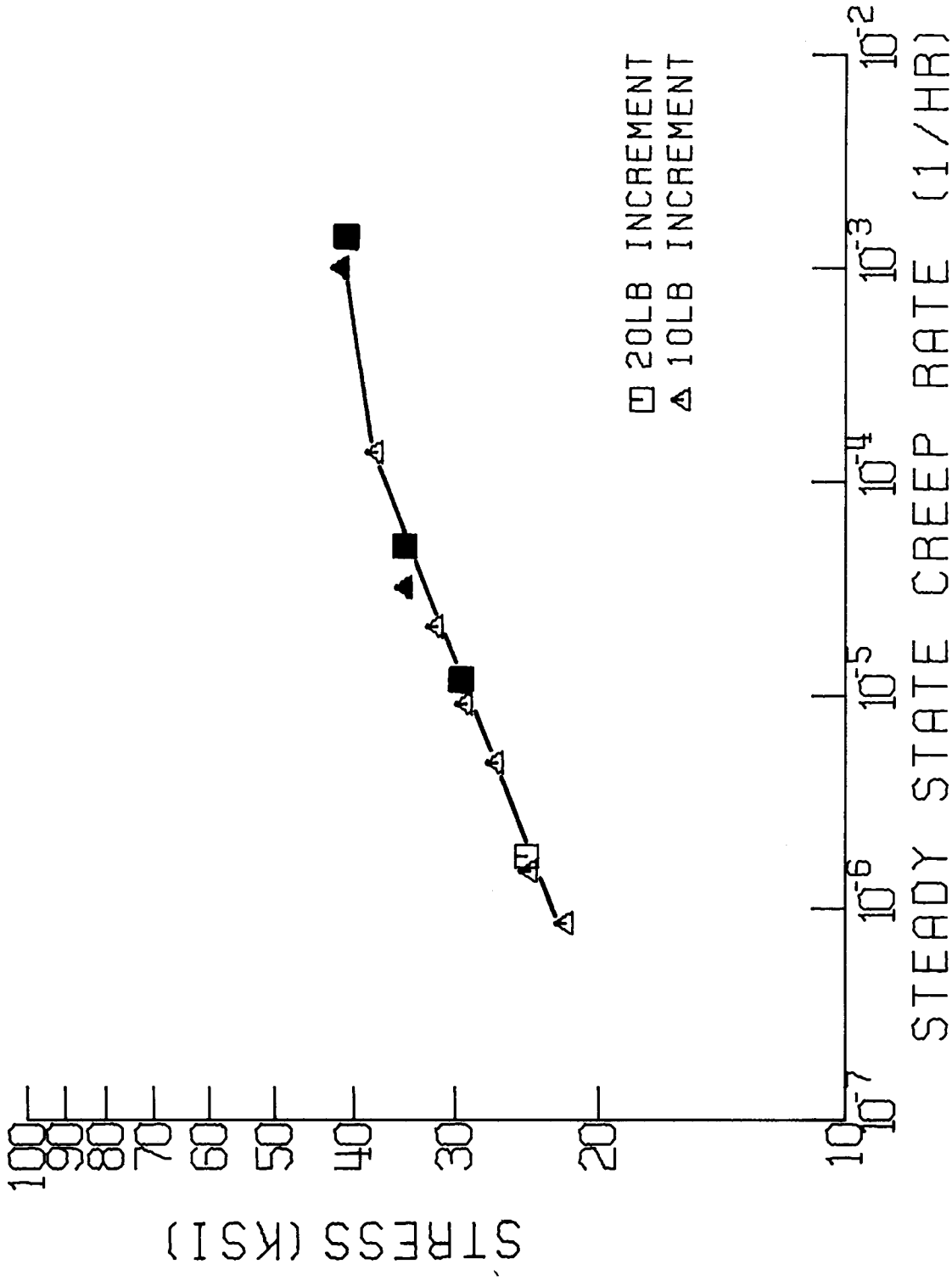


Fig. 16. Creep Stress vs. Steady State Creep Rate of Normalized and Tempered Alloy I, Tempered at 1050°F for 1 month. Test Temperature: 850°F.

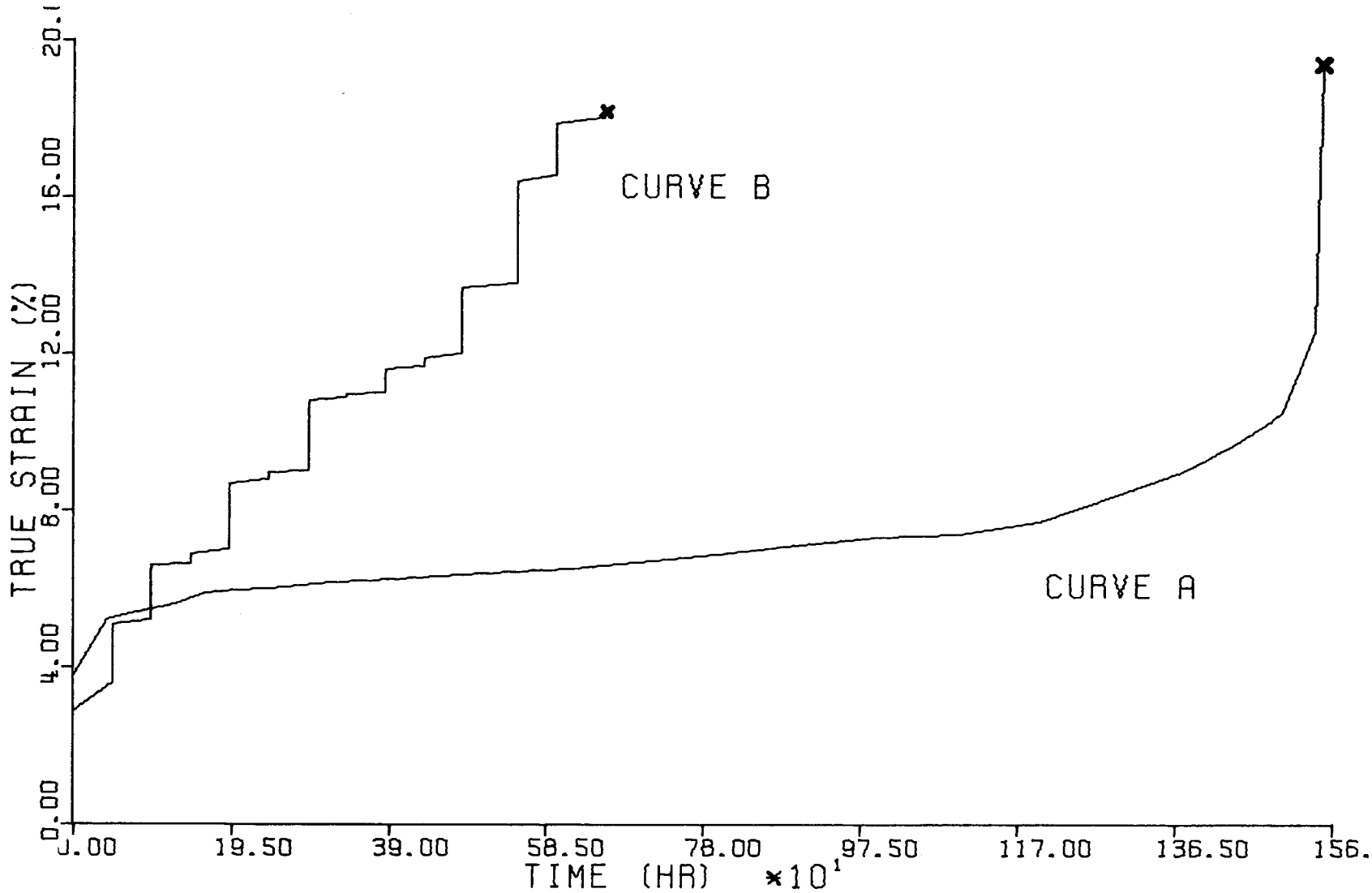


Fig. 17. Effects of Repeated Overlaodings on Creep Properties of Alloy LL at 850°F

The frequent recurrence of strain bursts reduces the creep rupture life if the rupture strain remains unchanged. This effect is shown in two creep curves in Fig. 17. Samples of Alloy LL, which has carbon content of 0.007% were employed in the N&T condition. Load of 180 lbs was applied to both specimens corresponding to the initial stress of 42 ksi. Specimen A was subjected to the constant load throughout the test, while a 20 lb additional weight was added for a period of 10 sec. to specimen B every 48 hours. The creep tests were conducted at 850°F. As expected, the rupture life was reduced. Note that the sum of strain bursts due to overloading contributed 89% of the rupture strain.

Commercial 2-1/4 Cr-1Mo steels have a typical carbon content of 0.12%, which corresponds to that of Alloy H in this study. Available data indicates that such a steel decarburizes to a carbon level of 0.02% in thirty years time at 965°F under the operating environment of LMFBR heat exchangers.[19] Since strain burst is absent in Alloy H within the service temperature range the occurance of possible damages from overloading spikes of 10 to 20% during the early stage of service life is remote. Meanwhile, microstructures will be stabilized progressively during long time exposure at service temperature, which again tends to eliminate the strain burst phenomenon even though the carbon contents are lowered. Therefore, it appears that strain bursts observed in the present study does not pose potential problems for the structural applications in LMFBR.

Attempts are now being made to find the possible mechanism governing the strain burst phenomenon. Since this appears analoguous to

strain aging observed during tensile tests, high temperature tensile tests will be conducted after initial creep deformation. Results of transmission electron microscopy and specimen surface examination before and after a strain burst will also be reported later.

### 7.2.4 REFERENCES


1. P. L. Jones and A. S. Tetelman, ORNL-5107, December 1975, p. 289.
2. Metals Handbook, Volume 2, American Society for Metals, Metals Park, Ohio, 1964, p. 113.
3. P. C. Paris and G.C.M. Sih, "Stress Analysis of Cracks," Fracture Toughness Testing and Applications, ASTM, STP 381, Philadelphia, Pennsylvania, 1965, p. 30.
4. O. Ajaja and A. J. Ardell, "Mechanical Properties Test Data for Structural Materials," Oak Ridge National Laboratory Quarterly Progress Report for period ending 31 January 1976, ORNL-5112, p. 249.
5. B. Weiss and R. Stickler, Met. Trans, 3 (1972) 851.
6. J. A. Mazza, J. Iron Steel Inst., 204 (1966) 783.
7. J. E. Spruiell, J. A. Scott, C. S. Ary and R. L. Hardin, Met. Trans., 4 (1973) 1533.
8. F. Garofalo, Trans. Met. Soc. AIME, 227 (1963) 251.
9. F. Garofalo, O. Richmond, W. F. Domis and F. von Gemmingen," Joint International Conference on Creep," Inst. Mech. Engrs. (London), 1963, p. 1-31.
10. J.C.M. Li, Acta Met., 11 (1963) 1269.
11. J.C.M. Li, Ibid, 13 (1965) 37.
12. N. S. Akulov, Ibid, 12 (1964) 1195.

13. G. A. Webster, A.P.D. Cox and J.E. Dorn, Metal. Sci. J., 3 (1969) 221.

14. A. Ahmadieh and A. K. Mukherjee, Mat. Sci and Engr., 21 (1975) 115.

15. A. Ahmadieh and A. K. Mukherjee, Scripta Met., 9 (1975) 1299.

16. P. L. Threadgill and B. Wilshire, Proceedings of a meeting on Creep Strength in Steel and High-Temperature Alloys, organized by the Iron and Steel Institute at the University of Sheffield, England, September 1972, p. 8.

17. P. A. Chalco, "Microstructure and Mechanical Properties of Cr-Mo Steels," Ph.D. Dissertation, UCLA, 1974.

18. P. A. Chalco, et al, "Mechanical Property Test Data for Structural Materials," ORNL-5103, pp. 343-356, October 1974.

19. D. E. Ellis, "Experience with Ferritic Steels in Reactor Systems," Low Carbon and Stablilized 2-1/4 Cr-1Mo Steels, ASM, pp. 1~12, October 1970.

# 8. GENERAL ELECTRIC COMPANY

K. D. Challenger

## 8.1 INTRODUCTION

The principal objective of mechanical properties testing at the General Electric Company is to characterize the behavior of 2¼Cr-1Mo and austenitic stainless steels in sodium environments relevent to LMFBR steam generators and intermediate heat transport systems. Under conditions predicted for the intermediate sodium system of the CRBRP, 2¼Cr-1Mo will lose carbon to the system and be weakened. The carbon will tend to carburize and embrittle stainless steel components in other portions of the system. The effects of a carburizing environment on creep rupture properties of Type 316 stainless steel will be evaluated along with an assessment of creep-fatigue interactions. In addition, studies of fatigue crack propagation rates in carburizing sodium will be performed in order to assess environmental effects under pertinent intermediate sodium loop loading conditions. The loss of carbon from 2¼Cr-1Mo steel components can result in increased creep rates of the decarburized surface layer with the possibility of ratchetting under cyclic straining. These effects will be evaluated for base metal and weld metal in a decarburizing sodium environment. Elastic-plastic fracture mechanics methods, including J-Integral and Crack Opening Displacement (COD) are being employed to determine the toughness ($K_{Ic}$) of 2¼Cr-1Mo steel at relevant temperatures and to compute the critical flaw sizes for the onset of rapid fracture. The effects of welding procedure, flaw location and thermal aging are being evaluated. The effect of melting practice and heat treatment on the mechanical behavior of 2¼Cr-1Mo is being evaluated to confirm that the properties of consumable remelted 2¼Cr-1Mo meet the appropriate requirements of the ASME B&PV Code for LMFBR steam generators.

## 8.2 MECHANICAL PROPERTIES OF STAINLESS STEEL IN CARBURIZING SODIUM

### 8.2.1 Fatigue Crack Growth Studies - J. F. Copeland/J. L. Yuen

The objective of this program is to determine the environmental influence of liquid sodium on the fatigue crack propagation rates for annealed Type 316 stainless steel and weldments. To be prototypic of expected LMFBR Intermediate Heat Transport System (IHTS) piping conditions, this testing is being done at low frequency (about 0.5 cycles per minute (cpm) and at 510°C[950°F]). Additionally, the existence of a high carburizing potential in the liquid sodium environment is a distinct possibility.[1] Since the exact carburizing potential of the IHTS sodium has not been determined, this experiment is being run under the most severe conditions, of carbon-saturated sodium. The use of carbon-saturated sodium also allows the acceleration of carburization in order to represent design life conditions with a relatively short-term test. Control tests in air are also being performed under the same loading conditions, in order to truly discern environmental effects. These results will show whether or not penalties or allowances for crack growth in secondary system sodium are required or warranted.

ASTM E399, 12.7 mm. (0.5 in.) thick, 3-point bend specimens were machined from annealed 15.9 mm. (5/8 in.) Type 316 plate[1] and fatigue precracked. Specimens to be tested in air were aged at 510°C(950°F) for 1000 hrs. in air. Those to be fatigued in high carbon sodium were pre-exposed in Loop A sodium with a Grade 1050 carbon steel source at 510°C (950°F) for 1000 hrs. The carburization incurred by these specimens during sodium pre-exposure is shown in Figure 8.1, and is typical of that anticipated[1] for a 30-year LMFBR design life with a 2¼Cr-1Mo steel carbon source.

Fatigue crack growth tests were performed in air and flowing, high carbon sodium in two specially designed fatigue test facilities.[1] Three tests could be run concurrently in each facility. After loading for an estimated number of cycles, the specimens were withdrawn and examined for crack growth. When the crack growth approximated 0.76 mm. (30 mils) the specimen was fractured to accurately measure crack growth. The crack

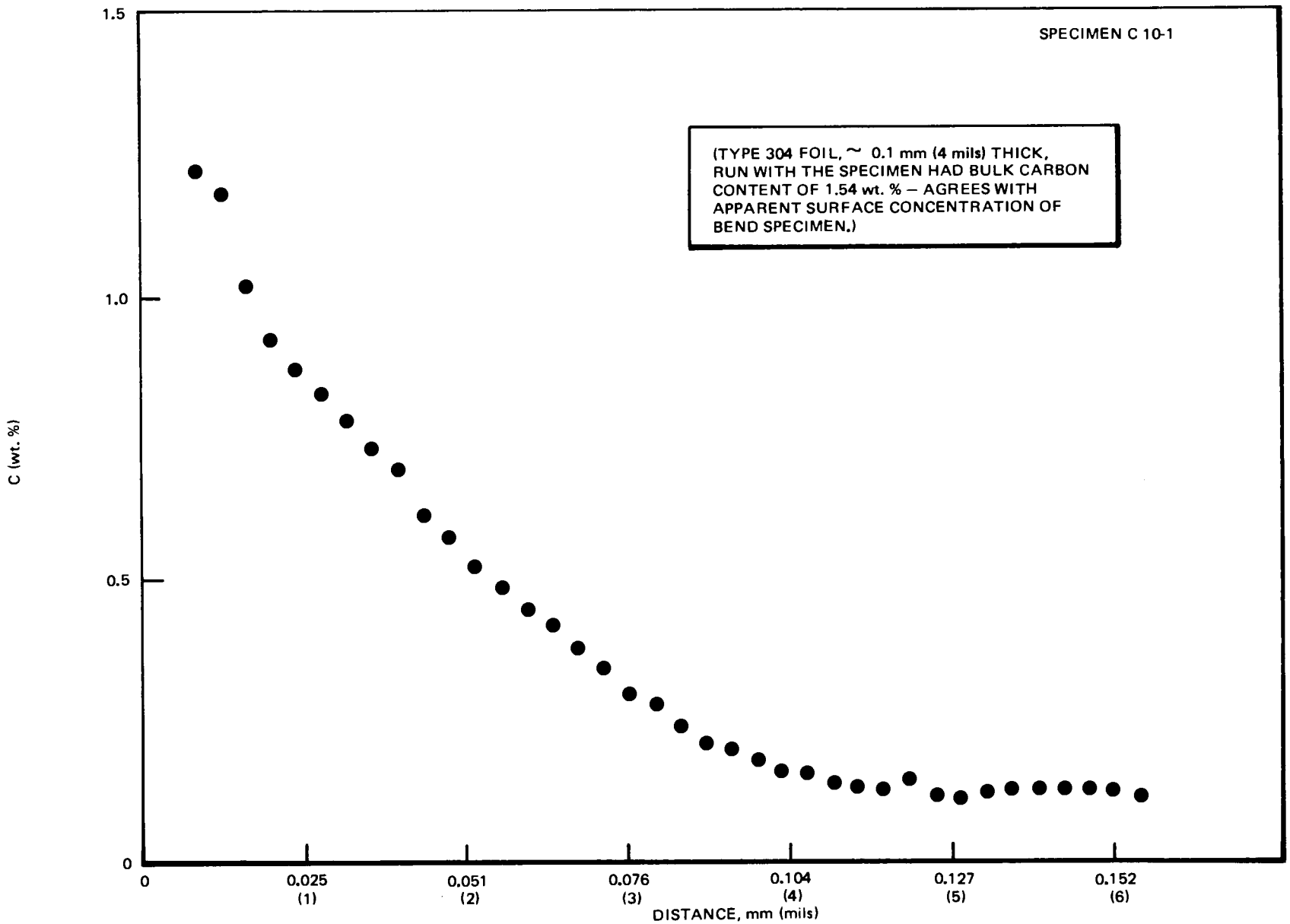


*Figure 8.1* *Carbon Profile (Electron Microprobe) on Annealed Type 316 12.7 mm (0.5 in.) Bend Specimen Aged in Loop A for 1000 hr at 510°C (950°F). 1050 Carbon Steel Source (Carbon – Saturated Sodium)*

growth rate was computed from the ratio of crack extension to cycles. The stress intensity factor range ($\Delta K$) was calculated at half the crack extension. Recently, a binocular microscope was employed to measure the crack growths, and a revised set of crack growth rates and stress intensity factors were calculated. The majority of the results were within $\pm$ 15% of the previously reported data. However, there were several specimens where the measurements yielded crack growth rates that differed by approximately 50%. The control air and sodium results are shown in Figure 8.2 and are compared to other data.[2,3,4,5] The revised control air data is in good agreement with the air data of HEDL and NRL. More tests will be run to determine the crack growth behavior under hold time and high stress ratio (R) conditions. Two sodium runs were completed this quarter. The first run evaluated the effects of zero hold at 0.5 cpm, the same as last quarter, but in an environment that had a higher carburizing potential. The reference TP 304S.S. foil monitors showed a much higher degree of carburization than the previous run. The results were lower than the air results, but higher than the 427°C(800°F) and 600°C(1112°F) of HEDL and CEGB. The second run in sodium, at 0.33 cpm, investigated the effects of 1) precarburizing the precrack crevice under load and testing with a hold time, 2) precarburizing the precrack crevice under load and testing with no hold time, and 3) precarburizing the precrack crevice with no load and testing with a hold time. The results, surprisingly, agree more closely with the carbon sodium results of HEDL and CEGB. A possible explanation could be crack tip blunting during the preload and hold times, which would retard crack growth. The reference foil monitors indicated an even higher carburizing potential of sodium than the previous run. These results indicated only a slight carburization effect, however, at the lower crack growth rates, where the environment is expected to have its greatest effects. Additional runs under the above conditions are required to define the crack growth behavior. Preliminary electron microprobe analysis of a sodium specimen (pre-exposed with no load) indicated that the degree of carburization of the crevice crack surfaces decreased rapidly from the machined chevron notch towards the crack tip. The surfaces near the crack extension zone did not show any significant

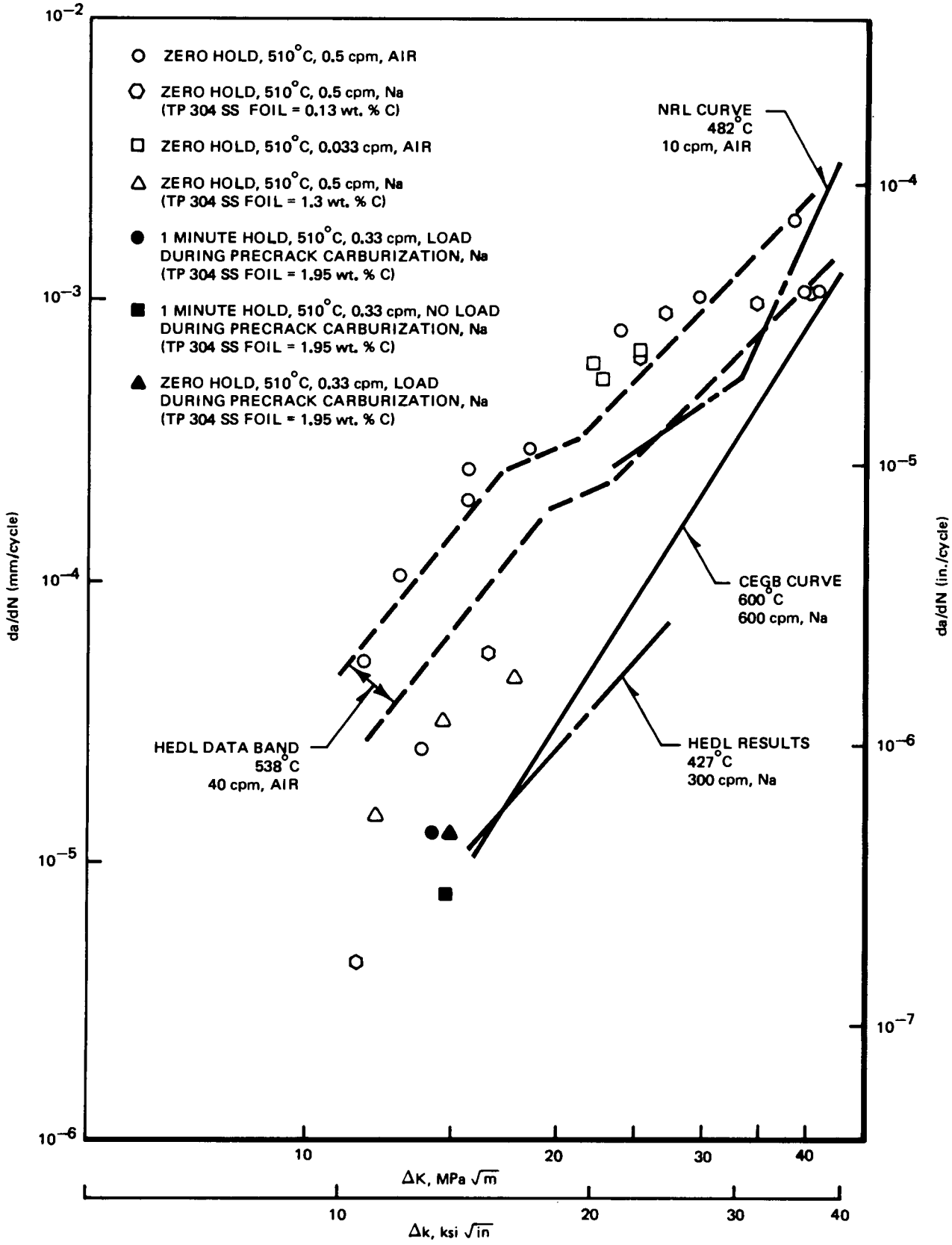


Figure 8.2 *Comparison of Fatigue Crack Propagation Rate Results for Annealed Type 316 Stainless Steel at Elevated Temperatures*

increase in the bulk carbon concentration, 0.06 wt%. A large percentage of the carbon in the sodium was probably removed by the relatively uncarburized surfaces of the crevice crack nearest the machined chevron notch; consequently, the sodium near the advancing crack front contained less carbon than anticipated. The carbon pick-up by the relatively uncarburized surfaces of the crevice crack may limit the effective carburized zone for a given crack opening. Flat annealed Type 316 stainless steel bars stacked at different openings (Figure 8.3) will be used to investigate the crack depth to opening ratio limitation of carburizing a crevice crack. Future testing may include slower cycle rates, the influence of load waves with hold times, and the effect of higher R values. Additional bend specimens fabricated from base metal and GTA weldments have been precracked. Machining of further bend specimens from the remaining GTA weldment has also been initiated. The pre-exposure of the control air specimens has begun. The control air test rig has been modified to apply a load wave with a high stress ratio, R, (where R = minimum stress/maximum stress) so that the crack tip will always be open to some extent. This situation is more realistic since some mean stress will always be present in the sodium piping. A control run in air to evaluate peak load hold time effects at high and low $\Delta K$'s and to determine the influence of an R value of 0.4 has been initiated. The sodium test rig will also be modified to perform high R tests. Emphasis during the next quarter will be on the testing of Type 316 weldment specimens.

### 8.2.2 Creep Investigation - P. P. Pizzo

The influence of carburization on the creep behavior of 316 H stainless steel is being investigated. Tubular creep specimens have been prepared for the second phase of testing. Two test matrices have been developed for this program and are presented in Table 8.1 and Table 8.2. Table 8.1 describes the creep test matrix for specimens strained at 510°C (950°F) under an initial strain rate of $10^{-3}s^{-1}$ prior to creep testing. Variation in creep properties as a function of pre-strain and exposure will be used to identify potential environmental influence. Six specimens,

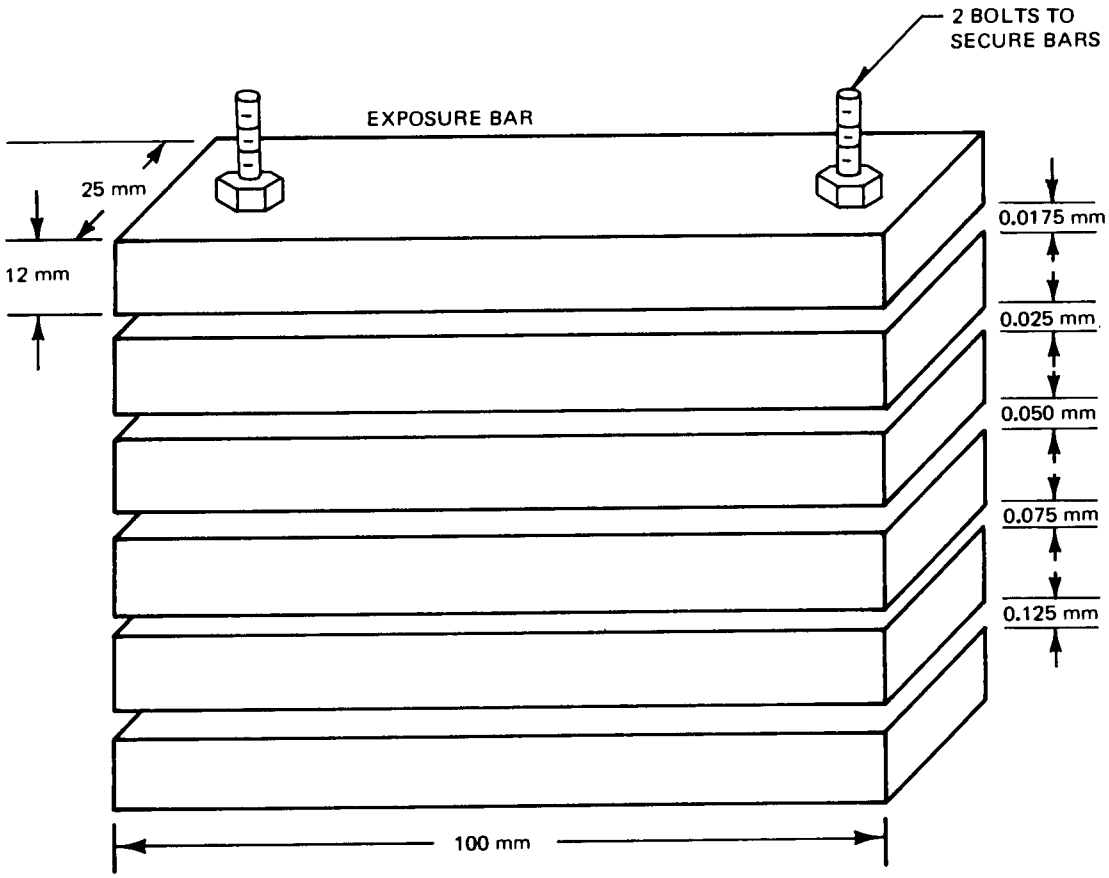


*Figure 8.3 Flat Type 316 Stainless Steel Exposure Bars Spaced at Different Openings*

TABLE 8.1

CREEP TEST MATRIX FOR PRE-STRAINED SPECIMENS

Material: Type 316 H Stainless Steel
Solution Annealed

Specimen Configuration: Tubular Creep Specimen

Creep Test Parameters: T = 510°C (950°F)
$\sigma$ = 377 MPa (54.7 Ksi)

| Specimen Design | Pre-Exposure Conditions Temp./Time (°C/hrs.) | Pre-Exposure Conditions Environment (I.D./O.D.) | Specimen ($\%\varepsilon_u$)[a] | Pre-Strain (mm/mm) | Creep Test Environment (I.D./O.D.) |
|---|---|---|---|---|---|
| C-26 | 510/1000 | Ar/Air | 35 | .065 | Ar/Air |
| C-34 | 510/1000 | Na/Air | 34 | .064 | Na/Air |
| C-27 | 510/1000 | Ar/Air | 52 | .098 | Ar/Air |
| C-33 | 510/1000 | Na/Air | 46 | .085 | Na/Air |
| C-30 | 510/1000 | Ar/Air | 85 | .159 | Ar/Air |
| C-32 | 510/1000 | Na/Air | 90 | .168 | Na/Air |

(a) $\varepsilon_u \equiv$ the strain corresponding to U.T.S. (at 510°C, $10^{-3}s^{-1}$) determined from hot tensile test of a 1000 hour, carbon saturated sodium exposed specimen.

(b) Specimens pre-strained after 1000 hour/510°C exposure.

(c) All specimens cooled under load control conditions from pre-straining operation.

(d) Creep tests to be initiated at 377 MPa.

(e) All sodium exposures are carbon saturated (1095 steel spring wire source).

TABLE 8.2

CREEP TEST MATRIX; MONOTONIC STRESS TESTS

Material: Type 316 H Stainless Steel Solution Annealed

Specimen Configuration: Tubular Creep Specimen

Test Temperature: T = 510°C/950°F

| Specimen Design | Pre-Exposure Conditions Temp./Time (°C/hrs.) | Pre-Exposure Conditions Environment (I.D./O.D.) | Applied Stress | Loading (mm/mm) | Initial Case Depth |
|---|---|---|---|---|---|
| C-29 | 510/1000 | Ar/Air | 377 MPa | .053 | -- |
| C-3 | 510/1000 | Na/Air | 377 MPa | .025 | 100μm |
| C-28 | 510/1000 | Ar/Air | 446 MPa | .145 | -- |
| C-36 | 510/1000 | Na/Air | 446 MPa | .069 | 100μm |

(a) All sodium exposures are carbon saturated (1095 steel spring wire source).

three exposed to carbon saturated sodium (510°C for 1000 hours) and three control (argon exposed at 510°C for 1000 hours), have been pre-strained to the levels indicated in the table. Specimens C-30 and C-32 are being readied for creep testing.

Four tubular specimens will undergo monotonic creep testing per the conditions established in Table 8.2. These specimens have also been pre-strained, but to a load equivalent to that necessary to achieve the applied stress listed in the table. The specimens were cooled under constant load conditions, and the strains tabulated in Table 8.2 represent the plastic strain upon loading for the respective creep tests. Specimens C-28 and C-36 are being prepared for creep testing during the next quarter.

In order to establish the criterion for pre-straining, Table 8.1, the elevated temperature properties of carburized and control tubular creep specimens were determined. Tensile curves for carburized and control specimens tested at an initial strain rate of $10^{-3}s^{-1}$ are presented in Figure 8.4. The argon control curve is found to exhibit a slightly greater 510°C (950°F) yield stress (176 MPa versus 153 MPa) and a lower U.T.S. (472 MPa versus 578 MPa) than the carburized specimen. The strain to failure is essentially equivalent for both conditions. Scanning electron microscopy revealed ductile transgranular fracture in both cases, with the argon control specimen exhibiting a similar reduction in area (73%) to that of the carburized specimen (62%).

A slightly lower (0.2%) Y.S. for the carburized specimens is substantiated in data obtained during the pre-straining of specimens identified in Tables 8.1 and 8.2. These data are presented in Figure 8.5. Attention to the scale of this figure indicates the sensitivity of the offset yield stress determination to the assumed modulus and to data scatter. The modulus plotted is the 510°C modulus of 300 series stainless recently reported by Hammond.[6] Carburized stainless may be predicted to exhibit a higher modulus as stiff chromium carbide particles are a significant constituent of the carburized case. This would, however, tend to produce an even lower yield stress value for the carburized data. The yield stress of 176 MPa for the 1000 hr./510°C exposed control specimen is comparable to a yield stress of 170 MPa measured for the as-recieved alloy.

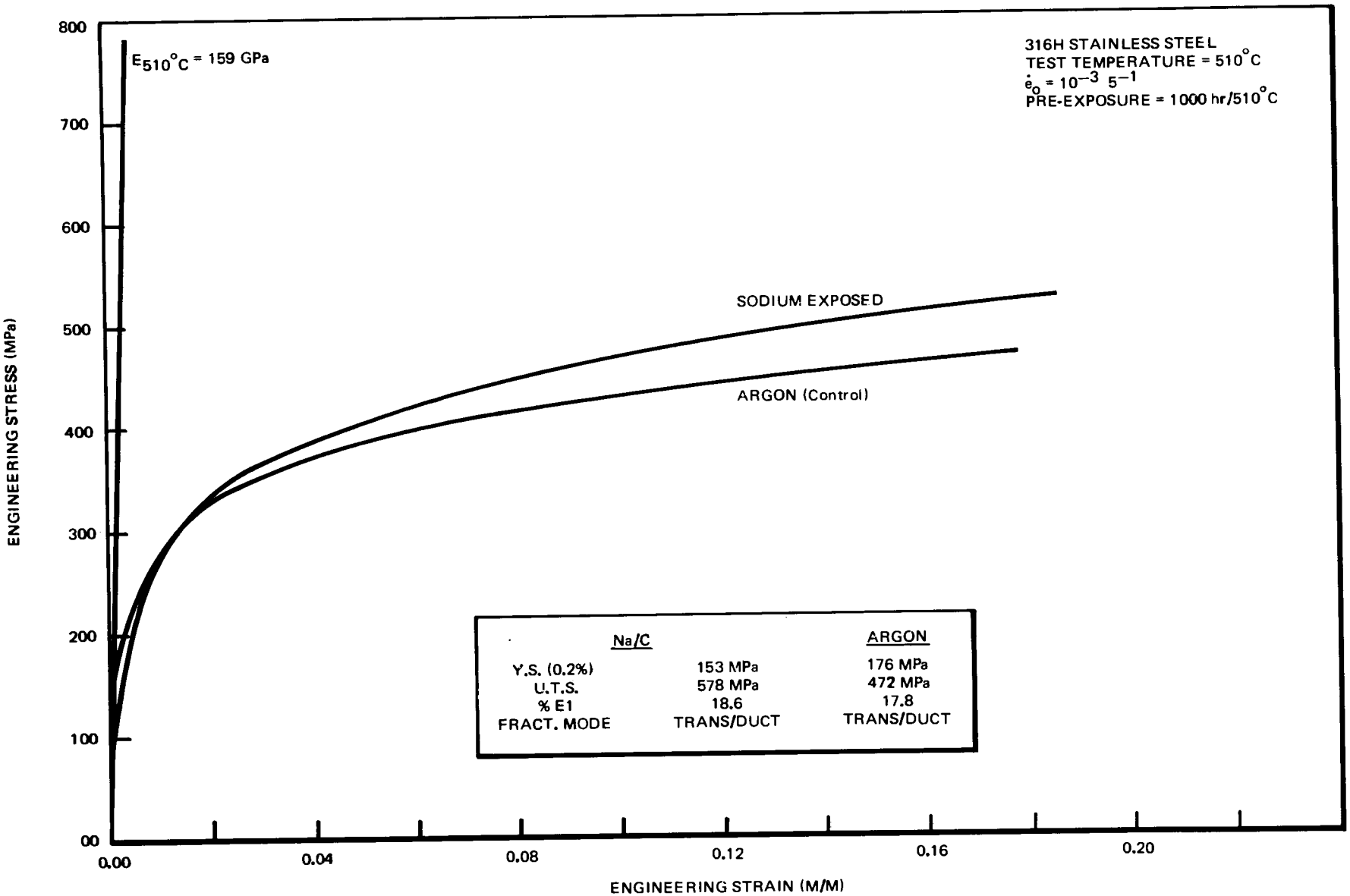


*Figure 8.4. Tensile Test at 510C 316H Stainless Tubular Creep Specimens*

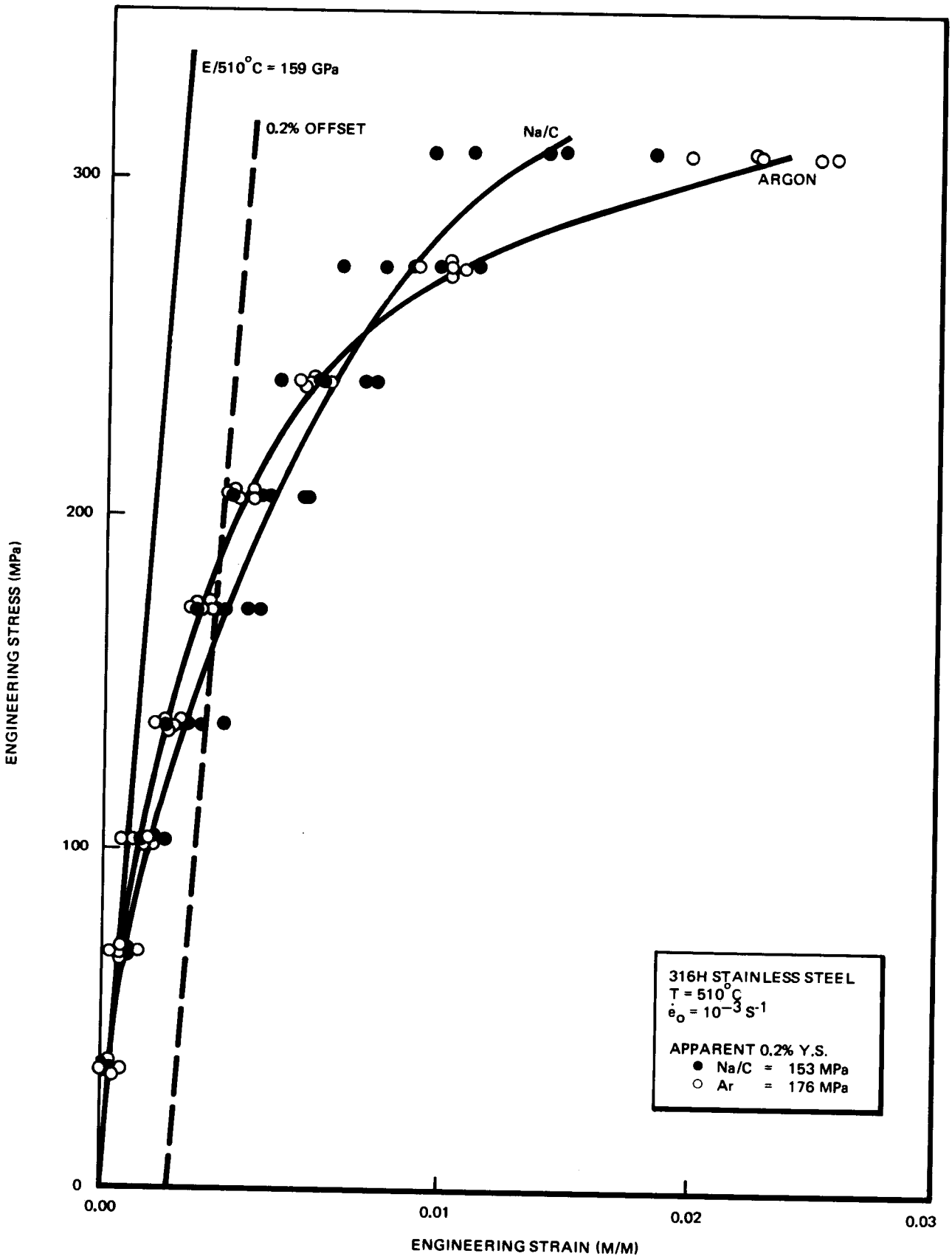


*Figure 8.5. Tensile Test at 510°C 316H Stainless Steel Tubular Creep Specimens*

The yield stress for the carburized stainless steel may best be termed an "apparent" yield stress. The extension at a given load for strains less than .005 are made up of intrinsic and extrinsic deflections. Extrinsic deflections are associated with microcracks distributed along the carburized case. These microcracks are characterized within this report, and they indeed may be responsible for the variation in tensile data observed in Figure 8.5.

The tensile properties of 316 H stainless steel tubular specimens investigated in this program are summarized in Table 8.3 The following trends are observed in the data;

1. The yield stress (0.2%) and the ultimate tensile stress at 510°C (950°F) are relatively unaffected by the 1000 hour pre-exposure.
2. The total specimen elongation is approximately halved by the 1000 hour pre-exposure, while the reduction in area is doubled.
3. Carburization decreases the "apparent" yield stress; however, the U.T.S. and the flow stress over a broad strain range are significantly increased (23% increase in U.T.S.).
4. The specimen elongation and reduction in area for carburized and control specimens are essentially equivalent.

The above data suggest that carburization affects the 510°C (950°F) tensile properties of 316 stainless steel up to the point of plastic instability. However, instability is reached at the same strain. The reduction in area is equivalent, and scanning electron microscopy confirmed that similar fracture processes occur in both the control and carburized specimens. No evidence of the 100μm carburized case could be detected in the fracture topography. The 100μm case has been found not to affect the hot tensile fracture behavior.

The data of Table 8.3 indicate that instability conditions and fracture processes are influenced by thermal aging. The argon environment of the 1000 hr. exposed specimen may contribute to the measured differences in %El. and %R.A.; however, thermal aging is believed to be the principal factor. In another study, 316 stainless steel aged at

TABLE 8.3

TEST MATERIAL CHARACTERIZATION - TENSION TESTS

Type 316 H Stainless Steel

¼ Schedule 80 Pipe Stock

Tubular Creep Specimens[a]

| | 0.2% Y.S. | | U.T.S. | | El. | R.A.[c] |
|---|---|---|---|---|---|---|
| | MPa | Ksi | MPa | Ksi | (%) | (%) |
| **Unexposed** | | | | | | |
| 22°C (72°F) | 272 | 39.4 | 623 | 90.4 | 50.0 | 55 |
| | 300 | 43.5 | 612 | 88.7 | 44.0 | 46 |
| 510°C (950°F) | 173 | 25.1 | 479 | 69.4 | 28.5 | 36 |
| | 166 | 24.0 | 491 | 71.2 | 32.5 | 37 |
| **Pre-exposed[b]** | | | | | | |
| Case Depth / Temp. | | | | | | |
| -- / 510°C | 176 | 25.5 | 472 | 68.5 | 17.8 | 73 |
| 100μm / 510°C | 153 | 22.2 | 578 | 83.8 | 18.6 | 62 |

(a) 8.6 mm. (0.34 in.) O.D. X 0.51 mm. (0.020 in.) wall X 50.8 mm. (2 in.) gage, approximate dimensions.

(b) Exposed at 510°C for 1000 hrs. in either (Argon/Air) or (Carbon Saturated Sodium/Air), (I.D./O.D.)

(c) All fractures ductile transgranular.

510°C (950°F) exhibited a nominal 20% reduction in both %El. and %R.A.[6] Thus, the data of this investigation exhibit somewhat anomalous behavior. The observed trend in ductility of the tubular specimens as a function of aging treatment is not understood, and it will receive further attention.

To date, several tubular creep specimens have been exposed to carbon saturated sodium. The following data characterize the resulting carburized case. Data are obtained from the 0.46 mm (18 mil) thick wall along the gage length of the tubular creep specimens unless otherwise stated.

Table 8.4 is a summary tabulation of data defining the depth of carburization. Bulk carbon content and the depth of carburization are presented as a function of increased 510°C (950°F) exposure. The following trends are evident;

1. The bulk carbon content increases from 0.056 wt.% for the as received alloy, to 0.326 wt.% carbon after an accumulated exposure of 3322 hours at 510°C (950°F).

2. The carburized case, as revealed by metallography (Glyceregia reagent), increases from a mean value of 70μm and standard deviation of 20μm for exposure between 1000 hrs. and 2000 hrs., to a mean value of 100μm and standard deviation of 7μm for total exposures between 2000 and 3000 hours.

3. A sharp transition from intergranular-to-transgranular fracture was detected on ruptured specimens by scanning electron microscopy. The intergranular fracture zone, measured from the specimen I.D. is found to penetrate the sample 120μm with a standard deviation of 32μm for total exposures lying between 1000 and 2000 hours. For accumulated exposures between 2000 and 3000 hours, intergranular fracture extends a mean distance of 150μm, and standard deviation of 40μm.

In summary, a sustained carburization potential has been confirmed for conditions established in this investigation. Static sodium, containing a 1095 carbon steel source, continues to provide carburization conditions for 316 stainless steel for exposures totaling 3000 hours. At 510°C (950°F), metallographic examination revealed a carburized case

# TABLE 8.4

## DEPTH OF CARBURIZATION OF 316 H STAINLESS STEEL EXPOSED TO CARBON SATURATED SODIUM

316 H Stainless Steel Tubular Creep Specimens

| Specimen Designation | Exposure Environment[f] (I.D./O.D.) | 510°C (950°F) Pre-Exposure | 510°C (950°F) Test Exposure[a] | 510°C (950°F) Total Exposure | 0.46mm. (18 mil) Wall Bulk Carbon | Carburized Case Depth (Optical Metallography)[e] | Intergranular-to-Transgranular Transition[d] |
|---|---|---|---|---|---|---|---|
| As Received Condition | -- | -- | -- | 0 hrs. | 0.056 wt.% | -- | -- |
| C02 | Ar/Air | 1000 hrs. | < 1 hrs. | 1000 hrs. | 0.061 wt.% | 0μm | (b) |
| C08 | Na/Air | 1000 hrs. | < 1 hrs. | 1000 hrs. | 0.187 wt.% | (b) | 0μm[e] |
| C16 | Na/Air | 1000 hrs. | 5 hrs. | 1005 hrs. | (b) | 51μm | 0μm[e] |
| C14 | Na/Air | 1000 hrs. | 423 hrs. | 1423 hrs. | (b) | 51μm | 150μm |
| C07 | Na/Air | 1000 hrs. | 428 hrs. | 1428 hrs. | 0.252 wt.% | 100μm | 152μm |
| C06 | Na/Air | 1000 hrs. | 680 hrs. | 1680 hrs. | 0.252 wt.% | 60μm | 130μm |
| C15 | Na/Air | 1000 hrs. | 842 hrs. | 1842 hrs. | (b) | 65μm | 115μm |
| C12 | Na/Air | 1000 hrs. | 904 hrs. | 1904 hrs. | (b) | 79μm | 100μm |
| C09 | Na/Air | 1000 hrs. | 917 hrs. | 1917 hrs. | (b) | 76μm | 67μm |
| C13 | Na/Air | 1000 hrs. | 1585 hrs. | 2585 hrs. | (b) | 102μm | 100μm |
| C18 | Na/Air | 1000 hrs. | 1860 hrs. | 2860 hrs. | (b) | 102μm | 166μm |
| C11 | Na/Air | 1000 hrs. | 2108 hrs. | 3108 hrs. | (b) | 94μm | 133μm |
| C19 | Na/Air | 1000 hrs. | 2322 hrs. | 3322 hrs. | .326 wt.% | 110μm | 200μm |

NOTES:
(a) Test exposure is equivalent to the time-to-rupture of the first phase creep experiments.
(b) Data point not obtained.
(c) Depth determined by optical microscopy. Clyceregia reagent used to etch carburized case.
(d) Determined by scanning electron microscopy of the fracture surface.
(e) Transgranular ductile fracture; carburized case not evident in fracture topography.
(f) All sodium exposure, carbon saturated (1095 steel spring wire source).

of about 76μm (or 3 mils) for exposures ranging from 1000 to 2000 hours. However, such specimens indicate an effective carburization zone influence of 120μm, or about 5 mils. This gives a ratio of effective zone width to apparent width of 1.6. When the exposure approaches 3000 hours at this temperature, the apparent zone width increases to 100μm (4 mils) and the ratio of effective to apparent width is found to be 1.5.

A typical carburization zone on the I.D. of a tubular creep specimen is indicated in Figure 8.6a. Heavy staining adjacent to the sodium/steel interface is characteristic of specimens etched with Glyceregia. Further into the metal, this reagent selectively highlights slip bands within the carburization region. These slip bands are present within the dark zone adjacent to the Na/metal interface as indicated in SEM, Figure 8.6b. Slip bands containing a high density of carbide precipitates have been noted in both strained and undeformed carburized specimens and are believed to be associated with the volume expansion accompanying carburization of the stainless steel. Although the matrix grains beyond the slip band region are relatively unattacked by the Glyceregia reagent, grain boundaries beyond this region are preferentially etched. At 510°C (950°F), grain boundary and pipe diffusion of carbon is much greater than diffusion through grains. The characteristics of the carburized region, slip band and grain boundary etching, are believed associated with this diffusion mechanism. Carbide particules precipitated along these defects, result in preferential etching. The fracture transition depth determined by scanning electron microscopy has been shown to be greater than the "apparent" carburization depth, and this transition may best be correlated with the extent of distinct grain boundary etching.

An alternate means of quantifying the carburization profile in stainless steel is to measure the microhardness profile. Charnock, et.al.[7] and Charnock and Ball[8] demonstrate that the microhardness profile in 316 stainless steel can be used to assess the degree of carburization. The hardness profile was found to extend about 2 times the penetration metallographically determined. Specimens of the present investigation were similarly evaluated; the results are plotted in Figure 8.7.

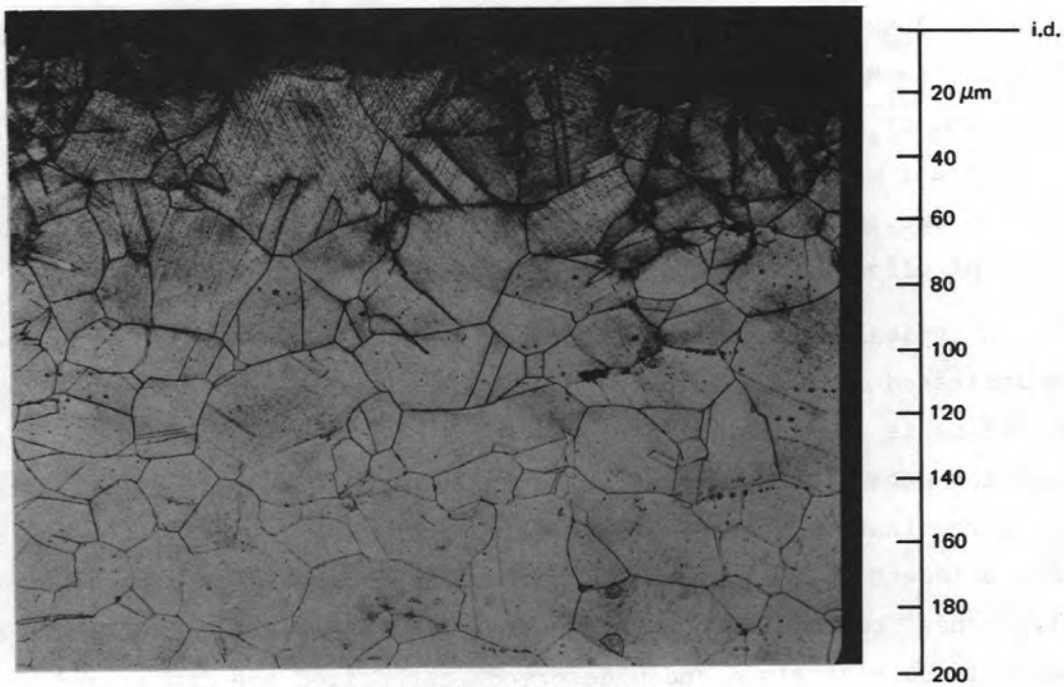


(a) OPTICAL MICROGRAPH OF THE CARBURIZATION ZONE (GLYCEREGIA REAGENT)

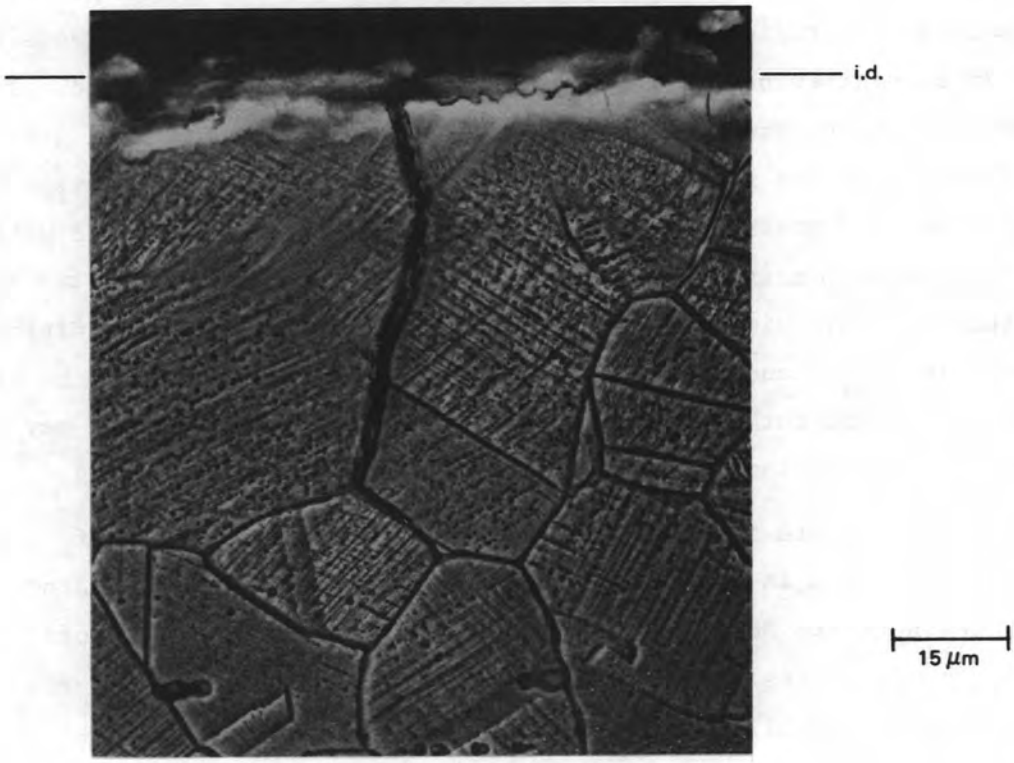


(b) SEM MICROGRAPH OF THE LIGHTLY ETCHED CASE

*Figure 8.6 Typical Carburization Zone for this Investigation*

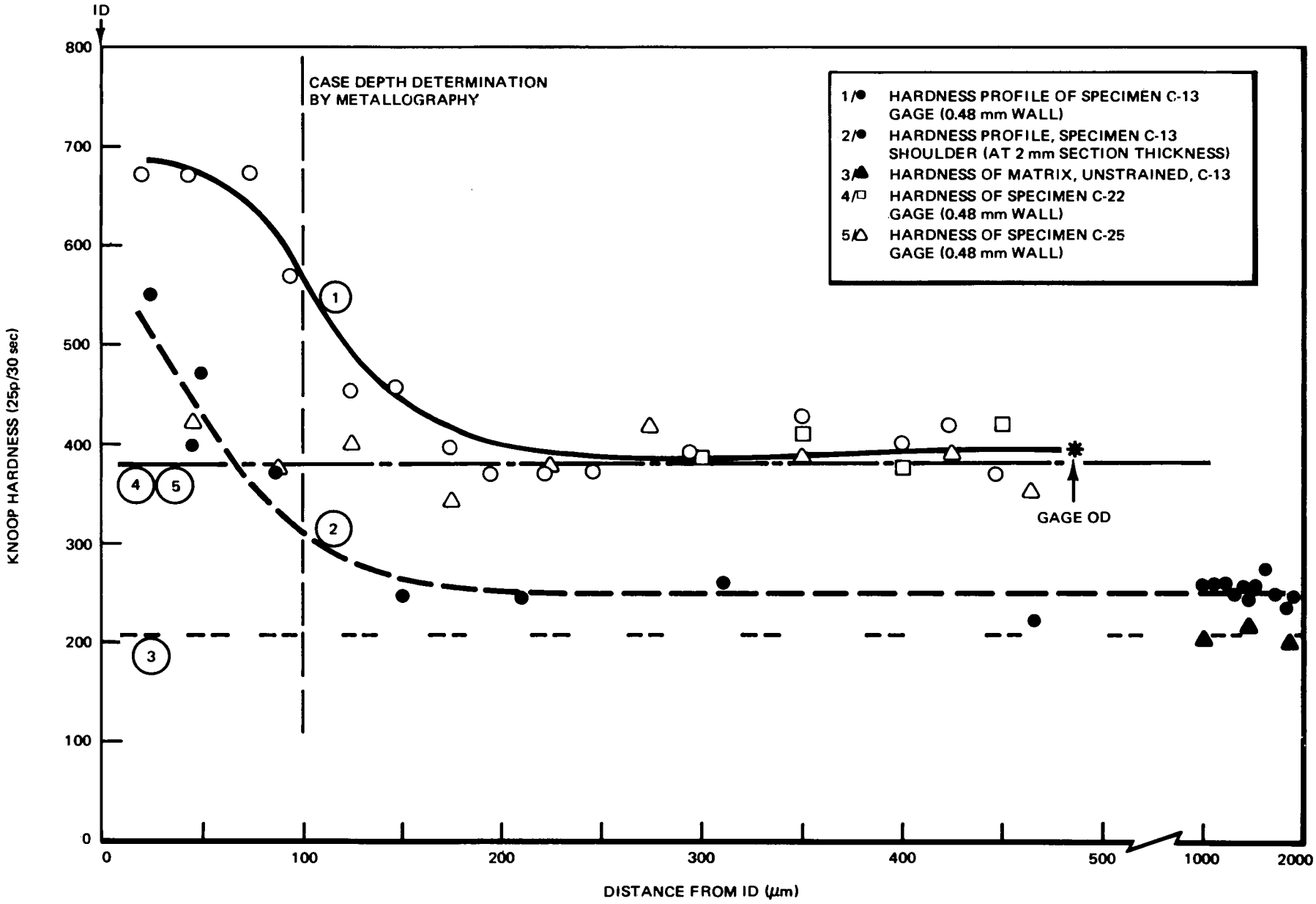


Figure 8.7 Microhardness Traverse Comparison

Specimen C-13 was a carburized creep specimen which failed in 2585 hours. Specimens C-22 and C-25 are both Ar control specimens, creep tested and hot tensile tested, respectively. Important comparisons are made within this figure;

1. Increased hardness is observed to extend to about twice the case depth determined from optical microscopy.
2. The hardness profile of unstrained material is uniformily raised after deformation.
3. The incremental increase in the lower shelf of the hardness profile is similar for carburized and control specimens, irrespective of whether the sample is strained under creep and/or hot tensile conditions.

The results of the microhardness survey are in good agreement with concurrent carburization studies.[7,8] Equivalent microhardness of the 316 H base metal, tensile and creep tests at 510°C (950°F) is to be expected since work hardening mechanisms dominate the mechanical behavior of 316 stainless steel at this temperature. As recovery mechanisms become more competitive at higher test temperatures, the matrix hardness of creep tested specimens would be expected to lie below that of hot tensile tested specimens.

An electron microprobe analysis of 1000 hour/510°C (950°F) carburized stainless steel, previously reported,[6] is included as Figure 8.8 for comparison purposes. The microprobe carbon profile compares favorably with the microhardness, optical, and SEM carburization zone results.

Table 8.5 is a comparison of the fracture characteristics of carburized and control tubular tensile specimens. Optical metallographic and SEM analysis techniques were used to identify the fracture mode and fracture topography of failed test specimens. The data indicate that fast fracture at 510°C (950°F), $\dot{\varepsilon} > 10^{-3}S^{-1}$, is ductile. Under such conditions, no evidence of the approximate 100μm case was detected in the fracture. Under slow deformation conditions, $\dot{\varepsilon} < 10^{-9}S^{-1}$, fracture processes are affected by the carburized case. Fracture is intergranular within the case, propagating along facets oriented perpendicular to the direction

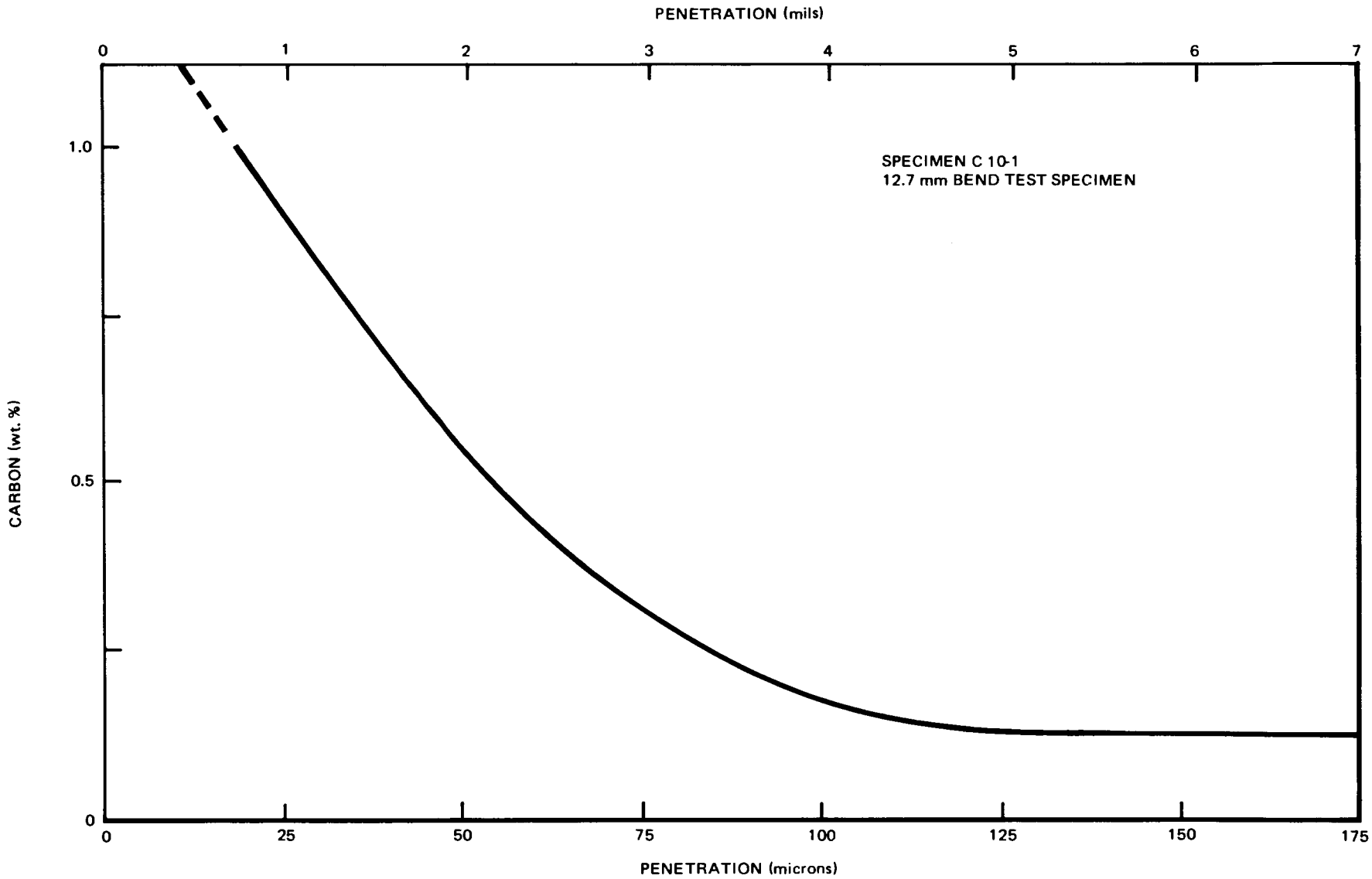


*Figure 8.8* *Electron Microprobe Carbon Profile of Annealed 316H Stainless Steel, Exposed in Carbon Saturated Sodium at 510°C (950°F) for 1000 Hours*

TABLE 8.5

A COMPARISON OF THE FRACTURE CHARACTERISTICS OF CARBURIZED AND UNCARBURIZED SPECIMENS

316 H Stainless Steel Tubular Creep Specimens

T = 510°C (950°F)

| Test Mode | Approximate Strain Rate | Pre-Exposure (I.D./O.D.) | R.A.(%) | Fracture Mode/Topography |
|---|---|---|---|---|
| Hot Tensile | $10^{-3}s^{-1}$ | Ar/Air | 73 | Transgranular/Flat |
| Hot Tensile | $10^{-3}s^{-1}$ | Na/Air | 62 | Transgranular/Flat |
| Creep[a] | $>10^{-2}s^{-1}$ | Ar/Air | >90 | Ductile/Chisel Point |
| Creep[a] | $>10^{-2}s^{-1}$ | Na/Air | >90 | Ductile/Chisel Point |
| Creep | $<10^{-9}s^{-1}$ | Ar/Air | 65 | Transgranular/Flat |
| Creep | $<10^{-9}s^{-1}$ | Na/Air | 47[b] | Intergranular Lip on I.D. to Transgranular Shear |

(a) Specimen failed upon first half-cycle of creep fatigue test program (P+ΔP loading)

(b) Standard deviation of 12% on 5 observations

of principal loading. Fracture through the remaining ligament, however, was transgranular, and grain deformation within the uncarburized material adjacent to the fracture region indicates extensive ductile deformation. Control specimens tested at 510°C (950°F) under similar slow conditions ($\dot{\varepsilon} < 10^{-9}S^{-1}$) failed in a ductile transgranular manner.

The scanning electron micrographs of Figure 8.9 compare the fracture topography of control specimens tested under hot tensile (Figure 8.9a) and creep (Figure 8.9b) test conditions. The topography is similar. More extensive microvoid coalescence is noted in the creep fracture. The fracture characteristics of the control specimen, Figure 8.9a, are identical to those of the carburized specimen tested at $\dot{\varepsilon} < 10^{-9}S^{-1}$ (reference Table 8.5).

In Figure 8.10, the fracture profiles of carburized specimens tested at two strain rates, $\dot{\varepsilon} > 10^{-2}S^{-1}$ (Figure 8.10a) and $\dot{\varepsilon} < 10^{-9}S^{-1}$ (Figure 8.10b), are compared. Both argon control and carburized specimens failed in the chisel point mode under rapid test conditions, Figure 8.10a. However, the variation in fracture characteristics under creep conditions is distinct. Figure 8.9b and Figure 8.10b provide this comparison. The transition between intergranular and transgranular fracture modes, used to establish the effective carburization depth for specimens of this investigation, is clearly identified in Figure 8.10b. This transition as revealed by scanning electron microscopy, is presented in Figure 8.11.

Intergranular fracture in the carburized case has its origin in microcracks developed upon loading and/or during deformation. Typical microcracks are characterized in Figure 8.12. These microcracks are intergranular in nature, and initially are discontinuous. Scanning electron microscopy of these cracks (Figure 8.12b) reveals "untorn ligaments" between open voids. These microcracks may develop as a result of microvoid coalescence about carbide precipitate particles distributed along grain boundaries within the carburized case. Kirman[9] found that local precipitation of $MgZn_2$ in the grain boundaries of 7000 series aluminum alloys can lead to ductile intergranular fracture, where microvoids are present on the individual grain facets. Such a mechanism would

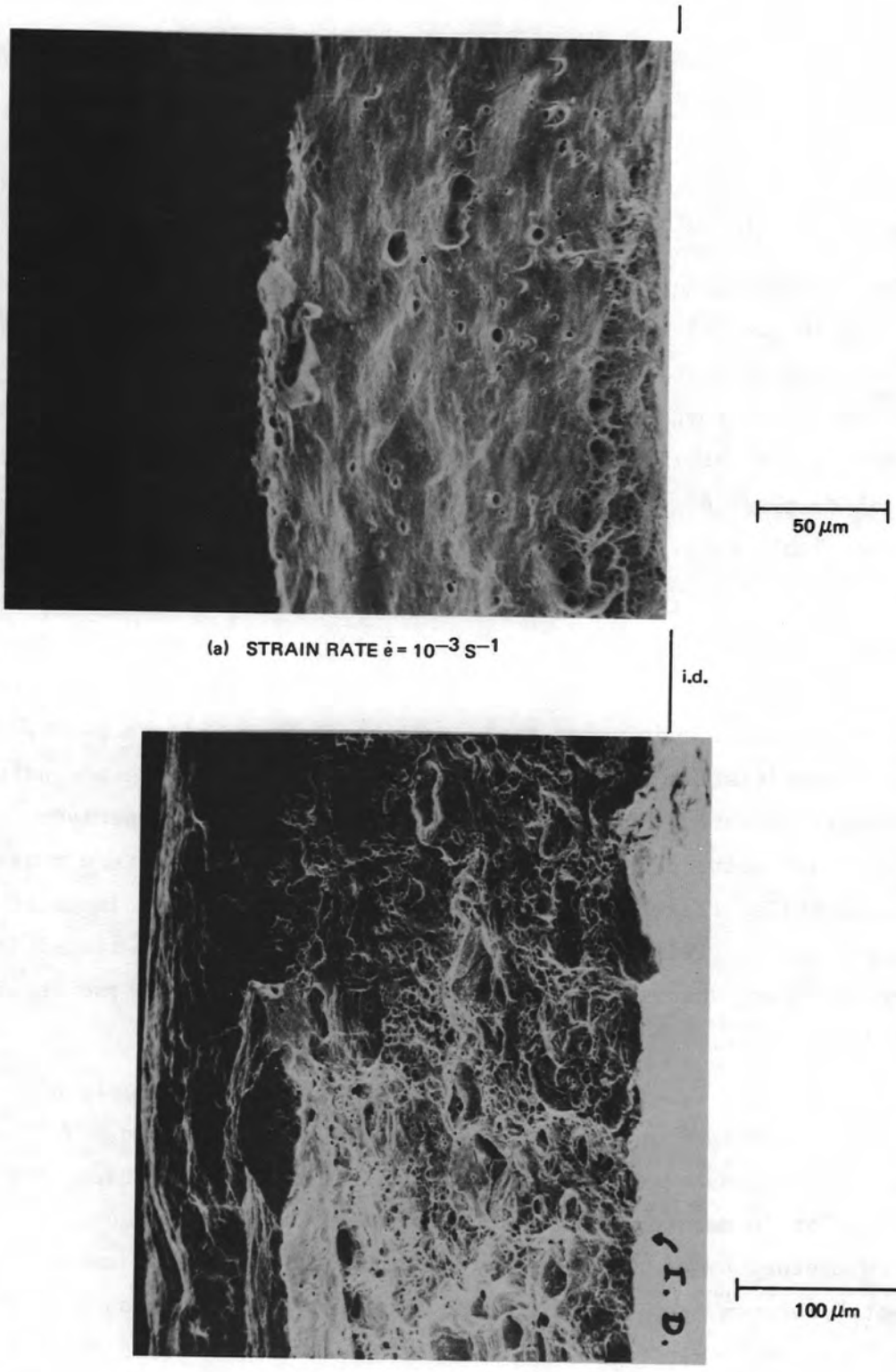


(a) STRAIN RATE $\dot{e} = 10^{-3}\ S^{-1}$

(b) STRAIN RATE $\dot{e} < 10^{-9}\ S^{-1}$

*Figure 8.9 SEM Comparison of the Fracture Topography of Control Specimens Tested at (a) $\dot{e} = 10^{-3}\ S^{-1}$ and (b) $\dot{e} < 10^{-9}\ S^{-1}$ ($T = 510°C$/316 Stainless Steel*

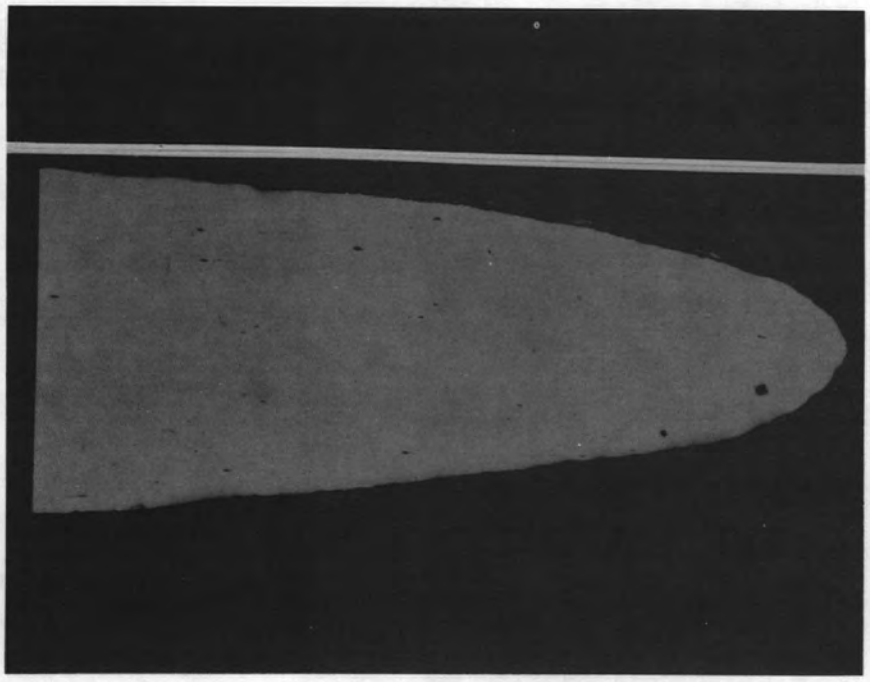


(a) $\dot{e} > 10^{-2}\ s^{-1}$

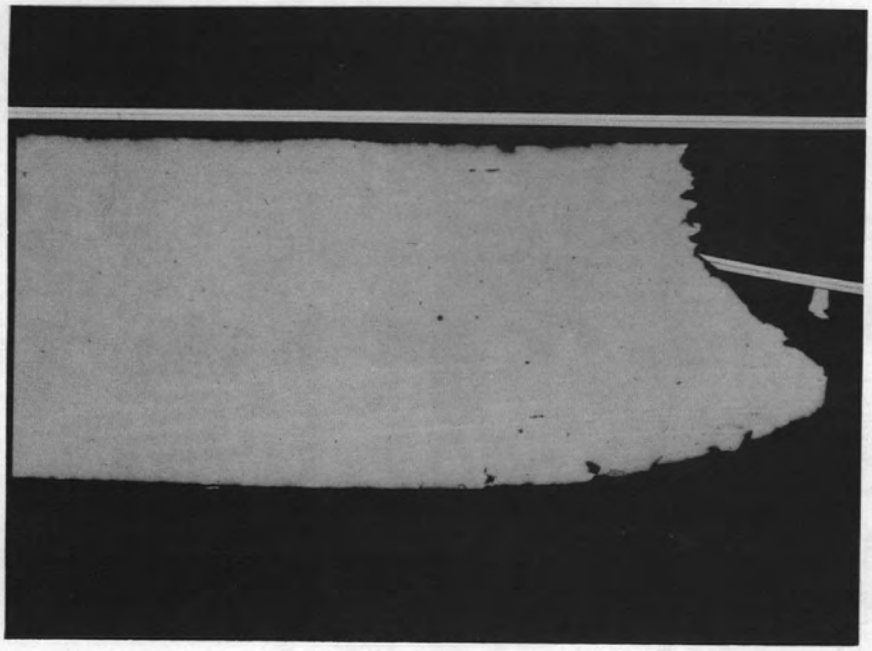


(b) $\dot{e} < 10^{-9}\ s^{-1}$

*Figure 8.10 A Comparison of Fracture Profiles as a Function of Deformation Rate at 510°C (a) Profile for Carburized Specimen where $\dot{e} > 10^{-2}\ s^{-1}$ (b) Profile for Carburized Specimen where $\dot{e} < 10^{-9}\ s^{-1}$*

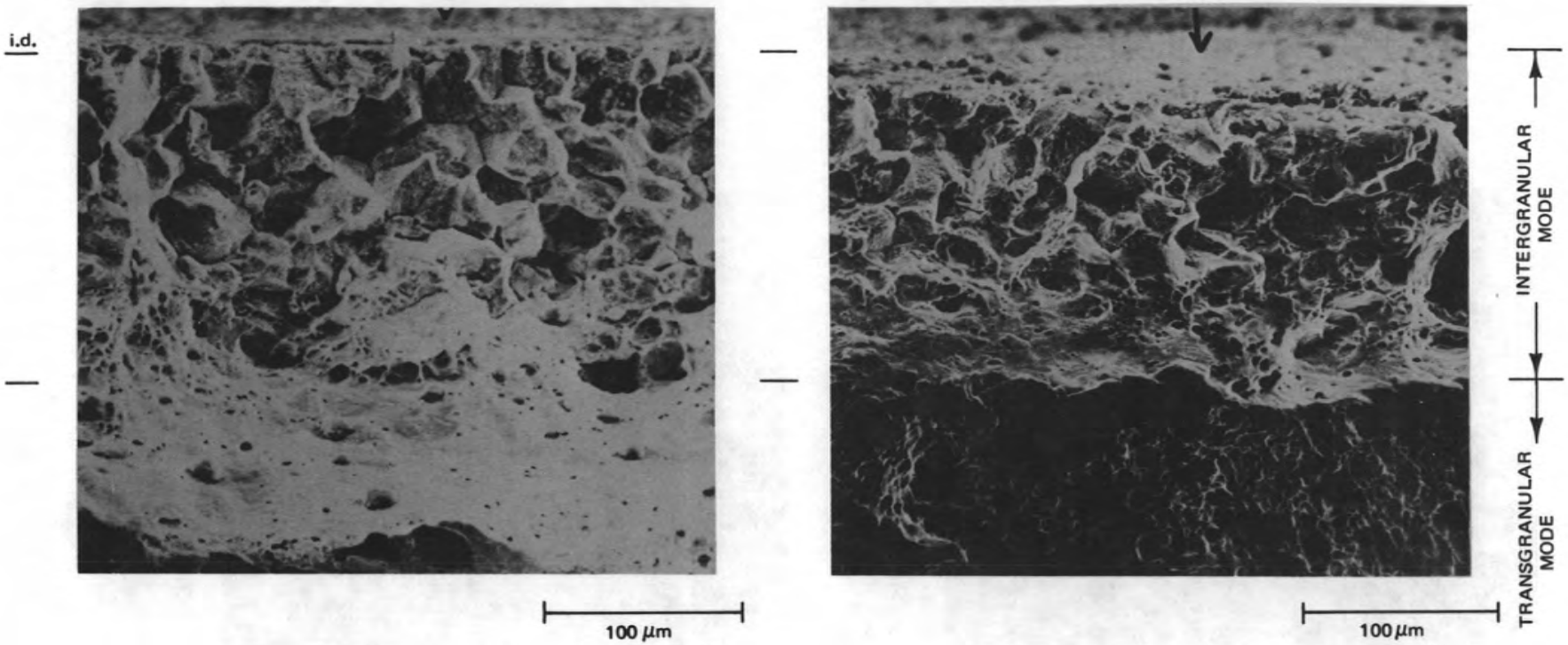


(a) SPECIMEN C09, ACCUMULATED EXPOSURE OF 2000 HOURS; SEM

(b) SPECIMEN C13, ACCUMULATED EXPOSURE OF 2000 HOURS; SEM

*Figure 8.11 Intergranular to Transgranular Transition in Carburized Specimens*

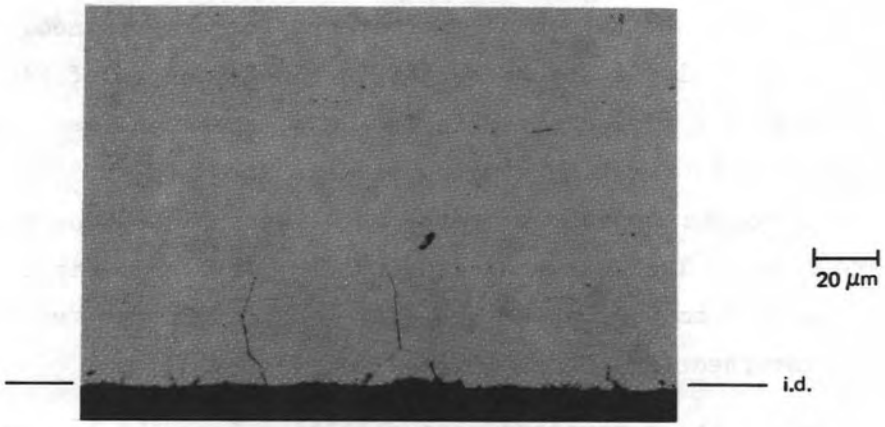


(a) TYPICAL MICROCRACKING IN THE CARBURIZED CASE OF 316 STAINLESS STEEL

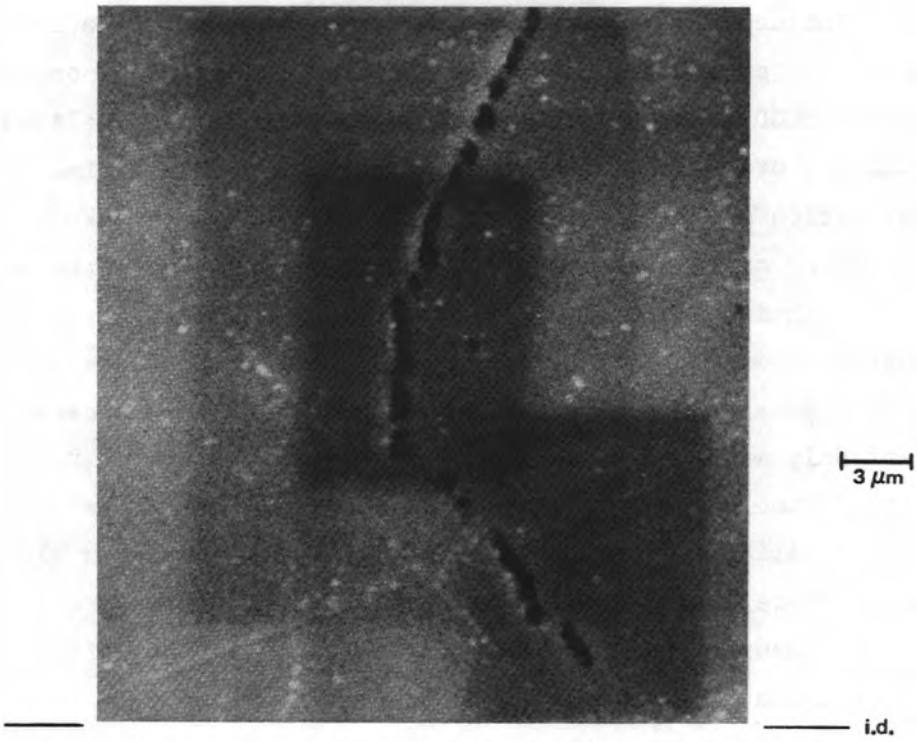


(b) SEM MICROGRAPH OF A MICROCRACK AT HIGH MAGNIFICATION

Figure 8.12 Microcracks Found Within the Carburized Case of 316H Stainless Steel

explain the strain rate sensitivity of fracture mode observed in the study and reported by other investigators.[10] Gage sections of the carburized specimens tested in the first phase of this investigation were examined, and the size and distribution of microcracks were determined. The results of this analysis are presented in the histogram of Figure 8.13. Although there is a wide scatter in the data, specimens sampled were found to contain microcracks ranging in depth from 10 to 50μm. In isolated regions, microcracks equivalent to the metallographically determined case depth were found. Typical crack density along a longitudinal section was found to be 4 $mm^{-1}$ or about one grain boundary crack for every six grain boundaries intersecting the carburized surface.

In summary, the carburized case resulting from the carbon-saturated sodium pre-exposure selected for this investigation has been characterized. Metallographic, microhardness, microprobe and fractographic techniques have been used to determine the effective carburization case depth with respect to influence on mechanical behavior. The effective carburization case depth is approximately 120μm (or 5 mils) for 510°C exposures ranging from 2000 to 3000 hours. This effective case is best correlated with grain boundary precipitation extending approximately 1.5 times the depth of carburization metallographically determined. Microcracks present along the gage extend approximately 45μm (or 2 mils) into the carburized case. Although a high density of microcracks are present within the carburized case, sustained carburization during slow deformation tests at 510°C only results in a general deeper penetration of the carburized case. Microcracks act only as perturbations in sample geometry and do not influence the point of sample instability. At instability, the deepest penetrating and/or most dense case cracks propagate along grain boundaries where a high density of carbide precipitates are present as a result of enhanced grain boundary diffusion at 510°C. Outside the carburization region, ductile/transgranular fracture is favored, and a transition in fracture mode results. There is no evidence in the current investigation that sustained carburization will accelerate the propagation of cracks under slow deformation ($\dot{\varepsilon} < 10^{-9} s^{-1}$) conditions. These results are consistent with observations made in recent CEGB studies.[11] The current creep program has been designed to ascertain whether this is indeed the case.

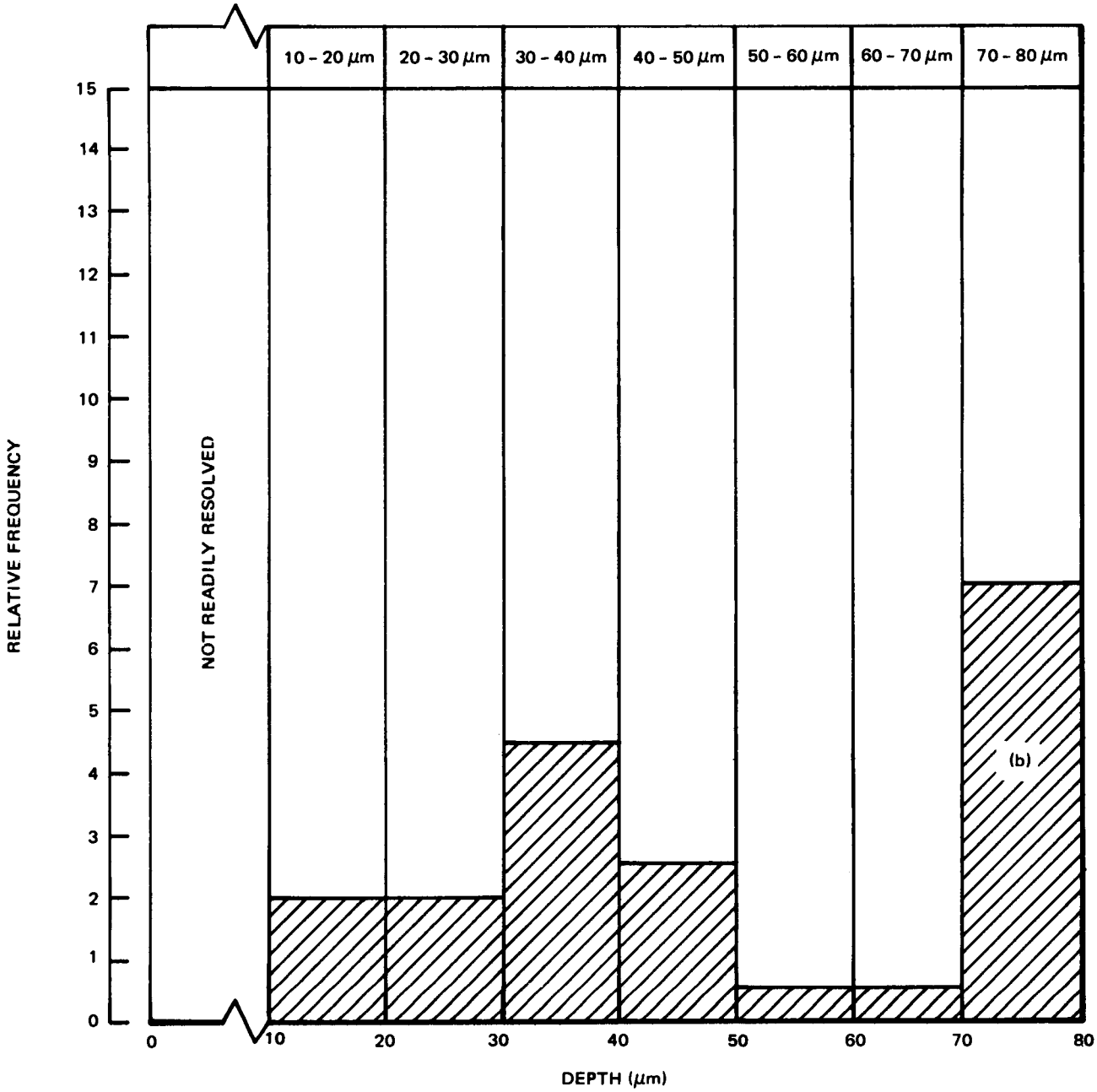


(a) TYPICAL CRACK DENSITY ALONG A LONGITUDINAL SECTION IS APPROXIMATELY 4 $mm^{-1}$ OR ABOUT ONE GRAIN BOUNDARY FOR EVERY SIX GRAIN BOUNDARIES INTERSECTING THE CARBURIZED SURFACE

(b) HIGH DENSITY OF DEEP MICROCRACKS OBSERVED IN ONE REGION OF SPECIMEN C-11

Figure 8.13 *Histogram Indicating the Size/Distribution of Microcracks Observed in Carburized Tubular Creep Specimens*

## 8.3 DECARBURIZATION KINETICS AND DESIGN METHODS VERIFICATION TESTING

P. P. Pizzo/L. V. Hampton/J. L. Krankota

### 8.3.1 Background

The selection of 2¼Cr-1Mo steel as the reference alloy for sodium-heated steam generators was based primarily upon its immunity to stress corrosion cracking in chloride or caustic contaminated environments, and its proven fabricability. One of the major concerns with the use of this material for sodium applications is its susceptibility to decarburization during service. Early analyses assumed that relatively thin sections, such as steam generator tubing, would completely decarburize during the LMFBR lifetime, with concomitant severe design stress penalties necessarily imposed. In addition to the assumed carbon losses, the potential for severe carburization of stainless steel components in the loop was also recognized as a potential difficulty.

In the absence of an acceptable theoretical model for decarburization of 2¼Cr-1Mo steel, an approach introduced by Armijo and Krankota[12] was used to analyze the results obtained from many different experiments. This technique treats carbon loss data as if it were corrosion data; that is, the loss of carbon per unit area is described as a function of time. A parabolic time dependence has been observed which suggests that the decarburization process is diffusion controlled. The decarburization rate constants, K*, from all available data were fit to an Arrhenius type expression for design use. Estimates of carbon loss and associated design

*Where K is defined by:

$$K = \frac{gm^c}{cm^2 - sec^{\frac{1}{2}}}$$

$$M = \left(\frac{gm^c}{cm^2}\right) = Kt^{\frac{1}{2}}$$

stress penalties can be made for steam generator components. These predictions of decarburization kinetics indicate that steam generator tubes would not be expected to lose more than 300 ppm carbon in the design life of the CRBRP. Only a small design stress penalty (<10%) is associated with this loss.

Design analysis for high temperature components requires a consideration of creep/fatigue interaction to accomodate the effects of transient loading. A recent study has provided creep/fatigue interaction information for 2¼Cr-1Mo[13] under conditions of uniform microstructure (i.e. no decarburized surface layer) with no ratcheting strains permitted. Steam generator tubes will experience cyclic loading with the potential to accumulate ratcheting strains, due to a weaker surface layer, as compared to the bulk metal. Interrupted creep tests on 2¼Cr-1Mo pipe, tubing and weld metal are being undertaken to assess the effects of such loading on partially decarburized material. Uniaxial tests will be performed on sodium-filled and inert gas-filled pipe samples in order to characterize the effect of stress cycling on creep strains. Tubing and all-weld-metal tubes will be internally pressurized in sodium and argon environments to assess the effects of creep/fatigue on rupture life in a decarburizing environment. Description of the samples, test facilities, and test matrix is included in earlier reports.[14,15,19]

### 8.3.2 Decarburization Studies

Current testing in the decarburization pot will yield data showing the effect of heat treatment variables on the decarburization kinetics of electroslag remelted (ESR), vacuum-arc remelted (VAR) and extra-low carbon (ELC) 2¼Cr-1Mo. Pot conditions remain the same as with previous runs, i.e., 510°C (950°F) static, titanium-gettered sodium. Foil specimens approximately 0.3 X 10 X 80 mm (0.0118 X 0.394 X 3.15 in.) were given the range of heat treatments listed in Table 8.6. Such treatments lead to a variety of microstructures, and possibly different decarburization rates in sodium. The effect of heat treatment on the carbon transport properties of 2¼Cr-1Mo has recently become a well-documented phenomenon.[16,17,18] The current study limits the heat treatments to those that produce the range of

microstructures that may be present in the Clinch River Plant steam generators. In addition, the more subtle effect of melting practice on the decarburization rate of 2¼Cr-1Mo in sodium is being studied. The test matrix for this phase of the decarburization study calls for exposure times of 1500 (DP-9), 6000 (DP-10) and 10,000 (DP-11) hours for each of the material treatments listed in Table 8.6.

Run DP-9 (1500 hours) has been completed, yielding the first carbon loss data for this series of experiments. Carbon analyses for this run have not yet been completed so the results will be reported at the next quarter.

Additional specimens were added to the pot for run DP-10 (4500 hours), due for completion in mid-December 1976. Included in this run will be ESR and VAR prototypic tubing material and 2¼Cr-1Mo weld material.

Extensive testing of 2¼Cr-1Mo tubing materials in both static and flowing sodium systems is planned for the coming fiscal year. As reported in the last monthly report (No. 16: May 1976), specimens of prototypic ESR and VAR 2¼Cr-1Mo tubing were shipped to Atomics International for attachment to the shrouds of both the evaporator and superheater modules (at sodium inlet and outlet regions) of the Few Tube Test Model. Also included for shroud attachment were reference heats of Alloy 800H (HH7055A) and 316 stainless steel (8092297) along with ESR and air-melted 2¼Cr-1Mo and 304 stainless steel specimens. These specimens will remain in the FTTM for ∿ 3 years, at which time the tubing will be analyzed for carbon gradient determination. Those tubular specimens included in the static pot for exposure will be retrieved after runs DP-10 and DP-11, and carbon gradient determinations will be made by precision machining of surface layers.

### 8.3.3 Mechanical Properties of 2¼Cr-1Mo Steel in Decarburizing Sodium

The ferritic alloy selected for the secondary loop of the sodium cooled fast breeder reactor will be subjected to decarburizing conditions during the design life of the reactor. Sodium-side surfaces will be depleted of carbon, and a composite structure, with bulk properties intermediate to the base alloy and the low-carbon surface region will result.

TABLE 8.6

TEST MATRIX

HEAT TREATMENT EFFECTS ON DECARBURIZATION

VAR, ESR and ELC* (Sumitomo)

A. Isothermal Anneal

927 ± 14°C (1700 ± 25°F) ½ hr.
cool to 716 ± 8°C (1320 ± 15°F)
in less than 10 minutes, hold
for ½, 1*, 1½ and 2 hrs.*

B. Same as A with PWHT 727°C (1340°F) - 4 hrs.

C. Normalize (Simulate Weld Heat Affected Zone)

927 ± 14°C (1700 ± 25°F) 1 hr.
Air cool to R.T.
PWHT 727 ± 19°C (1340 ± 35°F)
for 0, 1, 2 and 4 hrs.

D. Tube samples, VAR and ESR for Carbon Profile Determination

1. Isothermally annealed (as received) 927°C (1700°F) cool to 707°C (1305°F), hold for 2 hours, air cool.

2. Isothermally annealed and PWHT of 4 hours at 727 ± 19°C (1340 ± 35°F).

The purpose of effort within subtask A is twofold; first, to characterize the decarburization conditions expected to develop within the 30 year design life of the reactor, and secondly to quantify the influence of decarburization on the resultant mechanical behavior. Currently, the mechanical properties investigation is focused on creep and stress rupture behavior.

Details of the current mechanical properties investigation have been previously reported.[19] Three test matrices have been developed:

1. Tensile tests of 2¼Cr-1Mo sheet coupons at T = 510°C and a rate of $10^{-3}S^{-1}$ will be conducted. These tests are designed to measure the degradation in elevated temperature yield strength and tensile strength as a function of pre-exposure time in the specific titanium gettered environment selected for this investigation. The data of Charnock, Cordwell, Gwyther and Hobdell[15] suggest the importance of correlating mechanical properties changes with reproducible and consistent carbon activity excursions. The data from this program will be correlated with creep property measurements in order to isolate yield strength reduction in the analysis of creep strength degradation.

2. Uniaxial creep tests of ESR/2¼Cr-1Mo steel are being performed in order to determine the mechanical property variation as a function of pre-exposure conditions (time at 510°C). Tubular creep specimens with a 0.76 mm (0.030 in.) wall, decarburized on the I.D., are being tested. The properties to be evaluated are; (a) time to rupture, (b) minimum creep rate and, (c) strain-to-failure. The test matrix is designed to isolate pre-exposure influence on properties from effects associated with sustained decarburization potential.

3. Biaxial creep tests of pressure pin specimens are being conduted. The biaxial creep test program is also designed to determine property variations as a function of pre-exposure to decarburizing sodium. Rupture data over stresses ranging from 115 to 205 MPa (16.7 to 29.7 Ksi) are being generated.

The test matrix for the 510°C tensile test program is presented in Table 8.7. Tensile coupons have been given a thermal aging treatment, 510°C (950°F) in argon, such that when sodium pre-exposed, an accumulated 1000 hour thermal exposure will result. Respective pairs of coupons are encapsulated and await the sodium pre-exposure. Capsules will be filled from a sodium loop with a monitored decarburization potential. The decarburization potential will be maintained through use of titanium sponge enclosed within individual exposure capsules. Progress on this program is dependent on attaining a decarburization potential in the subject sodium loop, which previously was used in carburization studies. Hot trapping techniques are being used to getter the system of carbon, and progress is being monitored with 316 stainless steel, solution annealed foils. Progress on this program will be reported in the succeeding GE Quarterly.

The test matrix for the uniaxial creep test program is presented in Table 8.8. This matrix, previously reported as Table 3.3 in Reference 8, has been revised on the basis of data on electroslag re-melted (ESR) 2¼Cr-1Mo steel recently reported.[6] Data indicate that ESR material, annealed and isothermally annealed, exhibits creep properties consistent with existing Code Case 1592 minimum values for creep parameters pertinent to this study. The uniaxial creep specimens have been fabricated from ESR material, isothermally annealed and post weld heat treated, a proces-ing sequence prototypic of CRBRP steam generator tubing. The revised stress values reported in Table 8.8 are predicted to yield nominal 1000 hr. data. The base test plan has been expanded to investigate decarburization influence at three stress levels, 130 MPa, 150 MPa and 172 MPa. Tubular specimens are currently undergoing the control exposure (argon at 510°C [950°F]). The eight specimens requiring subsequent decarburization will be sodium filled using the sodium loop being adapted for this purpose. Testing of test specimen (A-19) has been initiated. Subsequent tests will be performed as specimens become available.

Based on the ESR/2¼Cr-1Mo steel data, the test plan for the biaxial creep program has also been revised, and the test matrix is presented in Table 8.9. However, prior to revision, testing of pressure pin specimens

TABLE 8.7

ELEVATED TEMPERATURE TENSILE TEST MATRIX

Material: 2¼Cr-1Mo Steel
Melting Practice - ESR
Isothermal Anneal
Post-Weld Treatment (727°C [1340°F] for 4 hours)

Specimen Configuration: Tensile Coupons (0.76 mm. [.030 in.] sheet)

Test Parameter: $T = 510°C$ (950°F)
$\dot{\varepsilon}_o = 10^{-3}\ sec^{-1}$ (strain rate)

| Quantity | Pre-Exposure time | Pre-Exposure Environment (one surface)[c] |
|---|---|---|
| 2 | 0 | -- |
| 2 | 100 | Na (Ti Gettered) |
| 2 | 200 | " |
| 2 | 300 | " |
| 2 | 400 | " |
| 2 | 500 | " |
| 2 | 750 | " |
| 2 | 1000 | " |

(a) All sodium exposures, titanium gettered.

(b) Test coupons given a 510°C (950°F) aging treatment in argon prior to sodium pre-exposure such that an accumulated 1000 hour total thermal exposure is attained prior to testing.

(c) 0.76 mm. (.030 in.) removed from one face of the initially 1.52 mm. (.060 in.) thick coupons.

TABLE 8.8

UNIAXIAL CREEP TEST MATRIX

Material: 2¼Cr-1Mo Steel
Electroslag Remelted
Isothermal Anneal
Post-Weld Heat Treatment (727°C [1340°F] for 4 hours)

Specimen Configuration: Tubular Creep Specimen

Test Parameters: T = 510°C (950°F)

| Quantity | Exposure History | | | | Test Environment (I.D./O.D.) | Creep Stress |
|---|---|---|---|---|---|---|
| | Control Exposure | | Decarburization Exposure | | | |
| | time | Environment (I.D./O.D.) | time | Environment (I.D./O.D.) | | |
| 1 | 0 | -- | 0 | -- | Ar/Air | 150 MPa (21.7 Ksi) |
| 1 | 750 | Ar/Ar | 250 | Na/Ar | Ar/Air | 150 MPa (21.7 Ksi) |
| 1 | 750 | Ar/Ar | 250 | Na/Ar | Na/Air | 150 MPa (21.7 Ksi) |
| 3 | 500 | Ar/Ar | 500 | Na/Ar | Na/Air | 150 MPa (21.7 Ksi) |
| 1 | 1000 | Ar/Ar | 0 | -- | Ar/Air | 150 MPa (21.7 Ksi) |
| 1 | 0 | -- | 1000 | Na/Ar | Na/Air | 150 MPa (21.7 Ksi) |
| 1 | 500 | Ar/Ar | 500 | Na/Ar | Na/Air | 130 MPa (18.9 Ksi) |
| 1 | 1000 | Ar/Ar | 0 | Ar/Ar | Ar/Air | 130 MPa (18.9 Ksi) |
| 1 | 500 | Ar/Ar | 500 | Na/Ar | Na/Air | 172 MPa (25.0 Ksi) |
| 1 | 1000 | Ar/Ar | 0 | -- | Ar/Air | 172 MPa (25.0 Ksi) |

NOTE: This is a revision of Table 3.3 of GEAP-14029-7

TABLE 8.9

BIAXIAL CREEP TEST MATRIX

Material: 2¼Cr-1Mo Steel
Melting Practice-ESR
Isothermal Anneal

Specimen Configuration: Pressure Pin Spcimens

Test Parameter: T = 510°C (950°F)

| Quantity | Pre-Exposure Time | Pre-Exposure Environment (ID/OD) | Test Environment (ID/OD | Stress MPa | Stress (ksi) |
|---|---|---|---|---|---|
| 2 | 0 | - | Ar/Na | 205 | (29.7) |
| 2 | 0 | - | Ar/Na | 172 | (25.0) |
| 2 | 0 | - | Ar/Na | 145 | (21.0) |
| 2 | 0 | - | Ar/Na | 130 | (18.9) |
| 2 | 0 | - | Ar/Na | 115 | (16.7) |
| 2 | 1000 | Ar/Ar | Ar/Na | 172 | (25.0) |
| 2 | 1000 | Ar/Ar | Ar/Na | 130 | (18.9) |
| 2 | 250 | Ar/Na | Ar/Na | 172 | (25.0) |
| 2 | 500 | Ar/Na | Ar/Na | 172 | (25.0) |
| 2 | 1000 | Ar/Na | Ar/Na | 172 | (25.0) |
| 2 | 250 | Ar/Na | Ar/Na | 130 | (18.9) |
| 2 | 500 | Ar/Na | Ar/Na | 130 | (18.9) |
| 2 | 1000 | Ar/Na | Ar/Na | 130 | (18.9) |
| 2 | 1000 | Ar/Na | Ar/Na | 205 | (29.7) |
| 2 | 1000 | Ar/Na | Ar/Na | 145 | (21.0) |
| 2 | 1000 | Ar/Na | Ar/Na | 115 | (16.7) |
| 4 | 0 | - | Ar/Ar | 172 | (25.0) |
| 4 | 0 | - | Ar/Ar | 130 | (18.9) |

NOTE: (a) All Na exposures titanium gettered. (b) This is a revision of Table 3.4 of GEAP-14029-7.

was begun. Three specimens, T05, T07 and T17 were tested. Specimens T05 and T07 were exposed to Ti-gettered sodium at 510°C (950°F) for 250 hours and 500 hours, respectively, prior to testing. Specimen T17 had been exposed 1000 hours at 510°C (950°F) in argon prior to testing. A fourth specimen, T04, was included in the run (unpressurized) in order to obtain a 1000 hour sodium pre-exposed pressure pin.

Tests of specimens T05, T07 and T17 were initiated at an equivalent stress of 210 MPa (30.5 Ksi). Rupture times were 49, 62 and 173 hours, respectively. Difficulty was encountered in maintaining system pressure after rupture of the second pressure pin specimen, and as a result, an effective stress was calculated to describe the behavior of specimen T17. Assuming a power law stress dependence ($n \sim -6$), the effective stress for specimen T17 was approximated to be 190 MPa (27.5 Ksi).

The above rupture data has been included on the log stress/log rupture time plot, Figure 8.14. This figure includes data obtained in the first phase of the biaxial creep program and summarized in previous reports.[19] Although the nominal rupture time is an order of magnitude lower than that desired for this investigation, this initial data demonstrate the following;

1. The biaxial creep data yields rupture times approximately equivalent to the ASME Code Case 1592 minimum, a trend consistent with uniaxial tensile creep data for ESR 2¼Cr-1Mo steel, isothermal annealed specimens.[6]

2. A small and resolvable reduction in creep strength is demonstrated as a function of pre-exposure condition.

The remaining data of Figure 8.14 represent results from the first phase biaxial stress rupture program. Included are rupture data for specimens which were inadvertently subjected to the sodium purification excursion (40 to 72 hours at 727°C [1340°F] in titanium gettered sodium) preceeding each run. These data were previously retracted because they were not representative of decarburization conditions required for the test program. Nevertheless, in terms of their resultant chemistry, they help illustrate an important point, and are thus presented in this summary report. The

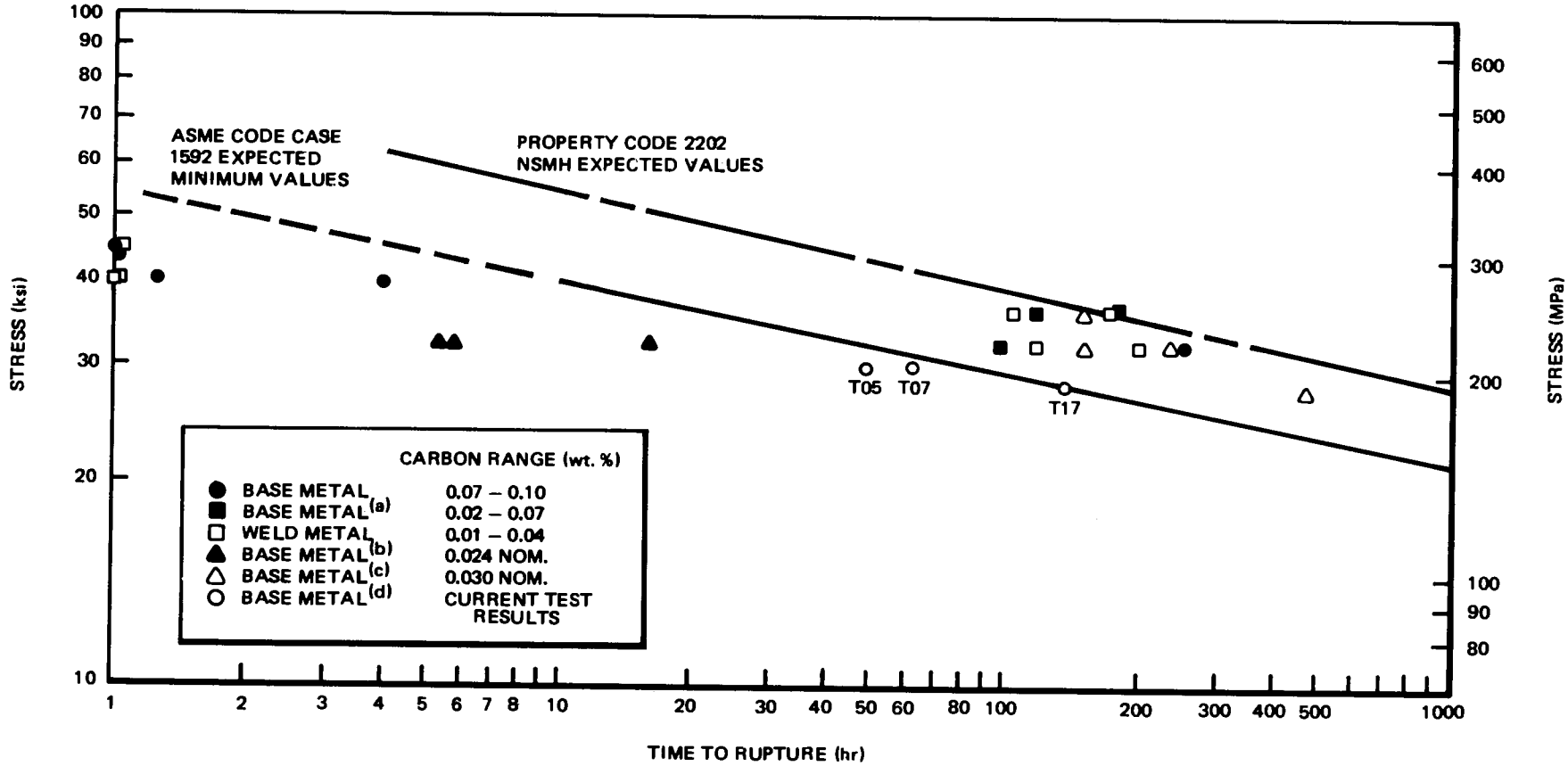


NOTES: (a) SINGLE EXPOSURE TO 727°C (1340°F)/40 HOUR EXCURSIONS IN Ti-GETTERED SODIUM AND TESTED IN SODIUM
(b) MULTIPLE EXPOSURE TO 727°C (1340°F/40 HOUR EXCURSIONS IN Ti–GETTERED SODIUM AND TESTED IN SODIUM
(c) MULTIPLE EXPOSURE TO 727°C (1340°F/40 HOUR EXCURSIONS IN Ti-GETTERED SODIUM AND TESTED IN ARGON
(d) CURRENT TEST PROGRAM, ESR MATERIAL (SPECIMENS ARE NOT YET AVAILABLE FOR CARBON ANALYSES)

Figure 8.14 Biaxial Stress Rupture Results

data of Figure 8.14 illustrate that the relatively short term stress rupture properties of 2¼Cr-1Mo steel are not greatly affected by large variations in bulk carbon content. Carbon determinations are catagorized in Figure 8.14 and tabulated in Table 8.10. Analysis of these specimens for carbon was done by a dry combustion technique (LECO) with a chromatographic measurement of the total oxidized carbon. The sensitivity of the analysis at the 0.2 wt.% carbon level is ±0.004 wt.%, and at the 0.5 wt.% level it is ±0.01 wt.% carbon. The following points are illustrated in Figure 8.14;

1. Data representative of base metal bulk carbon content ranging from approximately .030 to .100 wt.%, and those representative of weld metal with a nominal .020 wt.% carbon content, all fall within a common range typical of the spread between "expected" and "expected minimum" stress rupture behavior.

2. Only base metal specimens with a nominal bulk carbon content of .024 wt.% suffer a large decrement in creep strength.

The maintenance of relatively constant creep rupture strength for 0.03 < wt.% carbon < 0.10, with a sharp reduction in creep strength for carbon content less than .030 wt.%,has been previously reported.[6] However, this trend was established using a number of 2¼Cr-1Mo steel alloys with uniform carbon compositions. Figure 8.14 demonstrates a similar trend for specimens severly decarburized. Thus, the first phase results of the biaxial creep program confirm that

1. Stress rupture properties (short term) of 2¼Cr-1Mo steel are relatively constant within the carbon loss regime anticipated for the design life of CRBR.

2. Biaxial stress rupture data is directly comparable to uniaxial test results; thus, the design penalty associated with decarburization events can be determined from biaxial stress rupture test results.

Four samples of prototypic ESR tubing, scheduled for decarburization profile determination have accumulated a 2010 hour exposure to titanium gettered sodium at T = 510°C (950°F). These specimens will be used to characterize the specific decarburization conditions of this investigation.

TABLE 8.10

RELATIVE CARBON CONTENT FOR THE 2¼Cr-1Mo DATA OF FIGURE 8.14

| Key | | Carbon (Wt. %) Mean | Carbon (Wt. %) Std. Dev. | Melt History |
|---|---|---|---|---|
| ● | 2¼Cr-1Mo Base Metal | .094 | .008 | Air Melt |
| ■ | Base Metal[a] | .041 | .012 | Air Melt |
| □ | Weld Metal | .019 | .010 | Weld Metal |
| ⬭ | Base Metal[b] | .024 | .002 | Air Melt |
| △ | Base Metal[c] | .030 | .005 | Air Melt |
| ⊠ | Base Metal[d] | (not determined) | | Electroslag Remelted |

(a) Single exposure to 727°C (1340°F)/40 hour excursions in Ti-gettered sodium, tested in sodium at 510°C (950°F).

(b) Multiple exposure to 727°C (1340°F)/40 hour excursions in Ti-gettered sodium, tested in sodium at 510°C (950°F).

(c) Multiple exposure to 727°C (1340°F)/40 hour excursions in Ti-gettered sodium, tested in argon at 510°C (950°F).

(d) Current test program, ESR material, not yet available for carbon analysis.

(e) Bulk carbon determinations made on approximate 0.51 mm. (.020 in.) thick specimens.

## 8.4 METALLURGICAL CHARACTERIZATION OF VAR AND ESR 2¼Cr-1Mo STEEL

H. P. Offer

The objective of this activity is to generate mechanical property and microstructural characterization data for consumable remelted 2¼Cr-1Mo steel. The mechanical property data has been generated on vacuum arc remelted (VAR) and electroslag remelted (ESR) material. Heat treatments simulate the treatments used for the data base of ASME Code Case 1592, and the CRBR steam generator tubing and tubesheets before and after post weld heat treatment. This data is compared to the Code Case 1592 data base and to the Nuclear Systems Materials Handbook (NSMH) correlations, which both represent material without post weld heat treatment. The microstructural data is compared to RDT Standards M2-19 (tubesheets) and M3-33 (tubing), which are based on remelted material.

Data reported earlier[23] for two VAR heats (Nos. 56062 and 55262) and one ESR heat (No. R0110) include heat treatments, uniaxial tensile tests, drop-weight tests, Charpy V-notch tests, creep-rupture tests, chemical composition, microcleanliness, grain size and hardness, microstructure, and isothermal transformation data. Two additional heats are reported here - VAR heat 91506 and ESR heat 91505, which were remelted from the same vacuum induction melted heat. The data included for these heats are tensile tests from room temperature to 566°C (1050°F), creep-rupture tests at 454, 510, and 566°C (850, 950, and 1050°F), drop-weight and Charpy tests from -59 to 288°C (-75 to 550°F), heat treatments, chemical composition, and microinclusion data. Fracture toughness, uniaxial strain controlled fatigue, and additional creep-rupture tests are in progress for these heats. Tensile and creep results not reported previously for VAR heat 55262 and ESR heat R0110 are also included.

### 8.4.1 Summary of Results

Values of yield strength, tensile strength, elongation, reduction in area, yield strength ratio, and tensile strength ratio for the tensile tests are given in Table 8.11. In general, the strength of these heats is above the Code expected minimum curve for the short term isothermal

TABLE 8.11

TENSILE PROPERTIES OF 2¼Cr-1Mo STEEL

| Specimen Number | Heat Treatment | Test Temp. °C (°F) | Strength, MPa (KSI) Yield 0.2% Offset | Ultimate | Strength Ratio Yield | Ultimate | Total Elongation, % in 25.4 mm | Reduction in Area, % |
|---|---|---|---|---|---|---|---|---|
| Heat VAR 91506 - 0.10% C | | | | | | | | |
| VT1 | A | 24 (76) | 275 (39.9) | 461 (66.9) | 1.000 | 1.000 | 42.2 | 77.8 |
| VT2 | A | 204 (400) | 216 (31.4) | 396 (57.5) | .787 | .859 | 26.4 | 76.7 |
| VT3 | A | 371 (700) | 199 (28.9) | 450 (65.2) | .724 | .975 | 23.6 | 70.3 |
| VT4 | A | 454 (850) | 174 (25.3) | 413 (59.9) | .634 | .895 | 29.0 | 76.1 |
| VT5 | A | 510 (950) | 153 (22.2) | 372 (54.0) | .556 | .807 | 28.6 | 80.7 |
| VT6 | A | 566 (1050) | 148 (21.5) | 299 (43.3) | .539 | .649 | 39.3 | 89.2 |
| VT10 | A2 | 24 (76) | 260 (37.8) | 459 (66.6) | 1.000 | 1.000 | 40.5 | 77.1 |
| VT11 | A2 | 204 (400) | 236 (34.2) | 425 (61.7) | .905 | .926 | 26.6 | 74.5 |
| VT12 | A2 | 371 (700) | 201 (29.2) | 466 (67.6) | .772 | 1.015 | 24.3 | 68.9 |
| VT13 | A2 | 454 (850) | 161 (23.4) | 419 (60.8) | .619 | .913 | 28.2 | 76.5 |
| VT14 | A2 | 510 (950) | 161 (23.3) | 377 (54.7) | .616 | .821 | 30.3 | 80.9 |
| VT15 | A2 | 566 (1050) | 152 (22.0) | 308 (44.7) | .582 | .671 | 32.8 | 88.4 |
| VT19 | B | 24 (76) | 202 (29.3) | 440 (63.8) | 1.000 | 1.000 | 36.6 | 73.3 |
| VT20 | B | 204 (400) | 154 (22.3) | 365 (53.0) | .761 | .831 | 34.8 | 74.4 |
| VT21 | B | 371 (700) | 147 (21.3) | 381 (55.3) | .727 | .867 | 21.8 | 67.4 |
| VT22 | B | 454 (850) | 149 (21.6) | 356 (51.7) | .737 | .810 | 29.6 | 72.4 |
| VT23 | B | 510 (950) | 137 (19.8) | 312 (45.3) | .676 | .710 | 32.3 | 77.9 |
| VT24 | B | 566 (1050) | 139 (20.1) | 268 (38.8) | .686 | .608 | 28.8 | 86.2 |

TABLE 8.11

TENSILE PROPERTIES OF 2¼Cr-1Mo STEEL

| Specimen Number | Heat Treatment | Test Temp. °C (°F) | Strength, MPa (KSI) Yield 0.2% Offset | Ultimate | Strength Ratio Yield | Ultimate | Total Elongation, % in 25.4 mm | Reduction in Area, % |
|---|---|---|---|---|---|---|---|---|
| Heat VAR 91506 - 0.10% C | | | | | | | | |
| VT20 | D | 24 (76) | 228 (33.1) | 456 (66.1) | 1.000 | 1.000 | 34.5 | 73.8 |
| VT21 | D | 204 (400) | 197 (28.6) | 383 (55.6) | .864 | .841 | 31.1 | 72.2 |
| VT22 | D | 371 (700) | 173 (25.1) | 414 (60.0) | .758 | .908 | 24.7 | 66.5 |
| VT23 | D | 454 (850) | 151 (21.9) | 397 (57.6) | .622 | .871 | 28.4 | 71.6 |
| VT24 | D | 510 (950) | 156 (22.6) | 363 (52.6) | .683 | .796 | 31.2 | 79.0 |
| VT25 | D | 566 (1050) | 142 (20.6) | 314 (45.6) | .622 | .690 | 38.1 | 85.9 |
| VT27 | M | 24 (76) | 263 (38.1) | 467 (67.8) | 1.000 | 1.000 | 34.5 | 77.7 |
| VT28 | M | 204 (400) | 228 (33.0) | 425 (61.7) | .866 | .910 | 27.3 | 74.3 |
| VT29 | M | 371 (700) | 199 (28.8) | 465 (67.5) | .756 | .996 | 24.5 | 72.8 |
| VT30 | M | 454 (850) | 198 (28.7) | 439 (63.5) | .753 | .937 | 28.2 | 78.5 |
| VT31 | M | 510 (950) | 198 (28.7) | 406 (58.9) | .753 | .869 | 28.4 | 81.0 |
| VT32 | M | 566 (1050) | 183 (26.6) | 339 (49.1) | .698 | .724 | 37.6 | 85.9 |
| Heat ESR 91505 - 0.09% C | | | | | | | | |
| ET1 | A | 24 (76) | 261 (37.9) | 440 (63.8) | 1.000 | 1.000 | 38.3 | 79.1 |
| ET2 | A | 204 (400) | 203 (29.5) | 397 (57.6) | .778 | .903 | 30.7 | 78.0 |
| ET3 | A | 371 (700) | 188 (27.3) | 434 (63.0) | .720 | .987 | 24.5 | 71.1 |
| ET4 | A | 454 (850) | 159 (23.0) | 398 (57.7) | .607 | .904 | 26.6 | 75.9 |
| ET5 | A | 510 (950) | 153 (22.2) | 357 (51.8) | .586 | .812 | 28.3 | 80.2 |
| ET6 | A | 566 (1050) | 139 (20.1) | 290 (42.1) | .530 | .660 | 43.1 | 86.2 |

TABLE 8.11

TENSILE PROPERTIES OF 2¼Cr-1Mo STEEL

| Specimen Number | Heat Treatment | Test Temp. °C (°F) | Strength, MPa (KSI) Yield 0.2% Offset | Ultimate | Strength Ratio Yield | Ultimate | Total Elongation, % in 25.4 mm | Reduction in Area, % |
|---|---|---|---|---|---|---|---|---|
| Heat ESR 91505 - 0.09% C | | | | | | | | |
| ET10 | A2 | 24 (76) | 254 (36.9) | 434 (63.0) | 1.000 | 1.000 | 40.3 | 79.3 |
| ET11 | A2 | 204 (400) | 220 (31.9) | 398 (57.7) | .864 | .916 | 30.9 | 77.6 |
| ET12 | A2 | 371 (700) | 186 (27.0) | 429 (62.2) | .732 | .987 | 25.0 | 71.8 |
| ET13 | A2 | 454 (850) | 148 (21.4) | 394 (57.1) | .580 | .906 | 27.6 | 76.6 |
| ET14 | A2 | 510 (950) | 149 (21.6) | 359 (52.1) | .585 | .827 | 29.9 | 81.7 |
| ET15 | A2 | 566 (1050) | 139 (20.2) | 290 (42.1) | .547 | .668 | 37.6 | 86.8 |
| ET19 | B | 24 (76) | 187 (27.1) | 433 (62.8) | 1.000 | 1.000 | 37.3 | 74.5 |
| ET20 | B | 204 (400) | 154 (22.4) | 356 (51.6) | .827 | .822 | 26.6* | 76.6 |
| ET21 | B | 371 (700) | 143 (20.7) | 360 (52.2) | .764 | .831 | 25.8 | 71.0 |
| ET22 | B | 454 (850) | 134 (19.5) | 340 (49.3) | .720 | .785 | 30.9 | 74.5 |
| ET23 | B | 510 (950) | 128 (18.5) | 301 (43.6) | .683 | .694 | 24.2 | 77.8 |
| ET24 | B | 566 (1050) | 123 (17.9) | 248 (35.9) | .661 | .572 | 42.8 | 81.3 |
| ET20 | D | 24 (76) | 209 (30.3) | 436 (63.2) | 1.000 | 1.000 | 36.1 | 77.3 |
| ET21 | D | 204 (400) | 184 (26.7) | 361 (52.3) | .881 | .828 | 32.6 | 75.3 |
| ET22 | D | 371 (700) | 159 (23.1) | 388 (56.3) | .762 | .891 | 26.0 | 70.4 |
| ET23 | D | 454 (850) | 166 (24.1) | 372 (53.9) | .795 | .853 | 28.7 | 73.4 |
| ET24 | D | 510 (950) | 139 (20.1) | 334 (48.5) | .663 | .767 | 33.1 | 78.5 |
| ET25 | D | 566 (1050) | 137 (19.8) | 294 (42.7) | .653 | .676 | 42.3 | 84.3 |

TABLE 8.11

TENSILE PROPERTIES OF 2¼Cr-1Mo STEEL

| Specimen Number | Heat Treatment | Test Temp. °C (°F) | Strength, MPa (KSI) Yield 0.2% Offset | Ultimate | Strength Ratio Yield | Ultimate | Total Elongation, % in 25.4 mm | Reduction in Area, % |
|---|---|---|---|---|---|---|---|---|
| Heat ESR 91505 - 0.09% C | | | | | | | | |
| ET27 | M | 24 (76) | 262 (38.0) | 452 (65.5) | 1.000 | 1.000 | 35.4 | 78.5 |
| ET28 | M | 204 (400) | 209 (30.3) | 410 (59.5) | .797 | .908 | 28.0 | 74.8 |
| ET29 | M | 371 (700) | 185 (26.9) | 444 (64.4) | .708 | .983 | 25.5 | 72.3 |
| ET30 | M | 454 (850) | 183 (26.5) | 419 (60.8) | .697 | .928 | 28.4 | 77.5 |
| ET31 | M | 510 (950) | 166 (24.1) | 390 (56.5) | .634 | .863 | 29.1 | 82.3 |
| ET32 | M | 566 (1050) | 156 (22.6) | 329 (47.7) | .595 | .728 | 37.5 | 86.3 |
| ETS1 | N | 24 (76) | 235 (34.1) | 457 (66.3) | 1.000 | 1.000 | 34.3 | 69 |
| ETS2 | N | 204 (400) | 203 (29.5) | 407 (59.1) | .865 | .891 | 25.0 | 63 |
| ETS3 | N | 454 (850) | 207 (30.0) | 465 (67.5) | .880 | 1.018 | 16.8 | 61 |
| ETS4 | N | 510 (950) | 199 (28.9) | 425 (61.6) | .848 | .929 | 22.5 | 65 |
| ETS5 | O | 24 (76) | 236 (34.3) | 445 (64.6) | 1.000 | 1.000 | 34.1 | 70 |
| ETS6 | O | 204 (400) | 185 (26.8) | 369 (53.5) | .781 | .828 | 25.8 | 69 |
| ETS7 | O | 454 (850) | 175 (25.4) | 367 (53.2) | .741 | .824 | 22.3 | 64 |
| ETS8 | O | 510 (950) | 151 (21.9) | 323 (46.9) | .638 | .726 | 28.2 | 69 |
| ETS9 | D | 24 (76) | 243 (35.3) | 431 (62.5) | 1.000 | 1.000 | 34.3 | 69 |
| ETS10 | D | 204 (400) | 191 (27.7) | 358 (51.9) | .785 | .830 | 26.0 | 64 |
| ETS11 | D | 454 (850) | 156 (22.6) | 364 (52.8) | .640 | .845 | 24.7 | 59 |
| ETS12 | D | 510 (950) | 150 (21.8) | 329 (47.7) | .618 | .763 | 22.5 | 66 |

TABLE 8.11

TENSILE PROPERTIES OF 2¼Cr-1Mo STEEL

| Specimen Number | Heat Treatment | Test Temp. °C (°F) | Strength, MPa (KSI) Yield 0.2% Offset | Ultimate | Strength Ratio Yield | Ultimate | Total Elongation, % in 25.4 mm | Reduction in Area, % |
|---|---|---|---|---|---|---|---|---|
| Heat ESR R0110 - 0.10% C | | | | | | | | |
| D12-1 | L + A2 | 21 (70) | 340 (49.3) | 504 (73.1) | 1.000 | 1.000 | 31.2 | 71.8 |
| D12-2 | L + A2 | 371 (700) | 281 (40.8) | 504 (73.1) | .828 | 1.000 | 19.8 | 61.3 |
| D12-3 | L + A2 | 454 (850) | 279 (40.4) | 476 (69.1) | .820 | .945 | 21.1 | 68.6 |
| D12-4 | L + A2 | 510 (950) | 257 (37.3) | 440 (63.8) | .757 | .873 | 24.1 | 73.5 |
| D16-2 | L + H | 454 (850) | 199 (28.9) | 422 (61.2) | --- | --- | 27.4 | 66.8 |
| D16-3 | L + H | 510 (950) | 194 (28.1) | 384 (55.7) | --- | --- | 21.9 | 70.0 |
| D16-1 | L + H | 566 (1050) | 195 (28.3) | 320 (46.4) | --- | --- | 30.7 | 77.4 |
| D16-4 | L + H | 566 (1050) | 190 (27.5) | 336 (48.8) | --- | --- | 29.0 | 77.1 |
| Heat VAR 55262 - 0.10% C | | | | | | | | |
| T20 | M | 24 (76) | 241 (35.0) | 479 (69.5) | 1.000 | 1.000 | 31.6 | 72.4 |
| T21 | M | 204 (400) | 222 (32.2) | 421 (61.0) | .920 | .878 | 26.9 | 70.7 |
| T22 | M | 371 (700) | 256 (37.1) | 483 (70.0) | 1.060 | 1.007 | 21.8 | 62.7 |
| T23 | M | 454 (850) | 236 (34.2) | 475 (68.9) | .977 | .991 | 22.9 | 68.6 |
| T24 | M | 510 (950) | 243 (35.2) | 456 (66.2) | 1.006 | .953 | 25.9 | 72.9 |
| T25 | M | 566 (1050) | 215 (31.2) | 383 (55.5) | .891 | .799 | 31.0 | 80.1 |

TABLE 8.11

TENSILE PROPERTIES OF 2¼Cr-1Mo STEEL - 1½ INCH DIAMETER TUBING*

| Wall Thickness mm (in.) | Heat Treatment | Test Temp. °C (°F) | Strength, MPa (KSI) Yield 0.2% Offset | Ultimate | Strength Ratio Yield | Ultimate | Total Elongation, % in 25.4 mm | Reduction in Area, % |
|---|---|---|---|---|---|---|---|---|
| Heat Air X6216 - 0.11% C | | | | | | | | |
| 7.32 (.288) | N | 21 (70) | 306 (44.4) | 543 (78.7) | 1.00 | 1.00 | 21.2 | 75.0 |
| 8.92 (.351) | N | 21 (70) | 312 (45.2) | 541 (78.5) | 1.00 | 1.00 | 20.3 | 73.0 |
| 8.33 (.328) | N | 21 (70) | 410 (59.5) | 552 (80.0) | 1.00 | 1.00 | 19.0 | 72.7 |
| 8.97 (.353) | N | 21 (70) | 322 (46.7) | 546 (79.2) | 1.00 | 1.00 | 21.7 | 75.3 |
| 7.32 (.288) | N | 454 (850) | 271 (39.3) | 524 (76.0) | 0.89 | 0.97 | 15.5 | 75.1 |
| 8.92 (.351) | N | 454 (850 | 282 (40.9) | 538 (78.1) | 0.90 | 0.99 | 15.3 | 72.2 |
| 8.33 (.328) | N | 454 (850) | 350 (50.8) | 575 (83.4) | 0.85 | 1.04 | 14.1 | 70.8 |
| 8.97 (.353) | N | 454 (850) | 290 (42.0) | 541 (78.4) | 0.90 | 0.99 | 15.4 | 75.0 |
| 7.32 (.288) | N | 510 (950) | 270 (39.1) | 485 (70.3) | 0.88 | 0.89 | 17.2 | 79.6 |
| 8.92 (.315) | N | 510 (950) | 275 (39.9) | 496 (72.0) | 0.88 | 0.92 | 17.1 | 78.1 |
| 8.33 (.328) | N | 510 (950) | 345 (50.1) | 517 (75.0) | 0.84 | 0.94 | 16.0 | 75.4 |
| 8.97 (.353) | N | 510 (950) | 282 (40.9) | 503 (73.0) | 0.88 | 0.92 | 17.5 | 77.7 |
| Heat Air 72768 - 0.09% C | | | | | | | | |
| 8.97 (.353) | N | 21 (70) | 290 (42.0) | 488 (70.8) | 1.00 | 1.00 | 23.2 | 66.1 |
| 8.97 (.353) | N | 454 (850) | 232 (33.7) | 476 (69.1) | 0.80 | 0.98 | 17.1 | 76.4 |
| 8.97 (.353) | N | 510 (950) | 218 (31.6) | 448 (65.0) | 0.75 | 0.92 | 15.7 | 64.1 |

* ORNL Data (2)

anneals without post weld heat treatment. For the long term isothermal anneals or the full anneal, the strength is in some cases below the Code expected minimum. Post weld heat treatment reduces the strength of the short anneals below the Code expected minimum, and reduces the strength of the long isothermal anneals and the full anneal below the NSMH lower tolerance curve at elevated temperatures. Data generated by ORNL[24] on air-melted 2¼Cr-1Mo steel of approximately the same carbon content is included here for comparison with remelted data. The results for air melted material indicate that the relation of strength to temperature (incomplete vs. complete phase transformation) during heat treatment is independent of melting practice. A representative set of plots of these parameters versus temperature are shown in Figures 8.15 to 8.22. Charpy V-notch tests show that the VAR and ESR material has excellent upper shelf energy absorption. It also has satisfactory reference nil-ductility transition temperatures ($RT_{NDT}$) for hydrostatic testing of units fabricated from similar material at $RT_{NDT}$ + 33°C (60°F). The results of these tests are listed in Tables 8.12 and 8.13. These impact toughness results are a reflection of the low levels of non-metallic inclusions, primarily those containing phosphorus and sulfur. The chemical composition and microinclusion count are given in Tables 8.14 and 8.15, respectively. The cleanliness of these heats is also reflected in the relatively small increase in $RT_{NDT}$ after isothermal embrittlement heat treatment. The values of absorbed energy, lateral expansion, and precent shear fracture for ESR heat 91505 are shown in Figures 8.23, 8.24 and 8.25.

A summary of the creep-rupture results at 454, 510, and 566°C is given in Table 8.16. Plots of log stress-log minimum creep rate, log stress-log time to tertiary creep, and log stress-log rupture time at 510°C are given in Figures 8.26, 8.27, and 8.28. All of the minimum creep rate data can be seen to lie between the NSMH tolerance limits. The time to tertiary creep is consistently above the Code Case 1592 expected minimum curve* for the three heat treatments considered. Two of these three heat treatments show stress to rupture less than that of the Code Case 1592 expected minimum curve and the NSMH lower tolerance limit, for rupture times under 1000 hours. These heat treatments are a 90 minute -

*Derived from $S_t/0.8$, this assumes $S_t$ is set by time to tertiary creep.

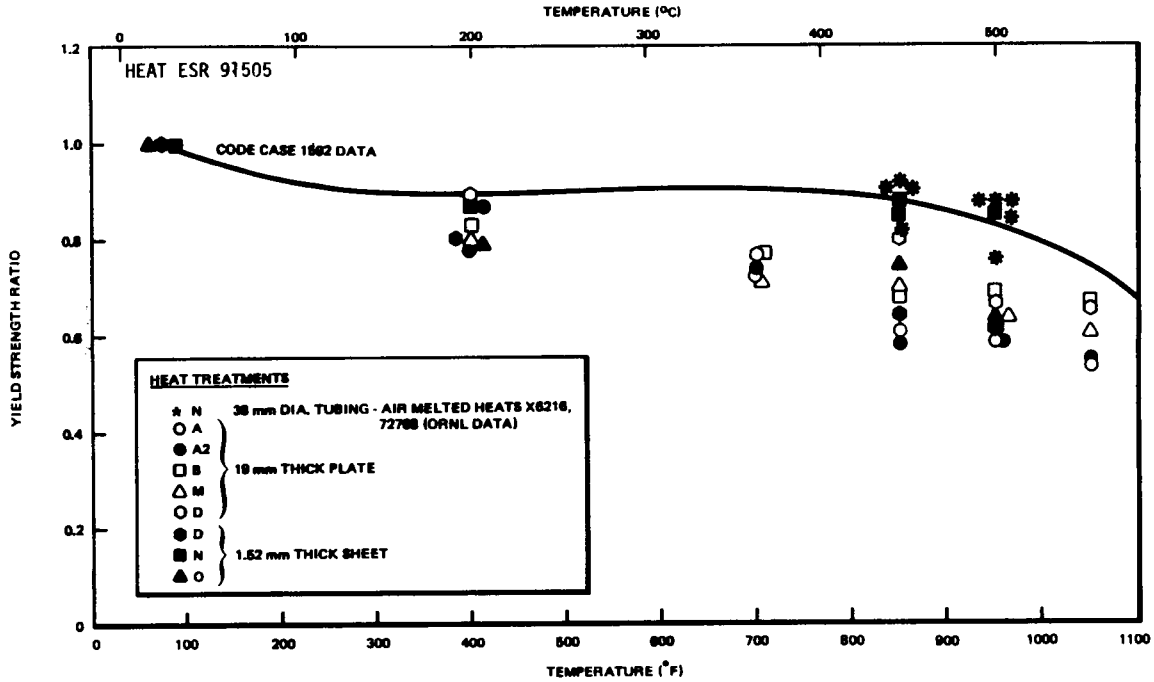


Figure 8.15 Variation of Yield Strength Ratio with Temperature

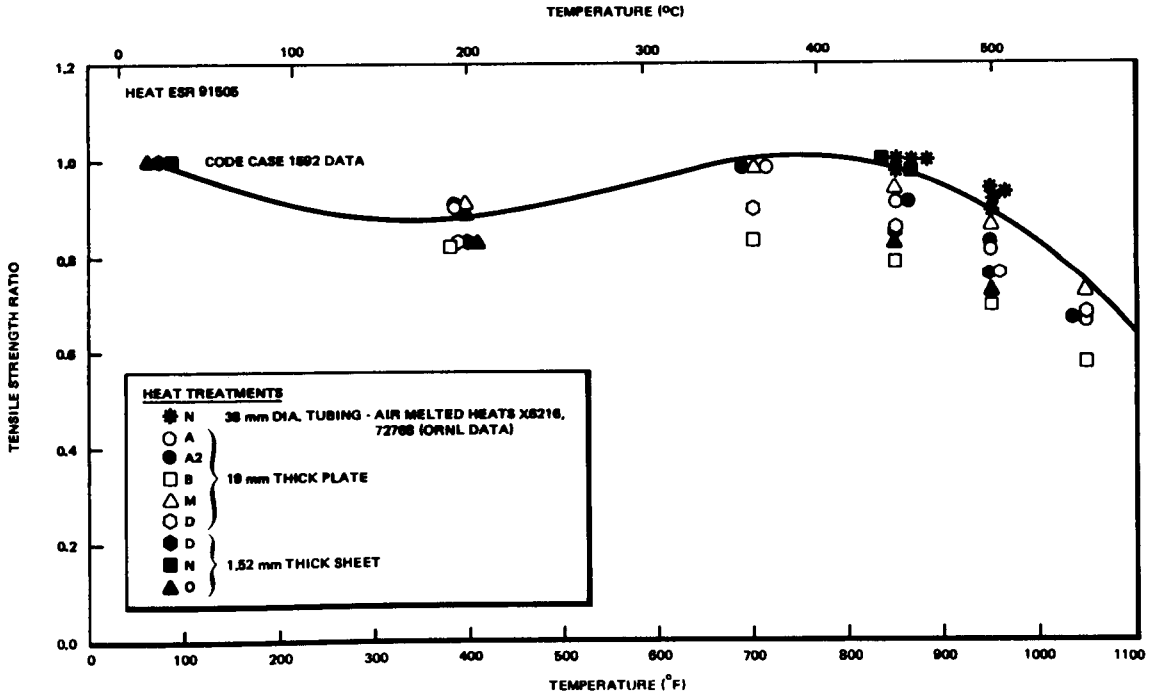


Figure 8.16 Variation of Tensile Strength Ratio with Temperature

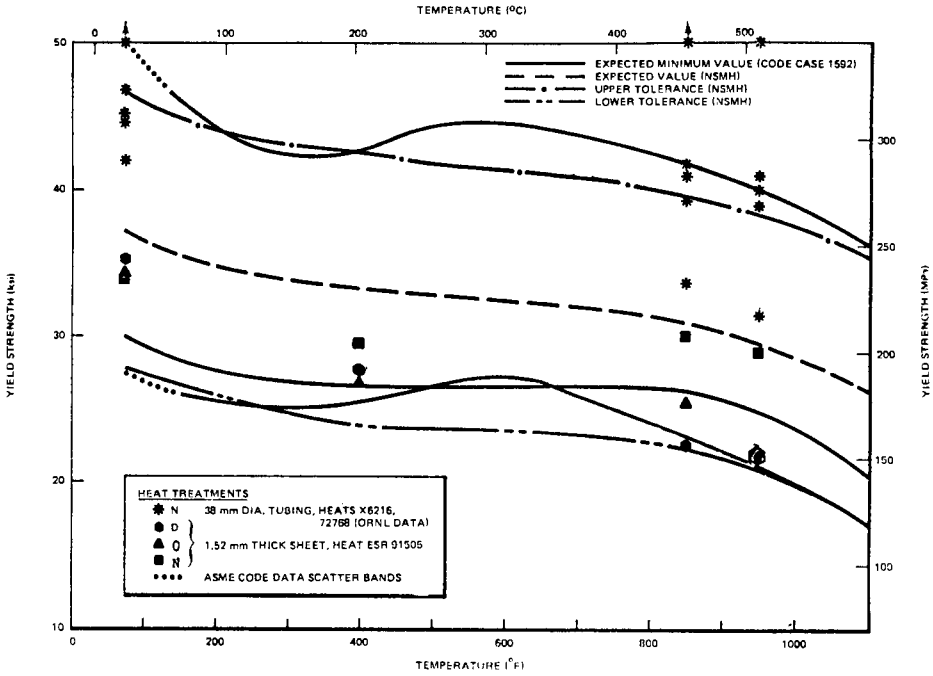


Figure 8.17 Variation of Yield Strength with Temperature

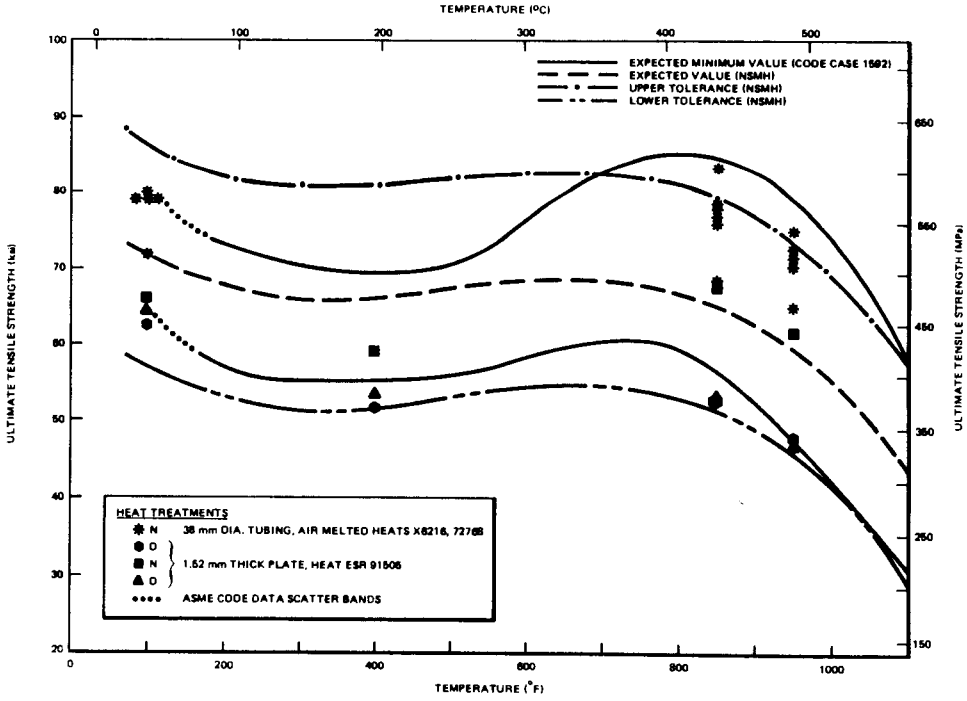


Figure 8.18 Variation of Ultimate Tensile Strength with Temperature

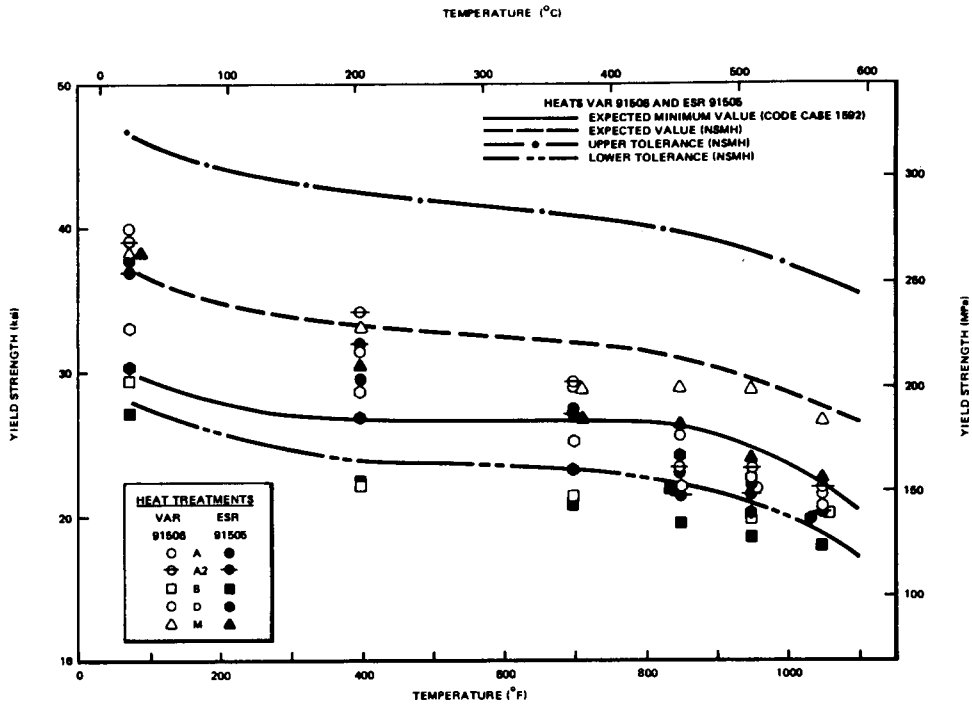


Figure 8.19 Variation of Yield Strength with Temperature

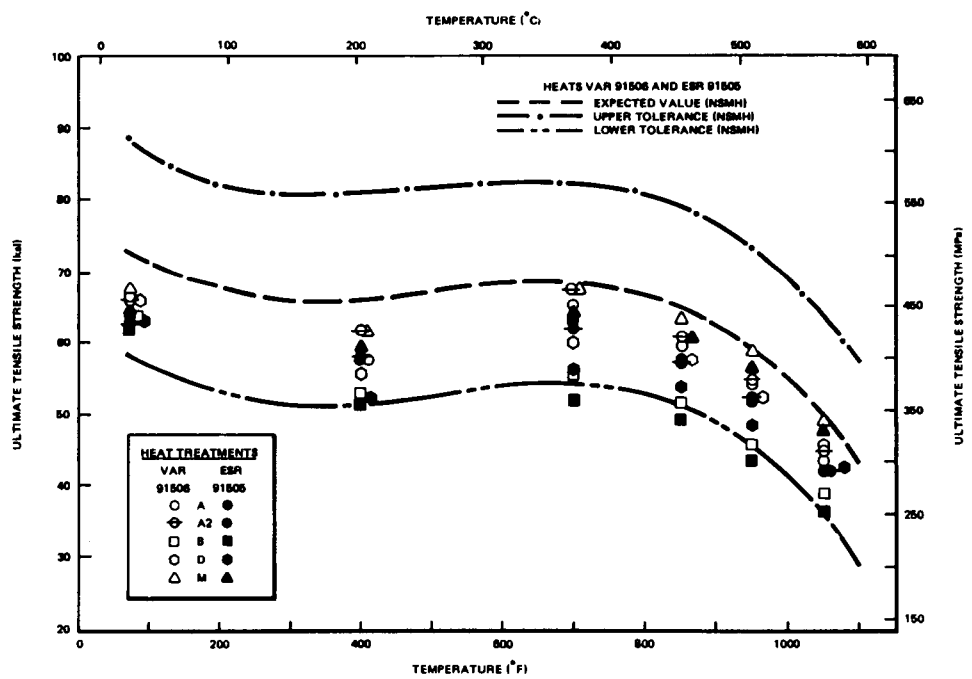


Figure 8.20 Variation of Ultimate Tensile Strength with Temperature

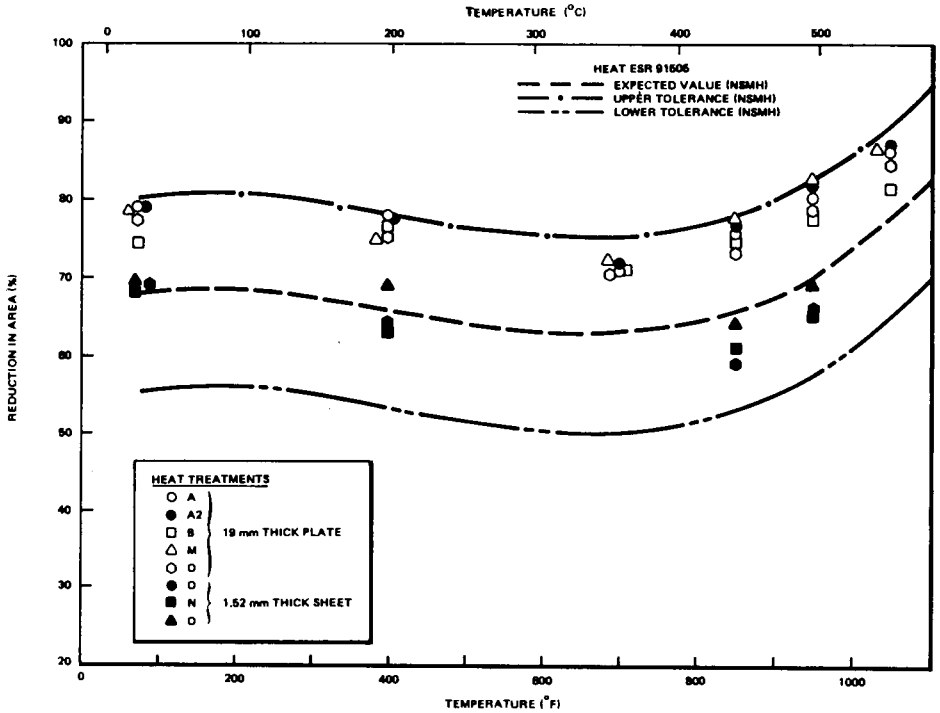


Figure 8.21 Variation of Reduction in Area with Temperature

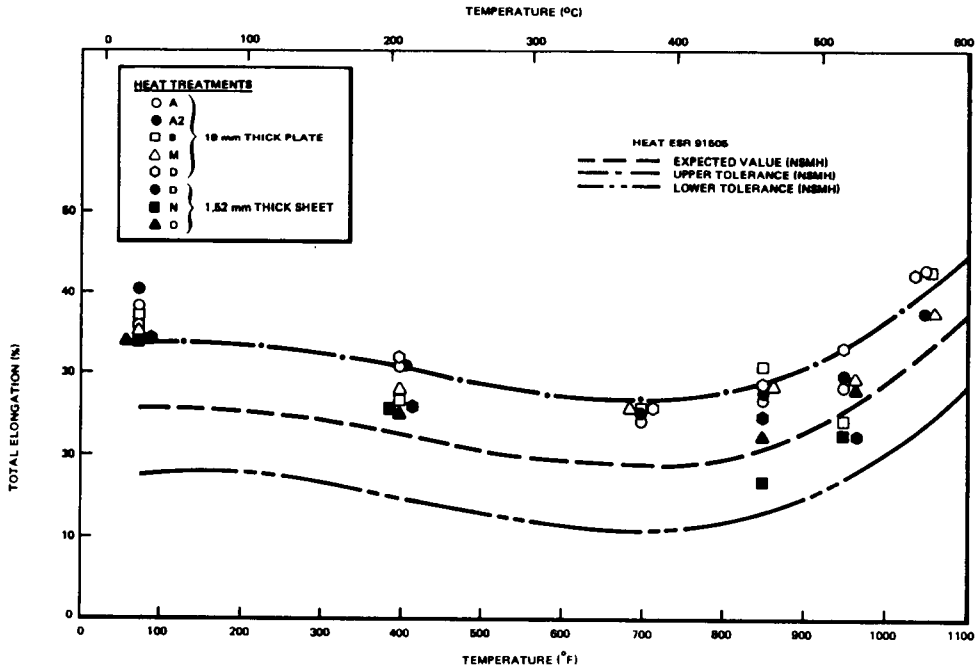


Figure 8.22 Variation of Total Elongation in 25.4 mm with Temperature

TABLE 8.12

CHARPY V-NOTCH RESULTS FOR 2¼Cr-1Mo STEEL

| Specimen No. | CVN J (ft.-lb.) | Temp. °C (°F) | Lateral Expansion µm (mils) | Shear Fracture (%) Observation Avg. of 3 | Heat. No. | Heat Treatment | Orientation |
|---|---|---|---|---|---|---|---|
| VV2 | 5.4 (4.0) | -46 (-50) | 102 (4) | 2 | VAR 91506 | A2 | Transverse |
| VV11 | 4.6 (3.4) | -32 (-25) | 127 (5) | 4 | VAR 91506 | A2 | Transverse |
| VV3 | 4.7 (3.5) | -32 (-25) | 152 (6) | 4 | VAR 91506 | A2 | Transverse |
| VV7 | 14.0 (10.3) | -29 (-20) | 305 (12) | 4 | VAR 91506 | A2 | Transverse |
| VV9 | 222.4 (164.0) | -29 (-20) | 2740 (108) | 66 | VAR 91506 | A2 | Transverse |
| VV5 | 146.6 (108.1) | -26 (-15) | 2760 (97) | 33 | VAR 91506 | A2 | Transverse |
| VV8 | 13.6 (10.0) | -23 (-10) | 279 (11) | 4 | VAR 91506 | A2 | Transverse |
| VV6 | 104.1 (76.8) | -23 (-10) | 1910 (75) | 21 | VAR 91506 | A2 | Transverse |
| VV10 | >322.7 (>238.0) | -21 (-5) | 2390 (94) | 100 | VAR 91506 | A2 | Transverse |
| VV4 | >324.0 (>239.0) | -17 (0) | 2240 (88) | 100 | VAR 91506 | A2 | Transverse |
| VV12 | >307.8 (>227.0) | 121 (250) | 2460 (97) | 100 | VAR 91506 | A2 | Transverse |
| VV13 | >279.3 (>206.0) | 288 (550) | 2620 (103) | 100 | VAR 91506 | A2 | Transverse |

TABLE 8.12

CHARPY V-NOTCH RESULTS FOR 2¼Cr-1Mo STEEL

| Specimen No. | CVN J (ft.-lb.) | Temp. °C (°F) | Lateral Expansion µm (mils) | Shear Fracture (%) Observation Avg. of 3 | Heat No. | Heat Treatment | Orientation |
|---|---|---|---|---|---|---|---|
| EV15 | 4.9 (3.6) | -46 (-50) | 76 (3) | 2 | ESR 91505 | B | Transverse |
| EV16 | 9.9 (7.3) | -32 (-25) | 254 (10) | 4 | ESR 91505 | B | Transverse |
| EV18 | 17.6 (13.0) | -26 (-15) | 432 (17) | 4 | ESR 91505 | B | Transverse |
| EV21 | 21.7 (16.0) | -23 (-10) | 533 (21) | 8 | ESR 91505 | B | Transverse |
| EV23 | 17.6 (13.0) | -23 (-10) | 432 (17) | 13 | ESR 91505 | B | Transverse |
| EV22 | 99.4 (73.3) | -21 (-5) | 1730 (68) | 27 | ESR 91505 | B | Transverse |
| EV14 | 108.4 (80.0) | -21 (-5) | 1980 (78) | 23 | ESR 91505 | B | Transverse |
| EV17 | 132.6 (97.8) | -17 (0) | 2290 (90) | 34 | ESR 91505 | B | Transverse |
| EV24 | 93.6 (69.0) | -15 (5) | 1700 (67) | 23 | ESR 91505 | B | Transverse |
| EV20 | >322.7 (>238.0) | -12 (10) | 2390 (94) | 100 | ESR 91505 | B | Transverse |
| EV19 | >322.7 (>238.0) | -3.9(25) | -- -- | 100 | ESR 91505 | B | Transverse |
| EV25 | >304.4 (>224.5) | 121 (250) | 1980 (78) | 100 | ESR 91505 | B | Transverse |
| EV26 | >260.0 (>192.0) | 288 (550) | 2010 (79) | 100 | ESR 91505 | B | Transverse |

TABLE 8.12

CHARPY V-NOTCH RESULTS FOR 2¼Cr-1Mo STEEL

| Specimen No. | CVN J (ft.-lb.) | Temp. °C (°F) | Lateral Expansion μm (mils) | Shear Fracture (%) Observation Avg. of 3 | Heat No. | Heat Treatment | Orientation |
|---|---|---|---|---|---|---|---|
| VV15 | 3.9 (2.9) | -46 (-50) | 76 (3) | 2 | VAR 91506 | B | Transverse |
| VV16 | 6.5 (4.8) | -32 (-25) | 127 (5) | 3 | VAR 91506 | B | Transverse |
| VV14 | 13.8 (10.2) | -21 (-5) | 330 (13) | 4 | VAR 91506 | B | Transverse |
| VV17 | 12.2 (9.0) | -17 (0) | 330 (13) | 8 | VAR 91506 | B | Transverse |
| VV23 | 116.6 (86.0) | -9.4 (15) | 2080 (82) | 23 | VAR 91506 | B | Transverse |
| VV19 | 39.3 (29.0) | -6.7 (20) | 864 (34) | 10 | VAR 91506 | B | Transverse |
| VV18 | 108.4 (80.0) | -3.9 (25) | 2010 (79) | 23 | VAR 91506 | B | Transverse |
| VV21 | 108.4 (80.0) | -3.9 (25) | 1980 (78) | 23 | VAR 91506 | B | Transverse |
| VV20 | 148.9 (109.8) | 1.7 (35) | 2410 (95) | 40 | VAR 91506 | B | Transverse |
| VV24 | 149.1 (110.0) | 4.4 (40) | 2360 (93) | 35 | VAR 91506 | B | Transverse |
| VV22 | >324.0 (>239.0) | 7.2 (45) | -- -- | 100 | VAR 91506 | B | Transverse |
| VV25 | >282.7 (>208.5) | 121 (250) | 2490 (98) | 100 | VAR 91506 | B | Transverse |
| VV26 | >267.1 (>197.0) | 288 (550) | 2160 (85) | 100 | VAR 91506 | B | Transverse |

TABLE 8.12

CHARPY V-NOTCH RESULTS FOR 2¼Cr-1Mo STEEL

| Specimen No. | CVN J (ft.-lb.) | | Temp. °C (°F) | | Lateral Expansion μm (mils) | | Shear Fracture (%) Observation Avg. of 3 | Heat No. | Heat Treatment | Orientation |
|---|---|---|---|---|---|---|---|---|---|---|
| ED9-1 | 6.5 | (4.8) | -46 | (-50) | 102 | (4) | 2 | ESR 91505 | G | Transverse |
| ED9-2 | 5.4 | (4.0) | -46 | (-50) | 76 | (3) | 2 | ESR 91505 | G | Transverse |
| ED10-1 | 35.3 | (26.0) | -32 | (-25) | 711 | (28) | 7 | ESR 91505 | G | Transverse |
| ED10-2 | 5.4 | (4.0) | -32 | (-25) | 127 | (5) | 3 | ESR 91505 | G | Transverse |
| ED11-1 | 13.6 | (10.0) | -26 | (-15) | 229 | (9) | 7 | ESR 91505 | G | Transverse |
| ED11-2 | 7.6 | (5.6) | -26 | (-15) | 102 | (4) | 3 | ESR 91505 | G | Transverse |
| ED12-1 | 32.8 | (24.2) | -17 | (0) | 610 | (24) | 7 | ESR 91505 | G | Transverse |
| ED12-2 | 35.5 | (26.2) | -17 | (0) | 711 | (28) | 9 | ESR 91505 | G | Transverse |
| ED14-1 | 170.8 | (126.0) | -3.9 | (25) | 2410 | (95) | 50 | ESR 91505 | G | Transverse |
| ED14-2 | 141.0 | (104.0) | -3.9 | (25) | 2290 | (90) | 40 | ESR 91505 | G | Transverse |
| ED16-1 | -- | -- | 24 | (75) | 2260 | (89) | 45 | ESR 91505 | G | Transverse |

TABLE 8.12

CHARPY V-NOTCH RESULTS FOR 2¼Cr-1Mo STEEL

| Specimen No. | CVN J (ft.-lb.) | | Temp. °C (°F) | | Lateral Expansion µm (mils) | | Shear Fracture (%) Observation Avg. of 3 | Heat No. | Heat Treatment | Orientation |
|---|---|---|---|---|---|---|---|---|---|---|
| VD9-1 | 3.0 | (2.2) | -46 | (-50) | 51 | (2) | 1 | VAR 91506 | G | Transverse |
| VD9-2 | 4.1 | (3.0) | -46 | (-50) | 51 | (2) | 2 | VAR 91506 | G | Transverse |
| VD10-1 | 5.3 | (3.9) | -32 | (-25) | 76 | (3) | 2 | VAR 91506 | G | Transverse |
| VD10-2 | 4.1 | (3.0) | -32 | (-25) | 76 | (3) | 3 | VAR 91506 | G | Transverse |
| VD11-1 | 7.2 | (5.3) | -26 | (-15) | 127 | (5) | 2 | VAR 91506 | G | Transverse |
| VD11-2 | 14.9 | (11.0) | -26 | (-15) | 127 | (5) | 3 | VAR 91506 | G | Transverse |
| VD12-1 | 19.0 | (14.0) | -17 | (0) | 381 | (15) | 2 | VAR 91506 | G | Transverse |
| VD12-2 | 19.0 | (14.0) | -17 | (0) | 432 | (17) | 4 | VAR 91506 | G | Transverse |
| VD13-2 | 199.8 | (147.4) | -15 | (5) | 2520 | (99) | 70 | VAR 91506 | G | Transverse |
| VD14-1 | 93.6 | (69.0) | -3.9 | (25) | 1700 | (67) | 27 | VAR 91506 | G | Transverse |
| VD14-2 | 41.4 | (30.5) | -3.9 | (25) | 838 | (33) | 9 | VAR 91506 | G | Transverse |
| VD16-1 | 73.2 | (54.0) | 24 | (75) | 1350 | (53) | 25 | VAR 91506 | G | Transverse |
| VD16-2 | 242.7 | (>179.0) | 38 | (100) | 2210 | (87) | 100 | VAR 91506 | G | Transverse |

TABLE 8.12

CHARPY V-NOTCH RESULTS FOR 2¼Cr-1Mo STEEL

| Specimen No. | CVN J (ft.-lb.) | Temp. °C (°F) | Lateral Expansion μm (mils) | Shear Fracture (%) Observation Avg. of 3 | Heat No. | Heat Treatment | Orientation |
|---|---|---|---|---|---|---|---|
| EV9 | 3.4 (2.5) | -59 (-75) | 25 (1) | 2 | ESR 91505 | A2 | Transverse |
| EV2 | 16.0 (11.8) | -46 (-50) | 356 (14) | 4 | ESR 91505 | A2 | Transverse |
| EV7 | 16.3 (12.0) | -32 (-25) | 356 (14) | 5 | ESR 91505 | A2 | Transverse |
| EV6 | >324.0 (>239.0) | -29 (-20) | 2770 (109) | 100 | ESR 91505 | A2 | Transverse |
| EV8 | >322.7 (>238.0) | -29 (-20) | 2490 (98) | 100 | ESR 91505 | A2 | Transverse |
| EV11 | >324.0 (>239.0) | -29 (-20) | 2600 (102) | 100 | ESR 91505 | A2 | Transverse |
| EV5 | >324.0 (>239.0) | -26 (-15) | 2620 (103) | 100 | ESR 91505 | A2 | Transverse |
| EV4 | >324.0 (>239.0) | -17 (0) | 2460 (97) | 100 | ESR 91505 | A2 | Transverse |
| EV1 | >324.0 (>239.0) | 24 (75) | 2260 (89) | 100 | ESR 91505 | A2 | Transverse |
| EV10 | >322.7 (>238.0) | 66 (150) | -- -- | 100 | ESR 91505 | A2 | Transverse |
| EV12 | >308.9 (>227.8) | 121 (250) | 1910 (75) | 100 | ESR 91505 | A2 | Transverse |
| EV13 | >284.7 (>210.0) | 288 (550) | 2160 (85) | 100 | ESR 91505 | A2 | Transverse |

TABLE 8.13

SUMMARY OF CHARPY IMPACT AND DROP-WEIGHT TEST DATA FOR 2¼Cr-1Mo STEEL

ASTM Standard E23-72

| Heat No. | Heat Treatment | Orientation | 67.5 J (50 ft.-lb.) Energy Temp. °C (°F) | 0.889 mm (35 mils) Lateral Expansion Temp. °C (°F) | 50% Shear Fracture Temp. °C (°F) | Nil Ductility Temp., **(NDT) °C (°F) | Reference NDT*** °C (°F) | Upper Shelf Energy J (ft.-lb.) |
|---|---|---|---|---|---|---|---|---|
| VAR 91506 | A2 | Transverse | -26 (-15) | -23 (-10) | -23 (-10) | -- | -- | >324 (240) |
| VAR 91506 | B | Transverse | -3.9 (25) | -6.7 (20) | 1.7 (35) | -18 (0) | -18 (0) | >324 (240) |
| VAR 91506 | G | Transverse | 10 (50)* | 24 (75)* | 32 (90)* | -6.7 (20) | 24 (75)* | >324 (240) |
| ESR 91505 | A2 | Transverse | -32 (-25) | -32 (-25) | -6.7 (-20) | -- | -- | >324 (240) |
| ESR 91505 | B | Transverse | -15 (5) | -18 (0) | -15 (5) | -18 (0) | -18 (0) | >324 (240) |
| ESR 91505 | G | Transverse | -12 (10) | -15 (5) | -3.9 (25) | -18 (0) | -18 (0) | >324 (240) |

* Approximate temperatures - insufficient data to determine precise values
** Determined from Drop-weight Tests
*** Determined according to NB-2300

TABLE 8.14

CHEMICAL ANALYSIS OF 2¼Cr-1Mo STEEL

| | VAR 91506 Check Chemical Analysis (Anamet) | ESR 91505 Check Chemical Analysis (Anamet) | Estimated Detection Limits | RDT M2-19 RDT M3-33 Minimum | Maximum |
|---|---|---|---|---|---|
| Aluminum | <0.005% | 0.017% | 0.005% | | |
| Antimony | <0.002% | <0.002% | 0.002% | | |
| Arsenic | 0.006% | 0.006% | 0.002% | | |
| Carbon | 0.102% | 0.087% | 0.005% | 0.070% | 0.110% |
| Chromium | 2.32% | 2.31% | 0.01% | 1.90% | 2.60% |
| Cobalt | 0.008% | 0.007% | 0.005% | | |
| Copper | 0.04% | 0.04% | 0.01% | | 0.35% |
| Hydrogen | 0.0009% | 0.0007% | 0.0001% | | |
| Manganese | 0.42% | 0.47% | 0.01% | 0.30% | 0.60% |
| Molybdenum | 1.00% | 0.99% | 0.01% | 0.87% | 1.13% |
| Nickel | 0.06% | 0.05% | 0.005% | 0.25% | |
| Nitrogen | 0.009% | 0.008% | 0.001% | | |
| Oxygen | 0.005% | 0.013% | 0.001% | | |
| Phosphorus | 0.007% | 0.007% | 0.003% | | 0.015% |
| Silicon | 0.32% | 0.26% | 0.01% | 0.20% | 0.40% |
| Sulfur | 0.008% | 0.003% | 0.002% | | 0.015% |
| Tin | <0.002% | <0.002% | 0.002% | | |
| Titanium | 0.003% | <0.002% | 0.002% | | 0.03% |
| Vanadium | 0.006% | 0.006% | 0.002% | | 0.03% |

TABLE 8.15

INCLUSION CONTENT DETERMINATION BY ASTM E45-D

| Position | Inclusion Type | | | |
|---|---|---|---|---|
| | A | B | C | D |
| | **191 mm (7.5 in.) Square Billets** | | | |
| **VAR Heat #91506** | | | | |
| Edge | | | | |
| Thin | --- | --- | --- | 1 |
| Heavy | --- | --- | --- | --- |
| Midsection | | | | |
| Thin | --- | --- | --- | 1 |
| Heavy | --- | 1 | --- | --- |
| Center | | | | |
| Thin | --- | --- | --- | 1 |
| Heavy | --- | 1 | --- | --- |
| **ESR Heat #91505** | | | | |
| Edge | | | | |
| Thin | --- | --- | --- | 1 |
| Heavy | --- | --- | --- | --- |
| Midsection | | | | |
| Thin | --- | --- | --- | 1 |
| Heavy | --- | --- | --- | --- |
| Center | | | | |
| Thin | --- | --- | --- | 1 |
| Heavy | --- | --- | --- | --- |
| | **19.1 mm (.75 in.) Thick Plates** | | | |
| **VAR Heat #91506** | | | | |
| Edge | | | | |
| Thin | --- | --- | ½ | --- |
| Heavy | --- | --- | --- | --- |
| Midsection | | | | |
| Thin | --- | --- | --- | 1 |
| Heavy | --- | --- | --- | --- |
| Center | | | | |
| Thin | --- | ½ | --- | --- |
| Heavy | --- | --- | --- | ½ |

TABLE 8.15

INCLUSION CONTENT DETERMINATION BY ASTM E45-D

| Position | Inclusion Type | | | |
|---|---|---|---|---|
| | A | B | C | D |
| | 19.1 mm (.75 in.) Thick Plates | | | |
| ESR Heat #91505 | | | | |
| Edge | | | | |
| Thin | --- | --- | --- | --- |
| Heavy | --- | 1½ | --- | 1 |
| Midsection | | | | |
| Thin | --- | --- | --- | 1 |
| Heavy | --- | 1 | --- | --- |
| Center | | | | |
| Thin | --- | --- | --- | 1 |
| Heavy | --- | 1½ | --- | --- |
| | RDT M3-33 and M2-19 | | | |
| Thin | 1½ | 1½ | 1½ | 1½ |
| Heavy | 1 | 1 | 1 | 1 |

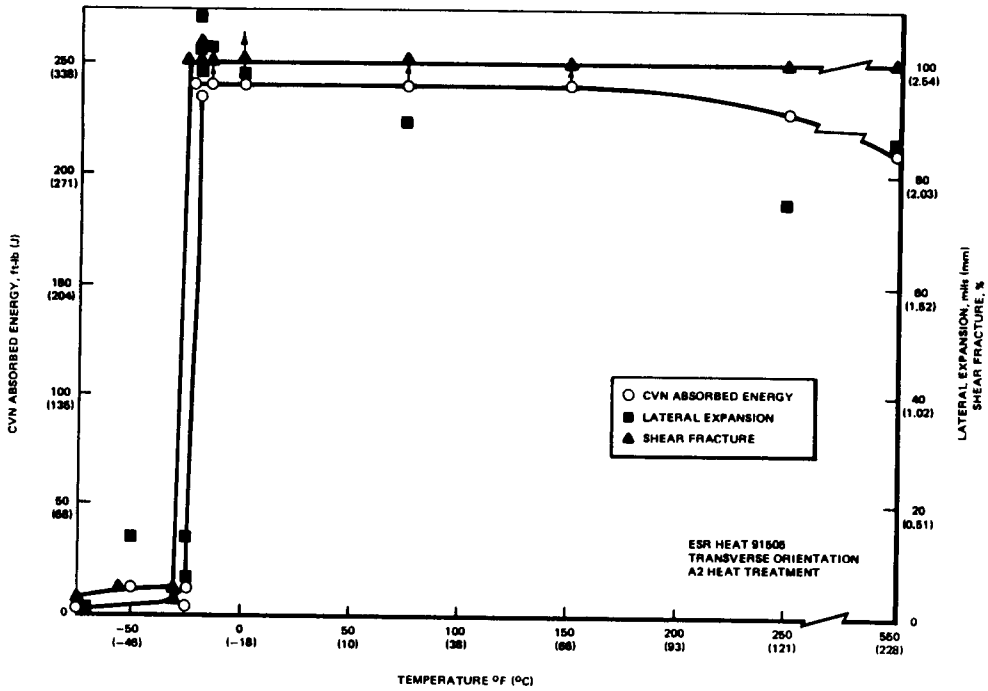


Figure 8.23 Variation of Charpy Impact Properties with Temperature for 19 mm Thick Plate

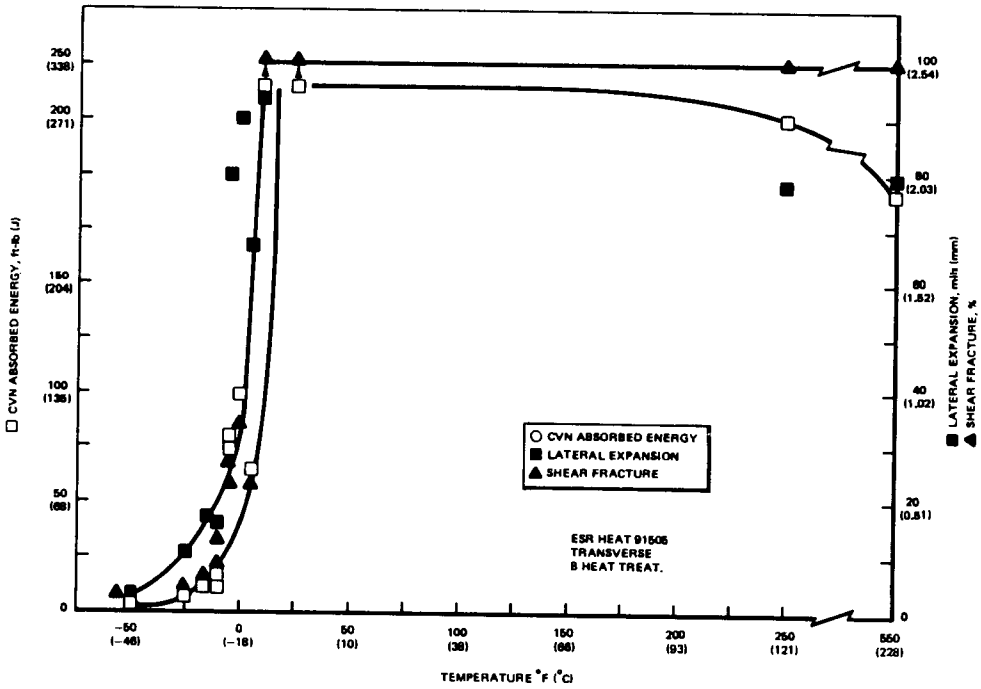


Figure 8.24 Variation of Charpy Impact Properties with Temperature for 19 mm Thick Plates

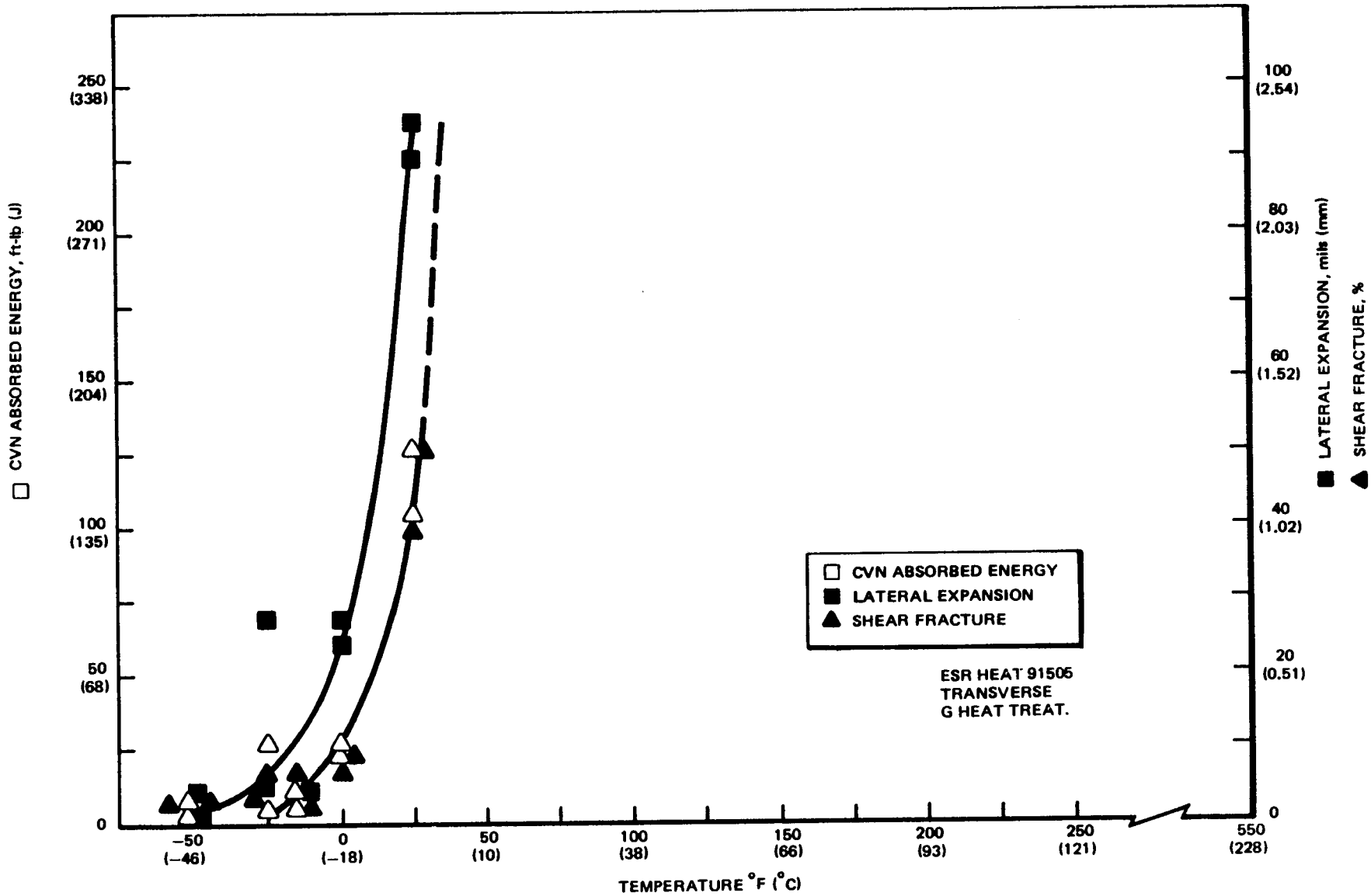


Figure 8.25 Variation of Charpy Impact Properties with Temperature for 19 mm Thick Plates

TABLE 8.16

CREEP-RUPTURE DATA FOR 2¼Cr-1Mo STEEL

| SPECIMEN NUMBER | HEAT TREATMENT | STRESS MPa (KSI) | RUPTURE TIME (hr.) | TIME TO THIRD* STAGE (hr.) | STRAIN TO THIRD* STAGE (%) | MINIMUM CREEP* RATE (%/hr.) | ELONGATION (%) | REDUCTION IN AREA (%) | PLASTIC ON LOADING (%) |
|---|---|---|---|---|---|---|---|---|---|
| Heat VAR 91506 | | | | | 454°C (850°F) | | | | |
| VC1 | A2 | 379.2 (55) | 78.6 | 51.8 | 2.95 | 0.0392 | 25.4 | 75.2 | 6.0+ |
| VC16 | B | 379.2 (55) | ** | --- | --- | --- | 24.1 | 70.7 | 8.0+ |
| VC4 | A2 | 358.5 (52) | 141.9 | 96.6 | 3.25 | 0.0249 | 25.5 | 75.2 | 5.9 |
| VC19 | B | 358.5 (52) | ** | --- | --- | --- | 25.0 | 69.5 | 7.0+ |
| VC7 | A2 | 330.9 (48) | 422.0 | 235 | 2.59 | 0.00660 | 27.6 | 78.1 | 3.1 |
| VC22 | B | 330.9 (48) | 3.1 | 2.6 | 8.90 | 2.15 | 29.9 | 72.7 | 6.0+ |
| VC25 | B | 275.8 (40) | 273.8 | 158 | 8.38 | 0.0454 | 36.3 | 76.7 | 2.9 |
| VC28 | B | 241.3 (35) | 1456.0 | 338 | 11.20 | 0.0312 | 42.5 | 81.3 | 2.1 |
| | | | | | 510°C (950°F) | | | | |
| VC2 | A2 | 241.3 (35) | 104.0 | 36.8 | 1.99 | 0.0397 | 41.0 | 84.4 | 1.4 |
| VC17 | B | 241.3 (35) | 20.3 | 5.0 | 4.90 | 0.756 | 45.3 | 83.4 | 2.3 |
| VT17 | H | 241.3 (35) | 16.2 | 8.9 | 7.20 | 0.751 | 41.0 | 82.2 | 2.2 |
| VC5 | A2 | 206.8 (30) | 235.1 | 59.9 | 1.50 | 0.188 | 49.1 | 85.7 | 0.9 |
| VC20 | B | 206.8 (30) | 113.9 | 32.2 | 5.80 | 0.151 | 52.3 | 83.8 | 1.4 |
| VT18 | H | 206.8 (30) | 57.7 | 15.4 | 3.85 | 0.203 | 49.5 | 86.2 | 1.5 |
| VC8 | A2 | 172.4 (25) | 790.4 | 114 | 1.17 | 0.00722 | 59.7 | 89.3 | 0.4 |
| VC23 | B | 172.4 (25) | 602.0 | 190 | 7.55 | 0.0358 | 59.7 | 86.2 | 0.6 |
| VF5 | H | 172.4 (25) | 318.9 | 85.8 | 4.87 | 0.0544 | 61.3 | 86.2 | 0.7 |
| VC11 | A2 | 151.7 (22) | 1778.6 | 153 | 0.64 | 0.00288 | 56.0 | 89.8 | 0.2 |
| VC26 | B | 151.7 (22) | 1429.1 | 503 | 9.10 | 0.0161 | 66.9 | 87.7 | 0.4 |
| VF6 | H | 151.7 (22) | 783.9 | 312 | 9.20 | 0.0288 | 61.9 | 90.6 | 0.4 |

* Determined by 0.2% strain offset
** Specimen failed on loading

TABLE 8.16

CREEP-RUPTURE DATA FOR 2¼Cr-1Mo STEEL

| SPECIMEN NUMBER | HEAT TREATMENT | STRESS MPa (KSI) | RUPTURE TIME (hr.) | TIME TO THIRD* STAGE (hr.) | STRAIN TO THIRD* STAGE (%) | MINIMUM CREEP* RATE (%/hr.) | ELONGATION (%) | REDUCTION IN AREA (%) | PLASTIC ON LOADING (%) |
|---|---|---|---|---|---|---|---|---|---|
| Heat VAR 91506 | | | | | 566°C (1050°F) | | | | |
| VC3 | A2 | 172.4 (25) | 19.3 | 3.3 | 3.02 | 0.789 | 61.7 | 88.5 | 0.8 |
| VC18 | B | 172.4 (25) | 15.4 | 5.4 | 9.20 | 1.47 | 75.0 | 87.1 | 1.1 |
| VC6 | A2 | 151.7 (22) | 51.6 | 11.2 | 5.10 | 0.411 | 68.7 | 90.5 | 0.3 |
| VC21 | B | 151.7 (22) | 43.8 | 16.4 | 10.55 | 0.564 | 70.7 | 90.6 | 0.6 |
| VC9 | A2 | 124.1 (18) | 201.5 | 18.5 | 8.70 | 0.101 | 56.2 | 90.3 | 0.1 |
| VC24 | B | 124.1 (18) | 213.9 | 73.5 | 8.80 | 0.102 | 68.8 | 90.8 | 0.3 |
| VC12 | A2 | 96.53(14) | 1716.3 | 700 | 8.20 | 0.0106 | 62.7 | 92.8 | 0.0 |
| VC27 | B | 96.53(14) | 1124.0 | 533 | 11.60 | 0.0198 | 68.9 | 93.3 | 0.0 |
| Heat ESR 91505 | | | | | 454°C (850°F) | | | | |
| EC1 | A2 | 379.2 (55) | 14.3 | 7.9 | 1.66 | 0.183 | 23.6 | 75.0 | 6.0+ |
| EC16 | B | 379.2 (55) | ** | --- | --- | --- | 24.9 | 72.1 | 6.0+ |
| EC4 | A2 | 358.5 (52) | 51.1 | 31.3 | 2.50 | 0.0614 | 25.0 | 75.9 | 5.2 |
| EC19 | B | 358.5 (52) | ** | --- | --- | --- | 23.7 | 72.9 | 6.0+ |
| EC7 | A2 | 330.9 (48) | 349.0 | 185 | 3.68 | 0.0139 | 27.3 | 75.2 | 3.7 |
| EC22 | B | 330.9 (48) | 0.2 | --- | --- | --- | 28.7 | 73.3 | 6.0+ |
| EC25 | B | 275.8 (40) | 90.3 | 46.2 | 8.55 | 0.159 | 36.0 | 81.4 | 3.4 |
| EC13 | A2 | 241.3 (35) | *** | --- | --- | --- | --- | --- | --- |
| EC28 | B | 241.3 (35) | 568.0 | 217 | 6.50 | 0.0249 | 43.3 | 81.9 | 2.1 |

* Determined by 0.2% strain offset
** Specimen failed on loading
*** Machine malfunction - no test

TABLE 8.16

CREEP-RUPTURE DATA FOR 2¼Cr-1Mo STEEL

| SPECIMEN NUMBER | HEAT TREATMENT | STRESS MPa (KSI) | RUPTURE TIME (hr.) | TIME TO THIRD* STAGE (hr.) | STRAIN TO THIRD* STAGE (%) | MINIMUM CREEP* RATE (%/hr.) | ELONGATION (%) | REDUCTION IN AREA (%) | PLASTIC ON LOADING (%) |
|---|---|---|---|---|---|---|---|---|---|
| Heat ESR 91505 | | | | | 510°C (950°F) | | | | |
| EC2 | A2 | 241.3 (35) | 85.8 | 25.2 | 1.85 | 0.0488 | 40.4 | 83.6 | 1.8 |
| EC17 | B | 241.3 (35) | 8.2 | 4.2 | 9.40 | 1.99 | 42.8 | 80.9 | 3.0 |
| ET17 | H | 241.3 (35) | 7.6 | 503 | 9.10 | 0.0161 | 42.8 | 83.2 | 2.6 |
| EC5 | A2 | 206.8 (30) | 205.3 | 40.0 | 1.21 | 0.0186 | 48.6 | 85.7 | 1.2 |
| EC20 | B | 206.8 (30) | 56.0 | 4.3 | 8.60 | 1.78 | 49.6 | 84.8 | 1.6 |
| ET18 | H | 206.8 (30) | 44.0 | 10.3 | 3.60 | 0.286 | 41.9 | 85.4 | 1.8 |
| EC8 | A2 | 172.4 (25) | 664.7 | 110 | 1.08 | 0.00509 | 55.6 | 89.8 | 0.4 |
| EC23 | B | 172.4 (25) | 289.0 | 117 | 12.70 | 0.104 | 61.2 | 87.5 | 1.0 |
| EF5 | H | 172.4 (25) | 243.8 | 177 | 6.20 | 0.0327 | 59.6 | 87.1 | 0.9 |
| EC11 | A2 | 151.7 (22) | 1327.0 | 114 | 0.382 | 0.00265 | 60.4 | 89.7 | 0.2 |
| EC26 | B | 151.7 (22) | 741.7 | 588 | 6.09 | 0.00781 | 61.2 | 88.0 | 0.5 |
| EF6 | H | 151.7 (22) | 568.7 | 155 | 5.35 | 0.0326 | 60.1 | 87.7 | 0.5 |
| | | | | | 566°C (1050°F) | | | | |
| EC3 | A2 | 172.4 (25) | 16.3 | 5.3 | 6.35 | 1.09 | 61.8 | 89.7 | 0.9 |
| EC18 | B | 172.4 (25) | 8.8 | 6.6 | 19.00 | 2.72 | 62.2 | 88.3 | 1.4 |
| EC6 | A2 | 151.7 (22) | 41.2 | 19.4 | 14.30 | 0.727 | 71.2 | 90.0 | 0.6 |
| EC21 | B | 151.7 (22) | 26.7 | 10.2 | 8.20 | 0.650 | 69.2 | 88.6 | 0.9 |
| EC9 | A2 | 124.1 (18) | 187.4 | 73.2 | 10.30 | 0.135 | 75.7 | 90.6 | 0.2 |
| EC24 | B | 124.1 (18) | 133.7 | 61.0 | 13.80 | 0.207 | 78.0 | 92.2 | 0.5 |
| EC12 | A2 | 96.53(14) | 1002.9 | 525 | 13.00 | 0.0235 | 70.2 | 93.0 | 0.0 |
| EC27 | B | 96.53(14) | 781.7 | 325 | 11.50 | 0.0314 | 77.5 | 90.3 | 0.0 |
| | | | | | 510°C (950°F) | | | | |
| Heat ESR R0110 | | | | | | | | | |
| | D | 151.7 (22) | 7236.2 | 1845 | 1.34 | 0.000499 | 35.0 | 60.7 | 0.2 |

* Determined by 0.2% strain offset

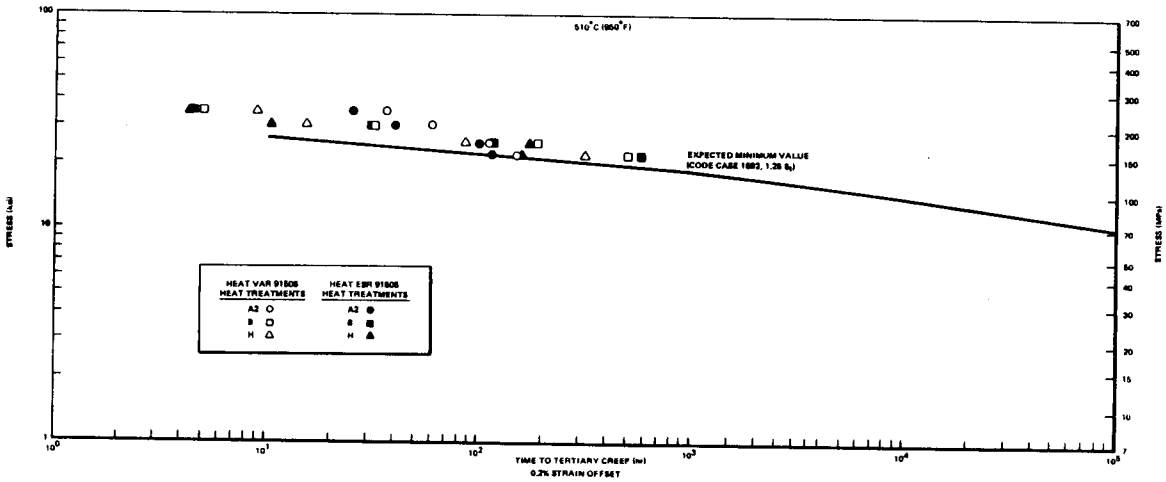


Figure 8.26 Variation of Stress and Time to Tertiary Creep in Uniaxial Tension

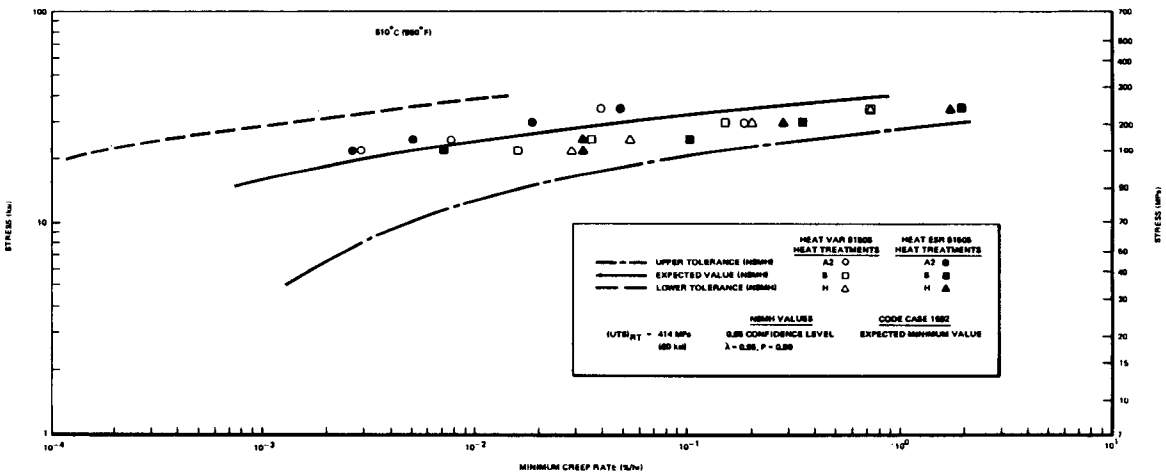


Figure 8.27. Variation of Stress and Minimum Creep Rate in Uniaxial Tension

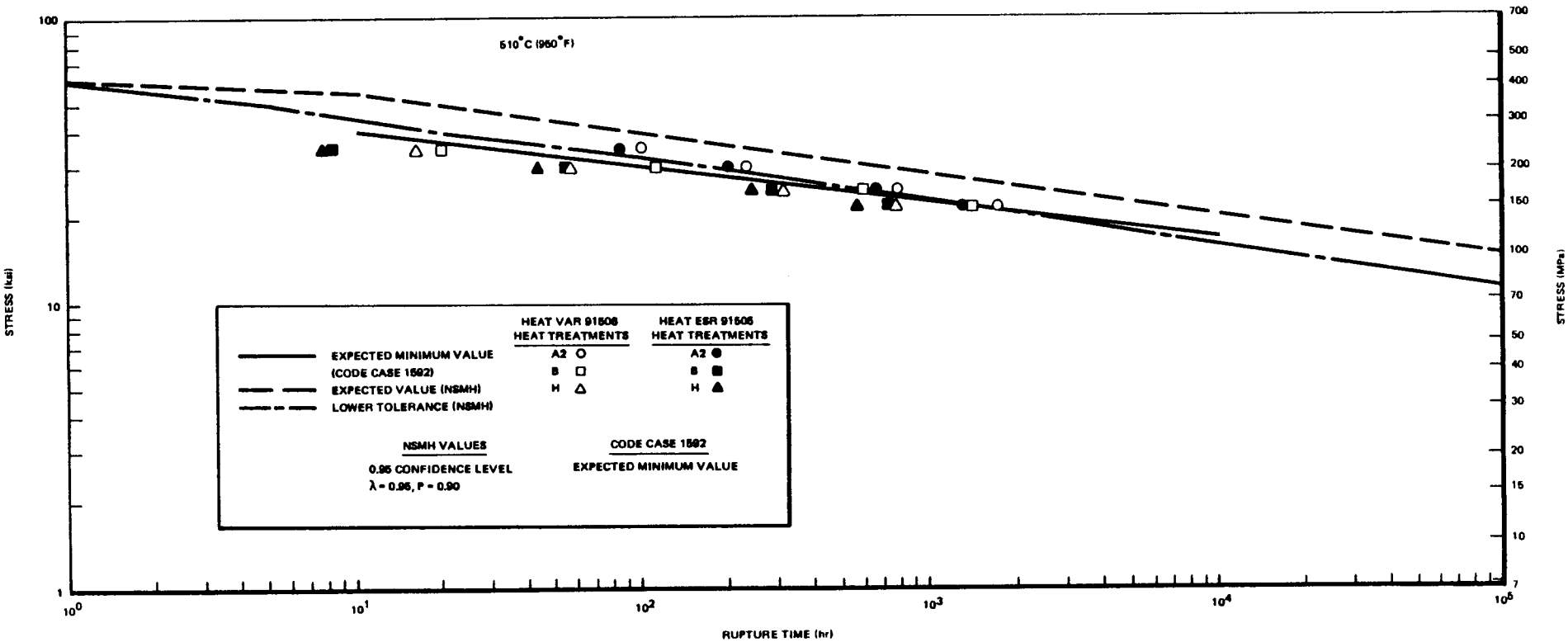


Figure 8.28 Variation of Stress and Rupture Time in Uniaxial Tension

704°C (1300°F) isothermal anneal with a 40 hour - 727°C (1340°F) PWHT, and a full anneal with a 4 hour - 727°C PWHT. The heat treatment which fell above these minimums was a 90 minute isothermal anneal plus a 4 hour - 727°C PWHT. It should be noted that the data falling below the minimum lines decreases relatively less with longer rupture times, and crosses above these lines at about 1000 hours. That is, although the data are below the minimum curve at short times, they have a higher stress dependence. Thus the heat treatments producing lower strength material, as reflected by low tensile strengths and by low short-term rupture times, have superior long-term rupture times as expected due to their more stable carbide structure.

## 8.5 FRACTURE TOUGHNESS OF LMFBR STEAM GENERATOR MATERIALS

J. F. Copeland/J. L. Yuen

### 8.5.1 Background

The objective of this program is to determine fracture toughness values ($K_{Ic}$) at 24°C (75°F) and higher temperatures, for potential LMFBR steam generator shell and tubesheet materials. These results will be combined with Charpy V-notch and drop-weight test values ($RT_{NDT}$ determinations) and tensile test results to evaluate resistence to fracture. The essence of this approach to prevent fracture is set forth in the $K_{IR}$ curve of Appendix G to Section III of the ASME Boiler and Pressure Vessel Code. No toughness data on 2¼Cr-1Mo steel was included in the derivation of the Code $K_{IR}$ curve. Therefore, testing is required at hydrostatic test and at service temperatures to assure that the present $K_{IR}$ curve approach is adequate for this material. In order to evaluate the fracture toughness of 2¼Cr-1Mo above the Nil Ductility Transition Temperature (NDTT), it is necessary to employ elastic-plastic fracture toughness testing methods, such as the J-Integral approach.

Thick section 2¼Cr-1Mo steel plates were procured for this program and heat treated to represent potential LMFBR material conditions. The emphasis is on air melted (AM) material, although some testing has been done on Vacuum Arc Remelted (VAR) steel. Information on test material

chemical composition is given in Table 8.17. The air melted material is in the form of 89 mm. (3.5 in.) thick plate, while the VAR steel is 51 mm. (2 in.) thick plate. Two 122 cm. (48 in.) long, 8.9 cm. (3.5 in.) thick SMAW weldments were prepared from the AM plates as described in Appendix 8.1. These weldments passed the nondestructive examination and appear to be excellent test welds. The "K"-shaped joint was specified to provide a relatively straight edged fusion line for heat affected zone (HAZ) tests.

Initial tensile, Charpy V-notch (CVN), drop weight NDT, and fracture toughness ($J_{Ic}$, $K_{Ic}$) test results on base material are reported in Reference 26. Summaries of these results, along with the recent results, are presented in this report in order to give a complete story to date.

### 8.5.2 Current Progress

Test material conditions are described in Table 8.18 These conditions include SMAW weld metal and HAZ tests. Specimen notch and gage length locations relative to these weldment zones are shown in Figures 8.29 - 8.31. Tensile test results are presented in Table 8.19 for material conditions A-E. The room temperature results were discussed previously.[21] Additional room temperature and elevated temperature tests are shown which were performed last quarter. These results are required for crack opening displacement (COD) toughness calculations and, additionally, give insight into the influence of post weld heat treatment (PWHT) on strength. It appears that for this heat, in the laboratory full anneal condition, there is a small decrease in yield strength and a larger decrease in ultimate tensile strength (UTS) resulting from the 4 hour PWHT at 727°C (1340°F). Hot tensile tests on conditions D, F, and G will be performed during the next quarter.

CVN energy, lateral expansion, and fracture appearance data and curves are shown in Figures 8.32 - 8.41 for all material conditions. These results supplement and extend previously reported[21] data. Transition temperature criteria used to determine $RT_{NDT}$ values for ASME Code applications are summarized in Table 8.20. The effect heat treatment was previously discussed.[21] The weld tests indicate that the weld metal and HAZ CVN transition temperature behavior is essentially the same as for the

TABLE 8.17

CHEMICAL COMPOSITIONS OF 2¼Cr-1Mo STEEL PLATES FOR FRACTURE TOUGHNESS TESTING (wt. %)

| Melting Process | Heat No. | | C | Mn | P | S | Si | Cr | Ni | Mo | Al | As | Sb | Sn |
|---|---|---|---|---|---|---|---|---|---|---|---|---|---|---|
| AM | 86693 | Melt | 0.11 | 0.45 | 0.009 | 0.028 | 0.20 | 2.01 | -- | 1.04 | -- | -- | -- | -- |
| | | Check | 0.11 | 0.41 | 0.014 | 0.026 | 0.19 | 2.00 | 0.12 | 1.00 | <0.005 | 0.013 | 0.007 | 0.012 |
| VAR | 55262 | Melt | 0.09 | 0.52 | 0.016 | 0.014 | 0.08 | 2.22 | -- | 1.01 | -- | -- | -- | -- |
| | | Check | 0.10 | 0.50 | 0.013 | 0.016 | 0.07 | 2.26 | 0.15 | 1.00 | <0.005 | 0.008 | <0.002 | 0.004 |

TABLE 8.18

MATERIAL CONDITION OF 2¼Cr-1Mo STEEL PLATES FOR FRACTURE TOUGHNESS TESTING

A. Anneal (AM Heat 86693)

927°C (1700°F) for 3 hr., furnace cool at max. rate of 55.5°C (100°F) per hr. to less than 482°C (900°F)

B. Anneal + Post Weld Heat Treatment (PWHT) (AM Heat 86693)

927°C (1700°F) for 3 hr., furnace cool at max. rate of 55.5°C (100°F) per hr. to less than 482°C (900°F)
+727°C (1340°F) for 4 hrs., air cool or furnace cool

C. Anneal + PWHT (VAR Heat 55262)

927°C (1700°F) for 3 hr., furnace cool at max. rate of 55.5°C (100°F) per hr. to less than 482°C (900°F)
+727°C (1340°F) for 4 hr., air cool

D. Anneal + PWHT + Embrittlement Treatment (AM Heat 86693)

927°C (1700°F) for 3 hr., furnace cool at max. rate of 55.5°C (100°F) per hr. to less than 482°C (900°F)
+727°C (1340°F) for 4 hr., air cool or furnace cool
+510°C (950°F) for 1000 hr., air cool

E. Normalize + Temper (AM Heat 86693)

927°C (1700°F) for 3 hr., air cool
+ 727°C (1340°F) for 4 hr., air cool

F. SMAW Weld Metal (AM Heat 86693)

915°C (1680°F) for 3.5 hr., furnace cool at max. rate of 55.5°C (100°F) per hour to less than 482°C (900°F)
+SMAW (see weld procedure)
+727°C (1340°F) for 12 hr., furnace cool at max. rate of 55.5°C (100°F) per hour

G. SMAW Heat Affected Zone (HAZ) (AM Heat 86693)

915°C (1680°F) for 3.5 hr., furnace cool at max. rate of 55.5°C (100°F) per hour to less than 482°C (900°F)
+SMAW (see weld procedure)
+727°C (1340°F) for 12 hr., furnace cool at max. rate of 55.5°C (100°F) per hour

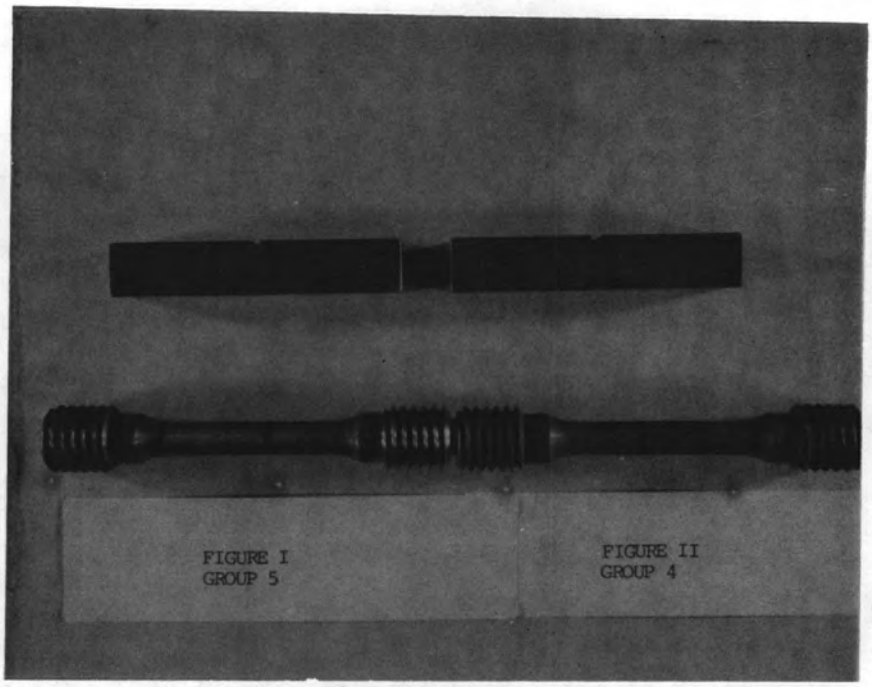


*Figure 8.29 Notch and Gage Length Location with Regard to SMAW Weld Deposit (Outlined on Etched Specimens). I-5 Specimens are Weld Metal Tests, and II-4 Specimens are HAZ Tests, with the Notch ~3 mm (0.12 in.) from the Straight Weld Fusion Line of the "K" joint.*

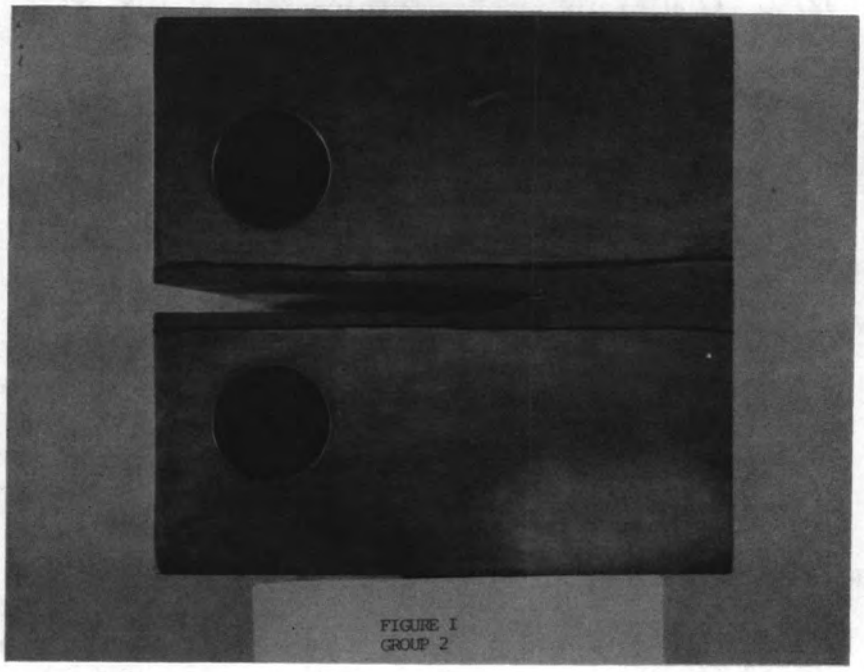


*Figure 8.30 Notch Location on SMAW Weld Metal Test (Weld Deposit Outlined on Etched Specimen) for Compact Tension Specimen I-2*

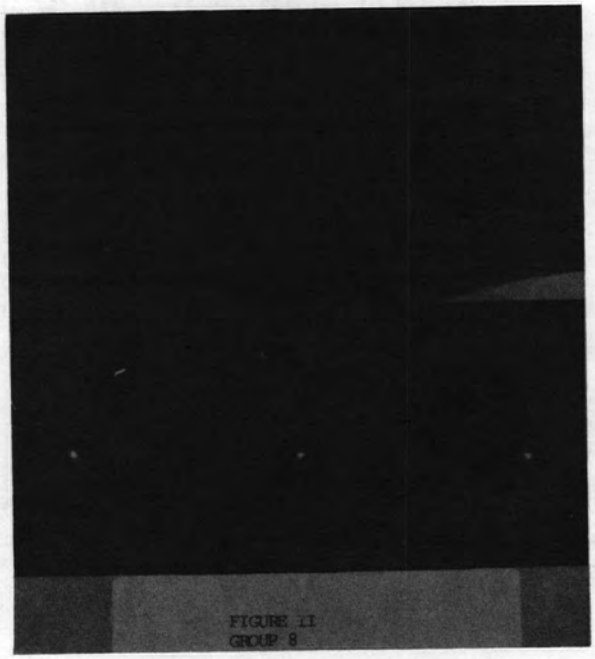


*Figure 8.31 Notch Location on SMAW HAZ Test (Weld Deposit Outlined on Etched Specimen) for Compact Tension Specimen 11-8. Notch is ~3 mm (0.12 in.) from the Straight Weld Fusion Line of the "K" Joint.*

TABLE 8.19

Tensile Test Properties at 24°C (75°F) for 2¼Cr-1Mo Heat 86693. Air-Melt 89 mm. (3.5 in.) Thick Plate, Properties at ¼ T Location. Strain Rate = 0.04 min.$^{-1}$. Also, results for VAR Heat 55262.

| Treatment | Test Temperature °C (°F) | Yield Point MPa (Ksi) | 0.2% Y.S. MPa (Ksi) | U.T.S. MPa (Ksi) | %El. (25.4 mm) | % R.A. |
|---|---|---|---|---|---|---|
| A (Anneal) | 24 (75) | 270 (39.2) | 243 (35.2) | 472 (68.5) | 39.6 | 65.3 |
| | | 262 (38.0) | 243 (35.2) | 466 (67.6) | 38.2 | 66.1 |
| | | 260 (37.7) | 235 (34.1) | 470 (68.2) | 41.5 | 66.9 |
| | 371 (700) | 169 (24.5) | 168 (24.3) | 450 (65.3) | 23.5 | 50.7 |
| | 454 (850) | - - | 160 (23.2) | 449 (65.1) | 23.8 | 49.5 |
| | 510 (950) | - - | 156 (22.6) | 410 (59.5) | 26.5 | 60.3 |
| | 566 (1050) | - - | 154 (22.4) | 363 (52.7) | 36.4 | 72.5 |
| B (Anneal + PWHT) | 24 (75) | 295 (42.8) | 261 (37.9) | 466 (67.6) | 33.3 | 65.9 |
| | | 297 (43.1) | 267 (38.7) | 467 (67.7) | 34.6 | 65.1 |
| | | - - | - - | 453 (65.7) | 32.7 | 69.5 |
| | | 243 (35.2) | 231 (33.5) | 448 (65.0) | 41.3 | 68.7 |
| | 177 (350) | 196 (28.4) | 192 (27.8) | 374 (54.2) | 36.5 | 68.3 |
| | | 209 (30.3) | 198 (28.7) | 372 (53.9) | 38.0 | 70.4 |
| | 288 (550) | 194 (28.2) | 181 (26.2) | 298 (57.7) | 24.9 | 59.7 |
| | 399 (750) | - - | 146 (21.2) | 399 (57.9) | 24.0 | 54.3 |
| | 454 (850) | - - | 152 (22.0) | 386 (56.0) | 27.8 | 56.2 |
| | 510 (950) | - - | 143 (20.7) | 340 (49.3) | 33.2 | 65.1 |
| | 566 (1050) | - - | 133 (19.3) | 292 (42.3) | 43.6 | 76.6 |
| C VAR* (Anneal + PWHT) | 24 (75) | - - | 275 (39.9) | 439 (63.7) | 36.1 | 51.6 |
| D (Anneal + PWHT + 510°C, 1000 hr.) | 24 (75) | 234 (33.9) | 221 (32.1) | 459 (66.6) | 34.8 | 64.4 |
| | | 223 (32.4) | 220 (31.9) | 465 (67.4) | 38.1 | 67.2 |
| E (Norm. + Temp.) | 24 (75) | 298 (43.2) | 285 (41.4) | 462 (67.0) | 38.4 | 68.7 |
| | | 285 (41.4) | 264 (38.3) | 460 (66.7) | 40.0 | 68.8 |

*Results by H. P. Offer (GE) on same VAR Heat No. (55262) - different plate, funded under 189a-SG029.

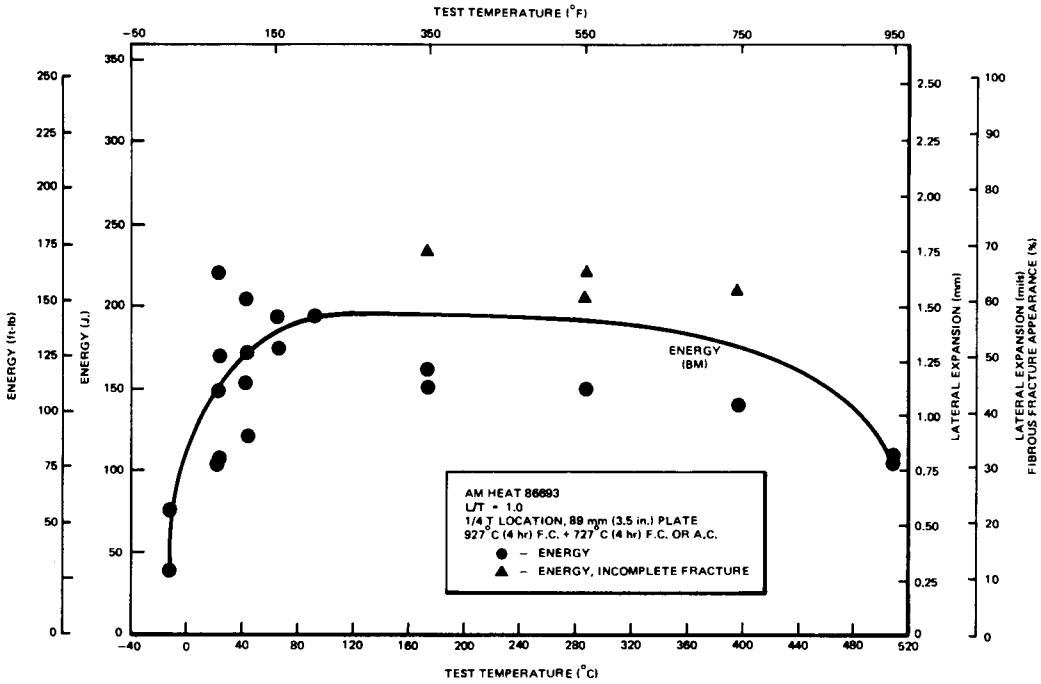


Figure 8.32 Charpy V-Notch Impact Test Energy Curve. Material Condition B

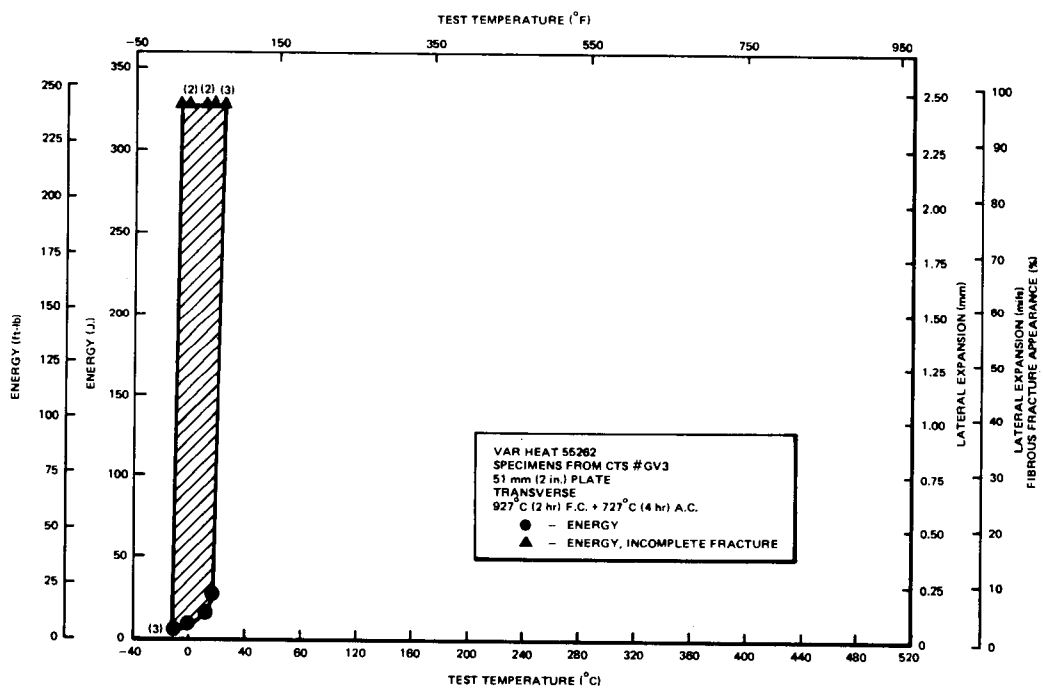


Figure 8.33 Charpy V-Notch Impact Test Energy Plot. Material Condition C

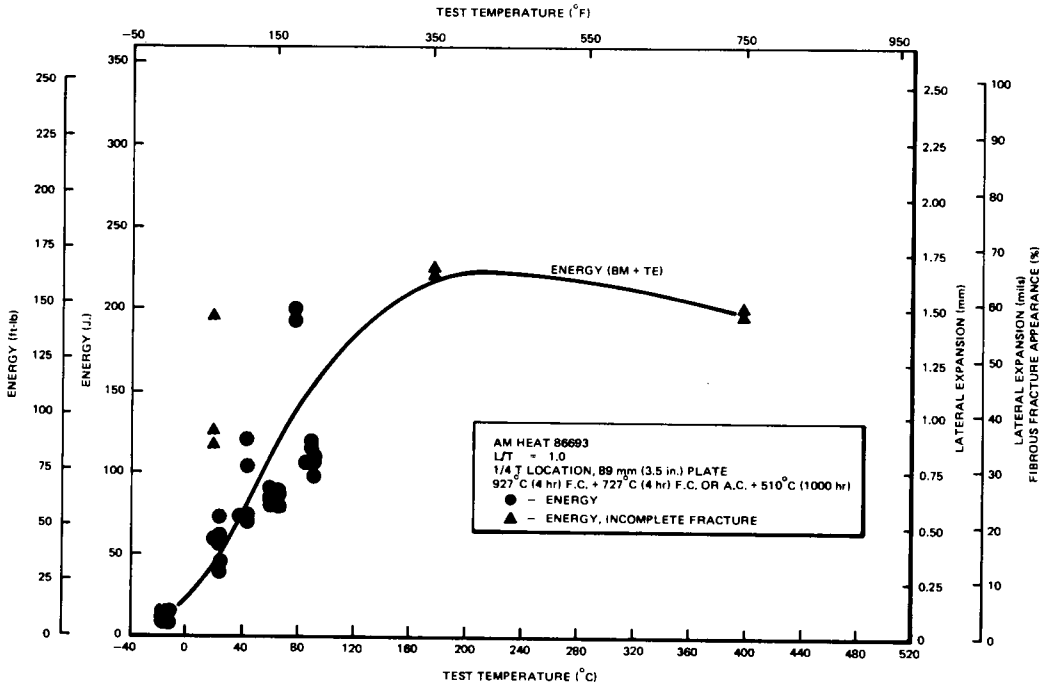


Figure 8.34 Charpy V-Notch Impact Test Energy Curve. Material Condition D

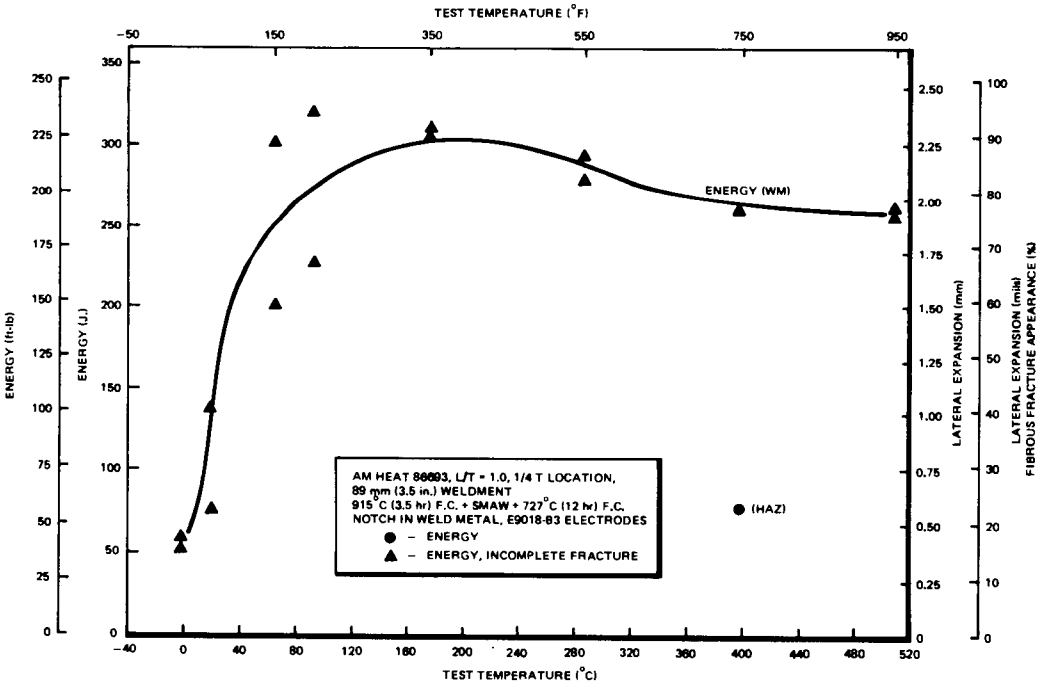


Figure 8.35 Charpy V-Notch Impact Test Energy Curve. Material Condition F

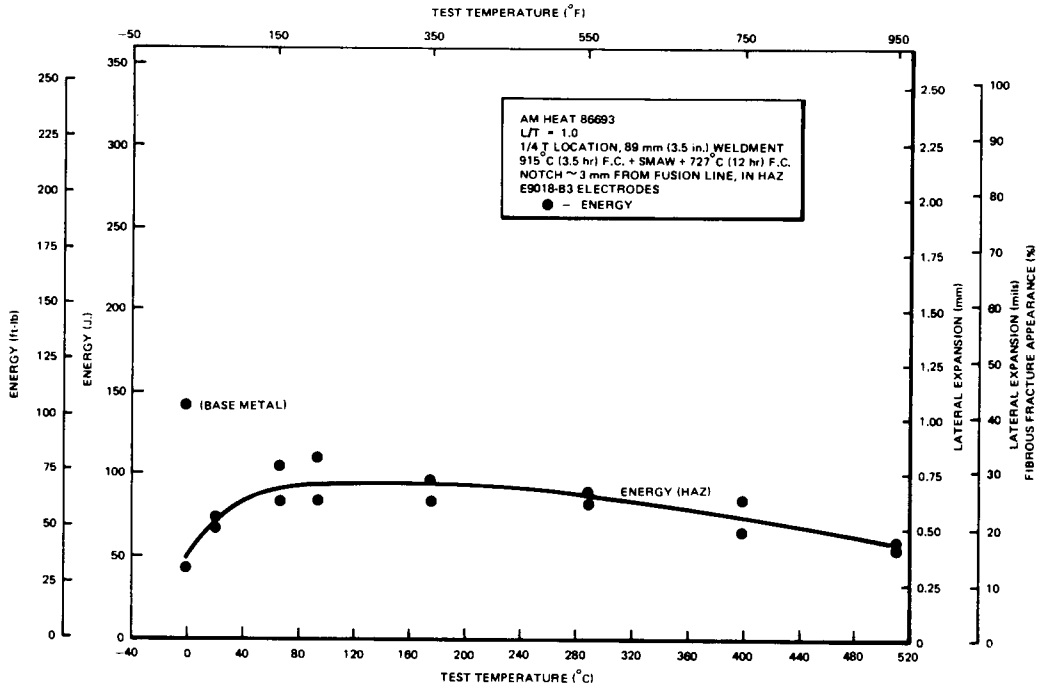


Figure 8.36 Charpy V-Notch Impact Test Energy Curve. Material Condition G

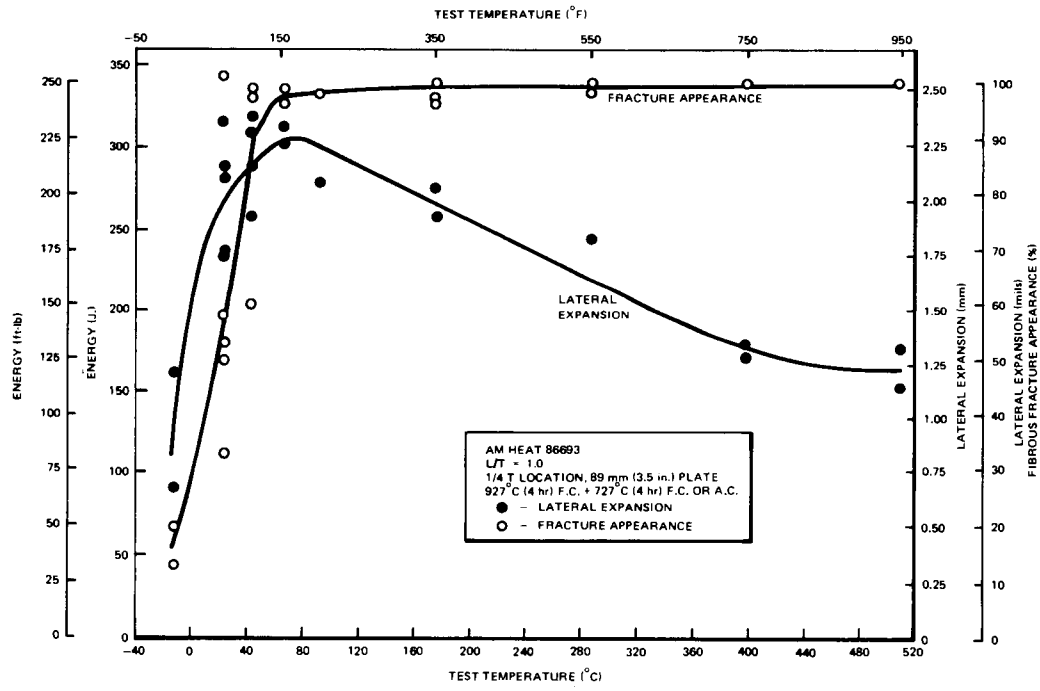


Figure 8.37 Charpy V-Notch Impact Test Lateral Expansion and Fracture Appearance Curves. Material Condition B

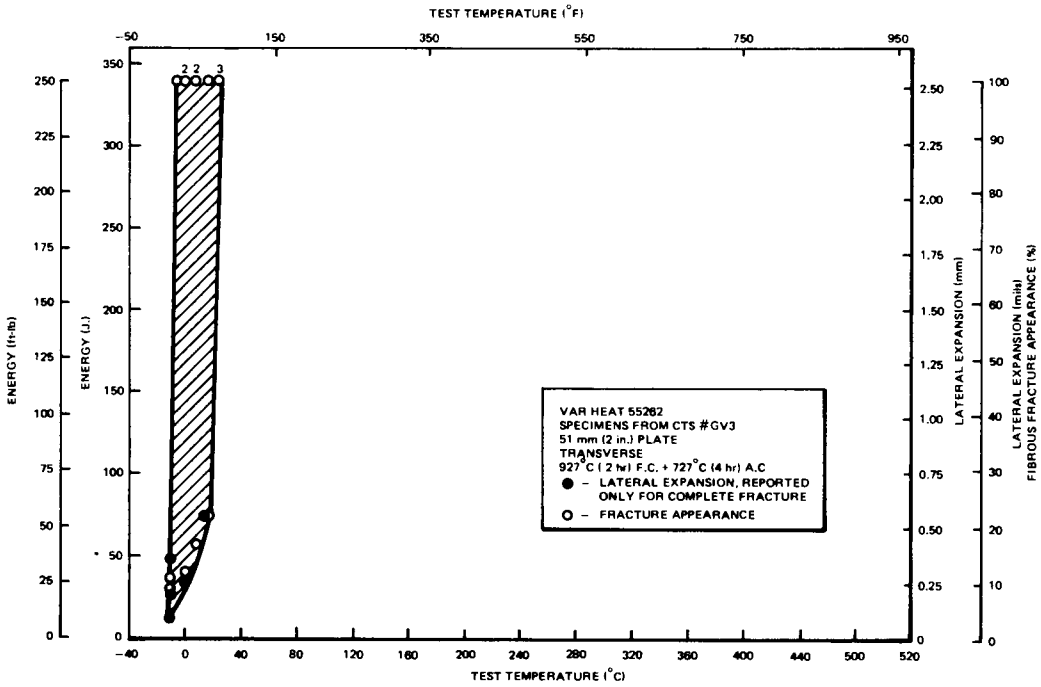


Figure 8.38 Charpy V-Notch Impact Test Lateral Expansion and Fracture Appearance Curves. Material Condition C

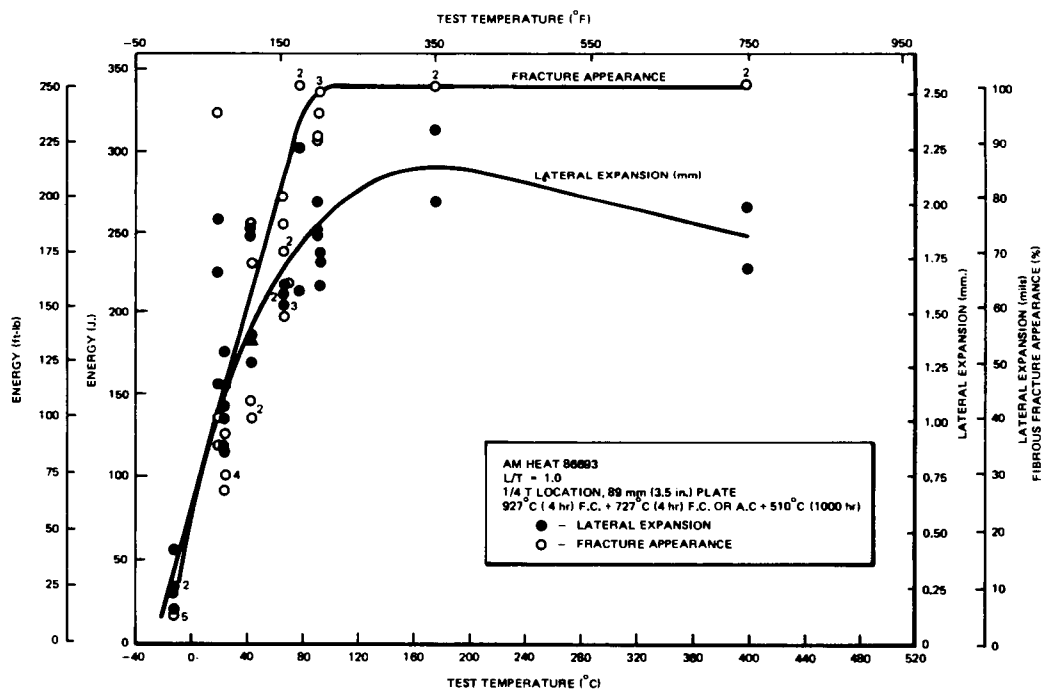


Figure 8.39 Charpy V-Notch Impact Test Lateral Expansion and Fracture Appearance Curves. Material Condition D

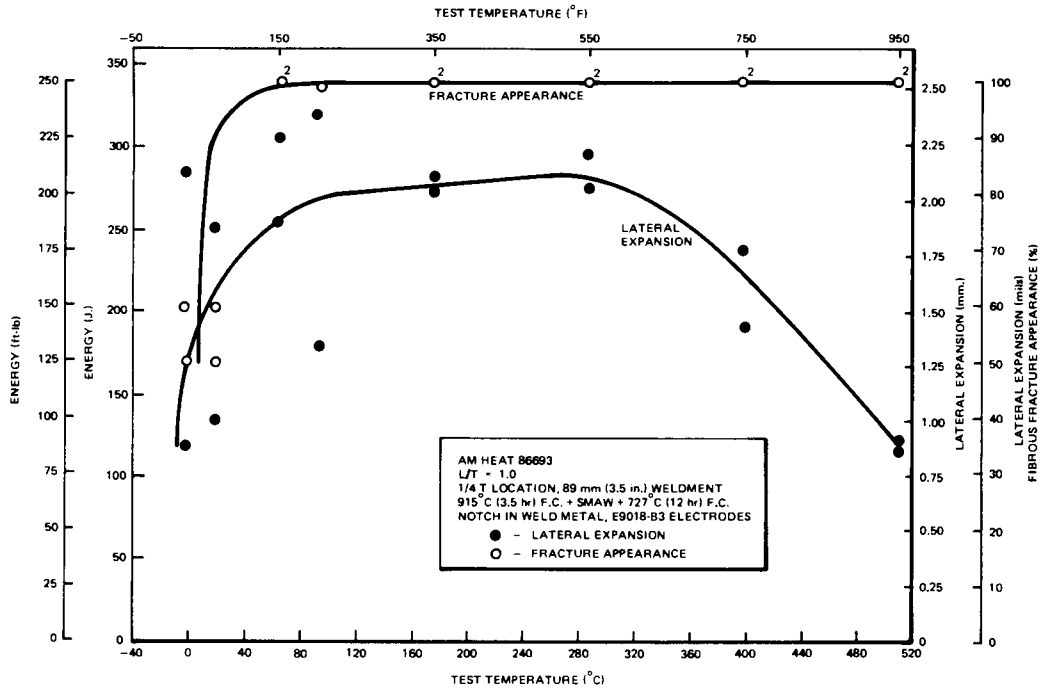


Figure 8.40 Charpy V-Notch Impact Test Lateral Expansion and Fracture Appearance Curves. Material Condition F

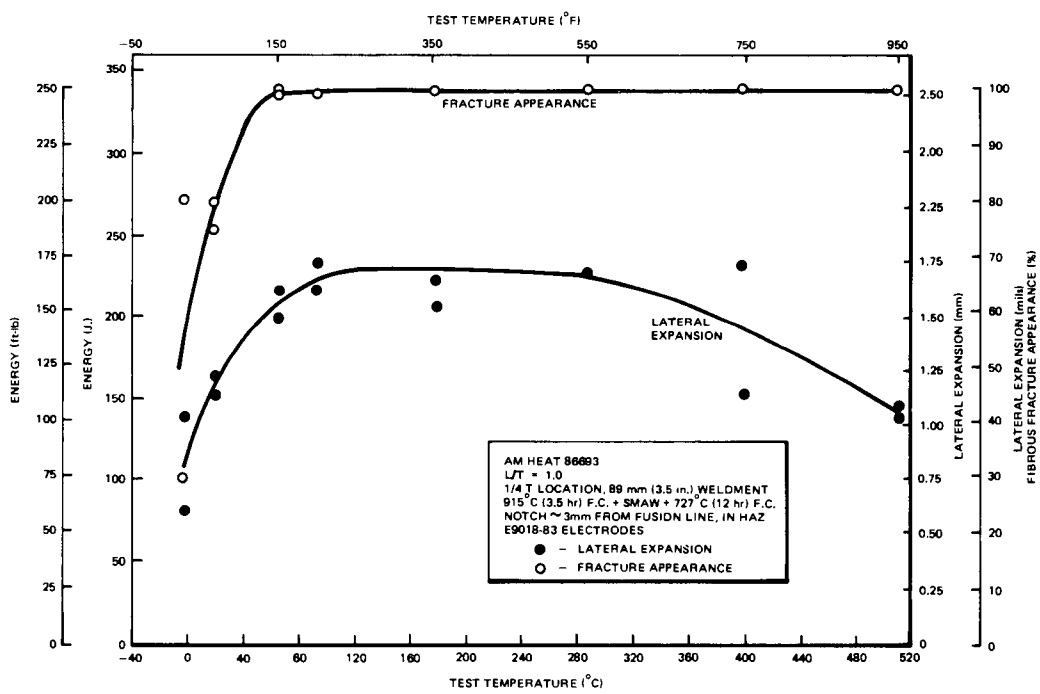


Figure 8.41 Charpy V-Notch Impact Test Lateral Expansion and Fracture Appearance Curves. Material Condition G

TABLE 8.20

Charpy V-Notch Toughness Criteria and P-3 Drop-Weight Nil Ductility Transition (NDT) Results for 2¼Cr-1Mo Heat 86693. Air-Melt 89mm. (3.5 in.) Thick Plate. Properties at ¼ T Location. Rolling Ratio of 1.0. Also, Transverse Results for VAR Heat 55262, 51mm. (2 in.) Thick Plate.

| Material Condition | 68 J. (50 ft-lb) Transition Temp. °C | (°F) | 0.89mm., (35 mils) Lateral Expans. Transition Temp. °C | (°F) | 50% Fract. Appear. Transition Temp. °C | (°F) | NDT °C | (°F) | Reference NDT ($RT_{NDT}$)* °C | (°F) |
|---|---|---|---|---|---|---|---|---|---|---|
| A | 29 | (84) | 11 | (52) | 32 | (90) | -1 | (30) | -1 | (30) |
| B | -10 | (14) | -13 | (8) | 19 | (66) | -1 | (30) | -1 | (30) |
| C (VAR)** | 18 | (64) | -4 | (25) | 29 | (85) | -7 | (20) | -7 | (20) |
| D | 36 | (96) | 14 | (58) | 30 | (86) | -7 | (20) | -7 | (20) |
| E | 13 | (56) | 7 | (45) | 19 | (66) | -1 | (30) | -1 | (30) |
| F | 7 | (45) | -8 | (18) | 8 | (46) | | | -1 | (30)*** |
| G | 15 | (59) | 0 | (32) | -5 | (23) | | | -1 | (30)*** |

* Determined according to ASME B&PV Code, Section III, NB-2300.

** Bimodal fracture behavior at a given temperature resulted in a 33C° (59F°) wide transition scatter band; values in this table are at the high temperature side of the scatter band.

*** Since Charpy transition values are similar to those of conditions A-E, assume that NDT is limiting and results in an $RT_{NDT}$ of -1°C (30°F).

base material (condition B). Some decrease in toughness is shown following the isothermal temper embrittlement treatment (condition D versus B). CVN tests were cut from a VAR (C) compact tension specimen in order to explain the relatively low fracture toughness.[21] The CVN transition plots indicate bimodal fracture behavior (Figure 8.33) which results in a broad transition range. This, taken in combination with notch sensitivity effects, satisfactorily explains the VAR $K_{Ic}$ results. Other important new information which was produced last quarter is on CVN upper shelf behavior up to 510°C (950°F). No known toughness data had previously been available at such high test temperatures, although tests on other materials had indicated a slight decreasing trend in toughness at 288°C (550°F). These upper shelf toughness results are summarized in Table 8.21. It is apparent from this Table and from the curves that there is a very significant decrease in toughness, especially at 510°C (950°F), which must be considered. The upper shelf toughness of 193 J. (142 ft-lb.) at 93°C (200°F) for condition B is almost halved at 510°C (950°F). Also, at these higher test temperature (177°C [350°F]) and above), there is no significant effect of the temper embrittlement treatment on shelf toughness. Weld metal toughness (F) is seen to be superior to that of the base metal (B) and does not suffer as much decrease in toughness at 510°C (950°F). However, condition G (the HAZ) has the lowest toughness of all conditions. Although the low temperature transition criteria (Table 8.20 are good for G, the upper shelf energy is quite low, even at 93°C (200°F) and drops off at 510°C (950°F) to 57 J. (42 ft-lb.). This valve is below the 68 J. (50 ft-lb.) ASME Code NB 2300 criteria which is supposed to quarantee a high upper shelf energy level. These high temperature results, thus, invalidate that aspect of the Code toughness requirements, and must be considered in design. Further discussion on temperature effects on toughness will follow when the $J_{Ic}$, $K_{Ic}$ results are presented in this report. Microstructures along the CVN fracture edge for conditions B, F, and G are shown in Figures 8.42 - 8.44. The structure of the base material is ferrite-pearlite-tempered bainite, and for the weld metal is tempered bainite. The structure of the HAZ appears to have resulted from an intercritical (two phase) treatment

TABLE 8.21

Charpy V-Notch Upper Shelf Energy Values* for 2¼Cr-1Mo Heat 86693. Air Melt 89mm. (3.5 in.) Thick Plate. Properties at ¼ T. Rolling Ratio of 1.0. Also, Transverse Results for VAR Heat 55262 51mm. (2 in.) Thick Plate.

| Material Condition | 93°C (200°F) J. | (Ft-lb.) | 177°C (350°F) J. | (Ft-lb.) | 288°C (550°F) J. | (Ft-lb.) | 399°C (750°F) J. | (Ft-lb.) | 510°C (950°F) J. | (Ft-lb.) |
|---|---|---|---|---|---|---|---|---|---|---|
| A | 118 | (87) | - | - | - | - | - | - | - | - |
| B | 193 | (142) | 195 | (144) | 193 | (142) | 175 | (129) | 106 | (78) |
| C | >324 | (239) | - | - | - | - | - | - | - | - |
| D | 153 | (113) | 217 | (160) | 217 | (160) | 197 | (145) | - | - |
| E | 129 | (95) | - | - | - | - | - | - | - | - |
| F | 271 | (200) | 302 | (223) | 288 | (212) | 263 | (194) | 258 | (190) |
| G | 95 | (70) | 95 | (70) | 88 | (65) | 75 | (55) | 57 | (42) |

*Values from CVN curves. All tabulated energy values correspond to 100% fibrous (ductile or shear) fracture appearance.

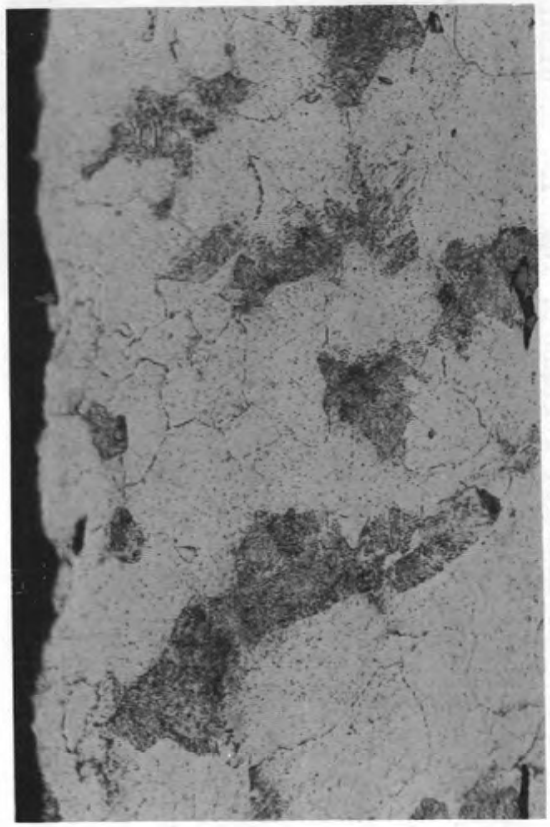

400X

*Figure 8.42* *Microstructure at CVN Fracture Edge. Material Condition B (Base Metal).*

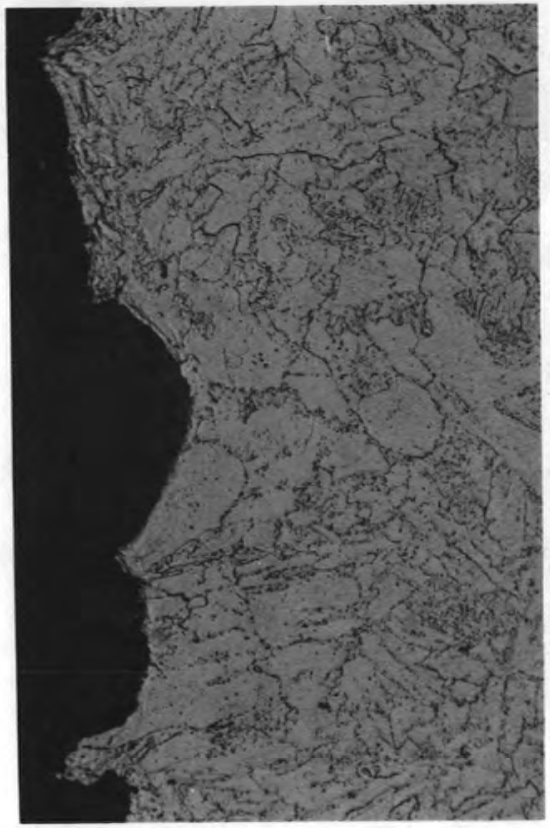

400X

*Figure 8.43* *Microstructure at CVN Fracture Edge. Material Condition G (SMAW HAZ)*

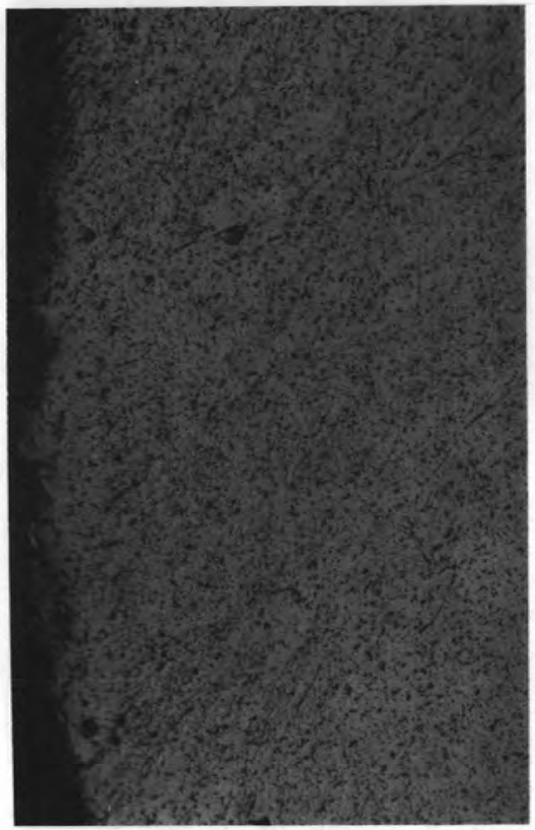

400X

*Figure 8.44* *Microstructure at CVN Fracture Edge. Material Condition F (SMAW Weld Metal).*

which produced lamellar regions or ferrite and tempered bainite or martensite. Electron microscopic examination of the HAZ microstructure is required to be more certain of its identity.

J-Integral test fracture toughness results are tabulated in Table 8.19. The multiple specimen analysis results were previously discussed.[21] Subsequent to those tests a crack opening displacement gage technique[25] was developed to allow the determination of ductile crack growth initiation for single specimen evaluation of fracture toughness. This method has proven successful, and as shown in Table 8.22, greatly increases the information gleaned from a given number of compact tension specimens (CTS). The CTS is described in Reference 26. The single specimen method was employed for specimens G-19 through I-5 in Table 8.22. Specimens G-19, G-20, and G-22 (24°C [75°F], condition B) gave somewhat higher $K_{Ic}$ results than did G-6, G-7, and G-8. This is a real difference in toughness, and is not caused by the method of analysis, since a multiple specimen analysis of G-19, G-20, and G-22 also gives a high result. This difference may have resulted from some variation in heat treatment, eg. the earlier specimens were air cooled from the PWHT, whereas the more recent ones were furnace cooled. Higher temperature $K_{Ic}$ results on condition B show a decreasing trend in toughness, similar to the CVN data, as temperature is increased. A specially devised clip gage with ceramic arms was employed for these high temperature measurements. Heating was successfully performed with an induction coil and was monitored with thermocouples on the crack tip and ligament regions of the CTS. Typical clip gage results to determine the onset of ductile crack growth (where $J_{Ic}$ and $K_{Ic}$ are computed) are shown in Figure 8.45. As theorized[25] there is an increase in crack tip gage opening rate as the crack grows. An added bonus is the occurrence of perturbations or "blips" in this curve as the crack grows. The first perturbation is taken as the onset of crack growth. It is planned to attempt accoustic emission measurements during a test in the future to gain further confidence that these perturbations represent crack extension. Confidence is gained that this is a meaningful measurement by the plots shown in Figure 8.46. The total amount of ductile crack extension (measured after the test) correlates

TABLE 8.22

COMPACT TENSION SPECIMEN (50.8 mm. [2 in.] THICK) FRACTURE TOUGHNESS RESULTS FOR 2¼Cr-1Mo HEAT 86693. AIR MELT 89 mm. (3.5 in.) THICK WELDMENTS AND PLATE WITH ROLLING RATIO OF 1.0. ALSO, TRANSVERSE RESULTS FOR VAR HEAT 55262, 50.8 mm. (2 in.) THICK PLATE. SPECIMEN LOAD POINT DISPLACEMENT RATE OF 1.52 mm./min. (0.06 in./min.).

| Spec.* No. | Material Condition | Test Temperature °C | (°F) | Ductile Crack Extension, Δa, at Unload. mm. | (in.) | Remarks | Δpc mm. | (in.) | J at COS** or Δpc, $J_{Ic}$ J./mm² | (in-lb/in.²) | $K_{Ic}$ MPa√m. | (Ksi√in.) |
|---|---|---|---|---|---|---|---|---|---|---|---|---|
| G1 | | | | 0.25 | (0.0099) | COS* only. | | | | | | |
| G2 | A | 24 | (75) | 3.00 | (0.1180) | Stable Δa. | - | - | 18.4 | (1050) | 206 | (187) |
| G3 | | | | 0.76 | (0.030) | Δa, Pop-in. | | | | | | |
| G6 | | | | 0.70 | (0.0276) | Δa, Pop-in. | | | | | | |
| G7 | B | 24 | (75) | 3.00 | (0.1180) | Stable Δa. | - | - | 20.3 | (1160) | 216 | (196) |
| G8 | | | | 2.90 | (0.1140) | Stable Δa. | | | | | | |
| GV1 | | | | - | - | Pop-in. | | | 9.3 | (530) | 145 | (132) |
| GV2 | C (VAR) | 24 | (75) | - | - | Pop-in. | - | - | 11.7 | (670) | 164 | (149) |
| GV3 | | | | - | - | Pop-in. | | | 6.5 | (370) | 121 | (110) |
| G10 | | | | | | Δa, Pop-in. | | | | | | |
| G11 | D | 24 | (75) | 0.30 | (0.0118) | Δa, Pop-in. | - | - | 24.5 | (1400) | 236 | (215) |
| G12 | | | | | | Stable Δa. | | | | | | |
| G14 | | | | 0.30 | (0.0118) | Δa, Pop-in. | | | | | | |
| G15 | E | 24 | (75) | 1.00 | (0.0394) | Stable Δa. | - | - | 22.9 | (1310) | 229 | (208) |
| G16 | | | | 3.50 | (0.1380) | Stable Δa. | | | | | | |

* Specimens G1 - G16 were analysed by multiple specimen method (intersect J versus Δa curve with COS line for $J_{Ic}$) since Δpc was not determined.

** Crack Opening Stretch - no real crack extension.

TABLE 8.22 (Cont'd.)

| Spec.* No. | Material Condition | Test Temperature °C | (°F) | Ductile Crack Extension, Δa, at Unload. mm. | (in.) | Remarks | Δpc mm. | (in.) | J at COS** or Δpc, $J_{Ic}$ J./mm² | (in-lb/in.²) | $K_{Ic}$ MPa√m. | (Ksi√in.) |
|---|---|---|---|---|---|---|---|---|---|---|---|---|
| G19 | B | 24 | (75) | 1.1 | (0.043) | Ductile Crack Extension | 5.588 | (0.2200) | 44.5 | (2544) | 319 | (290) |
| G20 | | | | 1.5 | (0.059) | | 5.334 | (0.2100) | 44.4 | (2536) | 318 | (289) |
| G22 | | | | 0.6 | (0.024) | | 5.207 | (0.2050) | 40.0 | (2287) | 303 | (275) |
| G21 | | 177 | (350) | 1.5 | (0.059) | | 4.445 | (0.1750) | 28.7 | (1639) | 250 | (227) |
| G26 | | 288 | (550) | 0.6 | (0.024) | | 2.985 | (0.1175) | 17.1 | (975) | 190 | (173) |
| G23 | | 399 | (750) | 1.3 | (0.051) | | 2.972 | (0.1170) | 16.0 | (914) | 179 | (163) |
| G24 | | 510 | (950) | 0.3 | (0.012) | | 2.794 | (0.1100) | 12.4 | (708) | 149 | (135) |
| G25 | | | | 0.6 | (0.024) | | 3.048 | (0.1200) | 15.7 | (897) | 167 | (152) |
| I-3 | F | 24 | (75) | Not Measurable | | Ductile Crack Extension with Small Pop-in's | 1.803 | (0.0710) | 12.5 | (713) | 168 | (153)*** |
| | | | | | | | 4.597 | (0.1810) | 39.7 | (2267) | 300 | (273)**** |
| I-5 | | | | Not Measurable | | | 2.337 | (0.0920) | 15.1 | (863) | 185 | (168)*** |
| | | | | | | | 3.912 | (0.154) | 30.8 | (1758) | 264 | (240)**** |

* Specimens G19 to I-5 were analysed based on Δpc (specimen load point displacement at the onset of crack extension) determined by a clip gage at crack tip.

** Crack Opening Stretch - no real crack extension.

*** Values based on Δpc at first pop-in (may have occurred in small amount of HAZ).

**** Values based on Δpc at onset of ductile crack extension (probably indicates weld metal toughness).

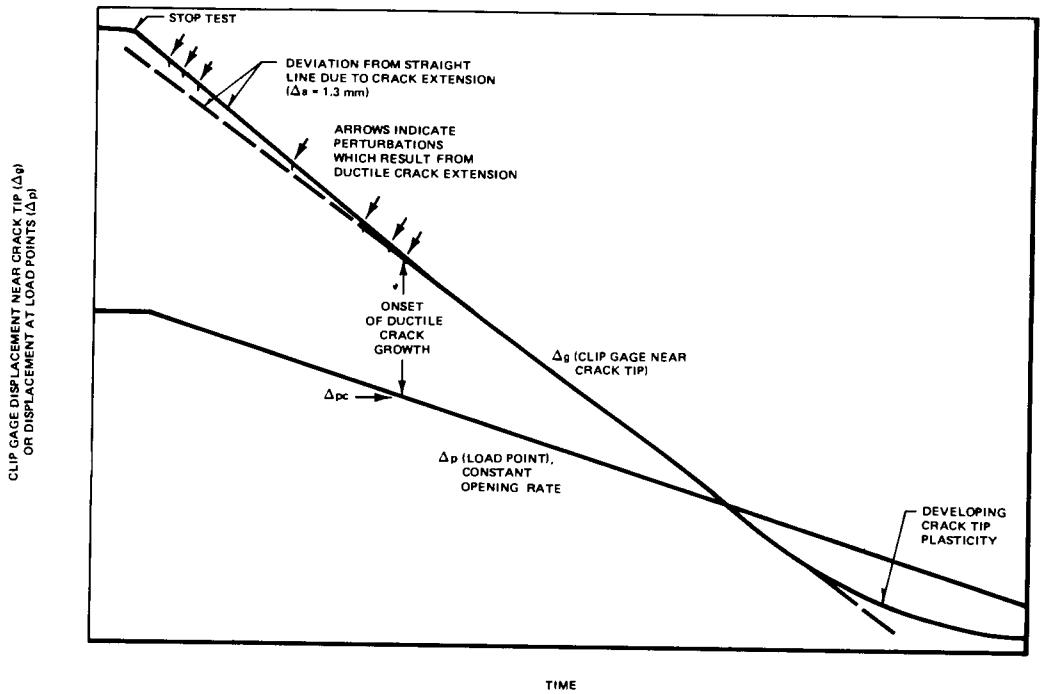


Figure 8.45 Displacement Gage Strip Chart Readings for Specimen G23 (J Integral Test) Used to Determine where Crack Extension Initiates (Δpc)

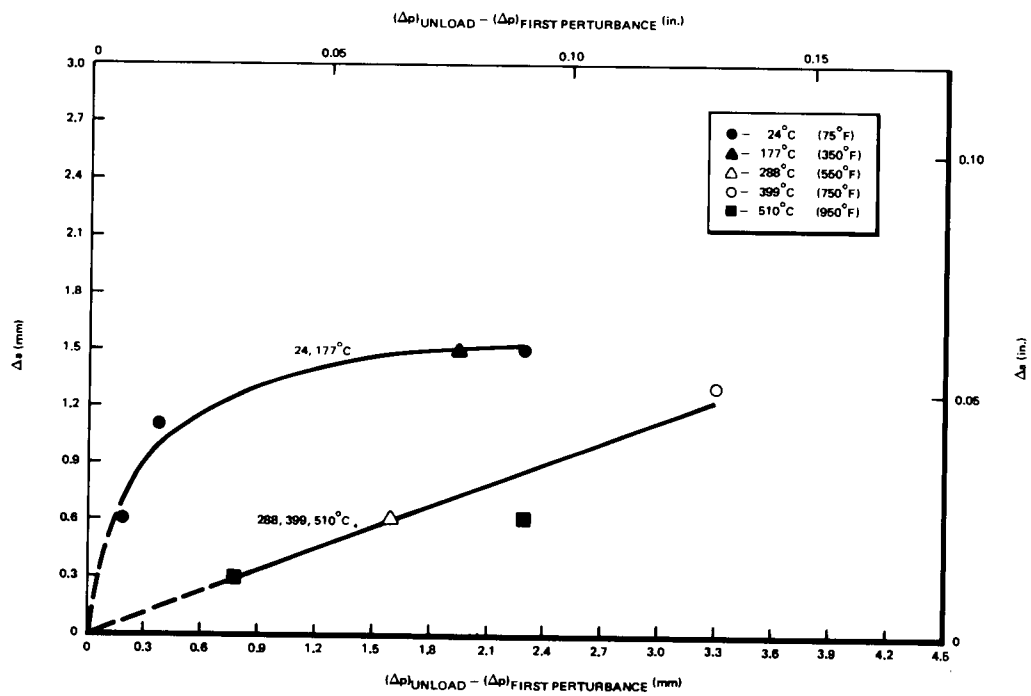


Figure 8.46 Crack Extension (Δa) Versus Load Point Displacement Beyond Δpc (as Determined at the First Perturbance on the Crack Tip Opening Curve)

nicely with the additional load point displacement applied to the specimen after the first perturbation. The fact that these curves extrapolate through the zero point of the graph indicates that the first perturbation signals the onset of crack extension. This figure also shows that high temperature ductile cracks grow differently than lower temperature ductile ones. After crack growth initiates the lower temperature cracks experience an initial "spurt" in growth with little applied increase in load point displacement. On the other hand, the higher temperature cracks require more applied displacement to grow the crack once it is initiated. Some of the reasons for the decreased fracture toughness at higher temperatures are illustrated in Figure 8.47. These are actual load-load point displacement ($\Delta p$) test curves which are used to compute $J_{Ic}$ and $K_{Ic}$ from the area under the curve to the onset of crack growth ($\Delta pc$). Lower toughness at 510°C (950°F) results from lower valves of flow stress, $\Delta pc$, and elastic modulus. Weld metal results (F) are also given in Table 8.22. These tests both showed numberous, audible pop-in's as reflected on the test curve in Figure 8.48. The usual ductile crack extension, as determined by the crack tip gage plots occurred at a higher displacement. Figure 8.49 shows the fracture surfaces from these weld metal tests. It appears that there is a small region of HAZ material, which the crack ran through, resulting from an imperfect "K" - joint in the weld. This region is at exactly the correct location in the specimen thickness for such an explanation. It is further reasoned that the early pop-in's occurred in this more brittle HAZ region (based on CVN results). Therefore, the correct measurement of $J_{Ic}$ and $K_{Ic}$ for the weld metal is probably represented by the higher values in Table 8.22, derived from the onset of ductile crack growth. This is consistent with the CVN results, since the weld metal toughness is approximately equal to the base material toughness (condition B). HAZ tests, planned for next quarter, will show whether or not the lower (pop-in) valves represent HAZ fracture toughness. All $K_{Ic}$ results from Table 8.22 are plotted and compared with the ASME Code Section III, Appendix G $K_{IR}$ curve in Figure 8.50. All results fall above this curve, as desired for conservative design, at the test temperature of 24°C (75°F). However, at higher temperatures the base material (B) falls considerably

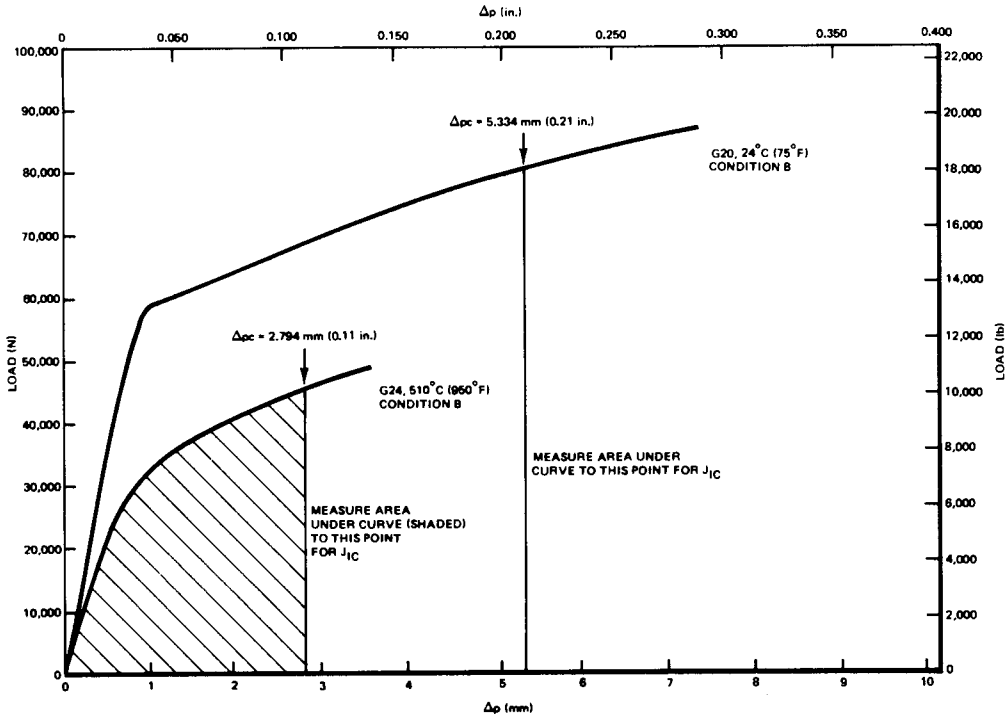


Figure 8.47 Load Versus Load Point Displacement (Δp) Curves Showing Influence of Test Temperature on $J_{IC}$ for Material Condition B

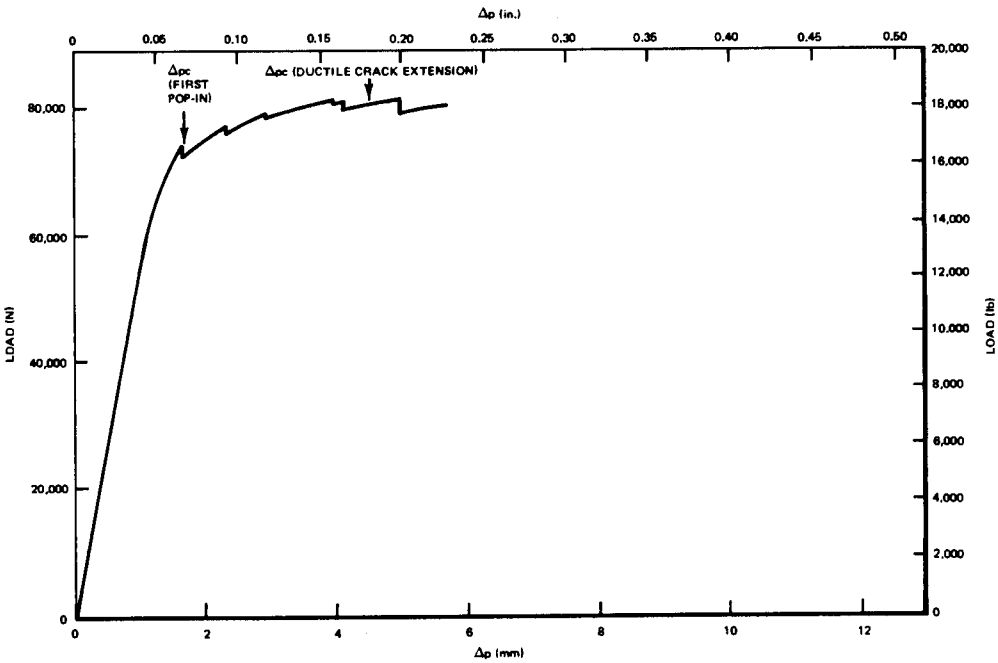


Figure 8.48 Load Versus Load Point Displacement (Δp) Curve for Specimen 1-3 J-Integral Test Showing Pop-In Behavior Believed to be Caused by Small Region of Relatively Brittle HAZ Material in this Weld Metal Test (Material Condition F)

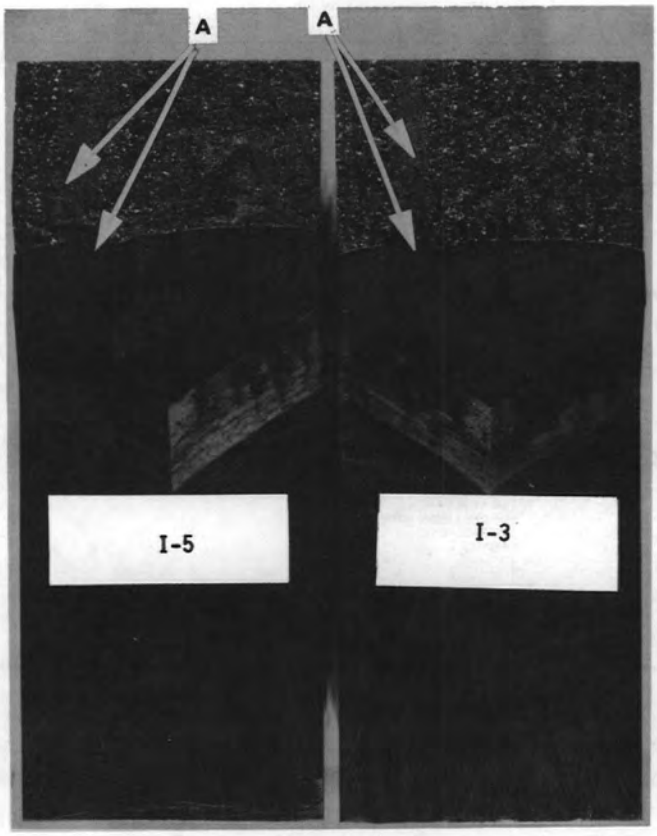


Figure 8.49 Fracture Surfaces of 50.8 mm (2 in.) Thick Compact Tension Specimens for Weld Metal Tests 1-3 and 1-5 (Material Condition F) Showing Small Regions of HAZ, Marked A

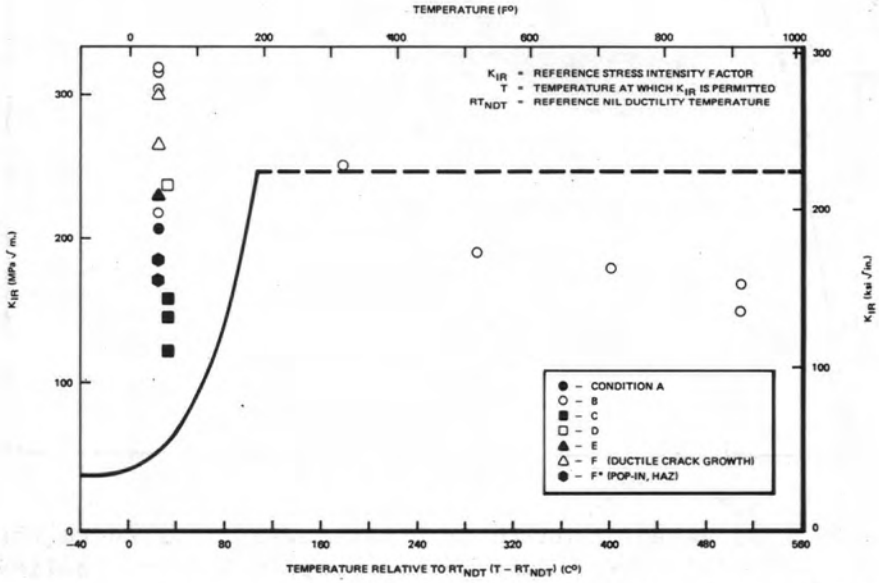


Figure 8.50 Comparison of Fracture Toughness Data with ASME Code Section III $K_{IR}$ Curve

below the assumed shelf to the $K_{IR}$ curve. This is not in conflict with derivation of the $K_{IR}$ curve since it was derived for materials other than 2¼Cr-1Mo steel. Also, no tests had been performed at temperatures as high as those of this study. However, these test results do indicate that current design concepts for the prevention of fracture are unconservative for 2¼Cr-1Mo steel at high service temperatures. This effect, which probably will be even greater for the lower toughness HAZ (G) material when tested at high temperature, must be considered in design. The amount of crack growth to expect in a component under these conditions is unknown, although it is expected that a leak-before-break behavior would exist, since this is not a brittle fracture, but is a low energy tear fracture. In the face of crack arrest uncertainties and the undesirability of a leak, design should be based on the results of this study. Such design would be reflected in allowable defect sizes and applied stresses.

High temperature weld metal and HAZ tests, as well as further base metal tests are planned for the next quarter. Preparation of another SMAW weldment has been initiated to evaluate weld toughness after temper embrittlement.

## 8.6 REFERENCES


1. "Program for the Development of Design Data - LMFBR Steam Generator Materials" prepared for the ERDA under contract AT(04-3)-893 Task 10-G and Task 18, July 16 & 17, 1975.

2. L. A. James, "Effect of Thermal Aging Upon the Fatigue-Crack Propagation of Austenitic Stainless Steels", Met. Trans., Vol. 5, Apr. 1974, pp. 831-838.

3. P. Shahinian, et al, "Fatigue Crack Growth in Type 316 Stainless Steel at High Temperature", Trans. ASME, Nov. 1971, pp. 976-980.

4. P. Marshall, "The Fatigue Behavior of Annealed AISI 316 Stainless Steel in Air and High Temperature Sodium: Review and Preliminary Results", Central Electricity Generating Board, Report RD/B/N 3236, Nov. 1974.

5. L. A. James and R. L. Knecht, "Fatigue-Crack Propagation Behavior of Type 304 Stainless Steel in a Liquid Sodium Environment", Met. Trans., Vol. 6A, Jan. 1975, pp. 109-116.

6. Mechanical Properties Test Data for Structural Materials, Quarterly Progress Report, Jan. 31, 1976; ORNL-5112.

7. W. Charnock, J. E. Cordwell, J. R. Gwythro, M. R. Hobdell, P. Marshall and I. R. McLaughlin, CEGB Report RD/B/N2670, July 1973.

8. W. Charnock and D. J. Ball, CEGB Report RD/B/N2848, dated Dec. 1973.

9. I. Kirman, Met. Trans. 2, 1761 (1971).

10. P. L. Jones and A. S. Tetelman, Section 7.2.5, ORNL-5103, Oct. 1974.

11. W. Charnock, Creep Cracking of AISI 316 in Liquid Sodium, (to be published).

12. J. L. Krankota and J. S. Armijo, "Decarburization Kinetics of Low Alloy Ferritic Steels in Sodium", Met. Trans., 3, pp. 2515-2523, Sept. 1972.

13. R. M. Curran and B. M. Wundt, "A Study of Low-Cycle Fatigue and Creep Interactions in Steels at Elevated Temperatures", presented at the Annual ASME Meeting in New York City, Nov. 21, 1974.

14. Steam Generator Materials Engineering - First Quarterly Report, GEAP 14029-1, (Oct. 1974).

15. Steam Generator Materials Engineering - Second Quarterly Report, GEAP 14029-2, (Jan. 1975).

16. K. Natesan, et.al., (ANL), Compatibility of Fe-2¼Cr-1Mo Steel in Sodium Environment. Presented at Int. Conf. on Mat'l. for Nucl. Steam Generator (Sept. 1975), Gatlenburg, Tenn.

17. T. Yukitoshi, et.al., (Sumitomo, Ltd.), Comparison of Various Chromium-Molybdenum Low Alloy Steels for LMFBR Steam Generators, Nuclear Technology, Vol. 28, pp. 506-515 (Mar. 1976).

18. K. Matsumoto, et al., Carbon Transfer Behavior of Materials for LMFBR Steam Generators, to be published in Nuclear Technology.

19. Seventh Quarterly Report, Steam Generator Materials Engineering, Jan.-Mar. 1976, GEAP-14029-7, ERDA Contract E(04-3)-893, Task 18, Apr. 1976.

20. W. Charnock, J. R. Cordwell, J. R. Gwyther and M. R. Hobdell, CEGB Report RD/B/N2980, Oct. 1974.

21. Sixth Quarterly Report, Steam Generator Materials Engineering, Oct.-Dec. 1975, GEAP 14029-6, Jan. 1976.

22. G. J. Licina and J. F. Copeland, A Review of 2¼Cr-1Mo Steel for Steam Generator Application in CRBRP; GEAP-20589, Oct. 1974.

23. H. P. Offer, "Metallurgical Characterization of VAR and ESR 2¼Cr-1Mo Alloy Steel", LMFBR Steam Generator Materials - Program for the Development of Design Data, January 29 and 30, 1976, prepared for ERDA under GE Contract AT(04-3)-893, Task 10 and 18.

24. D. A. Canonico, "Influence of Processing History on Microstructure and Tensile Properties of 1½ in. Diam. 2¼Cr-1Mo Steel Tubing", CRBRP Steam Generator Materials Program Review Meeting, June 5-6, 1974.

25. Seventh Quarterly Report, Steam Generator Materials Engineering, January-March 1976, GEAP-14029-7, U.S. ERDA Contract E(04-3)-893, Task 18, April 1976.

# APPENDIX 8.1

## SHIELDED METAL ARC WELD (SMAW) PROCEDURE DETAILS FOR 89 mm. (3.5 in.) THICK 2¼Cr-1Mo STEEL TEST PLATES

Double Bevel (AWS Prequalified Joint 220-PA)

Complete Penetration Groove Weld:

| | | |
|---|---|---|
| Length | - | 122 cm. (48 in.); Width - two 31 cm. (12 in. ) plates. |
| Plate | - | SA 387 Grade 22, Class 1. |
| Preheat | - | 121°C (250°F) Min. |
| Interpass | - | 121°C (250°F) - 177°C (350°F) (Maintain at 121°C (250°F) min. after welding commences until placed in PWHT furnace at 316°C [600°F]). |
| PWHT | - | 727°C ± 14°C (1340°F ± 25°F) for 12 hours, then furnace cool at less than 55.5°C (100°F) per hr. to at least 316°C (600°F). |
| Process | - | SMAW (Shielded Metal Arc weld). |
| Electrode Type | - | E9018-B3 |
| Position | - | Flat (Downhand) |
| Restraint | - | None required |

Suggested Weld Procedure:

1. Attach suitable length Run-off tabs at fit-up (V-shape tabs). Preheat for tack welding at fit-up.
2. Side #1 - In flat position deposit three stringer passes at root with 3.18 mm. (1/8 in.) electrodes (Use preheat).
3. Side #2 - Arc air gouge Side #1 root to sound metal, roughly maintaining the 9.53 mm. (3/8 in.) radius groove contour. Check by Magna flux, while maintaining heat. Acceptance criteria is no indication using ASME Specified technique.

4. Apply two to three stringer passes with 3.18 mm. (1/8 in.) electrode in downhand (flat) position in Side #2.

5. Continue filling groove, alternating sides with each layer applied, to maintain flatness, and using appropriately large diameter electrodes (3.97 mm. [5/32 in.]) to flush.

6. Maintain chart showing (and numbering) each pass applied. Also, show approximate amps, volts, and travel speed on each pass. Large beads are desirable, but keep heat input at reasonable level (measure).

Testing Requirements:

1. Prior to first root weld, but after fit-up, place punch marks across joint (on both sides) to measure shrinkage.

2. Radiograph after PWHT. Meet ASME Boiler and Pressure Vessel Code Section VIII, Div. 1 requirements UW-51. Report any radiographic indications and their locations, even acceptable defects.

Results:

1. All radiographs on 2 weld test plates are satisfactory to ASME Code. No indications on radiograph reports of the 2 welds.

2. Welding parameters

   Initial 2-6 passes:

   135 - 145 amps
   20 - 22 volts
   15.2 - 17.8 cm. (6-7 in.) per min. travel
   9.1 - 11.8 KJ/cm. (23-30 KJ/in.) heat input

   Remaining passes:

   195 - 200 amps
   21 Volts
   15.2 - 25.4 cm. (6-10 in.) per min. travel
   9.8 - 19.3 KJ/cm. (25-49 KJ/in.) heat input

3. Joint geometry and bead sequence. See following figure.

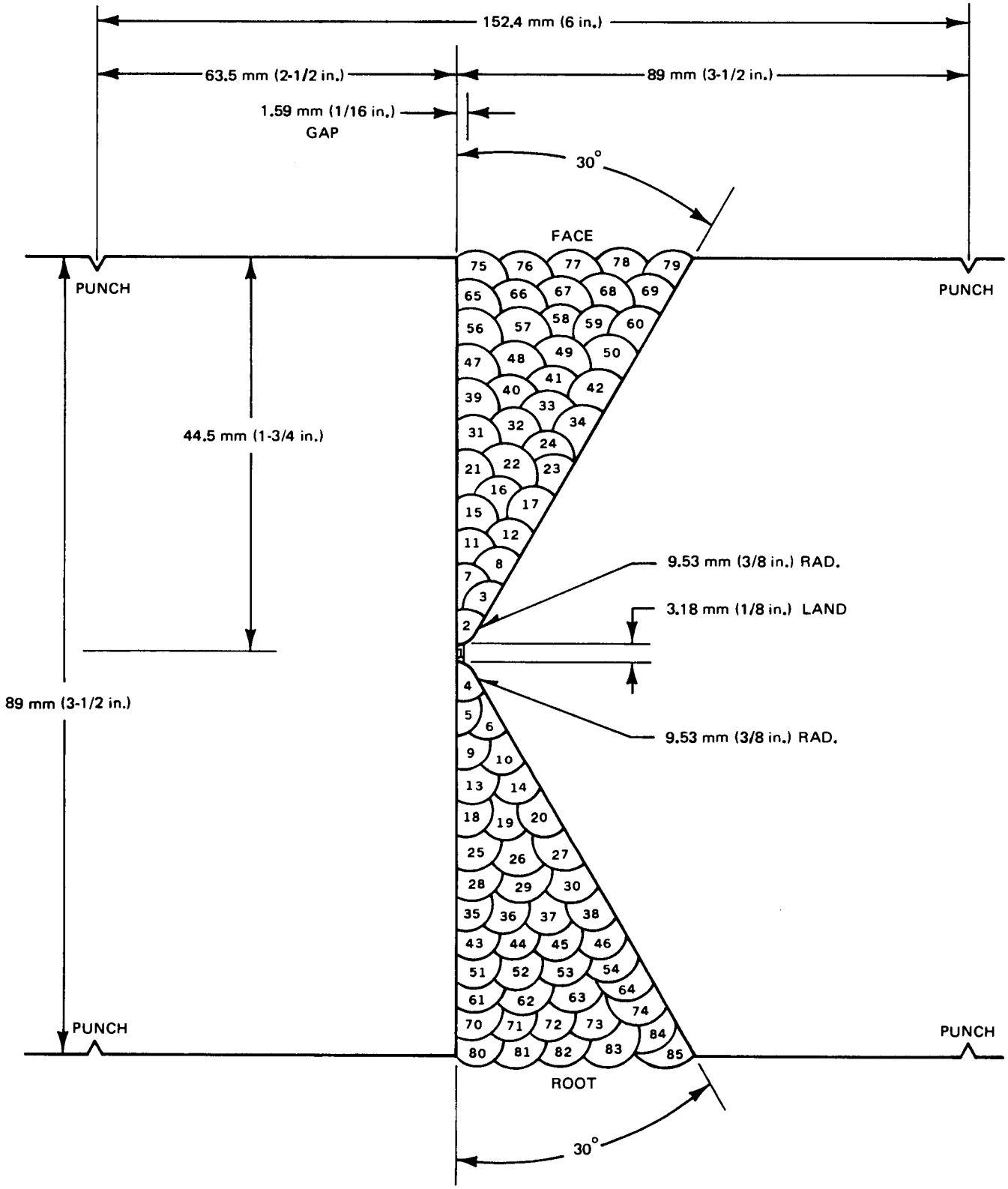


Weld Joint Geometry and Bead Sequence

INDEX


| Test | Material | Page |
|---|---|---|
| Chemical Analysis Data | | |
| | Inconel 718 . . . . . | 293 |
| Creep Test Data | | |
| Base-Line Data | | |
| | alloy 718 . . . . . | 2–4 |
| | 2 1/4 Cr-1 Mo steel . . . . . | 252–254, 446–488 |
| | 2 1/4 Cr-1 Mo weld metal . . . . | 446–488 |
| | 16-8-2 weld metal . . . . . | 149–150 |
| | Inconel 82 weld metal . . . . . | 227–230, 256 |
| | Inconel 600 . . . . . | 305–307, 309–313 |
| | type 304 SS bar . . . . . | 257–258 |
| | type 304 SS plate . . . . . | 75–81, 142–148, 340–347 |
| | type 304 SS tube . . . . . | 348 |
| | type 304 welded plate . . . . . | 347 |
| | type 308 SS weld metal . . . . . | 142–148 |
| | type 316 SS pipe . . . . . | 255–256 |
| | type 316 SS plate . . . . . | 88, 244–249 |
| | type 316 SS tube . . . . . | 347–348, 422–444 |
| | type 330 SS . . . . . | 365–367 |
| Correlations | | |
| | Inconel 600 . . . . . | 303–313 |
| | type 304 SS . . . . . | 78–86, 89–128, 230–241 |
| Effect of Cold Work | | |
| | type 304 SS . . . . . | 386–400 |
| Effect of Cycling | | |
| | 2 1/4 Cr-1 Mo tube, weld metal . | 446–488 |
| | type 316 SS tube . . . . . | 422–444 |

| Test | Material | Page |
|---|---|---|
| Creep Test Data (Continued) | | |
| Effect of Environment | | |
| | 2 1/4 Cr-1 Mo steel . . . . . | 265–267 |
| | Hastelloy X . . . . . | 266–268 |
| Effect of Heat Treatment | | |
| | 2 1/4 Cr-1 Mo steel . . . . . | 154–167 |
| Effect of Hold Time | | |
| | type 316 SS . . . . . | 422–444 |
| Effect of Sodium Exposure | | |
| | 2 1/4 Cr-1 Mo steel . . . . . | 446–488 |
| | type 316 SS tube (carburizing) . | 422–444 |
| Effect of Thermal Cycling | | |
| | type 304 SS . . . . . | 234–236 |
| Grain Boundary Sliding | | |
| | type 304 SS . . . . . | 374–379 |
| Heat-to-Heat Variation | | |
| | type 304 SS . . . . . | 89–109 |
| Microstructure Evaluation | | |
| | type 330 SS . . . . . | 365–367 |
| Multiaxial Tests | | |
| | type 304 SS . . . . . | 257–264 |
| Step-Load Tests | | |
| | 2 1/4 Cr-1 Mo steel . . . . . | 401–414 |
| Elastic Constants | | |
| Dynamic Measurements | | |
| | 2 1/4 Cr-1 Mo steel . . . . . | 139–141 |
| | Hastelloy X . . . . . | 130–135 |
| | type 304 SS . . . . . | 132–141 |
| Use in Stress Analysis | | |
| | type 304 SS weld metal . . . . . | 149–154 |
| Fatigue Test Data | | |
| Base-Line Data | | |
| | alloy 718 . . . . . | 2–6 |
| | type 316 SS tube . . . . . | 3–10 |

| Test | Material | Page |
|---|---|---|
| Fatigue Test Data, Base-Line Data (Continued) | | |
| | 2 1/4 Cr-1 Mo weld metal . . . . | 11–20 |
| | 2 1/4 Cr-1 Mo steel . . . . . | 11–20, 18–25 |
| Crack Growth Rate | | |
| Base-Line Data | | |
| | ASME SA-387 Grades C and D . . . | 314–327 |
| | SA-516 Grade 60 . . . . . | 315–317 |
| | SA-533 Grade B Class 1 . . . . . | 319–326 |
| | type 304 SS . . . . . | 381–385 |
| | type 316 SS plate, weld . . . . . | 418–422 |
| Effect of Cold Work | | |
| | type 316 SS plate . . . . . | 287–291 |
| Effect of Composition | | |
| | type 316 SS plate . . . . . | 287–291 |
| Effect of Environment | | |
| | 2 1/4 Cr-1 Mo steel . . . . . | 273–275 |
| Effect of Frequency | | |
| | 2 1/4 Cr-1 Mo steel . . . . . | 271–272 |
| | type 316 SS plate, weld . . . . . | 418–422 |
| Effect of Hold Time | | |
| | type 316 SS plate . . . . . | 287–291 |
| | type 316 SS plate, weld . . . . . | 418–422 |
| | Inconel 718 . . . . . | 291–300 |
| Effect of Static Load | | |
| | Inconel 718 . . . . . | 291–300 |
| Effect of Stress Intensity Factor | | |
| | type 316 SS plate, weld . . . . . | 418–422 |
| Effect of Sodium Exposure | | |
| | type 316 SS plate, weld . . . . . | 418–422 |
| Effect of Specimen Geometry . . . . . | | 273 |
| Effect of Temperature | | |
| | Inconel 718 . . . . . | 291–300 |
| Effect of Thermal Aging | | |
| | type 316 SS plate . . . . . | 287–291 |

| Test | Material | Page |
|---|---|---|
| Fatigue Test Data (Continued) | | |
| Cyclic Fatigue Test Data | | |
| | Inconel 82 weld metal . . . . . | 230–231 |
| Cyclic Hardening Behavior | | |
| | type 304 SS . . . . . | 60–71 |
| Effect of Cold Work | | |
| | type 316 SS plate . . . . . | 287–291 |
| Effect of Composition | | |
| | type 316 SS plate . . . . . | 287–291 |
| Effect of Heat Treatment | | |
| | type 304 SS . . . . . | 28–30 |
| Effect of Hold Time | | |
| | alloy 718 . . . . . | 2–8 |
| | type 316 SS plate . . . . . | 287–291 |
| | Inconel 82 weld metal . . . . . | 232–233 |
| | Inconel 718 . . . . . | 291–300 |
| Effect of Porosity | | |
| | Inconel 82 weld metal . . . . . | 231–233 |
| Effect of Sodium Environment | | |
| | type 316 SS plate . . . . . | 351–356 |
| | Inconel 718 . . . . . | 356–361 |
| Effect of Temperature | | |
| | Inconel 718 . . . . . | 291–300 |
| Heat-to-Heat Variation | | |
| | type 304 SS . . . . . | 24–28 |
| Interlaboratory Variation | | |
| | type 304 SS . . . . . | 21–24 |
| Life Prediction . . . . . | | 185–219 |
| | 2 1/4 Cr-1 Mo steel . . . . . | 40–41 |
| | Incoloy 800 . . . . . | 38–40 |
| | type 304 SS . . . . . | 31–38, 43–60 |
| | type 316 SS . . . . . | 40–43 |
| Mean Stress Effects | | |
| | alloy 718 . . . . . | 7–15 |

| Test | Material | Page |
|---|---|---|
| Fatigue Test Data (Continued) | | |
| Strain-Controlled Tests | | |
| | type 316 SS plate . . . . . | 242–245 |
| Hardness Data | | |
| Activation Energy | | |
| | type 330 SS . . . . . | 370–372 |
| Correlations | | |
| | 2 1/4 Cr-1 Mo steel . . . . . | 372–374 |
| Isothermal Transformation | | |
| | 2 1/4 Cr-1 Mo steel . . . . . | 459–511 |
| Relaxation Data | | |
| | 2 1/4 Cr-1 Mo steel . . . . . | 219–227 |
| | type 316 SS . . . . . | 248–252 |
| Tensile Test Data | | |
| Base-Line Data | | |
| | type 316 SS . . . . . | 241–243 |
| Correlations | | |
| | type 304 SS . . . . . | 78–86 |
| Effect of Heat Treatment | | |
| | 2 1/4 Cr-1 Mo steel . . . . . | 168–181 |
| Effect of Product Form | | |
| | type 316 SS . . . . . | 87–88 |
| Effect of Sodium Exposure | | |
| | 2 1/4 Cr-1 Mo steel . . . . . | 181–184 |
| Toughness | | |
| Charpy V-Notch | | |
| | 2 1/4 Cr-1 Mo steel, weld . . . . | 488–511 |
| J-Integral | | |
| | 2 1/4 Cr-1 Mo steel, weld . . . . | 488–511 |
| | Inconel X-750 . . . . . | 327–335 |
| | Inconel 718 . . . . . | 327–335 |
| Drop Weight NDT | | |
| | 2 1/4 Cr-1 Mo steel . . . . . | 459–511 |

ORNL-5200
Distribution
Category UC-79b, -h, -k

## INTERNAL DISTRIBUTION

1–2. Central Research Library
3. Document Reference Section
4–6. Laboratory Records Department
7. Laboratory Records, ORNL RC
8. ORNL Patent Office
9. R. J. Beaver
10. R. G. Berggren
11. J. J. Blass
12. M. K. Booker
13. C. R. Brinkman
14. D. A. Canonico
15. J. Corum
16. W. R. Corwin
17. F. L. Culler
18. J. E. Cunningham
19. J. H. DeVan
20. R. G. Donnelly
21. D. P. Edmonds
22. G. Fee
23. M. H. Fontana
24. W. R. Gall
25. B. L. Greenstreet
26. J. C. Griess, Jr.
27. J. P. Hammond
28. W. O. Harms
29. R. L. Heestand
30. R. F. Hibbs
31–33. M. R. Hill
34. D. O. Hobson
35. H. Inouye
36. P. R. Kasten
37. J. F. King
38. R. T. King
39. R. L. Klueh
40. K. C. Liu
41. C. T. Liu
42. A. L. Lotts
43–63. W. R. Martin
64. W. J. McAfee
65. H. E. McCoy
66. H. C. McCurdy
67. C. J. McHargue
68. J. Merkle
69. P. Patriarca
70. S. Peterson
71. H. Postma
72. C. E. Pugh
73. P. L. Rittenhouse
74. D. N. Robinson
75. T. Roche
76. J. L. Scott
77. Myrtleen Sheldon
78. V. K. Sikka
79. G. M. Slaughter
80. W. J. Stelzman
81. J. P. Strizak
82. R. W. Swindeman
83. D. B. Trauger
84. J. R. Weir, Jr.
85. G. D. Whitman
86. T. Yahr
87. Paul M. Brister (consultant)
88. John Moteff (consultant)
89. Hayne Palmour III (consultant)
90. J. W. Prados (consultant)
91. N. E. Promisel (consultant)
92. D. F. Stein (consultant)

EXTERNAL DISTRIBUTION

93—94. ERDA DIVISION OF NUCLEAR FUEL CYCLE AND PRODUCTION, Washington, DC 20545

Director

95—96. ERDA DIVISION OF NUCLEAR RESEARCH AND APPLICATIONS, Washington, DC 20545

Director

97—98. ERDA DIVISION OF REACTOR RESEARCH AND DEVELOPMENT, Washington, DC 20545

Director

99—100. ERDA OAK RIDGE OPERATIONS OFFICE, P.O. Box E, Oak Ridge, TN 37830

Research and Technical Support Division
Director, Reactor Division

101-400. ERDA TECHNICAL INFORMATION CENTER, Office of Information Services, P.O. Box 62, Oak Ridge, TN 37830

For distribution as shown in TID-4500 Distribution Category, UC-79b (Fuels and Materials Engineering Development); UC-79h (Structural Materials Design Engineering); UC-79k (Components)

☆ U.S. GOVERNMENT PRINTING OFFICE: 1976-748-189/483